CONF-9505200--

Proceedings of the THIRTEENTH SYMPOSIUM ON ENERGY ENGINEERING SCIENCES

Fluid/Thermal Processes; Systems Analysis and Control

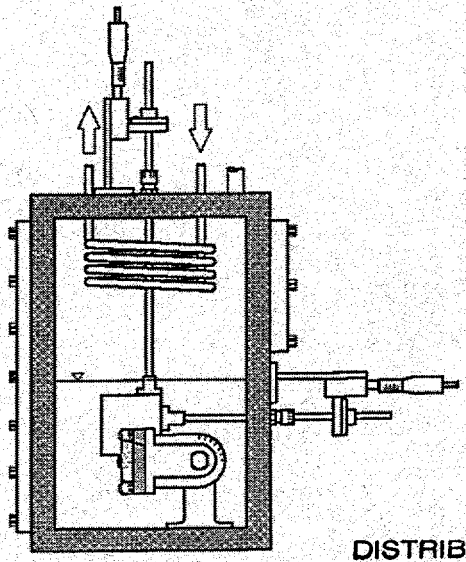

May 15-17, 1995
at
Argonne
National Laboratory
Argonne, Illinois

Reproduced from the best available copy.

Available to DOE and DOE contractors from the
Office of Scientific and Technical Information
P.O. Box 62
Oak Ridge, TN 37831
Prices available from (615) 576-8401

Available to the public from the
National Technical Information Service
U.S. Department of Commerce
5285 Port Royal Road
Springfield, VA 22161

CONF-9505200

Proceedings of the

THIRTEENTH SYMPOSIUM ON ENERGY ENGINEERING SCIENCES
Fluid/Thermal Processes; Systems Analysis and Control

May 15-17, 1995

at

ARGONNE NATIONAL LABORATORY

Argonne, Illinois

Cosponsored by

Office of Basic Energy Sciences
U.S. DEPARTMENT OF ENERGY

and

Energy Technology Division
ARGONNE NATIONAL LABORATORY

Coordinated by

Argonne National Laboratory
9700 South Cass Avenue
Argonne, Illinois 60439

DISCLAIMER

Portions of this document may be illegible electronic image products. Images are produced from the best available original document.

THIRTEENTH SYMPOSIUM ON ENERGY ENGINEERING SCIENCES
Fluid/Thermal Processes; Systems Analysis and Control

FOREWORD

This Proceedings Volume includes the technical papers that were presented during the Thirteenth Symposium on Energy Engineering Sciences on May 15-17, 1995, at Argonne National Laboratory, Argonne, Illinois. The Symposium was organized into nine technical sessions, which included 33 individual presentations followed by discussion and interaction with the audience. A copy of the schedule and a list of participants is appended to this volume.

This was the thirteenth annual Symposium sponsored by the Engineering Research Program of the Office of Basic Energy Sciences of the U.S. Department of Energy. The technical areas encompassed in this year's Symposium were fluid and thermal processes, and systems analysis and control. The dominant theme was fluid mechanics, which constituted five of the sessions and included 19 individual presentations. Each paper dealt with the research effort being sponsored by the Engineering Research Program.

The DOE Office of Basic Energy Sciences, of which Engineering Research is a component program, is responsible for the long-term mission-oriented research in the Department. It has the prime responsibility for establishing the basic scientific foundation upon which the Nation's future energy options will have to be identified, developed, and built. It is committed to the generation of new knowledge necessary for the solution of present and future problems of energy exploration, production, conversion, and utilization, consistent with respect for the environment.

Consistent with the DOE/BES mission, the Engineering Research Program is charged with the identification, initiation, and management of fundamental research on broad, generic topics addressing energy-related engineering problems. Its stated goals are: 1) to improve and extend the body of knowledge underlying current engineering practice so as to create new options for enhancing energy savings and production, for prolonging useful life of energy-related structures and equipment, and for developing advanced manufacturing technologies and materials processing with emphasis on reducing costs with improved industrial production and performance quality; and 2) to expand the store of fundamental concepts for solving anticipated and unforeseen engineering problems in the energy technologies.

In achieving these goals, the Engineering Research Program supports approximately 130 research projects covering a broad spectrum of topics cutting across traditional engineering disciplines with a focus on three areas: 1) mechanical sciences, 2) control systems and instrumentation, and 3) engineering data and analysis. The Thirteenth Symposium involved approximately one-fourth of the research projects currently sponsored by the DOE/BES Engineering Research Program.

The Thirteenth Symposium was held under the joint sponsorship of the DOE Office of Basic Energy Sciences and Argonne National Laboratory. Local arrangements were handled by Ms. Jacquie Habenicht of ANL Conference Services. Ms. Nina Daly of the ANL Office of Technical Communication Services was responsible for assembling these proceedings and attending to their publication.

I am grateful to all who contributed to the success of the program, particularly to the participants for their uniformly excellent presentations, their active involvement in discussions, and their

infectious enthusiasm. The resulting interactions made this Symposium a most stimulating and enjoyable experience.

James R. Welty, ER-15
Division of Engineering and Geosciences
Office of Basic Energy Sciences

THIRTEENTH SYMPOSIUM ON ENERGY ENGINEERING SCIENCES

May 15-17, 1995

Argonne National Laboratory

Argonne, IL

FINAL PROGRAM

Monday, May 15

8:00 a.m. Registration

9:00 a.m. Welcome

9:05 a.m. General Remarks
Oscar P. Manley, U.S. Department of Energy

9:10 a.m. Introductory Comments
James R. Welty, U.S. Department of Energy

TECHNICAL SESSION 1 - Fluid Mechanics I: Fundamental Properties

Chair: E. Fukushima, Lovelace Foundation

9:15 a.m. Viscosity of Colloidal Suspensions
E.G.D. Cohen, The Rockefeller Univ., New York and I.M. de Schepper, Delft University of Technology, The Netherlands

9:40 a.m. Gelation Under Shear
B.D. Butler, H.J.M. Hanley, G.C. Straty, and C.D. Muzny, NIST, Boulder, CO

10:05 a.m. Transport Properties of Porous Media from the Microstructure
S. Torquato, Princeton Univ., Princeton, NJ

10:30 a.m. BREAK

TECHNICAL SESSION 2 - Fluid Mechanics II: Two-Phase Flow

Chair: S. Torquato, Princeton University

10:45 a.m. NMR Studies of Multiphase Flows. II
S.A. Altobelli, A. Caprihan, E. Fukushima, I.J. Lowe, and L.Z. Wang, The Lovelace Inst., Albuquerque, NM

11:10 a.m.	Initiation of Slug Flow T.J. Hanratty and B.D. Woods, Univ. of Illinois, Urbana, IL
11:35 a.m.	The Drift Force on an Object in an Inviscid Weakly-Varying Rotational Flow G.B. Wallis, Dartmouth College, Hanover, NH
12:00 noon	LUNCH

TECHNICAL SESSION 3 - Thermal Processes

Chair: G. Pomraning, U.C.L.A.

1:00 p.m.	Active Control of Convection H.H. Bau, Univ. of Pennsylvania, Philadelphia, PA
1:25 p.m.	Effect of Steady and Time-Harmonic Magnetic Fields on Macrosegregation in Alloy Solidification F.P. Incropera and P.J. Prescott, Purdue U., W. Lafayette, IN
1:50 p.m.	Theoretical Modeling of CHF for Near-Saturated Pool Boiling and Flow Boiling from Short Heaters Using the Interfacial Lift-Off Criterion I. Mudawar, J.E. Galloway, C.O. Gersey, S.J. Reed, and D.D. Hall, Purdue Univ., W. Lafayette, IN
2:15 p.m.	Short-Pulse Laser Interactions with Disordered Materials and Liquids L.M. Phinney, C.H. Goldman, J.P. Longtin, and C.-L. Tien, Univ. of California, Berkeley, CA
2:50 p.m.	BREAK

TECHNICAL SESSION 4 - Fluid Mechanics III

Chair: I. Mudawar, Purdue University

3:05 p.m.	Studies on the Formulation of Thermodynamics and Stochastic Theory for Systems Far From Equilibrium J. Ross, Stanford Univ., Stanford, CA
3:30 p.m.	Linear Kinetic Theory and Particle Transport in Stochastic Mixtures G.C. Pomraning, UCLA, Los Angeles, CA
3:55 p.m.	Dynamics of Miscible Displacements in Round Tubes E. Meiburg, T. Maxworthy, P. Petijeans, and C.-Y. Chen, Univ. of Southern California, Los Angeles, CA
4:20 p.m.	Superconducting Coherence in a Vortex Line Liquid T. Chen and S. Teitel, Univ. of Rochester, Rochester, NY

5:30 p.m. RECEPTION

6:00 p.m. SYMPOSIUM DINNER

Tuesday, May 16

TECHNICAL SESSION 5 - Process Analysis and Control

Chair: J.B. McLaughlin, Clarkson University

8:25 a.m. Systematic Process Synthesis and Design Methods for Cost Effective Waste Minimization
L.T. Biegler, I.E. Grossmann, and A.W. Westerberg, Carnegie Mellon Univ., Pittsburgh, PA

8:50 a.m. Integrated Approaches to the Application of Advanced Modeling Technology in Process Development and Optimization
R.J. Allgor, W.F. Feehery, J.E. Tolsma, L.B. Evans, and P.I. Barton, MIT, Cambridge, MA

9:15 a.m. Intelligent Control of Mixed-Culture Bioprocesses
D.L. Stoner, E.D. Larsen, K.S. Miller, G.F. Andrews, and J.A. Johnson, INEL, Idaho Falls, ID

9:40 a.m. Control of Complex Dynamics and Chaos in Distributed Parameter Systems
S. Chakravarti, M. Marek, and W.H. Ray, Univ. of Wisconsin, Madison, WI

10:05 a.m. BREAK

TECHNICAL SESSION 6 - Fluid Mechanics IV: Turbulence

Chair: J. Ottino, Northwestern University

10:20 a.m. Turbulence Generation by Waves
D. Kaftori, X.S. Nan, and S. Banerjee, Univ. of California, Santa Barbara, CA

10:45 a.m. Numerical Simulation of High Reynolds Number Bubble Motion
J.B. McLaughlin, Clarkson Univ., Potsdam, NY

11:10 a.m. Structure and Modeling of Turbulence
E.A. Novikov, Univ. of Calif., San Diego, CA

11:35 a.m. Contaminant Dispersal in Bounded Turbulent Shear Flow
J.M. Wallace, P.S. Bernard, K.-F. Chiang, and L. Ong, Univ. of Maryland, College Park, MD

12:00 noon — Anomalous Scaling of a Scalar Field Advected by Turbulence
R.H. Kraichnan, R.H. Kraichnan, Inc., Santa Fe, NM

12:25 — LUNCH

TECHNICAL SESSION 7 - Fluid Mechanics V: Chaos

Chair: J. Wallace, University of Maryland

1:25 p.m. — Convection in a Nematic Liquid Crystal With Homeotropic Alignment and Heated From Below
G. Ahlers, Univ. of California, Santa Barbara, CA

1:50 p.m. — Modeling of Mixing Processes: Fluids, Particulates, and Powders
J.M. Ottino and S. Hansen, Northwestern Univ., Evanston, IL

2:15 p.m. — Spatiotemporal Patterns in a Reaction-Diffusion System and in a Vibrated Granular Bed
H.L. Swinney, K.J. Lee, W.D. McCormick, F. Melo, and P. Umbanhowar, Univ. of Texas, Austin, TX

2:40 p.m. — BREAK

TECHNICAL SESSION 8 - Materials Issues

Chair: J. Heberlein, University of Minnesota

2:55 p.m. — Deformation and Crack Growth Response Under Cyclic Creep Conditions
F.W. Brust, Jr., Battelle Mem. Inst., Columbus, OH

3:20 p.m. — Advanced Laser Diagnostics for Diamond Deposition Research
C.H. Kruger, T.G. Owano, and E.H. Wahl, Stanford Univ., Stanford, CA

3:45 p.m. — Physical Models of Polarization Mode Dispersion
C.R. Menyuk and P.K.A. Wai, Univ. of Maryland, Baltimore, MD

4:10 p.m. — Conditions for Synchronization in Josephson-Junction Arrays
A.A. Chernikov and G. Schmidt, Stevens Inst. of Tech., Hoboken, NJ

Wednesday, May 17

TECHNICAL SESSION 9 - Plasma Processes

Chair: J. Welty, U.S. Department of Energy

8:25 a.m. — Modeling Electronegative Plasma Discharge
A.J. Lichtenberg and M.A. Lieberman, Univ. of California, Berkeley, CA

8:50 a.m.	Plasma Characterization Studies for Materials Processing E. Pfender and J. Heberlein, Univ. of Minnesota, Minneapolis, MN
9:15 a.m.	Hydrodynamic Theory of Diffusion in Two-Temperature Multicomponent Plasmas J.D. Ramshaw and C.H. Chang, INEL, Idaho Falls, ID
9:40 a.m.	Closing Remarks Oscar P. Manley, U.S. Department of Energy
10:00 a.m.	Meeting Adjourns

Table of Contents

VISCOSITY OF COLLOIDAL SUSPENSIONS

E. G. D. Cohen*
and
I. M. de Schepper**

*The Rockefeller University
New York, NY 10021, U.S.A.
**Delft University of Technology
2629 JB Delft, The Netherlands

ABSTRACT

Simple expressions are given for the effective Newtonian viscosity as a function of concentration as well as for the effective visco-elastic response as a function of concentration and imposed frequency, of monodisperse neutral colloidal suspensions over the entire fluid range. The basic physical mechanisms underlying these formulae are discussed. The agreement with existing experiments is very good.

INTRODUCTION

We discuss here suspensions consisting of monodisperse spherical neutral colloidal particles with a diameter σ. The problem we address is: in the absence of hydrodynamic interactions, what is the effective viscosity of such a suspension, i.e., its viscosity as different from η_s, the viscosity of the pure solvent? We are interested in this as a function of the volume fraction $\phi = \pi n \sigma^3/6$ of the colloidal particles, viz. $\eta^{\text{eff}}(\phi)$, its effective Newtonian viscosity or $\eta^{\text{eff}}(\phi;\omega)$ its effective visco-elastic viscosity, when an imposed oscillatory shear rate $\gamma(t) = \gamma e^{i\omega t}$ of frequency ω is present. Here n is the number density of the colloidal particles and γ the amplitude of the imposed shear rate.

This is a very difficult problem, since it concerns a strongly interacting many particle system, especially at large volume fractions. It is part of a large class of "effective" behavior problems, which can usually only be treated in a systematic way at small ϕ by cluster expansions. Here we outline an approximate, yet satisfactory solution of this problem, derived from first principles, which leads to explicit formulae for $\eta^{\text{eff}}(\phi) \equiv \eta^{\text{eff}}(\phi;\omega = 0)$ and $\eta^{\text{eff}}(\phi;\omega)$, which agree with experiment and therefore appear to contain the right physics. In the next section we briefly outline the steps that lead from the fundamental Smoluchowski equation to the basic equation we use to compute $\eta^{\text{eff}}(\phi;\omega)$. In the following section we present the solution of this equation, the explicit formulae for $\eta^{\text{eff}}(\phi)$ and $\eta^{\text{eff}}(\phi;\omega)$ and a comparison of them with experiment. In the last section, we discuss our results.

THEORY

Basic Equation.

Starting from the N particle Smoluchowski equation in the absence of hydrodynamic interactions and integrating this equation over the positions of all particles but two, one obtains an

equation for the nonequilibrium pair distribution function $P_2(\mathbf{R};\mathbf{r};\phi;\omega;t)$ of the suspension, involving the three-particle distribution function P_3. Neglecting P_3 and the dependence of P_2 on the center of mass $\mathbf{R} = (\mathbf{r}_1 + \mathbf{r}_2)/2$ of the two particles at positions $\mathbf{r}_i (i = 1, 2)$, respectively, and making a Fourier transform of P_2 with respect to the relative coordinate $\mathbf{r} = \mathbf{r}_1 - \mathbf{r}_2$, one arrives at an equation of the form[1,2]

$$[\frac{\partial}{\partial t} + \frac{2}{\tau(k;\phi)} - \gamma e^{i\omega t} k_y \frac{\partial}{\partial k_x}]\delta S(\mathbf{k};\phi;\omega;t) = \gamma e^{i\omega t} k_y \frac{\partial}{\partial k_x} S_{eq}(k;\phi) \qquad (1)$$

Here $\delta S(\mathbf{k};\phi;\omega;t) = S(\mathbf{k};\phi;\omega;t) - S_{eq}(k;\phi)$ is the deviation of the nonequilibrium structure factor $S(\mathbf{k};\phi;\omega;t)$, the Fourier transform of $P_2(\mathbf{r};\phi;\omega;t)$, from that in equilibrium $S_{eq}(k;\phi)$, the Fourier transform of the equilibrium radial distribution function $g(r;\phi)$, where $r = |\mathbf{r}|$ and $k = |\mathbf{k}|$. $S_{eq}(k;\phi)$ is known for hard spheres[3] and exhibits for $0.3 < \phi < 0.55$ a very sharp maximum at $k \approx k^*$, where $k^*\sigma \approx 2\pi$, i.e., for periodic particle configurations with a wave length $\lambda^* = 2\pi/k^* \approx \sigma$ (cf.fig.1). This sharp maximum at these large ϕ reflects a highly ordered state of the colloidal particles in the suspension on this length scale (cf.fig.2), where each particle finds itself in a cage formed by its nearest neighbors, out of which it can only escape, i.e., diffuse, with difficulty[2,4]. At

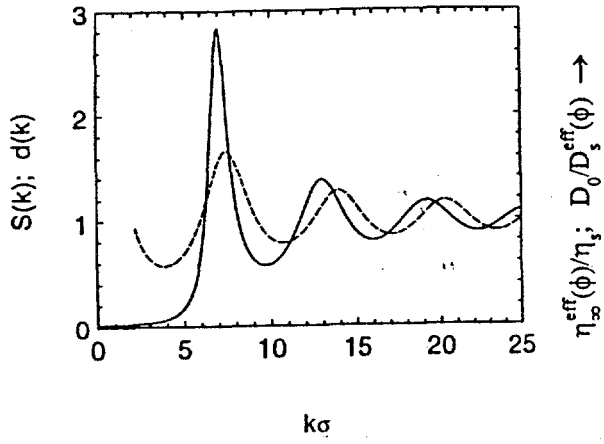

Figure 1 (left). Hard sphere S(k) for $\phi = 0.49$ (solid line, cf.Ref.3) and d(k) (dashed line, cf.below Eq.2), as functions of $k\sigma$.

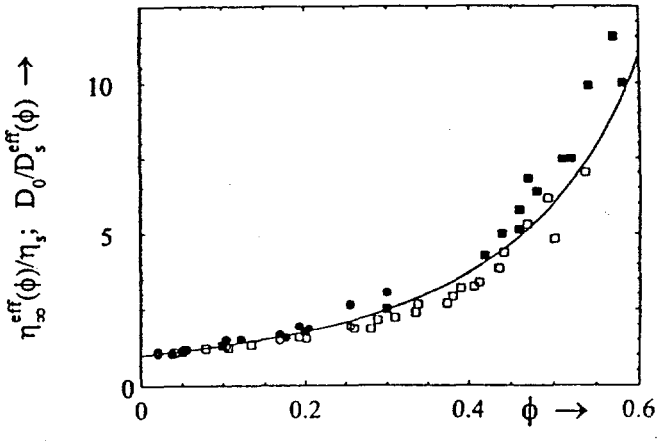

Figure 3 (right). Reduced high frequency viscosity $\eta_\infty^{eff}(\phi)/\eta_s$ (closed symbols) and inverse self diffusion $D_0/D_s^{eff}(\phi)$ (open symbols) as a function of ϕ. Open and closed circles from Ref.9(a), open squares from Ref.9(b) and closed squares from Ref.10. The solid line is $\chi(\phi)$ (cf.Eq.(4)); deviations due to hydrodynamic effects for intermediate ϕ (open squares) are visible.

small ϕ, $S_{eq}(k;\phi)$ displays no such maximum and the colloidal particle diffusion approaches that of free colloidal particles characterized by D_0, the Stokes-Einstein diffusion coefficient. The inverse relaxation time $1/\tau(k;\phi)$ in eq.(1) approaches D_0k^2 for small ϕ and is determined for large ϕ, by a cage-diffusion coefficient $D_c(k)$, derived from the analogous cage diffusion process in (pure) dense hard sphere fluids, by replacing the low density hard sphere gas Boltzmann diffusion coefficient D_B by the Stokes-Einstein diffusion coefficient D_0, relevant for dilute colloidal suspensions[1,2,4-7]:

$$1/\tau(k;\phi) = D_c(k)k^2 = \frac{D_0k^2}{\chi(\phi)S_{eq}(k;\phi)}d(k) \;\; (0.3 < \phi < 0.55) \qquad (2)$$

Here the equilibrium radial distribution function $g(r;\phi)$ at contact $r = \sigma : g(\sigma;\phi) \equiv \chi(\phi)$ is given very well by the Carnahan-Starling approximation $\chi(\phi) \approx (1 - \phi/2)(1 - \phi)^{-3} = 1 + \frac{5}{2}\phi + O(\phi^2)$, where the $O(\phi)$) term is exact (cf.fig.3) and $d(k) = 1/[1 - j_0(k\sigma) + 2j_2(k\sigma)]$, with $j_\ell(k\sigma)$ the ℓ-th spherical Bessel function (cf.fig.1). $1/\tau(k;\phi)$ is sketched and compared with the results of light scattering experiments in fig.4 for a typical large ϕ[6,7].

Solution and effective viscosity.

Solving the eq.(1) for $\delta S(\mathbf{k};\phi;\omega;t)$, integrating the solution over k and t and setting $\gamma = 0$, one obtains for the visco-elastic behavior of the colloidal suspension:

$$\eta^{\text{eff}}(\phi;\omega) = \eta^{\text{eff}}_{\infty}(\phi) + \frac{k_B T}{60\pi^2}\int_0^{\infty} dk\, k^4 [\frac{S'_{eq}(k;\phi)}{S_{eq}(k;\phi)}]^2 \frac{1}{2D_c(k)k^2 - i\omega} \quad (3)$$

Here $\eta^{\text{eff}}_{\infty}(\phi)$ is the infinite frequency, i.e., very short time, approximation to $\eta^{\text{eff}}(\phi;\omega)$ given by:

$$\eta^{\text{eff}}_{\infty}(\phi) = \eta_s \chi(\phi) \quad (4)$$

while $S'_{eq}(k;\phi) = dS_{eq}(k;\phi)/dk$. The second term on the right hand side of (3) is the contribution due to cage-diffusion.

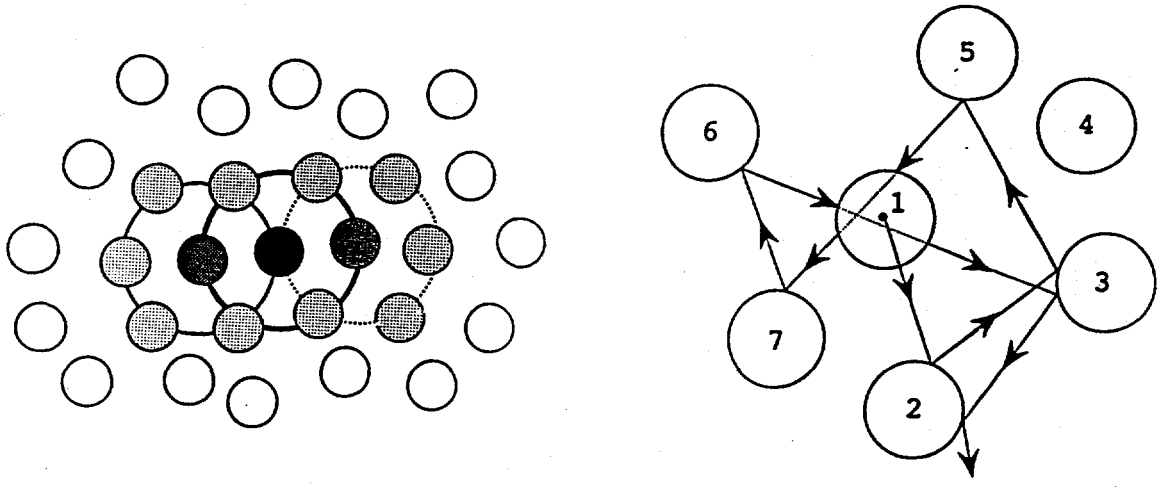

Figure 2. (a) The central particle (black) is in a cage whose wall is formed by the particles connected by the thick black line. Each wall particle is itself the center of a cage, of which the black particle is part of the wall. This is illustrated for two wall particles of the black particle, for which the cage walls are formed by particles connected by a solid line or a dotted line, respectively; (b) cage diffusion collisions of central particle 1 for fixed wall particles 2 to 7. The interparticle distances have been considerably enlarged for clarity.

The high frequency part $\eta^{\text{eff}}_{\infty}(\phi)$ of $\eta^{\text{eff}}(\phi;\omega)$ has been studied experimentally by a variety of methods and the expression (4) is in very good agreement with experiment for all $0 < \phi < 0.55$ (cf.fig.3). The physical interpretation of (4) is that for very short times, even smaller than the (Brownian) time $t_B = \sigma^2/4\nu_s \approx 10^{-7}$ sec, where ν_s is the kinematic viscosity of the solvent, the suspension viscosity is determined not only by that of the pure solvent viscosity η_s, but also by a correction factor $\chi(\phi)$ which gives the increase in effective suspension viscosity due to the pairs of touching ($r = \sigma$) particles present in the suspension. This is a very short time contribution to $\eta^{\text{eff}}(\phi;\omega)$, due to statistical thermodynamic, (i.e., hard sphere excluded volume) interactions, arising from the canonical equilibrium distribution of the colloidal particles, rather than the usually considered hydrodynamic interaction contributions. The time scale of the contributions of the second term in (3) is much longer than that of the first term and is related to the time scale on which the cage diffusion takes place, viz., the Péclet time $t_P = \sigma^2/4D_0 \approx 10^{-3}$ sec.

For $\omega = 0$, one obtains then from (3) for the effective Newtonian viscosity $\eta^{\text{eff}}(\phi) \equiv \eta^{\text{eff}}(\phi;0)$ of the suspension, with (2), the simple expression:

$$\eta^{\text{eff}}(\phi) = \eta_s \chi(\phi)[1 + \frac{1}{40\pi}\int_0^{\infty} d\kappa \frac{\kappa^2 [S'_{eq}(\kappa;\phi)]^2}{d(\kappa) S_{eq}(\kappa;\phi)}] \quad (5)$$

with $\kappa = k\sigma$.

Although this expression for $\eta^{\rm eff}(\phi)$ has been derived for large ϕ $(0.3 < \phi < 0.55)$ it is also applicable to small $\phi < 0.3$, since the second term in the square brackets mainly contributes for $\phi > 0.3$ and the first term $\eta_s\chi(\phi)$ adequately describes the smaller ϕ behavior (cf.fig.5).

For $\omega \neq 0$, one obtains the effective visco-elastic behavior of the suspension. Since $\eta^{\rm eff}(\phi;\omega)$ is complex one can consider its real and imaginary parts $\eta^{\rm eff}(\phi;\omega) = \eta_R^{\rm eff}(\phi;\omega) - i\eta_I^{\rm eff}(\phi;\omega)$ or equivalently those of $\eta^*(\phi;\omega) = [\eta^{\rm eff}(\phi;\omega) - \eta^{\rm eff}(\phi;\infty)]/[\eta^{\rm eff}(\phi;0) - \eta^{\rm eff}(\phi;\infty)]$, where $\eta^{\rm eff}(\phi;\infty) \equiv \eta_\infty^{\rm eff}(\phi)$, used before. In fig.6 they are plotted as a function of ω and compared with experiment[8,9]. They show a virtual absence of any concentration dependence within the spread of the experimental data. The theoretical asymptotic large ω behavior $\sim (\omega\tau_P)^{-1/2}$ for all ϕ, is consistent with what is found experimentally.

Discussion

We conclude with a number of remarks.

1. The Newtonian viscosity of a colloidal suspension in the fluid phase $0 < \phi < 0.55$ can be obtained without adjustable parameters for all concentrations from eq.(5). All that is needed, apart from D_0, is the hard sphere diameter σ to define the system. This can be obtained directly from electron microscopy or, for concentrated suspensions, from the first sharp maximum of $S_{eq}(k;\phi)$[4,7].
2. The good agreement between theory (eq.(5)) and experiment (figs.3,5), appears to confirm the correctness of the two basic physical mechanisms, which are at the heart of the eq.(5): statistical thermodynamic forces for very short times $(\leq t_B)$ and cage diffusion for longer times $(\geq t_P)$.
3. Hydrodynamic interactions are relevant on a time scale $\gg t_B$, but their effect is not detectable on the scale on which $\eta^{\rm eff}(\phi)$ is plotted in fig.5, where an almost hundred-fold increase of the effective viscosity of the suspension occurs over the fluid range $0 < \phi < 0.55$. They are surely present (cf.fig.3), but relatively small at small ϕ and appear to be quenched at large ϕ.
4. This leads to the prediction that the same behavior for $\eta^{\rm eff}(\phi)$ and $\eta^{\rm eff}(\phi,\omega)$ will be observed for *charged* colloidal suspensions, at least at large $\phi > 0.3$, if (a) one identifies the hard sphere diameter σ with the *Debye sphere diameter* and (b) ω is not such that deformations of the Debye spheres are relevant.

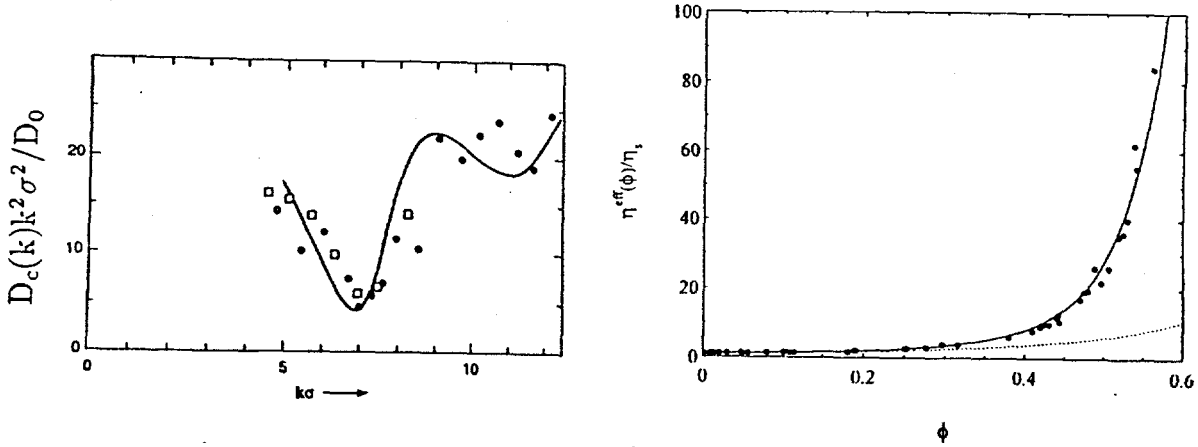

Figure 4 (left). Reduced cage diffusion coefficient $D_c(k)k^2\sigma^2/D_0$ as function of $k\sigma$ from light scattering for a charged colloid (closed circles; Ref.8(a), $\sigma = 600$nm, $\phi = 0.48$), a neutral colloid (open squares; Ref.8(b), $\sigma = 335$nm, $\phi = 0.49$) and from theory (solid line; Eq.(2)). The two minima correspond to the first two maxima of $S(k)$.
Figure 5 (right). Reduced Newtonian viscosity $\eta^{\rm eff}(\phi)/\eta_s$ as a function of ϕ from experiment (closed circles, Ref.10) and theory (solid line, cf.Eq.(5)). The dashed curve is $\chi(\phi)$.

5. For the very high frequency behavior $\eta_\infty^{\rm eff}(\phi)$ an Einstein relation holds for all $0 < \phi < 0.55$:

$$\eta_\infty^{\rm eff}(\phi) = \frac{k_B T}{6\pi D_s^{\rm eff}(\phi)(\sigma/2)} \tag{6}$$

Here $D_s^{\rm eff}(\phi)$ is the (effective) self-diffusion coefficient of the colloidal suspension at volume fraction ϕ, i.e., the diffusion coefficient of a tagged colloidal particle with respect to the other (identical) colloidal particles. In so far as $D_s^{\rm eff}(\phi)$ can be measured by light scattering techniques[8,9], $D_s^{\rm eff}(\phi)$, which characterizes the diffusive decay of density fluctuations, allows a non-mechanical determination of $\eta_\infty^{\rm eff}(\phi)$. Together with the usual Einstein relation and eq.(4),(6) leads to: $\eta_\infty^{\rm eff}(\phi)/\eta_s = D_0/D_s^{\rm eff}(\phi) = \chi(\phi)$ (cf.fig.4).

The physical origin of the validity of (6) is the inert character of the suspension surrounding two touching particles, at high frequencies, i.e., at very short times.

6. For large $\phi > 0.3$ an expression for the Newtonian viscosity of an atomic liquid very similar to (3) for $\omega = 0$, has been derived. This illustrates a close physical analogy of concentrated colloidal suspensions consisting of spherical particles on the one hand and simple atomic liquids, like liquid argon or liquid methane, on the other hand[4,7,12]. This analogy is based on a similarity of both fluid systems to dense hard sphere fluids, a similarity used above (in section 2) to obtain the crucial relation (2) for the colloidal suspension. The physical origin of this similarity is based on (a) the similarity of Brownian and Newtonian motion on large time scales ($t \gg t_B$)[13] and (b) the similarity of the cage-diffusion process in the two fluid systems. For further details we refer to the literature[4,12].

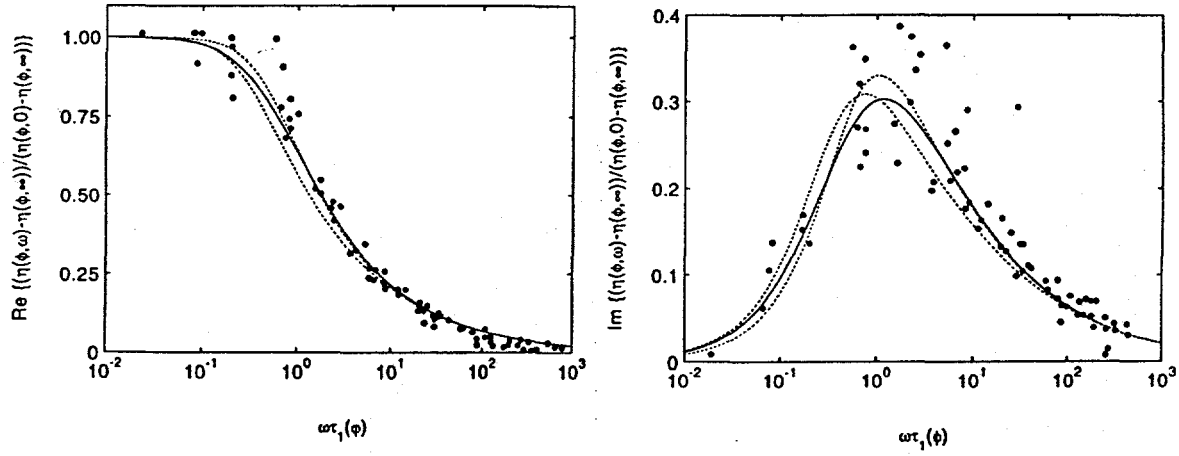

Figure 6. Real part (a) and imaginary part (b) of the reduced complex shear viscosity $\eta^*(\phi,\omega)$, as a function of reduced frequency $\omega\tau_1(\phi)$ (with $\tau_1(\phi) \approx \tau_P/4$ cf.Ref.1). The closed circles are from Ref.10. The dashed curves are from Eq. 3 for $\phi = 0.4$ and 0.5 (from left to right, respectively). The solid curve, for $\phi = 0$, is exact and from Ref.11.

ACKNOWLEDGEMENT

One of us (EGDC) is indebted to the Department of Energy grant number DE-FG 02-88-ER13847 for financial support.

REFERENCES

[1]. I. M. DE SCHEPPER, H. E. SMORENBURG and E. G. D. COHEN, *Phys. Rev. Lett.* 70, 2178 (1993).

[2]. I. M. DE SCHEPPER and E. G. D. COHEN, *Int. J. of Thermod.* 15, 1179 (1994).
[3]. D. HENDERSON and E. W. GRUNDKE, *J. Chem. Phys.* 63, 601 (1975).
[4]. E. G. D. COHEN and I. M. DE SCHEPPER, *Recent Progress in Many-Body Theories 3*, ed. T. L. Ainsworth, C. E. Campbell, B. E. Clements, and E. Krotscheck, (Plenum, New York, 1992) p. 387; *Slow Dynamics in Condensed Matter*, First Tohwa University International Symposium, Fukuoka, Japan, ed. K. Kawasaki, T. Kawaskatsu and M. Tokuyama (American Institute of Physics, New York, 1992) p. 359.
[5]. I. M. DE SCHEPPER, E. G. D. COHEN and H. J. ZUILHOF, *Phys. Lett. A*101, 399 (1984).
[6]. E. G. D. COHEN and I. M. DE SCHEPPER, *J. Stat. Phys.* 63, 241, 419 (1991).
[7]. I. M. DE SCHEPPER, E. G. D. COHEN, P. N. PUSEY and H. N. W. LEKKERKERKER, *J. Phys. Condens. Matter* 1, 6503 (1989); P. N. PUSEY, H. N. W. LEKKERKERKER, E. G. D. COHEN and I. M. DE SCHEPPER, *Physica A*164, 12 (1990).
[8]. (a) T. W. TAYLOR and B. J. ACKERSON, *J. Chem. Phys.*, 83, 2441 (1985); (b) P. N. PUSEY and W. VAN MEGEN, *Phys. Rev. Lett.* 59, 2083 (1987).
[9]. (a) J. X. ZHU, D. J. DURIAN, J. MÜLLER, D. A. WEITZ, and D. J. PINE, *Phys. Rev. Lett.* 68, 2559 (1992); (b) W. VAN MEGEN, S. M. UNDERWOOD, R. H. OTTEWILL, N. WILLIAMS and P.N. PUSEY, *Faraday Discuss. Chem. Soc.*, 83, 47 (1987).
[10]. J. C. VAN DER WERFF, C. G. DE KRUIF, C. BLOM and J. MELLEMA, *Phys. Rev. A*39, 795 (1989); J. C. VAN DER WERFF and C. G. DE KRUIF, *J. Rheol.* 33, 421 (1989).
[11]. B. CICHOCKI and B. U. FELDERHOF, *Phys. Rev. A*43, 5405 (1989).
[12]. E. G. D. COHEN, *Physica A*194, 229 (1993); id., *Twenty-five Years of Non-Equilibrium Statistical Mechanics*, XIII Sitges Conference, *Lecture Notes in Physics*, Springer (1995).
[13]. H. LÖWEN, J. P. HANSEN and J. N. ROUX, *Phys. Rev. A* 44, 1169 (1991).

GELATION UNDER SHEAR[1]

B.D. Butler, H.J.M. Hanley, and G.C. Straty

Thermophysics Division
National Institute of Standards and Technology
Boulder, Colorado, 80303, U.S.A

C.D. Muzny

Department of Physics, University of Colorado
Boulder, Colorado, 80309, U.S.A.

ABSTRACT

An experimental small angle neutron scattering (SANS) study of dense silica gels, prepared from suspensions of 24 nm colloidal silica particles at several volume fractions ϕ is discussed. Provided that $\phi \lesssim 0.18$, the scattered intensity at small wave vectors q increases as the gelation proceeds, and the structure factor $S(q,t \to \infty)$ of the gel exhibits apparent power law behavior. Power law behavior is also observed, even for samples with $\phi > 0.18$, when the gel is formed under an applied shear. Shear also enhances the diffraction maximum corresponding to the inter-particle contact distance of the gel. Difficulties encountered when trying to interpret SANS data from these dense systems are outlined. Results of computer simulations intended to mimic gel formation, including computations of $S(q,t)$, are discussed. Comments on a method to extract a fractal dimension characterizing the gel are included.

INTRODUCTION

The gelation of silica is of current interest both because gelation contains some interesting physics and because silica gel technology is an essential factor in the preparation and fabrication of modern ceramic materials [1]. A theme which has driven progress in the understanding and subsequent improvement in design of many material systems is the relationship between the properties of materials (mechanical, thermal, electrical, etc.) and their structure. Surprisingly, structural studies are relatively rare in the technologically relevant dense gels. This paper

[1] Contribution of the National Institute of Standards and Technology, not subject to copyright in the U.S.

summarizes some small angle neutron scattering (SANS) data which help to interpret the structural changes that take place during the gelation of silica. Specifically, the motivation was to understand better the evolution of the structure, on mesoscopic scales, of dense gelling silica spheres both with and without the influence of an applied shear. We report on: (1) the evolution of the structure factor in a gelling silica suspension (sol) subjected to an applied shear and compare this to similar systems without shear; and (2) the methods we use to interpret SANS data from *dense* gelling systems.

Experiments to probe the influence of shear on these systems are novel, but we anticipate that shear will impact the structure and formation mechanism of gels. Consider a gel as a mechanically and thermodynamically unstable microscopic network made up of some defined unit, for example, a particle or segment of a polymer chain. Instability is frozen when the network growth and/or rearrangement is restricted by the finite size of the container and the experimental conditions [2]. It is, however, known [3] that a shear rate γ applied to a system will affect its equation of state, its thermodynamic properties, and therefore its phase stability criteria. Thus, a sheared system may have phase behavior which is perturbed or even qualitatively different from its counterpart formed in isolation. Since gelation can be treated as a phase change, a shear applied to the precursor or sol can be expected to influence the final gel structure.

EXPERIMENT

This study [4] was carried out with colloidal silica particles, of nominal diameter $\sigma = 24$ nm, on the 30 m SANS instruments at the NIST Cold Neutron Research Facility. Silica spheres were suspended in a 70% H_2O - 30% D_2O medium (to reduce the effect of multiple scattering) at volume fractions ϕ of 0.10, 0.12, 0.18, 0.24, and 0.30. Gelation was initiated by lowering the pH of the suspensions to 5.8 ± 0.1 with the addition of 0.1M HCl. For gelation to proceed at a reasonable pace, NaCl was added to some designated samples until the solutions reached 0.4M NaCl.

The samples were placed in quartz cells of path length 1 mm, and the spectrometer was configured to an incident wavelength of 0.6 nm at a detector distance of 13 m. The scattered intensity was measured using a 2D position sensitive detector system, and, since asymmetry was not observed in any of the samples, the detector counts were averaged azimuthally. The measured scattered intensities were corrected for cell background and detector efficiency and were placed on an absolute scale by normalizing to the scattering from an appropriate standard. The structure factor was obtained by dividing this normalized intensity by a theoretical polydisperse form factor [4] modified to allow for instrument smearing. Data were collected after gel initiation at 10 min intervals for the first 3 h and then hourly until gelation was complete. Gelation was considered complete when the measured intensity became time independent (usually after 6-10 h).

For the shear studies, the SANS instrument was configured at 13 m and 8 m at a wavelength of 0.6 nm with the NIST 0.5 mm gap-width Couette shearing cell [5] in the sample holder position with the incident beam perpendicular to the flow direction. A gelation-initiated sample was loaded into the Couette cell, subjected to a shear rate $\gamma = 4500\ s^{-1}$, and the intensity recorded. A sector average of the sheared intensities indicated possible weak anisotropy at the higher volume fractions, but the data were circularly averaged and reduced following the procedure for the unsheared suspensions and gels. Intensities were measured at regular intervals until the scattering pattern from the shearing system was time-independent. At this point the shear was removed and

the intensity remeasured. Only very small relaxation was noted; in effect, the intensity did not change significantly when the shear was removed.

RESULTS

The presentation of these results and their interpretation is a distillation of the discussions of our work reported in Refs. [4, 6-8]. The data are summarized in Figures 1 and 2. Figure 1 (a) shows a typical sequence of the variation of the structure factor $S(q,t)$ as a function of time after gel initiation for a $\phi = 0.10$ sample gelling in the absence of an applied shear. At the very earliest times there is no appreciable small angle scattering, indicating the initial solution is relatively homogeneous at the length scales probed by this experiment (several particle diameters). As the gelation proceeds, however, there is a marked increase in the scattering at low q and this becomes more pronounced at longer times. At these later times, $S(q,t)$ displays an apparent power-law increase with decreasing q. Behavior qualitatively similar to this was observed in all samples, sheared and unsheared, that had silica volume fractions $\phi \leq 0.18$, with the lowest volume fractions showing the most intense small angle scattering. Quantitative differences between the samples with $\phi \leq 0.18$ measured with and without an applied shear were small.

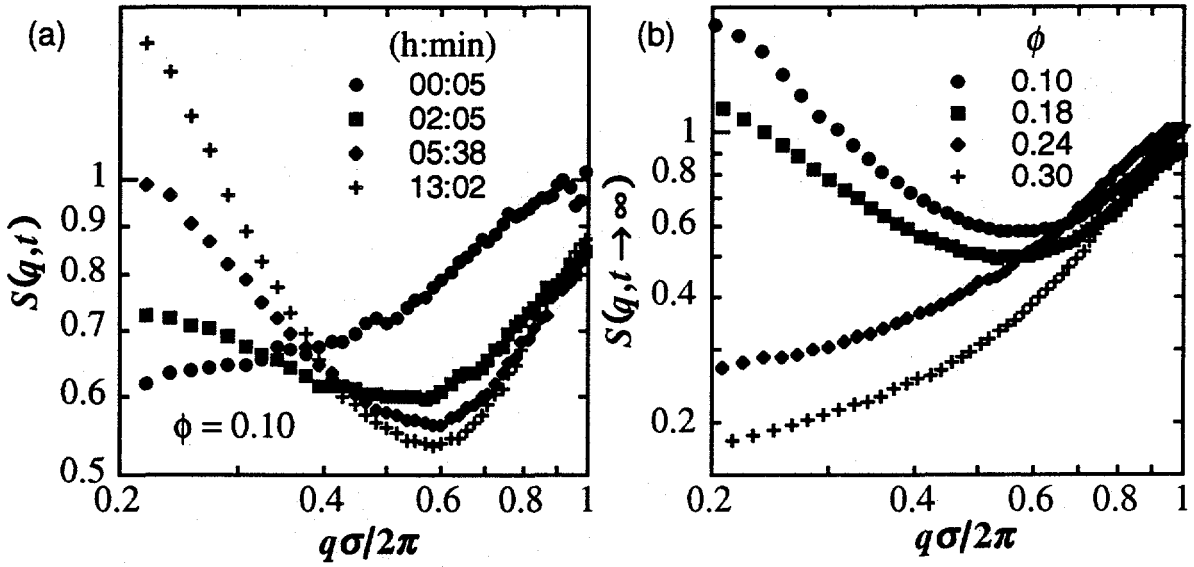

Figure 1: Measurered structure factors at $\gamma = 0$: (a) as a function of time since gel initiation, and (b), as a function of volume fraction after the gel has formed.

In contrast, samples with silica volume fractions above 0.18 ($\phi = 0.24,\ 0.30$) did not display a rise in the small angle scattering (even at very long times) when a shear was not applied. This result is apparent from Fig. 1 (b), which shows the scattering from the final gels as a function of volume fraction. Thus, the power-law increase in the scattering at small angles observed in the more dilute systems is not seen in the denser system. This power-law behavior in $S(q,t)$ returns, however, when shear is applied during the gelation of the higher density samples (Fig. 2). Furthermore, in addition to this large increase in small angle scattering with shear, there is a significant change observed in the particle-particle 'contact' peak located near $q\sigma/2\pi \approx 1$. This peak is broad and weak in the unsheared sample, but is much sharper and more intense in the sample gelled under shear.

Qualitatively, the increase in small angle scattering at low q indicates that the samples evolve from an initially homogeneous suspension of silica particles to an arrangement that contains structural inhomogeneities at length scales of the order of several particle diameters. These inhomogeneities apparently do not form at all in samples with volume fractions greater than 0.18 unless a shear is applied. This is a surprising result. We might anticipate that a shear will disorder the gel so as to prevent the formation of inhomogeneities; apparently the opposite is true. Moreover, the distinct particle-particle contact peak seen in the higher density sheared gels (Fig. 2) indicates that relatively dense clusters of these spherical silica particles have formed.

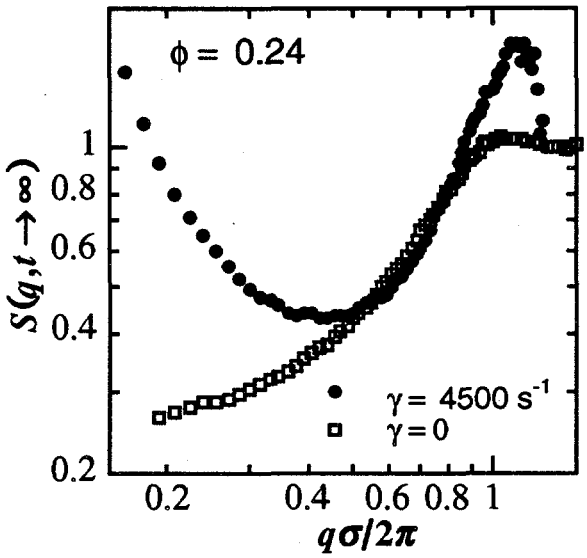

Figure 2: Measurered structure factors for the $\phi = 0.24$ gelled samples with and without an applied shear. The results for $\phi = 0.30$ are similar.

ANALYSIS

In *low* density gels, small angle x-ray [9], neutron [10], and light-scattering [11] studies show a characteristic power-law increase in intensity with decreasing wavevector. This power-law behavior, characteristic of fractal aggregation processes [12, 13], predicts that the mass of an aggregate varies as $m \sim \xi^{d_f}$, where ξ is a length characterizing the aggregate size and d_f is a fractal dimension. It is easily shown that the structure factor $S(q)$ of a collection of such objects is given by

$$S(q) \sim q^{-d_f} \tag{1}$$

at wavevectors in the range $2\pi/\xi << q << 2\pi/\sigma$, *provided* that there are no correlations between aggregates. The power-law slopes in the measured small-angle diffraction patterns of these low density gels (where correlations can be expected to be small) are thus related to the fractal dimension of the aggregates that form the gel.

It is tempting to apply Eq. (1) to our data and derive a fractal dimension from the slope of the measured structure factors. But, in this study, the small angle neutron scattering measurements

were performed on dense gels for which an assumption that the collection of aggregates or clusters of particles formed during gelation are uncorrelated *cannot* be justified. In these dense systems, the small angle scattering can be described only by a much more complicated function of the cluster shapes, cluster-cluster correlations, as well as the particle arrangements inside individual clusters [7]. Cluster growth and/or cluster-cluster correlations must, therefore, be included in the interpretation of the increased scattering at low angles. In other words, it is not necessarily the internal arrangements of the silica particles inside a cluster that cause the rise in scattering as it is in low density systems; rather, the size and shape of the clusters coupled with their correlation must be a factor.

COMPUTER SIMULATION

The direct interpretation of such complicated scattering patterns requires that we evoke some model of the particle rearrangement. We chose to simulate the gelation in a dense 2D system where it is possible both to observe the particle positions as a function of time and to compare this to an $S(q,t)$ computed from these configurations. In this way it is possible to gain insight into how cluster morphologies contribute to particular features of the corresponding diffraction patterns and therefore be better able to interpret the measurements. Furthermore, it is possible to simulate the effect of shear on the particle morphologies, and thus $S(q,t)$, and to compare this to our scattering measurements.

Details of the computer simulation are presented elsewhere [6], but, in brief, it consisted of quenching (by molecular dynamics methods) a large (N = 14336), dense (ρ = 0.325), 2D Lennard-Jones system, from a high temperature disordered fluid into the vapor/solid coexistence region and observing the subsequent aggregation both with and without an applied shear. The quench is intended to mimic the sudden change in interaction potential used to initiate gelation in real systems – the subsequent evolution of the real and simulated systems should therefore be qualitatively similar. In order to compare these simulations to experiment, $S(q,t)$ was computed from the simulation and compared with the experimental data and the simulated particle morphologies. Typical results from the simulations are presented in Fig. 3.

Figures 3 (a) and (b) are taken from a simulation with no applied shear after a total reduced time t = 500 since the quench. At this relatively late stage in the evolution of the system several large clusters with elongated shapes have formed which, overall, shows an interconnected morphology. Most interesting for our present purposes is the form of the computed $S(q,t)$. Like the experiments reported earlier, $S(q,t)$ shows a power-law-like rise with decreasing wavevector, but, in this case, the origin of the small angle scattering in the simulation is clear; there is a peak in $S(q,t)$ at low angles which results from the cluster-cluster correlations evident in Fig. 3 (a). The power-law slope cannot be identified with any particular internal feature of the clusters but instead depends on specific details of the correlations which give rise to the peak in $S(q,t)$.

Similar plots after the same time are presented in Figs. 3 (c) and (d) for the case where a shear is applied. Here we find that the coarsening of the clusters has proceeded much more rapidly than in the simulation where no shear was applied. While this might not be expected, as we may anticipate that shear will *disorder* the system, it is consistent with our experimental observation that the application of a shear in the dense gels gives rise to small angle scattering where none is present in the unsheared gels.

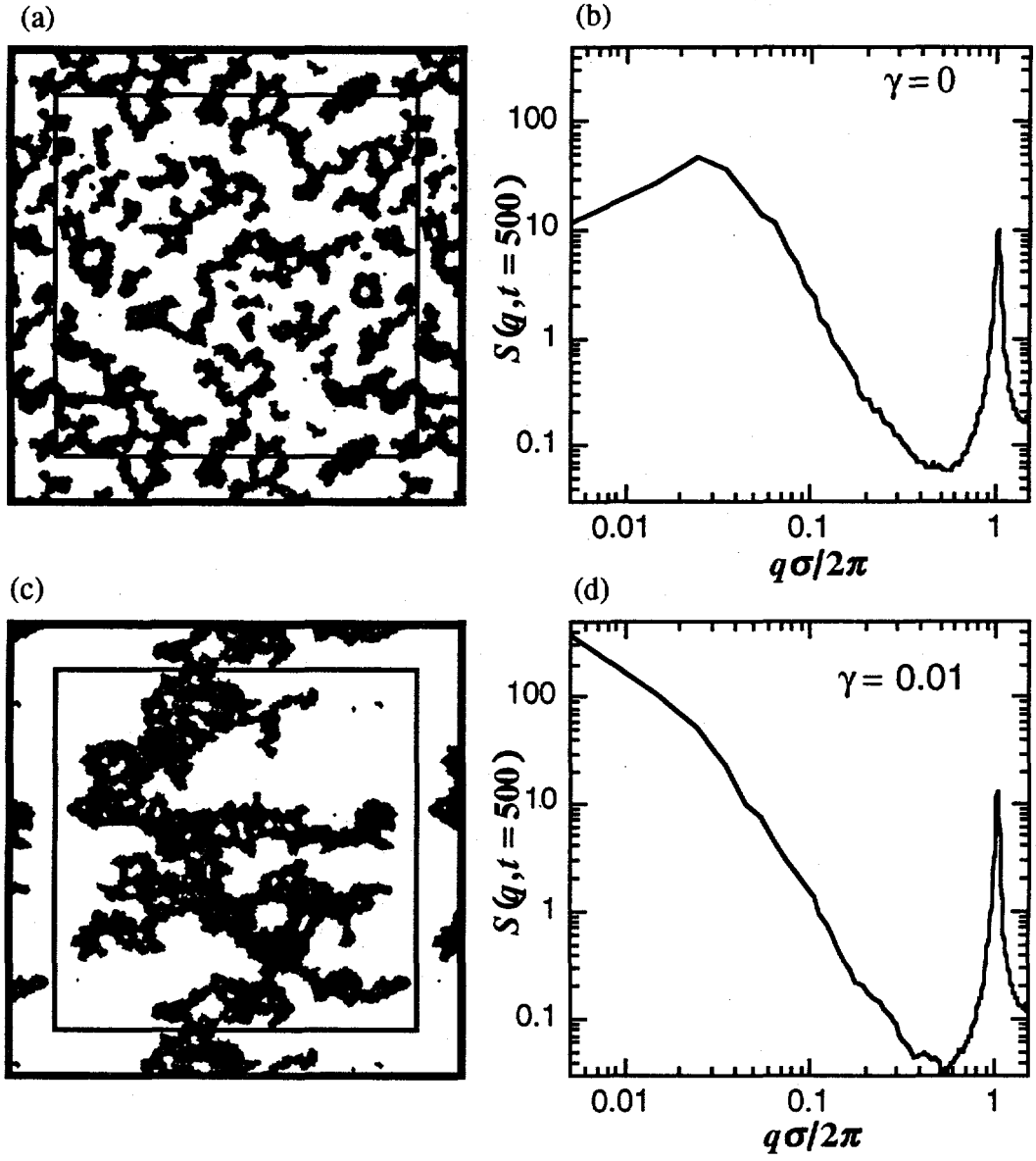

Figure 3: Molecular dynamics computer simulations of quenched Lennard-Jones disks: (a) and (c) are particle configurations at a reduced time $t = 500$ without and with an applied shear; (b) and (d) are the corresponding $S(q)$.

A DYNAMIC SCALING LAW

Close examination of the evolution of the cluster morphology showed that the aggregation proceeds in such a way that, except for a change in scale, the morphologies are similar. That is, the structure evolves in a temporally self-similar manner. If the clusters are mass fractals, the corresponding structure factors should, therefore, scale as [8]

$$S(q/q_m(t)) \sim q_m(t)^{-d_f} \tilde{S}(q/\tilde{q}_m) \tag{2}$$

where $q_m(t)$ is the location of the low angle peak in $S(q,t)$ and $\tilde{S}(q/\tilde{q}_m)$ is a time-independent characteristic structure function which peaks at $\tilde{q}_m$. The fractal dimension d_f is allowed to take on any value less than or equal to the dimensionality of the system and will depend on the structure of the evolving clusters. For the simulations presented here, this relation is satisfied well provided d_f is assigned a value of 1.85 ± 0.05. This result is presented in Fig. 4. Here the computed $S(q,t)$ have been scaled according to Eq. 2 and are found to lie on a universal curve. This result is important because it suggests a way to obtain information (the fractal dimension) about the structure of the evolving system, even in a dense system where correlations are inevitable, by observing the time dependence of the structure factor.

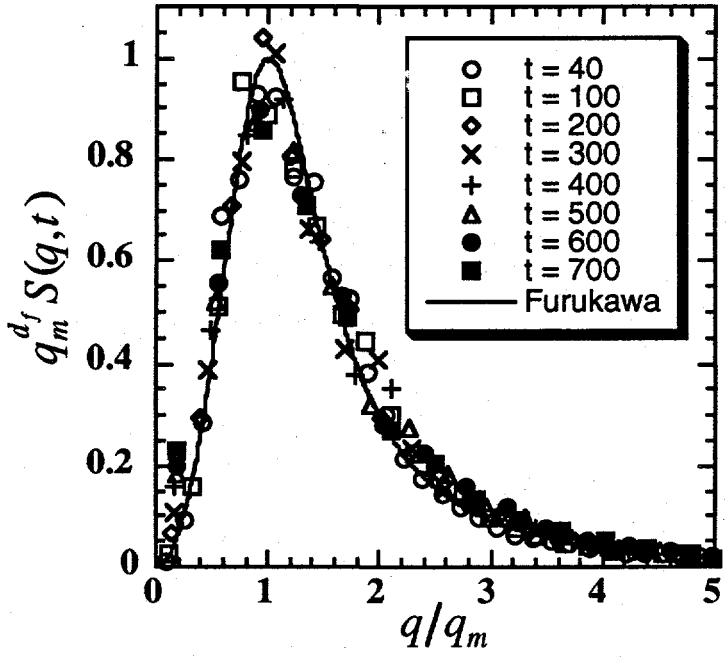

Figure 4: Computed stucture factors at different times during the evolution of the MD computer simulation (no shear) scaled according to Eq. (2). The solid line is the phenomenological theory of Furukawa [14] which has no adjustable parameters. See Ref. [8].

CONCLUSION

Measurement of SANS data on silica gels ranging in volume fraction ϕ from 0.10 to 0.30, were made with and without an applied shear. Those samples with $\phi \leq 0.18$ showed apparent power-law increases in their structure factors regardless of shear. The two higher density samples only displayed power-law rises in $S(q,t)$ when a shear was applied, indicating that shear actually assists the gelation processes that operate at lower density. A computer model based on the quenching of a Leonard-Jones system reproduces many features of the measured diffraction data – a power-law behavior and an increased tendency for ordering when a shear is applied. Comparing the simulation results with the data, we conclude that the power law behavior originates from the presence of cluster-cluster correlations and not from the internal fractal structure of these clusters. We present a dynamic scaling relation which can instead be used to derive the fractal dimension of

the evolving system even in the presence of these correlations.

ACKNOWLEDGEMENTS

This work was supported in part by a grant from the Office of Basic Energy Sciences, Division of Engineering and Geosciences, US Department of Energy. BDB was supported by a National Research Council Research Associateship. We are grateful to William O. Roberts, Du Pont, for supplying the silica samples and for valuable discussions. Part of the neutron studies were carried out on the NIST SANS instrument supported by the National Science Foundation under Agreement No. DMR-9122444.

REFERENCES

1. See, for example, C.J. Brinker and G.W. Scherer, *Sol-Gel Science: The Physics and Chemistry of Sol-Gel Processing*, Academic, San Diego (1990).
2. Experiment supports this view, for example; (a) a suspension can be gelled very slowly giving either an amorphous liquid-like solid phase (as for a slowly dried silica gel) or a crystal (as in opal formation); (b) on aging, a gel can rearrange to a metastable amorphous solid or to a stable crystal (See Ref. [1]).
3. H.J.M. Hanley and D.J. Evans, J. Chem. Phys. 76, 3225 (1982).
4. C.D. Muzny, G.C. Straty and H.J.M. Hanley, Phys. Rev. E. 50, R675 (1994).
5. G.C. Straty, H.J.M. Hanley, and C.J. Glinka, J. Stat. Phys. 62, 1015 (1991).
6. C. D. Muzny, D. Hansen, G, C,. Straty, D. J. Evans and H. J. M. Hanley, Simulation and SANS studies of gelation under shear, *Int. J. Thermophysics*, 16, 337 (1995).
7. B.D. Butler, H.J.M. Hanley, C.D. Muzny and G.C. Straty, Mat. Res. Soc. Symp. Proc., *Neutron Scattering in Materials Science* 376, *in press*.
8. B.D. Butler, H.J.M. Hanley, D. Hansen and D.J. Evans, Phys. Rev. Lett., *in press* (1995).
9. D.W. Schaefer, J.E. Martin, P. Wiltzius, and D.S. Cannell, *Phys. Rev. Lett.* **52**, 2371 (1984).
10. R. Vacher, T. Woignier, J. Pelous, and E. Courtens, *Phys. Rev. B* **37**, 6500 (1988).
11. G. Dietler, C. Aubert, D.S. Cannell, and P. Wiltzius, *Phys. Rev. Lett.* **57**, 3117 (1986).
12. P. Meakin, *Ann. Rev. Phys. Chem.* **39**, 237 (1988).
13. J. E. Martin and B.J. Ackerson, *Phys. Rev. A* **31**, 1180 (1985).
14. H. Furukawa, Adv. Phys. 34, 703 (1985).

TRANSPORT PROPERTIES OF POROUS MEDIA FROM THE MICROSTRUCTURE

S. Torquato

Department of Civil Engineering & Operations Research and Princeton Materials Institute
Princeton University, Princeton, N.J. 08544

ABSTRACT

The determination of the effective transport properties of a random porous medium remains a challenging area of research because the properties depend on the microstructure in a highly complex fashion. This paper reviews recent theoretical and experimental progress that we have made on various aspects of this problem. A unified approach is taken to characterize the microstructure and the seemingly disparate properties of the medium.

I. INTRODUCTION

The purpose of this paper is to review progress that we have made in the last several years on five basic aspects of the problem of determining effective transport properties of random porous media: (i) derivation of rigorous bounds on transport properties in terms of statistical correlation functions; (ii) quantitative characterization of the microstructure of nontrivial models; (iii) 3D imaging of porous media using x-ray tomography; (iv) and derivation of rigorous cross-property relations.

II. AVERAGED EQUATIONS

The random porous medium is a domain of space $\mathcal{V}(\omega) \in \boldsymbol{R}^3$ (where the realization $\boldsymbol{\Omega}$ is taken from some probability space ω) of volume V which is composed of two regions: the pore region $\mathcal{V}_1(\omega)$ (in which transport occurs) of volume fraction (porosity) ϕ_1 and a solid-phase region $\mathcal{V}_2(\omega)$ of volume fraction ϕ_2. Let $\partial\mathcal{V}(\omega)$ be the surface between $\mathcal{V}_1$ and $\mathcal{V}_2$.

A. Time Scales for NMR Relaxation

Nuclear magnetic resonance (NMR) is a powerful noninvasive technique for the study of fluid-saturated porous media [1]. The relaxation times of water contained in a porous medium are substantially smaller than those of bulk water, primarily because of enhanced

relaxation mechanisms at the pore-solid interface. NMR relaxation depends upon the characteristic length scales of the pore space and on the surface rate constant κ. The decay of the magnetization density $m(\mathbf{x},t)$ at local position $\mathbf{x}$ and time t is governed by a time-dependent diffusion equation, the solution of which can be expressed as an expansion in orthonormal eigenfunctions $\{\psi_n\}$:

$$\frac{m(\mathbf{x},t)}{m_o} = \sum_{n=1}^{\infty} a_n e^{-t/T_n} \psi_n(\mathbf{x}) \,, \tag{1}$$

where the coefficients a_n are simply related to the pore-volume average of ψ_n [2]. The diffusion relaxation times T_n are inversely proportional to the eigenvalues λ_n.

The net magnetization, usually the quantity of principal interest in NMR experiments, is defined as

$$M(t) = \int_{\mathcal{V}_1} m(\mathbf{x},t) d\mathbf{x} \,. \tag{2}$$

The *mean survival time* τ of a diffusing particle before it gets completely demagnetized is given by [2]

$$\tau = \int_0^{\infty} \frac{M(t)}{M_o} dt, \tag{3}$$

where $M_o \equiv M(t=0)$. The mean survival time τ depends on the diffusion coeffcient, D, κ, and the microstructure.

B. Effective Conductivity

The effective conductivity σ_e is given by an averaged Ohm's law:

$$< \mathbf{J}(\mathbf{x}) >= \sigma_e < \mathbf{E}(\mathbf{x}) > \tag{4}$$

where $< \mathbf{E}(\mathbf{x}) >$ and $< \mathbf{J}(\mathbf{x}) >$ represent the *ensemble average* of the local electric and current density fields, respectively. The local fields satisfy the usual steady-state conduction equations [3].

By mathematical analogy, results for σ_e translate into equivalent results for the thermal conductivity, magnetic permeability, dielectric constant, and diffusion coefficient.

C. Fluid Permeability

The fluid permeabilty k of a porous medium, defined by Darcy's law,

$$< \mathbf{u}(\mathbf{x}) >= -\frac{k}{\mu} \nabla p_o(\mathbf{x}) \,, \tag{5}$$

governs the rate at which a viscous fluid flows through it [4]. Here $< \mathbf{u}(\mathbf{x}) >$ is the ensemble average of the local fluid velocity which satisfies the steady-state Stokes equations [5], $\nabla p_o(\mathbf{x})$ is the applied pressure gradient, and μ is the dynamic viscosity. k depends nontrivially on the pore geometry and may be regarded to be an *effective cross-sectional area of pore channels.*

III. MICROSTRUCTURE/PROPERTY CONNECTION

A. Minimum Energy Principles

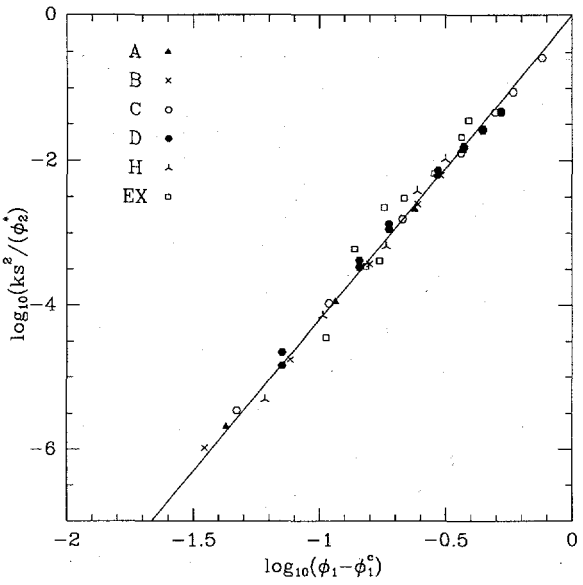

Figure 1: The log of $ks^2/2\phi_2$ vs. log of $\phi_1 - \phi_1^c$ for several different model microstructures and a sandstone. Here s is the specfic surface and ϕ_1^c is the porosity at which the pore phase becomes disconnected.

For general random media, the complexity of the microstructure prevents one from obtaining the effective properties of the system exactly. Therefore, any rigorous statement about the properties must be in the form of an inequality, i.e., rigorous bounds on the effective properties. Bounds are useful since they: (i) enable one to test the merits of theories and computer experiments; (ii) as successfully more microstructural information is incorporated, the bounds become progressively narrower; and (iii) one of the bounds can typically provide a good estimate of the property for a wide range of conditions, even when the reciprocal bound diverges from it.

Bounds are usually derived using *minimum energy principles* [3]. Recently, the mean survival time τ has been bounded from below in terms of moments of the *pore size distribution function* $P(\delta)$ [2,6]. $P(\delta)\,d\delta$ is the probability that a point in the pore region $\mathcal{V}_1$ lies at a distance between δ and $\delta + d\delta$ from the nearest point on the interface $\partial\mathcal{V}$.

The nearest-neighbor distribution function $H(r)$ has been shown to arise in rigorous bounds on the effective conductivity σ_e, mean survival time τ, and the fluild permeability k for suspensions of spheres [6]. $H(r)\,dr$ gives the probability of finding nearest neighbors in a spherical shell of thickness dr at a distance r from the center of a reference particle.

More recently, we have derived the sharpest available bounds on the effective conductivity and elastic moduli of two-phase heterogeneous materials that are given in terms of the n-point probability functions S_1, S_2,..., S_n [7]. $S_n(\mathbf{r}_1, ..., \mathbf{r}_n)$ gives the probability of finding n point at positions $\mathbf{r}_1$,...,$\mathbf{r}_n$ in one of the phases.

Guided by rigorous bounds on the permeability, we have found a universal scaling for the permeability of a class of porous media [8]. As Figure 1 demonstrates this includes various sphere packings as well as a sandstone.

B. Brownian-Motion Simulation Technique

We have applied our Brownian-motion simulation technique to compute effective diffusion properties, such as the effective conductivity of packings of spheroids [9] and mean survival time associated with diffusion-controlled reactions in *digitized, synthetic* heteroge-

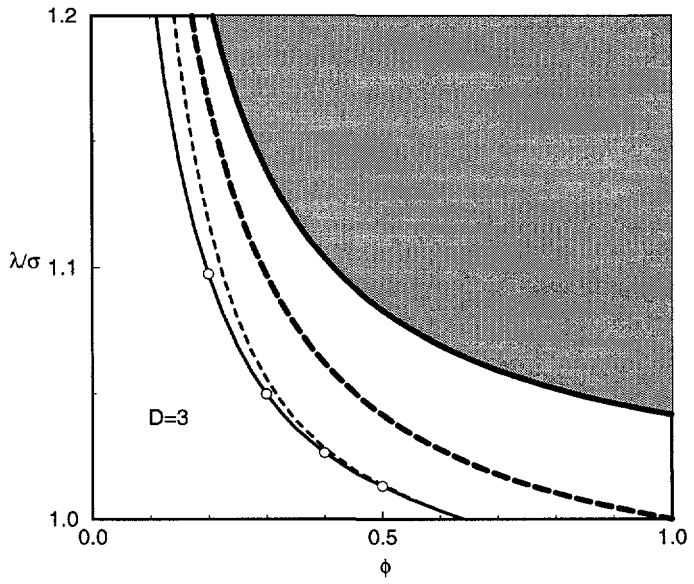

Figure 2: Dimensionless mean nearest-neighbor distance λ/σ vs. packing fraction ϕ for hard spheres. Thin solid line is theoretical prediction. Open circles are simulation data. Thin dashed line, thick dashed line, and solid lines are upper bounds.

neous media [10]. The latter work can be used to understand the critical issues involved when examining a digitized image of an actual material sample.

IV. MICROSTRUCTURE CHARACTERIZATION

Some of the different types of statistical correlation functions that have arisen in rigorous bounds on transport properties were described in the previous section. Until recently, application of such bounds (although in existence for almost thirty years in some cases) was virtually nonexistent because of the difficulty involved in ascertaining the correlation functions.

A. Unified Theoretical Approach

For statistically inhomogeneous systems of N identical d-dimensional spheres, Torquato [11] has introduced the general n-point distribution function $H_n(\mathbf{x}^m; \mathbf{x}^{p-m}; \mathbf{r}^q)$ and found a series representation of H_n which enables one to compute it. From the general quantity H_n one can obtain all of the aforementioned correlation functions and their generalizations [11]. This formalism has been generalized to treat polydispersed spheres, anisotropic media (e.g., aligned ellipsoids and cylinders), and cell models [3,6].

We have developed analytical expressions for the *chord-length distribution function* for models of porous media with a *polydispersivity in size* [12,13]. A new *coarse-graining* procedure has been obtained to generate and analyze a wide class of model microstructures [14].

The nearest-neighbor distribution function $H(r)$ is a fundamental quantity that statistically characterizes a random system of particles (including liquid structure). We have found analytical expressions for $H(r)$ for nontrivial particulate models up to the *random*

close-packing density [15].

Using $H(r)$ we have been able to obtain new and fundamental rigorous results for the *mean nearest-neighbor distance* λ between particles [16]. In particular, we have found an excellent approximation to λ for equilibrium hard spheres that is valid up to random close packing and rigorous upper bounds on λ. We have proven that a certain region in the ϕ-λ plane is prohibited to ergodic, isotropic hard spheres. (shaded region in Fig. 2).

We have very recently developed an exact algorithm to compute $H(r)$ and other void statistics [17]. Moreover, we have extracted various statistical measures from digitized representations of consolidated-sphere models [18].

The important topological property of connectedness is reflected in the two-point *cluster function* which we have evaluated exactly for a certain contimuum percolation model [19].

B. 3D Imaging Using X-Ray Tomography

We have very recently obtained high-resolution $3D$ digitized representation of a Fountainbleu sandstone using x-ray tomographic techniques [20]. This digitized representation is used to extract a number of morphological characteristics of the sample. Figure 3 shows a slice of the sandstone which has a porosity of 0.15. Figure 4 depicts the two-point probability function obtained from all of the slices.

V. CROSS-PROPERTY RELATIONS

An intriguing fundamental as well as practical question in the study of heterogeneous materials is the following: Can different properties of the medium be *rigorously* linked to one another? Such cross-property relations become especially useful if one property is more easily measured than another property. For example, it is difficult to measure the permeability k in situ.

Torquato [21] derived the first rigorous relation connecting the permeability k to the mean survival time τ of a porous medium:

$$k \leq D\phi_1\tau \,. \tag{6}$$

Generally, inequality (6) is not sharp because τ is a reflection of the entire pore space, whereas k is a reflection of the *dynamically connected* part of the pore space.

More recently, Avellaneda and Torquato [22] derived the first rigorous *equality* connecting the permeability to the *effective electrical conductivity* of a porous medium *containing a conducting fluid of conductivity* σ_1 *and an insulating solid phase*:

$$k = \frac{L^2}{8F} \,, \tag{7}$$

where $F = \sigma_1/\sigma_e$ is the *formation factor* and L is a length parameter which is a weighted sum over the viscous relaxation times associated with the time-dependent Stokes equations.

It has been conjectured that for isotropic media possessing an arbitrary but connected pore space, the following relation holds [23]:

$$k \leq \frac{D\tau}{F} \,. \tag{8}$$

We have continued to seek and test cross-property relations that connect the fluid permeability of porous media with diffusion properties, such as diffusion relaxation times, obtainable from NMR experiments, and the *electrical conductivity* [24,25]. Based on the above rigorous results, it has been proposed [24] that the approximate relation

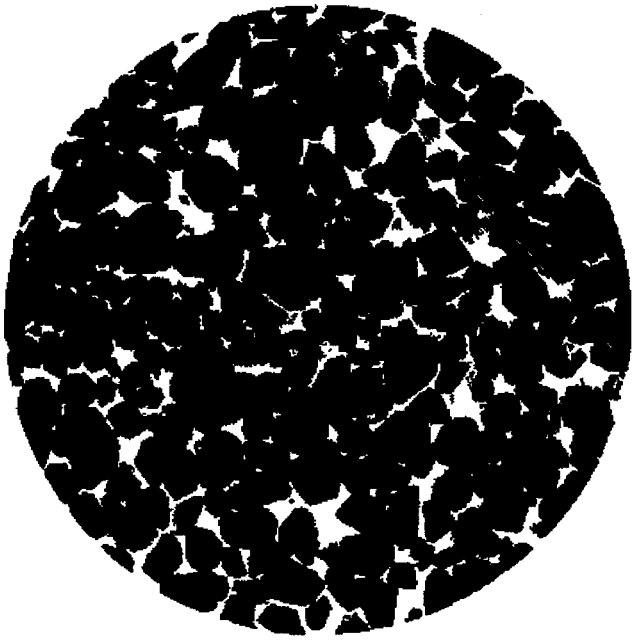

Figure 3: Sample filtered slice of Fountainbleu sandstone. The black region corresponds to the grain phase.

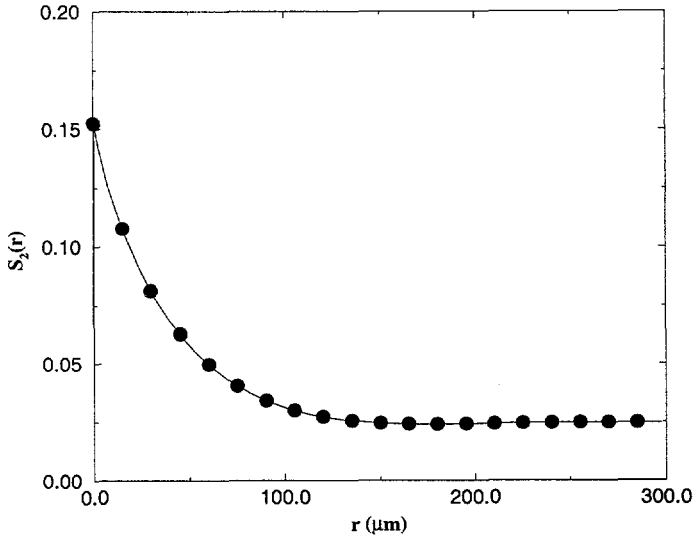

Figure 4: Two-point probability function vs. distance for Fountainbleu sandstone.

$$k \approx \phi_1 \frac{D\tau}{F} . \tag{9}$$

should be accurate for a large class of porous media.

To test cross-property relation (9), we have recently analyzed the 3D tomographic image of the aforementioned Fountainbleu sandstone (see Fig. 3) [20]. The quantity τD was determined to be 154 μm^2 from Brownian-motion simulations, F^{-1} was rigorously bounded from above by the value 0.089 using three-point information [7], and ϕ_1 was found to be 0.15. Thus, relation (9) predicts $k \approx 2.1 \mu m^2$, which is in relatively good agreement with the experimental value [25] of 1.3 μm^2.

The attentuation of elastic waves in fluid-saturated porous media depends on their effective elastic moduli. We have rigorously linked the conductivity to the elastic moduli of the medium [26-28].

ACKNOWLEDGMENTS

Support for this work was provided by the DOE under Grant DE-FG05-92ER14275.

REFERENCES

1. A. H. Thompson et. al., "Deuterium Magnetic Resonance and Permeability in Porous Media," *J. Appl. Phys.* **65**, 3259 (1989).
2. S. Torquato and M. Avellaneda, "Diffusion and Reaction in Heterogeneous Media," *J. Chem. Phys.* **95**, 6477 (1991).
3. S. Torquato, "Random Heterogeneous Media: Microstructure and Improved Bounds on Effective Properties," *Appl. Mech. Rev.* **44**, 37 (1991).
4. A. E. Scheidegger, *The Physics of Flow through Porous Media* (University of Toronto Press, Toronto, 1974).
5. J. Rubinstein and S. Torquato, "Flow in Random Porous Media: Mathematical Formulation, Variational Principles, and Rigorous Bounds," *J. Fluid Mech.* **206**, 25 (1989).
6. S. Torquato, "Unified Methodology to Quantify the Morphology and Properties of Inhomogeneous Media," *Physica A*, 79 (1994).
7. L. V. Gibiansky and S. Torquato, "Geometrical Parameter Bounds on Effective Properties of Composites," *J. Mech. Phys. Solids*, in press.
8. N. Martys, S. Torquato, and D. P. Bentz, "Universal Scaling of Fluid Permeability for Sphere Packings," *Physical Review E*, **50**, 403 (1994).
9. I. C. Kim and S. Torquato, "Effective Conductivity of Composites Containing Spheroids: Simulations and Comparison to Theory," *Journal of Applied Physics*, **74**, 1844 (1993).
10. D. Coker and S. Torquato, "Simulation of Diffusion and Reaction in Digitized Heterogeneous Media," *Journal of Applied Physics*, **77** (1995).
11. S. Torquato, "Microstructure Characterization and Bulk Properties of Disordered Two-Phase Media," *J. Stat. Phys.* **45**, 843 (1986).
12. B. Lu and S. Torquato, "Chord-Length and Free-Path Distribution Functions in Many-Body Systems," *Journal of Chemical Physics* **98**, 6472 (1993).
13. S. Torquato and B. Lu, "Chord-Length Distribution Function for Two-Phase Random Media," *Physical Review E*, **47**, 2950 (1993).
14. R. Blumenfeld and S. Torquato, "A Coarse-Graining Procedure to Generate and Analyze Heterogeneous Materials: Theory," *Physical Review E*, **48**, 4492 (1993).

15. S. Torquato, "Nearest-Neighbor Statistics for Random Packings of Hard Spheres and Disks," *Physical Review E*, **51**, 3170 (1995).
16. S. Torquato, "Mean Nearest-Neighbor Distance in Random Packings of D-Dimensional Hard Spheres," *Physical Review Letters*, **74**, 2156 (1995).
17. M. D. Rintoul and S. Torquato, "An Exact Algorithm to Compute Void Statistics for Random Arrays of Disks," submitted to *Physical Review E.*
18. D. Coker and S. Torquato, "Extraction of Morphological Quantities from a Digitized Image," *Journal of Applied Physics*, **77** (1995).
19. E. Cinlar and S. Torquato, "Exact Determination of the Two-Point Cluster Function for One-Dimensional Continuum Percolation," *Journal of Statistical Physics*, **78**, 827 (1995).
20. D. Coker, S. Torquato, and J. Dunsmuir "Morphological and Physical Properties of Fountainebleu Sandstone from Tomographic Analysis," to be submitted to *Journal of Applied Physics*
21. S. Torquato, "Relationship Between Permeability and Diffusion-Controlled Trapping Constant of Porous Media," *Phys. Rev. Lett.* **64**, 2644 (1990).
22. M. Avellaneda and S. Torquato, "Rigorous Link Between Fluid Permeability, Electrical Conductivity, and Relaxation Times for Transport in Porous Media," *Phys. Fluids A* **3**, 2529 (1991).
23. S. Torquato and I. C. Kim, "Cross-Property Relations for Momentum and Diffusional Transport in Porous Media," *Journal of Applied Physics*, **72**, 2612 (1992).
24. L. M. Schwartz, N. Martys, D. P. Bentz, E. J. Garboczi, and S. Torquato, "Cross-Property Relations and Permeability Estimation in Model Porous Media," *Physical Review E*, **48**, 4584 (1993).
25. L. M. Schwartz, F. Auzerais, J. Dunsmuir, N. Martys, and S. Torquato, "Transport and Diffusion in Three Dimensional Composite Media," *Physica A*, **207**, 28 (1994).
26. L. V. Gibiansky and S. Torquato, "Link Between the Conductivity and Elastic Moduli of Composite Materials," *Physical Review Letters*, **18**, 2927 (1993).
27. L. V. Gibiansky and S. Torquato, "Rigorous Link Between the Conductivity and Elastic Moduli of Fiber-Reinforced Composite Materials," *Philosophical Transactions of the Royal Society*, in press.
28. L. V. Gibiansky and S. Torquato, "Connection Between the Conductivity and Elastic Moduli of Isotropic Composite Materials," *Proceedings of the Royal Society of London A*, in press.

NMR STUDIES OF MULTIPHASE FLOWS. II

S. A. Altobelli, A. Caprihan, E. Fukushima, I. J. Lowe, and L. Z. Wang

The Lovelace Institutes
2425 Ridgecrest Dr., SE, Albuquerque, NM 87108 USA

ABSTRACT

NMR techniques for measurements of spatial distribution of material phase, velocity and velocity fluctuation are being developed and refined. Versions of these techniques which provide time average liquid fraction and fluid phase velocity have been applied to several concentrated suspension systems which will not be discussed extensively here. Technical developments required to further extend the use of NMR to the multi-phase flow arena and to provide measurements of previously unobtainable parameters are the focus of this report.

INTRODUCTION AND HISTORY

Nuclear magnetic resonance (NMR) has been used to study flowing fluids at The Lovelace Institutes (TLI) for the past ten years. The advantage of the NMR method for flow measurements is many-fold. Among the more obvious are that it is non-invasive and that, for certain materials, it can examine a flow system without any opaqueness problems. Among the possibly less obvious advantages is that the technique can measure many flow parameters not limited simply to velocity and concentration but also to diffusion, turbulence, acceleration, etc., as primary parameters (as opposed to secondary parameters that are derived from the primary parameters). The advent of NMR imaging (NMRI) allows us to spatially resolve all such parameters.

We have embarked on a program to study various properties of multiphase flows by NMR. In particular, we wish to develop new techniques and apply them to problems in various fields. The initial objective, five years ago under BES funding, of showing that spatially resolved measurements of velocity and concentration of liquid/solid multiphase flows was possible at any concentration of the solid component, has been fulfilled and some results were presented at the Tenth Symposium on Energy Engineering Sciences in 1992 [1]. Our current objectives are, on the one hand, to extend such measurements to higher order parameters such as diffusion and fluctuations of velocity and, on the other hand, to improve the NMR hardware to permit faster data acquisition which will yield better data for such parameters. In flows of concentrated suspensions and granular materials velocity fluctuations are hypothesized to be a crucial element of multi-phase transport processes [2, 3]. In this report, we describe progress made in several of these areas which represent pre-conditions to actually making such measurements in multiphase flows.

NMR AND LDA VELOCIMETRY IN A CURVED DUCT

In theory, NMR velocity measurements can produce 2- and 3-d datasets and arbitrary velocity components can be measured. In practice, mainly simple flows have been used to validate NMR methods, and the accuracy and precision of NMR velocity measurement techniques in complicated flows have not been assessed. An NMR velocity measurement system based on first order phase methods, and appropriate for measurement of a complex flow field with a primary velocity component and two smaller "secondary" components was implemented. Velocity dependent mis-registration was minimized by placing the phase-encoding interval immediately before the read-out interval and using a short echo-time. A geometry amenable to reliable measurement with transmission mode laser Doppler anemometry was chosen. The LDA measurements were done at the University of New Mexico in the laboratory of Prof. R. Truman.

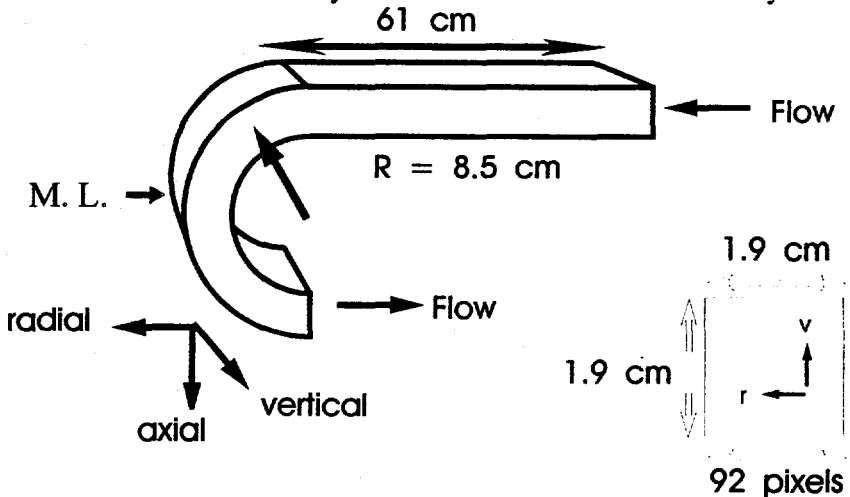

Figure 1. The dimensions of the Plexiglas flow phantom are shown. Flowing water entered a 61 cm straight duct, and turned in a section with centerline radius of 8.5 cm. Velocity components were measured after 90 ° of bend (M.L.). The cross section of the duct was 1.9 cm on a side.

A duct having square cross-section (1.9 ± 0.05 cm on a side) was constructed from Plexiglas sheet and cylinder stock. The dimensions of the duct are shown in Figure 1. Water from a constant height reservoir flowed through flexible tubing into a 61 cm straight section of square duct, turned through a 180° section of duct, with centerline radius 8.5 cm, and exited through a circular orifice into a second flexible tube. Tap water was used in the laser Doppler measurements. Water doped with Gd ($T_1 \approx 0.25$ s) was used in the NMR measurements.

The rf coil was modified to allow insertion of the phantom in the configuration shown. Slots were cut in the outer can and between the "rungs" in the resonant circuit. To install the flow model, the coil was partially disassembled, the curved section inserted through the rungs, the efflux tube connected, and the rf coil reassembled. The fact that the downstream end of the curved section was interrupted was less than optimal from the standpoint of comparison with previous results.

Three orthogonal components of velocity in a curved duct of square cross-section were measured with NMR, and two velocity components were also measured with laser Doppler techniques. Comparison between the two methods showed that accurate measurements of 3-dimensional flows can be made with NMR phase methods. Experiments using static references gave the most reliable measurements in low velocity regions. In Figure 2, a set of low flow rate measurements are shown.

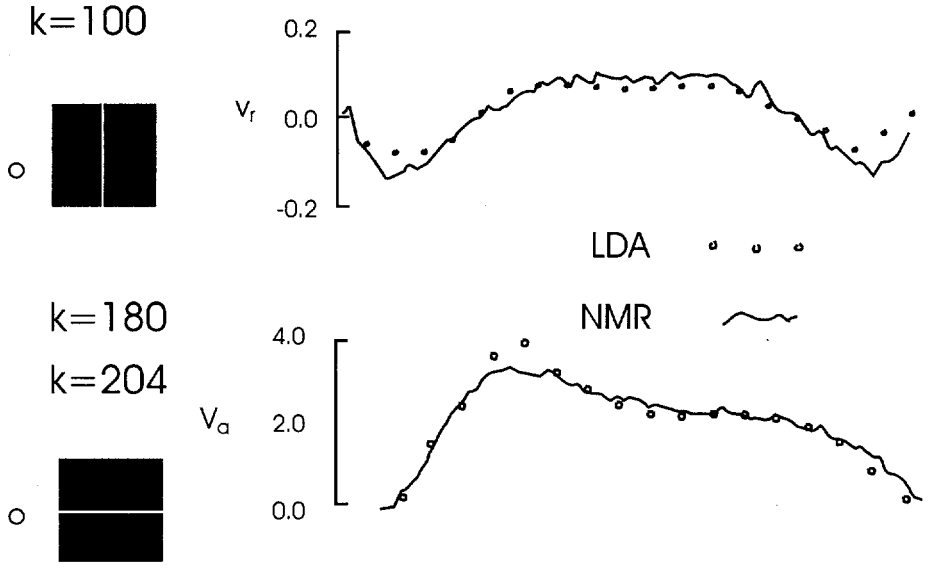

Figure 2. Comparisons between NMR (continuous lines) and LDA (points) are shown for the two velocity components measured with LDA. The schematics on the left show the locations of the measurement traverses, "O" refers to the outside of the curved tube.

At low flow rates, a single pair of vortices similar to low Dean number flow in a curved tube, symmetric about the plane containing the duct axis, is observed. The sense of the secondary flow is also the same as in a curved tube -- outward along the axis of symmetry, and inward along the walls. NMR velocimetry provides measurements over the cross-section, as opposed to measurements along a single line, and an example obtained at a higher flow rate is given in Figure 3. A vector plot shows the distribution of the secondary velocity components in the duct.

Below the vector plot, images of the velocity components are shown. The outer curved wall is shown on the left of the images and the vector plot. At this flow, two vortex pairs are prominent. The LDA confirmed the qualitative differences observed with NMR as a function of flow rate.

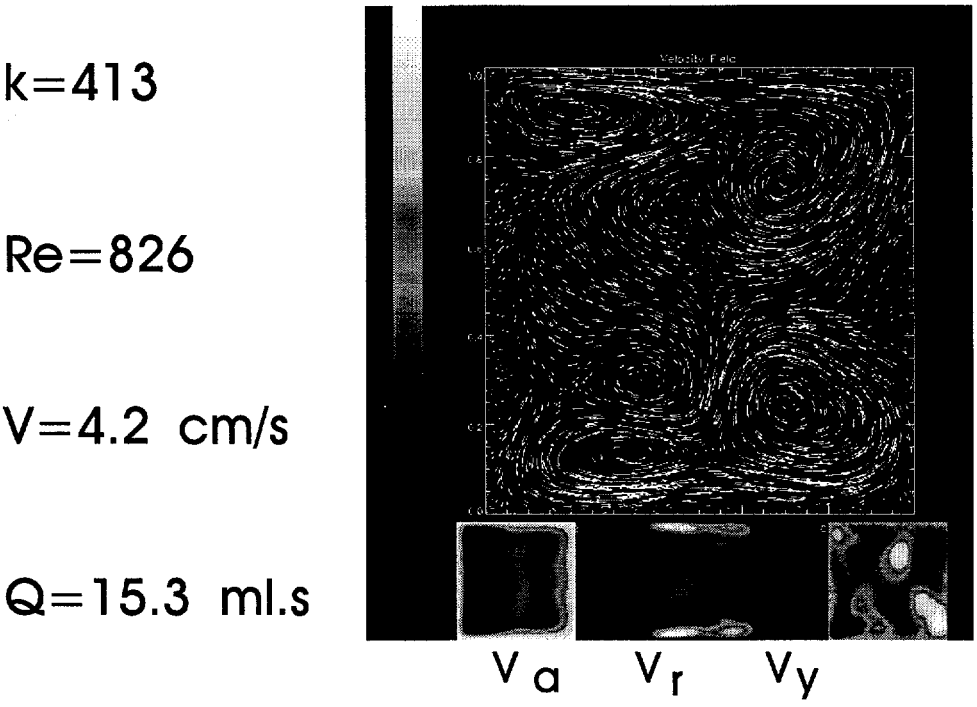

Figure 3. NMR data obtained in the curved duct at a flow of 15.3 cm^3/s are shown. a vector plot shows the presence of multiple pairs of vortices. The outer edge of the curved duct is on the left, as in Figures 1 and 2.

NMR DIFFUSION AND TURBULENCE MEASUREMENTS

Some of the techniques for measuring flow velocity by NMR were reviewed three years ago [1] and will not be reviewed here but the NMR methods for measuring molecular diffusion and turbulent diffusivity will be described.

Molecular diffusion measurements by NMR is an area we have gone into in the past two years. NMR can measure diffusion in the following way. In any NMR experiment, the nuclei with gyromagnetic ratio γ precess about the magnetic field B at frequency f according to the Larmor theorem: $f=(\gamma/2\pi)B$. Suppose an ensemble of spins is made phase coherent at $t=0$ and a magnetic field gradient g is applied for a time δ. The gradient causes spins at different locations z, to precess in a magnetic field intensity distributed according to gz, i.e., the spread of frequency across a distance z is $(\gamma/2\pi)gz$ and the incremental phase gain (or less) is $(\gamma/2\pi)gz\delta$. If, an equal but opposite gradient is applied at some later time Δ, the incremental phase changes reverse exactly and the ensemble finds itself with a regained coherence, leading to an unattenuated NMR signal. If, however, there is diffusion during the interval Δ, the full coherence will not be regained because the incremental phase changes during the two gradient pulses will not be equal

and opposite. Thus, NMR can be used to measure the diffusion coefficient by the signal attenuation caused by the diffusive motion of the molecules during an appropriately designed pulse sequence. In fact, any other incoherent motion will also attenuate the signal and this fact is used to study turbulent diffusivity.

Diffusion in restricted spaces can be studied by NMR, too, because the technique, as described above, measures the spin displacements in the interval Δ and the barriers to diffusion modifies the range of displacements. Because barriers can only limit the range of molecular motion, diffusion in restricted spaces can only increase the signal amplitude over unrestricted diffusion. There is an inherent difficulty that as more restrictive or, equivalently, more diffusive systems are studied, the gradient pulses that are used to define the range of incoherence will need to be made more effective. In the expression for the phase increment, given above, the only variables that can be changed for any given system are g and δ, the amplitude and duration of gradients. Because there is a practical limit to how large the gradient amplitude g can be made, there is a need to consider lengthening the duration δ. This is the root cause of much of our present research because much of the past derivations relating the diffusion coefficient D, the restricted spacing a, and the signal, depend on an assumption that the gradient pulse length δ obeys the relation $\delta << a^2/D$, i.e., it must be short enough that the molecule will not diffuse across the restricted region of dimension a during δ.

NARROW PULSE APPROXIMATION IN RESTRICTED DIFFUSION

An alternative manifestation of NMR signals being sensitive to molecular motion, besides the measurements of velocities, is the use of NMR to investigate molecular diffusion and the influence of barriers on such diffusion. Qualitatively, this is possible because any random molecular motion that takes place between two gradient pulses, one to dephase the spins and the other to rephase them, leads to an incomplete rephasing of the spins and shows up as a signal attenuation. Standard techniques for microstructure determination has existed for over three decades provided the magnetic field gradients used can be considered so short that no diffusion takes place during them.

The problem of diffusion in the presence of barriers, considered in this and next sections of this report, is an important one in many multiphase flow applications. The interphase boundaries usually represent significant barriers to diffusion so that any information on such boundaries leads to information about the multiphase structure.

Barriers to diffusion reduces the attenuation caused by diffusion because they reduce the range of translational motion for the spins. Therefore, ever stronger gradients must be used to study smaller and smaller restricted spaces. Because there is a limit to the strength of magnetic field gradients that can be created, there is a need to increase the duration of the gradient pulses. Thus, it is possible to violate the condition of "infinitely" narrow pulses, as diffusion is studied for smaller restricted regions. With the recent impetus for probing diffusion in ever smaller restricted spaces, this has become a meaningful question. A general expression for the attenuation has been derived from stochastic theory of random spin motion with an assumption of Gaussian displacements. The echo attenuation is divided into contributions A and B. A represents the contribution in the presence of the gradient while B is the contribution with the gradient off so that $F=A/(A+B)$ must be small for the narrow pulse approximation to hold.

Figure 4 is a plot of equal values of F as a function of two times, the duration of the gradient pulses δ, and the interval between the gradient pulses Δ, both in units of a^2/D which is the time for a molecule to diffuse with a diffusion coefficient D across the restricted space of dimension a.

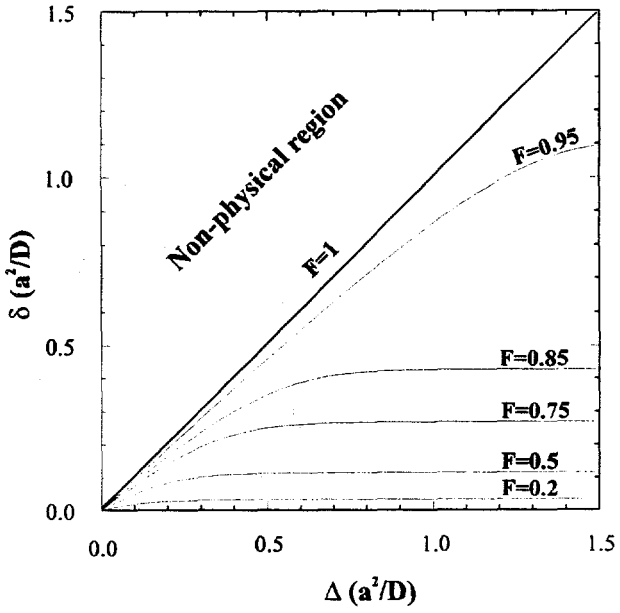

Figure 4. The fraction F of the total attenuation occurring during the application of the gradient pulses or a PGSE experiment as a function of the time intervals δ and Ω.

We have performed an alternative derivation of the same criterion for the validity of narrow pulse expressions for restricted diffusion from the diffraction-like behavior of NMR signal attenuation as a function of $qa=\gamma g\delta a/2\pi$, where q is, in effect, a reciprocal lattice vector for restricted diffusion [4]. In the narrow pulse approximation, the signal has minima at multiples of $q=1/a$. From the results of Blees [5], we plotted contour lines of constant fractional deviation of a particular minimum as a function of $\delta D/a^2$ and $\Delta D/a^2$ as before and the curves have shapes identical to those of Fig. 2.

We have found that the condition $F<<0.1$ is equivalent to a 5% shift in the second minimum position in qa. Although neither of these conditions seems very strict, they lead to the conclusion that gradient pulse duration δ must be much shorter than $0.02D/a^2$ in order for the narrow pulse expressions to be valid, a surprisingly strong criterion.

ANALYTICAL EXPRESSION FOR TIME-VARYING GRADIENTS

Although analytic expressions for NMR echo signals from an assembly of atomic nuclei undergoing diffusion in free and confined spaces were derived more than 30 years ago, a general expression without the assumption that molecular diffusion does not take place during the gradient pulses still does not exist. This is a problem that is gaining in importance as more and more smaller spaces or larger diffusion coefficients are studied. That this is so can be seen by the fact that the appropriate time unit for these problems is a^2/D which is how long a molecule with

diffusion coefficient D takes to diffuse across a restricted space a. Thus, smaller restricted spaces has the same effect as larger D.

We have derived an approximate analytical solution for diffusion in the presence of a gradient pulse that is not infinitesimally short by approximating the pulse with a series of gradient impulses each of which has a known narrow-pulse solution. We examined the convergence of the solution as a function of the order of the approximation, i.e., the number of impulses used, and found that 8 impulses is sufficient for most combinations of parameters. Because the method is general, it can be used for any shape gradient pulse, and its use is not limited only to rectangular pulses. Furthermore, the formalism is also applicable to non-uniform initial magnetization distribution.

STUDIES OF DIFFUSIVE AND TURBULENT SPECTRA

There have been suggestions of using gradient pulses that are tailored to probe particular frequency components of spectral density associated with coherent or incoherent motion [4]. We have derived relations for the signal attenuation as a function of sine and cosine coefficients of sinusoidal magnetic field gradients used during an otherwise standard NMR pulsed gradient spin echo diffusion experiments. We then performed experiments in three model systems: 1) diffusion measurements of water in an effectively unconfined space; 2) measurements of water diffusing between mica sheets spaced 25 μm apart; and 3) measurements turbulent diffusivity of water flowing in a circular pipe.

For water at room temperature in an unconfined space, the spectral density for diffusion is independent of frequency in the range studied, up to 100 Hz, as expected. On the other hand, in restricted spaces, deviation from the unconfined behavior is expected at the lower frequencies where the molecules have enough time to encounter walls. Experimentally, we measure the expected behavior, i.e., the spectral density is flat above 22 Hz but decreases below this threshold which is consistent with the known spacing between the mica sheets of 25 μm, as shown in Fig. 5.

We wish to extend this technique to the measurement of turbulent diffusivity. A preliminary experiment in water flowing in a circular pipe with Reynolds numbers between 2,000 and 12,000, yielded spectral densities that did not follow the correlation time-based curves used to fit spectral density for diffusion. This is to be expected because in turbulent diffusivity, the eddies are not uncorrelated as smaller ones are subdivided from the larger ones in order that the energy can be dissipated.

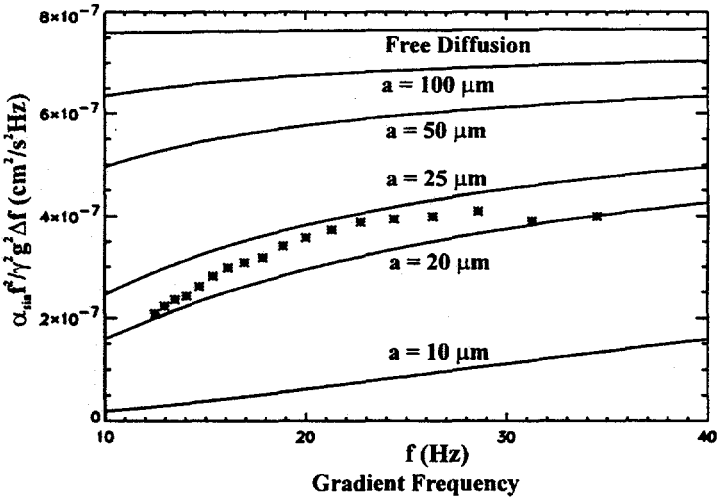

Figure 5. Results from spectral density of diffusion measurements (points) in a stack with 25 μm spacing shows good agreement with theoretical prediction. The technique is being evaluated for measurement of the size spectrum of turbulent eddies.

ACKNOWLEDGMENTS

This work was supported, in part, by the U. S. Department of Energy (DOE), Office of Basic Energy Sciences, via contract DE-FG03-93ER14316. Such support does not constitute an endorsement by DOE of the views expressed in this article. We benefited greatly from collaborations with R. C. Givler and L. A. Mondy of Sandia National Laboratories and A. L. Graham of Los Alamos National Laboratory in matters of multiphase flows.

1. S. A. Altobelli, A. Caprihan, E. Fukushima, and E.-K. Jeong, "Recent Results: NMR of Multiphase Flows," in Proceedings of the Tenth Symposium on Energy Engineering Sciences, May 11-13, 1992, Argonne National Laboratory, CONF-9205147; pp. 68-75.
2. J. T. Jenkins and D. F. McTigue, "Transport Processes in Concentrated Suspensions: The Role of Particle Fluctuations", In *Two Phase Flows and Waves* (D. D. Joseph and D. G. Schaeffer, eds.), Springer, 1990.
3 P. R. Nott and J. F. Brady, "Pressure-driven flow of suspensions: Simulation and Theory", *JFM* 1994, **275**, 157-199.
4. P. T. Callaghan, " Principles of Nuclear Magnetic Resonance Microscopy," Ch. 6-8, Oxford Univ. Press, New York, 1991.
5. M. H. Blees, J. Magn. Reson. A 109, 203 (1994).

INITIATION OF SLUG FLOW

Thomas J. Hanratty and Bennett D. Woods

University of Illinois
Urbana, Illinois 61801, U.S.A.

ABSTRACT

The initiation of slug flow in a horizontal pipe can be predicted either by considering the stability of a slug or by considering the stability of a stratified flow. Measurements of the shedding rate of slugs are used to define necessary conditions for the existence of a slug. Recent results show that slugs develop from an unstable stratified flow through the evolution of small wavelength waves into large wavelength waves that have the possibility of growing to form a slug. The mechanism appears to be quite different for fluids with viscosities close to water than for fluids with large viscosities (20 centipoise).

INTRODUCTION

The prediction of flow regimes is a central problem in the analysis of gas-liquid flows in pipes. Early work had used two-dimensional flow maps that employed variables such as the superficial gas and liquid velocities. These have proven unsatisfactory since they cannot represent the influence of the large number of variables that define multiphase systems. Pioneering works in this area are the papers presented by Dukler and his coworkers [1][2]. These papers suggest physical criteria and equations that define transitions from one regime to another. Flow maps can then be constructed for particular situations.

During the past 15 years the mechanisms suggested in references [1] and [2] have been examined more carefully and we now realize that some of the physics is flawed. This accounts for the failure of this approach to explain many observed phenomena. There is a need to develop an updated equation-based approach which utilizes improvements in our understanding of this problem.

This paper presents recent results on the transition from a stratified flow to a slug flow

in a horizontal pipe. Taitel & Dukler [1] suggest, on the basis of geometric arguments, that the height of the liquid in the stratified flow, h_L, needs to be larger than one-half of the pipe diameter, D, in order for a slug to form. This constitutes a necessary condition for the existence of slugs. A closer examination of data reveals that the proposed critical h_L/D is too large.

This paper summarizes results of a M.S. thesis from this laboratory [3] which relates the stability of slugs to the height of the liquid. The idea behind the analysis is quite simple: Slugs pick up liquid at the front as they propagate downstream and shed liquid at the rear. If the pickup rate is smaller than the shedding rate, slugs will decay. The critical problem is to define the volumetric shedding rate, Q_L.

Ruder et al [4] developed this idea by assuming the back of the tail as a Benjamin bubble so that

$$Q_L = A\left[0.542\ (gD)^{0.5}\right] \tag{1}$$

where A is the pipe area and D is the pipe diameter. This assumption provides only a limiting value of the critical h_L/D at small gas velocities. A series of studies were, therefore, carried out in which Q_L was measured for individual slugs. The system was air and water flowing in a horizontal pipe. The results of this study provide a necessary condition for the existence of a stable slug that is consistent with measurements.

For large h_L/D, Wallis and Dobson [5] suggested that the initiation of slugs might be considered to result from the stability of a stratified flow to long wavelength disturbances. The following critical condition was suggested:

$$U-u = K\left[\frac{g\rho_L H_G}{\rho_G}\right]^{\frac{1}{2}} \tag{2}$$

where U is the gas velocity, u, the liquid velocity and H_G, the height of the gas space. The use of an inviscid analysis gives K=1, but Wallis found for air and water that $K\approx\frac{1}{2}$. Taitel and Dukler adapted (2) to the geometry of a circular pipe and suggested that

$$K = \left(1-\frac{h_L}{D}\right) \tag{3}$$

The inviscid analysis yields a wave velocity, C, equal to u. Therefore, the inertia of the liquid is neither stabilizing nor destabilizing. Lin & Hanratty [6] carried out a viscous long wavelength analysis. The wave velocity is, then, not equal to u and liquid inertia is destabilizing. They found that K is a function of liquid viscosity. For water $K\approx\frac{1}{2}$; for liquids with viscosities greater than 20 centipoise, K=1.

Equation (2) has two important features. It suggests that a slug evolves directly from

a long wavelength disturbance that grows until it reaches the top of the pipe. It also suggests that the gas velocity needed to generate a slug increases with $D^{1/2}$. Measurements with air and water agree with this analysis [7]. However, studies with viscous liquids [8] reveal no influence of pipe diameter if the liquid viscosity is 20 centipoise or greater.

This disagreement suggests that the physical mechanism suggested by (2) is incorrect even though it correctly predicts the transition for an air-water flow. This paper summarizes recent results which show that slugs evolve from small wavelength waves and not from the direct growth of a large wavelength instability.

The implications of these new results from the viewpoint of predicting flow regimes is discussed.

STABILITY OF A SLUG

If conservation of mass is used in a frame of reference moving with a slug, the following equation is obtained for incompressible fluids:

$$\left(C-u_{LI}\right) A_{LI} - Q_L = A\left(1-\alpha\right)\frac{dL}{dt}, \tag{4}$$

where C is the slug velocity, u_{L1} the velocity of the liquid in the layer in front of the slug, A_{LI}, the area occupied by the liquid in front of the slug, α, the void fraction in the slug, L, the length of the slug and t, time. For a neutrally stable slug, dL/dt=0, and

$$A_{LI}^{C} = \frac{Q_L}{C-u_{LI}} \tag{5}$$

For $A_{L1}<A_{L1}^{C}$ slugs will decay; for $A_{L1}>A_{L1}^{C}$ slugs will grow.

If the back of a slug can be modelled as the nose of a bubble an equation for C similar to what is used for elongated bubbles in vertical tubes can be explored:

$$C=C_{\infty} + C_o u_{L3}, \tag{6}$$

where C_{∞} is the bubble velocity in a stationary fluid and u_{L3} is the average liquid velocity

$$u_{L3}=\frac{U_{SG} + U_{SL}}{1-(S-1)\alpha} \tag{7}$$

where U_{SG} is the superficial gas velocity, U_{SL}, the superficial liquid velocity and S the ratio of the gas and liquid velocities in the slug.

The second term in (7) represents the contribution of fluid convection to the slug velocity. For vertical flow with a turbulent liquid C_o has a value approximately equal to the ratio of the centerline and average velocities, $C_o \approx 1.2$.

The motion of the bubble relative to the liquid causes a displacement of liquid inside the slug given by

$$Q_L = \left(C - u_{L3}\right) A\left(1-\alpha\right) \tag{8}$$

Now if (6) is substituted into (8) and (5) the following relations are obtained:

$$Q_L = \left[C_\infty + \left(C_o - 1\right) u_{L3}\right] A\left(1-\alpha\right) \tag{9}$$

$$A_{LI}^{C} = \frac{\left[C_\infty + \left(C_o - 1\right) u_{L3}\right] 1-\alpha}{\left[C_\infty + C_o u_{L3} - u_{LI}\right]} \tag{10}$$

At large gas velocities u_{L1} can be neglected and $C_\infty << C_o u_{L3}$ so

$$A_{LI}^{C} = \frac{\left(C_o - 1\right)\left(1-\alpha\right)}{\left(C_o\right)} \tag{11}$$

If C_o=1.3 and $(1-\alpha) \approx 0.3$, equation (11) gives

$$\frac{A_{LI}}{A} = 0.16 \tag{12}$$

$$\frac{h_{LI}}{D} = 0.21 \tag{13}$$

DESCRIPTION OF EXPERIMENTS

The flow facility consists of a horizontal pipeline with a diameter of 0.0953 m and a length of 26.5 m. The experiments were conducted at atmospheric conditions. The gas and liquid phases were combined at the beginning of the pipeline in a tee section with the liquid phase flowing in the run and the gas phase entering from the top of the tee.

Measurements of the variation of the liquid holdup were obtained with a conductance probe that consists of two parallel chromel wires. A complete description of the film height analyzer, including a circuit diagram, may be found in Williams [9].

Conductance probes were used at $\frac{L}{D}$ = 200, 220, and 250. Two conductance probes are needed to measure the slug velocity and the flow of liquid out the tail of the slug. A third conductance probe is added in order to observe changes in a slug as it progresses along the pipeline. The third probe also provides better measurements of C and Q_L by averaging results from the first and second probes and from the second and third probes.

Pressure pulsations associated with the passage of a slug were measured with a piezoresistive pressure transducer located 0.127 m downstream of the first conductance probe.

The transducer was mounted flush with the wall so that no disturbances were introduced into the flow.

The magnitude of the signals from the conductance probes give the liquid holdup, $(1-\alpha)$, when a slug passes and the height of the liquid layer when a stratified flow was present. The slug velocity, C, was determined from the time needed for a slug to move between two of the measuring stations.

Values of Q_L were obtained from measurements at two stations using the equation

$$Q_L = \left(C - u_{Ll}\right) A_{Ll} - \frac{dV}{dt} \tag{14}$$

This was accomplished by attaching a control volume fixed to back of the slug.

Term dV/dt was determined by measuring the change of the volume of the liquid inside the control volume between two stations. The front of the control volume was located sufficiently ahead of the slug so that the area of the stratified flow in the front of the slug, A_{Ll}, was the same at all three stations. Velocity u_{Ll} was calculated from A_{Ll} and the gas velocity by using stratified flow relations developed by Andritsos and Hanratty [10].

STABILITY OF SLUGS

Measurements of Q_L are presented in Figure 1. It is noted that they agree with the Benjamin solution only for small values of U_{SG}. These measurements and equation (5) were used to calculate critical values of A_{Ll} (or h_{Ll}/D). A trace obtained from the conductance probes is shown in Figure 2. Peaks could be identified as slugs from measurements of pressure pulses. Neutral stability is designated by the line indicating the stability height. The correlation is not perfect, but there is a tendency to find growing slugs when $A_{Ll} > A_{Ll}^{C}$ and decaying slugs when $A_{Ll} < A_{Ll}^{C}$.

Values of the critical h_{Ll}/D for different U_{SG}, calculated from (5) are shown as the dashed curve in Figure 3. The solid curve is the stability condition for a stratified flow. The points are the observed h_L/D at which slugs appear for a fixed gas flow. At low gas velocities the necessary condition for the existence of slugs lies below the stability condition for a stratified flow. However, at high gas velocities the opposite is the case. Good agreement is noted between the observed transition at large U_{SG} and the necessary condition for the existence of a slug.

The curve representing the stability of a stratified flow would be shifted to the left with increasing gas density. Therefore, at sufficiently high gas densities one could expect that the initiation of slugging would be defined by stability conditions for a slug at all gas flows, rather than just at high gas flows.

The asymptotic behavior of the dashed curve in Figure 3 gives a critical $h_L/D \approx 0.21$. This is exactly the prediction from (11) if $C_o = 1.31$. Measurements of slug velocity are represented quite well by the equation

$$C = \left\{ \left[0.541 (gD)^{\frac{1}{2}} \right]^2 + \left[1.31 \left(U_{SG} + U_{SL} \right) \right]^2 \right\}^{\frac{1}{2}} \tag{15}$$

From (7) and (15) it is observed that

$$\frac{C_o}{1 + (S-1)\alpha} = 1.31 \tag{16}$$

Therefore C_o=1.31 corresponds to a slip ratio of 1.

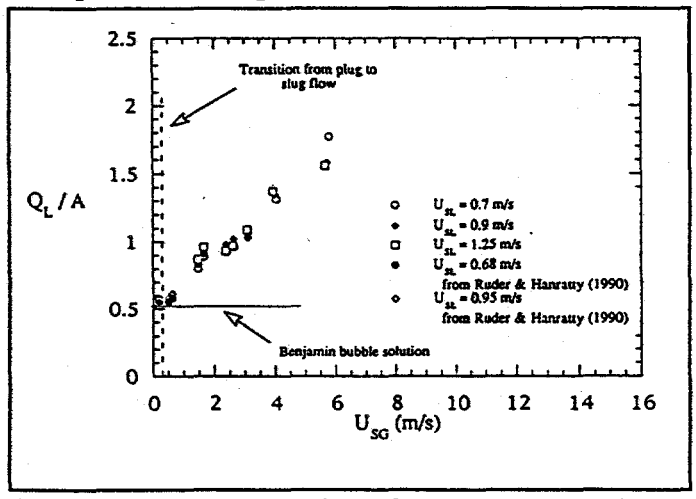

Figure 1 The mean value of the shedding velocity Q_L/A at each experimental flow condition as a function of the local superficial gas velocity.

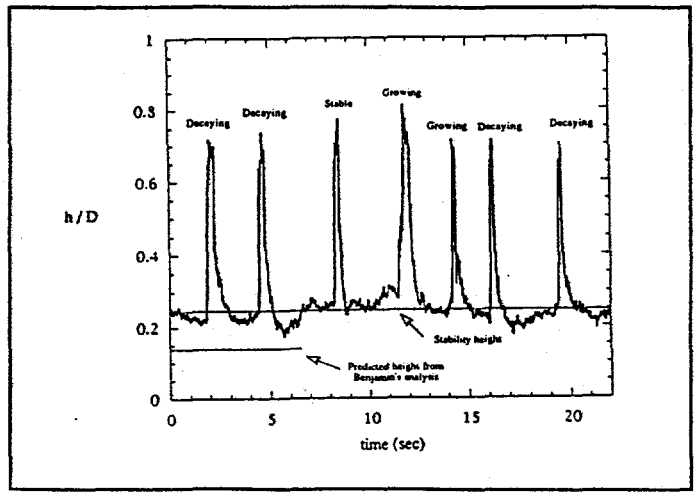

Figure 2 Liquid holdup profile at L/D=250 for U_{SG}=4.35 m/s and U_{SL} = 0.7 m/s.

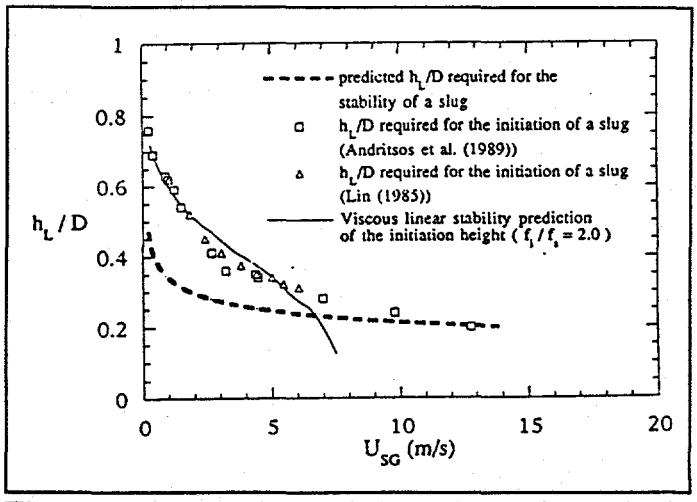

Figure 3 Comparison of the height of the liquid layer required for a stable slug with observations of the height of the liquid required to initiate a slug. (D=0.0953 m, Air - water system)

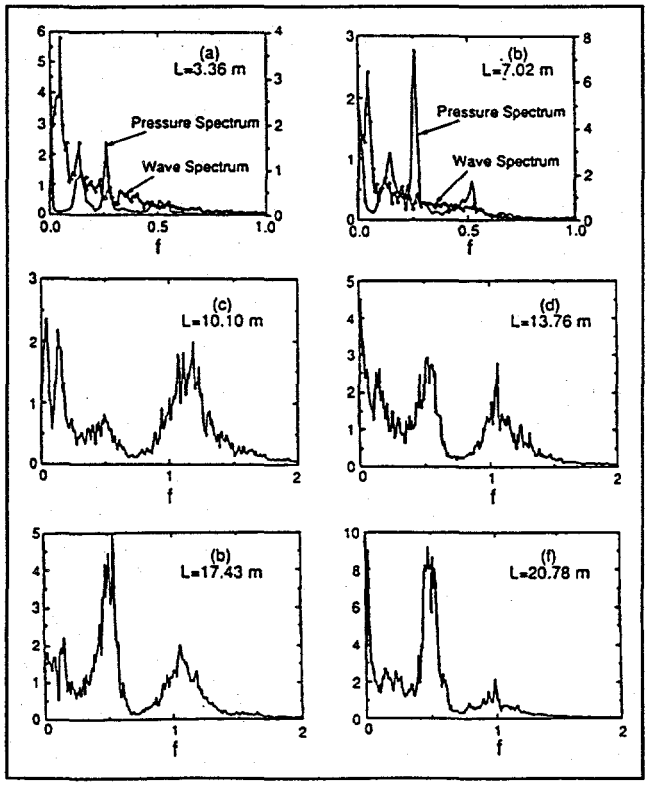

Figure 4. Power spectra of a liquid flow close to transition (u_{SG}=1.0m/s). The dimensionless spectra density functions are multiplied by 10^6. Wave spectra are on the left ordinate. Pressure spectra are on the right.

STABILITY OF A STRATIFIED FLOW

The transition to slug flow shown in Figure 3 for small gas velocities is governed by the stability of stratified flow. The mechanism for this transition for air/water has recently been explored by Fan et al [11]. A carefully designed entry was used to bring the gas and liquid together smoothly. Conductance probes were located along the pipeline to study the evolution of waves to form a slug.

Measured wave spectra are shown in Figure 4 for U_{SG}=1 m/s. The abscissa is the frequency (in cps) made dimensionless with $\sqrt{gD}$. The ordinate is the dimensionless spectral density function. The measurements at L=3.36 m and at L=7.02 m show a primary peak at f=0.06 (0.6 cps) and a secondary peak at f=0.12 (1.2 cps). These would correspond to very long wavelength waves that are observed visually as a swell. They would be predicted to appear by long wavelength theory. These waves do not evolve into a slug. Two peaks at f=0.12 and f=0.25 are observed in the spectral density function for the pressure fluctuations.

The peaks at f=0.06 and f=0.12 are still evident at L=10.1 m, but a peak with a large amount of energy appears at f=1.2 (12 cps). This corresponds to a capillary-gravity wave generated by Jeffrey's sheltering mechanism. A peak with a smaller amount of energy is also observed at f=0.5 (5 cps). As discussed in [11] the larger wavelength wave evolves from the f=1.2 wave through a resonance mechanism. This peak grows with distance downstream and the higher frequency peak shifts from f=1.2 to f=1.0. At 20.78 m, the f=0.5 wave is dominant. In a longer pipe this wave could stabilize to a fixed height (at which energy fed by the gas flow is balanced by viscous dissipation) or it could continue to grow until it breaks or forms a slug. There appears to be a critical liquid height (larger than that required for the existence of a stable slug), below which slugs cannot form from these waves.

The mechanism for the formation of slugs in these experiments at low gas flows appears to be different from what is suggested by (2). This is a paradox since equation (2) does a good job in predicting the initiation of slugs for liquids with viscosities close to that of water.

Figure 5 shows transition data obtained for a 100 cp liquid in a 9.53 cm pipe. The open triangular points represent a transition to slugs. The open squares indicate a transition to large amplitude waves. Because of the large viscosity, waves of the type described in Figure 4 are not present. The stratified flow that exists to left of the triangles has a smooth interface.

The transition points at large U_{SG} are, more than likely, defined by the stability condition for a slug, equation (5). However, it is noted by comparing Figures 3 and 5 that transition occurs at slightly higher h_L/D for the more viscous liquid. This suggests that C_o in (6) could be larger for large viscosity liquids, as has been found for large bubbles in a vertical tube.

At small gas flows the initiation of slugs, shown in Figure 5, occurs because of an instability of the stratified flow. A comparison of Figures 3 and 5 shows that larger values of h_L/D are required for an instability to occur with large viscosity liquids. The waves described in Figure 4 cannot occur. The first instability of the stratified flow occurs when the gas gap becomes small enough (for a given gas flow, U_{SG}) that the gas velocity above the liquid can cause a Kelvin-Helmholtz instability. The first disturbances that appear at the interface are capillary-gravity waves. These rapidly evolve into slugs by a mechanism which

has not been identified. The solid curve in Figure 5 represents the critical condition for the initiation of a Kelvin-Helmholtz instability.

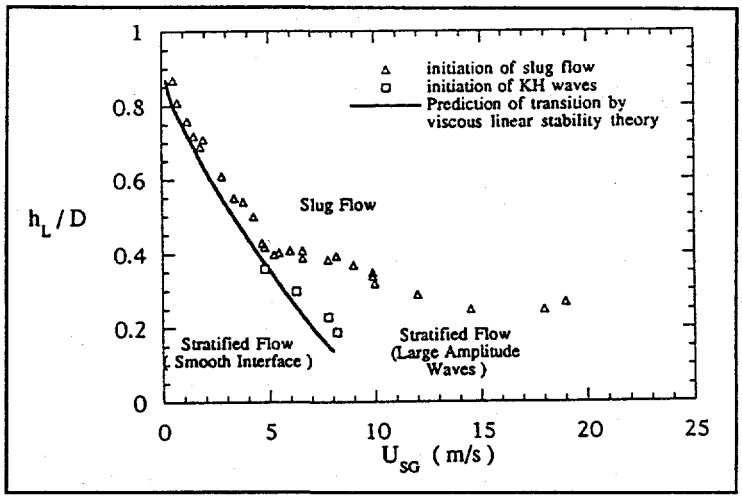

Figure 5 Initiation of slug flow or KH waves for a 100 cp liquid in a horizontal 9.53 cm pipe.

DISCUSSION

The flow regime criteria developed by Dukler and his coworkers have had an important impact on the analysis of two-phase flows. They are widely used - despite the recognition that they do not always give accurate results. Recently, more careful attention has been given to the physics defining the transitions. It is now possible to use these new insights to develop improved predictions of flow regimes.

A necessary condition for the existence of slugs of $h_L/D=0.5$ was suggested in [1] on the basis of geometric arguments. This paper develops an improved definition of this condition by considering the stability of slugs.

Equation (2) along with the long wavelength viscous analysis of Lin & Hanratty [6] does a good job in predicting the evolution of slugs from the instability of a stratified flow if the liquid viscosity is close to that of water. However, the observed mechanism appears to be different from what is suggested by (2). This issue needs to be resolved.

The waves which eventually evolve into slugs for stratified air-water flows are generated by a mechanism whereby energy fed to the waves by gas phase pressure variations in phase with the wave slope is larger than energy dissipated by viscous effects. As the viscosity of the liquid increases the critical gas velocity for the appearance of these waves also increases. For large enough liquid viscosities these waves are not present. In this case slugs evolve from capillary-gravity waves generated by a Kelvin-Helmholtz mechanism, whereby destabilization results from pressure variations 180° out of phase with the wave height. When the height of the liquid layer is too small to sustain a stable slug these Kelvin-Helmholtz waves evolve into large amplitude irregular waves. Under these conditions the initiation of slugging is governed by the stability condition for slugs.

REFERENCES

1. Y. TAITEL and A. E. DUKLER, "A Model for Predicting Flow Regime Transitions in Horizontal and near Horizontal Gas-Liquid Flow," *Int. J. Multiphase Flow* 13, 577 (1977).
2. Y. TAITEL, D. BARNEA and A. E. DUKLER, "Modeling Flow Pattern Transitions for Steady Upward Gas-Liquid Flow in Vertical Tubes," *A.I.Ch.E. Journal* 26, 345 (1980).
3. B. K. WOODS, "Shedding Rates of Slugs in Two Phase Horizontal Pipe Flow," Ph.D. thesis, Univ. of Illinois, Urbana (1995).
4. Z. RUDER, P. J. HANRATTY and T. J. HANRATTY, "Necessary Conditions for the Existence of Slugs," *Int. J. Multiphase Flow* 15, 135 (1989).
5. G. B. WALLIS and J. E. DOBSON, "The Onset of Slugging in Horizontal Stratified Air-Water Flow," *Int. J. Multiphase Flow* 1, 173 (1973).
6. P. Y. LIN and T. J. HANRATTY, "Prediction of the Initiation of Slugs with Linear Stability Theory," *Int. J. Multiphase Flow* 12, 79 (1986).
7. P. Y. LIN and T. J. HANRATTY, "Effect of Pipe Diameter on Flow Patterns for Air-Water Flow in Horizontal Pipes," *Int. J. Multiphase Flow*, 13, 13 (1987).
8. N. ANDRITSOS, L. WILLIAMS and T. J. HANRATTY, "Effect of Liquid Viscosity on the Stratified-Slug Transition in Horizontal Pipe Flow," *Int. J. Multiphase Flow*, 15, 877 (1989).
9. L. R. WILLIAMS, "Effect of Pipe Diameter on Horizontal Annular Two-Phase Flow," Ph.D. thesis, Univ. of Illinois, Urbana (1990).
10. N. ANDRITSOS and T. J. HANRATTY, "Influence of Interfacial Waves in Stratified Gas-Liquid Flows," *A.I.Ch.E. Journal* 33, 444 (1987).
11. L. FAN, F. LUSSEYRAN and T. J. HANRATTY, "Initiation of Slugs in Horizontal Gas-Liquid Flows," *A.I.Ch.E. Journal* 11, 1741 (1993).

THE DRIFT FORCE ON AN OBJECT IN AN INVISCID WEAKLY-VARYING ROTATIONAL FLOW

Graham B. Wallis

Thayer School of Engineering, Dartmouth College
Hanover, NH 03755 U.S.A.

ABSTRACT

The force on any stationary object in an inviscid incompressible extensive steady flow is derived in terms of the added mass tensor and gradient of velocity of the undisturbed fluid. Taylor's theorem is extended to flows with weak vorticity. There are possible applications to constitutive equations for two-phase flow.

INTRODUCTION

Any vector field (e.g., velocity) may be generated by a combination of flux and circulation sources. For example, an object in a potential flow may be "created" by putting a distribution of dipoles over its surface, to represent the jump in potential there, or a set of circulation source loops around its surface, to account for the jump in velocity [1]. A set of internal sources and sinks could also be used. Though various combinations of these elements can be selected, the resulting system has a unique dipole moment or **polarization**, characterizing a particular object in a certain environment [2].

Flux sources, which are simpler conceptually, usually have little physical meaning and resemble mathematical devices for setting up a real flow situation. Circulation sources are physically evident as vortex lines which have a clearer manifestation and actually exist in a real flow with rotation. The contribution of this paper is to show how weak vorticity in an inviscid flow interacts with a solid object. The results are of a general nature and apply to objects of any shape. Vorticity is bound in the fluid and is "entrained" by the object in much the same way as fluid is entrained by "drift". The added mass tensor provides the theoretical key to the solution of both problems.

FLUX SOURCES

An object of volume V moving at velocity $\mathbf{v}$ in an irrotational flow may be generated by internal sources and sinks of strength m_i located at $\mathbf{r}$.

The dipole moment of these sources is [1]

$$\mathbf{D} = \int \mathbf{r} m_i = \int \phi \mathbf{ds} + V\mathbf{v} \tag{1}$$

If the object is moving in an extensive fluid at rest far away, the added mass tensor $\underline{\underline{C}}$ is defined by

$$\int \phi \mathbf{ds} = \underline{\underline{C}} \cdot \mathbf{v}V \tag{2}$$

which does not depend on the details of conditions "at infinity" in the way that the induced net momentum does. Because of the linearity of Laplace's equation in this situation we may define the **polarizability**, $\underline{\underline{D}}$, such that

$$\mathbf{D} = \underline{\underline{D}} \cdot \mathbf{v}V \tag{3}$$

Combining (1) to (3) the two tensors are simply related by

$$\underline{\underline{D}} = \underline{\underline{C}} + \underline{\underline{I}} \tag{4}$$

Since $\underline{\underline{C}}$ is a symmetric tensor depending only on the shape of the object, so is $\underline{\underline{D}}$.

When the same object is at rest in fluid with a uniform velocity $\mathbf{U}$ far away, the sources and sinks are the same and dependent on the relative motion so that

$$\mathbf{D} = -\underline{\underline{D}} \cdot \mathbf{U}V \tag{5}$$

The force on a flux source is $-\rho \mathbf{U} m_i$. Forces between sources are mutual and cancel. There is no net force from the fluid on the sources (i.e., on the object) because $\sum m_i = 0$. The moment of the forces from the fluid on the object is, using (4) and (5),

$$\begin{aligned} \mathbf{M} &= -\sum \mathbf{r} \times \rho \mathbf{U} m_i = \rho \mathbf{U} \times \sum \mathbf{r} m_i \\ &= \rho \mathbf{U} \times \mathbf{D} = -\rho V \mathbf{U} \times \underline{\underline{D}} \cdot \mathbf{U} = \rho V \mathbf{U} \cdot \underline{\underline{C}} \times \mathbf{U} \end{aligned} \tag{6}$$

which is a compact version of the result given by Lamb [3].

When the object is in an irrotational flow that varies slowly on the scale of the object and can be described by a velocity

$$\mathbf{u} = \mathbf{U} + \mathbf{r} \cdot \nabla \mathbf{U} \tag{7}$$

before insertion of the sources, the resultant force is

$$F_p = \sum -\rho(m_i + m_i')(\mathbf{U} + \mathbf{r} \cdot \nabla \mathbf{U}) \tag{8}$$

where m_i' represents a small perturbation,with $\sum m_i' = 0$, in response to the gradient in the external field. To first order, (8) reduces to

$$\mathbf{F}_p = -\rho \sum m_i \mathbf{r} \cdot \nabla \mathbf{U} = -\rho \mathbf{D} \cdot \nabla \mathbf{U} \tag{9}$$

which we call the "polarization force" representing an interaction between the polarization and the external velocity gradient. Using (4) and (5), (9) can be put in the form

$$\mathbf{F}_p = \rho V(\mathbf{U} \cdot \nabla \mathbf{U} + \mathbf{U} \cdot \underline{\underline{C}} \cdot \nabla \mathbf{U}) \tag{10}$$

where the first term is the "buoyancy" force due to the external pressure gradient and the second term is compatible with a result derived by Taylor [4] and described by Lamb [3] in the alternative form

$$\mathbf{U} \cdot \underline{\underline{C}} \cdot \nabla \mathbf{U} = \nabla(\frac{1}{2}\mathbf{U} \cdot \underline{\underline{C}} \cdot \mathbf{U}) \tag{11}$$

which follows because $\underline{\underline{C}}$ is symmetric and $\nabla \times \mathbf{U} = 0$ in an irrotational flow.

CIRCULATION SOURCES

When a flow is rotational it contains vortices (circulation sources) that travel with the fluid. If a certain vortex line is marked, it will follow a trajectory which is the same as for a "time-line" recording the position of elements of fluid composing the vortex at subsequent intervals of time. If the vorticity is weak, these trajectories are determined by the "main" flow, the effect of vortices on each other being small. This picture formed the basis of Lighthill's analysis [5] of the wake of an object in a shear flow, and was later used by Auton [6] to derive the "lift" force on a sphere.

A vortex line passing close to an object will be deformed and will "drift" just as elements of fluid do. The velocity field from the vortex may be countered by internal sources m_i'. Since these have zero total sum and are "small" for "small" vorticity they contribute no net force, as in (8), to first order. Moreover, in an inviscid fluid, no net circulation is generated on the object. "Bound" vorticity would have to be generated some other way and it not part of the present analysis.

CROSS-STREAM VORTICITY

Let the main flow past a stationary object have velocity $\mathbf{U}$ in the x-direction. Let the oncoming flow have uniform vorticity in the cross-stream z-direction. Because of the component C_{xx} of the added mass coefficient, and the resulting impulse on the fluid by way of (2), there is a drift volume in the wake of the object representing fluid, and corresponding vorticity, that is retarded by the presence of the object.

We now consider a rectangular control volume around the object, with faces normal to the coordinate axes and large compared with the object. The total z-direction vorticity in this volume is augmented by an amount $C_{xx}V\omega_z$ because of the drift of fluid into this volume, as described by Lighthill [5] and sketched in Figure 1. The corresponding perturbations in velocity on the boundaries of the control volume may be determined from the basic equation of vector field theory:

$$\int \boldsymbol{\omega} dV = -\int \mathbf{u} \times \mathbf{ds} \tag{12}$$

This is to be applied to the z-component of vorticity, and therefore picks up the following components on the x- and y-faces of the control volume,

$$C_{xx}V\omega_z = \int \omega_z dV = \int \tilde{u}_y ds_x - \int \tilde{u}_x ds_y \tag{13}$$

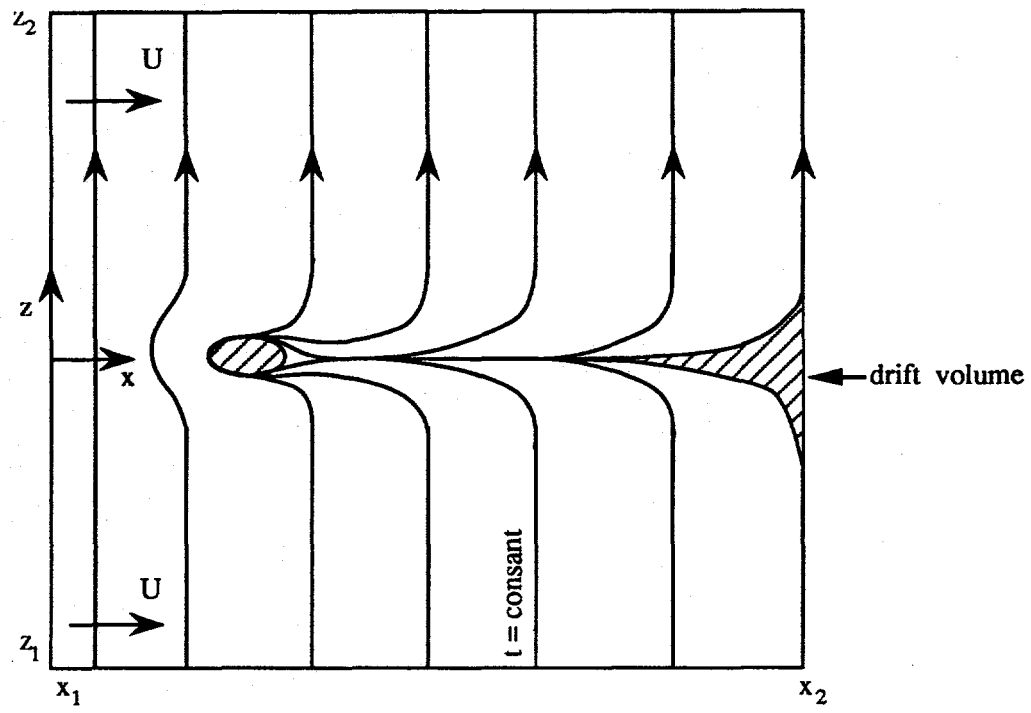

Figure 1. Vortex Lines, Originally in the z-Direction, Stretched Around an Object and Entrained by Drift in the Wake

Multiplying by ρU we get

$$\rho V C_{xx} U \omega_z = \int \rho U \tilde{u}_y ds_x - \int \rho U \tilde{u}_x ds_y \tag{14}$$

Now, on the y-faces far from the object the main flow is in the x-direction and therefore the perturbation in pressure is given by Bernoulli's equation as

$$\tilde{p} = -\rho U \tilde{u}_x \tag{15}$$

Using (15) in (14), the right-hand side is recognizable as the sum of the y-direction momentum flux through the x-faces and the pressure over the y-faces, which are exactly the terms in a momentum balance which shows the "drift" force from the fluid on the object in the y-direction to be,

$$F_{dy} = -\rho V C_{xx} U \omega_z \tag{16}$$

A more detailed derivation of this force is given in [7], where it is also related to the x-component of vorticity induced in the wake by bending of the vortex lines, originally in the z-direction. This x-vorticity in the wake loops around the object, the overall appearance resembling the bound vorticity and trailing vortex system for a conventional lifting surface.

Now, if the object is not oriented with one of its principal axes of added mass in the direction of the main flow, there will also be components of "interphase impulse", given by (2), in the transverse directions. For instance, the component C_{xy} (since $\underline{\underline{C}}$ is symmetric, it is not necessary to be fussy about the order of the subscripts) leads to displacement of the fluid streamlines in the y-direction due to relative velocity in the x-direction. The z-direction vortex lines that were

parallel upstream of the object are then bent in the wake as a result of this transverse "drift". If we look upstream in the negative x-direction from the far wake, these vortex lines will all be bent into the same shapes, independent of x, and form a set of vortex sheets, representing "streamlines" for vorticity (Figure 2). The z-direction vorticity in the wake is related to the corresponding velocity variations by

$$\omega_z = \frac{\partial u_y}{\partial x} - \frac{\partial u_x}{\partial y} \tag{17}$$

but $\partial u_y/\partial x = 0$ in a fully-developed wake and therefore

$$u_x = -\int \omega_z dy \tag{18}$$

The right hand side of (18) represents the z-vorticity flux which is constant along a "streamline" for vorticity. Therefore the cross-sections of vortex sheets in Figure 2 also represent contours of constant u_x. The perturbation in u_x is

$$\tilde{u}_x = -\int \tilde{\omega}_z dy = \omega_z Y \tag{19}$$

where Y is the displacement of a vortex line now lying at the point of interest. When (19) is integrated over the entire face of the control volume lying in the wake, there is a perturbation in outgoing mass flux in the amount

$$\dot{m} = \rho \int \tilde{u}_x dy dz = \rho\omega_z \int Y dy dz = -\rho\omega_z V C_{xy} \tag{20}$$

where the concept of "drift volume" in the y-direction has been used. The negative sign is needed because $\mathbf{v}$ in (2) is replaced by $-\mathbf{U}$. The increased mass flux $\dot{m}$ comes from fluid that is drawn into the sides of the control volume. The mechanism for "pumping" this secondary flow is the perturbation in vorticity in the wake. These perturbations form loops in the y-z plane that add to the original uniform vorticity to produce the pattern shown in Figure 2. In the extended wake these loops form cylindrical sheets of secondary vorticity that generate axial velocity much as the coils on a solenoid generate its axial magnetic field.

A fully developed wake cannot maintain pressure perturbations (which would lead to further "development") and the momentum flux out of the control volume on the wake side is increased by

$$\rho \int \left[(U + \tilde{u})^2 - U^2\right] dy dz = 2U\dot{m} \tag{21}$$

Combining (21) with the flux of momentum into the sides of the control volume, $\rho U\dot{m}$, the net force due to velocity perturbations induced by vorticity is

$$F_{dx} = \rho V U C_{xy} \omega_z \tag{22}$$

Results similar to (16) and (22) follow if there is vorticity in the transverse y-direction.

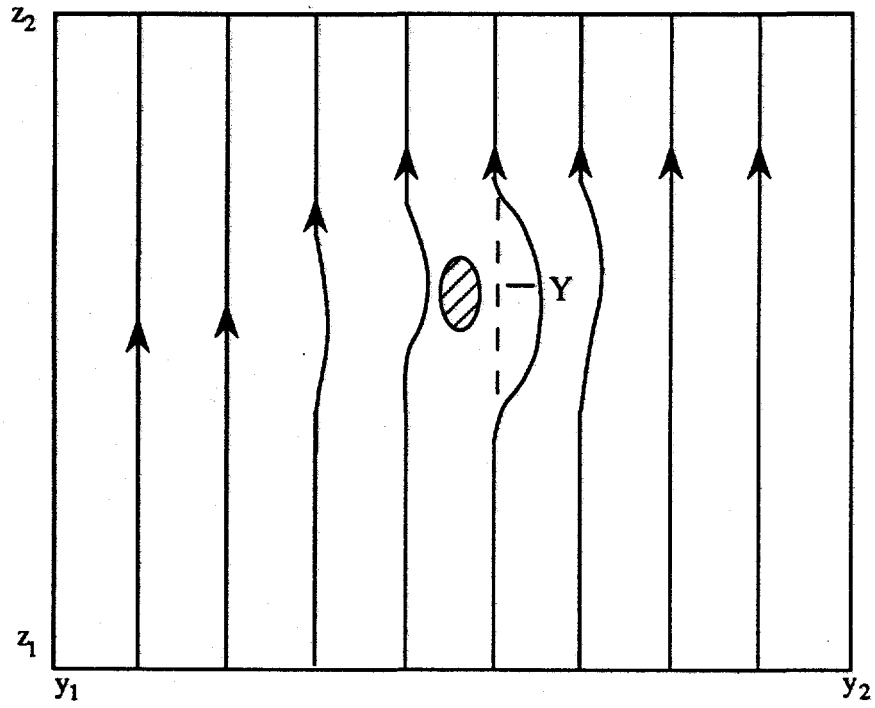

Figure 2. Drift of z-Direction Vortex Lines in the y-Direction Behind an Asymmetric Object

STREAMWISE VORTICITY

A uniform upstream vorticity ω_x is carried along the streamlines of the primary flow and will be diverted sideways in the wake if there are components C_{xy} and C_{xz} to the added mass tensor. The effect of C_{xy} is to displace streamlines in the y-direction, which can also be represented by Figure 2 which now represents the location in the wake of vortex sheets originally in the x-z plane. These contours now represent constant values of $\tilde{u}_z$ in the amount $-Y\omega_z$, by arguments resembling those leading to (19). This produces negligible effect on the sides of the control volume but introduces a perturbation in the flux of z-momentum in the wake and a corresponding drift force in the amount

$$F_{dz} = \rho V U C_{xy} \omega_x \tag{23}$$

similar effects occur if there is a C_{xz}, with corresponding results.

SYNTHESIS

All of the components of "drift force" derived above may be added together, assuming each is small so that interactions can be neglected, to give

$$\mathbf{F}_d = \rho V \mathbf{U} \cdot \underline{\underline{C}} \times \omega \tag{24}$$

This must be added to the polarization force in (10) to obtain the net force

$$\mathbf{F} = \rho V (\mathbf{U} \cdot \nabla \mathbf{U} + \mathbf{U} \cdot \underline{\underline{C}} \cdot \nabla \mathbf{U}^T) \tag{25}$$

Since $\underline{\underline{C}}$ is symmetric, the second term in (25) is exactly equal to Taylor's Force derived in (11) for inviscid flows. Therefore Taylor's Force is equally valid in flows with weak rotation.

DISCUSSION

The derivations in this paper are given with more detail in [7] where they are shown to be compatible with Auton [6] and Auton et al. [8]. Some results are derived there for an oncoming shear flow passing over an object in a tube, showing that it is not necessary for the control volume to be "large" or for the flow to be unbounded.

The quantity appearing in $\frac{1}{2}\mathbf{U}\cdot\underline{\underline{C}}\cdot\mathbf{U}$, when multiplied by ρV, has the form of the "kinetic energy due to relative motion" which plays a key role in effective continuum conservation equations for inviscid two-phase dispersions developed by Geurst [9,10] and Wallis [11,12]. Indeed, the forces described by (24) and (25) are recovered from Wallis [12], equation (87), in the limit when $\underline{\underline{C}}$ is isotropic, the volume of the particle is constant, there is no unsteady flow and the particle is at rest. Geurst's equations have the desirable property of being objective. It appears that the drift force is necessary in order to make the overall interaction force objective, as discussed in a more restricted case by Drew and Lahey [13,14].

Since the mean pressure gradient in the fluid flow is

$$\nabla\overline{p} = -\rho\mathbf{U}\cdot\nabla\mathbf{U} \tag{26}$$

the force in (25) is equivalent to minus the volume of the object times the gradient of a "particle pressure":

$$p_p = \overline{p} - \frac{1}{2}\rho\mathbf{U}\cdot\underline{\underline{C}}\cdot\mathbf{U} \tag{27}$$

which can be shown (Wallis [15]) to be the same as the mean bulk stress in the object when a uniform flow is oriented along a principal axis of $\underline{\underline{C}}$ and no external forces act on the object, or more generally when the restraining torque in (3) is applied by simple couples composed of equal and opposite forces acting perpendicular to a lever arm between them.

ACKNOWLEDGEMENT

This work was performed under the U.S. Department of Energy, Contract #DE-FG02-86ER13528, administered by Dr. Oscar Manley.

REFERENCES

1. Cai, X. and G.B.Wallis 1993 The Added Mass Coefficient for Rows and Arrays of Spheres Oscillating Along the Axes of Tubes, *Phys. Fluids A* **A5** (7), 1614-1629.

2. Wallis, G.B. 1993 The Concept of Polarization in Dispersed Two-Phase Potential Flow, *Nuclear Engineering and Design*, **141**, 329-342.

3. Lamb, H. 1932 *Hydrodynamics*, 6th ed., Cambridge University Press.

4. Taylor, G.I. 1928 The Forces on a Body Placed in a Curved or Converging Stream of Fluid. *Proc. Roy. Soc.*, **A120**, 260-283.

5. Lighthill, J. 1956 Drift, *J. Fluid Mechanics*, **1**, 31-53.

6. Auton, T.R. 1987 The Lift Force on a Spherical Body in a Rotational Flow, *J. Fluid Mech.*, **183**, 199-218.

7. Wallis, G.B. 1995 The Drift Force on an Object in an Inviscid Weakly-Varying Incompressible Flow, being revised for *J. Fluid Mechanics.*

8. Auton, T.R., Hunt J.C.R. and Prud'homme, M. 1988 The Force Exerted on a Body in Inviscid Unsteady Non-uniform Flow, *J. Fluid Mechanics*, **197**, 241-257.

9. Geurst, J.A. 1985 Virtual Mass in Two-Phase Bubbly Flow, *Physica*, **129A**, 233-261.

10. Geurst, J.A. 1986 Variational Principles and Two-Fluid Hydrodynamics of Bubbly Liquid/Gas Mixtures, *Physica*, **135A**, 455-486.

11. Wallis, G.B. 1989 Inertial Coupling in Two-Phase Flow: Macroscopic Properties of Suspensions in an Inviscid Fluid, *Multiphase Science and Technology*, **5**, 239-361.

12. Wallis, G.B. 1991 The Averaged Bernoulli Equation and Macroscopic Equations of Motion for the Potential Flow of a Dispersion, *Int. J. Multiphase Flow*, **17**(6), 683-695.

13. Drew, D.A. and Lahey, R.T., Jr. 1987 The Virtual Mass and Lift Force on a Sphere in Rotating and Straining Inviscid Flow, *Int. J. Multiphase Flow*, **13**, 113-121.

14. Drew, D.A. and Lahey, R.T., Jr. 1990 Some Supplemental Analysis Concerning the Virtual Mass and Lift Force on a Sphere in a Rotating and Straining Flow, *Int. J. Multiphase Flow*, **16**, 1127-1130.

15. Wallis, G.B. 1994 The Particle Pressure of Arrays in a Potential Flow, *Nuclear Engineering and Design*, **151**, 1-14.

ACTIVE CONTROL of CONVECTION

Haim H. Bau

Department of Mechanical Engineering and Applied Mechanics, University of Pennsylvania, Philadelphia, PA 19104-6315

ABSTRACT

Using stability theory, numerical simulations, and in some instances experiments, it is demonstrated that the critical Rayleigh number for the bifurcation (i) from the no-motion (conduction) state to the motion state and (ii) from time-independent convection to time-dependent, oscillatory convection in the thermal convection loop and Rayleigh-Bénard problems can be significantly increased or decreased. This is accomplished through the use of a feedback controller effectuating small perturbations in the boundary data. The controller consists of sensors which detect deviations in the fluid's temperature from the motionless, conductive values and then direct actuators to respond to these deviations in such a way as to suppress the naturally occurring flow instabilities. Actuators which modify the boundary's temperature/heat flux are considered. The feedback controller can also be used to control flow patterns and generate complex dynamic behavior at relatively low Rayleigh numbers.

INTRODUCTION

Until recently, most of the scientific community's work in the convection field has focused on identifying and describing various physical phenomena. In contrast, our work focuses on directing convective systems to behave in desired ways. The ability to control flow patterns is important from both the technological and the theoretical points of view. In many material processing applications, convection plays an important role. The ability to control the flow may lead to better quality products and more economical processes than are currently possible. In some processes, it may be desirable to operate at Rayleigh (R) numbers higher than the one at which convection occurs and yet have no convection. In other processes, it may be desirable to suppress (laminarize) chaotic or turbulent motions and maintain a steady, time-independent flow in order to minimize flow unpredictability, remove temperature oscillations which may exceed safe operational conditions, and/or reduce drag. In still other processes, it may be advantageous to induce chaos, under conditions at which it would not normally occur, so as to enhance mixing, heat transport or chemical reactions. From the theoretical point of view, the ability to control the transition and routes to chaos and to stabilize otherwise nonstable equilibrium states may assist us in obtaining a better understanding of the dynamics of convective systems and the transition to turbulence.

Our work on active feedback control of convection has focused on two simple paradigms: the thermal convection loop which is an experimental analog of the celebrated Lorenz equations [1] and

the classical Rayleigh-Bénard problem. The thermal convection loop has the advantage that its flow dynamics can be approximated by a low-dimension, dynamic model and that the theoretical predictions can be verified by relatively simple experiments. After succeeding in controlling flow patterns in the thermal convection loop, we utilized the physical insights we gained there to modify the flow patterns of a more complicated convective system, the Rayleigh-Bénard problem which is a paradigm of convective phenomena occurring in various material processes. Our work on these problems had proven applicable to other flow phenomena as well. For instance, we have successfully demonstrated that the loss of stability of planar Poiseuille flow can be significantly delayed or advanced through active feedback control [2].

THE THERMAL CONVECTION LOOP

The thermal convection loop is made of a pipe, bent into a torus, standing in the vertical plane. The lower and upper halves of the torus are heated and cooled, respectively. The heating and cooling conditions are symmetric with respect to the loop axis that is parallel to the gravity vector. In the absence of a controller, as the temperature difference between the heated and cooled sections of the thermal convection loop increases, the flow in the loop changes from no-motion to steady, time-independent motion to temporally oscillatory, chaotic motion with occasional reversals in the direction of the flow. The bifurcation diagram of the uncontrolled system is depicted in Fig. 1. With the use of a feedback controller making small perturbations in the boundary conditions, we have demonstrated that it is possible to:

(i) maintain the no-motion state at significantly higher temperature differences between the heated and the cooled portions of the loop than the critical one corresponding to the onset of convection in the uncontrolled system [3];
(ii) maintain steady, time-independent flow under conditions in which the flow would otherwise be chaotic [4,5].
(iii) stabilize periodic, non-stable orbits which exist in the chaotic regime of the uncontrolled system [3];
(iv) induce chaos in otherwise laminar (fully predictable), non-chaotic flow [5]; and
(v) render a subcritical bifurcation supercritical through the use of a nonlinear controller [6].

To make some of this work more concrete, we report in Figs. 2-4 a sample of our observations. Fig. 1 depicts the bifurcation diagram for the flow in the uncontrolled loop. For Rayleigh numbers $R<R_1$, the no-motion state is globally stable. As R is increased above R_1, the no-motion state loses stability and is replaced by time-independent motion either in the clockwise or the counterclockwise direction. When R is further increased to $R=R_2$, a second bifurcation occurs, and the time-independent motion loses stability. The loss of stability occurs through a subcritical Hopf bifurcation into a non-stable, limit cycle. Above R_2, the time-independent motion is replaced with a complicated time-dependent, chaotic motion. Fig. 2 depicts the experimentally observed temperature difference ($\Delta T_{3\text{-}9}$) between positions *3* and *9* o'clock around the loop as a function of time in the chaotic regime of the uncontrolled system. Changes in the sign of $\Delta T_{3\text{-}9}$ indicate a change in the flow direction. When $\Delta T_{3\text{-}9}>0$ (<0), the flow is in the counterclockwise (clockwise) direction. Fig. 3 shows the effect of the controller. To highlight this effect, the figure depicts the experimentally measured $\Delta T_{3\text{-}9}$ as a function of time both before and after the activation of the controller. Witness that once the controller has been engaged, the seemingly random, violent oscillations of Fig. 2 disappear and the flow is laminarized. The boundary conditions corresponding to Fig. 2 were altered only slightly to produce the almost time-independent flow shown in Fig. 3 for $t>33$ minutes. The feedback controller operates by sensing any deviation of $\Delta T_{3\text{-}9}$ from its desired value and altering slightly the heating rate, according to a prescribed control rule, in such a way as to nullify the deviation. The observed behavior is in agreement with our theoretical predictions.

The Hopf bifurcation occurring in the thermal convection loop as well as in many other flow systems (i.e., shear flows) is subcritical. In the case of subcritical bifurcations, often the size of the domain of attraction of the time-independent state is limited. In fact, in shear flows, the transition to turbulence typically occurs at subcritical Reynolds numbers. This is apparently due to disturbances

which grow sufficiently large so as to escape the domain of attraction of the laminar state and cause the system to snap through the nonstable limit cycle to a possibly chaotic or turbulent attractor. In order to increase the domain of attraction of the time-independent state, we drew inspiration from [7] and used nonlinear control to render the subcritical bifurcation supercritical. The bifurcation diagram of the thermal convection loop with and without nonlinear (cubic) control is depicted in Fig. 4. The theoretical predictions were successfully verified in experiments.

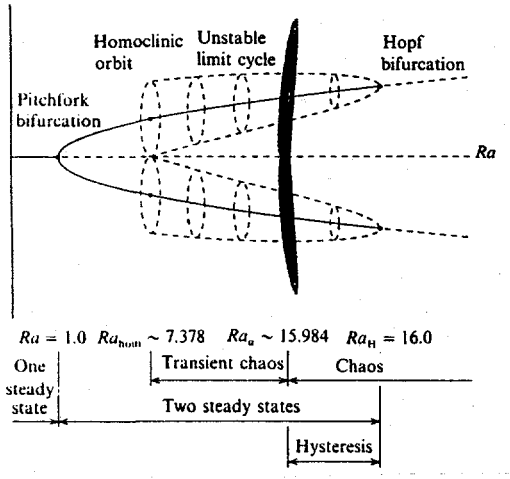

Fig. 1: The (unscaled) bifurcation diagram depicting various flow patterns in the uncontrolled loop as a function of the Rayleigh number. Stable and nonstable states are denoted by solid and dashed lines, respectively. The dark region represents the appearance of the strange attractor, which exists for $R>Ra_a$.

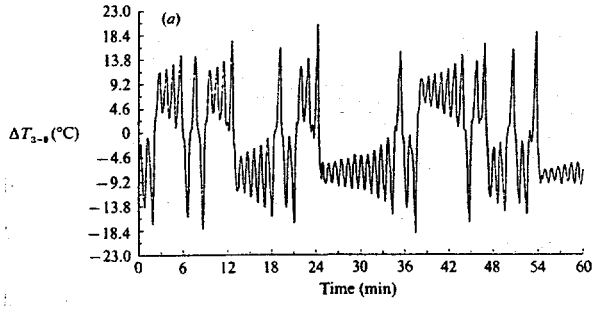

Fig. 2: The experimentally observed temperature difference, $\Delta T_{3\text{-}9}$, is depicted as a function of time for the uncontrolled thermal convection loop.

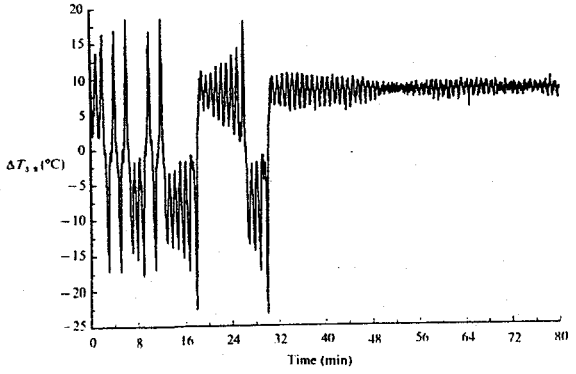

Fig. 3: The experimentally observed temperature difference, $\Delta T_{3\text{-}9}$, is depicted as a function of time both before and after activation of the controller. The controller was activated 33 minutes into the run. Observe the difference between the chaotic oscillations and the controlled (laminarized) flow.

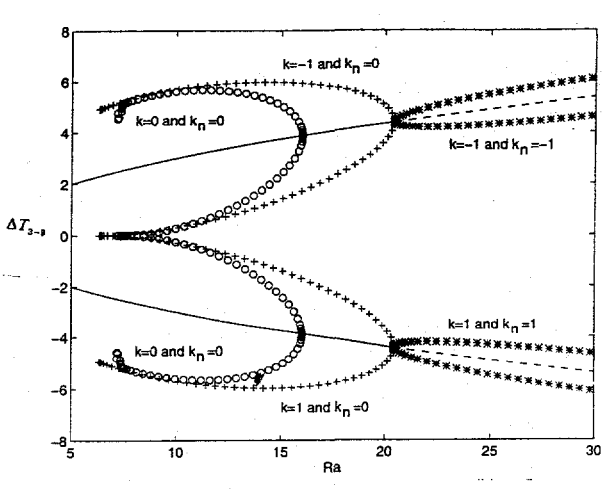

Fig. 4: The Hopf bifurcation in the thermal convection loop problem is shown without control $\{k, k_n\}=\{0,0\}$, with linear proportional control $\{k, k_n\}=\{-1,0\}$, and with linear and nonlinear controllers $\{k, k_n\}=\{-1,-1\}$. k and k_n denote, respectively, the linear and nonlinear controller gains.

THE STABILIZATION OF THE NO-MOTION STATE IN THE RAYLEIGH-BÉNARD PROBLEM

Encouraged by our success with the thermal convection loop, we implemented similar ideas in two more complicated flow systems: the Rayleigh-Bénard problem of a Newtonian fluid and the Lapwood problem of a saturated porous medium heated from below and cooled from above. In both cases, as the Rayleigh number, R, increases, the uncontrolled system undergoes a sequence of bifurcations from no-motion to time-independent motion (at $R=R_1$) to time-dependent motion (at $R=R_2$). The magnitude of R_1 depends on the container's geometry. The magnitude of R_2 depends on both the container's geometry and the fluid's Prandtl number (Pr). As the Prandtl number decreases so does the magnitude of R_2. In this section, we describe the stabilization of the no motion state. In other words, we use a controller to increase the magnitude of R_1.

The controller consists of sensors and actuators. The bottom surface consists of individual heaters, each equipped with a separately controlled power supply. The heaters serve a dual purpose. They supply the nominal heat flow needed to drive the convection as well as serve as actuators which effectuate the control. The sensors are diodes embedded on the heated surface and located at the layer's mid-height. They detect deviations in the fluid's temperature from the desired conductive values and direct the actuators to act in such a way as to enhance the disturbance-dissipating mechanisms in the fluid. More specifically, when the sensors detect an increase (decrease) in the fluid's temperature caused by an ascending (descending) column of fluid, they direct the actuators to reduce (increase) slightly the container's bottom temperature beneath the ascending (descending) fluid column. Through this action, the buoyant forces are reduced, thereby increasing the time available for conduction to dissipate disturbances before they have the opportunity to manifest themselves. Once the disturbances have been dissipated, the container's bottom temperature is restored to its nominal, uniform value.

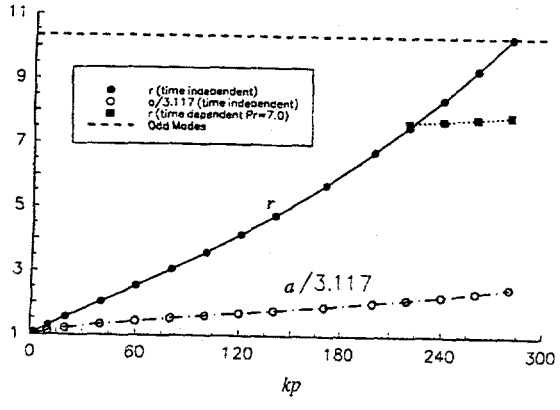

Fig. 5: The normalized critical Rayleigh ($r=\frac{R}{1707.762}$) and wave ($a/3.117$) numbers are depicted as functions of the thermal controller's gain (Kp) for $Pr=7$. The solid and dotted curves describe the loss of stability through, respectively, a simple eigenvalue (exchange of stability) and a Hopf bifurcation. The dashed curve describes loss of stability of the first odd mode.

For example, in the case of a linear, proportional control, the control law can be written as $\tilde{q}=\mathbf{K}\tilde{e}$ where $\tilde{e}$ is a n-dimensional vector describing the deviations of the measured temperatures from their desired values, $\tilde{q}$ is a m-dimensional vector describing the actuators' output, and $\mathbf{K}$ is a $m\times n$ matrix whose entries are the controller gains. The simplest situation, which we have studied thus far, is that of a single sensor being linked to a single actuator through a feedback loop. In such a case, the matrix $\mathbf{K}$ is square and diagonal. In the future, we will also study other scenarios such as when the matrix $\mathbf{K}$ is not diagonal as well as nonlinear control schemes.

Due to its accessibility to analytical treatment, we initially focused our attention on the problem of an unbounded, horizontal fluid layer. Using linear stability analysis, we first demonstrated that R_1, in a saturated porous layer (the Lapwood problem) could be significantly increased [8]. The porous media problem was studied for three reasons: (i) it is relevant to various technological processes such as transport in the mushy region of solidification processes and gel electrophoresis of macromolecules; (ii) it allows simpler and more complete analytic treatment; and (iii) if necessary, experiments in porous media can be conducted in a cruder and less expensive apparatus than would be required in the Newtonian fluid case since the onset of convection in porous media occurs at much higher temperature differences between the container's bottom and top than it does in a Newtonian fluid.

Subsequently, we carried out stability analyses of the controlled, no-motion state of a Newtonian fluid (the Rayleigh-Bénard problem) heated with a uniform temperature [9,10] and with uniform flux [11]. For example, for the uniform temperature heating and cooling, we demonstrated that the critical Rayleigh number for the onset of convection can be postponed from *1708* (in the uncontrolled system) to at least about *17,000* (in the controlled system). It is likely that with more sophisticated control strategies than the ones we have used, additional increases in R_1 would be possible. Fig. 5 depicts a stability diagram which shows the normalized Rayleigh number ($R_1/1708$) as a function of a proportional controller gain.

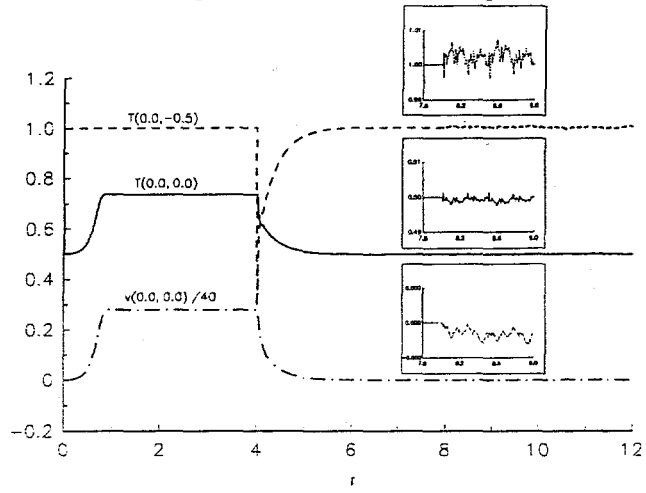

Fig. 6: The temperatures, $T(0,0)$ (solid line) and $T(0,-0.5)$ (dashed line), and the , vertical velocity $v(0,0)$ are depicted as functions of nondimensional time (t) for $R=3000$ and $Pr=0.7$. For $0<t<4$, the controller is off. For $4<t<8$, the controller with gain A is active. For $t>8$, the controller counteracts the action of random disturbances.

In order to study the supercritical flow dynamics in the uncontrolled and controlled systems and the stability in cylindrical containers, we developed numerical codes. The numerical simulations demonstrated that the controller can successfully suppress non-linear disturbances. Fig. 6 illustrates the controlled system's response to random disturbances. For Rayleigh number, $R=3000$, $Pr=0.7$, and controller gain $Kp=3$, Fig. 6 depicts, as functions of time (t), the mid-height temperature (solid line), the bottom temperature (dashed line), and the mid-height, vertical velocity (dot-dashed line) on the left hand side of the computational domain. For the controlled system, the critical Rayleigh number, wavenumber, and cell width are, respectively, $Rc=3538$, $a_c=3.877$, and $L_x=0.81$.

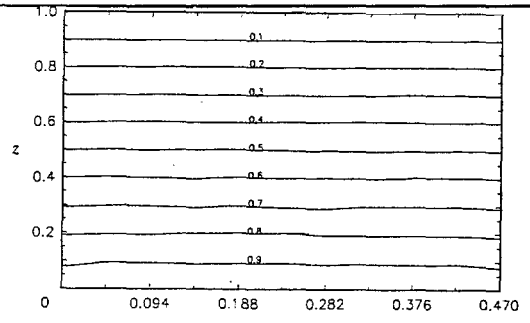

Fig. 7: The temperature field (isotherms) for $R=10,000$ and $Pr=0.7$ in the presence of a controller with gain $K_p=8.0$ and random fluctuations in the temperature field. The almost horizontal isotherms indicate lack of convection. This figure should be contrasted with Fig. 8.

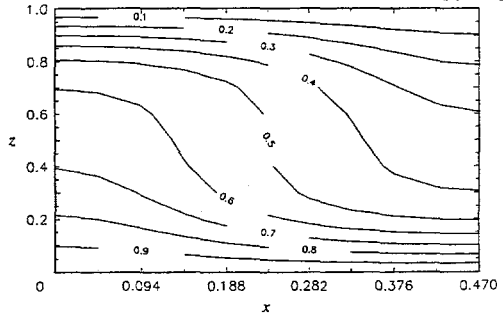

Fig. 8: The temperature field (isotherms) associated with time-independent flow in the absence of a controller for $R=10,000$ and $Pr=0.7$. The boundary conditions are similar to the ones in Fig. 7.

The initial conditions in Fig. 6 correspond to a no-motion state (t=0). In the beginning, the controller is off and the nondimensional bottom ($z=-0.5$) temperature is uniform, $T(0,-0.5)=1$. As a result of a thermal disturbance intentionally introduced at point $(0,0)$, counter-clockwise motion begins. In order to contrast the controlled and uncontrolled states, we allow the motion state to achieve equilibrium (this normally will never happen when the controller is active). At time $t=4$, the proportional controller with a gain $Kp=3$ is switched on. Since, in this case, we are dealing with established motion, the controller alters significantly the container's bottom temperature. This alteration in the container's bottom temperature causes a prompt reduction in the buoyancy force,

which, in turn, causes the flow to slow down. This slow down provides sufficient time for thermal dissipation to restore the conductive temperature field. As a result, the motion is successfully suppressed. The fact that the controller succeeded in suppressing an established motion suggests that it has a large domain of attraction. Once the motion has been suppressed, the controller restores the bottom's nondimensional temperature to its nominal, uniform value of *1*, the mid-plane's nondimensional temperature to its conductive value of *0.5*, and the vertical velocity to its no-motion value of zero. A glance at the temperature field (not shown here) reveals perfectly horizontal isotherms. In other words, for $4<t<8$, a stable, no-motion state is sustained for supercritical Rayleigh numbers with boundary conditions identical to the ones of the uncontrolled system.

We also tested the controller's response to small disturbances for $t>8$. We introduced random fluctuations in the temperature of magnitude up to $\pm 1\%$. Despite these disturbances, the container's bottom temperature remained close to its nominal value of one and there was essentially no motion in the fluid. In order to illustrate the temperature and velocity variations, it was necessary to stretch the vertical axis (see the insert in Fig. 6).

Fig. 7 depicts a snapshot of the temperature field (isotherms) for a controlled layer ($Kp=8$) with $R=10{,}000$ ($r\sim 5.85$). The temperature field was subject to random disturbances of magnitude up to $\pm 1\%$ of the grid point's temperature. The fact that the isotherms remained essentially horizontal suggests the absence of convective motion. This figure should be contrasted with Fig. 8 which depicts the temperature field for the same conditions in the absence of a controller. Fig. 7 clearly illustrates that the controller has successfully maintained a no-motion state under conditions in which convection normally would occur.

Although the controller preserves the classical no-motion state of the Rayleigh-Bénard problem, it has a profound effect on the supercritical behavior. The stability diagrams indicate that the controller can cause a transition from the no-motion state to complicated, time-dependent, supercritical motions at relatively low Rayleigh numbers. This suggests yet another potential application of the controller. Rather than stabilizing an equilibrium state of a given system, the controller could be used to create flow structures to suit particular requirements.

Before constructing an experimental apparatus to verify the numerical predictions, we needed to determine the optimal number and location of the sensors and actuators required to effectuate the control. We modified our numerical codes to analyze 3-D convection in an upright, circular cylinder. Preliminary results were presented in [12]. Since the three-dimensional, time-dependent computations required a considerable amount of computer time, a great effort went into code optimization. Computations have been carried out to determine the magnitudes of R_1 and R_2 as functions of apparatus geometry, various control strategies, the number of sensors and actuators, and potential time delays.

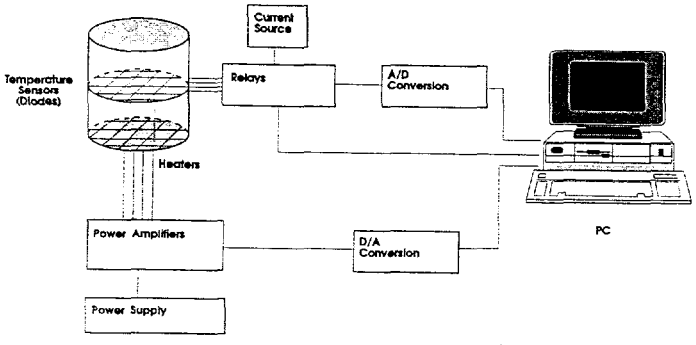

Fig. 9: A schematic description (not drawn to scale) of the experimental set-up.

We are now in the process of constructing an experimental apparatus. The experimental set-up is described schematically in Fig. 9. Briefly, the experimental apparatus consists of an upright cylinder, *0.06m* in diameter, heated from below and cooled from above. The height of the fluid layer and the aspect ratio of the apparatus (radius/height) can be varied. About *40* sensors and *40* actuators are used to facilitate the control. The bottom of the apparatus contains a network of individually controlled heaters.

The need to use a relatively large number of sensors and actuators has required us to devise novel solutions. Since we were not able to purchase the necessary actuators, we were forced to microfabricate them ourselves. The heaters were manufactured by growing an oxide layer on the back of a silicon wafer and spattering a thin nichrome layer on top of the oxide. Using photolithography, we shaped the heaters to the desired form. Next, we spattered silicon nitride on top

of the nichrome layer and etched windows in the silicon nitride to allow the deposition of gold electrodes on top of the heaters. The electrodes are used to assure uniform current density in each heater. Bonding pads were deposed on top of the silicon nitride layer to accommodate electrical leads for the supply of power .

Our theoretical studies suggest that the most effective location of the sensors is at the fluid layer's midheight. We have selected diodes to serve as temperature sensors. Because the diodes allow only unidirectional current flow, we have been able to significantly reduce the number of lead wires and multiplexer channels compared to what would be required if we were to use other sensing devices such as thermistors and/or thermocouples. The diodes are interconnected with two sets of intersecting wires (Fig. 9). We denoted one set of parallel wires with letters *A, B,* ... and the other set with numbers *1, 2,....* The temperature sensed by diode *C4* can be read by measuring the potential across wires *C* and *4*. In order to measure n^2 diodes, we need only two sets of n intersecting wires and a multiplexer with $2n$ channels. In contrast, if we were to use thermistors or thermocouples, the number of lead wires and multiplexer channels would be proportional to n^2. We tested the operation of the diode arrays, individually calibrated the diodes, and demonstrated that we can detect temperatures with a precision better than *0.01K*.

Via a multiplexer, the sensors' output is transmitted to a computer. Any of the sensors can control any of the actuators. According to a predetermined control law, the computer modulates the actuators' power.

For the onset of convection experiments, we will use Dow-Corning 200 fluids. We can customize the fluid to obtain the desired temperature difference between bottom and top at the onset of convection. For example, for Dow Corning 200 with a viscosity of *1000cs* and a layer height of *0.02m*, the critical temperature difference at onset is about *3K*.

Initially, experiments will be conducted in the absence of a controller to determine, as a function of the apparatus' aspect ratio and the working fluid, the critical Rayleigh numbers for the onset of convection in the uncontrolled system. A description of the post-critical flow patterns in our apparatus will also be obtained. The measured results will be compared with our theoretical predictions for the uncontrolled system. Subsequently, we will repeat the experiments in the presence of a controller and observe the effect of the controller on the stability of the no-motion state as well as on the supercritical flow patterns.

SUPPRESSION OF OSCILLATORY RAYLEIGH BÉNARD FLOWS

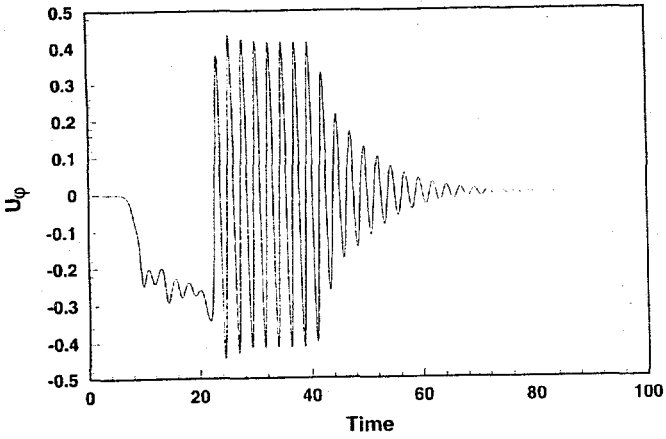

Fig. 10: The angular velocity u_ϕ at a point on the cylinder's midplane is depicted as a function of time. The system is (not) controlled for *(t<40) t>40. R=5000.*

Another objective of our research work is to delay or advance the secondary bifurcation from time-independent flow into oscillatory flow. The design of a controller is complicated by the fact that the system is highly nonlinear and closed form expressions for the time-independent flow from which the oscillatory flow bifurcates are not available. We are using the numerical code we described earlier to identify the critical Rayleigh numbers and the flow dynamics in an uncontrolled system. To verify the code we are comparing our theoretical predictions with experiments [13]. The numerical simulations allow us to obtain a wealth of information which can not be readily measured in experiments and enhance our understanding of the flow dynamics at high Rayleigh numbers.

For example, for a cylindrical container, with an aspect ratio (radius/height) of one, containing Newtonian fluid of *Pr=0.02* (i.e., gallium), we found that the first bifurcation from no-motion to time-independent motion occurs at $R_1 \sim 2200$. A second bifurcation from time-independent flow to

time-dependent flow occurs at $R_2 \sim 4800$. A sequence of additional bifurcations follows in quick succession until chaotic flow is observed for $R > 9000$.

For $R < R_2$, the flow consists of two counterrotating cells. With the onset of oscillatory behavior, the two cells oscillate angularly at relatively low amplitude. Using control strategies similar to ones we described in the previous section, we were able to suppress the oscillatory behavior. Fig. 10 depicts the angular velocity u_ϕ at a point on the cylinder's midplane for $R = 5000$. The initial conditions correspond to a no-motion state. For t<40, the system was not controlled and oscillatory motion has evolved. For $t > 40$, the controller is active. The controller successfully suppresses the oscillatory behavior and retains time-independent convection under the same conditions in which, in the absence of a controller the motion would have been oscillatory.

CONCLUSIONS

We have tackled the complicated problem of controlling highly nonlinear, distributed parameter systems. Through analysis, numerical simulations, and experiments (in the case of the thermal convection loop only), we have demonstrated that flow patterns can be controlled. Our immediate challenge now is to obtain experimental verification for our theoretical predictions for the Rayleigh Bénard problem. If successful, this research may provide the material processing community with an enabling technology.

ACKNOWLEDGMENT

Our work on the Rayleigh-Bénard problem was performed under the auspices of the U.S. Department of Energy.

REFERENCES

1. Lorenz, E. N., 1963, J. Atmospheric Sci. 20, 130-141.

2. Hu, H., and Bau, H. H., 1994, "Feedback Control to Delay or Advance Linear Loss of Stability in Planar Poiseuille Flow," Proceedings Royal Society A, 447, 299-312.

3. Singer, J. and Bau, H.H.,1991b, "Active Control of Convection," Physics of Fluids A, 3, 2859-2865.

4. Singer, J., Wang, Y-Z and Bau, H. H., 1991, "Controlling a Chaotic System," Physical Review Letters 66, 1123-1125.

5. Wang, Y-Z, Singer J., and Bau, H. H., 1992, "Controlling Chaos in a Thermal convection Loop," J. Fluid Mechanics, 237, 479-498.

6. Yuen, P., and Bau, H. H., 1995, "Rendering a Subcritical Bifurcation Supercritical," in preparation.

7. Abed, E. H., and Fu, J-H, 1986, "Local Feedback Stabilization and Bifurcation Control, I-Hopf Bifurcation," Systems Control Letters, 7, 11-17.

8. Tang, J., and Bau, H. H., 1993, "Feedback Control Stabilization of the No-motion State of a Fluid Confined in a Horizontal, Porous Layer Heated from Below," J. Fluid Mechanics, 257, 485-505.

9. Tang, J., and Bau, H. H., 1993, "Stabilization of the No-motion State in Rayleigh-Bénard Convection Through the use of Feedback Control," Physical Review Letters, 70, 1795-1798.

10. Tang, J., and Bau, H. H., 1994, "Stabilization of the No-motion State in the Rayleigh-Bénard Problem," Proceedings Royal Society A, 447, 587-607.

11 Tang, J., and Bau, H. H., 1995, "Stabilization of the No-motion state of a Horizontal Fluid Layer Heated from Below with Joule Heating," to appear in Trans. ASME-J. Heat Transfer.

12. Tang, J., and Bau, H. H., 1993, "Stabilization of the No-Motion State in Rayleigh-Bénard Convection in an Upright, Circular Cylinder," Fundamentals of Natural Convection, Boyd, R. D, and Kroeger, P. G., editors, ASME-HTD-264, 39-48.

13. Heslot, F., Casting, B., and Libchaber, A., 1987, "Transition to Turbulence in Helium Gas," Physical Review A, 36, 5870-5873.

EFFECT OF STEADY AND TIME-HARMONIC MAGNETIC FIELDS ON MACROSEGREGATION IN ALLOY SOLIDIFICATION

F. P. Incropera and P.J. Prescott

School of Mechanical Engineering
Purdue University
W. Lafayette, IN 47907

ABSTRACT

Buoyancy-induced convection during the solidification of alloys can contribute significantly to the redistribution of alloy constituents, thereby creating large composition gradients in the final ingot. Termed *macrosegregation,* the condition diminishes the quality of the casting and, in the extreme, may require that the casting be remelted. The deleterious effects of buoyancy-driven flows may be suppressed through application of an external magnetic field, and in this study the effects of both steady and time-harmonic fields have been considered. For a steady magnetic field, extremely large field strengths would be required to effectively dampen convection patterns that contribute to macrosegregation. However, by reducing spatial variations in temperature and composition, turbulent mixing induced by a time-harmonic field reduces the number and severity of segregates in the final casting.

INTRODUCTION

During solidification of an off-eutectic metal alloy, zones of pure solid and liquid are separated by a two-phase (solid/liquid), or *mushy*, region, consisting of fluid saturated dendritic structures. When solidification is induced by chilling a static mold from the side and/or from below, dendritic crystals which initially form at the cold surface may reject a lighter constituent which is redistributed by the combined influence of solutal and thermal buoyancy forces in the mushy and molten zones. Composition changes within the mushy zone may also induce regions of localized remelting in which channels develop and provide preferential paths for the flow of interdendritic fluid. The channels ultimately become sites of large composition gradients (termed *segregates*), and the large-scale redistribution of constituents in a fully solidified ingot is termed *macrosegregation.* One objective of research on alloy solidification is to reduce

macrosegregation by altering patterns of natural convection inherent in the solidification process. Options include solidification in a μ-gravity environment or active control of the process by thermal, mechanical or electromagnetic means. In the following sections consideration is given to the effects of both steady and time-harmonic magnetic fields on flow and macrosegregation occurring during solidification.

Regardless of the manner in which a magnetic field is applied, the induced Lorentz force is determined by a cross product of the current density and the field strength, $\mathbf{F_L} = \mathbf{J} \times \mathbf{B}$. For a moving medium, the current density follows from Ohm's law, $\mathbf{J} = \sigma_e(\mathbf{E} + \mathbf{V} \times \mathbf{B})$, where σ_e is the electrical conductivity of the medium, $\mathbf{E}$ is an externally applied electric field, and $\mathbf{V} \times \mathbf{B}$ is the electric field induced by fluid motion through the magnetic field. *Magnetic damping* occurs when an electrically conducting fluid flows transversely through a steady magnetic induction field, and with $\mathbf{E} = 0$, the Lorentz force reduces to $\mathbf{F_L} = \sigma_e(\mathbf{V} \times \mathbf{B}) \times \mathbf{B}$. In contrast to the passive (dissipative) influence exerted by a steady (d.c.) magnetic field on a convecting liquid metal, a time-harmonic (a.c.) magnetic field has an active influence which involves stirring of the molten alloy. The electric field induced by a time-varying magnetic field drives eddy currents, which interact with the magnetic field to induce the Lorentz forces. In this study an external inductor is configured to provide a traveling magnetic field in a vertical, annular mold. The field is characterized by its angular frequency ω, axial phase variation (wave number) k_ϕ, and phase velocity $V_\phi = \omega/k_\phi$.

MATHEMATICAL MODEL

A continuum model for transport phenomena in binary, solid-liquid phase change systems (Prescott et al., 1994) has been extended to account for the effects of magnetic damping or electromagnetic stirring (EMS). Assuming two-dimensional (r,z) conditions in a vertical, annular mold, the model transport equations for conservation of total mass, axial and radial momentum, energy and species may be expressed as

$$\frac{\partial \rho}{\partial t} + \nabla\cdot(\rho \mathbf{V}) = 0 \tag{1}$$

$$\frac{\partial}{\partial t}(\rho u) + \nabla\cdot(\rho \mathbf{V} u) = \nabla\cdot\left[(\mu_l + \mu_t)\frac{\rho}{\rho_l}\nabla u\right] - \frac{\mu_l}{K}\frac{\rho}{\rho_l}(u - u_s) + \rho_l B_{lz} - \frac{\partial P}{\partial z} + F_{L,z} \tag{2}$$

$$\frac{\partial}{\partial t}(\rho v) + \nabla\cdot(\rho \mathbf{V} v) = \nabla\cdot\left[(\mu_l + \mu_t)\frac{\rho}{\rho_l}\nabla v\right] - (\mu_l + \mu_t)\frac{\rho}{\rho_l}\frac{(v - f_s v_s)}{r^2} - \frac{\mu_l}{K}\frac{\rho}{\rho_l}(v - v_s) - \frac{\partial P}{\partial r} + F_{L,r} \tag{3}$$

$$\frac{\partial}{\partial t}(\rho h) + \nabla\cdot(\rho \mathbf{V} h) = \nabla\cdot\left[\left(\frac{k}{c_s^*} + \frac{g_l \mu_t c_l}{Pr_t\, c_s^*}\right)\nabla h\right] + \nabla\cdot\left[\left(\frac{k}{c_s^*} + \frac{g_l \mu_t c_l}{Pr_t\, c_s^*}\right)\nabla\left(h_s^* - h\right)\right] - \nabla\cdot[f_s \rho(\mathbf{V} - \mathbf{V_s})(h_l - h_s)] \tag{4}$$

$$\frac{\partial}{\partial t}\left(\rho f^\alpha\right) + \nabla\cdot(\rho \mathbf{V} f^\alpha) = \nabla\cdot\left[\left(\rho D + \frac{f_l \mu_t}{Sc_t}\right)\nabla f^\alpha\right] + \nabla\cdot\left[\left(\rho D + \frac{f_l \mu_t}{Sc_t}\right)\nabla\left(f_l^\alpha - f^\alpha\right)\right] - \nabla\cdot[f_s \rho(\mathbf{V} - \mathbf{V_s})(f_l^\alpha - f_s^\alpha)] \tag{5}$$

where B_{1z} is the net (thermal/solutal) buoyancy force per unit mass of liquid and F_L is the Lorentz force.

For the magnetic damping conditions of this study, the Lorentz force is oriented exclusively in the radial direction ($F_{L,z} = 0$) and the corresponding force component is $F_{L,r} = -\sigma_e B_z^2 v$. Moreover, since turbulence generation is negligible, $\mu_t = 0$. In contrast, for EMS, Lorentz forces are manifested principally in the vertical direction and turbulent mixing is a likely consequence of the stirring action. The radial dependence of $F_{L,z}$ has been determined (Prescott and Incropera, 1994), and a low Reynolds number k-ε model (Launder and Spalding, 1974) has been used to evaluate the turbulent viscosity μ_t (Prescott and Incropera, 1995). Turbulence has the effect of increasing the effective viscosity, $\mu_{eff} = \mu_l + \mu_t$, and a dimensionless viscosity may be defined as $\mu^* = (\mu_l + \mu_t)/\mu_l$. Effective Prandtl and Schmidt numbers may also be defined as $Pr_{eff} = \nu_{eff}/\alpha_{eff} = Pr\,\mu^*/\left[1 + Pr(\mu^* - 1)/Pr_t\right]$ and $Sc_{eff} = \nu_{eff}/D_{eff} = Sc\mu^*/\left[1 + Sc(\mu^* - 1)/Sc_t\right]$. For the Pb-Sn system, Pr = 0.02 and Sc = 172 (Le = Sc/Pr = 8600). Hence, for representative values of $\mu^* = 100$, $Pr_t = 1.2$, and $Sc_t = 1.0$, $Pr_{eff} = 0.75$ and $Sc_{eff} = 1$, yielding an effective Lewis number of 1.33. Although the respective molecular diffusion rates of momentum, energy, and species are highly disparate, turbulence has the effect of approximately equalizing these diffusion rates. Furthermore, by increasing the effective diffusion coefficients for all field variables, turbulence reduces the influence of advection, rendering all transport rates less sensitive to velocity *vectors* and more sensitive to *gradients* in the respective field variables.

Calculations were performed for an experimental mold cavity of height H = 150 mm and inner and outer radii of $r_i = 15.9$ and $r_o = 63.5$ mm, respectively. The mold contains a molten charge of Pb-19 wt pct Sn, which is initially at 305°C, and solidification is initiated by subjecting the side wall to cooling characterized by a chill temperature of $T_c = 13$°C and an overall coefficient of $U = 35$ W/m^2·K. For magnetic damping, field strengths of $B_z = 0.1$ and 0.5 T are considered. For EMS a downward magnetic field characterized by $\omega = 377$ rad/s, $k_\phi = -29$ rad/m and $B_r(r_o) = 2.9$ mT (rms) is considered.

RESULTS

Magnetic Damping. Three simulations, corresponding to values of $B_z = 0$, 0.1 and 0.5 T, were performed to assess the effects of magnetic damping. For the base case, $B_z = 0$ (Fig. 1), a strong, counterclockwise thermal convection cell is established shortly after the sidewall is chilled, and within t = 120 s, crystals begin to precipitate at the bottom of the mold wall, thereby forming a two-phase (mushy) zone. As cooling continues, the mushy zone grows, with the liquidus interface moving vertically upward and radially inward. At t = 140 s, a thin mushy zone of nonuniform thickness is attached to the bottom one-third of the cooled mold wall. The precipitation of solid is accompanied by solute (Sn) enrichment of interdendritic liquid, Fig. 1i (d), which induces solutal buoyancy forces acting upward on the interdendritic liquid and opposing thermal buoyancy forces caused by the radial temperature gradient, Fig. 1i (c). Because the density of Sn is significantly less than that of Pb, solutal forces dominate within the mushy zone. Interdendritic fluid which escapes from the mushy zone at $z^* \approx 0.27$, Figs. 1i (a) and (b), is turned

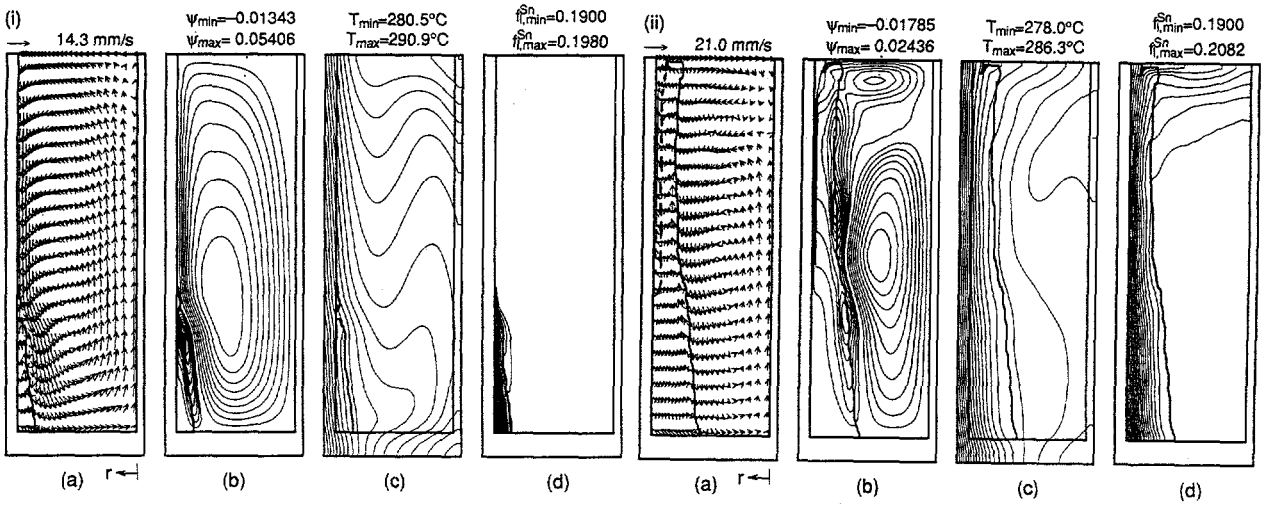

Fig. 1 Convection conditions after (i) t = 140 s and (ii) t = 175 s of cooling with no magnetic field: (a) velocity vectors, (b) streamlines, (c) isotherms, and (d) liquid isocomps.

downward along the liquidus interface by the momentum of the thermal convection cell, thereby confining the liquid composition gradient primarily within the mushy zone, Fig. 1i (d).

With time, the liquidus interface moves radially inward and vertically upward along the cooled mold wall. As this process occurs, fluid is exchanged between the mushy and melt zones in a relatively confined region near the top of the mushy zone, where a strong, solutally driven (Sn-rich) flow emerges from the mushy zone and interacts with thermally driven flow in the bulk melt, Fig. 1ii (b). Since the Pb-Sn system is characterized by a large Lewis number (Le ≈ 8600), fluid within the solutal convection cell readily exchanges energy with the bulk liquid but largely retains its composition. As shown in Fig. 1ii (a), these conditions favor the development of a channel within the mushy zone. Since fluid ascending along the cooled mold wall is enriched with Sn, there is a depression in the local liquidus temperature, which is conducive to remelting. In addition, due to the advection of warm, Sn-rich fluid from the melt into the mushy zone, remelting is enhanced and a channel is spawned. The channel is aligned vertically along the mold wall and is delineated by a thick dashed line in Fig. 1ii (a). In addition to the exchange of liquid between the mush and melt promoted by the channel, three small recirculation cells are active along the liquidus interface at $z^* \approx 0.3$, 0.6, and 0.8, Fig. 1ii (b). Such recirculations are responsible for establishing preferred flow paths of interdendritic liquid at later times. Fluid of nominal composition enters the mushy zone at the bottom of these recirculation zones and displaces fluid of higher Sn concentration. Thus, a small Sn depleted region, with an increased solid fraction and decreased permeability, is created. At the top of a recirculation cell, there exists a Sn enriched zone with decreased solid fraction and increased permeability. The position of these interfacial recirculation cells moves as the liquidus interface advances inward and upward, thereby creating a series of channels, which manifest themselves as A-segregates in the final casting. The momentum associated with the thermal convection cell gradually decreases, as temperature gradients in the melt diminish and opposing solutal buoyancy forces increase.

For $B_z = 0.1$ T, development of the mushy zone and the solutally driven convection cell, Fig. 2i (b), is accelerated. Magnetic damping reduces the strength of the thermally driven

circulation, thereby decreasing heat transfer between the melt and the cooled mold wall. Furthermore, due to the decreased momentum associated with the thermally driven downflow along the outer mold wall, Sn rich fluid from the mushy zone penetrates further into the melt, Fig. 2i (d). Since the thermal cell is weakened by the magnetic field, it is less effective at opposing the discharge of Sn rich liquid from the mushy zone, and the propensity for channel development is increased. A fully melted channel which turns radially inward from the outer mold wall, Fig. 2ii (a), provides a preferred flow path for interdendritic fluid, Fig. 2ii (b), facilitating its transfer to the top of the mold cavity, where Sn rich layers of liquid are forming, Fig. 2ii (d).

By increasing the induction field to 0.5 T, radial damping increases twenty-five fold, significantly reducing thermal convection and thermal stratification during the initial cooling period. At t = 140 s, Fig. 3i, a mushy zone covers nearly 90% of the vertical extent of the outer mold wall, the temperature gradient is primarily radial, and the positive buoyancy associated with the Sn concentration gradient in the interdendritic fluid produces an annular plume of Sn rich liquid ascending from the mushy zone. Since the magnetic field strongly dampens thermal convection during the initial cooling period, this solutal upwelling is virtually unopposed and is responsible for the channel which forms along the mold wall, where the local liquidus temperature is depressed. The strong magnetic damping causes the thermal and solutal convection cells to be sharply divided by a hypothetical cylindrical surface whose radius corresponds closely with the liquidus interface, Fig. 3i (b). With time, the mushy zone and the vertical interface between thermal and solutal convection cells move radially inward. Since vertical motion is undamped, solutal buoyancy forces continue to accelerate interdendritic fluid to relatively large velocities within the channel adjacent to the outer mold wall, while magnetic damping has the effect of minimizing radial motion. At t = 210 s, the counterclockwise thermal cell is virtually nonexistent, Fig. 3ii (b), and with the dominance of solutal buoyancy, solutal stratification eventually occurs.

Macrosegregation patterns at a time for which fluid flow is negligible and macrosegregation is essentially complete are shown in Fig. 4. The *A-segregates* of Fig. 4 (a)

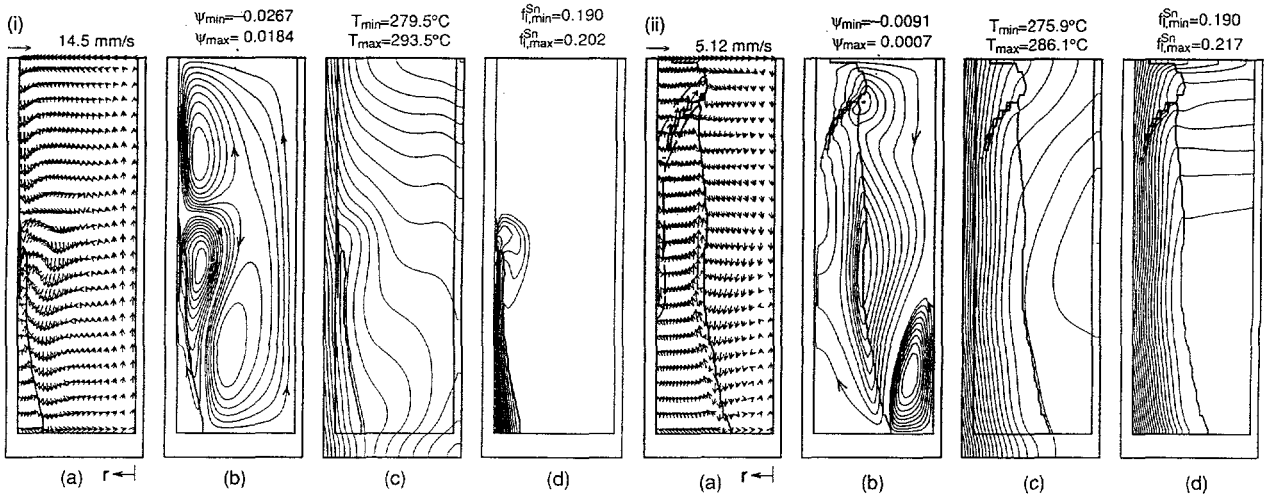

Fig. 2 Convection conditions after (i) t = 140 s and (ii) t = 210 s of cooling with B_z = 0.1 T: (a) velocity vectors, (b) streamlines, (c) isotherms, and (d) liquid isocomps.

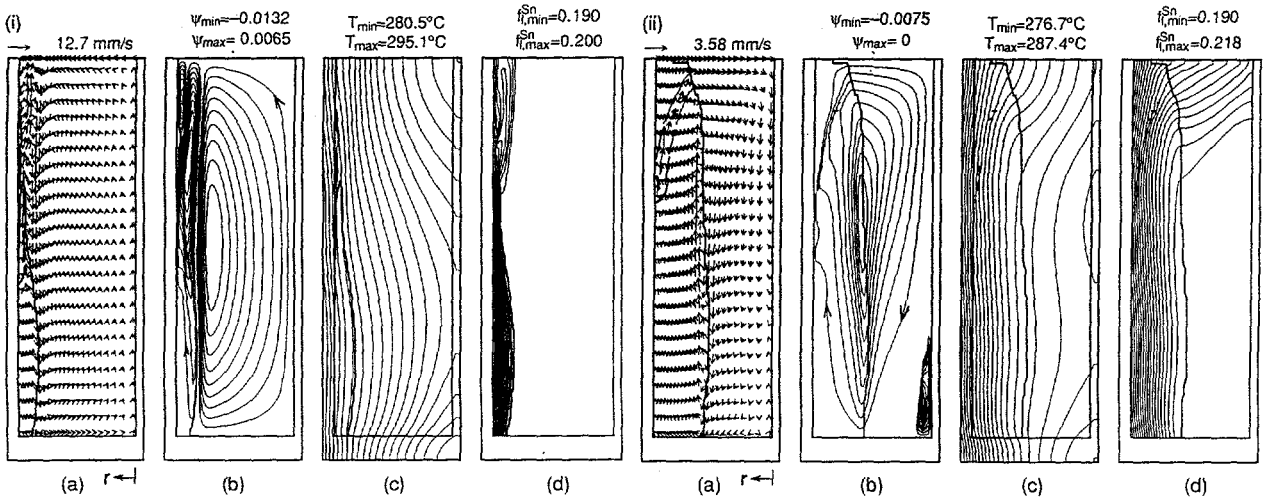

Fig. 3 Convection conditions after (i) t = 140 s and (ii) t = 210 s of cooling with $B_z = 0.5$ T: (a) velocity vectors, (b) streamlines, (c) isotherms, and (d) liquid isocomps.

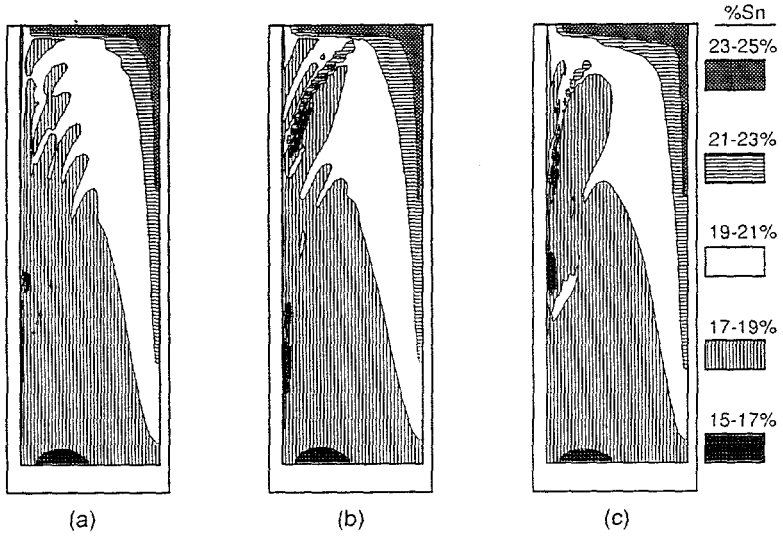

Fig. 4 Macrosegregation pattersn after 600 seconds of cooling: (a) without magnetic damping, (b) with $B_z = 0.1$ T, and (c) $B_z = 0.5$ T.

correspond to a series of Sn-rich pockets extending upward and radially inward from a Sn-depleted region. In addition to the pattern of *A-segregates*, there is a large *cone segregate* of Sn-rich material, which extends downward from the top of the ingot and results from solutally induced flow during intermediate stages of solidification. Application of the magnetic field has virtually no influence on development of the cone of positive segregation, but does affect the patter of A-segregates. For B = 0.1 T, Fig. 4 (b), the channel that existed at earlier times yielded a highly segregated zone among the array of A-segregates, which consists of adjacent extremes in positive (Sn-rich) and negative (Sn-depleted) segregation. Although the number and severity of the A-segregates are reduced for $B_z = 0.5$ T, Fig. 4 (c), overall segregation remains pronounced.

Magnetic Stirring. With application of a downward traveling magnetic field ($k_\phi < 0$), the Lorentz force acts in the downward direction and decreases with decreasing radius. Hence, the corresponding recirculation is one for which fluid ascends near the inner radius of the cavity and descends near the outer radius, thereby augmenting and opposing thermal and solutal buoyancy forces, respectively.

Predictions based on the turbulent model yielded a large convection cell and melt velocities during the early stages of solidification. However, correspondingly large values of the effective viscosity suppressed development of the velocity field, and at t = 160 s, Fig. 5i, the maximum velocity is 12.1 mm/s, with $\mu^* = 208$. Solidification has progressed for approximately 10 s, and a mushy zone of highly nonuniform thickness covers approximately 60% of the mold wall. The main convection cell, Fig. 5i (b), is driven by Lorentz forces, while a solutally driven convection cell is developing near the bottom within the confines of the mushy zone. Although $\mu^* = 1$ along the mold walls, Fig. 5i (e), large levels of turbulence exist throughout the melt. Due to the combined effects of local turbulence generation and distance from the walls, at which the turbulence kinetic energy, k_e, is zero, the maximum effective viscosity μ^*_{max} occurs at $r^* \approx 0.5$ and $z^* \approx 0.7$, Fig. 5i (e). Turbulence is damped in the mushy zone, but significant turbulent mixing still occurs near the liquidus interface within the mushy zone and is responsible for reducing gradients in the liquid Sn concentration, Fig. 5i (d,e).

With rapid growth of the mushy zone and a concomitant reduction in fluid velocities, the mushy zone occupies almost the entire mold cavity at t = 180 s, Fig. 5ii. Although the turbulence intensity has also decreased significantly, Fig. 5ii (e), it still enhances mixing in the interior of the cavity, thereby maintaining nearly uniform temperatures and concentrations in much of the mushy zone, Fig. 5ii (c,d). The turbulence intensity is a maximum for $r^* \approx 0.5$ at the top surface, Fig. 5ii (e), where damping is small due to small volume fractions of solid. The solutal convection cell is growing and eventually dominates flow conditions in the cavity. However, because Lorentz forces oppose solutal buoyancy forces, the clockwise convection cell in Fig. 5ii (b) grows more slowly than it would without electromagnetic stirring. At t = 195 s, most of the turbulence has been dissipated by damping, and its influence is confined to relatively small interior regions near the very top and bottom of the cavity, Fig. 5iii (e), where solid volume fractions are relatively small. However, under the influence of prior, turbulence-induced mixing, uniform temperatures and liquid compositions persist in much of the mushy region, Fig. 5iii (c,d).

The solutal convection cell continues to grow, while the electromagnetically driven cell and turbulence gradually decay. By t = 210 s, solutal buoyancy dominates convection, forming layers of Sn-rich liquid and causing dendrites to remelt at the top. Convection conditions representative of intermediate stages of solidification are shown in Fig. 5iv, which corresponds to t = 240 s. Turbulence is virtually fully decayed, Fig. 5iv (e), and interdendritic liquid is recirculated through the cavity in one large convection cell, Fig. 5iv (a,b). The small, counterclockwise recirculation cell at the bottom of the cavity vanishes completely shortly after t = 240 s, due to the increasing radial gradient in liquid Sn concentration. The convection pattern supplies cool Sn-rich liquid to the top interior region of the cavity, Fig. 5iv (c,d), thereby establishing vertical gradients of temperature and liquid Sn concentration. In the outer periphery of the mold cavity, gradients in temperature and liquid concentration are primarily radial and nearly uniform in the vertical direction.

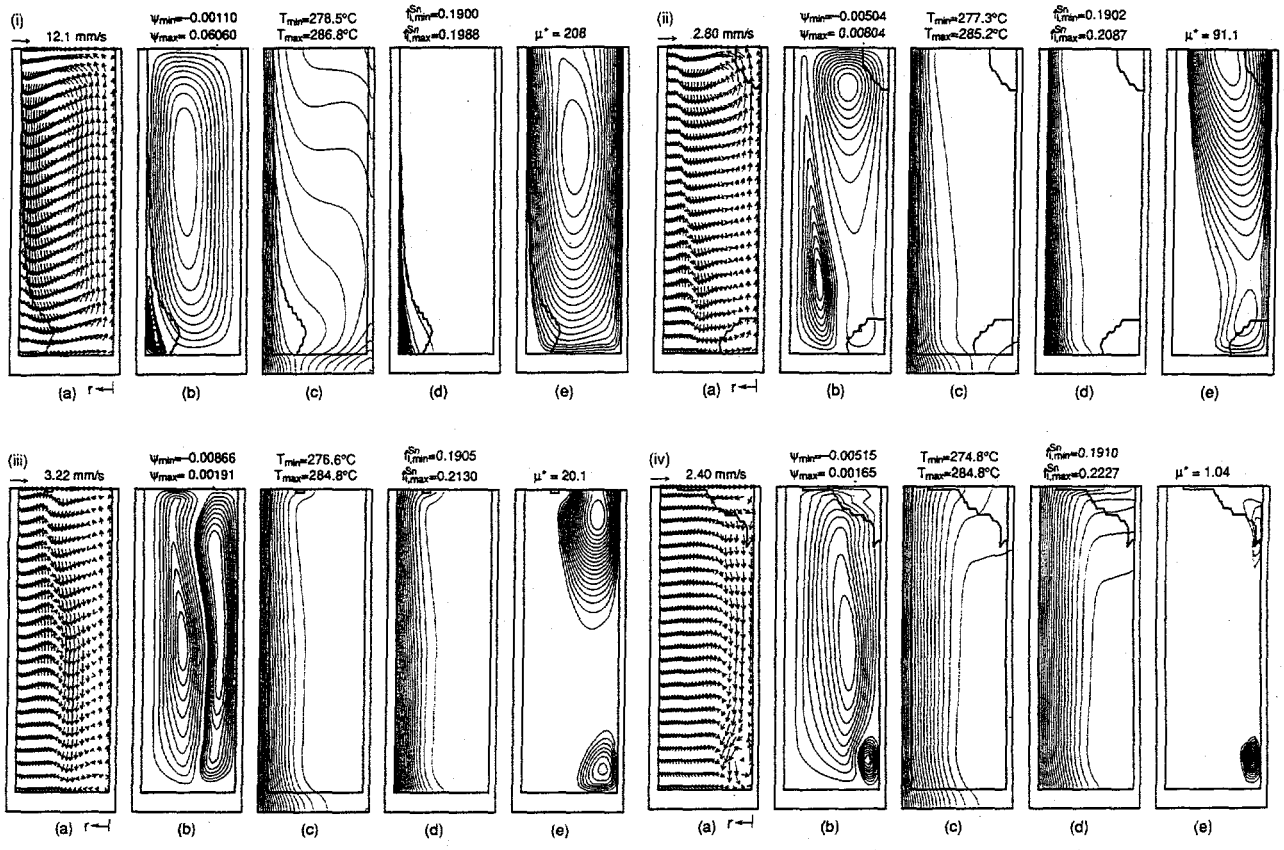

Fig. 5 Effect of EMS on conditions at (i) t = 160 s, (ii) t = 180 s, (iii) t = 195s and (iv) t = 240 s: (a) velocity vectors, (b) streamlines, (c) isotherms, (d) liquid isocomps, and (e) effective visocity (turbulence).

The subsequent development of macrosegregation patterns is shown in Fig. 6. At t = 240 s, Fig. 6 (a), macrosegregation is slight, with more than 95% of the partially solidified ingot remaining within 0.66% of the nominal composition. However, the solutal convection pattern of Fig. 5iv (b) is ultimately responsible for the formation of a cone of positive segregation at the top of the ingot, Fig. 6 (e), and although the overall rms macrosegregation is less than that predicted without electromagnetic stirring, the cone segregate of Fig. 6 (e) is only slightly smaller than that predicted without a magnetic field, Fig. 4 (a).

Turbulence has the effect of diminishing perturbations in the temperature and liquid concentration fields, thereby inhibiting the formation of channels in the mushy zone. With increased turbulent mixing, effective diffusion coefficients for momentum, energy, and species transfer are essentially equalized, decreasing the relative effect of advection and causing gradients in temperature and liquid Sn concentration to remain primarily radial and nearly uniform in the vertical direction. During early stages of solidification, counter-rotating convection cells driven by solutal buoyancy and Lorentz forces occupied the outer and inner portions of the cavity, respectively, with minimal mutual interactions and hence reduced the propensity for forming severely segregated regions associated with channels.

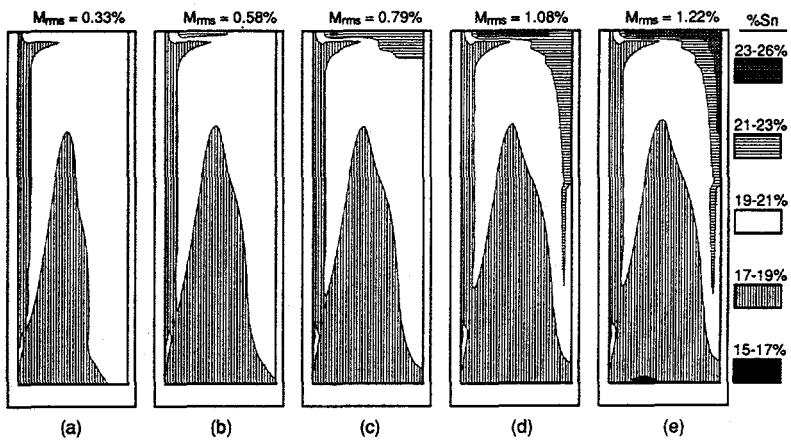

Fig. 6 Effect of EMS on macrosegregation patterns at (a) t = 240 s, (b) t = 300 s, (c) t = 360 s, (d) t = 480 s, and (e) t = 600 s.

SUMMARY

Options for suppressing the effects of natural convection on macrosegregation during the casting of molten alloys include active control of the solidification process by thermal, mechanical and/or electromagnetic means. However, results of this study indicate that, without unreasonably large field strengths, use of a *steady* magnetic field to *dampen* convection is not a viable option. In contrast, through a *stirring* action, use of a time-varying magnetic field of moderate strength has been shown to reduce the severity of macrosegregation.

ACKNOWLEDGEMENT

This work was performed under the auspices of the U.S. Department of Energy.

REFERENCES

1. Launder, B.E., and Spalding, D.B., 1974, "The Numerical Computation of Turbulent Flows," *Computer Methods in Applied Mechanics and Engineering,* Vol. 3, pp. 269-289.

2. Prescott, P.J., and Incropera, F.P., 1994, "Convective Transport Phenomena during Solidification of Binary Metal Alloys and the Effect of Magnetic Fields," TR DOE/ER/13759-7, School of Mechanical Engineering, Purdue University.

3. Prescott, P.J., and Incropera, F.P., 1995, "The Effect of Turbulence on Solidification of a Binary Metal Alloy with Electromagnetic Stirring," *J. Heat Transfer*, In Press.

THEORETICAL MODELING OF CHF FOR NEAR-SATURATED POOL BOILING AND FLOW BOILING FROM SHORT HEATERS USING THE INTERFACIAL LIFT-OFF CRITERION

Issam Mudawar†, Jesse E. Galloway‡, Christopher O. Gersey‡,
Stanley J. Reed‡, and David D. Hall‡

Boiling and Two-Phase Flow Laboratory
School of Mechanical Engineering, Purdue University
West Lafayette, IN 47907, U.S.A.

ABSTRACT

Pool boiling and flow boiling were examined for near-saturated bulk conditions in order to determine the critical heat flux (CHF) trigger mechanism for each. Photographic studies of the wall region revealed features common to both situations. At fluxes below CHF, the vapor coalesces into a wavy layer which permits wetting only in wetting fronts, the portions of the liquid-vapor interface which contact the wall as a result of the interfacial waviness. Close examination of the interfacial features revealed the waves are generated from the lower edge of the heater in pool boiling and the heater's upstream region in flow boiling. Wavelengths follow predictions based upon the Kelvin-Helmholtz instability criterion. Critical heat flux in both cases occurs when the pressure force exerted upon the interface due to interfacial curvature, which tends to preserve interfacial contact with the wall prior to CHF, is overcome by the momentum of vapor at the site of the first wetting front, causing the interface to lift away from the wall. It is shown this interfacial lift-off criterion facilitates accurate theoretical modeling of CHF in pool boiling and in flow boiling in both straight and curved channels.

† Professor and Director of the Purdue University Boiling and Two-Phase Flow Laboratory; author to whom correspondence should be addressed

‡ Graduate Student

1. INTRODUCTION

Predicting CHF has been the focus of a considerable body of research spanning over three decades. For pool boiling, the well known CHF model of Zuber *et al.* [1] has maintained its popularity because of its theoretical appeal and use of well-established hydrodynamic instability hypotheses in determining limits on liquid access to a horizontal surface. Many attempts have been made to alter this model in order to account for effects the original model did not address. These include finite heater size, heater geometry, and surface orientation. The latter of these effects, particularly the case of a vertical surface, is of special interest to the present study.

While the model by Zuber *et al.* [1] predicts zero CHF for vertical surfaces, experimental evidence proves CHF for this orientation and all orientations between horizontal and vertical are only slightly smaller than for a horizontal surface. Not only does this negate the suitability of this model for vertical surfaces, but it also raises questions concerning the CHF trigger mechanism on which the model is founded, even for horizontal surfaces. It is one of the key objectives of the present study to develop a new model for pool boiling CHF from vertical surfaces.

With regard to flow boiling, six main types of models have been proposed which encompass virtually all of the CHF research. These are *boundary layer separation* [2, 3, 4], *mechanical energy criterion* [5, 6], *bubble crowding* [7, 8, 9], *sublayer dryout* [10, 11, 12], and *interfacial lift-off* [13, 14, 15, 16]. The latter is the model discussed in the present paper.

Numerous, fairly reliable empirical CHF correlations also exist in the literature. However, in recent years, many researchers have refocused their efforts on determining the key physical mechanisms responsible for initiating CHF in pursuit of a universal CHF model.

The present study will first explore the trigger mechanism for CHF from a short vertical surface in near-saturated flow boiling using an apparatus which lends itself to high resolution photographic study of interfacial features. A model is proposed the validity of which will be tested for both straight and curved flow boiling. The curved flow configuration facilitates an assessment of the accuracy of the model in predicting the enhancement effects measured by many researchers due to curvature [17, 18, 19, 20]. This study will then treat pool boiling on a vertical surface simply as a limiting condition of flow boiling corresponding to zero liquid velocity. It will then be shown the proposed model reduces to a simple expression for pool boiling CHF.

2. EXPERIMENTAL METHODS

Straight and Curved Flow Boiling Visualization Facility

A CHF flow visualization apparatus was designed to maximize photographic access to interfacial features in close proximity to the heater surface in both straight and curved flows. The apparatus consisted of a curved flow channel having a 4.19-cm outer radius of curvature, which was located downstream from a straight channel. A 1.27-cm long heater was inserted in each of the straight and curved regions of the channel. As shown in Fig. 1, the flow channel was formed by milling a 0.16 cm $\times$ 0.64 cm slot into a transparent polycarbonate plastic (Lexan) plate. A second Lexan plate was clamped onto the first plate trapping an o-ring seal. The centerline of the curved heater was positioned at a 135-degree angle relative to the inlet flow. Both the straight and curved heaters were constructed from copper and heated by a thick-film electrical resistor silver soldered to the outer protruding surface. The heaters were inserted into insulating flanges made from G-10 fiberglass plastic. An o-ring was pressed between the base of each heater assembly

and the flow channel plate providing a leak proof seal. FC-87, a 3M dielectric fluid, was tested at a pressure of 1.37 bars (T_{sat} = 39 °C) with 8 °C inlet subcooling. Tilting the entire flow channel module allowed all tests to be conducted in an upflow configuration with respect to the tested heater. Only one heater was operated at a time.

Pool Boiling Facility

Figure 2 shows a schematic of the pool boiling test chamber which was constructed of G-10 fiberglass plastic and fitted on the front and back with Lexan windows. The chamber was equipped with two condensers and three cartridge heaters. The condenser coiled inside the chamber effectively recovered all of the vaporized liquid. An external reflux condenser connected to the chamber's vent acted as a final barrier to any escaping vapor during both deaeration and testing. To prevent the boiling on the cartridge heaters from influencing CHF on the primary test heater, the cartridge heaters were placed at the back of the test chamber, isolated from the test heater by a baffle plate. Water and FC-72, another 3M dielectric fluid, were tested at atmospheric pressure. The FC-72 test heater consisted of a 12.7 × 12.7 mm^2 copper block which was heated by a thick-film electrical resistor silver soldered to its back. A similar configuration was used for pool boiling of water but with a heater measuring 12.0 × 62.0 mm^2. Each heater was mounted on an angular rotation platform to facilitate testing at different surface orientations.

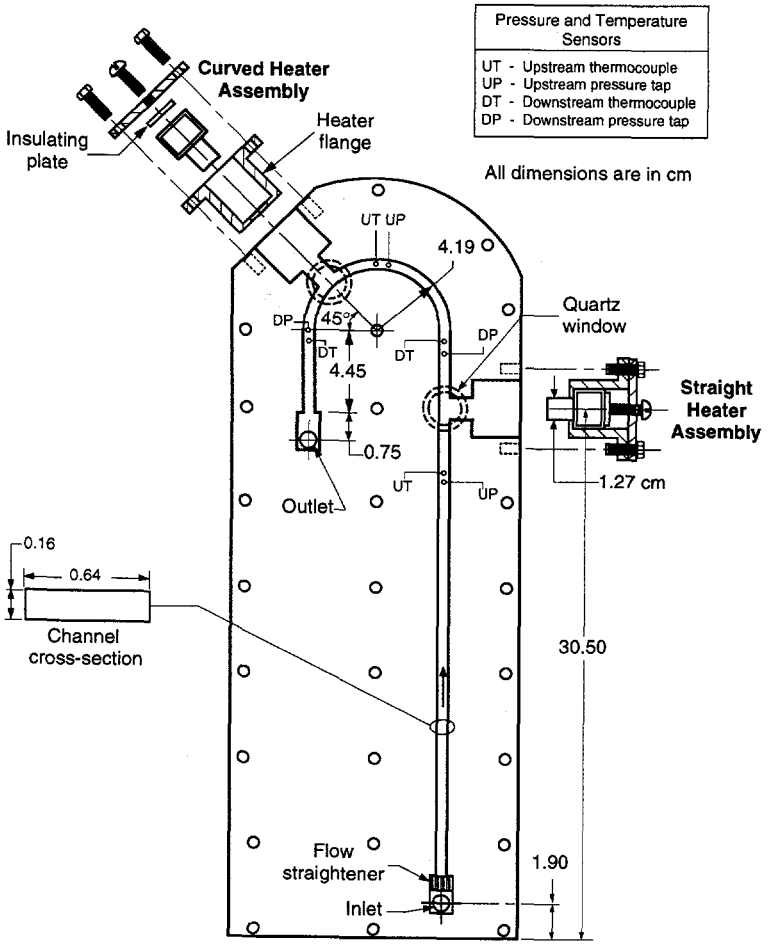

Figure 1. Flow Boiling Apparatus

3. PHOTOGRAPHIC STUDY OF VAPOR LAYER INTERFACIAL FEATURES

The flow and pool boiling facilities showed similar vapor production behavior at conditions leading to CHF. At a heat flux of about 85% of CHF, large coalescent bubbles were observed sliding over the heater surface. The length of these coalescent bubbles increased with increasing heat flux until, eventually, a fairly continuous wavy vapor layer was formed over the heater surface at heat fluxes below CHF. Boiling was sustained by liquid entrainment near the lower edge of the heater in pool boiling and the heater's upstream edge in flow boiling, as well as in *wetting fronts*, where the liquid-vapor interface made contact with the heater surface. Experimental evidence supporting this wetting front description is also available from studies by Fiori and Bergles [21], Hino and Ueda [22, 23], and Galloway and Mudawar [20]; all of whom measured fluctuations in heater surface temperature synchronous with the passage of vapor slugs.

Figure 3 shows the vapor layer formation on the curved heater in flow boiling corresponding to heat fluxes equal to 99% of CHF. Using a magnification better than 50×, no vapor jets could be seen emanating from the heater surface. Rather, a violent surge of small bubbles in the wetting fronts was observed to be feeding the vapor layer. The wavelength for both the straight and curved heaters decreased with increasing velocity. However, the curved heater exhibited significant differences in the shape of the wavy vapor layer as compared to the straight heater. For equal inlet velocities, the interfacial wavelength was greater for the straight heater than for the curved heater and, occasionally, at inlet velocities greater than 1.25 m/s, the curved heater projected vapor away from its surface in the form of vapor slugs which protruded from the wave peaks. No such behavior was observed with the straight heater.

Vapor layer mean thickness and wavelength were measured from high-speed video images captured by a 6000 partial frames per second Kodak EktaPro 1000 motion analyzer, which were later analyzed on a 55-cm wide screen; only still photography was used in the pool boiling tests. Thirty measurements were made for each inlet velocity to quantify the randomness of the interfacial features. Figure 4 shows the wavelength for the straight heater was greater than for the curved heater and the wavelengths for both heaters decreased with increasing inlet velocity. Figure 4 also compares the ratio of wavelength to mean thickness of the vapor layer for both heaters.

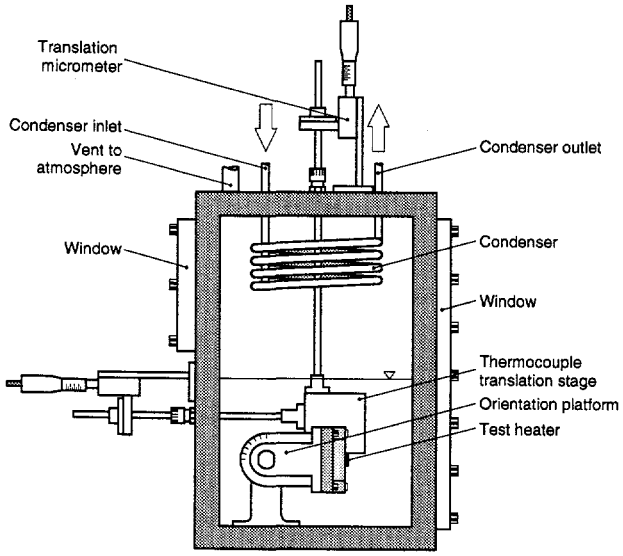

Figure 2. Pool Boiling Test Chamber

4. CHF MODEL

Model Assumptions

The proposed CHF model is built upon physical observations from extensive high speed video imaging studies as discussed in the previous section and illustrated in Fig. 5: (1) at heat fluxes approaching CHF, vapor coalesces to form a fairly continuous wavy vapor layer; (2) liquid is entrained at wetting fronts where the liquid-vapor interface contacts the heater surface; (3) vigorous boiling persists near the leading edge of the heater and in the wetting fronts while regions between neighboring wetting fronts dry out; (4) CHF commences when the liquid-vapor interface separates from the heater surface at the location of the most upstream wetting front; and (5) remaining wetting fronts are separated, in succession, after separation of the upstream wetting front.

As shown in Fig. 5, the first wetting front is established at a distance z^* from the leading edge and then propagates along the heater surface at a speed c_r. The vapor layer interfacial wavelength, $2\lambda_c$, was determined from hydrodynamic instability theory (discussed below) and observations made using the high-speed video imaging. When the liquid-vapor interface is unstable, a disturbance having a wavelength equal to λ_c is assumed to touch the heater surface at $z = z^*$ (z^* is

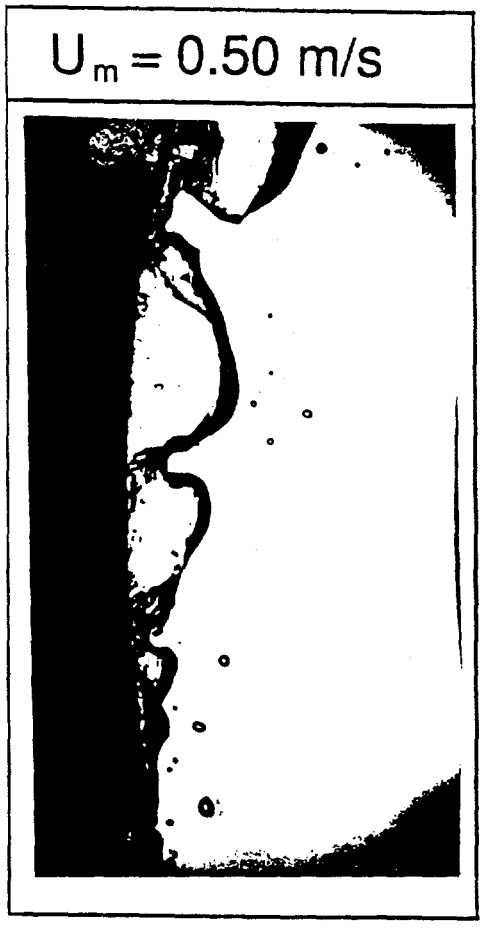

Figure 3. Wavy Vapor Layer Development on Curved Heater in Flow Boiling Just Prior to CHF

slightly greater than λ_c, the difference being a negligible distance z_0 over which the vapor velocity just exceeds the liquid velocity as discussed by Galloway and Mudawar [14]), enabling liquid to contact the heater over a localized region. A short time later, at $t = \lambda_c/c_r$, another disturbance approaching the heater surface will be forced away by the momentum of vapor emanating from residual liquid at $z = z^*$ left after the passage of the previous wetting front. Not until a later time $t = 2\lambda_c/c_r$, after the residual liquid has been consumed at the location of the first wetting front, will a new wetting front be established on the heater surface. Wetting is, therefore, skipped every other cycle and wetting fronts are separated by $2\lambda_c$ wavelengths.

Surface Energy Balance at CHF

A Lagrangian frame of reference is used to model heat transfer to the moving wetting fronts illustrated in Fig. 5. Equation (1) sums the transient energy removed from the heater by the passage of all wetting fronts in contact with the heater between the time a wetting front first forms on the heater surface and the time the next wetting front is established at the same location. Equation (1) also accounts for the steady heat removal from the continuous wetting zone, $0 < z < z^*$.

$$q_m = \frac{c_r / \left(2\,\lambda_c\right)}{L - z^*} \left[\int_0^{\tau} \int_{z^*}^{L} q_{s,1}\, dz\, dt + \cdots + \int_0^{\tau} \int_{z^*}^{L} q_{s,n}\, dz\, dt \right], \tag{1}$$

where $q_{s,1}, q_{s,2}, \ldots, q_{s,n}$ are the local heat fluxes corresponding to wetting fronts 1, 2, . . , n, respectively. Where a wetting front is present, q_s is equal to some localized heat flux value, q_l, otherwise q_s is essentially zero where the heater surface is dry.

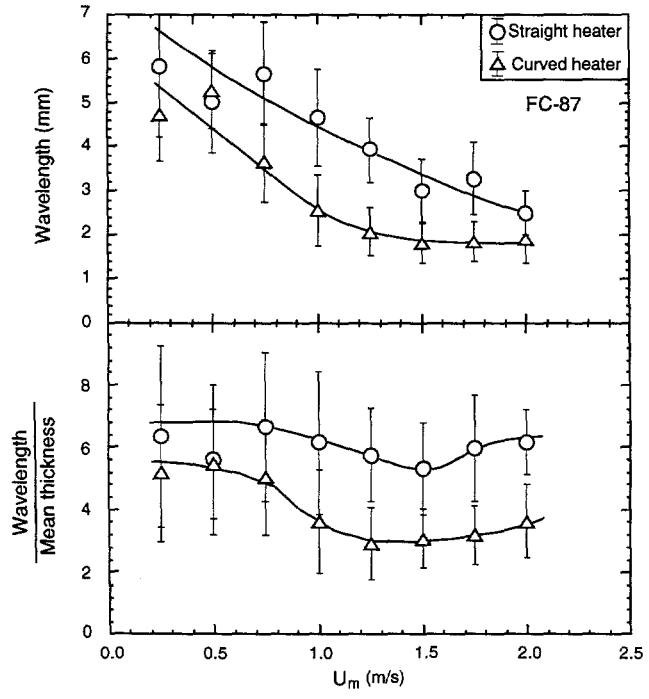

Figure 4. Vapor Layer Wavelength and Ratio of Wavelength to Mean Thickness Just Prior to CHF

The photographic study and data base revealed the span (length) of each wetting front was one-fourth the separation distance between wetting fronts; *i.e.*, CHF is about one-fourth the heat flux concentrated in the wetting fronts. A surface energy balance detailed by Galloway and Mudawar [14] reduces equation (1) to the following expression for CHF:

$$q_m = \left[1 - \frac{\lambda_c}{16\left(L - z^*\right)}\right] \frac{q_l}{4}, \tag{2}$$

where the coefficient in the brackets is close to unity for most operating conditions and accounts for continuous wetting in the region $0 < z < z^*$ and any partial wetting fronts in the downstream region, and q_l is the heat flux required to cause lifting of the most upstream wetting front.

CHF Trigger Mechanism: Lift-off Criterion

The lift-off heat flux will develop when the normal momentum of vapor generated in the wetting front just exceeds the pressure force exerted upon the interface as a result of interfacial curvature.

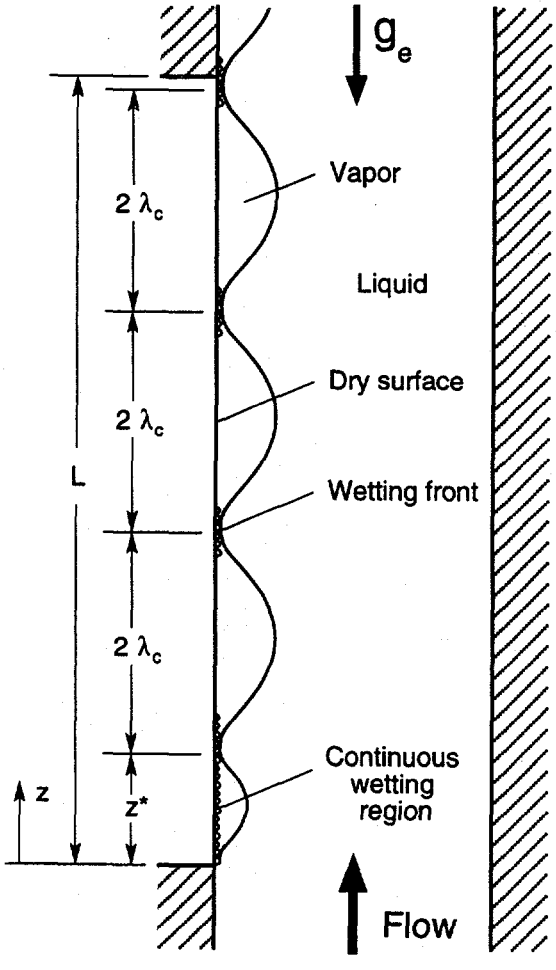

Figure 5. Wetting Front Propagation along a Vertical Surface

$$\rho_g \left[\frac{q_l}{\rho_g h_{fg} \left(1 + \frac{c_{p,f} \Delta T_{sub}}{h_{fg}} \right)} \right]^2 = \overline{P_f - P_g}, \tag{3}$$

where the average pressure difference across the interface, $\overline{P_f - P_g}$, is calculated by integrating the pressure difference over the span of the most upstream wetting front.

Combining equations (2) and (3) yields an expression for CHF which is applicable to both straight and curved heaters.

$$q_m = \frac{1}{4} \rho_g h_{fg} \left(1 - \frac{\lambda_c}{16\left(L - z^*\right)} \right) \left(1 + \frac{c_{p,f} \Delta T_{sub}}{h_{fg}} \right) \left[\frac{\overline{P_f - P_g}}{\rho_g} \right]^{1/2}. \tag{4}$$

Equation (4) shows predicting CHF requires estimation of $\overline{P_f - P_g}$. The next section will discuss an instability model which will be used to predict this key parameter for both straight and curved heaters.

The lift-off criterion alone can explain why, in flow boiling, CHF is greater for the curved, concave heater than the straight heater. For an assumed sinusoidal wave with wavelength λ and amplitude η_0, curvature at the wave peak is proportional to $(\eta_0 / \lambda)^2 / \eta_0$. Although the straight and curved heaters produced waves with fairly equal amplitudes, Fig. 4 indicates the waves acquired greater curvature over the curved heater than they did over the straight heater. This increased curvature resulted in a greater pressure force exerted upon the interface and, consequently, increases both the lift-off heat flux in the wetting fronts and CHF relative to the straight heater. As will be shown later, the curved heater produced an average enhancement of 23% compared to the straight heater.

Interfacial Instability of Vapor Layer

The interfacial waviness illustrated in Fig. 5 can be idealized as a hydrodynamic instability of an interface between a vapor layer of velocity $\bar{u}_{g,m}$ and height H_g and a liquid layer of velocity $\bar{u}_{f,m}$ and height H_f. Using classical instability theories [24, 25], the interfacial pressure difference resulting from a sinusoidal disturbance of the form $\eta(z,t) = \eta_0 e^{ik(z-ct)}$ perpendicular to the unperturbed interface can be expressed as [14]

$$P_f - P_g = -\eta k \left[\rho_f^{"} \left(c - \bar{u}_{f,m} \right)^2 + \rho_g^{"} \left(\bar{u}_{g,m} - c \right)^2 \right] - \left(\rho_f - \rho_g \right) g_n \eta = -\sigma k^2 \eta, \tag{5}$$

where g_n is the body force per unit mass perpendicular to the unperturbed interface ($g_n = 0$ for vertical upflow over a straight heater), and the modified density terms for a straight channel are expressed as [14]

$$\rho_f^{"} = \rho_f \coth\left(k H_f\right), \tag{6a}$$

$$\rho_g^{"} = \rho_g \coth\left(k H_g\right). \tag{6b}$$

Solving equation (5) yields the following equation for c:

$$c = \frac{\rho_g'' \bar{u}_{g,m} + \rho_f'' \bar{u}_{f,m}}{\left(\rho_g'' + \rho_f''\right)} \pm \sqrt{\frac{\sigma k}{\left(\rho_g'' + \rho_f''\right)} - \frac{g_n\left(\rho_f - \rho_g\right)}{k\left(\rho_g'' + \rho_f''\right)} - \frac{\rho_g'' \rho_f''\left(\bar{u}_{g,m} - \bar{u}_{f,m}\right)^2}{\left(\rho_g'' + \rho_f''\right)^2}} \quad . \tag{7}$$

The critical wavelength is defined as the wavelength that produces a neutrally stable wave. This wavelength can be calculated by setting the argument of c in equation (7) equal to zero.

$$\frac{2\pi}{\lambda_c} = k_c = \frac{\rho_f'' \rho_g''\left(\bar{u}_{g,m} - \bar{u}_{f,m}\right)^2}{2\sigma\left(\rho_f'' + \rho_g''\right)} + \sqrt{\left[\frac{\rho_f'' \rho_g''\left(\bar{u}_{g,m} - \bar{u}_{f,m}\right)^2}{2\sigma\left(\rho_f'' + \rho_g''\right)}\right]^2 + \frac{g_n\left(\rho_f - \rho_g\right)}{\sigma}} \quad . \tag{8}$$

This classical hydrodynamic instability model is not applicable to curved flow. Recently, Galloway and Mudawar [26] developed a new model for hydrodynamic instability along a curved interface. Interestingly, the above instability model was proven equally valid for curved flow, provided the liquid and vapor velocities in equations (5), (7) and (8) are calculated along the interface, and the modified density terms are replaced by the following:

$$\rho_f''' = \rho_f \left[\frac{\left(\frac{R_0}{R_1}\right)^{2kR_0} + 1}{\left(\frac{R_0}{R_1}\right)^{2kR_0} - 1}\right], \tag{9a}$$

$$\rho_g''' = \rho_g \left[\frac{\left(\frac{R_0}{R_2}\right)^{2kR_0} + 1}{1 - \left(\frac{R_0}{R_2}\right)^{2kR_0}}\right]. \tag{9b}$$

CHF Model Predictions for Straight and Curved Flow Boiling

A separated flow model given by Galloway and Mudawar [14, 26] was employed to predict local mean values of vapor layer thickness and velocities of the liquid and vapor layers in terms of inlet velocity, subcooling, and heat flux. These local values are required in order to predict the interfacial wavelength and $\overline{P_f - P_g}$.

Figure 6 shows the CHF model predicts the experimental data for the straight and the curved heaters with mean absolute errors of 7% and 14%, respectively. The accuracy of the model predictions is proof of the validity of assumptions used in constructing the surface energy balance and of the lift-off criterion. The CHF enhancement obtained with the curved heater over the straight heater is a direct consequence of the increased curvature of the individual interfacial waves

causing an increase in the net pressure force exerted upon the interface in the wetting fronts.

As for the limitations of the present model, several conditions exist for which the assumptions used may not be valid. They include (a) near-critical pressure, (b) highly subcooled flow, where the vapor layer development may be strongly influenced by condensation along the vapor-liquid interface, (c) high inlet velocities corresponding to $g_n = U_m^2 / R_2 > 10\, g_e$, where vapor slugs begin to detach from peaks in the wavy vapor-liquid interface, and (d) long heaters. A recent study by two of the authors [15, 16] explored the stream-wise changes in the interfacial features at CHF over long heaters. The vapor waves between wetting fronts maintained equal wavelengths over an axial distance close to the length of the heaters used in the present study, but were found to grow downstream due to merging of adjacent waves. This behavior increased the distance between wetting fronts resulting in smaller CHF for long heaters as compared to heaters close in size to the one used in the present study. These findings, while determined from straight heater experiments, clearly indicate the present model should not be applied in its present form to long straight or curved heaters.

5. THEORETICAL MODEL FOR POOL BOILING CHF FROM A VERTICAL SURFACE

Growth of Vapor Layer

Figure 7 shows pool boiling data for water for orientations ranging from horizontal ($\theta = 0$ degrees) to vertical (90 degrees), compared with predictions of the model by Zuber *et al.* [1], modified by replacing g_e by $g_e \cos\theta$. CHF decreases with increasing angle of orientation following, to some degree, the predicted trend. However, while the model predicts zero CHF for the vertical orientation, the data show an increase in CHF between 75 and 90 degrees. Obviously, the mechanism proposed by Zuber *et al.* is not suitable for near-vertical orientations.

In pool boiling on a vertical surface, the mean velocity of liquid outside the vapor layer is zero. Equations for the mean vapor velocity, $\bar{u}_{g,m}$, and vapor layer thickness, δ, can be derived by applying mass, momentum, and energy conservation for a control volume of the vapor layer of length Δz. Combining both mass and energy conservation for this control volume and integrating with respect to z gives

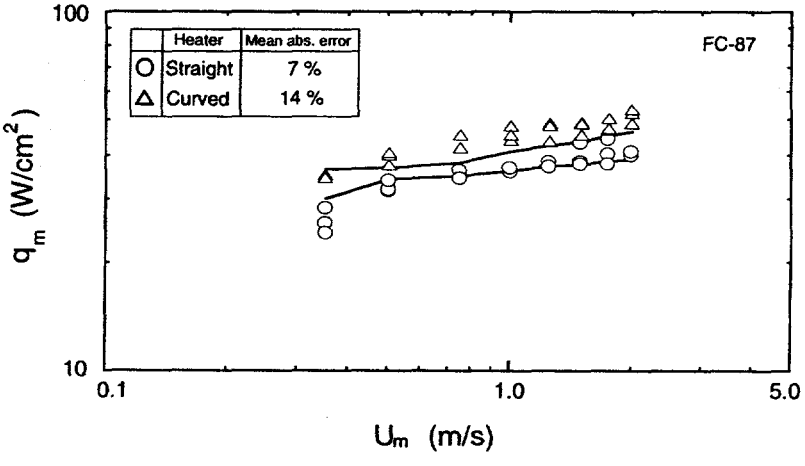

Figure 6. Comparison of Model Predictions and Flow Boiling CHF Data for Straight and Curved Heaters

$$\rho_g \bar{u}_{g,m} \delta = \frac{q_m z}{h_{fg}\left[1 + \frac{c_{p,f}\Delta T_{sub}}{h_{fg}}\right]} . \tag{10}$$

A momentum balance on the same control volume yields

$$\frac{d}{dz}\left[\rho_g \bar{u}_{g,m}^2 \delta\right] = \left(\rho_f - \rho_g\right) g_e \delta . \tag{11}$$

Combining equations (10) and (11) gives a differential equation relating $\bar{u}_{g,m}$ to z. The solution for this equation is

$$\bar{u}_{g,m} = \left[\frac{2}{3}\left(\frac{\rho_f - \rho_g}{\rho_g}\right) g_e z\right]^{1/2} . \tag{12}$$

Substituting for $\bar{u}_{g,m}$ using equation (12) in equation (10) gives the variation of δ with z.

$$\delta = \frac{q_m}{\rho_g h_{fg}\left[1 + \frac{c_{p,f}\Delta T_{sub}}{h_{fg}}\right]} \left[\frac{2}{3}\left(\frac{\rho_f - \rho_g}{\rho_g}\right) g_e\right]^{-1/2} \sqrt{z} . \tag{13}$$

The critical wavelength corresponding to the onset of instability can be derived from equation (8) by setting g_n and $\bar{u}_{f,m}$ equal to zero; further simplification is also possible because, for the conditions of the pool boiling study, $\rho_g'' \equiv \rho_g$.

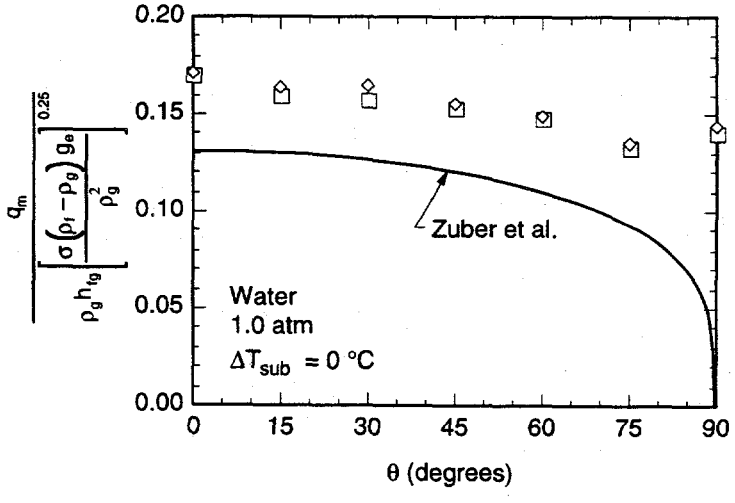

Figure 7. Comparison of Pool Boiling CHF Data for Different Orientations with Predictions of the Modified Model by Zuber *et al.* [1]

$$\lambda_c = \frac{2\pi}{k_c} = \frac{2\pi\,\sigma\left(\rho_f + \rho_g\right)}{\rho_f \rho_g'' \bar{u}_{g,m}^2}. \tag{14}$$

The mean interfacial pressure force over the wetting front for a sinusoidal wave with $k = 2\pi/(2\lambda_c)$ becomes

$$\overline{P_f - P_g} = 2\sqrt{2}\,\pi \frac{\sigma\delta}{\lambda_c^2}. \tag{15}$$

Substituting the above expression in equation (4), neglecting the coefficient due to the upstream continuous wetting zone and the downstream partial wetting front, gives

$$q_m = \frac{1}{4}\rho_g h_{fg}\left[1 + \frac{c_{p,f}\Delta T_{\text{sub}}}{h_{fg}}\right]\left[\left(2\sqrt{2}\,\pi\right)\frac{\sigma\delta}{\rho_g \lambda_c^2}\right]^{1/2}. \tag{16}$$

Since the first wetting front is centered at $z = \lambda_c$, the critical wavelength, equation (14), can be expressed in terms of $\bar{u}_{g,m}$, equation (12), corresponding to $z = \lambda_c$. This gives

$$\lambda_c = \left[3\pi\left(\frac{\rho_f + \rho_g}{\rho_f - \rho_g}\right)\frac{\sigma}{\rho_f g_e}\right]^{1/2}. \tag{17}$$

Substituting the expressions for δ (based on $z = \lambda_c$), equation (13), and λ_c, equation (17), in equation (16) yields the following CHF relation

$$q_m = \frac{1}{8}\left(\frac{\pi}{3}\right)^{1/4}\left[1 + \frac{c_{p,f}\Delta T_{\text{sub}}}{h_{fg}}\right]\left[\frac{\rho_f}{\rho_f + \rho_g}\right]^{3/4}\rho_g h_{fg}\left[\frac{\sigma\left(\rho_f - \rho_g\right)g_e}{\rho_g^2}\right]^{1/4}. \tag{18}$$

The above equation can be further simplified for saturated conditions, and pressures much smaller than critical to

$$q_m = 0.126\,\rho_g h_{fg}\left[\frac{\sigma\left(\rho_f - \rho_g\right)g_e}{\rho_g^2}\right]^{1/4}. \tag{19}$$

Interestingly, equation (19) is identical in form to the model by Zuber *et al.* [1], although the mechanisms proposed in the individual models are distinctly different. Also, while the model by Zuber *et al.* predicts zero CHF for vertical surfaces, the present model, as shown in Fig. 7, predicts a CHF value for the same orientation only 11% smaller than the data.

6. CONCLUSIONS

Experiments involving pool and flow boiling from vertical surfaces were performed to ascertain the CHF trigger mechanism for each. The flow boiling experiments included both straight and curved surfaces. Key conclusions from the study are as follows:

(1) A fairly continuous wavy vapor layer engulfs the heater surface at heat fluxes smaller than CHF in both pool and flow boiling. Boiling remains active in wetting fronts, where the interface of the vapor layer contacts the heater surface. CHF is triggered when the normal momentum of the vapor produced in the wetting front exceeds the pressure force exerted upon the interface due to interfacial curvature.

(2) A CHF model constructed from these observations predicts flow boiling CHF data for the straight and curved heaters with mean absolute errors of 7% and 14%, respectively.

(3) In flow boiling, CHF is higher for the curved heater than for the straight heater because of a greater pressure resistance to interfacial separation in the case of the curved heater.

(4) For pool boiling, the present model reduces to an expression identical in form to the model by Zuber *et al.* [1], although the mechanisms proposed in the individual models are distinctly different. However, while the model by Zuber *et al.* predicts zero CHF for vertical surfaces and is therefore unsuitable for vertical surfaces, the present model predicts a CHF value for the same orientation only 11% smaller than the data.

ACKNOWLEDGMENT

The authors are grateful for the support of the Office of Basic Energy Sciences of the U.S. Department of Energy (Grant No. DE-FE02-93ER14394).

NOMENCLATURE

c	wave speed
c_p	specific heat at constant pressure
c_r	real component of wave speed
g_e	Earth gravity
g_n	component of body force per unit mass normal to liquid-vapor interface
H	channel height, $H_f + H_g$, $R_2 - R_1$
H_f	liquid layer thickness
H_g	vapor layer thickness
h_{fg}	latent heat of vaporization
k	wave number, $2\pi/\lambda$
k_c	critical wave number, $2\pi/\lambda_c$
L	heater length
n	number of wetting fronts
P	pressure
$\overline{P_f - P_g}$	mean interfacial pressure difference in wetting front

q_l heat flux (at CHF) corresponding to wetting front separation (lift-off)
q_m critical heat flux (CHF)
R_0 radius of unperturbed interface in curved flow
R_1 inner radius of curved channel
R_2 outer radius of curved channel and curved heater surface
t time
T temperature
ΔT_{sub} liquid subcooling
u_m mean velocity across liquid or vapor layer
U_m mean liquid velocity upstream of heater in flow boiling
z spatial coordinate in the stream-wise direction
z^* distance from leading edge of heater to center of first wetting front, $z_0 + \lambda_c(z^*)$
z_0 position from leading edge where the liquid and vapor velocities become equal

Greek Symbols
δ mean vapor layer thickness ($= H_g$)
η_0 interfacial displacement
η amplitude of interfacial displacement
θ surface angle of orientation
λ wavelength of interfacial perturbation
λ_c critical wavelength corresponding to onset of instability
ρ density
ρ'' modified density defined in equations (6a) and (6b)
ρ''' modified density defined in equations (9a) and (9b)
σ surface tension
τ wetting period

Subscripts
f saturated liquid
g saturated vapor
m mean
sub subcooling

REFERENCES

1. N. ZUBER, M. TRIBUS and J. M. WESTWATER, "The Hydrodynamic Crisis in Pool Boiling of Saturated and Subcooled Liquid," *International Developments in Heat Transfer*, Boulder, CO, Part II, 230-236 (1961).

2. S. S. KUTATELADZE and A. I. LEONT'EV, "Some Applications of the Asymptotic Theory of the Turbulent Boundary Layer," *Proc. 3rd Int. Heat Transfer Conf.*, Chicago, IL, Vol. 3, pp. 1-6 (1966).

3. L. S. TONG, "Boundary-Layer Analysis of the Flow Boiling Crisis," *Int. J. Heat Mass Transfer* 11, 1208-1211 (1968).

4. L. S. TONG, "A Phenomenological Study of Critical Heat Flux," ASME Paper 75-HT-68 (1975).

5. J. H. LIENHARD and R. EICHHORN, "Peak Boiling Heat Flux on Cylinders in a Cross Flow," *Int. J. Heat Mass Transfer* 19, 1135-1142 (1976).

6. J. H. LIENHARD and M. M. HASAN, "On Predicting Boiling Burnout with the Mechanical Energy Stability Criterion," *ASME J. Heat Transfer* 101, 276-279 (1979).

7. G. J. KIRBY, R. STANIFORTH and J. H. KINNEIR, "A Visual Study of Forced Convection Boiling Part 2: Flow Patterns and Burnout for a Round Test Section," Report AEEW-R 506, United Kingdom Atomic Energy Authority, Atomic Energy Establishment, Winfrith, England (1967).

8. W. HEBEL, W. DETAVERNIER and M. DECRETON, "A Contribution to the Hydrodynamics of Boiling Crisis in a Forced Flow of Water," *Nucl. Engng Des.* 64, 433-445 (1981).

9. J. WEISMAN and B. S. PEI, "Prediction of Critical Heat Flux in Flow Boiling at Low Qualities," *Int. J. Heat Mass Transfer* 26, 1463-1477 (1983).

10. C. H. LEE and I. MUDAWAR, "A Mechanistic Critical Heat Flux Model for Subcooled Flow Boiling based on Local Bulk Flow Conditions," *Int. J. Multiphase Flow* 14, 711-728 (1988).

11. Y. KATTO, "A Physical Approach to Critical Heat Flux of Subcooled Flow Boiling in Round Tubes," *Int. J. Heat Mass Transfer* 33, 611-620 (1990).

12. Y. KATTO, "Prediction of Critical Heat Flux of Subcooled Flow Boiling in Round Tubes," *Int. J. Heat Mass Transfer* 33, 1921-1928 (1990).

13. J. E. GALLOWAY and I. MUDAWAR, "CHF Mechanism in Flow Boiling from a Short Heated Wall - Part 1. Examination of Near-Wall Conditions with the aid of Photomicrography and High-Speed Video Imaging," *Int. J. Heat Mass Transfer* 36, 2511-2526 (1993).

14. J. E. GALLOWAY and I. MUDAWAR, "CHF Mechanism in Flow Boiling from a Short Heated Wall - Part 2. Theoretical CHF Model," *Int. J. Heat and Mass Transfer* 36, 2527-2540 (1993).

15. C. O. GERSEY and I. MUDAWAR, "Effects of Heater Length and Orientation on the Trigger Mechanism for Near-Saturated Flow Boiling CHF - Part 1. Photographic and Statistical Characterization of the Near-Wall Interfacial Features," *Int. J. Heat Mass Transfer* 38, 629-642 (1995).

16. C. O. GERSEY and I. MUDAWAR, "Effects of Heater Length and Orientation on the Trigger Mechanism for Near-Saturated Flow Boiling CHF - Part 2. CHF Model," *Int. J. Heat Mass Transfer* 38, 643-654 (1995).

17. W. R. GAMBILL and N. D. GREENE, "Boiling Burnout with Water in Vortex Flow," *Chem. Engng Prog.* 54(10), 68-76 (1958).

18. Z. L. MIROPOL'SKIY and V. Y. PIKUS, "Critical Boiling Heat Fluxes in Curved Channels," *Heat Transfer-Soviet Research* 1, 74-79 (1969).

19. T. G. HUGHES and D. R. OLSON, "Critical Heat Fluxes for Curved Surface during Subcooled Flow Boiling," *Trans. Canadian Soc. Mech. Eng.* 3, 122-130 (1975).

20. J. E. GALLOWAY and I. MUDAWAR, "Critical Heat Flux Enhancement by means of Liquid Subcooling and Centrifugal Force Induced by Flow Curvature," *Int. J. Heat Mass Transfer* 35, 1247-1260 (1992).

21. M. P. FIORI and A. E. BERGLES, "Model of Critical Heat Flux in Subcooled Flow Boiling," *Proc. 4th Int. Heat Transfer Conf.*, Versailles, France, Vol. 6, pp. 354-355 (1970).

22. R. HINO and T. UEDA, "Studies on Heat Transfer and Flow Characteristics in Subcooled Flow Boiling-Part 1. Boiling Characteristics," *Int. J. Multiphase Flow* 11, 269-281 (1985).

23. R. HINO and T. UEDA, "Studies on Heat Transfer and Flow Characteristics in Subcooled Flow Boiling-Part 2. Flow Characteristics," *Int. J. Multiphase Flow* 11, 283-297 (1985).

24. H. LAMB, *Hydrodynamics* (6th Edn), p. 371. Dover Publications, New York (1945).

25. L. M. MILNE-THOMPSON, *Theoretical Hydrodynamics* (4th Edn), p. 409. Macmillan, New York (1960).

26. J. E. GALLOWAY and I. MUDAWAR, "A Theoretical Model for Flow Boiling CHF from Short Concave Heaters," *ASME J. Heat Transfer*, in press.

SHORT-PULSE LASER INTERACTIONS WITH DISORDERED MATERIALS AND LIQUIDS

Leslie M. Phinney, Cynthia H. Goldman, Jon P. Longtin, and Chang-Lin Tien

Department of Mechanical Engineering
University of California at Berkeley
Berkeley, California 94720

ABSTRACT

High-power, short-pulse lasers in the picosecond and subpicosecond range are utilized in an increasing number of technologies, including materials processing and diagnostics, micro-electronics and devices, and medicine. In these applications, the short-pulse radiation interacts with a wide range of media encompassing disordered materials and liquids. Examples of disordered materials include porous media, polymers, organic tissues, and amorphous forms of silicon, silicon nitride, and silicon dioxide. In order to accurately model, efficiently control, and optimize short-pulse, laser-material interactions, a thorough understanding of the energy transport mechanisms is necessary. Thus, fractals and percolation theory are used to analyze the anomalous diffusion regime in random media. In liquids, the thermal aspects of saturable and multiphoton absorption are examined. Finally, a novel application of short-pulse laser radiation to reduce surface adhesion forces in microstructures through short-pulse laser-induced water desorption is presented.

INTRODUCTION

Since their invention thirty years ago, lasers have altered the direction and rate of the development of science and technology. Laser applications have fundamentally influenced modern technology in the areas of measurement, materials, manufacturing, information, and communication [1]. Short-pulse lasers are being applied to materials processing and diagnostics, electronic device fabrication and maintenance, and medical procedures. In these varied applications, short-pulse laser radiation interacts with a multitude of different materials, including, but not limited to, metals, semiconductors, polymers, porous media, liquids, and biological tissue.

Examples of short-pulse laser applications in materials processing and diagnostics include annealing of radiation damage in ion-implanted semiconductors, recrystallization of amorphous (noncrystalline) and polycrystalline silicon, rapid thermal cleaning, deposition of thin films, creation of metastable alloys, and thin-film and atomic-level diagnostics [2]. The increased temporal resolution of optical observations in diagnostics allows detailed "stop action" observations of previously inaccessible phenomena. In addition, the ultrashort laser-material interaction time permits highly localized observation and processing due to the short-range of diffusion during the interaction time.

In these applications, laser interactions with random media such as amorphous materials, porous media, and composites are often required. Amorphous forms of materials such as silicon dioxide, silicon nitride, and silicon are widely used in microelectronics and micro-sensor/actuator fabrication. Many nanostructured and metastable materials formed by laser processing are also amorphous [3]. Also, porous silicon, porous metal "black" coatings, polymers, and composites are becoming increasingly important. Nanosecond and picosecond laser pulses have also been used to ablate atherosclerotic tissue [4], a biological tissue which is random in nature.

Additionally, the interaction of high-power, pulsed laser radiation with liquids is fundamental to applications in many contemporary technologies, including ophthalmic microsurgery and gall-stone fragmentation [5], laser-induced desorption of thin films [6], laser particle removal [7], photothermal spectroscopy, and laser pulse generation and modification [8,9]. The liquid phase is also present in both laser melting and vaporization processes. Moisture induced device failure is a significant and persistent problem in the microelectronics industry [10,11], with incomplete moisture removal from electronic devices being a cause of leakage current, oxidation, and contamination [11]. Microelectromechanical systems are also subject to liquid related problems during fabrication and operation. Sticking and the accompanying high static friction between a tiny movable part and an underlying substrate, termed *stiction*, is a major problem for microstructures and is mainly due to capillary forces from residual water [12,13].

In laser-assisted processes and laser design, temperature control is a major consideration necessitating the accurate characterization and modeling of energy transport during laser-material interactions. As the pulse width of lasers used in many applications has decreased into the picosecond and subpicosecond range, the applicability of conventional models of energy transport is questionable [1,14]. Short-pulse laser heating of metals has been recently researched for both single- and multi-layer metal films [15,16,17], but the interaction between short-pulse laser radiation and random media or liquids is not fully understood and will be discussed in this paper. An application of short-pulse laser radiation to reduce the surface adhesion of silicon microstructures is also presented.

TRANSPORT IN AMORPHOUS AND NANOSTRUCTURED MATERIALS

In short time-scale applications involving random media, a regime of anomalous diffusion is observed, where the thermal diffusivity is time dependent. In this anomalous regime, transport is slowed compared to that which occurs during normal diffusion. Fournier and Boccara [18] observed anomalous diffusion in an assembly of weakly-bonded, copper spheres (~ 100 μm in diameter) heated by a short-pulse (~ 1 ns) laser. By measuring the transient surface temperature, they were able to distinguish the anomalous diffusion region from those in which normal diffusion occurred. Gefen et al. [19] predicted that anomalous diffusion will have an important effect on the AC electrical conductivity of a percolating network in high frequency (short time-scale) applications. Similarly, Goldman et al. [20] predicted that anomalous diffusion will have a significant effect on thermal transport in amorphous materials on short time scales such as short-pulse laser-material interactions.

The range and impact of anomalous diffusion in transient thermal transport in random media was studied using fractals and percolation theory. A fractal is a shape that is made up of parts similar to the whole in some way [21]. A percolation network is characterized by its correlation length, ξ, a length scale below which the network exhibits fractal behavior and above which it appears homogeneous. Figure 1 shows the temporal behavior of surface temperature of a random medium heated by an instantaneous plane source. Three distinct regimes are present. In the first regime, the heat is absorbed by the basic unit of the percolating network which is Euclidean, so the temperature follows that predicted for normal diffusion. An example of a basic unit of a percolating network is a porous silica particle in a silica aerogel [22,23]. Next, the energy

is transmitted from one site to another in the fractal cluster and diffusion is anomalous. Finally, the energy carriers have traveled a distance greater than the correlation length in the material, the material appears homogeneous, and diffusion is once again normal.

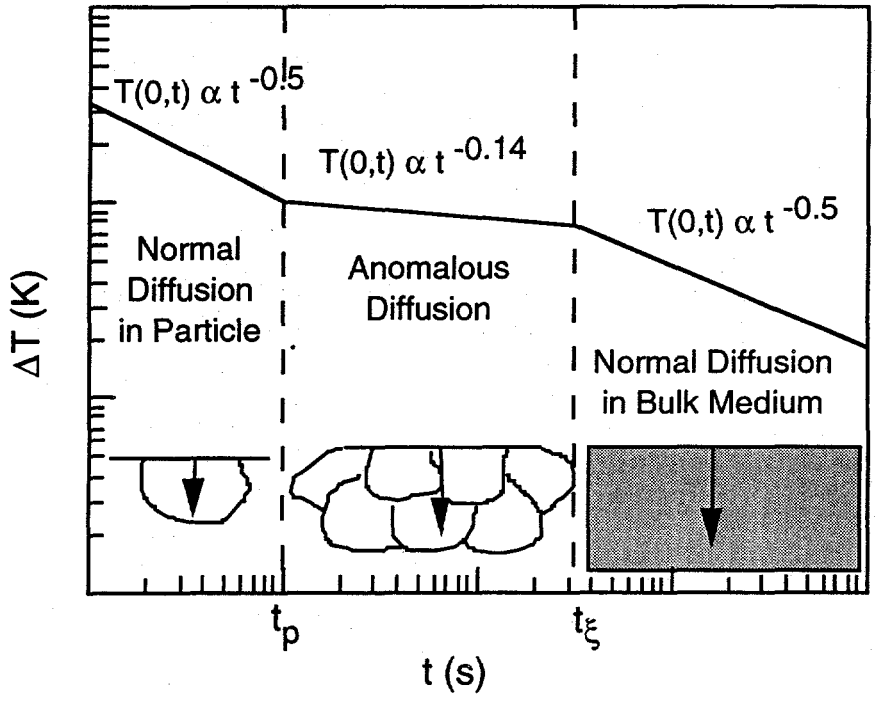

Figure 1. Regimes of Diffusion in Random Media [24]

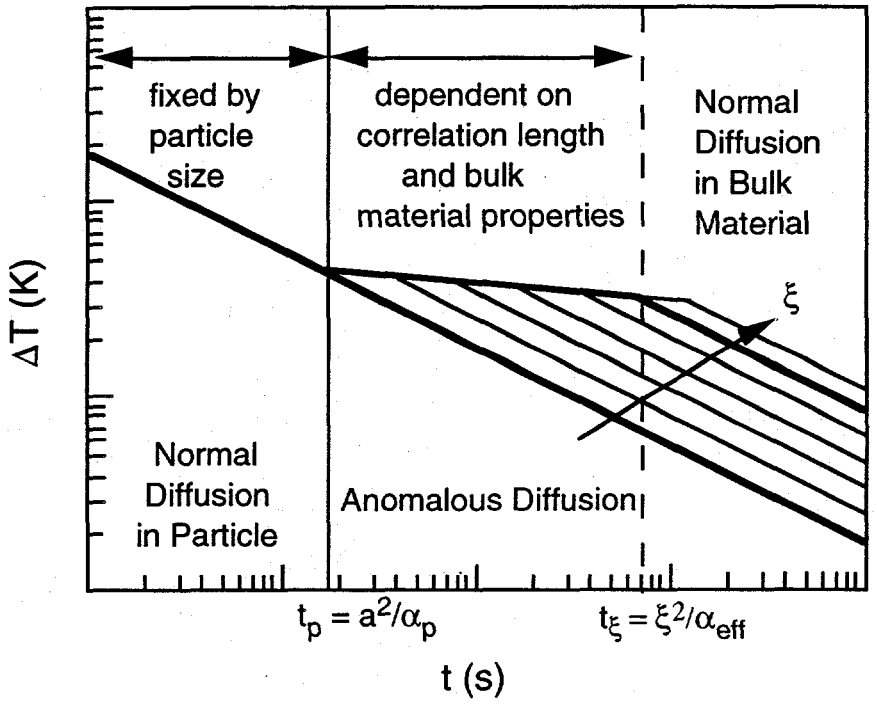

Figure 2. Scaling of Anomalous Diffusion Regime [24]

The impact of anomalous diffusion can be determined by considering the characteristic time and length-scales of heating and other transport mechanisms relative to the time and length-scales of anomalous diffusion[24]. Anomalous diffusion is expected to occur when the length-scale of transport is on the order of the correlation length. The characteristic crossover times, t_p and t_ξ, depend on the particle size, a, and correlation length, ξ, respectively, as well as the diffusivities, α_p and α_{eff}. Figure 2 illustrates the dependence of the anomalous diffusion regimes on particle size, correlation length, and diffusivity of the particle or random medium.

SHORT-PULSE, HIGH-INTENSITY LASER-LIQUID INTERACTIONS

When exposed to laser irradiation, liquid molecules absorb photons and transition to excited states, which usually have different absorption characteristics than the initial (ground) state. After a characteristic relaxation time, τ_p, ~10^{-12}-10^{-10} s, the molecule will relax back to the ground state. At low intensities, relaxation occurs fast enough to keep the majority of the molecules in the ground state; the absorption is then linear, obeying an exponential decay with distance into the liquid (Beer's law). At high laser intensities, however, enough molecules can be promoted to excited states to alter the bulk transmission and heating effects [25]. This is called *saturable absorption*, and occurs in both pure liquids and solutions, including organic dyes, alcohols, and water. In Figure 3, plots of the temperature rise as a function of distance x into a common saturable absorber (Eastman dye # 9470) are shown. One-hundred 35 ps laser pulses with wavelength of 1064 nm and pulse energy of 70 mJ pass through a 1 cm dye cell. The dye concentration is $8.1 \cdot 10^{-6}$ mol/liter in a 1,2 dichloroethane solvent. The threshold intensity I_s represents the onset of saturation, and the intensity is increased by an order of magnitude in each frame. The dashed lines are classical, low-intensity model results; the solid lines represent the microscopic model. The deviation from low-intensity models (Beer's law) is seen to be very significant at high intensities.

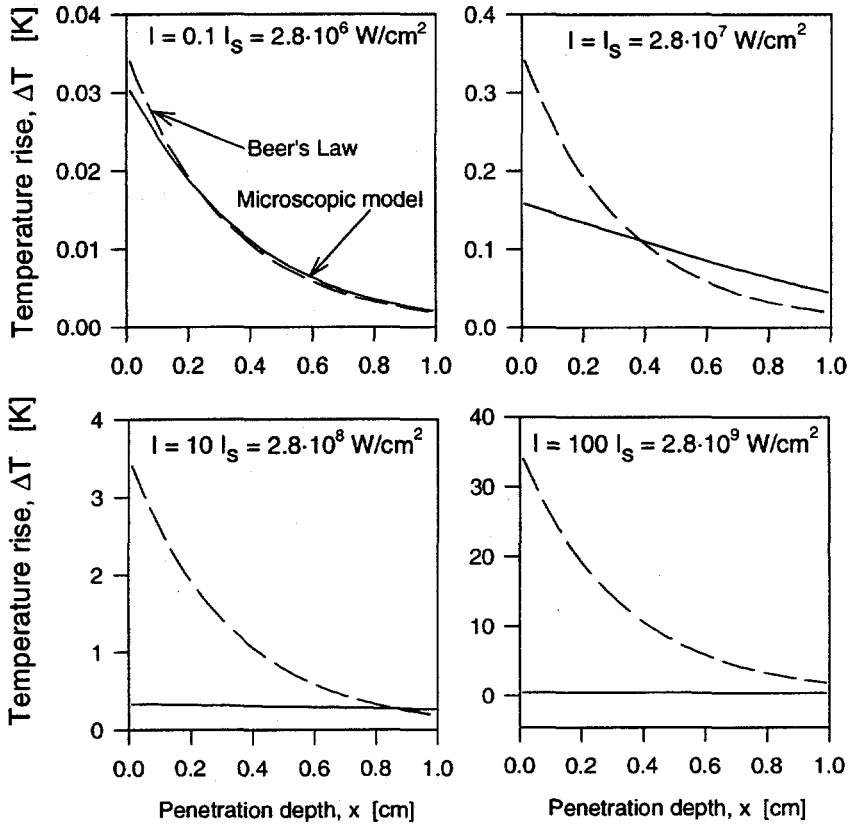

Figure 3. Intensity-dependent temperature during saturable absorption [25]

At even higher intensities the molecule can absorb enough photons to either ionize, which removes an electron completely, or dissociate into simpler constituent products. This process, called *multiphoton absorption and photolysis*, results in a combination of free electrons, ionized cations, and dissociation products that can interact strongly with the incident laser pulse, strongly altering the absorption and heating properties of the liquid [26]. Figure 4 shows the temperature profiles in 1 cm of water irradiated by a combination of 532 nm and 266 nm laser pulses of 1 ns duration at intensities of $1 \cdot 10^9$ and $1 \cdot 10^{10}$ W/cm^2. For the high-intensity pulse, the temperature rise varies over one to two orders of magnitude from the front to the back of the liquid. The total temperature rise due to the 266 nm and 532 nm laser pulses can exceed 40 K, which is three to four orders of magnitude greater than that predicted by classical models [26]. Also, the temperature rise is a strong function of intensity, thus precise control of heating in the liquid can be accomplished by varying the intensity.

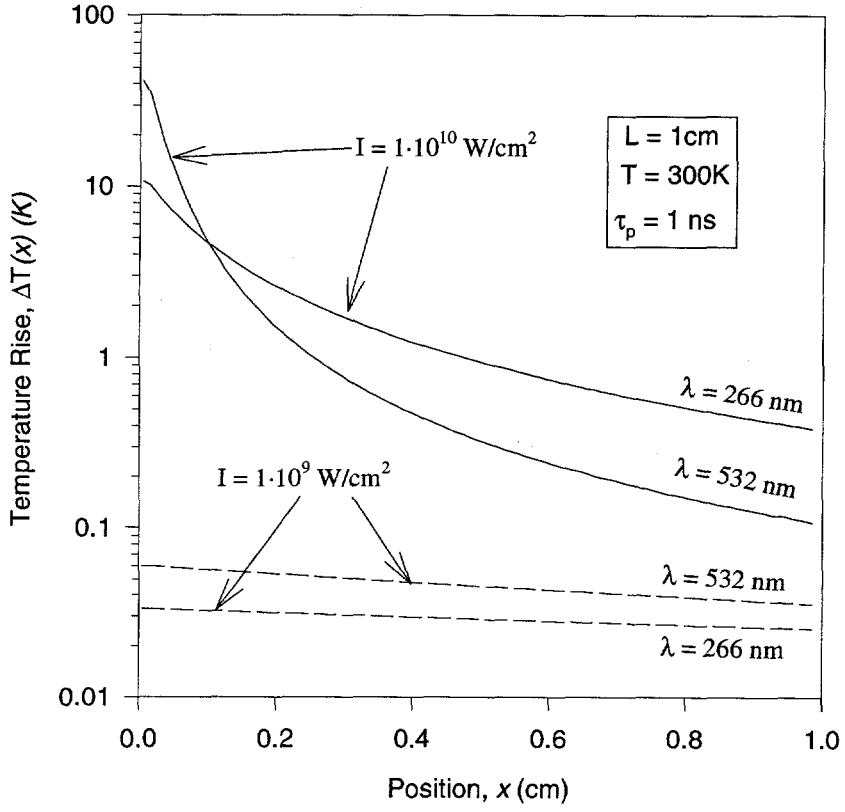

Figure 4. Temperature profiles in water during multiphoton absorption [26]

REDUCTION OF STICTION USING SHORT-PULSE LASER RADIATION

Stiction, the high surface adhesion between microelectromechanical surfaces, is often the result of forces from capillary liquids during the microdevice release process. Residual water molecules can be present underneath the silicon microstructures stuck on the underlying substrate. The desorption of trapped liquid molecules should reduce the adhesion force on the structures. Desorption induced by ultrashort-pulse laser radiation for metals and resulting electronic excitations was first reported by Prybyla et al. [27]. After irradiating a Pd surface with 200 femtoseconds (fs), 620 nm laser pulses, they measured the desorption rate of NO molecules from the Pd surface and showed that the total desorption yield varies superlinearly with the absorbed laser fluence. Since the desorption yield is proportional to the fluence at pulse durations longer than nanoseconds [28], a desorption mechanism other than thermal desorption due to lattice vibrations was involved. The role of the extremely high electron temperature was later confirmed by Prybyla et al. [29], and a model of desorption yield was proposed by Kao et al. [30].

Calculations for silicon microstructures (~ 2 μm thick) irradiated by short-pulse lasers (< 5 ps) indicate that high electron temperatures would exist at short times at both the front and rear surfaces (where the front surface is the surface irradiated by the laser) [31]. At the same time, the lattice temperature does not significantly increase. Therefore, the possibility for short-pulse laser-induced water desorption and a subsequent reduction in stiction is possible. If the adhesion force is reduced below the value of the restoring force of the microstructures, structures stuck to underlying surfaces will be freed as shown in the schematic in Figure 5.

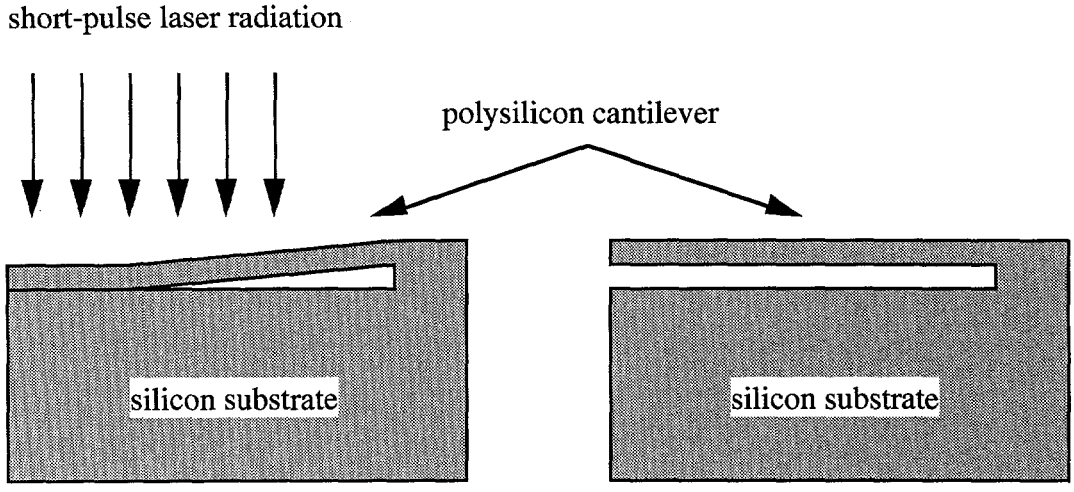

Figure 5. Schematic of the Stiction Reduction Experiment

Experiments to determine the feasibility of using short-pulse laser radiation to reduce the surface adhesion in silicon microstructures were conducted using a 790-nm-wavelength Ti:Sapphire laser [32]. The pulse duration and repetition rate were 150 fs and 1 kHz, respectively. The laser fluence had maximum value of 17 mJ/cm^2. A stiction test structure consisting of cantilevers ranging in length from 60 μm to 1 mm at 20 μm increments was fabricated on an undoped polysilicon substrate. All of the cantilevers have same width (5 μm) and thickness (2 μm), and the free separation between a cantilever and the substrate is 1.5 μm. After the drying process, cantilevers longer than 100 μm on the test structure were stuck to the substrate. An image of the test structure after five seconds of irradiation by the laser beam showed the release of two cantilevers of length 100 μm and 120 μm from the substrate due to the ultrashort-pulse laser irradiation. Thus, the experiments indicated the feasibility of using short-pulse laser radiation to reduce stiction by the possible mechanism of water desorption induced by electronic excitations.

CONCLUSIONS

Short-pulse laser-material interactions are examined for disordered or random materials. Using fractals and percolation theory, an analysis of short time-scale energy transport in random media delineates three regimes of heat transport. The three regimes correspond to transport over the basic percolation unit (particle), the fractal cluster, and the homogeneous medium. Scaling shows that the anomalous diffusion regime is bounded by characteristic times depending on the material properties and structure.

In high-power, laser-liquid interactions, the saturable and multiphoton absorption mechanisms of energy deposition are investigated. Saturable absorption occurs when a sufficient number of molecules have been promoted to excited states by incoming laser radiation, thus affecting bulk transmission and absorption. In multiphoton absorption and photolysis, molecules

absorb a sufficient number of photons to ionize or dissociate. This results in a combination of free electrons, ionized cations, and dissociation products which can interact strongly with the incident laser pulse, altering the absorption and heating properties of the liquid. Temperature profiles calculated considering the effects of saturable absorption or multiphoton absorption and photolysis differ considerably from those predicted by classical heating models.

An application of short-pulse laser radiation is the reduction of surface adhesion in microstructures. Through short-pulse laser-induced desorption of liquid molecules present below a microstructure stuck to an underlying substrate, the adhesion forces on the structures can be reduced and device recovery achieved. This process could be used to both increase device yield during fabrication and extend the operation of microelectromechanical systems.

ACKNOWLEDGEMENT

This work was supported by the U.S. Department of Energy, under grant number DE-FG03-92ER14287.

REFERENCES

1. C. L. TIEN, T. Q. QIU, and P. M. NORRIS, "Microscale Thermal Phenomena in Contemporary Technology," *J. Thermal Science and Engineering* 2, 1 (1994).
2. VON DER LINDE, D., "Ultrashort Interactions in Solids," *Ultrashort Laser Pulses: Generation and Applications,* 2nd ed., W. Kaiser, ed., Springer-Verlag, New York, pp. 113-182 (1993).
3. G. C. HADJIPANYAYIS and R. W. SIEGEL, *Nanophase Materials: Synthesis, Properties, and Applications,* Kluwer Academic Publishers, Boston (1994).
4. A. A. ORAEVSKY, R. O. ESENALIEV, and V. S. LETOKHOV, "Temporal Characteristics and Mechanism of Atherosclerotic Tissue Ablation by Nanosecond and Picosecond Laser Pulses", *Lasers in the Life Sciences* 5, 75 (1992).
5. C. A. SACCHI, "Laser-Induced Electric Breakdown in Water", *J. Optical Society America B* 8, 337 (1991).
6. S. D. ALLEN, J. O. PORTEUS, W. N. FAITH, and J. B. FRANCK, "Contaminant and Defect Analysis of Optical Surfaces by Infrared Laser Induced Desorption", *Appl. Phys. Lett.* 45, 997 (1984).
7. S. J. LEE, K. IMEN, and S. D. ALLEN, "Laser-Assisted Particle Removal from Silicon Surfaces", *Microelectronic Engineering* 20, 145 (1993).
8. Y. B. BAND and B. SCHARF, "Engineering Reverse Saturable Absorbers for Desired Wavelengths", *Chemical Phys. Lett.* 127, 381 (1986).
9. M. STUKE, *Dye Lasers: 25 Years,* Springer-Verlag, Berlin (1992).
10. W. C. SHUMAY, "Corrosion in Electronics", *Advanced Materials and Processes* 132, 73 (1987).
11. C. S. LEECH, "Removing Moisture from Electronic Components and Assemblies", *Circuits Assembly* 5, 34 (1994).
12. R. L. ALLEY, G. J. CUAN, R. T. HOWE, and K. KOMVOPOULOS, "The Effect of Release-Etch Processing on Surface Microstructure Stiction", *Technical Digest, IEEE Solid-State Sensor and Actuator Workshop*, Hilton Head Island, South Carolina, pp. 202 (1992).
13. R. LEGTENBERG, H. A. C. TILMANS, J. ELDERS, and M. ELWENSPOEK, "Stiction of Surface Micromachined Structures after Rinsing and Drying: Model and Investigation of Adhesion Mechanisms", *Sensors and Actuators A* A43, 230 (1994).
14. T. Q. QIU and C. L. TIEN, "Heat Transfer Mechanisms During Short-Pulse Laser Heating of Metals," *J. Heat Transfer* 115, 835 (1993).
15. T. Q. QIU and C. L. TIEN, "Short-Pulse Laser Heating on Metals," *Int. J. Heat Mass Transfer* 35, 719 (1992).

16. T. Q. QIU and C. L. TIEN, "Femtosecond Laser Heating of Multi-Layer Metals–I. Analysis," *Int. J. Heat Mass Transfer* 37, 2789 (1994).
17. T. Q. QIU, T. JUHASZ, C. SUAREZ, W. E. BRON, and C. L. TIEN, "Femtosecond Laser Heating of Multi-Layer Metals–II. Experiments," *Int. J. Heat Mass Transfer* 37, 2799 (1994).
18. D. FOURNIER and A. C. BOCCARA, "Heterogeneous Media and Rough Surfaces: A Fractal Approach for Heat Diffusion Studies," *Physica A* 157, 587 (1989).
19. Y. GEFEN, A. AHARONY, and S. ALEXANDER, "Anomalous Diffusion on Percolating Clusters," *Phys. Rev. Lett.* 50, 77 (1983).
20. C. H. GOLDMAN, P. M. NORRIS, and C. L. TIEN, "Picosecond Energy Transport in Amorphous Materials," *Proceedings of the 1995 ASME/JSME Joint Thermal Engineering Conference* 1, 467 (1995).
21. B. B. MANDELBROT, *Fractals: Form, Chance, and Dimension,* Freeman, San Francisco (1977).
22. K. RICHTER, and C. L. TIEN, "Structure Simulation of Sparse Silica Aerogels," *Fractals* 2, 535 (1994).
23. K. RICHTER, P. M. NORRIS, and C. L. TIEN, "Aerogels: Applications, Structure, and Heat Transfer Phenomena," *Ann. Rev. Heat Transfer* 6, in press (1995).
24. C. H. GOLDMAN and C. L. TIEN, "Anomalous Diffusion in Short-Pulse Laser Interactions with Random Media," to be presented at the 1995 National Heat Transfer Conference, Portland, Oregon, August 5-9, 1995.
25. J. P. LONGTIN and C. L. TIEN, "Saturable Absorption during High-Intensity Laser Heating of Liquids," to be presented at the 1995 International Mechanical Engineering Congress and Exposition, San Francisco, California, November 12-17, 1995.
26. J. P. LONGTIN and C. L. TIEN, "High-Intensity Laser Heating in Liquids: Multiphoton Absorption," to be presented at the 1995 National Heat Transfer Conference, Portland, Oregon, August 5-9, 1995.
27. J. A. PRYBYLA, T. F. HEINZ, J. A. MISEWICH, M. M. T. LOY, and J. H. GLOWNIA, "Desorption Induced by Femtosecond Laser Pulses," *Phys. Rev. Lett.* 64, 1537 (1990).
28. F.-J. KAO, D. G. BUSCH, D. GOMES DA COSTA, and W. HO, "Femtosecond versus Nanosecond Surface Photochemistry: O_2 + CO on Pt(111) at 80 K," *Phys. Rev. Lett.* 70, 4098 (1993).
29. J. A. PRYBYLA, H. W. K. TOM, and G. D. AUMILLER, "Femtosecond Time-Resolved Surface Reaction: Desorption of CO from Cu(111) in < 325 fsec," *Phys. Rev. Lett.* 68, 503 (1992).
30. F.-J. KAO, D. G. BUSCH, D. COHEN, D. GOMES DA COSTA, and W. HO, "Femtosecond Laser Desorption of Molecularly Adsorbed Oxygen from Pt(111)," *Phys. Rev. Lett.* 71, 2094 (1993).
31. K. FUSHINOBU, L. M. PHINNEY, and N. C. TIEN, "Ultrashort-Pulse Laser-Induced Water Desorption from Silicon Surfaces," to be submitted to *Int. J. Heat Mass Transfer* (1995).
32. N. C. TIEN, S. JEONG, K. FUSHINOBU, L. M. PHINNEY, and J. BOKOR, "Reduction of Surface Adhesion in Silicon Microstructures Using Ultrashort-Pulse Laser Irradiation," private communication (1995).

STUDIES ON THE FORMULATION OF THERMODYNAMICS AND STOCHASTIC THEORY FOR SYSTEMS FAR FROM EQUILIBRIUM

John Ross
Department of Chemistry
Stanford University
Stanford, California 94305

ABSTRACT

We have been working for some time on the formulation of thermodynamics and the theory of fluctuations in systems far from equilibrium and progress in several aspects of that development are reported here.

THEORY

The theory is based on the concept of an excess work, ϕ, that is the work necessary for a differential displacement of a system in an arbitrary state, further away from a stationary state, minus the work of the same displacement away from the stationary state (or at a specified reference state). This excess work, ϕ, has the following properties: 1. the excess work, ϕ, provides necessary and sufficient conditions of global stability for systems with one or more stable stationary states. 2. ϕ is the thermodynamic driving force towards the stationary states and is a species-specific affinity. 3. ϕ is a Liapunov function with ϕ in the form of Boltzman's H theorem. 4. ϕ is a measurable excess work attainable from the spontaneous relaxation in a differential displacement along the deterministic trajectory minus the work of that same displacement from the stationary state. 5. ϕ provides a criterion of relative stability of two stable stationary states. 6. With proper reference states ϕ yields the stationary probability distribution of stochastic equations describing the given processes.

The structure of the theory is analogous to that at equilibrium and revolves into that theory as the system approaches an equilibrium point, rather than a stationary state.

We have established a new fluctuation-dissipation relation for one-variable nonlinear processes which connects the macroscopic deterministic net reaction rate, the probability diffusion coefficient, and the species-specific affinity. This fluctuation-dissipation relation may also be viewed as a force-flux relation. The main feature of this development is the symmetry with respect to the contributions of the forward and backward chemical processes to

fluctuations and relaxation. Two new physical interpretations of the probability diffusion coefficient are given: one corresponds to a measure of the strength of fluctuations at a steady state, and the other to a measure of the instability of a given fluctuation state. The dispersion of the number q of reaction events in a given time interval is given by a generalized Einstein relation: $\{\Delta q^2\}=2VD(x)t$, where V is the volume of the system. Further, the diffusion coefficient D(x) is proportional to the reciprocal value of the mean age $\{\tau(x)\}$ of a fluctuation state characterized by the concentration x: $D(x)=1/[2V\{\tau(x)\}]$. These interpretations are not related to the use of a Fokker-Planck approximation of the chemical master equation.

For single variable systems the excess work, ϕ, is a state function which, however, is not the case for multi-variable systems. Hence in the evaluation of the excess work for multi-variable systems a path of integration through the concentration space for chemical systems must be chosen. If the process to be described follows the deterministic equations of motion then that path is also the most probable path in a stochastic investigation and the excess work must then be evaluated along that path. If, however, we investigate fluctuations away from a stationary state then the excess work for such fluctuations must be evaluated along the most probable path of a fluctuation from a stationary state to a given nonstationary state. We have shown that, in general, deterministic paths of relaxation to stationary states are not the same as most probable fluctuational paths away from stationary states. We have investigated these issues by means of the eikonal (WKB type) solution of the master equation for two-variable chemical systems with multiple stationary states. If we suppose there to be two stable stationary states then these are separated by a deterministic separatrix and as well by a different fluctuational separatrix. Caustics occur in the system and require careful analysis. We have checked the validity of the eikonal approximation against a Monte Carol solution of the master equation and find the results accurate.

We have conducted extensive calculations and experiments to test our theory in regard to relative stability of two stable stationary states. Consider a volume such as a tube filled with the system, subject to given constraints, in one of the two stable stationary states. Next consider a similar volume for the same external constraints filled with the system in the other of the two stable stationary states. On connection of the two tubes there occurs a motion of the front between the two different stationary states such that the more stable stationary state eliminates the less stable stationary state. At equistability of the two stable stationary states the front velocity is zero. We have shown

that the excess work for creating the front between the two stable stationary states from either of the two stable stationary states provide the necessary criterion of relative stability. Thus if the excess work calculated from one of the stable stationary states to the stable front of the interface between the two stationary states exceeds that of the excess work from the other stable stationary state to that stable front then the interface moves in the direction of annihilating the region with the larger excess work. Experiments in relative stability in the bistable multivariable bromate-ferroin reaction confirm this result of the theory.

We have attempted an application of our theory to a thermodynamic theory of hydrodynamics. The thermodynamic potential (state) functions for irreversible processes approaching equilibrium are known: for example, the Gibbs free energy change for the processes at constant temperature and pressure. Changes in this Gibbs free energy yield the maximum work available from the changes. Then, by analogy, the goals of thermodynamics for hydrodynamic processes are the establishment of macroscopic evolution criteria (Liapunov functions) with physical significance, such as the connection with excess work; the work (and power) available from a transient decay to a stationary state; macroscopic necessary and sufficient criteria of stability; thermodynamic criteria for bifurcations; a thermodynamic criterion of relative stability of stable attractors in systems with more than one attractor, that is, a thermodynamic criterion of state selection; and finally a connection of the thermodynamic formulation to fluctuations.

We start with the Navier-Stokes equations and the Boussinesq approximation and then proceed according to the studies of Saltzmann, who reduces these equations to a set of ordinary differential equations by means of a spectrum expansion. In lowest order one then arrives at the Lorenz equations and we investigate the steady states of those equations. We construct the excess work and show that it has the following properties. 1. The differential of ϕ is expressed in terms of thermodynamic functions: the energy for viscous flow and the entropy for thermal conduction when taken separately. 2. ϕ is an extremum at all stationary states, a minimum (maximum) at stable (unstable) stationary states, and thus yields necessary and sufficient criteria for stability; 3. ϕ describes the bifurcation from homogeneous to inhomogeneous stationary states; 4. ϕ is a Liapunov function with physical significance parallel to that of the Gibbs free energy change (maximum work) on relaxation to an equilibrium state; 5. ϕ is the thermodynamic "driving force" (potential) towards stable stationary states; 6. ϕ is a component of the total dissipation during the relaxation towards a stable

stationary state; 7. for constraints leading to equilibrium ϕ reduces to the known thermodynamic function, which is the work of displacing the system from the equilibrium for those given constraints; and 8. ϕ qualitatively explains the positive energy release in both the destruction and formation of a convective structure in a Rayleigh-Bénard experiment.

References marked with a * denote accreditation to The Department of Energy/Basic Engineering Sciences Program.

302. "Experiments on relative stability in the bistable multivariable bromate-ferroin reaction", J. Phys. Chem. 97, 4708 (1993) Petra Foerster, Yi-Xue Zhang and John Ross.

* 303. "Tests of thermodynamic theory of relative stability in one-variable systems", J. Chem. Phys. 99, 3455 (1993), A. N. Wolff, A. Hjelmfelt, John Ross and P. M. Hunt.

304. "Thermodynamic and stochastic theory of reaction-diffusion systems with multiple stationary states", J. Chem Phys. 99, 3444 (1993) Xiaolin Chu, P. M. Hunt, K. L. C. Hunt and John Ross.

* 306. "Stationary probability distribution near stable limit cycles far from Hopf bifurcation points", Phys. Rev. E 48, 1646 (1993) Mark Dykman, Xiaolin Chu and John Ross.

* 307. "Towards a thermodynamic theory of hydrodynamics: The Lorenz equations", J. Phys. Fluids 6, 550 (1994) Manuel G. Velarde, Xiao-Xiaolin Chu, and John Ross.

* 310. "Large fluctuations and optimal paths in chemical kinetics", J. Chem. Phys. 100 5735, (1994) Mark I. Dykman, Eugenia Moria, and John Ross.

* 312. "H-theorem for telegrapher-type master equations", Phys. Let. A 184, 403 (1994) Marcel O. Vlad and John Ross.

314. "Fluctuation-dissipation relations for chemical systems far from equilibrium", J. Chem. Phys. 100 7268 (1994) Marcel O. Vlad and John Ross.

* 315. "Random paths and fluctuation-dissipation dynamics for one-variable chemical systems far from equilibrium", J. Chem. Phys. 100, 7279 (1994), Marcel O. Vlad and John Ross.

* 316. "Thermodynamic approach to nonequilibrium chemical fluctuations", J. Chem. Phys. 100, 7295 (1994) Marcel O. Vlad and John Ross.

* 318. "Generating functional approach to space-and time-dependent colored noise", Physical Review E 50, 798 (1994) Marcel O. Vlad, Michael C. Mackey, John Ross.

* 319. "Electro-chemical experiments on Thermodynamics at nonequilibrium steady states", J. Phys. Chem. 98, 9900 (1994) Allen Hjelmfelt and John Ross.

321. "Thermodynamic and stochastic theory of nonequilibrium systems: Fluctuation probabilities and excess work", J. Chem. Phys., Bo Peng, Katherine L. C. Hunt, Paul M. Hunt, Alberto Suàrez, and John Ross.

322. "Thermodynamic and stochastic theory of nonequilibrium systems: A Lagrangian approach to fluctuations and relation to excess work", J. Chem. Phys., Alberto Suàrez, John Ross, Bo Peng, Katherine L. C. Hunt, and Paul M. Hunt.

* 323. "A model of excitation and adaptation in bacterial chemotaxis", Biophys. Journal 68, 708 (1995), David C. Hauri and John Ross.

LINEAR KINETIC THEORY AND PARTICLE TRANSPORT IN STOCHASTIC MIXTURES

G. C. Pomraning

School of Engineering and Applied Science
University of California, Los Angeles
Los Angeles, CA 90095-1597

Abstract

We consider the formulation of linear transport and kinetic theory describing energy and particle flow in a random mixture of two or more immiscible materials . Following an introduction, we summarize early and fundamental work in this area, and we conclude with a brief discussion of recent results.

INTRODUCTION

In the last decade these has been considerable interest in the problem of describing linear particle transport in a stochastic medium consisting of two (or more) randomly mixed immiscible materials. The goal in this research has been to develop a relatively simple and accurate description for the ensemble-averaged solution of the stochastic transport problem. In this brief report, we will attempt to summarize the salient features of this work and present an overall view of the status of this research, with particular emphasis on the work of the present author.

The generic linear transport equation we will concerned with is written

$$\frac{1}{v}\frac{\partial \psi}{\partial t} + \mathbf{\Omega}\cdot\nabla\psi + \sigma\psi = \frac{\sigma_s}{4\pi}\varphi + S, \tag{1}$$

where

$$\varphi = \int_{4\pi} d\mathbf{\Omega}\psi(\mathbf{\Omega}). \tag{2}$$

In writing Eqs. (1) and (2) we have used the notation of neutron transport theory, but our considerations are equally applicable in any linear transport setting. The dependent variable in Eq. (1) is the angular flux $\psi(\mathbf{r},\mathbf{\Omega},t)$, with $\mathbf{r},\mathbf{\Omega}$, and t denoting the spatial, angular (neutron flight direction), and time variables, respectively. The quantity $\varphi(\mathbf{r},t)$ is

the scalar flux, v is the neutron speed, $\sigma(\mathbf{r},t)$ is the macroscopic total cross section, $\sigma_s(\mathbf{r},t)$ is the macroscopic scattering cross section, and $S(\mathbf{r},\mathbf{\Omega},t)$ denotes any internal source of neutrons. We have assumed isotropic and coherent (no energy exchange) scattering in Eq. (1), but this simplification is not necessary for the essentials of the considerations to follow. Thus Eq. (1) is a monoenergetic (one group) transport equation, and there is no need to display the independent energy variable which is simply a parameter.

To treat the case of a binary statistical mixture, the quantities σ, σ_s, and S in Eq. (1) are considered as discrete random variables, each of which assumes, at any $\mathbf{r}, \mathbf{\Omega}, t$, one of two sets of values characteristic of the two materials constituting the mixture. We denote the two materials by an index i, with $i = 0$, 1, and in the ith material these three quantities are denoted by $\sigma_i(\mathbf{r},t), \sigma_{si}(\mathbf{r},t)$ and $S_i(\mathbf{r},\mathbf{\Omega},t)$. That is, as a neutron traverses the mixture along any path, it encounters alternating segments of the two materials, each of which has known deterministic values of σ, σ_s, and S. The statistical nature of the problem enters through the statistics of the material mixing, i.e., through the probabilistic knowledge as to which material is present in the mixture at space point $\mathbf{r}$ and time t. Since σ, σ_s and S in Eq. (1) are (two state, discrete) random variables, the solution of Eqs. (1) and (2) for ψ and φ is stochastic, and we let $\langle\psi\rangle$ and $\langle\varphi\rangle$ denote the ensemble-averaged angular and scalar fluxes, respectively. The goal is to develop accurate and , hopefully, simple models for these ensemble-averages.

To discuss this problem in a qualitative way, it is convenient to consider the simple case of time-independent transport in a purely absorbing ($\sigma_s = 0$) medium. Then Eq. (1) reduces to

$$\frac{d\psi}{ds} + \sigma\psi = S, \tag{3}$$

where s denotes the spatial variable in the direction of propagation. If we write any random variable Q as the sum of its ensemble average $\langle Q\rangle$ and the deviation from this average $\tilde{Q}$, an ensemble averaging of Eq. (3) gives

$$\frac{d\langle\psi\rangle}{ds} + \langle\sigma\rangle\langle\psi\rangle + \langle\tilde{\sigma}\tilde{\psi}\rangle = \langle S\rangle. \tag{4}$$

It is clear from Eq. (4) that one needs to calculate (or approximate) the cross correlation term involving the ensemble average of the product of $\tilde{\sigma}$ and $\tilde{\psi}$ to obtain a formulation for the quantity of interest, namely $\langle\psi\rangle$.

On physical grounds, and it can also be shown mathematically by using asymptotics, it is clear that this term is very small and can be neglected when $\sigma_i l_i \ll 1$, where l_i is a characteristic chord length for the material packets of material i. However, when this inequality is not satisfied, the neglect of the cross correlation term in Eq. (4) can lead to large errors in $\langle\psi\rangle$. In particular, the attenuation of a beam of particles can be grossly overestimated by using Eq. (4) without the cross correlation term. Simply stated then, the challenge is to compute the cross correlation term in Eq. (4). To do this, one must specify

the statistics of the material mixing, and we discuss both Markovian and non-Markovian mixtures.

FUNDAMENTAL RESULTS

References to the original works for the material discussed in this section can be found in the recent book by the present author.[1]

We initially consider the simple transport equation given by Eq. (3), under the assumption of Markovian mixing. These mixing statistics are defined by a no-memory statement. Given that point s is in material i, the probability of point $s + ds$ being in material $j \neq i$ is given by

$$Prob(i \to j) = \frac{ds}{\lambda_i(s)}, \qquad j \neq i, \tag{5}$$

where the $\lambda_i(s)$ are the prescribed Markovian transition probabilities. The probability $p_i(s)$ of finding material i at position s, and the correlation length $\lambda_c(s)$ for the Markov mixture are uniquely and simply related to the $\lambda_i(s)$. With the mixing statistics defined by Eq. (5), one can obtain an exact description for $\langle\psi\rangle$ corresponding to the transport problem given by Eq. (3). This is given by the two coupled equations

$$\frac{d}{ds}\begin{bmatrix}\langle\psi\rangle \\ \chi\end{bmatrix} + \begin{bmatrix}\langle\sigma\rangle & \nu \\ \nu & \hat{\sigma}\end{bmatrix}\begin{bmatrix}\langle\psi\rangle \\ \chi\end{bmatrix} = \begin{bmatrix}\langle S\rangle \\ T\end{bmatrix}, \tag{6}$$

where

$$\nu\chi = \langle\tilde{\sigma}\tilde{\psi}\rangle, \qquad \nu = (p_0p_1)^{1/2}(\sigma_0 - \sigma_1), \tag{7}$$

$$\langle\sigma\rangle = p_0\sigma_0 + p_1\sigma_1, \qquad \hat{\sigma} = p_1\sigma_0 + p_0\sigma_1 + \frac{1}{\lambda_c}, \tag{8}$$

$$\langle S\rangle = p_0S_0 + p_1S_1, \qquad T = (p_0p_1)^{1/2}(S_0 - S_1). \tag{9}$$

Two derivations of Eq. (6) can be given. The first is based upon the so-called method of smoothing. Subtraction of Eq. (4) from Eq. (3) gives

$$\frac{d\tilde{\psi}}{ds} + \langle\sigma\rangle\tilde{\psi} + \left[\tilde{\sigma}\tilde{\psi} - \langle\tilde{\sigma}\tilde{\psi}\rangle\right] = \tilde{S} - \tilde{\sigma}\langle\psi\rangle. \tag{10}$$

Inserting a smallness parameter in front of the bracketted term in Eq. (10) and seeking a solution as a power series in this smallness parameter gives the Neumann series

$$\tilde{\psi} = \sum_{n=0}^{\infty}(-1)^n[G(I-P)\tilde{\sigma}]^nG(\tilde{S} - \tilde{\sigma}\langle\psi\rangle), \tag{11}$$

where I is the identity and G and P are Green's and projection operators defined by

$$Gf = \int_0^s ds' \left[exp - \int_{s'}^s d\xi \langle \sigma(\xi) \rangle \right] f(s'), \qquad Pf = \langle f \rangle. \tag{12}$$

For Markovian statistics, all of the terms in the sum of Eq. (11) can be evaluated and the infinite summation performed. The result of the these algebraic manipulations is just Eq. (6).

The second derivation of Eq. (6) is based upon the observation that the transport problem given by Eq. (3) describes a Markov process; it is an initial value problem with the spatial variable s playing the role of time. Thus, together with the assumed Markovian mixing, we have a joint Markov process and we can write a Liouville master equation for the joint probability $P_i(s, \psi)$, defined such that $P_i d\psi$ is the probability of finding material i and intensity ψ lying between ψ and $\psi + d\psi$ at position s. This master equation is given by

$$\frac{\partial P_i}{\partial s} - \frac{\partial}{\partial \psi}(\psi \sigma_i P_i - S_i P_i) = \frac{P_j}{\lambda_j} - \frac{P_i}{\lambda_i}, \quad j \neq i. \tag{13}$$

The probability $p_i(s)$ is just the integral of $P_i(s, \psi)$ over ψ, and the conditional ensemble-averaged intensity given that position s is in material i, $\psi_i(s)$, is the integral of $\psi P_i(s, \psi)$ over ψ, divided by p_i. Multiplying Eq. (13) by ψ and integrating over ψ gives two coupled equations for the ψ_i. Making the change of variables

$$\langle \psi \rangle = p_0 \psi_0 + p_1 \psi_1, \qquad \chi = (p_0 p_1)^{1/2} (\psi_0 - \psi_1) \tag{14}$$

once again leads to Eq. (6).

No such exact results are available when time-dependence and scattering are present in the transport problem, i.e., when Eq. (1) is the underlying stochastic transport equation. In this case, the algebra of the method of smoothing cannot be carried through. Further, with scattering the transport problem is not a Markov process (it is a boundary value problem) and hence the master equation approach cannot rigorously be used. Nevertheless, it has been suggested that the use of the master equation might lead to a useful, albeit approximate, model. This model is

$$\left(\frac{1}{v} \frac{\partial}{\partial t} + \mathbf{\Omega} \cdot \nabla + \mathbf{\Sigma} \right) \begin{bmatrix} \langle \psi \rangle \\ \chi \end{bmatrix} = \frac{1}{4\pi} \mathbf{\Sigma}_s \begin{bmatrix} \langle \varphi \rangle \\ \eta \end{bmatrix} + \begin{bmatrix} \langle S \rangle \\ T \end{bmatrix}, \tag{15}$$

where

$$\mathbf{\Sigma} = \begin{bmatrix} \langle \sigma \rangle & \nu \\ \nu & \hat{\sigma} \end{bmatrix}, \qquad \mathbf{\Sigma}_s = \begin{bmatrix} \langle \sigma_s \rangle & \nu_s \\ \nu_s & \hat{\sigma}_s \end{bmatrix}, \tag{16}$$

where, in addition to Eqs. (7) through (9), we have

$$\langle \varphi \rangle = \int_{4\pi} d\mathbf{\Omega} \langle \psi \rangle, \quad \eta = \int_{4\pi} d\mathbf{\Omega} \chi, \quad \nu_s = (p_0 p_1)^{1/2} (\sigma_{s0} - \sigma_{s1}), \tag{17}$$

$$\langle \sigma_s \rangle = p_0 \sigma_{s0} + p_1 \sigma_{s1}, \qquad \hat{\sigma}_s = p_1 \sigma_{s0} + p_0 \sigma_{s1}. \tag{18}$$

Several other derivations of this model are available. Sahni has shown that the assumption of independent particle flight paths leads to Eq. (15), and he has also shown that nuclear reactor noise techniques can be used to obtain this model. It has also been demonstrated that one can derive exact particle balance equations in this stochastic transport setting, but involving two ensemble averages conditioned upon being in material i, namely a volumetric average ψ_i and a surface (interface between materials) average $\bar{\psi}_i$. Making the approximation that these two ensemble averages are equal again yields the model given by Eq. (15). Numerical comparisons with exact Monte Carlo results shows the accuracy of this model to be of the order of ten percent or so, with the error being the largest, as expected, for problems with multiple scattering interactions.

Although no exact transport-like equation(s) formulation is available in general for $\langle\psi\rangle$ in the presence of time dependence and scattering, a few exact results have been reported for certain time-independent problems including the scattering interaction in rod (particles are restricted to move along a line) and planar geometry. Vanderhaegen and Deutsch considered the sourcefree purely scattering rod problem and used a Riccati transformation to convert the boundary value transport problem for the intensity to an initial value problem for the rod transmission. They then applied the master equation approach to this initial value problem. Their results were confirmed in a paper devoted to numerical and analytical solution methods for the Liouville master equation applicable to a large class of initial value problems. An exact formalism in rod and planar geometry has been developed for a restricted class of problems, in which σ_s/σ and S/σ are nonstochastic; the only stochasticity is the optical depth variable. The results of Vanderhaegen and Deutsch were again confirmed, and results for several classical halfspace and infinite medium transport problems were developed.

If one accepts Eq. (15) as a reasonable model of particle transport in a binary Markovian mixture, two simplifications involving certain asymptotic limits have been reported. The first of these corresponds to a small amount, of $O(\epsilon^2)$, of one material admixed with an $O(1)$ amount of the second material. Further, the first material has large, of $O(1/\epsilon^2)$, source and cross sections compared to $O(1)$ quantities for the second material. In this asymptotic limit, one finds a renormalized transport equation of the standard form given by

$$\left(\frac{1}{v}\frac{\partial}{\partial t} + \Omega\cdot\nabla + \sigma_{eff}\right)\langle\psi\rangle = \frac{\sigma_{s,eff}}{4\pi}\langle\varphi\rangle + S_{eff} + O(\epsilon^2), \tag{19}$$

with

$$\sigma_{eff} = \langle\sigma\rangle - \frac{\nu^2}{\hat{\sigma}}, \qquad \sigma_{s,eff} = \sigma_{eff} - \sigma_{a,eff}, \tag{20}$$

and

$$\sigma_{a,eff} = (\langle\sigma\rangle - \langle\sigma_s\rangle) - \frac{(\nu-\nu_s)^2}{(\hat{\sigma}-\hat{\sigma}_s)}, \qquad S_{eff} = \langle S\rangle - \frac{(\nu-\nu_s)}{(\hat{\sigma}-\hat{\sigma}_s)}T. \tag{21}$$

Equation (21) for S_{eff} assumes that the sources are isotropic, i.e., $S_i \neq S_i(\Omega)$. The corresponding expression for anisotropic sources is more complex. The result given by Eqs. (19) through (21) is robust in that all of these effective cross sections and source are always nonnegative, even when one is far from the asymptotic limit under consideration. This derivation of a renormalized transport equation as an asymptotic limit has been generalized to a mixture containing an arbitrary number of the material components, and leads to an entire class of reduced (in complexity) transport descriptions.

The second asymptotic limit of Eq. (15) is one in which the scattering interaction is dominant, of $O(1)$. Absorption, sources, and all derivatives are assumed small, of $O(\epsilon^2)$, except for the spatial derivative which is scaled to be $O(\epsilon)$. This scaling eliminates the angular variable in the transport problem, and is analogous to the Hilbert expansion which gives the Euler material equations from the Boltzmann equation. If we restrict ourselves to isotropic sources as well as an isotropic correlation length, one finds in this asymptotic limit two coupled diffusion equations given by

$$\left(\frac{1}{v}\frac{\partial}{\partial t} - \nabla \cdot \mathbf{D}\nabla + \mathbf{\Sigma}_a\right)\begin{bmatrix}\langle\varphi\rangle \\ \eta\end{bmatrix} = 4\pi\begin{bmatrix}\langle S\rangle \\ T\end{bmatrix} + O(\epsilon^2), \tag{22}$$

where $\mathbf{\Sigma}_a = \mathbf{\Sigma} - \mathbf{\Sigma}_s$ and

$$\mathbf{D} = \frac{1}{3}\mathbf{\Sigma}^{-1} = \frac{1}{3(\langle\sigma\rangle\hat{\sigma} - \nu^2)}\begin{bmatrix}\hat{\sigma} & -\nu \\ -\nu & \langle\sigma\rangle\end{bmatrix}. \tag{23}$$

It can easily be shown that the diffusion coefficient matrix $\mathbf{D}$ is positive definite under all choices of the physical parameters, thus assuring robustness in this diffusion approximation. Since the scaling which lead to Eq. (22) corresponds to a singular perturbation problem, both boundary and temporal layers exist. Performing the appropriate asymptotic matching analyses, one obtains boundary and initial conditions for Eq. (22). The boundary condition is of the mixed (Robbin) type, involving the number 0.710446... , the classic linear extrapolation distance for the Milne problem.

We note the suggestion that non-Markovian statistics of the renewal type can be treated by modifying the correlation length λ_c in Eq. (8). Specifically, if $Q_i(z)$ is the probability that a segment length in material i exceeds length z, then it has been proposed that Eq. (15) approximately describes this statistical situation, if λ_c in $\hat{\sigma}$ [see Eq. (8)] is replaced with $q\lambda_c$, where

$$q = \frac{1}{\sigma_0}\left(\frac{1}{\tilde{Q}_0(\sigma_0)} - \frac{1}{\lambda_0}\right) + \frac{1}{\sigma_1}\left(\frac{1}{\tilde{Q}(\sigma_1)} - \frac{1}{\lambda_1}\right) - 1. \tag{24}$$

Here $\tilde{Q}_i(\sigma_i)$ is the Laplace transform of $Q_i(z)$, evaluated at the transform variable σ_i. For Markovian statistics, $Q_i(z)$ is exponential with decay length λ_i, and in this case $q = 1$. Finally, most of these binary mixture considerations have been generalized to a mixture with more than two components.

RECENT RESULTS

We close this report with a very brief discussion of results obtained in the last few years.[2–18] Space limitations allow simply a listing of such results, and references where more detail can be found. One group of papers[3,12–14,18] deals with the generic problem of attempting to construct a more accurate model than that given by Eq. (15). One such model[14] retains the simplicity of two equations in two unknowns as in Eq. (15), but it incorporates small correlation length physics into these two equations.[13] Two other models[3,18] involve additional equations, yielding four equations in four unknowns. These models are obviously more complex, but are more accurate. An independent variational approach to stochastic transport has also been attempted,[12] with limited success. A paper has been published[6] which compares the accuracy of several models against Monte Carlo benchmark results. Such benchmark results are available for both Markovian and non-Markovian statistics.[10]

Another group of papers[4,5,7,8,16,17] deals with diffusive approximations to the two equation model given by Eq. (15). Two of these papers[4,17] develop flux-limited diffusion equations, a third deals with the P_2 approximation,[16] and the remaining three[5,7,8] develop various asymptotic diffusive limits which result from different scalings of the Markovian transition lengths.

Finally, four papers have been published concerned with applications of this stochastic transport formalism. Two of these[9,11] deal with the cloud-radiation interaction problem within the context of general circulation models of the atmosphere, one addresses a random heterogeneity problem in fission reactor fuels,[2] and one is concerned with beam transport and energy deposition as might be encountered in medical applications.[15]

Under continuing DOE support, we expect to report additional results from this line of research in the near future.

ACKNOWLEDGMENT

The work reported here was partially supported by the U.S. Department of Energy under grant DE-FG03-93ER14355.

REFERENCES

1. G. C. Pomraning, *Linear Kinetic Theory and Particle Transport in Stochastic Mixtures*, World Scientific Publishing, Singapore (1991).

2. R. Sanchez and G. C. Pomraning, *Ann. Nucl. Energy* **18**, 371 (1991).

3. G. C. Pomraning, *J. Quant. Spectrosc. Radiat. Transfer* **46**, 221 (1991).

4. M. Sammartino and G. C. Pomraning, *J. Quant. Spectrosc. Radiat. Transfer* **46**, 237 (1991).

5. M. Sammartino, F. Malvagi, and G. C. Pomraning, *J. Math. Phys.* **33**, 1480 (1992).

6. F. Malvagi and G. C. Pomraning, *Nucl. Sci. Eng.* **111**, 215 (1992).

7. F. Malvagi, G. C. Pomraning, and M. Sammartino, *Nucl. Sci. Eng.* **112**, 199 (1992).

8. G. C. Pomraning, *Ann. Nucl. Energy* **19**, 737 (1992).

9. F. Malvagi, R. N. Byrne, G. C. Pomraning, and R. C. J. Somerville, *J. Atmos. Sci.* **50**, 2146 (1993).

10. B. Su and G. C. Pomraning, *J. Quant. Spectrosc. Radiat. Transfer* **50**, 211 (1993).

11. F. Malvagi and G. C. Pomraning, *Atmospheric and Oceanic Optics* **6**, 610 (1993). Russian translation in same journal: **6**, 1064 (1993).

12. B. Su and G. C. Pomraning, *J. Quant. Spectrosc. Radiat. Transfer* **51**, 467 (1994).

13. B. Su and G. C. Pomraning, *J. Quant. Spectrosc. Radiat. Transfer* **51**, 893 (1994).

14. G. C. Pomraning and B. Su, "A Closure for Stochastic Transport Equations," *Proc. International Conference on Reactor Physics and Reactor Computations*, Ben-Gurion University of the Negev-Press, pp. 672-679 (1994).

15. G. C. Pomraning and A. K. Prinja, *Transport Th. Statis. Phys.* **24**, 565 (1995).

16. B. Su and G. C. Pomraning, "P_1, P_2, and Asymptotic Approximations for Stochastic Transport," *Nucl. Sci. Eng.*, accepted for publication.

17. G. C. Pomraning, "Flux-Limting in Three-Dimensional Stochastic Radiative Transfer," *J. Quant. Spectrosc. Radiat. Transfer*, accepted for publication.

18. B. Su and G. C. Pomraning, "Modification to a Previous Higher Order Model for Particle Transport in Binary Stochastic Media," *J. Quant. Spectrosc. Radiat. Transfer*, accepted for publication.

DYNAMICS OF MISCIBLE DISPLACEMENTS IN ROUND TUBES

E. Meiburg, T. Maxworthy, P. Petitjeans*, and C.-Y. Chen

Dept. of Aerospace Engineering
University of Southern California
Los Angeles, CA 90089-1191

*permanent address: Laboratoire de Physique et Mécanique des Milieux Hétérogenes
Ecole Supérieure de Physique et de Chimie Industrielles
10, rue Vauquelin, F-75231 Paris cedex 05, France

ABSTRACT

A combined experimental and numerical investigation of miscible two-phase flow in a capillary tube is reported. The fraction of fluid left behind on the wall is obtained as a function of the Peclet, Atwood, and Froude numbers. Scaling arguments are presented for two distinct flow regimes, dominated by diffusion and convection, respectively. In the latter one, an effective surface tension value can be estimated.

INTRODUCTION

An improved understanding of the dynamics of multiphase porous media flows remains an essential prerequisite for progress in the fields of enhanced oil recovery, fixed bed regeneration, hydrology, and filtration. From basic stability theory we know that, if the displacing fluid is less viscous than the displaced fluid, the unfavorable mobility profile is likely to lead to the well-known fingering instability, a topic that has been reviewed by Saffman [1] and Homsy [2]. Depending on whether the fluids are immiscible or miscible, one can distinguish two fundamentally different problems: In the *immiscible* case, where surface tension acts at the interface between the two fluids, the capillary number, which represents the ratio of viscous to surface tension forces, is a dynamically important parameter. It determines the most unstable wavelength of the fingering instability, as well as the dynamics of the evolving fingers. For *miscible* displacements, it is conventionally assumed that the dynamics are governed by the relative importance of convective and diffusive effects, as expressed by the Peclet number. However, the proper and accurate form of the governing equations and related boundary conditions in the area of contact between the miscible fluids is not known. Past investigations relied on ad hoc approaches that cannot be rigorously justified. Zimmermann and Homsy [3] have taken a first step towards more realistic conditions by assuming an anisotropic, velocity dependent Taylor dispersion approach. Within the present investigation, we address this issue by conducting physical as well as numerical experiments within

capillary tubes, which can be considered a simple model of the miscible displacement process within a single pore of a porous medium. In particular, we carry out Taylor's [4] experiment (cf. also the numerical investigation by Reinelt and Saffman [5]) in capillary tubes using miscible fluids. We discuss the possibility to define an "effective" surface tension and capillary number, on the basis of both computational and experimental results.

GOVERNING EQUATIONS

Our investigation concerns the displacement of a more viscous phase '2' by a less viscous one '1' in a capillary tube of diameter d. To this end, we consider the incompressible Stokes equations in axisymmetric form. The concentration field is governed by a convection-diffusion equation, in which the diffusion coefficient D is taken to be constant. This represents a simplifying assumption, as the experimental measurements to be discussed below reveal a concentration dependence of the diffusion coefficient. Density is assumed to vary linearly with the concentration, while the viscosity is taken to depend exponentially on it. After rendering the governing equations dimensionless by means of characteristic scales, we identify as the governing dimensionless parameters a Peclet, an Atwood, and a Froude number

$$Pe = \frac{Ud}{D} \quad , \quad At = \frac{\mu_2 - \mu_1}{\mu_2 + \mu_1} \quad , \quad F = \frac{gd^2}{\nu_2 U} \frac{\rho_2 - \rho_1}{\rho_2}$$

Here U represents the of the unperturbed Poiseuille flow far away from the mixing region, while g denotes the gravitational acceleration, which is assumed to act in or against the direction of the displacement. ρ indicates density.

NUMERICAL APPROACH

We solve the incompressible Stokes equations in axisymmetric form, employing streamfunction and vorticity variables. In this way, the pressure is eliminated, and the continuity equation is satisfied identically. At the tube wall and the centerline, we employ standard boundary conditions for the velocity components and the normal derivative of the concentration. At the in- and outflow boundaries, we set the second derivatives in the streamwise direction to zero. Test calculations for computational domains of different sizes confirm that these conditions are appropriate. The convective terms in the concentration equation are represented by four point upwind biased finite difference stencils, whereas the diffusive terms are discretized by five point central differences. The elliptic vorticity equation is solved by means of a standard multigrid technique.

COMPUTATIONAL RESULTS

$\underline{Pe \geq O(10^3)}$

The evolution of the flow in this parameter regime is exemplified by the case $Pe = 1,600$ and $At = 0.9866$, shown in figure 1 in a moving reference frame. Gravity is absent for this flow.

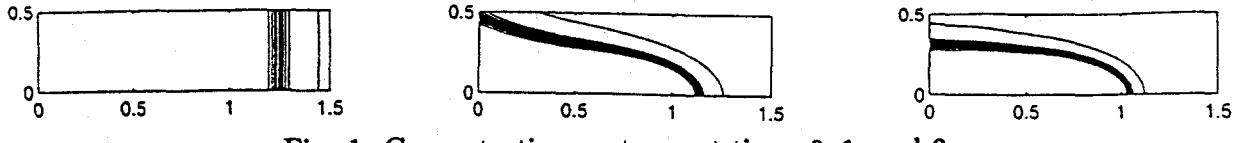

Fig. 1: Concentration contours at times 0, 1, and 3.

The initial condition specifies a one-dimensional error-function profile for the concentration, along

with axisymmetric Poiseuille flow for the velocity components. The velocity field results in an immediate strong deformation of the concentration distribution in the interior of the tube, while at the wall concentration changes are the result of diffusion only. The transient evolution of the concentration distribution, in turn, causes corresponding changes in the viscosity field, thereby modifying the velocity field. This effect distinguishes the present situation from the one analyzed by Taylor [6], in which there is no feedback by the concentration distribution onto the velocity field. For the present parameters, we observe the development of a well-defined finger of the less viscous fluid in the center of the tube. The finger tip consists of a steep concentration front, while its sides are formed by diffusively spreading layers over which the concentration varies. The figure indicates that the mixed inflow/outflow boundary to the left is handled well by the present set of numerical boundary conditions, as there are no detectable disturbances propagating from the boundary towards the finger tip.

By time $t = 2$, the finger tip shape and the associated concentration field have reached a quasisteady state. This is confirmed by the propagation velocity V_{tip} of the finger tip, which is defined as the velocity with which the $c = 0.5$ contour moves along the tube's axis. The steepness of the concentration front at the finger tip is determined by the local balance of strain and diffusion. The strength α of the local strain field is governed by the difference of the streamwise velocities ahead of and behind the finger tip. By assuming that this velocity difference of approximately $2(V_{tip} - 1)$ is achieved over a distance comparable to the tube radius, we obtain

$$\alpha \approx \frac{4(V_{tip} - 1)}{d}$$

A straightforward one-dimensional balance of strain and diffusion then yields for the front thickness δ_0 at the finger tip

$$\frac{\delta_0}{d} \approx \sqrt{\frac{D}{2(V_{tip} - 1)d}}$$

indicating that the front thickness scales with the square root of the inverse of the Peclet number formed with the velocity difference across the finger tip. For the present case, this results in $\delta_0/d \approx 1/30$, which is in good agreement with fig. 1. The one-dimensional analysis furthermore gives

$$\left.\frac{\partial c}{\partial x}\right|_{max} \approx \sqrt{\frac{2}{\pi}}\sqrt{\frac{(V_{tip} - 1)d}{D}}$$

which for the present parameters yields approximately 17. Considering the rough estimate of the strain intensity, this value is in reasonable agreement with the computational results of approximately 28, confirming that the concentration field near the finger tip is indeed determined by a nearly one-dimensional balance of strain and diffusion.

On the sides of the finger, the concentration layers grow diffusively with increasing distance from the finger tip. These layers will merge when $\delta/d \approx 0.5$. Straightforward scaling yields

$$\frac{\delta}{d} \approx \sqrt{\frac{Dt}{d^2}} \qquad , \qquad t \approx \frac{L_f}{V_{tip}}$$

where L_f represents the length of the finger as a function of time. Consequently, the diffusion layers will merge when the finger has reached a length $L_f = Ped/4$. Once the finger has grown to this length, the supply of uncontaminated fluid to the tip region will gradually be cut off, and

eventually the quasisteady state will begin to decay. The above scaling laws indicate that we can neither employ a sufficiently large computational domain, nor can we carry the simulation to sufficiently long times, in order to capture these effects for the present set of parameters.

For practical considerations, a relevant quantity is the fraction of more viscous fluid left behind on the walls of the tube once the quasi-steady state has developed. Taylor [4] calculates an effective film thickness of this fluid from the tip velocity of the finger as $m = 1 - 0.5/V_{tip}$ In particular, it will be of interest to record $m = m(At)$ in the limit of infinitely large Pe. Since grid based numerical simulations will not provide accurate results for this limit, we resort to an extrapolation procedure for $V_{tip} = f(Pe^{-1})$. These calculations demonstrate that the tip velocity for $Pe = 1,600$ is within less than one per cent of the extrapolated value for $Pe \to \infty$. In view of the considerable computational cost associated with carrying out several simulations at different large Pe for each value of At in order to perform the extrapolation, we will in the following present the simulation results for $Pe = 1,600$ in lieu of $Pe \to \infty$. In this way, we arrive at the (m, At)-relationship depicted in fig. 2. Notice that for $At = 0.5$ we obtain $m < 0.5$ as a result of the

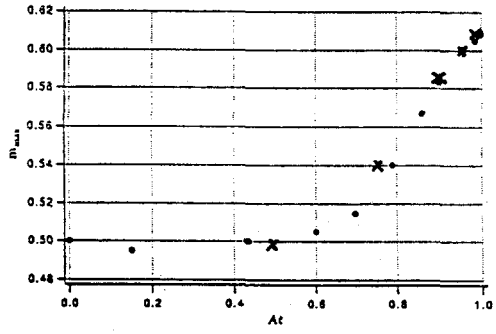

Fig. 2

× computational results
• experimental results

finite Pe-effects. These lead to a diffusive slowing of the finger tip, and thereby to a reduced film thickness. The agreement with the experimental results, also shown in fig. 2 and to be discussed below, is resonable, although not perfect. A possible reason for the observed discrepancy includes non-axisymmetric flow features in the experiment, due to density differences between the two phases. We remark that the value $m \approx 0.61$ for the film thickness in the limit $At \to 1, Pe \to \infty$ agrees well with the observations by Cox [7] for immiscible flow in the limit $At \to 1, Ca \to \infty$, where Ca denotes the capillary number. Taylor [4] previously found a maximum value of 0.56, but he suggested that higher values might be reached. This indicates that as diffusion or surface tension, respectively, become very small, their dynamical significance decays to zero in a smooth fashion, so that the shape of the finger tip is determined by the viscosity contrast alone.

$\underline{Pe \leq O(10^3)}$

For this range of lower Pe-numbers, the formation of a quasi-steady finger shape is not observed. Instead, as exemplified by the case of $Pe = 100, At = 0.9866$ (fig. 3), diffusion soon causes the concentration front to decay, thereby resulting in a progressively more spread out finger tip. As discussed above, at higher values of Pe a balance between strain and diffusion is in effect,

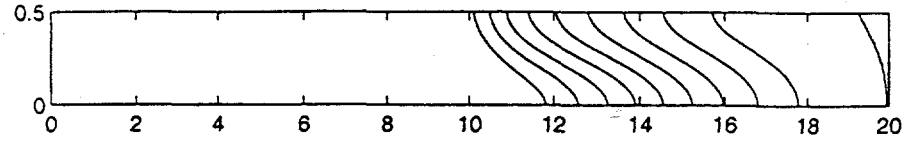

Fig.3

which maintains a steep concentration front. This quasi-one-dimensional balance can only exist if the front thickness at the tip, δ_0, is significantly smaller than the tube diameter. Consequently, there will be a critical level of diffusion beyond which the strain can no longer maintain a sufficiently steep front. In other words, below a critical value of Pe, the strain field will not be strong enough to counter the tendency of diffusion to smear out the finger front. The condition $\delta_0/d < const$ leads to an estimate for this critical value of Pe. With the above relationship for the ratio of front thickness and tube diameter, and with $V_{tip} \approx 1.25$, we obtain

$$\frac{\delta_0}{d} \approx \sqrt{\frac{2}{Pe}} < const$$

For $const = 1/10$ and $1/20$, this criterion yields $Pe_{crit} = 200$ and 800, respectively. Since the finger velocity, and consequently the strength of the strain field, depend on At, we expect Pe_{crit} to vary with At as well, although only weakly. Our numerical simulations for $At = 0.9866$ show the development of a quasi-steady finger with a steep front for $Pe \geq 800$, and a diffusing finger tip for $Pe \leq 400$. For lower values of At, we obtain diffusing fingers even for $Pe = 800$. These Pe-values are in reasonable agreement with the critical values estimated above.

The computational results of fig. 3 indicate that with increasing time the concentration field becomes progressively smoother. It is interesting to note that for $c \neq c(r)$, Poiseuille flow represents an exact solution to the Navier-Stokes equations, independent of the x-dependence of the concentration. As a result, we expect Taylor's [6] work on passive dispersion in Poiseuille flow to provide some guidance for the analysis of the flow development in the low Pe regime. In particular, under the assumption that axial diffusion is much less significant than radial diffusion, Taylor shows that convective effects on the concentration field will be small compared to diffusive effects if $\delta/d \gg Pe/58$, where δ is a measure of the thickness of the smeared out front. Consequently, we would expect to see Poiseuille flow under this condition. If we take δ as the distance along the centerline between the 0.1 and 0.9 concentration contours, then fig. 3 indicates that for $Pe = 100$ and $t = 10$ we have $\delta/d \approx 6$, while $Pe/58 \approx 1.7$. An examination of the fluid velocity confirms that by this time the velocity field has indeed decayed to near Poiseuille flow. The same observation can be made for $Pe = 200$ and $t = 22$, and for $Pe = 400$ and $t = 38$, when $\delta/d \approx 12.6$ and 23 for $Pe/58 \approx 3.4$ and 6.9, respectively. These results confirm the above scaling considerations, and we can conclude that Poiseuille flow will be reached approximately when $\delta/d \approx Pe/16$. Taylor furthermore observes that δ is related to time and the Taylor dispersion coefficient k as $\delta = 3.62\sqrt{kt}$. Here k depends on the tube diameter, the centerline velocity U of the Poiseuille flow, and the diffusion coefficient as $k = d^2U^2/768D$ With the above estimate for δ/d by the time Poiseuille flow is reached, we can now estimate the *time* it takes to approach Poiseuille flow as $t = 0.23Pe$. Consequently, after this time the cross-section-averaged concentration profile $c_m(x)$ should approach the shape of an error function. Equivalently, dc_m/dx should take the form of a Gaussian. This is confirmed by the numerical results, validating the above scaling arguments.

EXPERIMENTS

Apparatus

Two separate pieces of equipment were used in this study. The first, while not directly involved in the study of miscible displacements, was nontheless critical to its success. An extensive survey of the literature on the properties of the glycerine-water system, which was used in this study, failed to find any useful information on the molecular diffusivity D between the two

species. Since the major control parameter Pe involves this property, it was essential to measure it independently. This was accomplished by introducing a glycerine-water mixture on top of a pure glycerine layer in a thin cell. A thin laser beam was projected through the interface and its deflection related to the local refractive index n gradient. The distribution of ∇n was measured at various times and the resultant growth of the interface thickness used to calculate the coefficients of species diffusivity. Due to the differences in mobility between glycerine and water, the diffusivity of the mixture into glycerine is less than that of glycerine into the mixture. The results are shown in figure 4. The value used in the calculation of Pe is the sum of the two

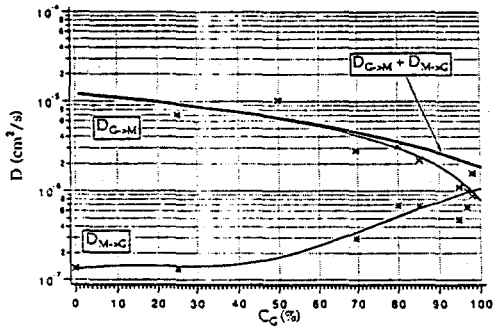

Fig. 4

individual diffusivities, which is dominated by the latter value except for values of c_G (glycerine concentration by weight) close to 100%.

The main piece of apparatus is shown in Figure 5. It is a minor adaptation of that due to

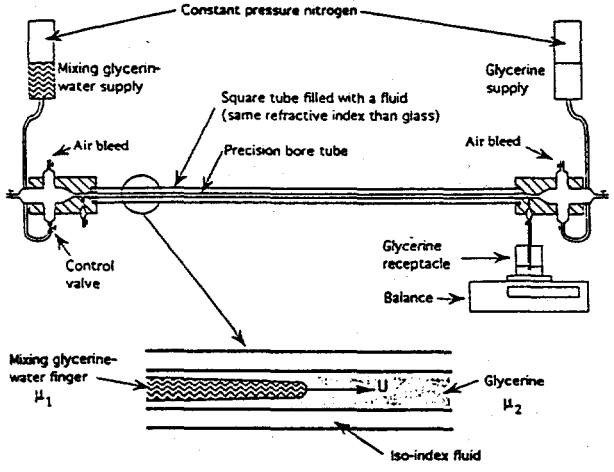

Fig. 5

Taylor [4]. It consists of two plastic manifolds connected by a precision bore capillary tube. Four different tube diameters d were used: 1,2,3 and $4mm$. For each experiment, the tube was first filled with pure glycerine from the right-hand reservoir. The desired mixture, dyed to improve its visibility, was then introduced at the left-hand end, the flow rate being controlled by a very precise compound needle valve. The motion of the nose of the intruding "finger" was timed between $10cm$ marks, and the amount of glycerine expelled from the tube during that time measured by an electronic balance to $1mg$. From these two measurements the effective film thickness m could

be calculated.

Results

A large number of experiments were performed for all four tubes, for several values of At and various tube orientations, i.e., horizontal, vertical with the heavier glycerine on the bottom, and vertical with glycerine on top. The former orientation introduced interesting, non-axisymmetric, gravitational distortions of the finger that need to be discussed in more detail than possible here. On the other hand, the vertical cases introduced distortions that were axisymmetric so that these could be used to determine the state of the finger when gravity was not present, i.e., by plotting m as a function of F and interpolating to $F = 0$. Thus we concentrate on some aspects of the vertical cases that appear to be of widest interest. Notice that for the experimental results the measured velocity of the finger tip was used for the calculation of the dimensionless governing parameters. In figure 6 we show curves of m vs. Pe for $At = 0.79$ and for the two vertical

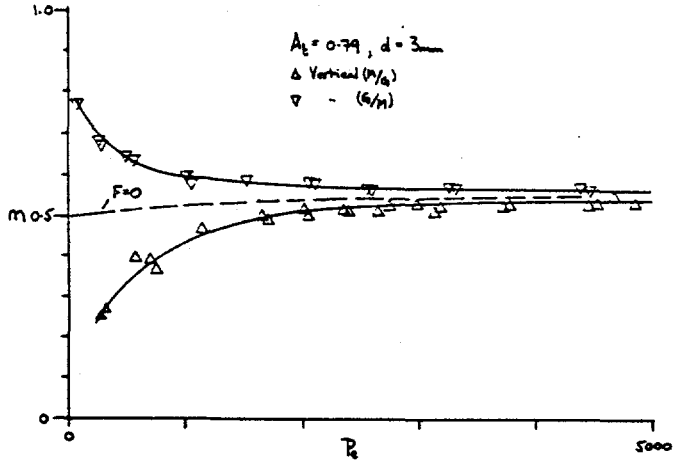

Fig. 6

orientations of a $3mm$ tube. Both curves asymptote $m = 0.54$ at large Pe. In fact, the curves for all values of At and all tube diameters asymptote a value of m that depends only on At (figure 2). At smaller values of Pe the curves diverge with one appearing to approach zero and the other unity. Repeating these measurements for other values of tube diameter, but the same value of At, allows us to construct curves of m or alternatively V_{tip} vs. F at a fixed value of Pe (figure 7). Interpolating to $F = 0$ gives the value of m for no gravitational effect, with the results for various

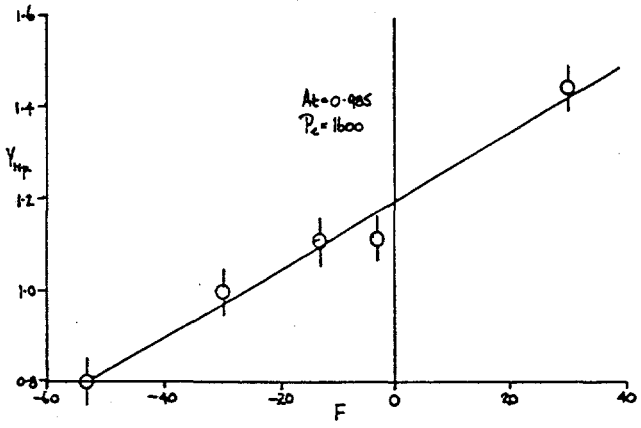

Fig. 7

values of Pe and for $At = 0.79$ given in figure 6. It appears that in this case $m \to 0.5$ as $Pe \to 0$,

as discussed in the previous section.

Two further observations are of interest. Firstly we note that when m is less than 0.5, Taylor [4] gives two possible streamline patterns for the flow relative to the moving nose. We have found that in such cases a thin needle of fluid is continuously ejected from the tip of the finger in a way that makes it clear that of the two flow pictures the one with a single stagnation ring on the finger surface is the one found in these experiments. Secondly, by matching Taylor's results of m vs. $Ca = \mu U/\sigma$ (where μ is the dynamic viscosity of the displaced fluid) for immiscible fluids, with the present measurements it is possible estimate an effective surface tension σ for the miscible interface for values of Pe greater than approximately 250, i.e., when a thin interface exists. Such a match is shown in figure 8 and results in an estimate for σ of

$$\sigma \approx \frac{1000}{3}\frac{\mu D}{d}$$

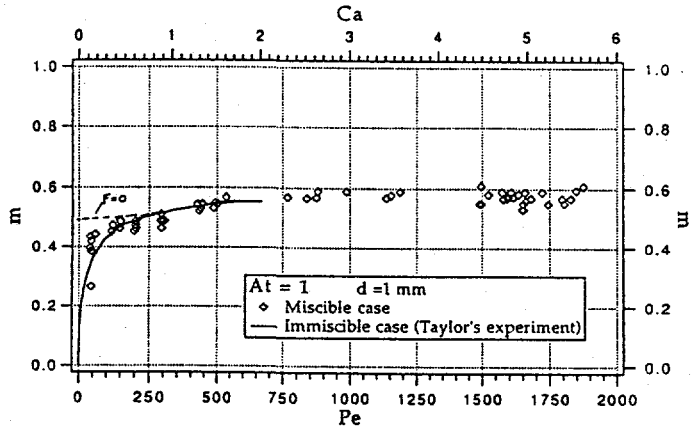

Fig. 8

ACKNOWLEDGMENTS

This work is being supported by the Department of Energy, Office of Basic Energy Sciences.

REFERENCES

1. P.G. SAFFMAN Viscous fingering in Hele-Shaw cells. J. Fluid Mech. 173, 73 (1986).
2. G.M. HOMSY Viscous fingering in porous media. Ann. Rev. Fluid Mech. 19, 271 (1987).
3. W. ZIMMERMANN and G.M. HOMSY Nonlinear viscous fingering in miscible displacement with anisotropic dispersion. Phys. Fluids A 3, 1859 (1991).
4. G.I. TAYLOR Deposition of a viscous fluid on the wall of a tube. J. Fluid Mech. 10, 161 (1961).
5. D.A. REINELT and P.G. SAFFMAN The penetration of a finger into a viscous fluid in a channel and tube. SIAM J. Sci. Stat. Comput. 6, 542 (1985).
6. G.I. TAYLOR Dispersion of soluble matter in solvent flowing slowly through a tube. Proc. R. Soc. A219, 186 (1953).
7. B.G. COX On driving a viscous fluid out of a tube. J. Fluid Mech. 14, 81 (1962).

SUPERCONDUCTING COHERENCE IN A VORTEX LINE LIQUID

Tao Chen and S. Teitel

Department of Physics and Astronomy
University of Rochester, Rochester, New York 14627

ABSTRACT

We carry out simulations of the anisotropic uniformly frustrated 3d XY model, as a model for vortex line fluctuations in high T_c superconductors. We compute the phase diagram as a function of temperature and anisotropy, for a fixed applied magnetic field B. We find two distinct phase transitions. Upon heating, there is first a lower $T_{c\perp}$ where the vortex line lattice melts and superconducting coherence perpendicular to the applied magnetic field vanishes. At a higher T_{cz}, within the vortex line liquid, superconducting coherence parallel to the applied magnetic field vanishes. For finite anisotropy, both $T_{c\perp}$ and T_{cz} lie well below the crossover from the vortex line liquid to the normal state.

INTRODUCTION

In the presence of an applied magnetic field, the low temperature state of a clean type II superconductor is the Abrikosov vortex line lattice, consisting of a triangular lattice of perfectly straight lines of vorticity in the phase of the complex superconducting wavefunction ψ. The lines are parallel to the magnetic field, with a density given by B/ϕ_0; B is the magnetic field that penetrates the sample ($B < H$), and $\phi_0 = hc/2e$ is the flux quantum. For a conventional "low temperature" superconductor, this vortex lattice persists up to a critical temperature $T_{c2}(H)$, where the amplitude of the spatially varying superconducting wavefunction vanishes, superconductivity is lost, and the normal metallic state is entered [1]. Experimentally, $T_{c2}(H)$ is signalled upon cooling, by the onset of a strong diamagnetism as well as by the vanishing of electrical resistance.

From a phenomenological point of view, the "high T_c" copper-oxide superconductors differ from conventional low T_c superconductors due to the dramatically enhanced role that thermal fluctuations play [2]. This is due to the high values of T_c, the very strong anisotropy arising from the layered nature of the materials, and the large ratio of magnetic penetration length $\lambda_\perp$ to coherence length ξ_0. For a magnetic field oriented perpendicular to the

copper-oxide planes, theoretical models have predicted [2–5] that thermal fluctuations will cause the vortex line lattice to melt at a T well below the T_{c2} where the amplitude of the locally fluctuating ψ vanishes. Between these two temperatures is a new vortex line liquid state. Experimentally, this picture has been supported by the observation that, in high T_c materials, the onset of reversible diamagnetism occurs at a temperature well above that where resistance vanishes [6]; the separation between these temperatures increases with increasing B. According to this picture, the onset of diamagnetism at $T_{c2}(H)$ is associated with a growth in superconducting correlations, giving rise on short length scales to a finite superconducting wavefunction $\psi(\mathbf{r})$ in terms of which vortex lines can be defined. This T_{c2} marks a strong cross-over region, rather than a sharp thermodynamic transition. In the resulting vortex line liquid, free diffusion of vortex lines gives rise to "flux flow" electrical resistance [1]. The vanishing of resistance only occurs at a lower T when the line liquid freezes into a lattice.

MODEL

To investigate the above scenario we have carried out Monte Carlo simulations using the uniformly frustrated XY model as a model for a fluctuating superconductor [7]. Making the London approximation that the amplitude of the superconducting wavefunction is constant outside of a vortex core, $\psi(\mathbf{r}) = |\psi| e^{i\theta(\mathbf{r})}$, and discretizing the continuum to a cubic mesh of points, the Hamiltonian for our system is

$$\mathcal{H}[\theta_i] = -\sum_{\langle ij \rangle} J_{ij} \cos(\theta_i - \theta_j - A_{ij}) \tag{1}$$

where θ_i is the phase of the wavefunction at site i of the cubic mesh, the sum is over nearest neighbor bonds, $A_{ij} = (2\pi/\phi_0) \int_i^j \mathbf{A} \cdot d\mathbf{l}$ is the integral of the magnetic vector potential across the bond, and $J_{ij} = J_z$ or $J_\perp$ is the anisotropic coupling in the direction of the bond. The argument of the cosine is the gauge invariant phase difference across the bond, and is thus proportional to the supercurrent flowing along the bond. Since cosine is quadratic for small arguments, Eq.(1) represents the kinetic energy of the flowing supercurrents. If we identify the discrete spacing along $\hat{\mathbf{z}}$ as the distance d between copper-oxide planes, and the discrete spacing in the xy plane as representing the short length cutoff for a vortex core of radius ξ_0, we have

$$J_\perp \equiv \frac{\phi_0^2 d}{16\pi^3 \lambda_\perp^2}, \qquad J_z = \frac{\phi_0^2 \xi_0^2}{16\pi^3 \lambda_z^2 d}, \tag{2}$$

where $\lambda_\perp$ and λ_z are the magnetic penetration lengths within and normal to the copper-oxide planes, respectively. We define an anisotropy parameter η as

$$\eta \equiv \sqrt{\frac{J_\perp}{J_z}} = \frac{\lambda_z}{\lambda_\perp} \frac{d}{\xi_0}. \tag{3}$$

In our model of Eq.(1) we ignore spatial variations and fluctuations in the internal magnetic field, taking $\nabla \times \mathbf{A} = B\hat{\mathbf{z}}$ a uniform constant. This should be valid provided

[7] that B is so large that the spacing between vortex lines $a_v = \sqrt{\phi_0/B} \ll \lambda_\perp$ (so the magnetic fields associated with each vortex line strongly overlap), yet B is small enough that $a_v \gg \xi_0$ (so details of the vortex cores are not important). The anisotropy must also be such that $d < \lambda_\perp^2/\lambda_z$, so that Josephson coupling between the planes dominates over magnetic coupling [5,8]. For our simulations, we thus take the A_{ij} as fixed constants, chosen to give a particular fractional density $f \equiv B\xi_0^2/\phi_0$ of vortex lines penetrating the xy plane [9].

To model a particular material, we would like to map out the phase diagram as a function of T and magnetic field B, for a fixed value of anisotropy η. However, due to commensurability difficulties between the triangular vortex lattice preferred in a continuum and the discrete sites permitted by our numerical mesh, different vortex line densities would form lattice structures of differing symmetry in the ground state. Since we are computationally limited to a fairly coarse mesh, this would make direct comparison of systems with different B difficult. We therefore choose to map out the phase diagram as a function of T and anisotropy η, for fixed B. We can see however, using dimensional arguments, that increasing η at fixed B, is similar to increasing B at fixed η. If we measure any transition temperature T_c in units of $J_\perp$, then the dimensionless $T_c/J_\perp$ can only depend on the other dimensionless parameters of the model, the anisotropy $\eta = \lambda_z d/\lambda_\perp \xi_0$, and the vortex line density $f = B\xi_0^2/\phi_0 = (\xi_0/a_v)^2$. Since our London approximation ignores details of the vortex cores, if we consider the continuum limit of our model, $a_v \gg \xi_0$, we expect that $T_c/J_\perp$ should be at most weakly dependent [10] on the core radius ξ_0. The only combination of η and f that is independent of ξ_0 is $\eta^2 f$. Thus, the dominant dependence of $T_c/J_\perp$ on η and f can only be through some function of $\eta^2 f \sim \eta^2 B$.

We can further argue how transition temperatures should depend on the quantity $\eta^2 f$. In the limit of extreme anisotropy, $\eta \to \infty$, we have completely decoupled planes, and the transition temperature should be independent of η; thus we expect $T_c \sim J_\perp$. In the limit of a nearly isotropic system, $\eta \sim 1$, we expect that T_c should be independent of the spacing between planes d; thus we expect $T_c \sim J_\perp/\eta\sqrt{f} = (\phi_0^2/16\pi^3\lambda_\perp^2)(\lambda_\perp/\lambda_z)(\phi_0/B)^{1/2}$. These are in fact the predictions for the melting temperature based on Lindemann criterion calculations [2].

RESULTS

We now simulate the Hamiltonian (1), using periodic boundary conditions in all directions, on mesh sizes $L_\perp^2 \times L_z$. To test for superconducting coherence, we compute the helicity moduli $Y_\perp(T)$ and $Y_z(T)$ which measure the stiffness with respect to applying a net gradient ("twist") in the phase of the wavefunction along directions perpendicular and parallel to the applied magnetic field [7]. The helicity modulus in direction $\hat{\mu}$ is given by the phase correlation

$$Y_\mu(T) = \left\langle \frac{1}{L_\perp^2 L_z} \sum_{\langle ij \rangle} J_{ij} \cos(\theta_i - \theta_j - A_{ij})(\hat{\mathbf{e}}_{ij} \cdot \hat{\mu})^2 \right\rangle$$

$$- \frac{1}{T L_\perp^2 L_z} \left\langle \left[\sum_{\langle ij \rangle} J_{ij} \sin(\theta_i - \theta_j - A_{ij})(\hat{\mathbf{e}}_{ij} \cdot \hat{\mu}) \right]^2 \right\rangle, \qquad (4)$$

where $\hat{\mathbf{e}}_{ij}$ is the unit vector from site i to j. $Y_\perp$ and Y_z are proportional to the density of superconducting electron pairs for currents flowing perpendicular and parallel to B. When Y_μ is positive, there is superconducting coherence in direction $\hat{\mu}$. When Y_μ vanishes, superconducting coherence is lost.

We also measure the specific heat of the system using the usual energy fluctuation formula. A peak in the specific heat locates the temperature at which, upon cooling, there is a dramatic freezing out of thermal fluctuations and the system looses the bulk of its entropy. We will take the location of the specific heat peak as indicating the cross-over temperature T_{c2} [11].

We carry out our simulations with a B yielding a fractional density of vortex lines $f = 1/15$. The ground state, shown in Fig. 1, is a nearly triangular vortex line lattice. Our runs are typically 10,000 sweeps through the mesh to equilibrate, followed by 128,000 sweeps to compute averages. These simulations are about 9 times longer than in our previous work [7].

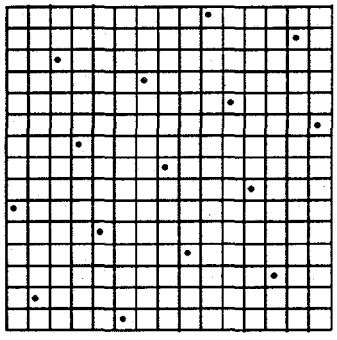

FIG. 1. Ground state locations of vortex lines in the xy plane for line density $f = 1/15$ on a cubic mesh. Vortices form a nearly triangular lattice with sides $\sqrt{18} \times \sqrt{18} \times \sqrt{17}$.

A sample of our results, for the case of $\eta = \sqrt{10}$ is shown in Fig. 2. We see that $Y_\perp$ vanishes at a $T_{c\perp}$ significantly lower than the T_{cz} where Y_z vanishes. We show data for heating and cooling, for three different mesh sizes, 15^3, 30^3, and $15^2 \times 120$. We see no appreciable hysteresis comparing heating and cooling, nor is there any apparent finite size effect as $L_\perp$ and L_z are varied. By computing the density-density correlation function of vortices in the xy plane, we identify $T_{c\perp}$ as locating the melting of the vortex line lattice [7].

For $T < T_{c\perp}$ we have an ordered vortex lattice which is commensurably pinned to the discrete mesh, resulting in a finite $Y_\perp$. For $T > T_{c\perp}$ we have a vortex line liquid of unpinned diffusing vortex lines; the resulting "flux flow" resistance drives $Y_\perp \to 0$. Between $T_{c\perp}$ and T_{cz} we have a vortex line liquid which retains superconducting coherence in the direction parallel to the applied magnetic field. These results are in complete agreement with our earlier simulations [7] on a similar *isotropic* model. In contrast to these earlier simulations however, we now see that, in agreement with experiment, both $T_{c\perp}$ and T_{cz} lie noticeably

below the cross-over T_{c2} as determined by the specific heat peak.

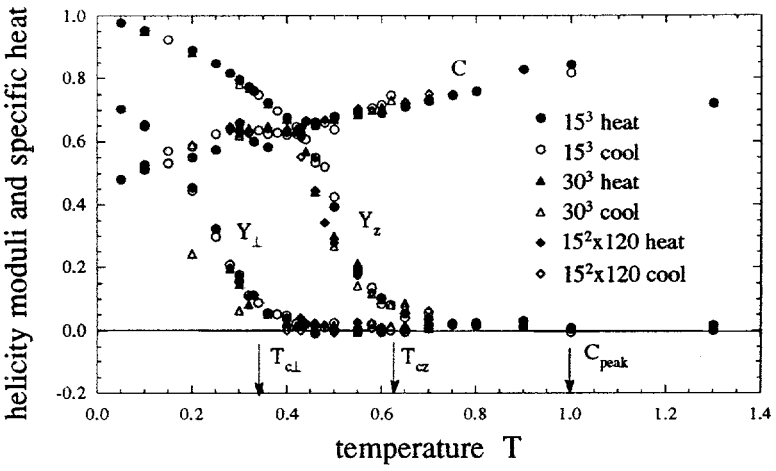

FIG. 2. Helicity moduli $Y_\perp$ and Y_z and specific heat C versus temperature T for anisotropy $\eta = \sqrt{10}$ and vortex line density $f = 1/15$. Heating and cooling for three different system sizes are shown. $Y_\perp$, Y_z, C, and T are all measured in units of $J_\perp$.

Carrying out simulations at other values η on a 15^3 size mesh, we show in Fig. 3 the resulting phase diagram in the $\eta - T$ plane. The $T_{c\perp}$ line locates the melting of the vortex line lattice. The T_{cz} line locates the loss of coherence parallel to the magnetic field. The line "C_{peak}" locates the peak of the specific heat, which we take as the cross-over temperature T_{c2}. For $T > T_{c2}$ we have the normal metal. For $T_{c2} > T > T_{cz}$ we have a vortex line liquid, with resistive behavior in all directions. For $T_{cz} > T > T_{c\perp}$ we have a vortex line liquid with superconducting coherence parallel to B. For $T_{c\perp} > T$ we have a pinned Abrikosov vortex line lattice.

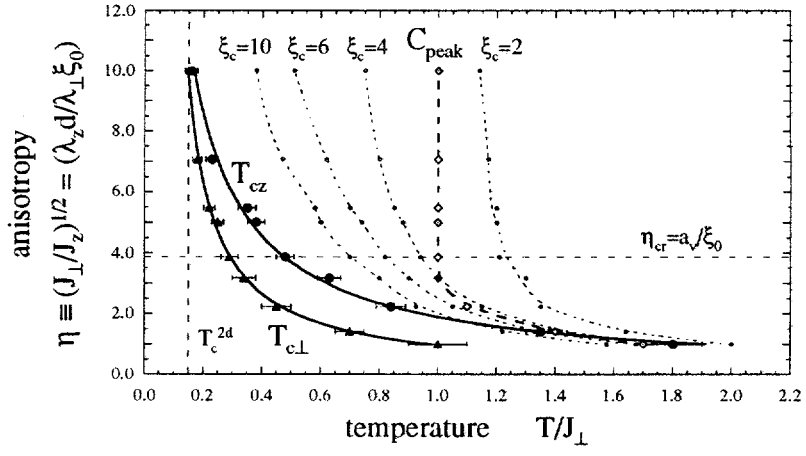

FIG. 3. Phase diagram in the anisotropy–temperature plane for vortex line density $f = 1/15$. T is measured in units of $J_\perp$ and ξ_c in units of d.

The solid phase boundary lines for $T_{c\perp}$ and T_{cz} are fits to a simple form $T = a + b/\eta$, as motivated by our discussion at the end of the preceding section. If we fit the lowest five data points (those for $\eta \leq \eta_{cr}$) to a power law, we find $T_{c\perp} \sim 1/\eta^{0.914}$ and $T_{cz} \sim 1/\eta^{0.966}$, in excellent agreement with our dimensional argument that characteristic temperatures at small η should scale as $T \sim 1/\eta$. We can also fit the melting temperature at these low η to the form predicted by a Lindemann criterion [2], $T_{c\perp} = 4c_L^2(\phi_0^2/16\pi^2\lambda_\perp^2)(\lambda_\perp/\lambda_z)(\phi_0/B)^{1/2} = 4\pi c_L^2 J_\perp/\eta\sqrt{f}$, where the Lindemann parameter $c_L^2 \equiv \langle u^2\rangle/a_v^2$ gives the average displacement of a vortex line from its equilibrium lattice position, at melting. We find $c_L = 0.14$. At large η, we see that $T_{c\perp}$ approaches a constant value T_c^{2d}, which we have found from independent simulations to be the melting temperature for an isolated two dimensional plane.

The cross-over from small to large η, where the discreteness of the layering along $\hat{\mathbf{z}}$ becomes important and one approaches the two dimensional limit, can be estimated, following our discussion at the end of the previous section, by the criterion $\eta_{cr}^2 f \simeq 1$, or, using $f = B\xi_0^2/\phi_0 = (\xi_0/a_v)^2$, as $\eta_{cr} = a_v/\xi_0$. Using an effective elastic medium approximation to describe vortex line fluctuations in the line lattice, one can show [2] that for $\eta < \eta_{cr}$, the dominant wavenumber q_z of fluctuations at melting satisfies the condition $d < \pi/q_z$, and hence the layering of the material is averaged over. For $\eta > \eta_{cr}$ however, the dominant wavenumber is at $d = \pi/q_z$, and layering is important. Some theoretical models [5] have predicted that η_{cr} will mark a dramatic change in behavior, reflecting a three dimensional to two dimensional cross-over. In Fig. 3 we indicate the cross-over η_{cr}. We see that the specific heat peak for $\eta > \eta_{cr}$ is independent of η. Thus at these high temperatures and anisotropies, our three dimensional system is behaving as effectively decoupled layers. However we see no dramatic change in behavior for $T_{c\perp}$ and T_{cz} as η_{cr} is crossed. In particular we continue to find $T_{cz} > T_{c\perp}$ for all $\eta > \eta_{cr}$.

An intriguing question concerning behavior in the vortex line liquid is how easily lines can cut through each other. This has important consequences for line diffusion. If lines cannot cut, they can be effectively pinned by their mutual entanglements [3,12]. To investigate this we have computed the average number of vortex line intersections, N_c, present in any instantaneous configuration of the system. An intersection is defined when two vortex lines enter and leave the same unit cell of the mesh, and corresponds to vortex lines with overlapping cores. Once two lines intersect, they are free to cut through each other, or even to detach and reconnect different ingoing and outgoing segments. We define the "cutting length" $\xi_c \equiv fL_\perp^2 L_z/N_c$ as the average distance (in units of d) along $\hat{\mathbf{z}}$ between cuts of the magnetic field induced vortex lines. ξ_c gives a crude measure of the average length over which a vortex line remains a well defined string, or equivalently a measure of the number of planes which remain correlated. In Fig. 3 we show contours of constant $\xi_c = 2$, 4, 6, and 10 in the $\eta - T$ plane. We see that planes are essentially uncorrelated at temperatures above the specific heat peak. Correlations grow as one starts to cool below the specific heat peak towards T_{cz}, but cutting remains relatively frequent throughout most of the vortex line liquid.

DISCUSSION

We have computed the phase diagram of a fluctuating type II superconductor in the anisotropy temperature plane. Our results are consistent with general experimental observations, that vortex lattice melting occurs well below the cross-over T_{c2} associated with the formation of local superconducting order. Our melting curve agrees well with that predicted by the Lindemann criterion. No dramatic change in critical behavior is seen at the so-called 3d-2d cross-over anisotropy η_{cr}. We find that vortex line cutting can occur over most of the vortex line liquid region. From our earlier isotropic simulations [7] we believe that cutting can be frozen out on long time scales only for $T < T_{cz}$.

We find a new distinct transition T_{cz}, inside the vortex line liquid [13]. For $T_{c\perp} < T < T_{cz}$ we have a vortex line liquid with superconducting coherence parallel to the applied magnetic field. Recent "flux transformer" experiments [14,15] on YBCO single crystals show that there is a temperature "T_{th}" below which vortex line correlations parallel to B become comparable to the thickness of the sample. "T_{th}" is clearly found to be above the "T_{irr}" where resistivity transverse to B vanishes. Resistivity parallel to B however appears to vanish at "T_{th}". A phenomenological fit [14] shows that the region over which correlations parallel to B grow, extends over the entire region between T_{c2} and "T_{th}". If we identify "T_{th}" with our T_{cz}, T_{irr} with our $T_{c\perp}$, and T_{c2} with our specific heat peak, our results are in complete accord with these experimental finding. These experiments on YBCO are carried out in the "3d" region corresponding to $\eta^2 f < 1$. Similar results in the "2d" region $\eta^2 f > 1$ have been reported in artificial MoGe/Ge multilayers [16].

By consideration of other properties of the vortex line system, such as vortex density-density correlation function, density of thermally activated vortex rings, and vortex winding, the picture we have formed of transitions in the anisotropic vortex line system is as follows [7]. Upon heating, the vortex line lattice melts into a vortex line liquid, in which vortex lines maintain a well defined identity in passing down the thickness of the system. As T increases, transverse fluctuations increase, and thermally excited vortex rings appear between adjacent xy planes. At T_{cz} these rings have so proliferated that they link up all the magnetic field induced vortex lines into a percolating tangle; one can find a connected path of vortex line segments that travels completely around the system in the direction transverse to the applied magnetic field. As T increases, the correlations between planes decreases, and each plane behaves more like an uncoupled two dimensional liquid of point vortices. Finally, as T_{c2} is reached, thermally excited vortex rings may now pierce the xy planes, creating the analog of vortex-antivortex pairs in a 2d layer. The proliferation of these rings leads to an explosion of vorticity in the planes, destroys the local fluctuating superconducting wavefunction in the plane, and results in the cross-over to the normal metallic state.

ACKNOWLEDGMENT

This work has been supported by the U.S. Department of Energy under grant DE-FG02-89ER14017.

REFERENCES

[1] M. Tinkham, *Introduction to Superconductivity*, (R.E. Krieger Co., Malabar, FL, 1980).

[2] D. S. Fisher, M. P. A. Fisher, and D. A. Huse, Phys. Rev. B **43**, 130 (1991).

[3] D. R. Nelson and H. S. Seung, Phys. Rev. B **39**, 9153 (1989).

[4] A. Houghton, R. A. Pelcovits and A. Sudbø, Phys. Rev. B **40**, 6763 (1989); E. H. Brandt, Phys. Rev. Lett. **63**, 1106 (1989).

[5] L. I. Glazman and A. E. Koshelev, Phys. Rev. B **43**, 2835 (1991).

[6] T. K. Worthington, F. H. Holtzberg and C. A. Field, Cryogenics **30**, 417 (1990); U. Welp, W. K. Kwok, G. W. Crabtree, K. G. Vandervoort and J. Z. Liu, Phys. Rev. Lett. **62**, 1908 (1989).

[7] Y.-H. Li and S. Teitel, Phys. Rev. B **47**, 359 (1993) and *ibid.* **49**, 4136 (1994).

[8] D. S. Fisher in *Phenomenology and Applications of High Temperature Superconductors*, edited by K. Bedell *et al.* (Addison-Wesley, Reading, MA, 1992), p.287.

[9] Recently we have suggested that differences between the uniform B model and a more exact treatment may also appear once the sample thickness is large compared to the length $\phi_0^2/8\pi T_m \simeq 1400\mu m$ (T_m is the vortex lattice melting temperature). Experimental samples however are typically thinner than this. See, T. Chen and S. Teitel, Phys. Rev. Lett. **74**, 2792 (1995).

[10] The interactions between different vortex lines are independent of the core size ξ_0. However the self interaction of a bending vortex line can depend on ξ_0. This may lead to weak logarithmic dependencies on ξ_0. See E. H. Brandt, J. Low Temp. Phys. **26**, 735 (1977).

[11] Because B is kept uniform and constant in our model, equivalent to a $\lambda_\perp \to \infty$ approximation, we cannot directly measure the magnetization in our system.

[12] M. C. Marchetti and D. R. Nelson, Phys. Rev. B **42**, 9938 (1990) and Physica C **174**, 40 (1991); S. P. Obukhov and M. Rubinstein, Phys. Rev. Lett. **65**, 1279 (1990) and *ibid.* **66**, 2279 (1991).

[13] M. V. Feigelman, Physica A **168**, 319 (1990); M. V. Feigelman, V. B. Geshkenbein and V. M. Vinokur, JETP Lett. **52**, 546 (1990); M. V. Feigelman, V. B. Geshkenbein, L. B. Ioffe, and A. I. Larkin, Phys. Rev. B **48**, 16641(1993).

[14] H. Safar, P. L. Gammel, D. A. Huse, S. N. Majumdar, L. F. Schneemeyer, D. J. Bishop, D. López, G. Nieva, and F. de la Cruz, Phys. Rev. Lett. **72**, 1272 (1994).

[15] F. de la Cruz, D. López, and G. Nieva, Phil. Mag. B **70**, 773 (1994); D. López, G. Nieva, and F. de la Cruz, Phys. Rev. B **50**, 7219 (1994).

[16] D. G. Steel, W. R. White and J. M. Graybeal, Phys. Rev. Lett. **71**, 161 (1993).

SYSTEMATIC PROCESS SYNTHESIS AND DESIGN METHODS FOR COST EFFECTIVE WASTE MINIMIZATION

Lorenz T. Biegler
Ignacio E. Grossmann
Arthur W. Westerberg

Dept. of Chemical Engineering
and the Engineering Design Research Center
Carnegie Mellon University
Pittsburgh, PA 15213

ABSTRACT

We present progress on our work to develop synthesis methods to aid in the design of cost effective approaches to waste minimization. Work continues to combine the approaches of Douglas and coworkers and of Grossmann and coworkers on a hierarchical approach where bounding information allows it to fit within a mixed integer programming approach. We continue work on the synthesis of reactors and of flexible separation processes. In the first instance, we strive for methods we can use to reduce the production of potential pollutants, while in the second we look for ways to recover and recycle solvents.

INTRODUCTION

We summarize progress made on the following topics which we are pursuing in this work.

1. Integration among design levels for process synthesis in order to develop cost effective waste minimizing processes.
2. Quantitative targeting approaches for the synthesis of reactor networks
3. Synthesis of nonideal separation sequences for byproduct recovery and reuse.

MULTILEVEL SYNTHESIS OF PROCESS FLOWSHEETS

The main objective of this project has been to develop a new framework for the synthesis of total processing systems that can address the issue of generation of superstructures and optimization under a methodology that combines preliminary screening and MINLP optimization. This challenge was in

fact proposed by the late David Rippin at the session on process synthesis at the FOCAPD Meeting in 1989.

The basic question that we have addressed over the past year is how to develop a search procedure that avoids solving a single flat MINLP that contains all the alternatives of interest for a process flowsheet, and that in principle is capable of producing the same result as if the single MINLP had been solved at once. The emphasis in this work has been on the development of a design methodology that integrates thermodynamic analysis (mostly second law analysis), the hierarchical decomposition by Douglas and the MINLP optimization developed by our group at Carnegie Mellon.

To provide a conceptual basis for our work we had developed in our previous work an abstract mathematical model for characterizing aggregated models. These models are higher level representations that are given in terms of algebraic relations for equations and variables that guarantee bounding properties with respect to the original problem. These aggregated models must be derived for each problem at hand, but one particularly useful framework is the one that relies on thermodynamic analysis as described below. Given aggregated models at various level of abstraction and that obey bounding properties, the question that arises is how to integrate these within a multilevel strategy for flowsheet synthesis.

We have developed a multilevel synthesis strategy that can be viewed as a hierarchically driven tree enumeration in which simultaneous optimization models at increasing levels of detail are considered for predicting bounds on the profit. The basic idea for the enumeration consists of applying a hierarchical decomposition that involves four major levels: input/output, reaction, separation and heat integration.

Rather than relying directly on Douglas' procedure, our approach consists of a branch and bound search coupled with aggregated or "black box" models that through their predicted bounds allow us to eliminate many alternatives in the search. The aggregated models consist of higher level representations that are physically based and that make use of stoichiometry and thermodynamic analysis. The basic idea is to combine high level or black box models with superstructure optimization models. In particular, at the input/output level thermodynamic availability is considered to estimate a lower bound for the energy requirements in addition to minimum material flows. At the reaction level, a superstructure model is considered together with thermodynamic models for separation and heat integration. At the separation level the reactor network is fixed while the heat integration is treated as a "black box" using the Duran and Grossmann model. Finally, at the heat integration level a fixed flowsheet is considered with a superstructure for a heat exchanger network. Note that each level gives rise to a simultaneous optimization model at different levels of complexity. Normally at the input/output level the optimization problem corresponds to an NLP subproblem, while at the heat integration level it corresponds to an MINLP problem.

The search of the optimal flowsheet involves the multiple levels within a rigorous tree search whose terminal nodes correspond to feasible NLP solutions of the flowsheet. One advantage of this strategy is that it involves the solution of NLP and MINLP subproblems which are much smaller than the original MINLP problem. The potential drawback is that the number of subproblems to be solved can be rather large. We tested this strategy with the HDA process by Douglas. In a restricted version of this problem, our proposed method required the enumeration of only few nodes. Furthermore, the predicted upper bounds on the profit were rather tight. This is due to the anticipation of energy requirements at the higher levels of decision (e.g. input-output structure). Shown in the figure below is the flowsheet obtained from the proposed method.

Mark Daichendt, the student working on this project is finalizing the writing of his Ph.D. thesis. The manuscript of this work [1] is currently under preparation. The next major step in this project is the integration of operational considerations as part of this design methodology.

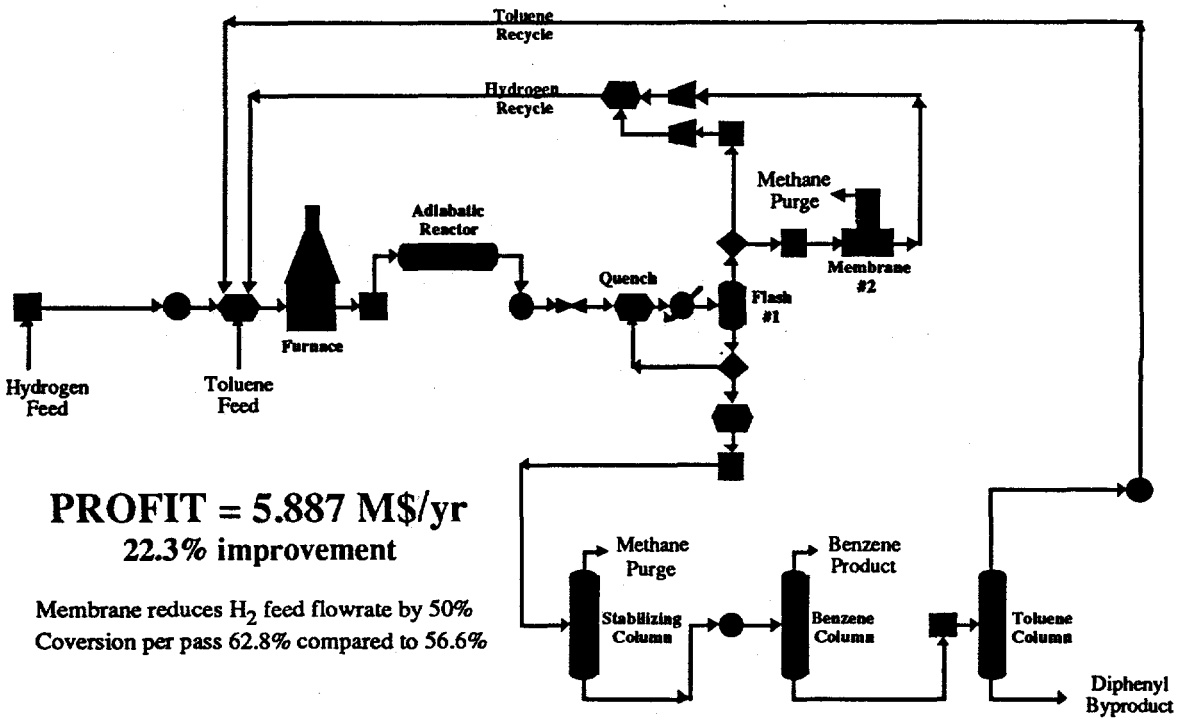

Figure 1. HDA process synthesized using proposed method

REACTOR NETWORK SYNTHESIS FOR WASTE MINIMIZING PROCESSES

The public is demanding processes that are environmentally benign. One of the most efficient approaches to designing such processes is to increase raw material conversion to product rather than wasteful byproducts. In this work we consider the development and application of optimization-based process synthesis tools to improve reactor and separation process performance to improve the environmental characteristics of processes.

We apply systematic process synthesis approaches to the design of the reactor network to maximize the overall conversion to useful product and thus minimize harmful byproducts. This approach is based on concepts of attainable regions in concentration space and is supported by powerful, large-scale optimization tools. Examples that can benefit from this approach are processes for the manufacture of chlorinated hydrocarbons especially allyl chloride and vinyl chloride, two high volume polymer intermediates. The improvements made by this approach can also validated by rigorous process simulation models.

We use these approaches to improve both economic and environmental performance. Specifically we describe recently developed techniques for process synthesis and extend them to consideration of reactor networks and their interaction with other process subsystems.

The nature of the reaction mechanism and the resulting reactor design frequently determines the entire character of a chemical process. Once a kinetic route is chosen and a quantitative (not necessarily a mechanistic) rate law has been established, the flow pattern, mixing characteristics and rates of heat addition or removal have a strong influence on product yield and selectivity. The reactor effluent then determines the downstream separation sequence which then impacts on the

energy network. More importantly, the generation of hazardous waste is almost always the result of the characteristics of the reactor network.

Over the past three decades process synthesis methodologies for heat exchanger and separation systems have seen considerable research activity. Many of the resulting synthesis methods are either rule-based or graphical techniques driven by physical insights; others can be formulated as well-characterized optimization problems. For example, efficient synthesis methods based on pinch technology have been established for heat exchanger networks [2]; design of simple separation networks has been formulated as a structural optimization problem and azeotropic separation sequences can be synthesized through phase plane analysis (see next section). However, relatively little research has been done for reactor network synthesis. Here well-known heuristics for single reactions or series-parallel systems [3, 4] may yield inconsistent or conflicting results when dealing with more complex systems. On the other hand, quantitative optimization approaches lead to difficulties as a result of nonlinear reactor models (frequently described by partial differential equations) and in solving large, nonconvex optimization problems.

A much more efficient approach was recently developed, based on the construction of an attainable region [5]. This approach uses geometric properties to find a region in concentration space that cannot be extended by further reaction or mixing. Once known, the determination of the optimum point is greatly simplified. Construction of the attainable region is accomplished by analyzing the rate vector field and determining a surface that is a) convex (all points can be mixed),, b) has no rate vectors pointing out of the region (cannot be extended by further reaction), and c) no rate vectors external to the region can be reversed back into the region (cannot be extended by a mixed reactor). Thus, a simple graphical approach can been used to derive superior reactor networks; this approach has been demonstrated for numerous reaction mechanisms.

The attainable region can be constructed efficiently in two and even in three dimensions [6], but, for larger reaction systems, a graphical approach has clear limitations. As a result, Balakrisnan and Biegler [7] adapted these attainable region concepts so that they can be formulated as small nonlinear optimization problems for reaction mechanisms of any dimension. Consequently, optimal reactor networks can now be synthesized for arbitrarily complicated reaction mechanisms, through small and inexpensive optimization problems. This approach has also been extended to nonisothermal systems [8] with only slightly more complicated optimization problems. Finally, Lakshmanan and Biegler [9] recently considered this approach for the synthesis of waste minimizing processes. In addition, refinements of this optimization-based approach using a compact MINLP strategy have been presented recently by Lakshmanan and Biegler [10].

While construction of the reactor network is not difficult from the boundary of the attainable region, the attainable region itself also provides information on the performance of the reactor network without explicitly constructing it. Instead, compact optimization formulations can be used to target reactor performance, and these can be embedded into larger process systems. For instance, an attainable region formulation can be substituted for a complex reactor model, and this can be coupled to the recycle and separation network as well as a heat exchanger network. By combining these systems, a resulting optimization formulation can exploit the interactions and the synergy among these subsystems, and far better processes can result. Balakrishna and Biegler [8, 11] have shown how this approach can be coupled to heat exchanger network and separation synthesis formulations with the result that very complex flowsheets can be synthesized and optimized simultaneously.

The waste minimization problem also forms an important component to be addressed by reactor targeting and here we also include the waste treatment step into the synthesis procedure. In our research we apply these synthesis techniques to processes for reaction mechanisms and rate laws that are well-known. As an example we consider a simple (allyl chloride) Van de Vusse process to illustrate the reactor targeting approach and demonstrate its potential.

Example Problem

Consider the simplified allyl chloride process shown in Figure 2. Propylene and chlorine are mixed and reacted at high temperature to allyl chloride, hydrogen chloride and dichlorinated byproducts. The reactor effluent is flashed to separate the unreacted propylene and chlorine and hydrogen chloride from the reaction products. This mixture is sent to a scrubber to recover the hydrogen chloride and recycle the reactants. On the other hand, the reaction products, allyl chloride, dichloropropene and dichloropropane, are further separated downstream and the dichlorinated compounds are discarded. The reaction can be described by rate expressions from Groll and Hearne [12] and, if chlorine is assumed in excess, the system follows van de Vusse kinetics: A --> B --> C, A --> D where A, B, C, and D are propylene, allyl chloride, dichloropropene and dichloropropane, respectively. This process is well-characterized and has been the subject of numerous studies [13, 14].

This process was modeled in GAMS, an optimization/modeling platform, using the targeting concepts explained above along with simplified separation models. The resulting formulation consists of 542 constraints and 523 variables and was solved in 3.0 CPU sec's on an HP 9000/720 workstation. Here it turns out that the optimal reactor network is a tubular reactor (as in practice) but with the falling temperature profile shown in Figure 3 (as opposed to the adiabatic profile used in practice). This falling profile can also be used to exploit the heat of reaction elsewhere in the process. While this is frequently done, the heat recovery network is usually constructed sequentially, without changing process conditions to its advantage. In fact, if we are able to synthesize the heat exchanger network simultaneously with the reactor system, the overall profit can be increased by over 90%. A comparison of the sequential and simultaneous optimization is given in Table 1. Note that the overall conversion of propylene to allyl chloride increases from 49.6% to 61.5%. This results from a higher selectivity to main product vs. waste, lower conversion per pass, higher recycle and lower feed requirements.

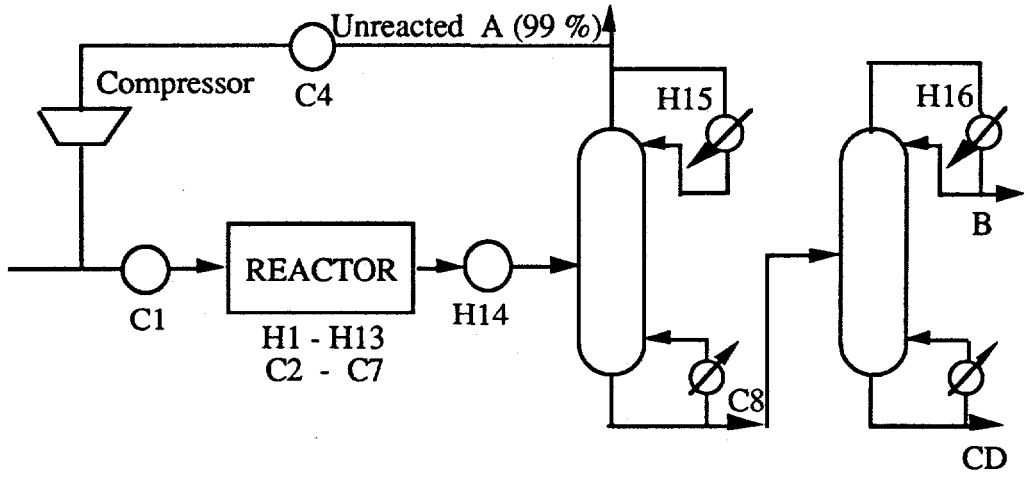

Figure 2. Allyl chloride process flowsheet

Additionally, we constrain the amount of hazardous waste being produced in the optimization formulation and can synthesize a maximum profit reactor network for a given waste limit. This allows us to establish an optimal trade-off curve of profit (before waste treatment) vs. waste generated, as shown in Figure 4. While waste treatment costs can be directly incorporated into this problem directly, the trade-off curve provides a very useful tool for decision-making when confronted with uncertain waste treatment costs and changing regulations.

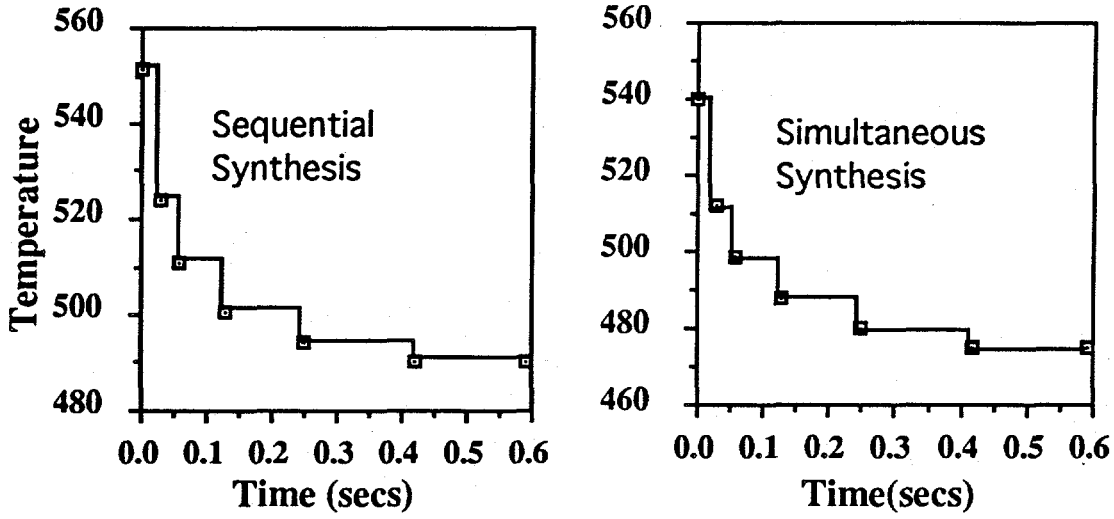

Figure 3: Reactor temperature profiles

Table 1. Comparison between sequential and simultaneous optimizations

	Sequential	Simultaneous
Overall Profit	$38.98 * 10^5$ \$/yr	$74.02 * 10^5$ \$/yr
Overall Conversion	49.6 %	61.55 %
Hot utility load	$3.101 * 10^5$ BTU/hr	$2.801 * 10^5$ BTU/hr
Cold utility load	$252.2 * 10^6$ BTU/hr	$168.5 * 10^6$ BTU/hr
Fresh Feed A	$8.057 * 10^4$ lb/hr	$6.466 * 10^4$ lb/hr
Degraded Product C	$3.112 * 10^4$ lb/hr	$1.44 * 10^4$ lb/hr
By-Product D	$0.933 * 10^4$ lb/hr	$1.00 * 10^4$ lb/hr
(Recycled) A	$1.22 * 10^4$ lb/hr	$1.963 * 10^4$ lb/hr

As future work we plan to consider and further develop the following topics:

- development of large-scale nonlinear programming tools for optimization formulations based on differential-algebraic models.
- advanced software environments for the rapid development and prototyping of reactor and process models
- development and enhancement of fundamental concepts for reactor targeting and extension to separation and waste treatment systems
- access to rigorous process models embedded within the ASPEN simulator as well as the CRDT reactor design program.

A major goal of our research will be the demonstration and refinement of an optimization-based process synthesis methodology for waste minimization of important chemical processes. Process models developed in ASPEN and CRDT along with the optimization formulations for reactor targeting can then be developed for more rigorous process evaluation.

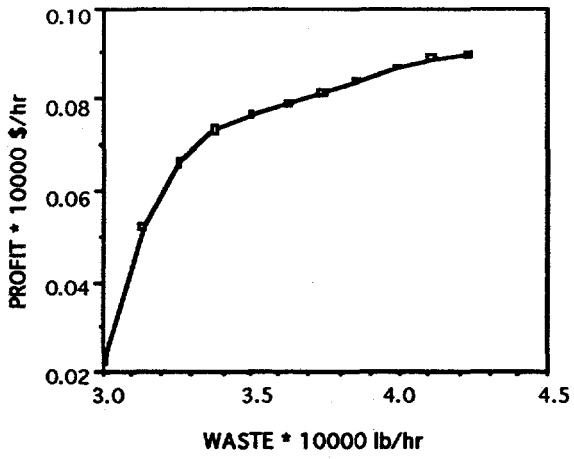

Figure 4: Allyl Chloride trade-off curve (noninferior curve)

SYNTHESIS OF NONIDEAL SEPARATION SEQUENCES FOR BYPRODUCT RECOVERY AND REUSE.

We have been working on methods to synthesize separation processes for liquid mixtures displaying azeotropic and liquid/liquid behavior since 1989. In this work we developed SPLIT, an expert system for the synthesis of such processes [15, 16, 17, 18]. We also developed many insights for separating mixtures that allowed, for example, the prediction of the all the reachable products that a conventional and an extractive three component distillation column can produce, where the operation of the column ranged from total reflux to reversible [19, 20, 21]. The pinch trajectories corresponding to reversible operation allowed the computation of how far column operation can cross the so-called residue and distillation curve boundaries. These trajectories can be very rich -- having multiple branches.

The computations to support each decision in the synthesis of separation processes for azeotropic mixtures are very extensive, causing us to term this approach "analysis-driven synthesis."

Synthesis of batch separation processes for azeotropic mixtures

We have recently extended the insights for continuous distillation processes to batch distillation-based processes [22]. In the course of developing these insights, we investigated unconventional batch column configurations such as those shown in Figure 5. The leftmost is a conventional batch still with a pot at the bottom. The second is a top pot column where the condenser has large holdup and one draws off a bottom product. The third is the most interesting and is a batch column with a center stage holdup. It has both a stripping and an enriching set of trays. It can be run with either heating or cooling of the pot. As Morari and coworkers [23] reported, this configuration cuts utility use in half (generally not economically significant, but interesting). It also allows one to double the throughput, making essentially two cuts in the time a conventional column can make one (more significant economically), but, of coure, it will be more expensive to purchase. We also show an optional extractive agent feed in the top section of the column. The fourth is a conventional batch column with an extractive agent fed continuously as one carries out the separation. We can break azeotropes with the last two configurations.

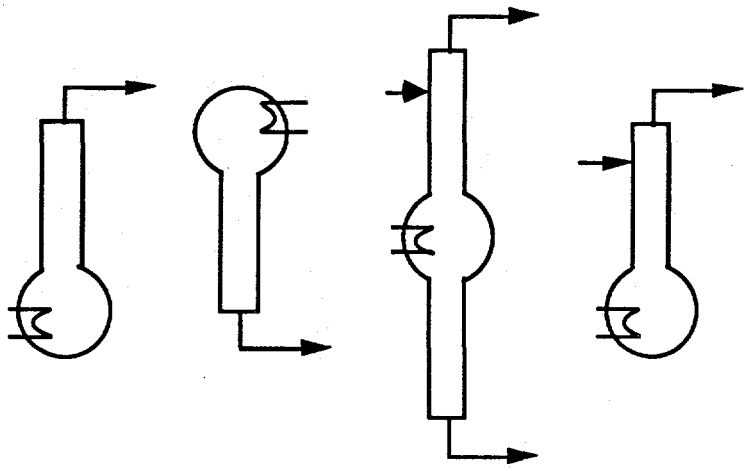

Figure 5. Conventional and unconventional batch columns

We are working on comparing the optimal operation as found using optimal control to how we would predict one should operate such a column using the above insights, where the insights give bounds on the solvent flow vs. reflux ratio vs. the amount of material separated [24].

Flexible separation processes

The recovery of solvents from processes is an important environmental problem. If several processes at a single site share a single solvent recovery system, then we find the need to design such a system to operate with a variety of potential feed compositions and flow rates.

Collocation models: To carry out the synthesis of flexible separation systems, we identified the need to reduce the analysis burden, especially to determine the detailed behavior of a column. We often needed to solve tray-by-tray models. Unfortunately these computations involve fixing the number of trays in each of the column sections and guessing the reflux ratio to use to effect a desired separation. It is difficult to know the number of trays and a suitable reflux a priori.

Based on work by others [25, 26, 27], we [28] developed a collocation model for distillation. Such models have had difficulty in producing accurate composition profiles when portions of the profiles flattened out, as in a column where there are too many trays or where one seeks high purity. We introduced two variable transformations to our collocation model. The first maps trays ranging in number from zero to infinity onto the range zero to one:

$$z = 1 - e^{-as}$$

where z is the transformed stage location and s is the original tray number. The second transformation mapped composition from the range zero to one into the range minus infinity to plus infinity:

$$-1 \le 2(x - 0.5) = \tanh(\xi) = \frac{e^{\xi} - e^{-\xi}}{e^{\xi} + e^{-\xi}} \le 1$$

where x is composition and ξ is the transformed composition. Both change the shape of the column profiles to those more easily characterized by low order polynomials.

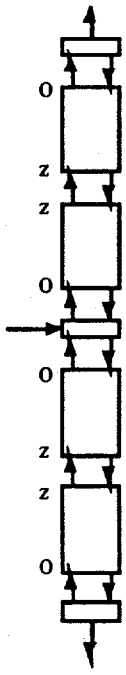

Figure 6. Reduced order column model

Our collocation model involves a feed tray, a condenser, a reboiler and two tray stacks, as shown in Fig. 6. We models the tray stacks as two opposing collocation sections, where the transformed tray number z is zero at the opposing ends of each section and nonzero where they merge. Testing of this model on several example problems, where the components range from displaying ideal to azeotropic behavior, shows it compares very favorably to that obtained using tray-by-tray computations, even for cases for sharp separation and too many trays. We have developed a robust computation method that creeps up on the solution (continuation for degree of separation and model refinement to move from ideal to nonideal equilibrium models).

Flexible design: We have used this model for column design and optimization. Our latest use is for the design of a single flexible column. We defined flexible operation as being able to operate at steady-state with any one of a given set of alternative feeds to the column. The designer sets the fraction of time each feed will exist for the column so we can compute appropriate operating costs relative to capital costs.

A conventional optimization code fails to simultaneously converge a column model and move to an optimum solution. We therefore use a grid of nine column designs -- using our robust procedure to creep up on the solutions for each column, one for each feed. For each feed we fit a quadratic polynomial to characterize a column's reflux ratio vs. total trays and feed tray location. The optimization code has no difficulty with this very reduced model in finding the optimal diameter and total number of trays for the column. It also picks which tray to feed and what reflux rate to use to operate the column for each feed.

If the optimal design is at the edge of the nine grid points used to characterize the model, we compute more column designs to place that point interior to the grid and repeat Tests include both nearly ideal and azeotropic mixtures.

Future work on flexible separation process synthesis: To design flexible complete processes comprising several columns, we are examining setting up a superstructure model for separating feeds from anywhere in a composition diagram using the ideas presented recently by Sargent [29]. He treats each azeotrope as a new species. For each distillation region, he puts the bounding components (pure and azeotropic) into an order that corresponds to their volatility and develops a superstructure for separating them. Curvature of the distillation boundary influences possible products. His rules also suggest where recycling should be allowed. We shall attempt to optimize this superstructure using the design approach we developed earlier for a single flexible column. We are also examining the potential of using A-teams [30] as an approach to carrying out the optimization. Our concern is that the optimization of superstructures is likely to have multiple local optima, a problem that A-teams may address effectively.

REFERENCES

1. Daichendt, M. and I.E. Grossmann, "Combined Hierarchical Decomposition and Mathematical Programming for the Synthesis of Process Flowsheets", manuscript under preparation (1995).
2. Linnhoff, B. and E. Hindmarsh, "The Pinch Design Method for Heat Exchanger Networks", Chem. Eng. Sci., 38, 745 (1983)
3. Levenspiel, O. Chemical Reaction Engineering, John Wiley, New York (1962)
4. Fogler, H. S., Elements of Chemical Reaction Engineering, Prentice-Hall, Englewood Cliffs, NJ (1992)
5. Glasser, D., C. Crowe, and D. Hildebrandt, "A Geometric Approach to Steady Flow Reactors: The Attainable Region and Optimization in Concentration Space," I&EC Res., 26(9),1803 (1987)
6. Hildebrandt, D. and D. Glasser, "The Attainable Region and Optimal Reactor Structures," Proc. ISCRE Meeting, Toronto (1990)
7. Balakrishna, S. and L. T.. Biegler, "Constructive Targeting Approaches for Synthesis of Chemical Reactor Networks," I & EC Research, 31, p. 300 (1992).
8. Balakrishna, S. and L. T. Biegler, "Targeting Strategies for the Synthesis and Heat Integration of Nonisothermal Reactor Networks" I & EC Research, 31, 9, p. 2152 (1992)
9. Lakshmanan, A. and L. T.. Biegler, "Reactor Network Targeting for Waste Minimization," submitted for publication (1994a)
10. Lakshmanan, A. and L. T.. Biegler, "An Improved MINLP formulation for Reactor Network Synthesis," presented at Annual AIChE meeting, San Francisco (1994b)
11. Balakrishna, S. and L. T. Biegler, "A Unified Approach for the Simultaneous Synthesis of Reaction, Energy and Separation Systems," I & EC Research, 32, p. 1372 (1993)
12. Groll, H. P. A., and G. Hearne, "Reaction of Vinyl Type Monochalides with Halogen," US Patent 2,060,303, Nov. 10 (1939).
13. Shell Chemical Corporation, "Allyl chloride and other allyl halides." Instituut voor Toegepaste Sociologie te Nijmegen, New York (1949)
14. McKetta, J. J. (ed.), Encyclopedia of Chemical Processing and Technology, 5th ed., Marcel Dekker, New York (1991)
15. Wahnschafft, O. M., T. P. Jurain and A. W. Westerberg, "SPLIT: a Separation Process Designer," Comput. Chem. Engng, 15, No. 8, 565-581 (1991).
16. Wahnschafft, O. M., J. P. LeRudulier, P. Blania and A. W. Westerberg, "SPLIT: II. Automated Synthesis of Hybrid Separation Systems" Computers Chem Engng, ESCAPE-I Supplement, pp S305-S312 (1992b).
17. Wahnschafft, O. M., J. P. LeRudulier and A. W. Westerberg, "A Problem Decomposition Approach for the Synthesis of Complex Separation Processes," Ind. Eng. Chem. Res., Vol. 32, 1121-1141 (1993a).
18. Wahnschafft, O. M., J. W. Koehler and A. W. Westerberg, "Homogeneous Azeotropic Distillation: Analysis of Separation Feasibility and Consequences for Entrainer Selection and Column Design," ESCAPE III Supplement, Comput. Chem. Engng, Vol. 18, S31-S35 (1993b).
19. Wahnschafft, O. M., J. W. Koehler, E. Blass and A. W. Westerberg, "The Product Composition Regions of Single-Feed Azeotropic Distillation Columns," I&EC Res, 31(10), 2345-2361 (1992a).
20. Wahnschafft, O. M., and A. W. Westerberg, "The Product Composition Regions of Azeotropic Distillation Columns: 2. Separability in Two-Feed Columns and Entrainer Selection," , Ind. Eng. Chem. Res., Vol. 32, 1108-1120 (1993).
21. Westerberg, A. W., and O. M. Wahnschafft, The Synthesis of Distillation-based Separation Systems, 124 page review submitted to Advances in Chemical Engineering (1995).
22. Safrit, B., U. Diwekar, O. M. Wahnschafft, A. W. Westerberg, "Extending Continuous Conventional and Extractive Distillation Insights to Batch Distillation," submitted (1994).

23. Meski, G. A.., and M. Morari, "Batch Distillation in a Column with a Middle Vessel," paper 152a, AIChE Annual Meeting, St. Louis, MO (1993).

24. Safrit, B., A. W. Westerberg, U. Diwekar, O. M. Wahnschafft, "Improved Operational Policies for Batch Extractive Distillation Columns," paper 82e, AIChE Spring National Meeting, Houston, TX (1995).

25. Cho, Y. S. and B. Joseph, "Reduced Order Steady-state and Dynamic Models for Separation Processes," AIChE J, 29, 261-269, 270-276 (1983)

26. Stewart, W. E., K. L. Levien, and M. Morari, "Collocation Methods in Distillation," in Westerberg, A. W., and H. H. Chien (eds.), Proc. Second Int'l Conf. Foundations Computer Aided Process Design (FOCAPD83), CACHE Corp., Ann Arbor, MI, pp535-569 (1984).

27. Seferlis, P., and A. N. Hrymak, "Reduced Order Models for Distillation Optimization" paper 152m, Annual AIChE Meeting, Los Angeles, CA (1991).

28. Huss, R. S., and A. W. Westerberg, "Collocation Methods for Distillation Design, paper 131c, Annual AIChE Meeting, San Francisco (1994).

29. Sargent, R. W. H., "A Functional Approach to Process Synthesis and its Application to Distillation Systems, manuscript from Centre for Process Systems Engineering, Imperial College of Science, Technology and Medicine, London SW7 2BY, UK (1994).

30. Talukdar, S., and P. de Souza, "Insects, Fish and Computer-based Super-agents," paper from Engineering Design Research Center, Carnegie Mellon University, Pittsburgh, PA 15213 (1995).

INTEGRATED APPROACHES TO THE APPLICATION OF ADVANCED MODELING TECHNOLOGY IN PROCESS DEVELOPMENT AND OPTIMIZATION

R. J. Allgor, W. F. Feehery, J. E. Tolsma, L. B. Evans, and P. I. Barton[‡]
Department of Chemical Engineering and Energy Laboratory
Massachusetts Institute of Technology
Cambridge, MA 02139

ABSTRACT

The batch process development problem serves as good candidate to guide the development of process modeling environments. It demonstrates that very robust numerical techniques are required within an environment that can collect, organize, and maintain the data and models required to address the batch process development problem. This paper focuses on improving the robustness and efficiency of the numerical algorithms required in such a modeling environment through the development of hybrid numerical and symbolic strategies.

1 INTRODUCTION

Over the past twenty five years process modeling technology has emerged as an invaluable and widely used tool for the solution of many problems in process design and operation [1]. A major current trend in this technology is the evolution of equation-based simulation tools, such as SpeedUp [2], ASCEND [3], POLYRED [4], or ABACUSS [7], into *process modeling environments* in which a common reusable process model may be used reliably for a variety of different computational tasks, such as steady-state and dynamic simulation, steady-state and dynamic optimization, data reconciliation and parameter estimation, etc. [6]. Concurrently to these advances in the underlying technology, it is necessary to investigate the complex process design tasks that might be addressed by such software. In this context, we can envision sophisticated software environments that can collect, organize, and maintain the data and models required to address complex design problems, and facilitate the seamless application of numerical algorithms to steps in the solution of the overall problem.

A process design task that serves as a good candidate for this approach is the batch process development problem recently formalized by Allgor *et al.*[5]. In the specialty chemical and pharmaceutical industries, major competitive advantages can be derived from the rapid development of efficient batch processes with low environmental impact. Allgor *et al.*[5] present an industrial case study in which the combined discrete/continuous simulation capabilities of ABACUSS [7] are used to develop a process design significantly more efficient than that resulting from a direct implementation of pilot scale experiments in the large scale plant. A prototype methodology in which process modeling technology is employed for batch process development is also presented.

Our current research is addressing two major issues in refining this methodology and making it accessible to the practicing engineer: development of a suitable software environment, Batch

[‡]Author to whom correspondence should be addressed.

Developer, that implements this methodology and coordinates the overall process development, and further developments of the underlying process simulation and optimization technologies driven by the challenging problems posed by the steps of the methodology. A simultaneous investigation of these two issues is proving particularly fruitful. This paper will focus on advances in the second category.

A major advantage of a process modeling environment, particularly when applied to problems such as batch process development, is the potential to decouple the process model from the numerical solution procedures applied to it. In addition to enabling a variety of different calculations to be performed with a single model, this feature frees the engineer to concentrate on the correct formulation of the model and the design, rather than the details of the numerical solution procedures. While this is a very desirable goal, it places very stringent demands and constraints on the robustness and generality of the solution procedures. Our experience has demonstrated that current technologies do not provide the level of robustness or efficiency required for routine application of modeling technology to the batch process development problem.

Detailed modeling of batch processes requires the use of combined discrete/continuous simulation applied to differential-algebraic models exhibiting complex and highly nonlinear behavior [8]. This problem is further complicated by the fact that during a batch operation state variables may vary over many orders of magnitude (e.g. the composition profile in a batch distillation column), and several physical regimes (e.g. the phase changes in a solvent switch operation). Recent research on combined discrete/continuous simulation [7, 9] has led to the development of what is termed an *interpretative* simulator architecture. In contrast to the more conventional code generation approach, in which the model is automatically coded as a FORTRAN subroutine and then linked with numerical solvers, the interpretative approach creates an image of the process model as data structures in machine memory, and during a simulation these data structures are 'interpreted' to pass residuals, partial derivatives, etc., to numerical solvers. The interpretative approach is ideally suited to discrete manipulation of the mathematical model at any point during the combined discrete/continuous simulation [10], and reporting and diagnosis of problems or errors in the solution process [11].

A further advantage of the intepretative architecture is that the complete functional form of the model is available in explicit symbolic form for analysis and/or manipulation throughout the entire simulation. This symbolic information has the potential to be extremely useful in addressing the issue of robustness discussed above. In addition, it prompts an investigation of hybrid symbolic and numerical strategies for more robust and efficient solution of simulation and optimization problems. This paper reports on the progress and results of our preliminary investigations. The current implementation of the interpretative architecture in ABACUSS serves as the platform for our efforts.

The next three sections of the paper identify areas in which the robustness and efficiency of existing numerical techniques can be improved. Section 2 demonstrates shortcomings of current numerical integration techniques for the solution DAEs and identifies improvements. Section 3 demonstrates the potential for exploiting the interpretative architecture for the efficient solution dynamic optimization problems. Finally, section 4 investigates a new method for the solution of large scale highly nonlinear optimization problems.

2 ROBUST NUMERICAL INTEGRATION OF DIFFERENTIAL-ALGEBRAIC SYSTEMS

As noted above, models of batch processes typically give rise to systems of differential-algebraic

equations (DAEs):

$$\begin{aligned} \mathbf{f}(\dot{\mathbf{x}}, \mathbf{x}, \mathbf{u}, t) &= \mathbf{0} \\ \mathbf{u} &= \mathbf{u}(t) \end{aligned} \tag{1}$$

where $\mathbf{x}, \dot{\mathbf{x}} \in \mathbf{R}^n$, $\mathbf{u} \in \mathbf{R}^l$ and $\mathbf{f} : \mathbf{R}^n \times \mathbf{R}^n \times \mathbf{R}^l \times \mathbf{R} \rightarrow \mathbf{R}^n$. Standard BDF codes for numerical integration of DAEs provide certain guarantees on the accuracy of the numerical approximation. Results from the application of ABACUSS as part of a batch process development strategy, particularly the batch distillation of certain wide-boiling mixtures, indicate that under certain situations these guarantees break down. This section demonstrates the new result that a breakdown of the error control mechanism can stem from an ill-conditioned corrector iteration matrix. Bounds are derived that define the conditions under which the accuracy can be guaranteed, and scaling techniques are investigated to mitigate the problem. ABACUSS is currently interfaced to the DASOLV [12] implementation for sparse unstructured systems. Comparisons of DASOLV are made with the widely used dense implementation DASSL [13]

Accuracy is maintained by adapting the step size to control the local truncation error (DASSL also controls the interpolation error, using the more restrictive criteria to determine the allowable step size.) The local truncation error is defined as follows for both DASOLV and DASSL [13]:

$$\text{error} = M \cdot \left\| \mathbf{x}^C - \mathbf{x}^P \right\| \leq 1.0 \tag{2}$$

where $\mathbf{x}^C$ is the corrected solution and $\mathbf{x}^P$ is the predicted solution. In DASOLV M is defined as the inverse of the step size (h); M varies with the order of the method and the step size in DASSL, but for a first order method when $h_{n+1} \ll h_n$, M approaches $\frac{h_{n+1}}{h_{n+1}+h_n}$. Note that in both cases the truncation error scales with the integration step size, and the user requested tolerances are buried in the definition of norm used in (2).

The DASOLV implementation allows the step size to be reduced up to eight times before declaring that the step is too small. This permits large differences between the predicted and corrected values of certain variables to be accepted when the step size becomes small.[1] For example, Figure 1 shows the trajectory of the condenser duty for a batch distillation simulation performed with ABACUSS. The model has no discontinuities, and the observed 'spikes' are the result of successful integration steps with a very small step size. Effectively, the error control mechanism has broken down but solution has continued. On the other hand, the DASSL implementation defines a minimum allowable step size. This criterion is more likely to cause the equally undesirable premature termination of the simulation (a familiar phenomenon to experienced users of these codes).

The fact that DASOLV continues integration has enabled elucidation of the source of the problem: an ill-conditioned corrector iteration matrix. The corrector employs a modified Newton method, terminating iterations based on the size of the update vector $\Delta\mathbf{x}$ calculated in exact arithmetic.

$$\|\Delta\mathbf{x}\| \leq \tau \tag{3}$$

Assuming that the predictor provides an initial guess within the region of convergence of Newton's method and that the operations are performed using exact arithmetic, the superlinear convergence of Newton's method [14] bounds the distance from the current iterate $\mathbf{x}_k$ to the solution $\mathbf{x}^*$ using the Newton update $\Delta\mathbf{x}$ and the convergence rate β_k as follows:

$$\|\mathbf{x}_{k+1} - \mathbf{x}^*\| \leq \frac{\beta_k}{1-\beta_k} \|\Delta\mathbf{x}_k\| \leq \tau \frac{\beta_k}{1-\beta_k} \tag{4}$$

[1]The norm employed in DASOLV, a weighted root mean square norm, is scaled by the system size, so it is less restrictive than a weighted infinity norm.

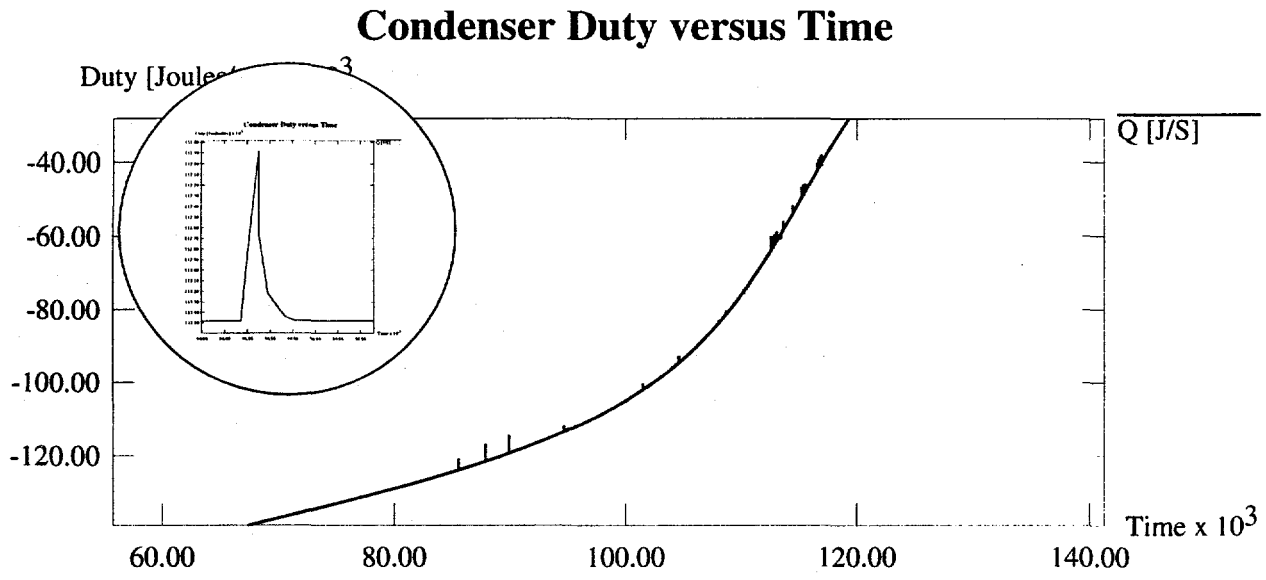

Figure 1: Plot of condenser duty resulting from ABACUSS simulation.

Unfortunately, the criterion defined in (3) cannot be applied directly because the only information available is the size of the Newton update $\overline{\Delta \mathbf{x}}$ calculated using floating point arithmetic. However, as long as the current iterate is within the region of convergence, we need only demonstrate that (3) is satisfied to attain the desired accuracy. The following linear error analysis uses $\overline{\Delta \mathbf{x}}$ and the condition number of the iteration matrix ($\kappa(\mathbf{J})$) to derive conditions under which (3) must hold.

The criterion of (3) dictates that $\Delta \mathbf{x}$ must lie in a closed neighborhood of the origin of radius τ, defined by $N_\tau(0)$. Although the exact location of $\Delta \mathbf{x}$ is not known, $\Delta \mathbf{x}$ must lie within a closed neighborhood of radius $r \geq \|\delta \boldsymbol{x}\|$ of the numerically calculated update $\overline{\Delta \mathbf{x}}$. Thus, (3) will hold as long as $N_r(\overline{\Delta \mathbf{x}}) \subset N_\tau(0)$. Linear error analysis is used to prove the following: If there exists a $\overline{\Delta \mathbf{x}}$ such that (5) and (6) are satisfied, then $N_r(\overline{\Delta \mathbf{x}}) \subset N_\tau(0)$.

$$\left\|\overline{\Delta \mathbf{x}}\right\| \leq \frac{\tau}{1+\kappa(\mathbf{J})\frac{\|\delta \boldsymbol{J}\|}{\|\mathbf{J}\|}} \tag{5}$$

$$\left\|\overline{\Delta \mathbf{x}}\right\| \leq \tau(1-\kappa(\mathbf{J})\frac{\|\delta \boldsymbol{f}\|}{\|\mathbf{f}\|}) \tag{6}$$

Linear perturbation analysis provides the following bounds.

$$\frac{\|\delta \boldsymbol{x}\|}{\|\Delta \mathbf{x}+\delta \boldsymbol{x}\|} \leq \kappa(\mathbf{J})\frac{\|\delta \boldsymbol{J}\|}{\|\mathbf{J}\|} \tag{7}$$

$$\frac{\|\delta \boldsymbol{x}\|}{\|\Delta \mathbf{x}\|} \leq \kappa(\mathbf{J})\frac{\|\delta \boldsymbol{f}\|}{\|\mathbf{f}\|} \tag{8}$$

Combining (5) and (7) using the triangle inequality produces (9) which shows that $\|\Delta \mathbf{x}\| \leq \tau$.

$$\tau \geq \left\|\overline{\Delta \mathbf{x}}\right\|(1+\kappa(\mathbf{J})\frac{\|\delta \boldsymbol{J}\|}{\|\mathbf{J}\|}) \geq \left\|\overline{\Delta \mathbf{x}}\right\| + \|\delta \boldsymbol{x}\| \geq \|\Delta \mathbf{x}\| \tag{9}$$

Given that $\|\Delta \mathbf{x}\| \leq \tau$, (8) provides an upper bound for $\|\delta \boldsymbol{x}\|$.

$$\|\delta \boldsymbol{x}\| \leq \kappa(\mathbf{J})\,\|\Delta \mathbf{x}\|\,\frac{\|\delta \boldsymbol{f}\|}{\|\mathbf{f}\|} \leq \kappa(\mathbf{J})\frac{\|\delta \boldsymbol{f}\|}{\|\mathbf{f}\|}\tau \;=\; r \tag{10}$$

(6) shows that $\left\|\overline{\Delta \mathbf{x}}\right\| + r$ is bounded from above by τ, which implies that $\|\delta \boldsymbol{x}\| \leq \tau$ by applying the triangle inequality. Thus, $N_r(\overline{\Delta \mathbf{x}}) \subset N_\tau(0)$, an (3) must hold.

In the best case, the only error in the calculation process comes from storing the original data, so the error in the data is bounded by the machine unit roundoff ϵ. In this case, $\|\delta \boldsymbol{f}\| \leq \epsilon \|\mathbf{f}\|$ and $\|\delta \boldsymbol{J}\| \leq \epsilon \|\mathbf{J}\|$. Thus, (6) reduces to (11).

$$\left\|\overline{\Delta \mathbf{x}}\right\| \leq \tau(1 - \kappa(J)\epsilon) \tag{11}$$

If the condition number is high, then we admit the possibility that the accuracy cannot be maintained. The condition number of the iteration matrices from the previously mentioned batch distillation experiments, show that it is impossible to find a $\overline{\Delta \mathbf{x}}$ to satisfy (11).

To obtain solutions to such numerical experiments, the condition number of the iteration matrix must be reduced, or the simulation must be performed in higher precision. Scaling the variables and the equations of the model offers the opportunity to improve the conditioning of the matrix. An ad hoc application of variable and equation scaling on the distillation model has shown significant improvement in the conditioning of the iteration matrix. Therefore, automated scaling techniques are currently being implemented within ABACUSS. Variables are adaptively scaled throughout the simulation, since a given variable may change over orders of magnitude during the simulation of a batch operation. The equations will be scaled based on their functional form.

3 HIGH-INDEX FORMULATIONS FOR DYNAMIC OPTIMIZATION

A subproblem of batch process development is the design of optimal operating policies for individual processing tasks [5]. For example, system level targets may require the selectivity from a reaction task to be maximized, and this can be achieved by searching for the optimal time profiles for reactant feed rate and reactor temperature. This subproblem can in principle be posed as a dynamic optimization problem. However, adequate models are relatively large and must reflect nonideal phase behavior, complex reaction kinetics, and discontinuous physical behavior. Further, formulations must accurately reflect equipment constraints such as design pressures, which typically translate into path inequality and equality constraints. The combination of these issues poses severe problems for current dynamic optimization algorithms [15, 16]. This section introduces a combined symbolic and numerical strategy that has the potential to solve large scale dynamic optimization problems with general path constraints in an efficient manner.

The *index* of a differential-algebraic system is defined as the smallest integer I such that the system formed from equations 1 and their first I time derivatives define $\dot{\mathbf{x}}(t)$ as locally unique functions of $\mathbf{x}(t)$ and t [13]. According to this definition, a system of ODEs is index-0. The term *high-index* is usually used to refer to systems with index ≥ 2. High-index DAEs can occur for two reasons. On the one hand, equations 1 may be inherently high index due to engineering assumptions made in the derivation of the model. On the other hand, the index of the system may be raised by the choice of which subset of model variables are specified as explicit functions of time $\mathbf{u}$ in order to satisfy the degrees of freedom (DOF). This latter property is of interest here. Note that in this context, even a system of ODEs may be made high index by specifying an output trajectory rather than an input trajectory.

In dynamic optimization, the functions $\mathbf{u}(t)$ are the decisions. If path equality constraints involving $\mathbf{x}$ are appended to equations 1, this reduces the DOF and raises the index. Path inequality constraints can be treated in a similar manner by introducing slack variables. In this case, the index is raised locally while the inequality is active. Hence, any solution method must adapt to changes in the index as the trajectory is traced.

The control parameterization approach to the solution of dynamic optimization problems [16] relies on a decomposition in which an augmented DAE system is repeatedly integrated to evaluate the objective function and gradients for a master NLP, which has as its decision variables the parameters of the basis functions chosen to approximate $\mathbf{u}(t)$. Current approaches [16] avoid the difficulties associated with integration of high-index systems [17] by removing path constraints from the DAE system, and lumping their violation over the entire time interval into terms in the master NLP. This infeasible path approach is less than satisfactory because the master NLP is provided with little information concerning the path constraints, and this leads to an excessive number of expensive DAE integrations.

We are investigating a feasible path control parameterization approach that includes all path constraints explicitly in the DAE subproblems. This should lead to a dramatic reduction in the number of DAE integrations required to solve path constrained problems. This work is predicated on the ability to solve high index systems reliably. Mattsson and Soderlind [18] have presented an algorithm in which the over-determined system of index-1 DAEs that can be derived from a high index system by differentiation is made fully-determined by the symbolic substitution of time derivative variables by 'dummy' algebraic variables. However, there are no reports on the application of this algorithm to anything other than small problems due to numerical issues associated with a large-scale implementation (dummy pivoting). We are currently resolving these issues and implementing the algorithm in ABACUSS.

Mattsson and Soderlind's approach uses Pantelides' [19] structural algorithm to identify which equations to differentiate in order to derive the index-1 system, and symbolic differentiation can perform the necessary differentiations. We have successfully implemented these two steps in ABACUSS and are currently using this feature for consistent initialization of large scale high-index DAE systems.

We have also demonstrated that certain classes of dynamic optimization problems can be solved extremely efficiently by deliberately making them high-index. In this case, the problem reduces to a NLP in terms of the model variables at a finite number of points. This is similar to the collocation approach [15] but gives rise to NLPs that are dramatically smaller.

4 ROBUST OPTIMIZATION OF LARGE SCALE HIGHLY NONLINEAR PROBLEMS

Many problems in process development and design give rise to large, highly nonlinear mathematical programming problems. Consider the following nonlinear program (NLP):

$$\min_{\mathbf{x}} f(\mathbf{x}) \tag{12}$$

$$\text{s.t. } \mathbf{h}(\mathbf{x}) = \mathbf{0} \tag{13}$$

$$\mathbf{g}(\mathbf{x}) \geq \mathbf{0} \tag{14}$$

The first-order necessary conditions for optimality are the well known Karush-Kuhn-Tucker (KKT) conditions, which are a mixture of nonlinear equations and inequalities. It is shown by Mangasarian that the complementary slackness condition in the KKT conditions can be reformulated as an equivalent set of nonlinear equations [20]. After applying Mangasarian's theorem, the KKT conditions become:

$$\nabla f(\mathbf{x}) - \nabla \mathbf{h}(\mathbf{x})^T \mathbf{v} - \nabla \mathbf{g}(\mathbf{x})^T \mathbf{u} = \mathbf{0} \tag{15}$$

$$\mathbf{h}(\mathbf{x}) = \mathbf{0} \tag{16}$$

$$M(|g_i(\mathbf{x}) - u_i|) - M(g_i(\mathbf{x})) - M(u_i) = 0 \quad \forall i \tag{17}$$

where $M : R \longrightarrow R$ is a strictly increasing function with $M(0) = 0$. This set of equations will be solved using the globally convergent homotopy continuation method. A similar approach has been proposed by Brengel and Seider [21] in an attempt to coordinate design and control optimization and by Sun and Seider [22] in Gibbs free energy minimizations. The ability to dervive equations (15–17) automatically by symbolic differentiation and manipulation in an equation-oriented simulation environment plays a pivotal role in this approach for solving large-scale NLPs. In addition, symbolic manipulation techniques are being investigated to improve the performance of the homotopy continuation method itself.

Homotopy continuation has been used in the past to solve systems of equations when a good starting point is not known or when the equations contain many singularities. Suppose $\mathbf{F}(\mathbf{x}) = 0$ is a set of equations we are interested in solving. One popular homotopy is the convex linear homotopy given by:

$$\mathbf{H}(\mathbf{x}, \lambda) = \lambda \mathbf{F}(\mathbf{x}) + (1 - \lambda)\mathbf{G}(\mathbf{x}) \tag{18}$$

where λ is the homotopy parameter and $\mathbf{G}(\mathbf{x})$ is set of equations which has a known solution $\mathbf{x}^0$. The idea behind homotopy continuation is to begin at $\lambda = 0$ and $\mathbf{x} = \mathbf{x}^0$, where $\mathbf{H}(\mathbf{x}^0, 0) = 0$, and track the homotopy path given by $\mathbf{H}(x, \lambda) = 0$ to $\lambda = 1$ and $\mathbf{x} = \mathbf{x}^*$, a solution of $\mathbf{F}(\mathbf{x}) = 0$.

One particular homotopy is the Newton homotopy where $\mathbf{G}(\mathbf{x}) = \mathbf{F}(\mathbf{x}) - \mathbf{F}(\mathbf{x}^0)$. The homotopy map is given by:

$$\mathbf{H}(\mathbf{x}, \lambda) = \mathbf{F}(\mathbf{x}) - (1 - \lambda)\mathbf{F}(\mathbf{x}^0) \tag{19}$$

Parameterizing $\mathbf{x}$ and λ with respect to the arclength of the homotopy path, and differentiating, we obtain:

$$\nabla \mathbf{F}(\mathbf{x}) \frac{d\mathbf{x}}{ds} + \mathbf{F}(\mathbf{x}^0) \frac{d\lambda}{ds} = 0 \tag{20}$$

Combining this equation with equation (19) and rearranging, we obtain:

$$\frac{d\mathbf{x}}{ds} = \frac{d\lambda/ds}{1 - \lambda} \nabla \mathbf{F}(\mathbf{x})^{-1} \mathbf{F}(\mathbf{x}) \tag{21}$$

Now consider the global Newton method. The global Newton method can be interpreted as the integration of the autonomous ODE system:

$$\frac{d\mathbf{x}}{dt} = -\nabla \mathbf{F}(\mathbf{x})^{-1} \mathbf{F}(\mathbf{x}) \tag{22}$$

A damped Newton method, given by the iteration formula

$$\mathbf{x}^{k+1} = \mathbf{x}^k - \alpha^k \nabla \mathbf{F}(\mathbf{x}^k)^{-1} \mathbf{F}(\mathbf{x}^k) \tag{23}$$

can be obtained by a first-order explicit integration of equation (22) with a stepsize, α^k, selected such that $\left\|\mathbf{F}(\mathbf{x}^{k+1})\right\| \leq \left\|\mathbf{F}(\mathbf{x}^k)\right\|$. Now consider the successive quadratic programming (SQP) algorithm for nonlinear optimization. SQP converges to an optimum by obtaining search directions from the solution of a quadratic program (QP) subproblem formed by taking quadratic approximations of the objective function and linear approximations of the constraints. The current point is updated by moving in the direction obtained in the QP a stepsize determined by minimizing some merit function. It can be shown that the directions obtained in the QP subproblem are the same as the directions obtained by applying Newton's method to the KKT conditions of the NLP, considering only the active constraints (i.e. inequality constraints equal to zero). Thus, SQP can be interpreted

as applying a damped Newton method to the KKT conditions. In the homotopy continuation approach for solving NLPs, the KKT conditions are solved using homotopy continuation. The relationship between homotopy continuation and the damped Newton method indicates that SQP and the homotopy continuation approach for solving NLPs are quite similar.

Although these two approaches are similar, using homotopy continuation has the following advantages. First, homotopy continuation can locate solutions where other methods fail due to both lack of a good initial guess and the presence of singularities. Homotopy continuation is globally convergent with probability 1 [23] and, unlike the related global Newton method, remains stable near singular points [24]. Second, under reasonable assumptions, the homotopy path given by (18) is a connected one-dimensional submanifold. This feature makes it possible to track out several solutions using homotopy continuation. Being able to track out multiple (possibly all) KKT points is, in many cases, better than obtaining a single global minimum (for example, the global minimum is useless if it is not possible to control the plant when operating at that point). Finally, deriving equations (15–17) does not change the sparsity of the original problem. Therefore, this approach should be able to handle large NLPs with many degrees of freedom. These properties suggest this approach has the potential to be effective in solving large-scale, non-convex NLPs with highly nonlinear constraints and many degrees of freedom, where the performance of SQP is seriously degraded.

Acknowledgments — This work was supported by the United States Department of Energy under grant DE-FG02-85ER13331.

References

[1] L. B. Evans, "Steady-state simulation: A state-of-the-art review," in *The Fifth International Symposium on Process Systems Engineering*, (Kyongju, Korea), pp. 953–967, July 1994.

[2] AspenTech, *SpeedUp User Manual Release 5.4*. Aspen Technology UK Ltd., 1993.

[3] A. W. Westerberg, K. Abbot, and B. Allan, "Plans for ASCEND IV: Our next generation equation-based modelling environment," in *AspenWorld 1994*, (Boston, Massachusetts), November 6–9 1994.

[4] H. W. Ray, "Dynamic modelling of polymerization process flowsheets using POLYRED," in *1st Industrial Chemical Engineering Technology Topical Conference, AIChE Annual Meeting*, (St. Louis, USA), November 7–12 1993.

[5] R. J. Allgor, M. D. Barrera, P. I. Barton, and L. B. Evans, "Optimal batch process development," in *The Fifth International Symposium on Process Systems Engineering*, (Kyongju, Korea), pp. 153–157, July 1994.

[6] C. C. Pantelides and P. I. Barton, "Equation-oriented dynamic simulation current status and future perspectives," *Computers Chem. Engng*, vol. 17, pp. S263–S285, 1993.

[7] P. I. Barton, *The Modelling and Simulation of Combined Discrete/Continuous Processes*. PhD thesis, University of London, 1992.

[8] P. I. Barton, "Batch process simulation: Why and how," in *AspenWorld 1994*, (Boston, Massachusetts), November 6–9 1994.

[9] P. I. Barton and C. C. Pantelides, "gPROMS – a combined discrete/continuous modelling environment for chemical processing systems," *Simulation Series*, vol. 25, no. 3, pp. 25–34, 1993.

[10] P. I. Barton and C. C. Pantelides, "The modelling of combined discrete/continuous processes," *AIChE Journal*, vol. 40, no. 6, pp. 966–979, 1994.

[11] P. C. Piela, *ASCEND An Object-Oriented Computer Environment for Modeling and Analysis.* PhD thesis, Carnegie-Mellon University, 1989.

[12] R. B. Jarvis and C. C. Pantelides, "DASOLV — a differential algebraic equation solver," tech. rep., Centre for Process Systems Engineering, Imperial College, London, March 1992.

[13] K. E. Brenan, S. L. Campbell, and L. R. Petzold, *Numerical Solution of Initial-Value Problems in Differential Algebraic Equations.* New York: Elsevier Science Publishing Co., Inc., 1989.

[14] J. J. Moré and D. C. Sorensen, "Newton's method," in *Studies in Numerical Analysis* (G. H. Golub, ed.), pp. 29–83, ??, 1984.

[15] J. E. Cuthrell and L. T. Biegler, "On the optimization of differential-algebraic process systems," *AIChE J.*, vol. 33, pp. 1257–1270, 1987.

[16] V. S. Vassiliadis, *Computational Solution of Dynamic Optimization Problems with General Differential-Algebraic Constraints.* PhD thesis, University of London, 1993.

[17] L. R. Petzold, "Differential/algebraix equations are not ODEs," *SIAM J. Sci. and Stat. Comp.*, vol. 3, pp. 367–384, 1982.

[18] S. E. Mattsson and G. Soderlind, "Index reductiion in differential-algebraic equations using dummy derivatives," *SIAM J. Sci. and Stat. Comp.*, vol. 14, pp. 677–692, 1992.

[19] C. C. Pantelides, "The consistent initialization of differential-algebraic systems," *SIAM J. Sci. and Stat. Comp.*, vol. 9, pp. 213–231, 1988.

[20] O. L. Mangasarian, "Equivalence of the complementarity problem to a system of nonlinear equations," *SIAM J. Appl. Math*, vol. 31, p. 89, 1976.

[21] D. D. Brengel and W. D. Seider, "Coordinated design and control optimization of nonlinear processes," *Computers and Chemical Engineering*, vol. 16, pp. 861–886, 1992.

[22] A. C. Sun and W. D. Seider, "Mapped homotopy continuation algorithm for global optimization," in *Recent Advances in Global Optimization*, 1991.

[23] L. T. Watson, "Hompack: A suite of codes for globally convergent homotopy algorithms," *ACM Transactions on Mathematical Software*, vol. 13, pp. 281–310, 1987.

[24] E. L. Allgower and K. Georg, *Numerical Continuation Methods.* New York: Springer-Verlag, 1990.

INTELLIGENT CONTROL OF MIXED-CULTURE BIOPROCESSES

D. L. Stoner, E. D. Larsen, K. S. Miller, G. F. Andrews, and J. A. Johnson

Idaho National Engineering Laboratory
Lockheed Idaho Technologies Company, Inc.
P. O. Box 1625, Idaho Falls, ID 83415-2203

ABSTRACT

A hierarchical control system is being developed and applied to a mixed culture bioprocess in a continuous stirred tank reactor. A bioreactor, with its inherent complexity and non-linear behavior was an interesting, yet, difficult application for control theory. The bottom level of the hierarchy was implemented as a number of integrated set point controls and data acquisition modules. Within the second level was a diagnostic system that used expert knowledge to determine the operational status of the sensors, actuators, and control modules. A diagnostic program was successfully implemented for the detection of stirrer malfunctions, and to monitor liquid delivery rates and recalibrate the pumps when deviations from desired flow rates occurred. The highest control level was a supervisory shell that was developed using expert knowledge and the history of the reactor operation to determine the set points required to meet a set of production criteria. At this stage the supervisory shell analyzed the data to determine the state of the system. In future implementations, this shell will determine the set points required to optimize a cost function using expert knowledge and adaptive learning techniques.

INTRODUCTION

Bioprocesses which utilize axenic cultures and sterile feeds predominate in the food, pharmaceutical and specialty chemical industries. However, large scale bioprocessing for the mining industry or waste water treatment utilize mixed populations of microorganisms for two main reasons. First, and most important, is that mixed populations of indigenous microorganisms are more effective and can ever improve the performance through natural selection. Not only do these naturally occurring microorganisms behave as consortia, bacteria which have been added to enhance

activity may not be maintained within the indigenous microbial population. Difficulties and the expense involved with the sterilization of feed stocks required for large scale processing is a second reason that large scale processes must accommodate the presence of mixed microbial populations.

Control of any biologically-based process is complicated by the fact that microbial activity can not be directly manipulated. Microbial activity can be indirectly influenced through the manipulation of the physical and chemical environment. Furthermore, while the microorganisms are controlled by their environment, the microbial culture's environment is being changed by the metabolic activities of the microorganisms. Mixed culture bioprocesses further compound control issues by the additional requirement that the process must be regulated in such a manner as to maintain the desired activities of all consortium members that are necessary for the process. Another important consideration is that the main process variable, the microbial activity, can not be measured on-line in a commercially reliable fashion.

An intelligent control system for mixed culture bioprocesses using acidophilic microorganisms is of increasing importance to the mining industry. The long-term objective is a control strategy that will optimize economics of bioprocess. To this end, a hierarchical control system is being developed and applied to a nonlinear, unstable, mixed culture bioprocess in a continuous stirred tank reactor (CSTR).[1] At the bottom of the hierarchy was a number of integrated set point controls and data acquisition modules. The next level was a diagnostic system that used expert knowledge to determine the operational status of the various sensors, actuators, and control modules. The top level was a supervisory shell that is currently under development. This stage was capable of identifying the bioreactor state by reading information from the low level sensors, control systems, and the diagnostic system. In its envisioned, full, implementation, the supervisory shell will control the operation of the reactor by using expert knowledge and the history of the reactor operation to determine the set points required to meet a set of production criteria. In this paper, we describe the microorganism, the integration of the diagnostic system and the results obtained to date as they will be implemented into the top level supervisory shell.

SYSTEM DESCRIPTION

Microbial Culture

The mixed culture bioprocess used as the model system for this program is one that would be utilized for the microbial desulfurization of coal. *Thiobacillus ferrooxidans*, the causative agent of acid mine drainage, is a valuable microorganism for the bacterial leaching of sulfide mineral ores and the oxidation of pyritic sulfur in coal. *T. ferrooxidans* is a microorganism that inhabits acidic environments, utilizes CO_2 as a carbon source and Fe^{2+} as the energy source. In our test system, this microorganism was defined as the biocatalyst with CO_2 and Fe^{2+} as substrates. Fe^{3+} and metabolic products were the product and byproduct, respectively. In natural environments, acidophilic heterotrophic microorganisms enhance the desulfurization activity of *T. ferrooxidans* by scavenging the metabolites and other inhibitory organic compounds. Thus, in later stages of the program, an acidophilic heterotrophic microorganism will be added that will utilize, as its growth and energy source, the metabolic products excreted by *T. ferrooxidans*.

T. ferrooxidans (ATCC 23270) was cultivated at 30°C using a modification of the basal salts medium of Johnson et al.[2] The medium (pH 1.8), contained per liter $(NH_4)_2SO_4$, 1.25 g; $MgSO_4 \cdot 7H_2O$, 0.50 g; K_2HPO_4, 0.25 g; trace elements solution, 1 mL and 50 mM $FeSO_4$.

Hardware

The bioreactor was a 2 liter continuous culture system (Multigen F-2000, New Brunswick Scientific Co., Inc.) that was modified to receive external control signals for stirrer speed and heating. A stainless steel lid was constructed and fitted with 4 liquid inlet ports; sampling port; thermocouple; heating probe; sensors for oxygen, pH and redox (Ingold Electrodes, Inc., Wilmington, MA); air exhaust through a demister/condensation column; and an impeller and aeration assembly. Air and CO_2 were humidified by sparging through sterile water. Five peristaltic pumps (Masterflex 7520-35; Cole-Parmer Instrument Co., Niles, IL) were used feed water, basal salts, iron solution, acid and base into the bioreactor. Passive over flow was used to maintain the working volume of the reactor. Each of the three main pumps, i.e., water, nutrients and iron, had a fuzzy logic control loop to maintain the desired flow rates.

A Macintosh IIx computer equipped with a NB-MIO-16HX multifunction Input/Output board and two NB-AO6 analog output boards (National Instruments, Austin TX). These boards provided a total capacity of 16 analog input, 14 analog output, and 32 digital I/O lines for the bioreactor system. The I/O lines were isolated and conditioned with 5B series back plane and isolation modules. Additionally, the Macintosh was equipped with a 4 port serial board. Combined with the computer's 2 ports, this provided six RS-422 serial lines. The RS-422 ports were wired with custom made cables that made them compatible with the RS-232 instruments used in the system. The pump subsystem of the bioreactor used 1 analog input, 5 analog outputs, and 4 serial lines. The computer and all of the instruments in the system were protected with a Fortress uninterruptable power supply (Best Power Technology, Inc., Nedcedah, WI). Computer programming, data acquisition and analysis was done using LabVIEW graphical programming language (National Instruments Corporation, Austin, TX). LabVIEW provided a convenient operator interface, as well as a sophisticated language interface to the I/O boards for data acquisition and control.

Analytical Methods

Off-line titration of Fe^{2+} species with potassium dichromate[3] was used to determine the concentration of Fe (II). The concentration of Fe^{3+} in solution was determined offline by absorption at 304 nm.[4] On line measures for total organic carbon (TOC) were obtained by difference of total carbon and inorganic carbon using a total organic carbon analyzer (Model TOC-5000, Shimadzu Corporation, Columbia, MD). Dissolved organic carbon determinations were obtained by off-line measures of a filtered (0.2 μm, Whatman Puradisc, polypropylene filter, Clifton, NJ) reactor fluid. Cell counts were made by staining cells filtered onto black polycarbonate membrane filters (0.2 μm, Poretics, Livermore, CA) with acridine orange (0.01% final concentration in water adjusted to a pH of 11 with NaOH). Prior to staining cells were washed with water adjusted to pH 1 with sulfuric acid then with water adjusted to pH 11 with NaOH. After staining cells were washed with deionized water and counted using an epifluorescence microscope.

Low-Level Sensing and Control System

On-line sensors were used to determine the pH, temperature, dissolved oxygen, redox potential, and air and carbon dioxide flow rates (Figure 1). In addition a carbon analyzer was used on line to

determine total organic carbon, dissolved organic carbon, and dissolved carbon dioxide. The difference between the TOC and DOC was used a measure of biomass. Off-line measurements included cell counts and $[Fe^{+2}]$ and $[Fe^{+3}]$ as described below. Fuzzy PID[5] controllers were implemented to control the pH and temperature of the reactor. The pH was controlled by activating one of two pumps to add acid or base as necessary and the temperature maintained at the desired set point above the ambient room temperature by turning on or off a heater. The flow of air and carbon dioxide was controlled by mass flow controllers. Substrate feed concentrations were controlled by setting the flow rates of two pumps that transferred basal salts and iron solution from reservoirs into the reactor and the dilution rate controlled by adding water through a third pump. The reservoirs were placed on scales and the pumps recalibrated every 24 hours using the scale measurements. In addition, the effluent mass was measured as a check on the dilution rate. The system accounted for the addition of acid or base for pH control when determining the water flow such that the dilution rate remains constant.

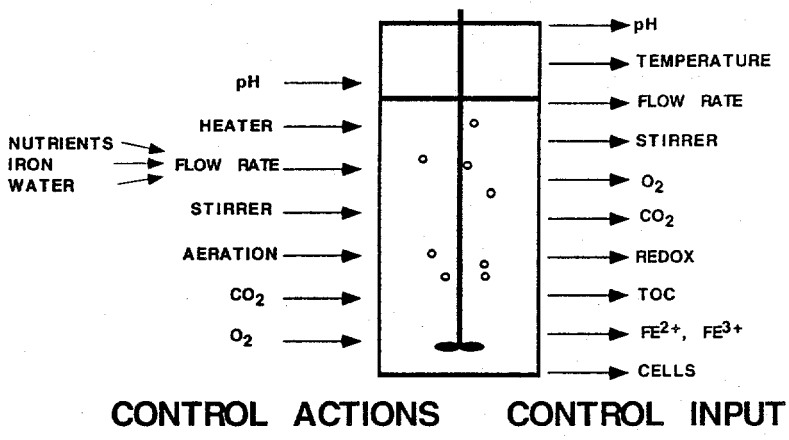

Figure 1. Schematic of reactor with control actions and control input variables obtained by on-line sensors and off-line analyses.

Diagnostic System

At the next level of control, a diagnostic system used expert knowledge to determine the operational status of the various sensors, actuators, and control modules. Sensed and controlled parameters were examined to be sure that the measured values were within the tolerance of the control system and, if not, the data was analyzed to determine the specific cause of the problem. Other problems were diagnosed indirectly from combinations of sensor data. For example, the increase in Redox and decrease in oxygen at 20 hours in Figure 2 was interpreted as a stopped stirrer by the diagnostics program. The importance of detection and diagnosis of instrument failures increases as run time increases. We have observed increased equipment malfunctions near the later stages of our extended bioreactor operations.

Supervisory Shell

The top level was a supervisory shell that is currently under development. At its current stage of development, the supervisory shell was capable of identifying the state of the bioreactor by reading information from the low level sensors and control systems and from the diagnostic system. In its envisioned implementation, the supervisory shell will be able to control the operation of the reactor by using expert knowledge and the history of the reactor operation to determine the set points required to meet a set of production criteria. This supervisor will observe the operation and make decisions to change the set points, adapting to the current status of the reactor and its inhabitants.

In this study, the supervisory shell monitored the acquired data to determine whether the bioreactor was in one of three operational states, 1) transition phase; 2) steady state or 3) washout. Transition phase is a transient state of the bioreactor that occurs when any operational parameter e.g., flow rates, substrate loading, or pH, has been changed. During the transition phase, as the reactor is approaching a new steady state, microbial activity is changing in response to the changes in the physical-chemical environment of the system. Steady state occurs when the microorganisms have achieved an approximate state of balanced growth in response to a steady environment. Once steady state has been achieved the human operator is prompted to modify operating parameters, i.e., flow rate if desired. While steady state can be defined in a variety of ways, our program defined steady state as a minimum of 5 reactor volumes, substrate (Fe^{2+}) and product (Fe^{3+}) concentrations that varied by less than 10% and biomass as determined by cell counts that varied by less than 25%. The latest installation of the program utilized TOC values that varied less than 10% instead of cell counts for the biomass measure. Washout condition is the operational state of the bioreactor in which the flow rate exceeds the maximum growth rate of the microorganisms and the cells are washed out of the reactor.

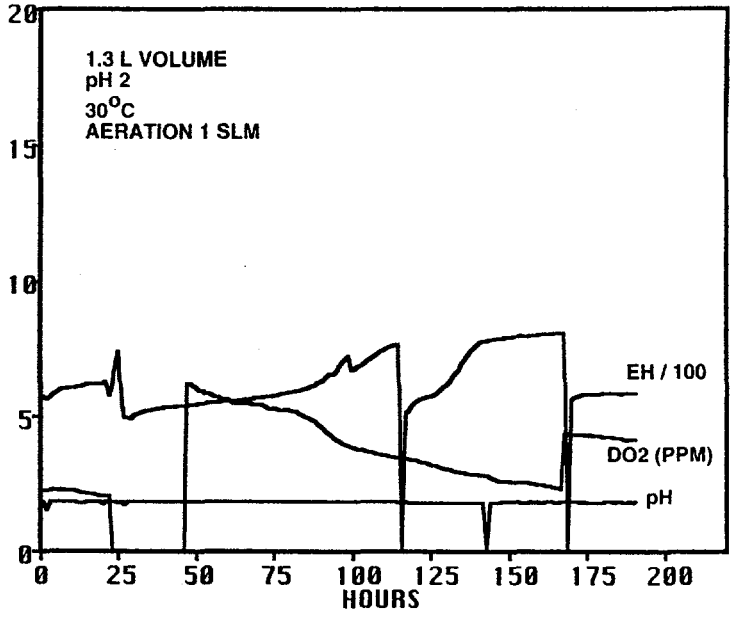

Figure 2. An example of the data set obtained by on-line Redox (mV), pH, and oxygen (ppm) determinations.

RESULTS AND DISCUSSION

We are developing and applying a hierarchical control system to a nonlinear mixed culture bioprocess in a CSTR. A CSTR bioreactor is inherently stable. However, we have introduced the dangers of instability by imposing an operating constraint that the volumetric productivity be a maximum. This requires that the bioreactor be operated near the washout point. To operate with an economic constraint also requires the minimum inputs of other nutrients. Data is reported here from a run of 47 days with a reactor volume of 1.3 L, air flow of 1 L/min, an iron feed concentration of 50 or 100 mM, and a range of dilution rates from $0.132\ hr^{-1} \leq D \leq 0.441\ hr^{-1}$ which corresponds to liquid delivery rates of 3 mls/min to 10 mls/min. The objectives were to test the lower-level control loops, to evaluate the ability of the diagnostic level to perform some simple tasks and to identify the limiting nutrient in order to start to construct rules by which the supervisory control system can move the system towards the optimal operating point.

Redox and oxygen probes were particularly subject to fouling problems, thus, were cleaned frequently. Differences in redox and oxygen values between fouled and cleaned probes was apparent from the data (Figure 2). Cell counts, and Fe^{2+} and Fe^{3+} concentrations were determined, at a

minimum, daily and entered into the data base (Figure 3). Excursions in TOC values occurred when the physical disturbance of the reactor resulted in the dislodging of solid material that had built up in dead zones in the reactor (Figure 3). While there was an increase in TOC during these excursions, there was little affect on the overall behavior of the reactor. In Figures 2 and 3, steady state was achieved at approximately 45 hours, and at 50 hours the flow rate was decreased from 10 mls/min to 6 mls/min. This corresponded to a decrease in dilution rate (D) from 0.441 hr^{-1} to 0.265 hr^{-1}. The decreased flow rate resulted in increased cell counts, and increased product (Fe^{3+}) concentration.

Redundant measures of process parameters will be used until the most effective and reliable means of assessing bioreactor performance are determined. While redox values provide an estimate the ratio of Fe(III) to Fe (II), they do not provide a measure of the concentration of the iron species. Total iron values obtained by the summation of values obtained for Fe (II) and Fe (III) by off-line quantitation agree with total iron concentrations obtained by atomic absorption spectroscopic methods (Data not shown). Fouling or coating of the redox probe and resulted in deviations from Redox potential of the bulk fluid. Graindorge et al.,[6] in relatively short bioreactor runs, utilized Redox measures as an estimate of biomass yield and biological activity. Because of errors introduced by fouling, Redox as a measure of microbial productivity could introduce error into our control decisions. Until a direct measure of microbial activity is developed in the context of this program, an indirect measure of activity will be biomass as measured by organic carbon measures and cell counting procedures. Initially, process monitoring and determination of steady state conditions was accomplished using cell counts as an estimate of microbial activity. With the addition of the total organic carbon (TOC) analyzer, on-line measures of organic carbon as an estimate of microbial growth and activity were used for the determination of steady state conditions.

The experimental plan that would determine the operational limits of the bioreactor was based on relationships for the kinetic behavior of a CSTR (Figure 4). Conventional treatment of kinetic data obtained from bioreactors assume that there is a single limiting nutrient in the liquid feed that, ultimately, controls the growth rate of the microorganisms. In our initial hypothesis, Fe^{2+} was the single limiting nutrient and that there would have been sufficient CO_2 introduced by aeration to support the growth of the microorganisms. The data from four steady-state conditions examined, plotted in Figure 5, show a pattern unlike that in Figure 4, indicating that microbial growth was not limited by Fe^{2+} or any other liquid-phase nutrient. Since dissolved oxygen was maintained at non-limiting values (4 -6 mg/L) throughout the experiment, the most likely hypothesis is that metabolism was limited by the availability of CO_2, the carbon source for the autotrophic *T. ferrooxidans*. Generally, on-line inorganic carbon values were less than 5

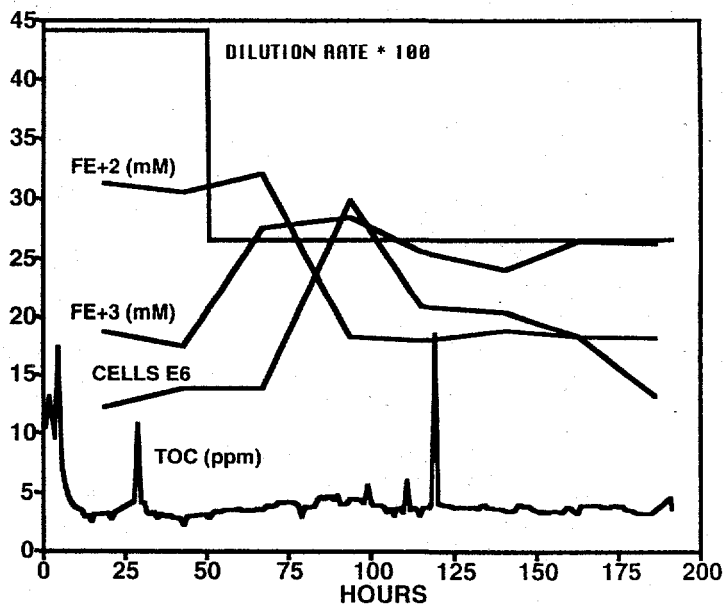

Figure 3. An example of the data set obtained for cell density (x E^6 cells/mL), Fe^{2+} concentration (mM), Fe^{3+} concentration (mM) and on-line total organic carbon determinations (ppm).

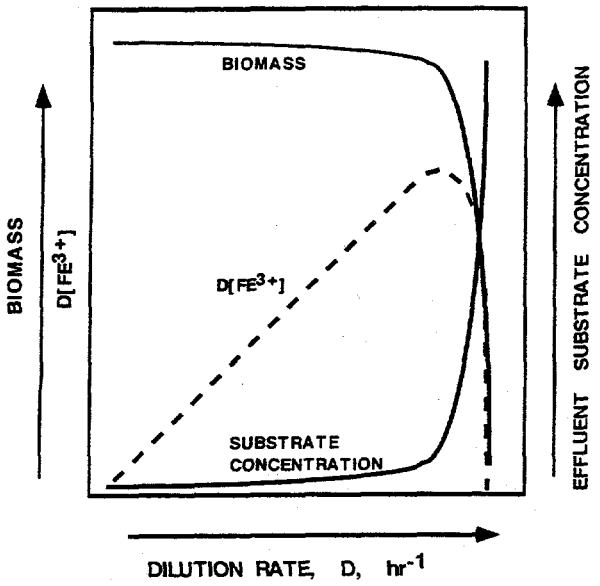

Figure 4. Expected relationships between dilution rate and cell yields, substrate concentration, or product concentration.

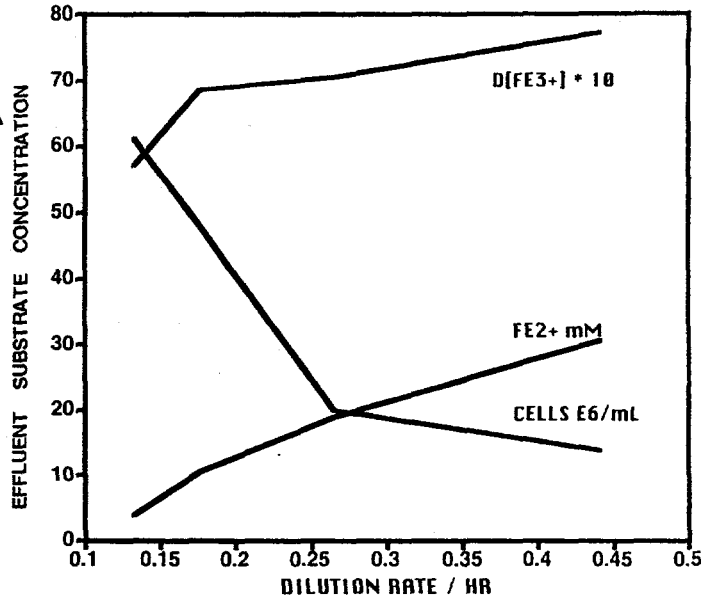

Figure 5. Experimentally determined relationships between dilution rate (Hr^{-1}), and effluent substrate concentration (mM), productivity (mM/Hr) and cell density (10^6 cells/mL).

ppb which suggested that the reactor was, indeed, operating under CO_2 limitation. Note that cell numbers did not rapidly approach zero as flow rate was increased (Figure 5). When the limiting nutrient must be transferred from the gas phase, cell washout did not occur was if would have if the limiting nutrient is dissolved in the liquid feed. Data obtained at steady state indicated that dilution rates greater than 0.176 (4 mL/min) resulted in marginal improvement in total Fe^{3+} yield (Figure 6). Maximum Fe^{3+} yield per unit biomass was observed for a dilution rate of 0.265 (6 mL/min). The observed CO_2 limitation at relatively low iron concentrations (~50 mM) has implications for the development of a control system that maximizes the iron oxidation rate. The feed must be enriched with CO_2 and controlled using on-line dissolved inorganic carbon measurements so as to maintain a reasonable non-limiting CO^2 concentration at reasonable cost.

SUMMARY

We have found that several lower-level control loops successfully performed control tasks such as pH and temperature control, accurate delivery of liquid feeds. Upper level control programs were successful in determining the operational state of the reactor and diagnosing equipment malfunctions. And working towards the goal of a supervisory control system, we have identified the limiting nutrient in order to start to construct rules by which this control system can move the system towards the optimal operating point. Problems such as analytical difficulties, equipment malfunctions and the complexity of the biological system which are typically encountered when running long term continuous processes must be accounted for and incorporated into any supervisory control program.

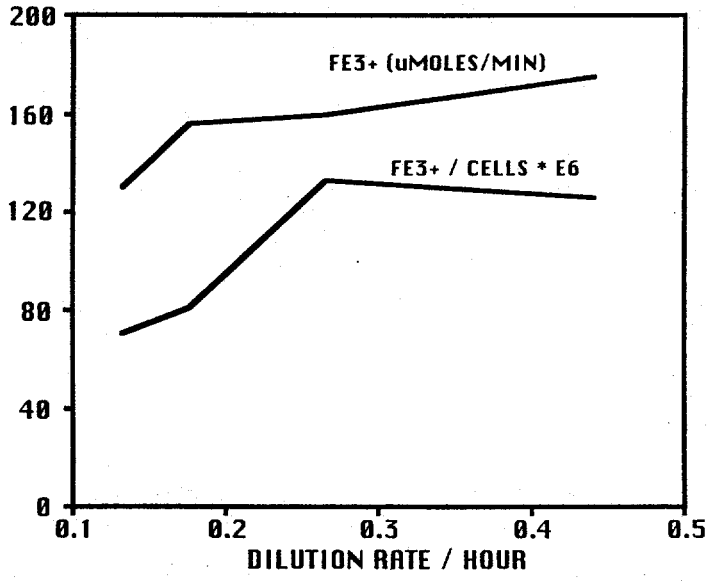

Figure 6. Relationship between total Fe^{3+} production (μmoles/min) and volumetric productivity (Fe^{3+}/cell numbers) and dilution rate.

ACKNOWLEDGMENTS

This work was supported by the U.S. Department of Energy, Office of Energy Research, Office of Basic Energy Sciences, under DOE Idaho Operations Office Contract No. DE-AC07-94ID13223.

REFERENCES

1. K. B. KONSTANTINOV and T. YOSHIDA, "Knowledge-Based Control of Fermentation Processes," *Biotechnol. Bioengineer.* 39, 479-486 (1992).

2. D. B. JOHNSON, J. H. M. MACVICAR, and S. WOLFE, "A New Solid Medium for the Isolation and Enumeration of *Thiobacillus Ferrooxidans* and Acidophilic Heterotrophic Bacteria," *J. Microbiol. Methods,* 7, 9-18 (1987).

3. D. A. SKOOG and D. M. WEST, *Fundamentals of Analytical Chemistry*, Holt, Rinehart and Winston, Inc., New York, 436-438 (1969).

4. M. STEINER and N. LAZAROFF, "Direct Method for Continuous Determination of Iron Oxidation by Autotrophic Bacteria," *Appl. Microbiol.*, 28, 872-880 (1974).

5. J. A. JOHNSON and H. B. SMARTT, "Advantages of an Alternative Form of Fuzzy Logic," *IEEE Transactions on Fuzzy Logic*, In Press, 1995.

6. P. GRAINDORGE, S. CHARBONNIER, J. P. MAGNIN, C. MAUVY, and A. CHERUY, A Software Sensor of Biological Activity Based on a Redox Probe for the Control of *Thiobacillus ferrooxidans* Cultures," *J. Biotechnol.* 35, 87-96 (1994).

Control of Complex Dynamics and Chaos in Distributed Parameter Systems

S. Chakravarti M. Marek* W. H. Ray†

Department of Chemical Engineering,
University of Wisconsin,
Madison, WI 53706

Abstract

This paper discusses a methodology for controlling complex dynamics and chaos in distributed parameter systems. The reaction-diffusion system with Brusselator kinetics, where the torus-doubling or quasi-periodic (two characteristic incommensurate frequencies) route to chaos exists in a defined range of parameter values, is used as an example. Poincaré maps are used for characterization of quasi-periodic and chaotic attractors. The dominant modes or topos, which are inherent properties of the system, are identified by means of the Singular Value Decomposition. Tested modal feedback control schemas based on identified dominant spatial modes confirm the possibility of stabilization of simple quasi-periodic trajectories in the complex quasi-periodic or chaotic spatiotemporal patterns.

Introduction

The discussion of problems connected with the development of a systematic framework for control of complex dynamics and chaos in distributed parameter systems is the subject of this work. The control of complex dynamics has significant practical implications. Transition to chaos via the quasi-periodic route occurs in a number of hydrodynamic and other systems. Control of such transitions could be used to improve characteristics of process systems. The issue of chaos control in distributed parameter systems (DPS) has been discussed in several papers [1]. However, there do not appear to be studies that address the problem of controlling chaos when it occurs through the quasi-periodic route in a DPS. The focus of this effort is to explore the possibility of controlling the chaotic attractor in a distributed system to one of the quasi-periodic attractors, namely tori from which it evolves based on an understanding of the underlying dynamics. The distributed parameter system considered is of the reaction-diffusion type with Brusselator kinetics. A quasi-periodic or torus doubling route to chaos is known to exist in the selected region of parameter space [2]. In order to achieve the desired control objective, it was found useful to combine ideas from previous work in the area of control of chaos in lumped parameter systems (LPS) and low dimensional maps [1], general methodology of identification and control of distributed parameter systems [3] and analysis of spatiotemporal patterns in distributed systems [4].

*Permanent Address: Dept. of Chemical Engineering, Prague Institute of Chemical Technology, Prague, Czech Republic

†Author to whom correspondence should be addressed

System description

The *Brusselator reaction kinetic scheme* is a standard model system used for the study of dissipative structures in nonlinear chemical systems [5]. The reaction scheme involves the transformation of initial components A and B into products D and E through the reaction intermediates X and Y.

$$\begin{aligned} A &\xrightarrow{k_1} X \\ B + X &\xrightarrow{k_2} Y + D \\ 2X + Y &\xrightarrow{k_3} 3X \\ X &\xrightarrow{k_4} E \end{aligned}$$

The case of the Brusselator reaction occurring in a membrane reactor is studied in this work. It is assumed that the reactor remains isothermal. A possible reactor design is shown in Figure (1). The reaction medium in the reactor is in a thin tube without radial variations in composition. The concentrations of A and B and of the products D and E in the reactor are controlled by a lateral semipermeable membrane between the reactor tube and the zoned chambers formed by the tube jacket. There are 19 such zoned chambers with concentrations being measured by sensors located at the mid-point of each zone. The only exceptions are the zones at either end which are 1.5 times longer than the rest and have measurement sensors at the two-thirds point. Separate membranes at the end of the reactor control the concentration of intermediates X, Y at each end of the tube. There is no convective contribution so that the system could be alternately viewed as a series of well mixed reaction cells coupled by diffusion. The governing set of partial differential equations for the Brusselator kinetics in a reaction-diffusion system can be expressed as [2, 5]:

$$\frac{\partial X}{\partial t} = \frac{D_X}{L^2}\frac{\partial^2 X}{\partial z^2} + X^2Y - (B+1)X + A \tag{1}$$

$$\frac{\partial Y}{\partial t} = \frac{D_Y}{L^2}\frac{\partial^2 Y}{\partial z^2} - X^2Y + BX \tag{2}$$

The length of the reactor L is chosen as the bifurcation parameter. The diffusion coefficients

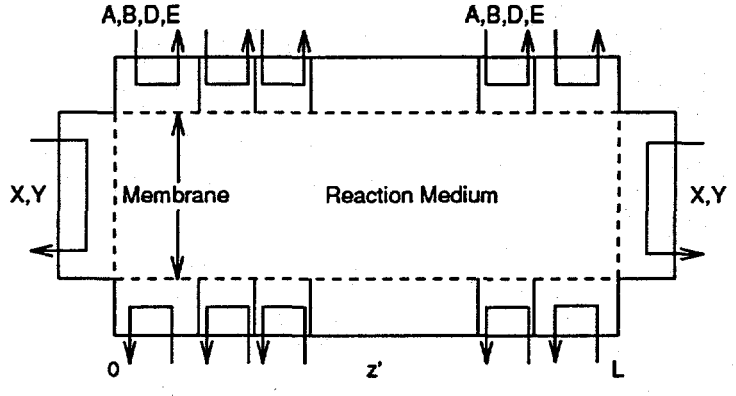

Figure 1: Membrane Reactor Geometry.

D_X, D_Y of X and Y are chosen as 0.008 and 0.004 respectively. The dimensionless distance coordinate z ranges from 0 to 1. Also, A and B are 2.0 and 5.45 respectively. The boundary conditions are of the Dirichlet type:

$$X(t,0) = X(t,1) = \bar{X}, \quad Y(t,0) = Y(t,1) = \bar{Y} \tag{3}$$

where $\bar{X}$ and $\bar{Y}$ are the steady state concentrations in the homogeneous system. Thus $\bar{X} = A = 2$ and $\bar{Y} = B/A = 2.725$.

For purposes of computation of spatiotemporal data for dynamic analysis, the finite difference approximation, where the spatial domain is discretized into 20 intervals of equal length, is used. Holodniok et al [2] observed that the leading eigenvalues of the monodromy matrix, a measure of the stability of the periodic solution, were almost identical for 20 and 40 intervals. Also, we found the results of the simulations performed with 40, 80, 160 intervals to be consistent with those for 20.

Poincaré maps

The nonlinear dynamics of interest can be studied by means of properly chosen Poincaré maps. The Poincaré map for the present problem essentially represents the intersection of the trajectory obtained by integration of equations (1) and (2) and a 37-dimensional hypersurface suitably defined. For example, the surface could be defined by the following equation:

$$X_{z=0.3}(t) = 2.0 \tag{4}$$

with $dX_{z=0.3}(t)/dt > 0$. The Poincaré map would then contain only those spatial profiles which satisfy the requirement of equation (4) as denoted by solid lines in Figures (2a) and (2b). To represent the Poincaré map in two dimensions it becomes necessary to project the map onto chosen two phase-space coordinates i.e. concentrations of X and Y at chosen location in the reactor. The concentrations of X and Y at $z = 0.5$ when the concentration of X at $z = 0.3$ is 2.0 and increasing (see points Q and R in Figure (2)) were used here. In such a 2D map, a single point denotes periodic behavior. A closed orbit indicates quasi-periodic behavior (or torus) while a double closed orbit would suggest a torus doubling.

Equations (1) and (2) were integrated using two sets of initial conditions. The first set of initial conditions, denoted by A (or IC-A) throughout this paper, corresponds to:

$$X = 2.32,\ Y = 1.75 \text{ for } z < 0.5 \text{ and } X = 3.32,\ Y = 2.75 \text{ for } z \geq 0.5$$

The second set of initial conditions, referred to as B (or IC-B) is the mirror image of the initial condition A. The Poincaré maps that result as L is varied from 1.403 to 1.43 are presented in Figure (3), which reveals the existence of two co-existing and mutually mirror-symmetric spatially asymmetric attractors. The symmetry arises from the symmetry in the geometry of the problem and the solution reached depends on the initial conditions used.

Singular Value Decomposition (SVD)

Spatiotemporal patterns can be better understood if they are decomposed into time-independent spatial structures and their time-varying amplitudes. This orthogonal decomposition can be accomplished by means of the Singular Value Decomposition [6]. Implementation of SVD in this context is in principle similar to the Karhunen-Loéve expansion. The SVD analysis is

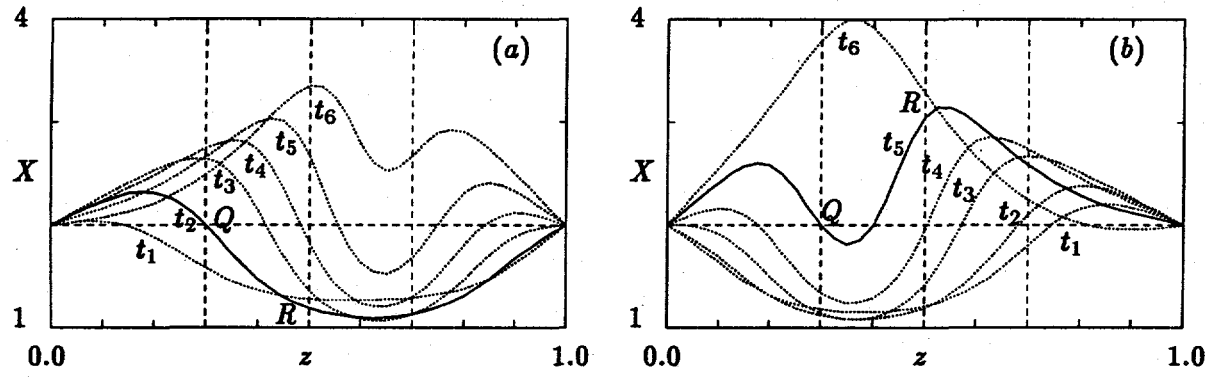

Figure 2: Selecting spatial profiles for Poincaré maps of DPS. (a) and (b) correspond to initial conditions A and B (cf. text). $t_1 < t_2 < t_3 < t_4 < t_5 < t_6$. Equation (4) defines the Poincaré surface.

applied to both reactants X and Y. The spatiotemporal data for reactant X typically consists of M snapshots at N points in space which constitutes an $N \times M$ matrix $\mathbf{X}'$. Application of the matrix SVD yields left and right unitary singular matrices and a diagonal singular value matrix. The columns of the left (spatially dependent) and right (time dependent) singular vectors are referred to as topos and chronos respectively.

Figure (4) illustrates the behavior of the topos, $\mathbf{w_i}(z)$, corresponding to the first two modes ($i = 1, 2$) when using initial condition A. Initial condition B yields a set of topos $\mathbf{w_i^*}(z)$ which satisfies the condition $\mathbf{w_i^*}(z) = \mathbf{w_i}(1 - z)$. The $(z, 1 - z)$ relation indicates that the symmetry is of the same mirror-image type seen in the Poincaré maps. The topos $\mathbf{w_i}(z)$ are *inherent properties* of the system and were found to fluctuate very little as L was varied.

From the square of the singular values, the relative energy of each mode can be assessed. The singular values are arranged in descending order. It was found that about 85% of the energy is concentrated in the first mode itself and another 12% in the second mode. Also the distribution of the energy amongst the dominant modes remained similar throughout the regime of transition to chaos i.e. $L = 1.403$—1.43. This observation coupled with the robustness of the topos lends support to the idea that in a feedback control framework, desirable performance could be achieved by controlling the first mode alone.

Modal Feedback Control

The primary goal is to develop a feedback control framework which would facilitate control of the chaotic attractor to any of the tori from which it evolves or vice-versa or from one torus to another. A modal feedback control methodology that accounts for the spatial nature of the output is schematically depicted in Figure (5). A detailed account of the different modal control schemes used can be found in [7].

First, let us suppose that we wish to control the chaotic attractor to the 1-torus. Let $X(z, t)$ in the open loop represent chaotic behavior and $X_{sp}(z, t)$ be indicative of the desired quasi-periodic behavior. Thus the set point is a dynamically varying profile. $\varepsilon(z, t)$ is the deviation

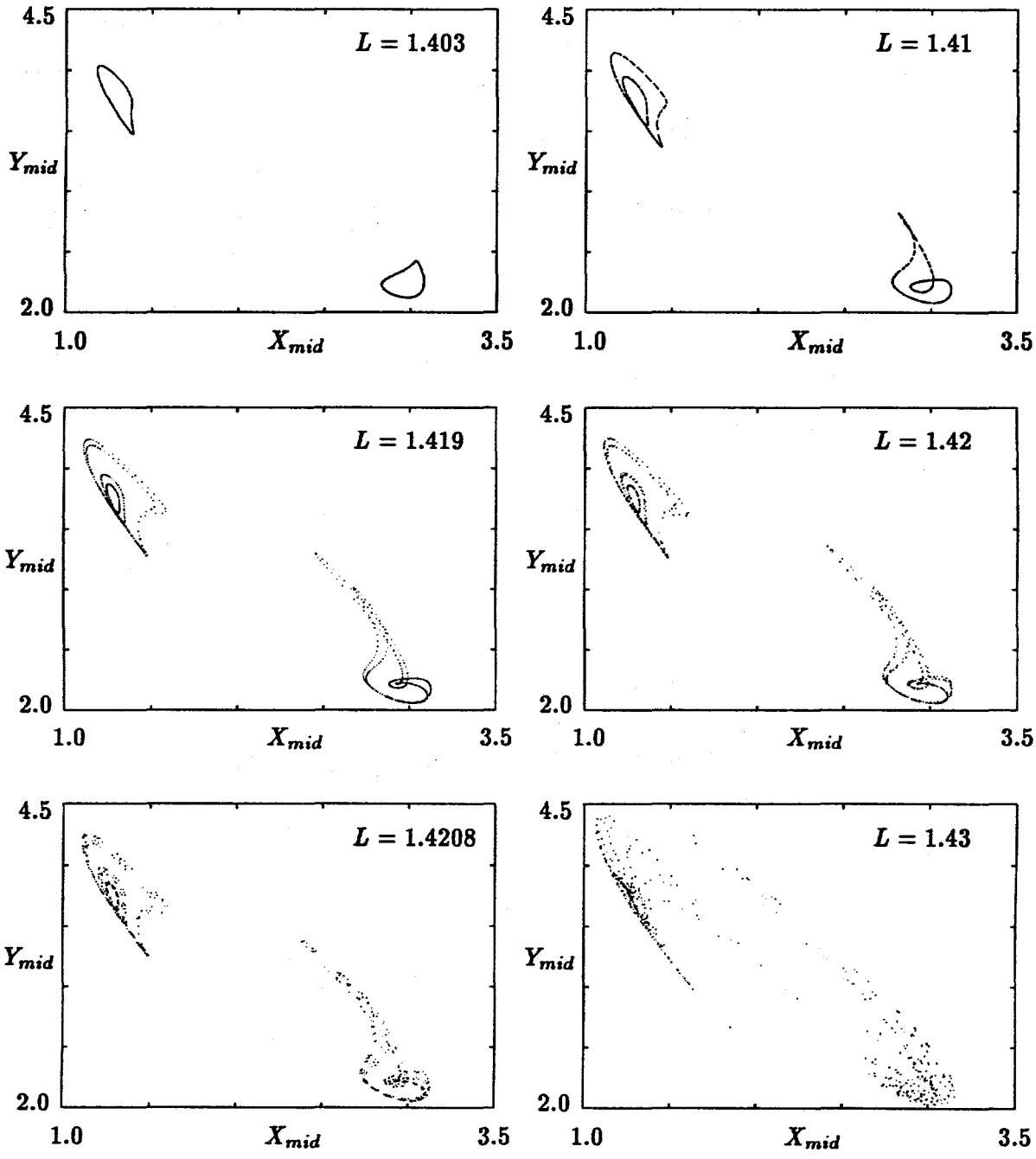

Figure 3: Poincaré maps. The horizontal and vertical axes represent the concentration of X and Y at the midpoint, $z = 0.5$. The attractors in the top left corner are obtained using initial condition A while the ones in the bottom right correspond to initial condition B. Equation (4) defines the Poincaré surface.

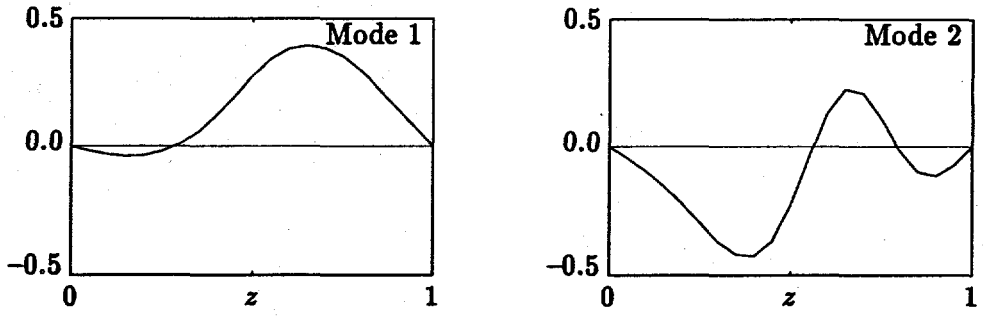

Figure 4: Topos for modes 1 and 2 with $L = 1.403$. Initial condition A is used. The horizontal axes denote the distance coordinate while the vertical axes represent the magnitude of the topos.

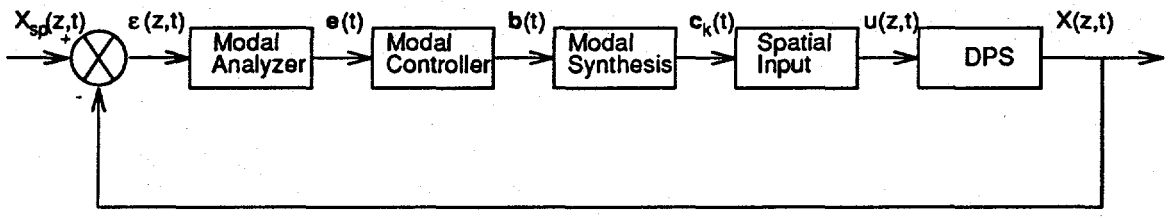

Figure 5: Modal feedback control scheme.

of the output profile $X(z,t)$ from the set point $X_{sp}(z,t)$:

$$\varepsilon(z,t) = X_{sp}(z,t) - X(z,t) \tag{5}$$

Since the topos $w_i(z)$ were shown to be intrinsic properties of the system (i.e. consistent throughout the transition regime), the modal error vector $\mathbf{e}(t)$ is obtained by projecting the deviation $\varepsilon(z,t)$ onto the topos.

$$e_i(t) = \int_0^1 \varepsilon(z,t) w_i(z)\, dz \tag{6}$$

The modal controller computes the control coefficients $b_i(t)$ corresponding to each $e_i(t)$. A suitable form of control law could be used. For instance, with proportional control, $b_i(t) = Ke_i(t)$. The control action $u(z,t)$ is then obtained as follows:

$$u(z,t) = \sum_{i=1}^{N} b_i(t) w_i(z) \tag{7}$$

Though a distributed parameter system is of infinite dimension (i.e. $N = \infty$), in practice N could be set to a value which ensures that the first N modes capture the desired amount (for example, 90%) of the original behavior. This information can be obtained from the singular values. It is difficult to practically implement a control action of the type described by equation (7) that is continuous in space. A more physically realizable technique would be having M zones of piecewise uniform control in the interval $z_k < z < z_{k+1}$ (cf. Figure (1) for an example). The

control action could then be expressed as:

$$u(z,t) = \sum_{k=1}^{M} c_k(t) g_k(z) \tag{8}$$

where $g_k(z) = H(z - z_k) - H(z - z_{k+1})$. $H(z)$ refers to the Heaviside step function. $c_k(t)$ can be obtained by using the orthogonality of $g_k(z)$, thus yielding the expression:

$$u(z,t) = \sum_{k=1}^{M} \sum_{i=1}^{N} K \left(\int_0^1 \left[X_{sp}(z',t) - X(z',t) \right] w_i(z')\, dz' \right) \left(\int_0^1 w_i(z') g_k(z')\, dz' \right) g_k(z) \tag{9}$$

In the reaction-diffusion system (equations (1) and (2)) control is physically accomplished by the addition or removal of reactants A and B as shown in Figure (1). The exact increments or decrements of A and B, referred to as u_X and u_Y, are computed based on the deviations of $X(z,t)$ and $Y(z,t)$ from $X_{sp}(z,t)$ and $Y_{sp}(z,t)$ respectively. Proportional feedback is used based on the observation that earlier works dealing with the problem of control of chaos have found such a scheme adequate for the purpose of stabilization of the strange attractor onto one of the embedded unstable orbits. With the inclusion of feedback control the governing equations (1) and (2) are transformed to:

$$\frac{\partial X}{\partial t} = \frac{D_X}{L^2} \frac{\partial^2 X}{\partial z^2} + X^2 Y - (B + u_Y + 1)X + (A + u_X) \tag{10}$$

$$\frac{\partial Y}{\partial t} = \frac{D_Y}{L^2} \frac{\partial^2 Y}{\partial z^2} - X^2 Y + (B + u_Y)X \tag{11}$$

The boundary conditions (equation (3)) remain unchanged. As in the case of dynamics, the computations are performed using the finite difference approximation with 20 intervals of equal length. The approach is to try several forms of modal control — 1 mode, 1 zone and 1 mode, 19 zones. Figure (6) illustrates the results of trying to direct the chaotic attractor to the 1 torus. Using 19 zones expectedly enhances the performance. The same modal feedback control scheme can also be used to control the chaotic attractor to any other torus and also any torus to the chaotic attractor or any other torus.

CONCLUSIONS

Through properly chosen Poincaré maps, it was observed that the dynamics of the reaction-diffusion system with Brusselator kinetics (in the parameter space of interest $L = 1.403$—1.43) is characterized by the presence of two co-existing and mutually mirror-symmetric spatially asymmetric attractors. The mirror-symmetry was initially ascertained from the use of mirror-symmetric sets of initial conditions. This finding was also corroborated from the relationship between the topos for the two sequences of attractors. Thus, Singular Value Decomposition proved to be a useful tool in detecting the presence of co-existing and mutually mirror-symmetric attractors. The consistency of the topos throughout the transition region coupled with the distribution of energy amongst the various modes suggested their possible use in the development of the control strategy.

Finally a modal control strategy was developed and applied to the control of chaos occurring through the torus doubling route in the reaction-diffusion system. The key idea was to compute the control action by projecting the deviation of the current dynamic behavior of the system

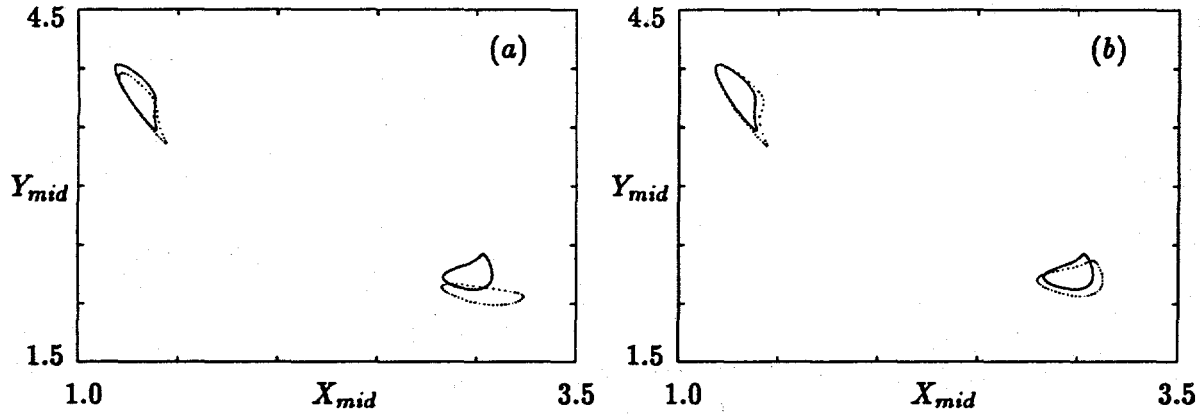

Figure 6: Poincaré map depicting the control of the open loop chaotic attractor ($L = 1.43$) to the underlying torus using (a) 1 zone, (b) 19 zones and the most dominant mode. Equation (4) defines the Poincaré surface. $K = 0.03$, solid line refers to the "set point" attractor, dots refer to the controlled attractor.

from the desired behavior onto the dominant modes. It was possible to obtain behavior close to any of the tori by suitably controlling the chaotic attractor and vice-versa. Although applied to an example which demonstrated a quasi-periodic route to chaos, the control scheme is essentially independent of the route to chaos and so could potentially be applied to instances of chaos in distributed parameter systems occurring through other routes too.

REFERENCES

[1] G. Chen. Control and Synchronization of Chaotic Systems (bibliography). EE Dept, Univ of Houston, TX - available from ftp: "uhoop.egr.uh.edu/pub/TeX/chaos.tex" (login name and password: both "anonymous").

[2] M. Holodniok, M. Kubíček, and M. Marek. Disintegration of an Invariant Torus in a Reaction-Diffusion System. Presented at the Fifth International Seminar NUMDIFF-5 held at the Martin-Luther-University, Halle, May 22-26, 1989.

[3] D. H. Gay and W. H. Ray. Identification and Control of Distributed Parameter Systems by means of the Singular Value Decomposition. *Chemical Engineering Science*, In Press.

[4] L. Sirovich. Turbulence and the Dynamics of Coherent Structures-Parts I,II,III. *Quarterly of Applied Mathematics*, XLV(3):561–590, October 1987.

[5] M. Marek and I. Schreiber. *Chaotic Behaviour of Deterministic Dissipative Systems.* Cambridge University Press, Cambridge, 1991.

[6] G. W. Stewart. On the Early History of Singular Value Decomposition. *SIAM Review*, 35(4):551–566, December 1993.

[7] S. Chakravarti, M. Marek, and W. H. Ray. Reaction-Diffusion System with Brusselator Kinetics — Control of Quasiperiodic Routes to Chaos. *Physical Review E*, In Press.

TURBULENCE GENERATION BY WAVES

D. Kaftori
X. S. Nan
S. Banerjee

Chemical Engineering Dept.
University of California Santa Barbara
Santa Barbara, CA 93106

ABSTRACT

The interaction between two-dimensional mechanically generated waves, and a turbulent stream was investigated experimentally in a horizontal channel, using a 3-D LDA synchronized with a surface position measuring device and a micro-bubble tracers flow visualization with high speed video.

Results show that although the wave induced orbital motion reached all the way to the wall, the characteristics of the turbulence wall structures and the turbulence intensity close to the wall were not altered. Nor was the streaky nature of the wall layer. On the other hand, the mean velocity profile became more uniform and the mean friction velocity was increased. Close to the free surface, the turbulence intensity was substantially increased as well. Even in predominantly laminar flows, the introduction of 2-D waves causes three dimensional turbulence. The turbulence enhancement is found to be proportional to the wave strength.

INTRODUCTION

This study is part of an ongoing research effort in our laboratory concerning turbulence at a gas-liquid interface. Previous works, both experimental and computational using direct numerical simulations, have focused on smooth turbulent open channel flows with and without imposed wind shear. In this work the question of turbulence in the presence of two-dimensional waves, moving with the current, and without wind is addressed.

One of the main effects of waves on a turbulent current is to increase the turbulence intensity close to the free surface (e.g. Kemp & Simons[1]). This may be most important in transport processes at the surface, particularly with sparingly soluble gases. The reason for the increased intensity is not clear. Rashidi et al.[2] examined this question by investigating the relationship be-

Table 1. Wave parameters

Re_h	h [mm]	H [mm]	f [Hz]	$\overline{u^*}$ [m/s]	λ [m]	Re_h	h [mm]	H [mm]	f [Hz]	$\overline{u^*}$ [m/s]	λ [m]
7500	37.2	7.0	1.90	9.4e-3	0.39	5000	40.8	6.13	2.40	6.1e-3	0.29
5000	55.0	8.4	1.90	4.8e-3	0.38	5000	41.3	12.13	2.37	6.1e-3	0.29
5000	40.5	6.4	1.62	6.5e-3	0.46	4400	39.5	5.55	2.37	6.0e-3	0.29

$Re_h = U_m h/\nu$ Reynolds number. ν is kinematic viscosity.
H Wave height.
$\overline{u^*}$ Mean friction velocity. See below.

tween the waves and the wall structures, because the structures are considered to be responsible for most of the turbulence production in the boundary layer. They found that the number of wall ejections increased in wavy flows and proposed that this may be the reason for the enhanced turbulence. However, the frequency of the bursts themselves (each containing a number of ejections), was not changed. Since it now seems that the large scale structures are the ones responsible for turbulence production (i.e., the bursts, or funnel-shaped vortices, as they were interpreted by Kaftori et al.[3]), rather than the internal structures (i.e., separate ejections), this question remains unresolved. In addition, Rashidi et al. could not make measurements very close to the wall and could not measure the variations in turbulence quantities there.

In this work the increased turbulence in wavy flow was examined. The rate of increase throughout the flow profile was measured in an attempt to identify the causes and mechanisms that govern it. Other turbulence characteristics, such as the velocity profile, friction velocity, and the wall structures, were also measured and observed. While the exact causes for the enhanced turbulence still remain unclear, the results obtained suggest that they are not related to the wall layer. Instead, it appears that they originate at the wavy interface. In addition, a relationship between the rate of increased intensity and the wave strength is presented.

EXPERIMENTS AND PROCEDURE

Experiments were conducted in an open water flume with waves superimposed onto the turbulent stream by a mechanical wedge-shaped wave maker. A diagram of the system is shown in

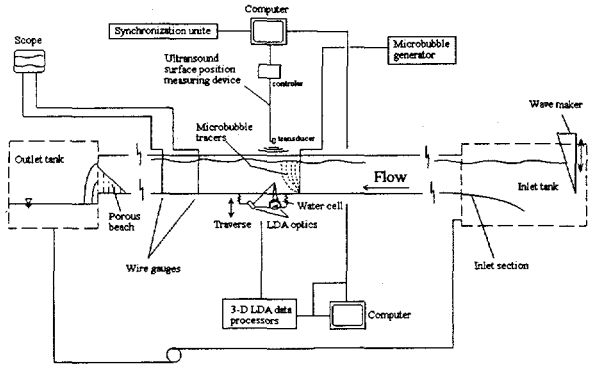

Figure 1: The experimental facility.

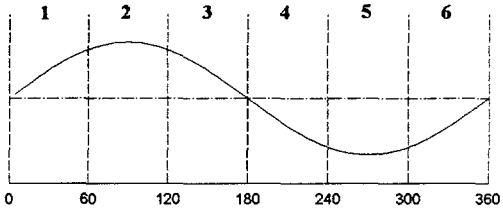

Figure 2: Wave phase division.

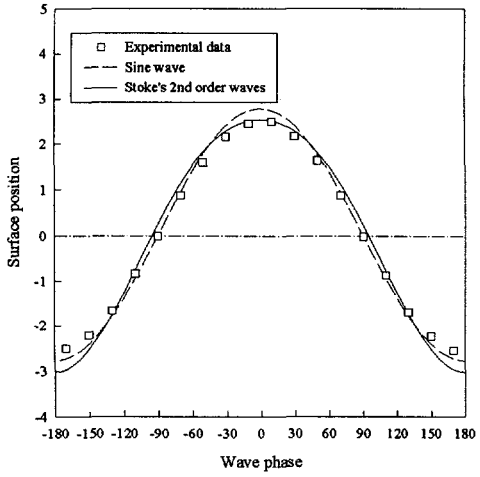

Figure 3: A comparison between a typical wave from the experiments, a sine wave, and a second order Stoke's wave.

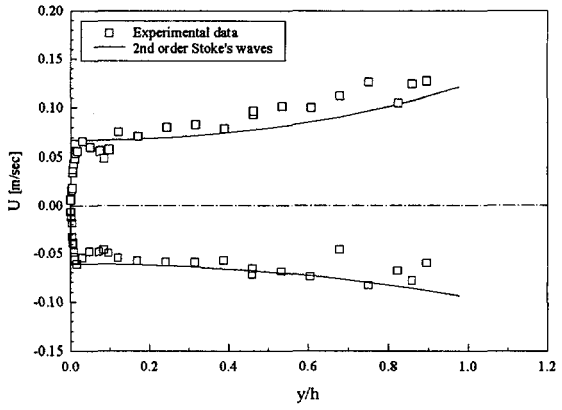

Figure 4: Wave velocity profile under the crest, in experiments and by assuming Stoke's second order waves.

Figure 1. The mean water depth in the channel was typically in the range of 40-55 mm.

The channel was equipped with a 3-D laser Doppler anemometry system for data acquisition, an ultrasound distance measuring device (Air gauge) for surface elevation measurements, and a microbubble tracers flow visualization apparatus with high speed video. The LDA and Air Gauge were synchronized so that each velocity data point could be related to the correct wave phase. In addition, two wire gauges, each measuring the instantaneous water depth, were used.

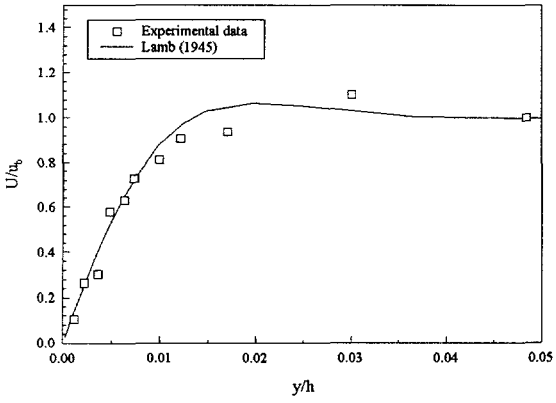

Figure 5: Wave velocity profile under the crest in the wave boundary layer, in experiments and according to Lamb[4]. Normalized by the velocity at the edge of the wave boundary layer.

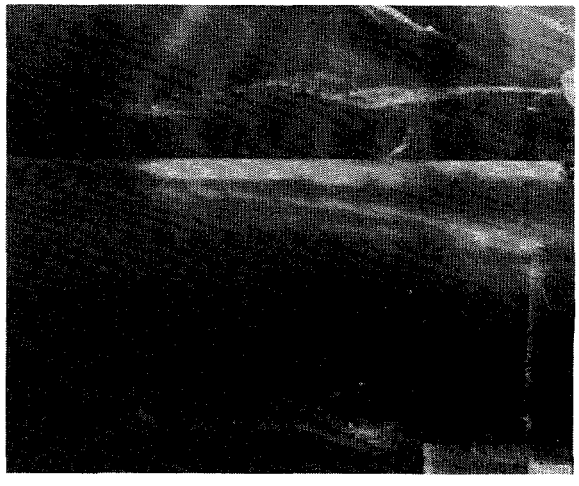

Figure 6: Funnel-shaped streamwise vortices in a wavy flow. Top - plan view from underneath. Bottom - side view. Microbubble tracers were generated only in the lower 1/3 of the flow. Scale: width of photo ~600 wall units.

The gauges were displaced in the streamwise direction so that the phase lag between them could be used as a measure of the wave length λ. The measured wave length was within 7% of the theoretical length, based on linear wave theory:

$$(\omega - kU_m)^2 = gk \cdot \tanh(kh) \quad , \tag{1}$$

where $\omega=2\pi f$ is wave period with f the wave frequency, $k=2\pi/\lambda$ is wave number, U_m is mean velocity of the turbulent current, g is gravitational acceleration, and h is mean water depth.

In all, 6 experiments with waves were conducted, along with several runs with a smooth surface. The wave parameters were varied between experiments and are detailed in Table 1.

In order to distinguish between the various contributions to the velocity field, each measured velocity data - u, was decomposed into mean velocity of the turbulent stream - U, wave induced fluctuations - u_w, and turbulence fluctuations - u', as:

$$u = U + u_w + u' \quad . \tag{2}$$

The average (mean) velocity was computed at each measuring point as:

$$U = \frac{1}{n}\sum u \quad , \tag{3}$$

where n is the number of data samples. The wave induced velocity was calculated for each phase of the waves by dividing the waves into 6 (or, in some experiments, 18) sections, each representing a phase, as in Figure 2. The average wave induced velocity was then calculated for each phase:

$$u_w\Big|_{ph} = \overline{u_i}\Big|_{ph} - U \quad . \tag{4}$$

Here $u_i\Big|_{ph}$ is a velocity data point at a given phase of the wave, and the overbar represents an average over all waves. In determining the wave phase of each data point, the information col-

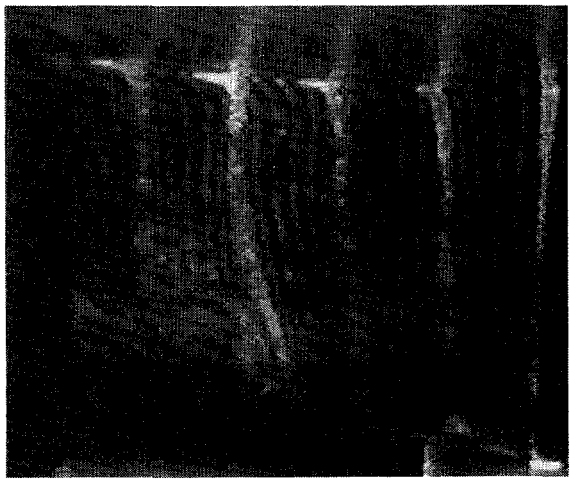

Figure 7: Instantaneous velocity profile under wave trough. Note flow reversal at the surface and close to the wall. Scale: width of photo ~340 wall units.

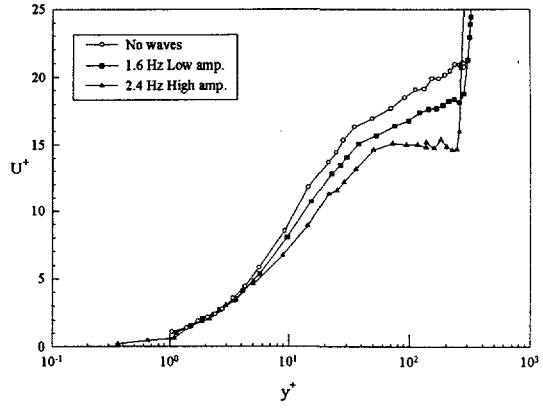

Figure 8: Normalized mean velocity profiles in smooth and wavy flows.

lected from the ultrasound surface elevation measurements was used. The fluctuating turbulence velocity component was deduced from Eq. (2).

In order to qualify the type of waves in the experiments, the measured velocities and wave forms were compared with some establish wave types. Figure 3 depicts a typical wave form measured in an experiment together with a sinusoidal wave form and a second order Stokes wave given by:

$$\eta = \frac{H}{2}\cos(kx-\omega t)+\frac{Hk}{16}\frac{\cosh(kh)}{\sinh^3(kh)}[2+\cosh(kh)]\cos[2(kx-\omega t)] \quad , \tag{5}$$

where x is the streamwise coordinate and t is time. The first term on the right is the sine wave in the figure. As can be seen, the waves were close to second order waves but with a somewhat sharper crest, implying a higher order of non-linearity. The wave velocity profile was also in agreement with that of second order Stoke's waves, as illustrated in Figure 4. Close to the wall the wave velocity was also in agreement with Lamb's[4] prediction, based on linear wave theory, as shown in Figure 5.

RESULTS

Wall Structures

The behavior of turbulence wall structures in wavy flow was examined and compared to smooth flow using microbubble tracers with high speed video. These observations show that the same structures which are seen in smooth flows appear in wavy flow as well. These funnel-shaped vortical structures (see Kaftori et al.[3]), originate close to the wall and stretch in the streamwise direction while expanding outward from the wall in a spiraling motion. In wavy flow the structures seem to be of the same size and shape, as shown in Figure 6. This was true in spite of the fact that the effect of the waves was apparent all the way to the wall, where the orbital wave induced velocity caused the flow to reverse at the wall, as shown in Figure 7.

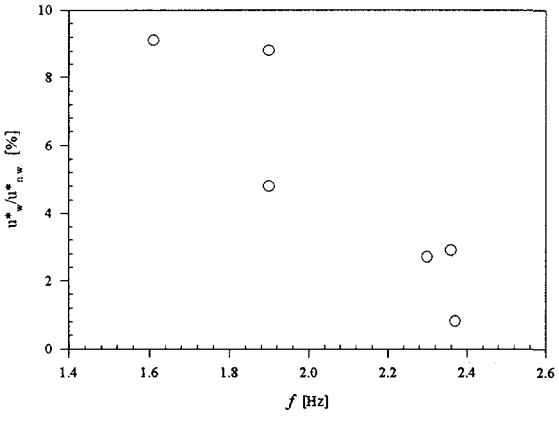

Figure 9: Percent increase in friction velocity as a function of wave frequency.

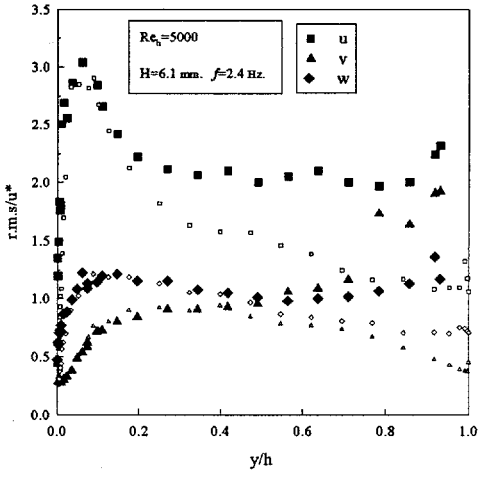

Figure 10: Turbulence intensities profile (wave induced velocity removed).

The streaky structure of the wall layer, typical to smooth flow, was also preserved when waves were introduced. The streak spacing seemed to remain approximately the same (~100 wall units). It seems that the streaks became better defined, with a larger difference between the streamwise velocity of the high- and low-speed regions. Similar observations were make by Rashidi et al.[2].

Velocity profile

The effect of surface waves on the mean velocity profile is shown in Figure 8. It appears that the waves reduce the mean velocity in the outer part of the flow but do not affect the profile in the wall layer. In general, the velocity profiles become more uniform and the effect is stronger with larger waves. The deficit in mass flow rate due to the lower velocities in the figure is balanced by the flow in the crest region of the waves. The instantaneous velocity profiles varied with wave phase. An example of the profile under a trough was given in Figure 7, where the velocity is reversed close to wall, positive in the mid section, and is negative again close to the free surface. The same type of instantaneous profile was recorded by Kemp & Simons[1].

The mean friction velocity $\overline{u^*}$, was calculated from the average velocity profile in the viscous layer ($y^+ \leq 5$). In wavy flows the friction velocity was up to 10% higher than in smooth flow. The increase was proportional to the wave length, and indirectly proportional to the frequency, as depicted in Figure 9.

Turbulence intensities

r.m.s velocity fluctuations of a wavy flow are compared to those of smooth flow in Figure 10 with the wave induced fluctuations removed, the r.m.s. curves are of the same shape as in smooth flow but the intensities of the three components are higher in the upper portion of the flow profile. The increase was larger for stronger waves. The waves did not affect the r.m.s close to the wall.

These results imply that turbulence production occurred in the upper portion of the flow as a result of the waves. While wave induced motion can be seen throughout the flow profile, they seem not to affect the turbulence wall structures, which are generally responsible for most of the turbulence production, nor alter the shape or magnitude of the turbulence intensities in the wall region. They do, however, significantly increase the intensities close to the free surface. Thus it appears that unlike simple turbulent open channel flow, where wall shear is the primary mechanism for turbulence production, in wavy flow there exists another production mechanism. This turbulence source is strongest close to the wave trough and weakens toward the wall.

In order to test this hypothesis, turbulence production in laminar wavy flow was examined using dye and particle tracers flow visualization. In these experiments dye diffusion and particle dispersion were observed and measured in both simple laminar flow, and in laminar flow with waves. Figure 11 is a sample of a dye diffusion experiments. In simple laminar flow there is hardly any diffusion at all. In the wavy flow, on the other hand, there is turbulent diffusion and the dye is dispersed immediately. The diffusion was three dimensional, with the same rate of dispersion in the spanwise direction as in the wall normal direction. The spanwise dispersion can only be accounted for by turbulence.

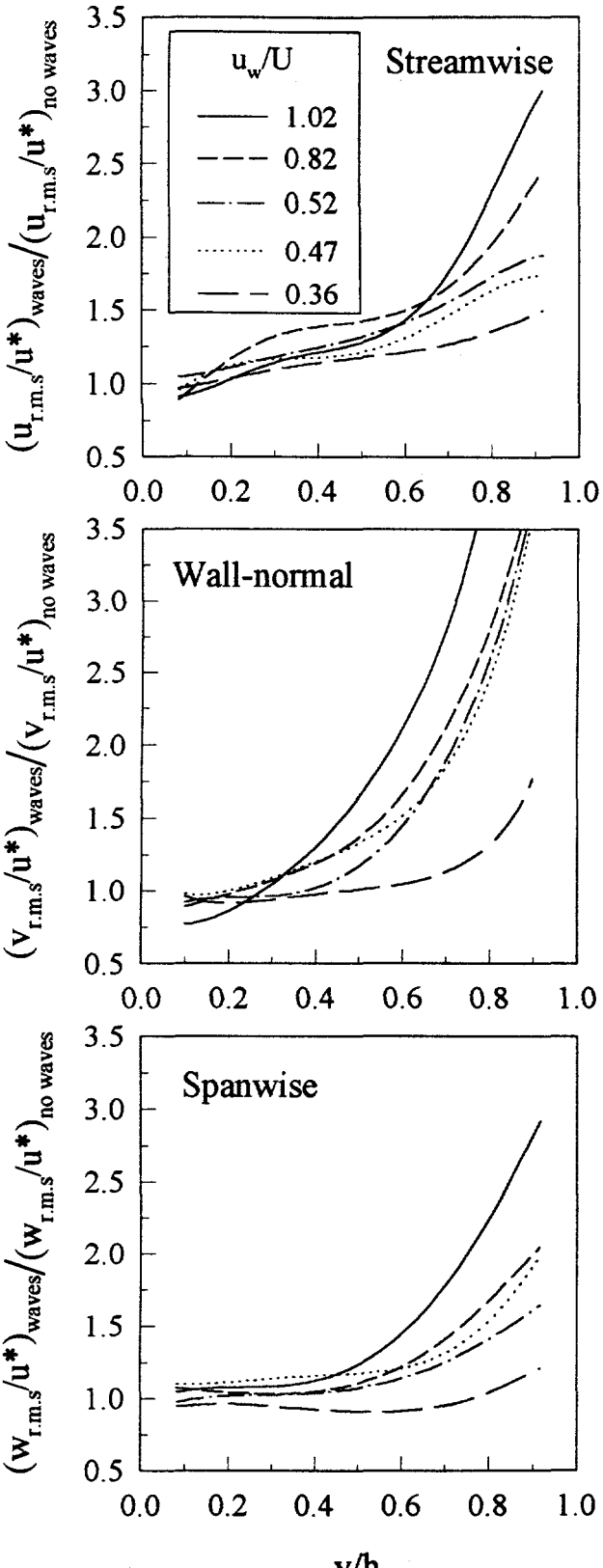

Figure 12: Increase in r.m.s level in wavy flow compared to smooth flow, as a function of wave strength. Lines are curve fits.

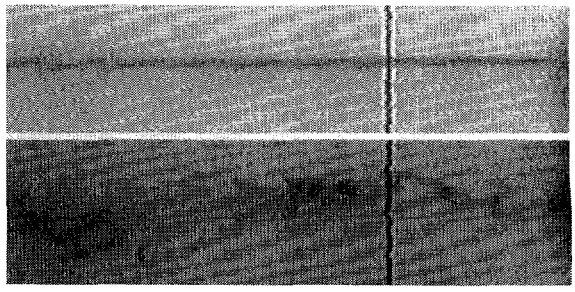

Figure 11: Dye diffusion experiment.
Top - Simple laminar flow.
Bottom - Laminar flow with waves.

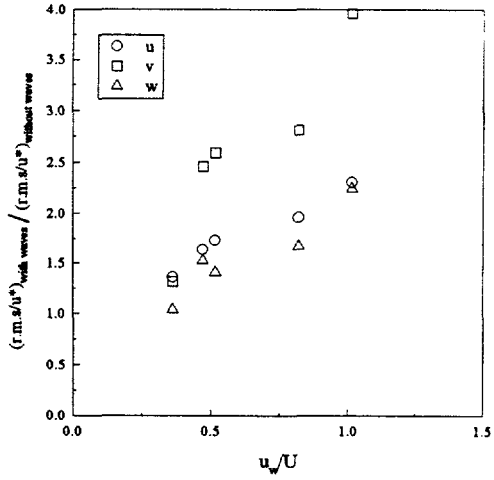

Figure 13: Increase in r.m.s levels with waves at y/h=0.8.

In the particle tracers experiments, polystyrene particles (specific density ~1.05, nominal diameter 275 μm) were released into the flow and were photographed using high speed video. Their spanwise displacement was then measured in order to examine the particle spanwise dispersion. Results show that in wavy flow the particle spanwise dispersion rate was up to three times higher compared to the non-wavy flow. These findings confirm that three-dimensional turbulence is generated by the predominantly two-dimensional waves.

As mentioned above, the rate of turbulence production due to waves increased with wave amplitude and frequency. Figure 12 shows the increase in turbulence intensities of the three velocity components as a function of wave strength, defined as the ratio of (a fluid) particle velocity to mean current velocity. The particle velocity at the mean water level was used. As can be seen, the r.m.s level in the upper half of the flow profile increases with increasing wave strength. In order to quantify this behavior, the r.m.s increases of all runs were compared at y/h=0.8. Results are in Figure 13. There it seems that the increase is directly proportional to wave strength.

The reason for the turbulence enhancement by the waves is still not clear. Evidently, it must be related to a coupling between the wave induced velocity fluctuations and the turbulence fluctuations, resulting in additional Reynolds stress-type terms in the momentum equation. In addition, since a wave induced drift usually exists in wavy flows (Phillips[5]), additional viscous shear may be introduced. These points and their relative importance are currently under investigation.

CONCLUSIONS

The introduction of 2-D waves onto a turbulent stream substantially increases the level of turbulence in the upper portion of the flow, while having only little effect on the turbulence in the wall layer. Even in laminar flow the introduction of waves causes the onset of turbulence. The enhancement seems to scale with the strength of the waves, namely the ratio of wave induced velocity to the mean current velocity. Since the turbulence characteristics close to the wall, and the nature of the wall structures, seemed to be unchanged by the waves, it appears that the enhanced turbulence is not related to increased shear at the wall or to turbulence in the wall layer. Rather, it seems that it may originate at the wavy region. This must be investigated further.

REFERENCES

1 P. H. Kemp and R. R. Simons, The interaction between waves and a turbulent current: waves propagating with the current," *J. Fluid Mech.* **116**, 227-250, (1982)

2 M. Rashidi, G. Hetsroni, and S. Banerjee, "Wave-turbulence interaction in free-surface channel flows," *Phys. Fluids A* **4** (12), 2727-2738, (1992).

3 D. Kaftori, G. Hetsroni, and S. Banerjee, "Funnel-shaped vortical structures in wall turbulence," *Phys. Fluids* **6** (9), 3035-3050, (1994).

4 H. Lamb, Hydrodynamics, Sixth edition, Dover Publications, New York (1945).

5 O. M. Phillips, The dynamics of upper ocean, Cambridge at the university press (1966).

NUMERICAL SIMULATION OF HIGH REYNOLDS NUMBER BUBBLE MOTION

John B. McLaughlin
Department of Chemical Engineering, Clarkson University
Potsdam, N.Y. 13699-5705, USA

ABSTRACT

This paper presents the results of numerical simulations of bubble motion. All the results are for single bubbles in unbounded fluids. The liquid phase is quiescent except for the motion created by the bubble, which is axisymmetric. The main focus of the paper is on bubbles that are of order $1mm$ in diameter in water. Of particular interest is the effect of surfactant molecules on bubble motion. Results for the "insoluble surfactant" model will be presented. These results extend research by other investigators to finite Reynolds numbers. The results indicate that, by assuming complete coverage of the bubble surface, one obtains good agreement with experimental observations of bubble motion in tap water. The effect of surfactant concentration on the separation angle is discussed.

INTRODUCTION

Bubble motion in liquids is of interest in many engineering problems. In the context of Bioreactors, bubbles are important in mass transfer, the hydrodynamics of the reactors, and because they represent a volume that is not available for reaction [1]. Visual inspection of fluidized bed ethanol Bioreactors indicates that the bubbles are typically on the order of a few millimeters in diameter [1, 2]. A characteristic of Bioreactors is that they typically contain surface active materials in the form of biopolymers that are generated by the microbes.

Thus, it is of interest to develop models for the effect of surfactants on bubble motion. Andrews et al. [2] took a step in this direction. They developed a boundary layer analysis to describe the surfactant concentration on the upper portion of bubble. Their analysis is valid up to the point of flow separation. An interesting result is that large concentrations of surfactant can cause the point of separation to move closer to the top of the bubble, suggesting that there may be a corresponding increase in wake volume.

The approach taken by Andrews et al. cannot provide information about the nature of the wake. Ryskin and Leal [3-5] developed a numerical simulation technique for axisymmetric bubbles. They presented results for bubble Reynolds numbers as large as 200 and Weber numbers as large as 20. A surprising result was that, as they increased the Weber number for a fixed Reynolds number, flow separation from a bubble was preceded by the formation of detached eddies.

Haberman and Morton [6], Saffman [7], and Hartunian and Sears [8] reported experimental results for bubble motion in water and a variety of other liquids. Bubble velocities in distilled water and tap water are virtually the same for bubbles with equivalent spherical diameters, d_e, smaller than about $1mm$. Bubbles of this size are approximately spherical and have approximately the same drag coefficient as a rigid sphere of the same diameter. For values of d_e between $1mm$ and about $6mm$, there are significant differences between distilled water and tap water. In distilled water, the bubble rise velocity exhibits a local maximum at $d_e = 1.4mm$. Bubbles of this size rise twice as fast in distilled water as in tap water ($35cm/s$ compared to $17cm/s$). The corresponding Reynolds numbers, based on d_e, are 490 and 240.

The differences between bubble motion in distilled water and tap water have been attributed to the presence of surfactants [6-8]. The air-water interface is particularly susceptible to surfactants because of the polarity of the water molecule. Sadhal and Johnson [9] devised a theory for the effects of surfactants

on bubbles and drops for Stokes flow. They assumed that the adsorption-desorption kinetics was slow and that one could neglect surface diffusion. This approximation has been referred to as the "insoluble surfactant" approximation. They showed that the surfactant would collect in a cap on the rear portion of the bubble, and obtained an exact solution.

The insoluble surfactant approximation has been used by Stone and Leal [10] to study the effect of surfactants on bubbles in two-dimensional straining flow. They studied only the Stokes flow limit.

Pan et al. [11] used the static pendant drop method to determine the kinetic rate constants for surfactant exchange between an aqueous sublayer and an air-water interface. A key feature of their approach is the use of high volume concentrations of surfactant. They showed theoretically that, by using sufficiently high volume concentrations of surfactant, one could distinguish kinetics from diffusion. The availability of such results opens the possibility of checking the conditions of the insoluble surfactant approximation for experiments with controlled amounts of a known surfactant.

GOVERNING EQUATIONS

The numerical techniques in this study were described by Ryskin and Leal [3-5]. Therefore, this section contains only a brief summary of the equations and the computational parameters.

In what follows, the equivalent spherical radius, r_e, the bubble rise velocity, U, the liquid density, ρ, the fluid kinematic viscosity, ν, the interfacial surface tension, γ ,and the acceleration of gravity, g, will be used to make quantities dimensionless. The gas density is assumed to be negligible. The Reynolds number, Re, the Weber number, W, and the Morton number, M, may be used to characterize the fluid mechanics problem for clean interfaces:

$$Re = \frac{d_e U}{\nu} \tag{1}$$

$$W = \frac{\rho(d_e)U^2}{\gamma} \tag{2}$$

$$M = \frac{g\mu^4}{\rho\gamma^3}. \tag{3}$$

The drag coefficient, C_D, is given by

$$C_D = \frac{4}{3}\frac{(d_e)g}{U^2}. \tag{4}$$

The above quantities are related by

$$M = \frac{3}{4}C_D\frac{W^3}{Re^4}. \tag{5}$$

Figure 1 shows a (σ, x) plane in a cylindrical coordinate system (σ,ϕ, x). Following Ryskin and Leal [3], it is convenient to introduce an orthogonal, curvilinear coordinate system (ξ,η,ϕ) in which the variables ξ and η lie between 0 and 1. The coordinate mesh is shown in Figure 1. The surface of the bubble is given by $\xi = 0$. The point at infinity corresponds to $\eta = 0$. The positive x axis corresponds to $\eta = 0$ and the negative x axis corresponds to $\eta = 1$. The coordinate mapping is determined by the covariant Laplace equations as described by Ryskin and Leal. For the bubble in Fig. 1, $Re = 200$ and $W = 5$. Only half the bubble is shown since the flow is axisymmetric.

The present study is limited to axisymmetric motion. Therefore, it is convenient to use the stream-function-vorticity method. For steady motion, the governing equations, written in dimensionless form, are

$$L^2(\omega\sigma) - \frac{Re}{2}\left(\frac{\partial\psi}{\partial\xi}\frac{\partial\omega/\sigma}{\partial\eta} - \frac{\partial\psi}{\partial\eta}\frac{\partial\omega/\sigma}{\partial\xi}\right) = 0 \tag{6}$$

$$L^2\psi + \omega = 0, \tag{7}$$

where the operator L^2 is defined by

$$L^2 = \frac{1}{h_\xi h_\eta}\left[\frac{\partial}{\partial\xi}\left(\frac{f}{\sigma}\frac{\partial}{\partial\xi}\right) + \frac{\partial}{\partial\eta}\left(\frac{1}{f\sigma}\frac{\partial}{\partial\eta}\right)\right]. \tag{8}$$

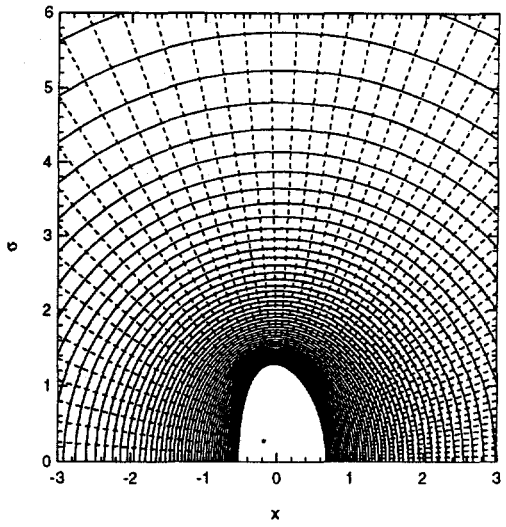

Figure 1: Coordinate Curves for a Bubble with $Re = 200$, $W = 5$

In Eqs. (6-8), ω is the ϕ component of the vorticity, ψ is the streamfunction, h_ξ and h_η are metric functions, and f is the ratio h_η/h_ξ. All quantities are dimensionless.

The pressure on the interface may be obtained by integrating the Navier-Stokes equation along the bubble surface:

$$p = \frac{3}{4}C_D x - u_\eta^2 - \frac{4}{Re}\int_0^\eta \frac{f}{\sigma}\frac{\partial}{\partial \xi}(\sigma\omega)d\eta, \tag{9}$$

where the pressure has arbitrarily been chosen to be zero at $\eta = 0$. By demanding that, in steady-state, the net force on the bubble vanishes, one may express C_D in terms of p_{dyn}, where p_{dyn} is the sum of the second and third terms on the right hand side of Eq.(9).

The boundary conditions at the surface of the bubble are as follows:

$$\psi = 0 \tag{10}$$

$$\omega - 2\kappa_\eta u_\eta = 0 \tag{11}$$

$$\tau_{\xi\xi} - \frac{4}{W}(\kappa_\eta + \kappa_\xi) = 0. \tag{12}$$

In Eqs.(10-12), κ_η and κ_ξ are the normal curvatures, u_η is the η component of the liquid velocity, and $\tau_{\xi\xi}$ is a component of the liquid stress tensor at the interface. The normal curvatures may be computed from expressions given by Ryskin and Leal [4].

The covariant Laplace equations and the streamfunction-vorticity equations are put into a canonical form discussed by Ryskin and Leal [4] and solved with the constant step ADI method suggested by Ryskin and Leal. In this iterative approach, one uses an artificial time step, Δt, and relaxation parameters for the vorticity boundary condition, β_ω and the normal stress balance, β_h.

When an insoluble surfactant is present, one must include the transport equation for the surface concentration of surfactant, Γ:

$$\nabla_s \cdot (\Gamma u_\eta - \frac{1}{P_s}\nabla_s \Gamma) = 0, \tag{13}$$

where ∇_s is the surface gradient operator and P_s is the surface Peclet number. If $P_s >> 1$, one obtains the Sadhal-Johnson result:

$$u_\eta = 0, \ \theta < \phi \tag{14}$$

$$\Gamma = 0, \ \theta > \phi, \tag{15}$$

where the angle ϕ is a cap angle in which the surfactant is concentrated. The angles ϕ and θ are measured from the positive x-axis. Thus, one may specify a cap angle and then use essentially the same procedure

as for the clean interface. The main modification is that one must impose a condition on the normal derivative of the streamfunction associated with the no-slip condition on the surfactant cap.

The calculations to be reported were performed for an "ideal gas" equation of state for the surfactant. This equation of state has the following form:

$$\gamma = \gamma_0 - RT\Gamma, \tag{16}$$

where γ is the surface tension, γ_0 is the surface tension of the clean interface, R is the gas law constant, T is the absolute temperature, and Γ is the surfactant concentration ($moles/m^2$) on the interface. This model is reasonable as long as the average distance between surfactant molecules remains large compared to the molecular size. For the calculations to be reported, this condition is satisfied.

To express Eq.(16) in dimensionless form, one can use γ_0 as the characteristic surface tension. The dimensionless surfactant concentration is defined by

$$\Gamma' = \frac{RT\Gamma}{\gamma_0}. \tag{17}$$

Thus, the dimensionless form of the ideal gas law is

$$\gamma' = 1 - \Gamma'. \tag{18}$$

The total amount of adsorbed surfactant, S, is given by the integral of Γ over the bubble surface. Using the axisymmetry of the problem, this integral may be reduced to the following form:

$$S = 2\pi r_e^2 \int_0^1 \Gamma \sigma h_\eta d\eta. \tag{19}$$

One way of characterizing the amount of surfactant is with the dimensionless parameter S' defined as follows:

$$S' = \frac{1}{4\pi r_e^2} \frac{SRT}{\gamma_0}. \tag{20}$$

One may also express S' in terms of the Marangoni number, Ma, the capillary number, C, and the dimensionless surface area, A', as follows:

$$S' = MaCA', \tag{21}$$

where

$$Ma = \frac{1}{A} \frac{SRT}{\mu U} \tag{22}$$

$$C = \frac{W}{Re} \tag{23}$$

$$A = 2\pi r_e^2 \int_0^1 \sigma h_\eta d\eta \tag{24}$$

and

$$A' = \frac{A}{4\pi r_e^2}. \tag{25}$$

NUMERICAL SIMULATIONS

Haberman and Morton [6] measured the bubble rise velocity in tap water and filtered water as well as a variety of other liquids. Figure 2 shows their measurements for tap water and filtered water. In filtered water, the bubble rise velocity reached a local maximum at $d_e = 1.4mm$. The corresponding values of Re and W are 490 and 2.35, respectively. The program was run with 61 equally spaced grid points in both the ξ and η coordinates. The computed Morton number, M, was $2.64 \cdot 10^{-11}$. The value of M for

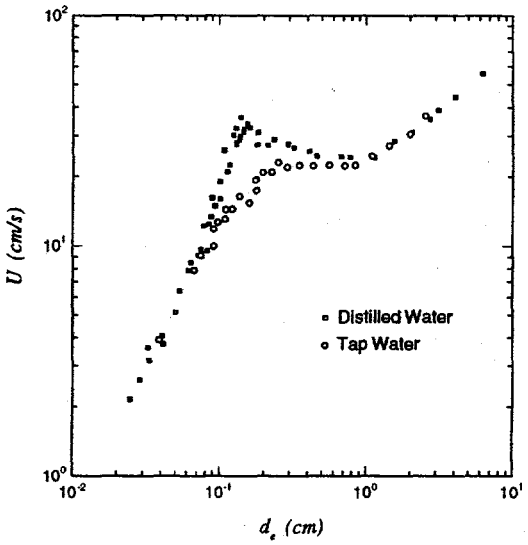

Figure 2: Bubble Rise Velocities Measured by Haberman and Morton [6]

the Haberman-Morton experiments was $2.55 \cdot 10^{-11}$. The flow did not separate, which is consistent with Hartunian and Sear's conclusion that flow separation occurs for $W > 3.2$ in clean, low Morton number fluids.

Numerous authors have suggested that the difference in bubble rise velocities between distilled water and tap water is due to the presence of surface active materials in tap water. A goal of the present work is to test this idea with computer simulations using the insoluble surfactant model. The program was tested by making a series of runs for $Re = 0.1$ and comparing the results with the Sadhal-Johnson theory. The results for the drag coefficient as a function of cap angle are shown in Fig. 3.

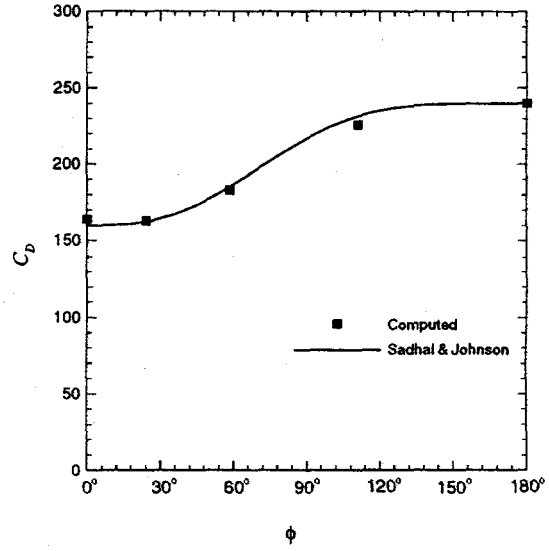

Figure 3: Computed Drag for $Re = 0.1, W = 0.02$ Compared with Sadhal and Johnson [9]

For tap water, Haberman and Morton's experiments indicate that the rise velocity of a bubble with $d_e = 1.4mm$ is approximately $17cm/s$. For such a bubble, $Re = 240$ and $W = 0.55$. A run was made with the latter values of Re and W and $\phi = 180°$. This corresponds to a bubble interface that is covered with surfactant (although the distribution is nonuniform). The computed Morton number was $2.62 \cdot 10^{-11}$. Table 1 contains a summary of runs with different cap angles, ϕ. For $\phi = 148°$, the Morton number is $2.55 \cdot 10^{-11}$. Thus, the insoluble surfactant model suggests that the rising bubbles are nearly covered

with surfactant. The value of S' is 0.0227. This may indicate that the ideal gas law is a reasonable way of estimating the surface tension. For example, Andrews et al. [2] estimated the maximum surface concentration of heptanoic acid to be $4.4 \cdot 10^{-10} cm^2/s$. The corresponding value of S' is 0.142. The average distance between molecules at close packing is about $6\mathring{A}$. Other molecules with comparable (low) solubilities in water will likely have about the same maximum surface concentration. The maximum bulk solubility of heptanoic acid in water at room temperature is $8mg/L$.

Table 1

Computer Runs for $Re = 240$, $W = 0.55$

ϕ	C_d	$M \cdot 10^{11}$	θ_{sep}	A'	χ	S
0^o	0.192	0.722		1.000	1.070	0
16.6^o	0.192	0.724		1.000	1.070	0.000011
26.0^o	0.194	0.729		1.000	1.070	0.000054
32.1^o	0.196	0.736		1.000	1.069	0.000120
36.5^o	0.198	0.744	8.06^o	1.000	1.068	0.00019
60.5^o	0.221	0.832	36.8^o	1.000	1.058	0.00139
90.8^o	0.353	1.33	58.1^o	1.000	1.039	0.00555
111.9^o	0.495	1.86	64.9^o	1.000	1.038	0.0103
134.8^o	0.633	2.38	67.3^o	1.000	1.041	0.0179
148.4^o	0.680	2.56	68.0^o	1.000	1.042	0.0227
166.4^o	0.697	2.62	68.5^o	1.000	1.043	0.0273
180^o	0.698	2.62	68.6^o	1.000	1.043	0.0287

Figure 4 shows the dimensionless surface tension as a function of the polar angle measured from the positive x-axis (i.e., measured from the direction of liquid motion in the bubble frame of reference). For this figure, $\phi = 180^o$. The surface tension varies by only a few percent even though this variation is sufficient to immobilize the interface. The surface tension at $\theta = 180^o$ is taken to be the surface tension of pure water. This assumption is not necessary. However, in modeling tap water, it produces results that agree well with experiment.

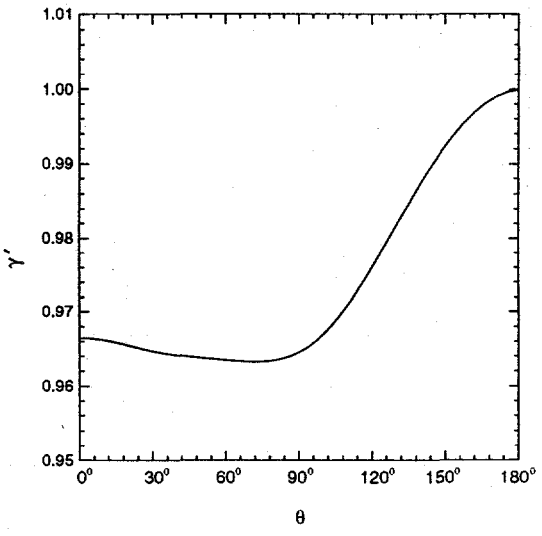

Figure 4: Dimensionless Surface Tension as a Function of Polar Angle for $Re = 240$, $W = 0.55$, and $\phi = 180^0$

Even in distilled water, bubbles that are smaller than about $0.8mm$ behave like rigid spheres. Thus, there is evidently enough surface active material to immobilize the surface of sufficiently small bubbles.

Does this low level of surfactant have an effect on the $1.4mm$ bubble considered earlier? Figure 5 shows the drag coefficient as a function of the cap angle for $Re = 490$, $W = 2.35$. One can obtain the observed rise velocity in two ways. One way is to assume that the interface is completely clean. The other way is to assume that the cap angle is approximately 105^o. The corresponding value of S' is 0.015, which is considerably lower than the value for tap water (0.023), but still significant. An important consequence of the adsorbed surfactant is that there is sizeable wake behind the bubble. The separation angle is close to 75^o. This may be consistent with the experimental observations made by Subramanian and Tien [12]. Subramanian and Tien performed visualization experiments using India ink. The experiments indicated the presence of a sizeable wake behind bubbles that were roughly $1mm$ in diameter even in distilled water. However, the ink may have acted as a surfactant. If the above inference is correct, it indicates that the boundary layer analyses based on potential flow theory such as those of Moore [13-14] are in inappropriate for bubbles in distilled water.

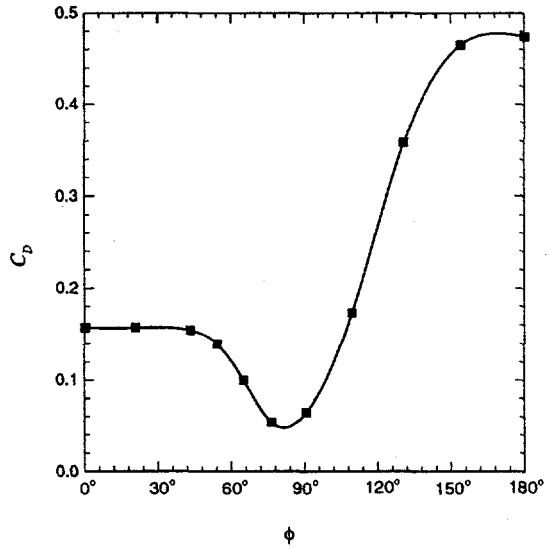

Figure 5: Drag Coefficient as a Function of Cap Angle for $Re = 490$, $W = 2.35$

The results for water indicate that surfactants have little effect on the rise velocities of bubbles with $W = 5$. The Reynolds number of these bubbles is 1600. Calculations at such a Reynolds number would be computationally expensive. According to Hartunian and Sears, the Reynolds number should have little effect on the stability of the bubble for $Re > 200$. Therefore, a run was made for a clean bubble with $Re = 200$ and $W = 5$. The corresponding Morton number is $4.26 \cdot 10^{-8}$. To determine the effect of surfactant on the wake, runs were made at smaller Reynolds numbers with different cap angles. To simplify the physical interpretation, the bubble volume was held constant. This was done by computing the Weber number as follows:

$$W = 5(\frac{Re}{200})^2. \tag{1}$$

For each Reynolds number, the cap angle was varied to obtain the correct Morton number. The Reynolds number for $\phi = 180^o$ is 167. Therefore, surfactant has relatively little effect of on the motion of bubbles of this size. However, the wake is considerably larger for contaminated interfaces. For the clean interface, the separation angle is 57.2^o, but, for complete coverage, the separation angle is 79.9^o. For a rigid sphere, the separation angle is 70.4^o.

CONCLUSIONS

The Ryskin-Leal simulation technique has been used to compute axisymmetric bubble motion at higher Reynolds numbers than previously reported. The effects of an insoluble surfactant have been included using

the ideal gas model. Assuming complete coverage, one obtains good agreement with the observations for a $1.4mm$ bubble in tap water. The computations predict the existence of a large wake behind the bubble. The computations also reveal the possibility that the bubble may possess a large wake in distilled water. This suggests that boundary layer treatments based on potential flow theory may be inappropriate even for distilled water.

Computations at large Weber numbers show that the the surfactant has little effect on the bubble rise velocity. However, the bubble wake is increased substantially.

ACKNOWLEDGEMENT

The author gratefully acknowledges helpful discussions with Dr. Brian Davison and Dr. Charles Maldarelli.

REFERENCES

1. R. BAJPAI, J.E. THOMPSON, and B.H. DAVISON, "Gas holdup in three-phase immobilized-cell Bioreactors," *Appl. Biochem. Biotech.* 24/25, 485-496 (1990).

2. G.F. ANDREWS, R. FIKE, and S. WONG, "Bubble hydrodynamics and mass transfer at high Reynolds number and surfactant concentration," *Chem. Eng. Sci.* 43, 1467-1477 (1988).

3. G. RYSKIN and L.G. LEAL, "Orthogonal mapping," *J. Comput. Phys.* 50, 71-100 (1983).

4. G. RYSKIN and L.G. LEAL, "Numerical solutions of free-boundary problems in fluid mechanics. Part 1. The finite difference technique," *J. Fluid Mech.* 148, 1-17 (1984).

5. G. RYSKIN and L.G. LEAL, "Numerical solutions of free-boundary problems in fluid mechanics. Part 2. Buoyancy-driven motion of a gas bubble through a quiescent liquid," *J. Fluid Mech.* 148, 19-35 (1984).

6. W.L. HABERMAN and R.K. MORTON, "An experimental investigation of the drag and shape of air bubbles rising in various liquids," *David Taylor Model Basin, Rep.* no. 802 (1953).

7. P.G. SAFFMAN, "On the rise of small air bubbles in water," *J. Fluid Mech.* 1, 249-275 (1956).

8. R.A. HARTUNIAN and W.R. SEARS, "On the instability of small gas bubbles moving uniformly in various liquids," *J. Fluid Mech.* 3, 27-47 (1957).

9. S.S. SADHAL and R.E. JOHNSON, "Stokes flow past bubbles and drops partially coated with thin films. Part 1. Stagnant cap of surfactant film - exact solution," *J. Fluid Mech.* 126 , 237-250 (1983).

10. H.A. STONE and L.G. LEAL, "The effects of surfactants on drop deformation and breakup," *J. Fluid Mech.* 220, 161-186 (1990).

11. R. PAN, C. MALDARELLI, B. ENNIS, and J. GREEN, "Mixed diffusive-kinetic control in the adsorption of the polyethoxylated surfactant $C_{12}E_6$ to the clean air/water interface," (submitted for publication, 1994).

12. G. SUBRAMANIAN and C. TIEN, "Longitudinal mixing in liquid columns due to bubble motion," Syracuse University, Final Report to Federal Water Pollution Control Administration for Grant No. WP 00922 (1970).

13. D.W. MOORE, "The rise of a gas bubble in a viscous liquid," *J. Fluid Mech.* 16, 113-130 (1963).

14. D.W. MOORE, "The velocity of rise of distorted gas bubbles in a liquid of small viscosity," *J. Fluid Mech.* 23, 749-766 (1965).

STRUCTURE AND MODELING OF TURBULENCE

E.A. Novikov

Institute for Nonlinear Science
University of California, San Diego
La Jolla, CA 92093-0402

ABSTRACT

The "vortex strings" scale $\ell_s \sim LRe^{-3/10}$ (L-external scale, Re - Reynolds number) is suggested as a grid scale for the large-eddy simulation. Various aspects of the structure of turbulence and subgrid modeling are described in terms of conditional averaging, Markov processes with dependent increments and infinitely divisible distributions.

The major request from the energy, naval, aerospace and environmental engineering communities to the theory of turbulence is to reduce the enormous number of degrees of freedom in turbulent flows to a level manageable by computer simulations. The vast majority of these degrees of freedom is in the small-scale motion. The study of the structure of turbulence provides a basis for subgrid-scale (SGS) models, which are necessary for the large-eddy simulations (LES). The general strategy, developed in this work is summarized in the Diagram.

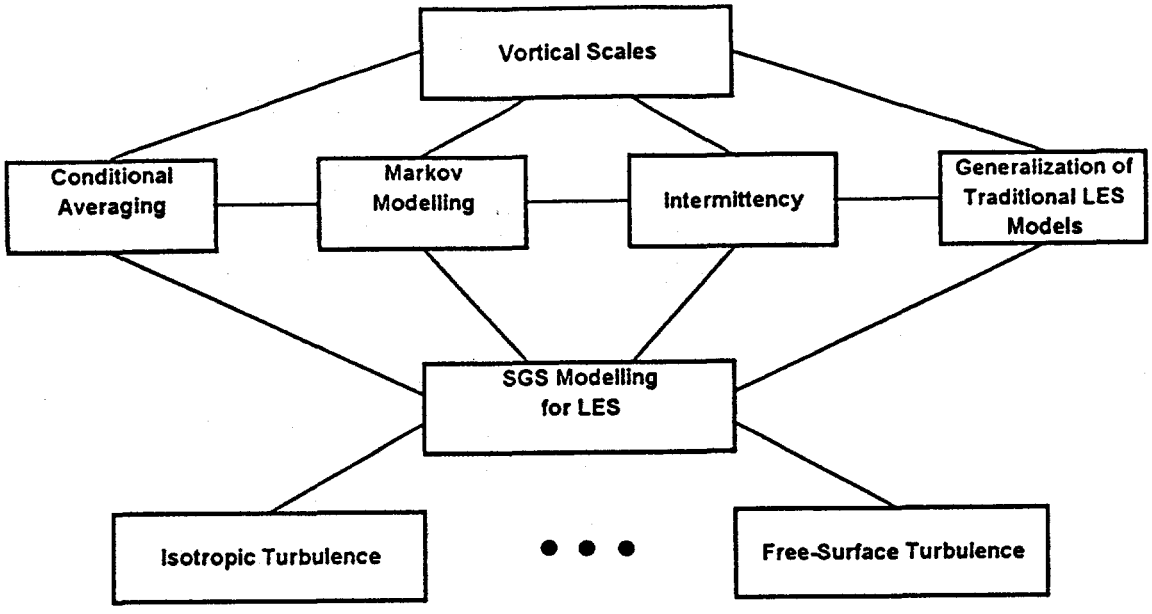

Diagram: Structure and Modeling of Turbulence

The first block in the Diagram ("vortical scales") is about an interface between numerics and a model. It seems natural to choose a grid scale for LES to be of the order of the "vortex strings" scale[1] $\ell_s \sim LR^{-3/10}$ (L-external scale, $Re = VL\nu^{-1}$ - Reynolds number, V - characteristic velocity, ν - molecular viscosity). At this scale, the most important (physically and numerically) nonlinear effect of vortex stretching in three-dimensional (3D) turbulence does not produce a flux in the vorticity correlations. Thus, we expect a smooth connection between numerics and modeling at this scale. The effective number of degrees of freedom with such grid scale is $N_s \sim (L/\ell_s)^3 \sim Re^{9/10}$. A potential reduction in the numerical capacity is huge if we compare N_s with the classical estimate[2] $N \sim Re^{9/4}$, based on the Kolmogorov internal scale $\ell_\nu = \nu^{3/4}\epsilon^{-1/4}$ (ϵ - mean rate of the energy dissipation).

Next in the Diagram is a horizontal row of four blocks, representing various aspects of the statistical structure of turbulence and ingredients of SGS modeling. The first block in this row refers to the conditional averaging of the Navier-Stokes equations with fixed vorticity in a point (for 3D flow). It was analytically predicted[3-5] that for high Re the effect of vortex stretching is statistically balanced with viscous dissipation on any level of fixed vorticity ω and other terms in the vorticity balance are $\sim Re^{-1/2}$. This prediction was recently confirmed by direct numerical simulations (DNS)[6], which also revealed that the conditionally averaged rates of vortex stretching and dissipation increase exponentially with ω. It was also predicted[3-5] and recently confirmed by DNS[7] that conditionally averaged vorticity field $\overline{\mathbf{\Omega}}(\mathbf{r},\omega)$, as a function of distance $\mathbf{r}$ from a point with fixed vorticity ω, has a characteristic twist of vortex lines, connected with the effect of vortex stretching. It was also argued[6] that local imbalance between vortex stretching and dissipation leads to the formation and destruction of twisted vortex strings with characteristic scale ℓ_s indicated above. Having the field $\overline{\mathbf{\Omega}}$, we can construct a relaxation scheme[8], which will make vorticity on a grid in LES to be consistent with $\overline{\mathbf{\Omega}}$. We plan to test such a scheme in the near future.

Let us note, that instead of vorticity we can use microcirculations (velocity circulations over infinitely small fluid contours), which are inviscid invariants of motion. Such approach separates the effect of vortex stretching into an additional linear equation (for fluid surface elements) with independent initial condition[9]. Conditional averaging was also applied to the free-surface turbulence[10] with the use of the fully nonlinear dynamical boundary condition on free surface.

The second block in the same row in the Diagram refers to the Lagrangian and Eulerian description of velocity increments in terms of Markov processes with dependent increments, consistent with the Navier-Stokes equations[11-14]. The 3D vector of velocity increments (vi) can be presented in the form:

$$u_i = v_i(\mathbf{x}+\mathbf{r}) - v_i(\mathbf{x}) = u_r n_i + \tilde{u}_i, \qquad n_i = r_i r^{-1} \tag{1}$$

Here $u_r = u_i n_i$ is the radial (longitudinal) component of vi, $\tilde{u}_i$ is the transversal vi, normal to the separation distance $\mathbf{r}$. In the inertial range ($\ell_\nu \ll r \ll L$) we have the Kolmogorov result:

$$< u_r^2 >= -\frac{4}{5}\epsilon r \tag{2}$$

which can be written in tensor form[11]:

$$< u_i u_j u_k >= -\frac{4}{15}\epsilon(r_i\delta_{jk} + r_j\delta_{ki} + r_k\delta_{ij}) \tag{3}$$

Here $< >$ means statistical (unconditional) averaging. The Kolmogorov result (2) has been originally obtained for decaying turbulence. The same result was derived[15], by using

a special functional formalism[15,16], for statistically stationary turbulence with large-scale random forces, supplying energy. This formalism was also used in the derivation of the balance equation for the vorticity correlations[1] leading to the indicated above scale ℓ_s.

Two components of *vi* are physically different, even simply because of incompressibility condition:

$$\frac{\partial}{\partial r_i} < u_i u_j >= 0 \tag{4}$$

Loosely speaking u_r and $\tilde{u}_i$ signify correspondingly deformation along the vector **r** and rotation around a vector, normal to **r**. Statistical preference of negative u_r, emphasized by (2), corresponds to compression of fluid element in the direction of **r** and (because of incompressibility) expansion in a normal direction. Since $\tilde{u}_i$ represents vortex, oriented normally to **r** , we can interpret (2) as an inertial range manifestation of the same effect of vortex stretching, which is analyzed by conditional averaging (see above). Probability density function (*pdf*) for the vector *vi* has unusual form[13,14]. Asymptotically (when $u^2 \gg < u^2 >$) it reduces to the function of peculiar argument:

$$P(u_r u_i, r) = (\epsilon r \tilde{u})^{-3/4} f\left[\frac{u_r^2 + \tilde{u}^2}{(\epsilon r \tilde{u})^{1/2}}\right] \tag{5}$$

$$\tilde{u}^2 \equiv \tilde{u}_i^2, \qquad f(z) = N_{\pm}^{-1} \exp\{-\theta_{\pm} z^{2/3}\} \tag{6}$$

Here constants N and θ are different for the cases $u_r > 0$ and $u_r < 0$, which is reflected by subscript $\pm$. This asymptotic was obtained[13] without Markovian assumption and corresponds to experimentally observed exponential behavior of *pdf* for u_r. The global *pdf* for the vector *vi* is obtained[13,14] assuming that relative velocity of fluid particles is Markovian with a local relaxation and simplest forcing (diffusion in the velocity space). The Markovian assumption is consistent with (3)-(6) and with the classical similarity. It also gives the Lagrangian description of turbulence[11–14], which corresponds, in particular, to the Richardson law:

$$< r^2(t) >_L \sim \epsilon t^2 \tag{7}$$

Here $r(t)$ is the distance between two fluid particles and subscript L indicates the Lagrangian ensemble of averaging. The exact relations between Lagrangian and Eulerian descriptions[17,18] are used in this approach.

Preliminary LES tests of a Markov type SGS model give positive results. However, intermittency effects, which are important physically and numerically, have to be included into SGS modeling. This leads to the next block in the same row in the Diagram. The intermittency is described in terms of the breakdown coefficients (*bdc*) for the energy dissipation[19,12,20]. The most recent progress is associated with the imbedding of self-similar intermittency into the theory of infinitely divisible distributions[20]. This gives us access to the well developed mathematical apparatus[21]. An intermittency correction in terms of *bdc* for a simple SGS model was obtained in Ref. [12]. For the comparison with the experiment we use data sets, obtained from the big Russian wind tunnel[22], and plan to use data sets from atmospheric boundary layer.

The last block in the same row in the Diagram refers to traditional SGS models (Smagorinsky[23], Bardina[24]) and their broad generalization[25,26].

All models are coming into a melting pot - block "SGS modeling for LES", which serves as a "free market" for SGS models. Here we use the test-filtering procedure (running LES with two different resolutions) in order to determine dynamically weighing coefficients to all models and to find optimal combinations of models for different applications. These

applications, represented in the last row in the Diagram, range from the simplest (isotropic turbulence) to the most complex (free-surface turbulent flows with fully nonlinear dynamical conditions on free surface).

Each of these blocks in the Diagram is an independent and fruitful area of research. By putting them together and focusing on LES implementation, we can see new connections and a more general picture of the structure and modeling of turbulence is developing.

ACKNOWLEDGEMENT

This work is supported by the U.S. Department of Energy under Grant No. DE-FG03-91ER13188, with Dr. Oscar P. Manley as program manager.

REFERENCES

1. E.A. NOVIKOV, *Phys. Rev. Let.* **71**, 2718 (1993).
2. L.D. LANDAU and E.M. LIFSHITZ, "*Fluid Mechanics*", Pergamon, 1959.
3. E.A. NOVIKOV, *Dokl. Akad. Nauk SSSR* **12**, 299 (1967) [*Sov. Phys. Dokl.* **12**, 1006 (1968)].
4. E.A. NOVIKOV, in Proc. of Monte-Verita Sympos. "New Approaches and Concepts in Turbulence" 1991, ed. T. Dracos and A. Tsinober (Birkauser, Basel, 1993); *J. Phys. A* **25**, L657 (1992).
5. E.A. NOVIKOV, *Fluid Dyn. Res.* **12**, 107 (1993); *Phys. Rev. E* **49**(2), R975 (1994); *J. Phys. A.* **27**, L797 (1994).
6. E.A. NOVIKOV and D.G. DOMMERMUTH, *Modern Phys. Lett. B* **8**(23), 1395 (1994).
7. D.G. DOMMERMUTH, R.C.Y. MUI and E.A. NOVIKOV, "Conditionally averaged vorticity field", in preparation.
8. E.A. NOVIKOV, "Conditionally averaged dynamics of turbulence, new scaling and stochastic modeling", in "Lévy Flights and Related Phenomena in Physics" (eds. U. Frish, B. Mandelbrot, M. Shlesinger and G. Zaslavsky), Springer, 1995, to be published.
9. E.A. NOVIKOV, "Microcirculations in Turbulent Flows", submitted to *Phys. Rev. E.*
10. E.A. NOVIKOV, "Conditional averaging of turbulent free surface", submitted to *Phys. Rev. E.*
11. E.A. NOVIKOV, *Phys. Fluids A* **1**, 326 (1989).
12. E.A. NOVIKOV, *Phys. Fluids A* **2**, 814 (1990).
13. E.A. NOVIKOV, *Phys. Rev. A* **46**(10), R6147 (1992).
14. G. PEDRIZZETTI and E.A. NOVIKOV, *J. Fluid Mech.* **280**, 69 (1994).

15. E.A. NOVIKOV, *Zh. Eksp. Teor. Fiz* **47**, 1919 (1964) [*Sov. Phys. JETP* **20**, 1290 (1965)].

16. W.D. McCOMB, "The Physics of Fluid Turbulence", Appendix H (Claredon, Oxford, 1990).

17. E.A. NOVIKOV, *Appl. Math. Mech* **33**, 862 (1969).

18. E.A. NOVIKOV, *Phys. Fluids* **29**, 3907 (1986).

19. E.A. NOVIKOV, *Appl. Math. Mech.* **35**, 231 (1971).

20. E.A. NOVIKOV, *Phys. Rev. E* **50**(5), R3303 (1994).

21. W. FELLER, "An Introduction to Probability Theory and its Applications" (Wiley, New York, 1991, reprinted from 1966 edition) Vol. 2.

22. A.A. PRASKOVSKY, private communication.

23. J. SMAGORINSKY, *Mon. Weather Rev.* **91**, 99 (1963).

24. J. BARDINA, J.H. FERZIGER and W.C. REYNOLDS, AIAA 80-1357 (1980).

25. T.S. LUND and E.A. NOVIKOV, *Ann. Res.*, CTR, Stanford, 27 (1992).

26. D.G. DOMMERMUTH and E.A. NOVIKOV, "Direct-numerical and large-eddy simulations of turbulent free-surface flows", Proc. Sixth Internat. Conf. on Numerical Ship Hydrodynamics, Iowa City, p. 239-270 (1993).

CONTAMINANT DISPERSAL IN BOUNDED TURBULENT SHEAR FLOW

James M. Wallace, Peter S. Bernard, Kwo-Fu Chiang & Lawrence Ong

Department of Mechanical Engineering
University of Maryland, College Park, MD 20742, U.S.A.

ABSTRACT

The dispersion of smoke downstream of a line source at the wall and at $y^+ = 30$ in a turbulent boundary layer has been predicted with a non-local model of the scalar fluxes, $\overline{uc}$ and $\overline{vc}$. The predicted plume from the wall source has been compared to high Schmidt number experimental measurements using a combination of hot-wire anemometry to obtain velocity component data synchronously with concentration data obtained optically. The predicted plumes from the source at $y^+ = 30$ and at the wall also have been compared to a low Schmidt number direct numerical simulation . Near the source, the non-local flux models give considerably better predictions than models which account solely for mean gradient transport. At a sufficient distance downstream the gradient models gives reasonably good predictions.

INTRODUCTION

The prediction of thermal and mass concentration fields diffusing within turbulent shear flows is of paramount importance in numerous applications in environmental science and engineering. Current prediction methods are mainly confined to simple Gaussian diffusion models [1], solutions of the Reynolds averaged equations for which the turbulent scalar flux rate must be modeled [2-4] and to random flight models which mimic the motion of individual tracers in turbulence through an assumed Markov process [5-8]. Closure models for the scalar flux correlation usually have adopted the gradient form in the absence of better knowledge about the physics of scalar transport, although it has long been recognized [9-11] that gradient transport is incapable of representing the short time dispersion near the source of contaminant plumes.

While many tests of the predictions of random flight and closure models have been made against experimental data, until recently [12-17] such comparisons have not been in controlled settings where accurate information about the turbulence scales and other correlations appearing in the models are available. As a result, it has been difficult to discern what the relative strengths of the two methodologies are, and especially whether the substantially greater computational cost of random flight methods in comparison to closure models pays off by providing greater accuracy in the prediction of the near field of scalar dispersal.

Past work of our research group [17] has provided a successful analysis of some important aspects of the physical mechanisms associated with the scalar flux in the near field of plumes. This uses a Lagrangian technique which had heretofore been instrumental in exploring the mechanisms of Reynolds stress and vorticity transport [18 - 20]. Among the accomplishments of this work was a demonstration that the turbulent flux in the near field of plumes is due to meandering of the turbulent field over the source, a physical process bearing no relationship to gradient diffusion. It was also shown, however, that gradient transport physics does emerge at locations far enough downstream of the source. Extensive tests of closure models versus random flight models were made for the case of Prandtl number 0.71 in which a direct numerical simulation (DNS) of the plume flow was used to supply an accurate solution. These tests showed the closure models to be

generally superior to the random flight approach both in speed and accuracy, though serious errors near the source were apparent due to the inappropriateness of the gradient model.

A new non-local turbulent transport theory has been derived as an outgrowth of the previous formal Lagrangian analysis of transport using ensembles of backward particle paths [21]. This is based on replacing ensemble averaging by spatial averaging over the initial locations of the fluid particles. The probability density function (*pdf*) of initial particle position – which plays a critical role in the theory – is derived heuristically and shown to be in good agreement with available data. Applications of the approach to the scalar field in a fully developed channel flow with a uniform source and to a spanwise line source plume, show the non-local formulation to offer some considerable improvements over gradient transport models.

We have carried out closely coordinated experimental, numerical and modeling studies of diffusion of near wall plumes. The inherent restriction of DNS to low Prandtl (or Schmidt) number plumes in relatively simple geometries at low Reynolds numbers places a high premium on well designed experiments to guide the development and testing of scalar transport models suitable for realistic complex flow conditions. For this purpose we have experimentally obtained the mean scalar concentration and concentration fluxes in plumes resulting from a spanwise line source of scalar smoke particles originating at the wall of a turbulent boundary layer. Comparisons for high Schmidt numbers, when combined with the $Pr = 0.71$ number model comparisons and evaluations with the DNS, give a fairly complete picture of the capabilities of current models under a significant range of shear flow conditions. Our analysis of the near source plume diffusion indicates how models need to be formulated to acquire a greater measure of physical accuracy. Implementation and testing of one such model, using experimental data as the essential and final arbiter for determining physical appropriateness, forms the main thrust of this paper.

EXPERIMENTAL FACILITY, INSTRUMENTATION AND METHOD

Experiments (cf.[22-23]) have been carried out in a turbulent boundary layer at $R_\tau \approx 725$ ($R_\theta \approx 1600$) in which smoke was seeped into the sublayer through a downstream facing slot at a location 7 m downstream of the boundary layer trip. The smoke, formed by smoldering incense, was passed through steel wool to remove the tar and then through a heat exchanger to bring it to the temperature of the flow. The smoke generation can be maintained in an equilibrium state for up to two hours and can be reproduced from experiment to experiment. The particle sizes ranged in diameter from $0.12 - 1.92$ μm, and thus follow the flow quite well. Care has been taken to control the smoke injection from the slot so as not to create a wall jet.

In oder to obtain concentration flux values, the U (streamwise, x-direction) and V (wall normal, y-direction) velocity components were measured with a calibrated 4-sensor hot-wire probe, which accounted for binormal cooling of the sensors. It was positioned in a sheet of laser light, oriented in the $x - y$ plane, which illuminates the dispersing scalar smoke particles. In order to create this light sheet, the beam from a 15 W copper-vapor pulsed laser was passed through a set of spherical and cylindrical lenses to form an approximately 1mm thick sheet. The illuminated smoke was photographed on Kodak TMAX instrumentation film (ASA 400 and resolution of 400 lines/mm) with a high speed Photonec 16 mm movie camera during the acquisition of synchronized hot-wire data. These photographs constitute an ensemble of images with light intensities which were subsequently mapped into quantitative values of scalar concentration by means of a calibration and transformation procedure, described below. Averaging over the ensemble yielded contours of mean concentration in the plane of illumination; the averaged products of the instantaneous velocity fluctuations, u and v, with the instantaneous concentration fluctuation values yielded the scalar fluxes.

The images recorded on film were digitized with a personal computer controlled image acquisition system, which consist of a Reticon 8 bit (256 grey levels), 2048 pixel line scanning camera and a motorized film transport device. The averaged digitized image was contrast-enhanced to maximize the range of usable grey levels. Particle sampling was carried out isokinetically at several locations above the wall. The grey level intensities from the images were calibrated against the measured number density of the smoke particles, sorted by particle size with a Laser Aerosol Spectrometer, over a matrix of locations for the same flow and particle emission conditions. The dependence of the light intensity on particle diameter, d, was accounted for by determining an effective number density, N_{eff}, for an arbitrarily chosen particle size (from within the size range), that would scatter

(4) which accounts for any systematic relationship between the velocity field and alterations to C along particle paths. These changes may occur either by diffusion or by the presence of sources in the flow.

Equation (4) may be made the basis for a physically consistent transport model by replacing the ensemble averages by averages over initial particle location. A detailed account of this methodology may be found in [21]. Here, some of the principal ideas are summarized together with numerical results. First, the theory appropriate to a uniform constant source of strength $2/R_eS_c$ is briefly discussed; to be followed by consideration of plume flows. For the wall normal flux in a channel flow (4) gives

$$\overline{vc}(y) = \overline{v_a(\overline{C}_b - \overline{C}_a)} + \overline{v_a(C_a - C_b)}. \tag{5}$$

The formal Lagrangian expansion

$$v_a = v_b + (\overline{V}_b - \overline{V}_a) + (V_a - V_b), \tag{6}$$

to which may be added the natural approximation

$$v_b \approx \frac{y - y'}{T_{22}}, \tag{7}$$

where y' denotes the y coordinate of the particle at b and T_{22} is a Lagrangian integral time scale, provides a basis for modeling v_a in (5). For channel flow $\overline{V}_b - \overline{V}_a = 0$ while the fluid particle acceleration can be modeled as

$$V_a - V_b = -T_{22}\frac{\partial \overline{P}^*}{\partial y}, \tag{8}$$

where the asterisk is meant to denote an average between y' and y. Similarly, the approximation

$$C_a - C_b = \frac{T_{22}}{R_eS_c}\left(\frac{d^2\overline{C}^*}{dy^2} + 2\right) \tag{9}$$

may be developed.

Now substituting volume averages over the initial locations of the fluid particles for the ensemble averages in (5), and using (6 - 9) it follows that

$$\overline{v_a(\overline{C}_b - \overline{C}_a)}(y) = -\int_0^h \frac{y' - y}{T_{22}}(\overline{C}(y') - \overline{C}(y))p(y', y)dy' - T_{22}\int_0^h (\overline{C}(y') - \overline{C}(y))\,\frac{\partial \overline{P}^*}{\partial y}\,p(y', y)\,dy', \tag{10}$$

and

$$\overline{v_a(C_a - C_b)} = -\int \frac{y' - y}{R_eS_c}\,\frac{d^2\overline{C}^*}{dy^2}\,p(y', y)\,dy' - \int \frac{\partial \overline{P}^*}{\partial y}\,\frac{T_{22}^2}{R_eS_c}\left(\frac{d^2\overline{C}^*}{dy^2} + 2\right), \tag{11}$$

where h is the channel height and $p(y', y)$ is the *pdf* for the chance that a fluid particle originating at y' travels to y over a mixing time. In each of the terms in (10), the identity $\overline{C}_b - \overline{C}_a = \overline{C}(y') - \overline{C}(y)$ is used.

Equations (10) and (11) are useful once an explicit formula for $p(y', y)$ is provided. If it is assumed that the *pdf* of v at any point in a flow is Gaussian, then it may be shown heuristically that

$$p(y', y) = \frac{1}{\sqrt{2\pi}l_2}e^{-\frac{(y'-y)^2}{2(l_2)^2}} \tag{12}$$

where $l_2 \equiv \sqrt{\overline{v^2}T_{22}}$. This equation is exact for the case of a linear distribution of $\overline{C}$ in homogeneous turbulence.

Near boundaries it can be expected that the *pdf* of v departs from Gaussianity, so some modification to (12) is necessary near solid walls. For a fixed wall at $y = 0$, $p(y', y) = 0$ for $y' = 0$,

the same amount of light as the poly-sized particle cloud:

$$I \propto \sum d_i^2 N_i = d_{eff}^2 N_{eff}, \tag{1}$$

where I is the average grey-level intensity at the corresponding concentration measurement location. Thus at each node of the calibration matrix,

$$N_{eff} = \left(\frac{d_i}{d_{eff}}\right)^2 N_i. \tag{2}$$

When this effective number density is plotted against the average light intensity, as shown in Fig. 1, a linear calibration relationship between these two variables is obtained. With this relationship, the grey level intensities in each instantaneous image were converted to effective concentration values. The value of the particle flux was determined across the vertical plane at $x^+ = 95$, and this value was used to set the release rate of the source term in the model, to be described below.

NUMERICAL SIMULATION AND MODELING

To analyze the physics of transport, ensembles of backward particle paths were obtained from a direct numerical simulation of a line source plume developing in turbulent channel flow. The paths were computed from a large set of previously computed and stored consecutive numerical velocity fields. The simulation [17] has a mesh with $96 \times 97 \times 96$ points in the streamwise, wall-normal and spanwise directions, respectively, and a computational box of dimensions $1822 \times 290 \times 683$, expressed in wall units. The numerical scheme consists of a pseudo-spectral method to solve the full incompressible 3D Navier-Stokes equations. The velocity and scalars on off nodal points needed in the path computations are obtained through tricubic interpolation [24]. The Reynolds number of the simulation is $R_\tau = U_\tau h/\nu = 145$, where U_τ is the friction velocity and h is the channel halfwidth. The mean velocity and Reynolds stresses for the simulation agree closely with those found in previous studies [25]. In a further test of the code, a spatially uniform source flow was computed and shown to agree very closely with previous simulations [12,13].

We have attempted to develop a physically accurate model of scalar transport using a Lagrangian decomposition of the scalar flux correlation, $\overline{u_i c}$, into identifiable physical processes. This correlation appears naturally in the averaged scalar transport equation

$$\frac{\partial \overline{C}}{\partial t} + \overline{U}_i \frac{\partial \overline{C}}{\partial x_i} = -\frac{\partial \overline{u_i c}}{\partial x_i} + \frac{1}{ReSc} \nabla^2 \overline{C} + Q, \tag{3}$$

where C is the concentration field, $\overline{C}$ and c are its mean and fluctuating parts with overbars denoting ensemble averaging, u_i is the velocity fluctuation vector, $\overline{U}_i$ is the mean velocity vector and Q is a source term for the scalar. The basis for the model described below is the identity

$$\overline{u_{i_a} c_a} = \overline{u_{i_a} c_b} + \overline{u_{i_a}(\overline{C}_b - \overline{C}_a)} + \overline{u_{i_a}(C_a, -C_b)}, \tag{4}$$

where the subscript a refers to the given endpoint of a large ensemble of fluid particle paths at time t which are at the random locations b at an earlier time $t - \tau$. As discussed elsewhere in related contexts and verified numerically [17-20], the mixing condition $\overline{u_{i_a} c_b} = 0$ is satisfied for τ large enough. We define the mixing time, say τ_m, as the smallest interval at which $\overline{u_{i_a} c_b} \approx 0$. τ_m may be thought of as the time over which events in the flow cause the correlation between u_i and c to develop. Equation (4) thus shows that for times $\tau > \tau_m$, $\overline{u_i c}$ is a result of the processes represented by the last two terms.

The second term on the right-hand side of (4) represents transport arising from the displacement of fluid particles. It is a formal statement of the classical argument that in the presence of a gradient in the mean scalar field, turbulent eddying motion should lead to a net transport. In particular, the resulting directional dependence of the scalar flux on the gradient of $\overline{C}$ is created by fluid particles carrying on average – without alteration – the local mean scalar field of their starting point to their final point over a mixing time. Non-gradient sources of transport are contained in the last term in

since fluid particles on the surface have no chance of migrating to interior points in the flow. A convenient means of enforcing this condition is to generalize (12) via

$$p(y',y) = \frac{1}{\sqrt{2\pi}l_2^*}\left(e^{-\frac{(y'-y)^2}{2(l_2^*)^2}} - e^{-\frac{(y'+y)^2}{2(l_2^*)^2}}\right) \tag{13}$$

where $l_2^* = \min\{l_2, y/3\sqrt{2}\}$, a condition assuring that $\int_0^h p(y',y)dy' \approx 1$ for y near the boundary. Numerical computations show that l_2^* slightly deviates from l_2 only in the region $y^+ \leq 25$.

Despite the heuristic derivation of (13), its general validity is supported by comparisons with measurements of $p(y',y)$ obtained in a turbulent channel flow. Fig. 2 shows predictions of $p(y',y)$ at $y^+ = 7.4$ and $y^+ = 36.6$ obtained from a direct numerical simulation compared to (13). It is clear that the latter gives a reasonable estimate of $p(y',y)$ including an excellent prediction of the scale of its support. The model curves do not show the effect of the boundary to the same degree as the DNS results, suggesting that (13) does not sufficiently take into account the departure of the *pdf* of v from Gaussianity near the wall. On the whole, however, (13) provides a sufficiently accurate description to make a useful implementation of the theory.

Application of (5) and equivalent formulas for $\overline{uc}$ give excellent predictions of channel flow containing a uniform source as shown in [21]. It was found that the first term in (10) is a dominant effect in wall normal transport and may be used by itself to most efficiently capture the important physics for predictive schemes. Now we concentrate on an extension of the method suitable for two-dimensional plumes. In this case, previous work [17] showed that the physics of transport along a plume is distinctly different near and far from the source. In the former case, transport is primarily due to the effect captured in the last term in (5), which represents fluid particles picking up the scalar as they meander through the source. Away from the source the physics are well accounted for by the first term in (10). Proceeding formally, we have that near the source the most important effect is

$$\overline{v_a(C_a - C_b)} = -\int \frac{y'-y}{T_{22}}\left(\int_{-T_{22}}^{0} Q(s)ds\right)\, p(\mathbf{x}',\mathbf{x})d\mathbf{x}' \tag{14}$$

where $\int Q(s)ds$ is the amount of scalar acquired by a fluid particle arriving at a given point $\mathbf{x}$ after leaving from $\mathbf{x}'$. Note that for constant Q, this term is zero, which is why it does not appear in (11). An estimate of $\int Q(s)ds$ for fluid particles traveling from $\mathbf{x}'$ to $\mathbf{x}$ must be found if (14) is to be evaluated. Here it will be assumed that the only paths for which $\int Q(s)ds \neq 0$ are those for which the source lies between $\mathbf{x}'$ and $\mathbf{x}$, i.e. $\mathbf{x}'$ lies in the 'shadow' behind the source as viewed from $\mathbf{x}$ (see Fig. 2). Thus, every fluid particle leaving from the region contained within the dashed line in the figure and arriving at $\mathbf{x}$ after a mixing time is assumed to pass over the source, while no others do so. This probabilistic model is consistent with the approximations such as (7) and our intuitive sense of where the particles most likely to cross the source come from.

To evaluate (14), the source region is discretized into small sections represented by the grid as shown in Fig. 3. For each of these, such as the one which is dark shaded, it is assumed that all fluid particles starting out in the region contained in the dashed outline will pass through this part of the source and thus have a non-zero value of $\int Q(s)ds$. The amount of $\int Q(s)ds$ can be estimated as the local magnitude of the source in a particular area, say Q_{ij} for the i,jth box, times the time it takes the fluid particle to cross it, say τ. The latter may be estimated as the characteristic dimension of the grid spacing Δx divided by the speed at which the fluid particle passes over this area. The estimate may then be made:

$$\int Q(s)ds = Q_{ij} \times \frac{\Delta x}{\sqrt{(x-x')^2 + (y-y')^2}/\tau} \tag{15}$$

The width of the dashed region behind the source element is given by the small number Δx, so that after substitution of (15) into (14), it is justifiable to collapse the area integral in (14) to just a line integral along the length of the shadow region in Fig. 3. Collecting these results together gives

$$\overline{vc}(y) = - \int \frac{y'-y}{T_{22}} (\overline{C}(\mathbf{x}') - \overline{C}(\mathbf{x})) p(\mathbf{x}', \mathbf{x}) d\mathbf{x}'$$

$$- \sum_{ij} \frac{Q^*_{ij} Y_{ij}}{2\pi l_1 \sqrt{1-\rho^2} R_{ij}} \int_{-\infty}^{-R_{ij}} da \, e^{-\frac{a^2 Y_{ij}^2}{2R_{ij}^2} - \frac{\left[a\left(\frac{X_{ij}}{R_{ij}} - \rho \frac{Y_{ij}}{R_{ij}}\right) + \overline{X}\right]^2}{2(1-\rho^2)}} \tag{16}$$

where $Q^*_{ij} = Q_{ij} \Delta A_{ij}$, ΔA_{ij} is the area of the (i,j)th source element, $X_{ij} = (x - x_{ij})/l_1$, $Y_{ij} = (y - y_{ij})/l_2$, $R_{ij} = \sqrt{(x-x_{ij})^2 + (y-y_{ij})^2}/l_1$ and $\overline{X} = \overline{U} T_{22}/l_1$.

An equivalent analysis of the streamwise flux may be performed with similar results. The complete non-local closure may be applied to the study of plume flows in a wide variety of circumstances.

RESULTS

Fig. 4 illustrates the improvement over a gradient law which is attainable from (16). Predictions of $\overline{vc}$ are given along the line $y^+ = 43.5$ through a plume centered at $x^+ = 0, y^+ = 30$. Equation (16) shows very good agreement with the DNS while the gradient model is subject to extremely large errors in the vicinity of the source. These only diminish to a reasonable level by $x^+ = 250$, after which point the gradient model appears to be a reasonable approximation. The different roles of the two terms in (16) is shown in Fig. 5. Near the origin of the plume the displacement effect is negligible and transport is entirely due to the source term. Downstream, the situation is reversed as the displacement mechanism begins to dominate transport by $x^+ = 200$. These results are fully consistent with the previous evaluation of (5) using ensembles of particle paths, [17]. It should be noted that the results from the DNS shown here have not been sufficiently averaged to remove some of the obvious statistical variations. This is most true of the gradient curve in Fig. 4 which was evaluated from finite differences of the mean scalar field computed in the DNS.

Contours plots of $\overline{C}$ determined from the gradient model, the DNS and experiment are shown in Fig. 6. Clearly the gradient model does not capture the character of the DNS plume near the source. This is shown even clearer in Fig. 7 where the values of $\overline{C}$ along the wall are plotted. Further downstream the gradient model, the DNS and the experiment are in relatively good agreement. Experimental values of the fluxes $\overline{uc}$ and $\overline{vc}$, were measured; they show the expected trend in sign and magnitude in the buffer layer and in the lower part of the logarithmic layer.

CONCLUSION

A non-local closure for turbulent scalar flux was derived as an extension of a previous Lagrangian transport analysis. Assuming the availability of the appropriate length and time scales of the underlying turbulent flow field, the closure was shown to be effective in capturing many aspects of scalar transport which are erroneously predicted by gradient closures, by comparison to experimental and DNS results.

REFERENCES

1. R. W. BOUBEL, D. FOX, D. TURNER and A. STERN, *Fundamentals of Air Pollution*, 3rd Ed., Academic Press, San Diego (1994).

2. A. YOSHIZAWA, "Statistical modeling of passive scalar diffusion in turbulent shear flows," *J. Fluid Mech.* 195, 541 (1988).

3. M. M. ROGERS, N. N. MANSOUR, and W. C. REYNOLDS, "An algebraic model for the turbulent flux of a passive scalar," *J. Fluid Mech.* 203, 77 (1989).

4. K. HORIUTI (1992), "Assessment of two-equation models of turbulent passive scalar diffusion in channel flow," *J. Fluid Mech.* 238, 405 (1992).

5. H. VAN DOP, F. T. M. NIEUWSTADT, and J. C. R. HUNT, "Random walk models for particle displacements in inhomogeneous unsteady turbulent flows," *Phys. Fluids* 28, 1639 (1985).

6. D. J. THOMSON, "A random walk model of dispersion in turbulent flows and its application to dispersion in a valley," *Quart. J. Roy. Met. Soc.* 112, 511 (1986).

7. Y. SHAO, "Turbulent dispersion in coastal atmospheric boundary layers: an application of a Lagrangian model," *Bound. Layer Met.* 59, 363 (1992).

8. J. M. MACINNES and F. V. BRACCO, "Stochastic particle dispersion modeling and the tracer-particle limit," *Physics Fluids A* 4, 2809 (1992).

9. M. R. RAUPACH, "A practical Lagrangian method for relating scalar concentrations to source distributions in vegetation canopies," *Quart. J. Royal Met. Soc.* 115, 609 (1989).

10. G. I. TAYLOR, "Diffusion by continuous movements," *Proc. London Math. Soc.* Ser. 2, 20, 196 (1921).

11. C. A. DEGRAZIA and O. L. L. MORAES, "A model for eddy diffusivity in a stable boundary layer," *Boundary Layer Met.* 58, 205 (1991).

12. W. C. REYNOLDS, M. M. ROGERS and N. D. Sandham, "Advances in turbulent transport modeling based on direct simulations of turbulence," *Transport Phenomena in Turbulent Flows: Theory, Experiment, and Numerical Simulation*, edited by M. Hirata, N. Kasagi, (Hemisphere, N. Y.), 701 (1988).

13. J. KIM and P. MOIN, "Transport of passive scalars in a turbulent channel flow," in *Turbulent Shear Flows 6*, edited by J.-C. Andre et al., (Springer, N. Y.), 5-2-1 (1987).

14. N. KASAGI and Y. OHTSUBO, "Direct numerical simulation of passive scalar field in a turbulent channel flow," *ASME J. Fluids Engrg.* 114, 598 (1992).

15. P. K. YEUNG, J. G. BRASSEUR and D. M. Bell, "Evolution of passive scalar sources in a numerically simulated boundary layer," in *Near Wall Turbulent Flows*, edited by R. M. C. So, C. G. Speziale and B. E. Launder, (Elsevier, Amsterdam) 307 (1993).

16. D. M. BELL and J. H. FERZIGER, "Turbulent boundary layer DNS with passive scalars," in *Near Wall Turbulent Flows*, edited by R. M. C. So, C. G. Speziale and B. E. Launder, (Elsevier, Amsterdam) 327 (1993).

17. P. S. BERNARD and A. L. ROVELSTAD, "On the physical accuracy of turbulent scalar transport models in inhomogeneous turbulence," *Physics Fluids* 6, 3093 (1993).

18. P. S. BERNARD, "Turbulent Vorticity Transport in Three Dimensions," *Theoretical and Computational Fluid Dynamics*, 2, pp. 165 (1990).

19. P. S. BERNARD and R. A. HANDLER, "Reynolds Stress and the Physics of Turbulent Momentum Transport," *Journal of Fluid Mechanics*, 220, pp. 99 (1990).

20. P. S. BERNARD, J. M. THOMAS and R. A. HANDLER, "Vortex Dynamics and the Production of Reynolds Stress," *J. of Fluid Mechanics*, 253, pp. 385 (1993).

21. P. S. BERNARD, "A Non-local Physically Consistent Turbulent Transport Model," to appear in Proceedings of Turbulent Shear Flows 10, Penn State Univ. (1995).

22. H. STAPOUNTZIS and R. E. BRITTER, "Turbulent diffusion behind a heated line source in a nearly homogeneous turbulent shear", in *Proc. 6th Turbulent Shear Flows 6*, (Springer-Verlag,Berlin), 9.2.1 (1987).

23. U. KARNIK and S. TAVOULARIS,"Measurements of heat diffusion from a continuous line source in a uniformly sheared turbulent flow", *J. Fluid Mech.* 202, 233 (1989).

24. A. L. ROVELSTAD, R. A. HANDLER and P. S. BERNARD, "The Effect of Interpolation Errors on the Lagrangian Analysis of Simulated Turbulent Channel Flow," *J. Computational Physics*, 110, pp. 190 (1994).

25. KIM, J., MOIN, P. and MOSER, R. D., 1987 "Turbulence statistics in fully-developed channel flow at low Reynolds number" *J. Fluid Mech.*, 177 (133).

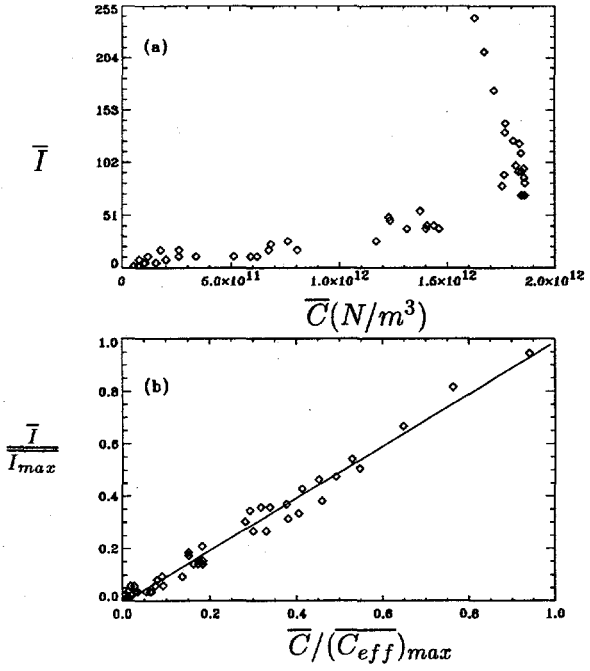

Figure 1: Calibration relationship between (a) the grey level intensity and the raw particle concentration, (b) the grey level intensity and the effective particle concentration.

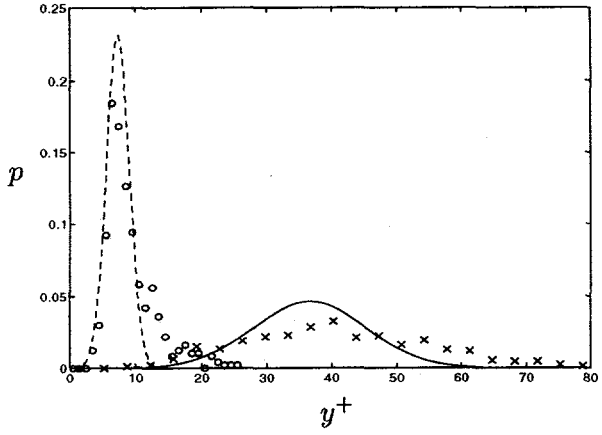

Figure 2: *pdf* of initial particle position. ∘, DNS for $y^+ = 7.4$; ×, DNS for $y^+ = 36.6$; – – –, Eq. (13) for $y^+ = 7.4$; and, ——, Eq. (13) for $y^+ = 36.6$.

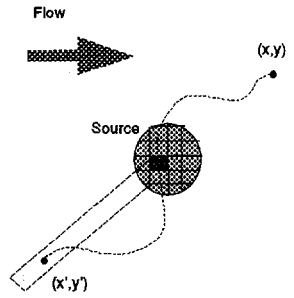

Figure 3: Model of transport due to source.

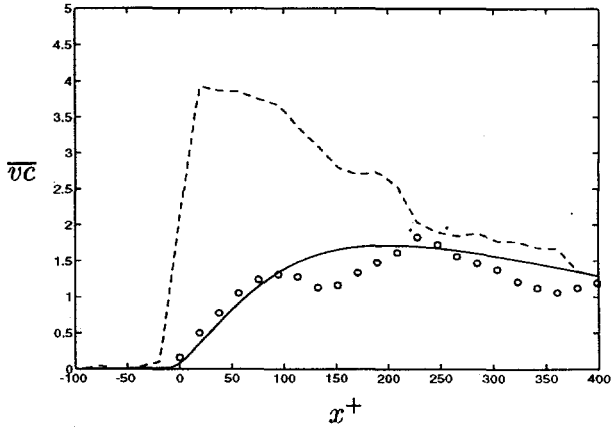

Figure 4: $\overline{vc}$ on line $y^+ = 43.5$: ∘, DNS; ——, Eq. (16); – – –, gradient model.

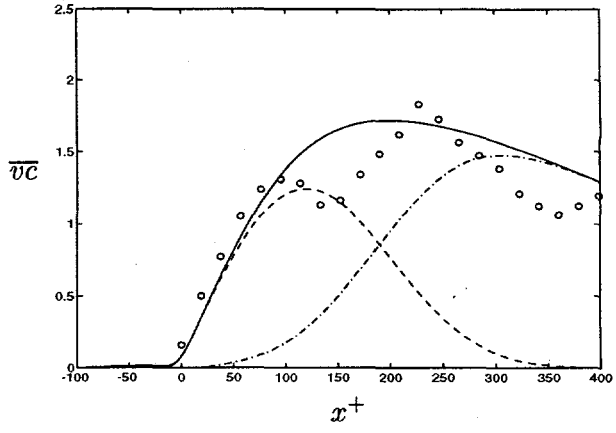

Figure 5: $\overline{vc}$ on line $y^+ = 43.5$: ∘, DNS; ——, Eq. (16); –·–, displacement term in (16); – – –, source term in (16).

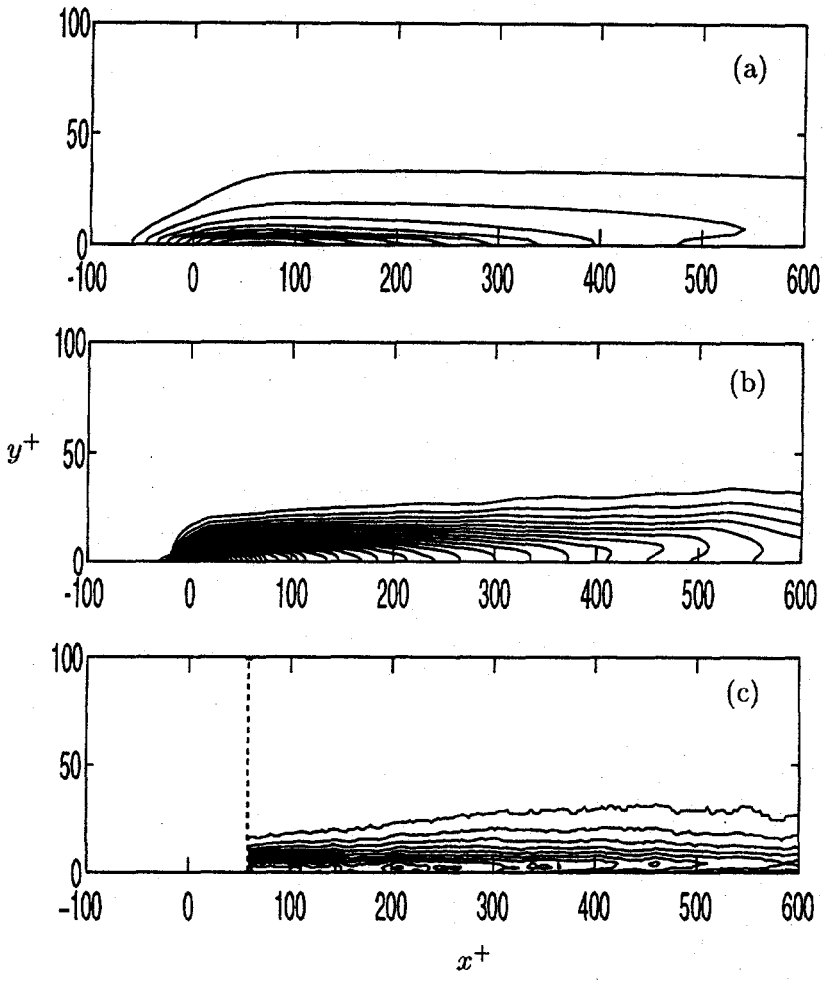

Figure 6: Concentration contours: (a) Gradient model, (b) DNS, (c) Experiment.

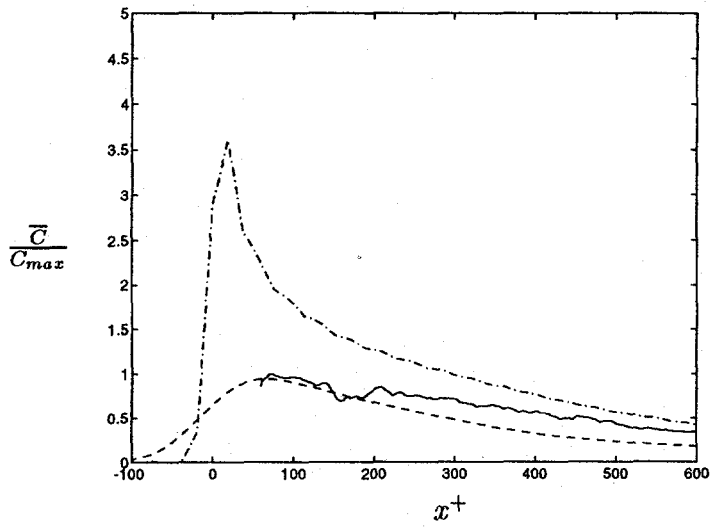

Figure 7: Streamwise concentration profile at $y^+ = 0$: $- \cdot - \cdot -$ DNS, $- - - -$ Gradient model, —— Experiment.

ANOMALOUS SCALING OF A SCALAR FIELD ADVECTED BY TURBULENCE

Robert H. Kraichnan

Robert H. Kraichnan, Inc.
369 Montezuma 108, Santa Fe, NM 87501-2626

ABSTRACT

Recent work leading to deduction of anomalous scaling exponents for the inertial range of an advected passive field from the equations of motion is reviewed. Implications for other turbulence problems are discussed

Understanding of the dynamics of the small scales of turbulence is essential to construction of improved parametrization of small scales in computer modeling of turbulence. It is also an outstanding challenge in non-equilibrium statistical mechanics. For over 50 years, thinking about the small scales of turbulence has been dominated by the cascade ideas first presented by Kolmogorov in 1941 and modified in 1962 to include phenomena associated with intermittency of dissipation [1]. It has long been recognized that the small scales of turbulence are intermittent and that the intermittency of the velocity derivatives increases with Reynolds number. An unsettled question is whether the increase persists to infinite Reynolds number so that the scaling exponents of the inertial-range structure functions at infinite Reynolds number differ from the total self-similarity by Kolmogorov in 1941 (K41) [1].

In the years since 1962, a very large number of models of intermittency in the inertial and dissipation ranges have been proposed and compared with experimental data [1]. In particular, many fractal models of inertial range structure have been offered, some of great sophistication and mathematical complexity. One thing conspicuously missing in almost all of this work is contact with the equations of motion; the models are not derived from the Navier-Stokes (NS) equation. The present paper reviews recent work in which this pattern has been broken in the case of a particular limit of the advection of a passive scalar contaminant field by a random incompressible velocity field. Non-trivial anomalous scaling exponents for the inertial-range structure functions of the scalar field are deduced from the equations of motion [2,3]. The implications of the scalar-field analysis for two other problems, Burgers and NS dynamics, are discussed qualitatively.

Successive random strainings of flow subvolumes containing a passively advected scalar field tend to produce intermittency in the gradient of the scalar field. If there were no counteracting mechanism, the probability distribution function of the scalar gradient would become ever more intermittent as the number of effective independent steps of straining increases. Thus the steady-state intermittency would increase with increase of ratio of macrolength scale to dissipation length scale (increase of Péclet number). A corresponding argument suggests an increase of intermittency

of vorticity with Reynolds number as a result of successive strainings. The increase is compounded by vorticity intensification as vortex tubes are stretched.

What can oppose the increase? One mechanism that can inhibit growth of intermittency is molecular diffusivity/viscosity, which relaxes a non-Gaussian field toward Gaussian statistics. Crudely speaking, this is because unusually strong spikes in the field are preferentially relaxed (spread in space). The same effect can come from the action of eddy diffusivity/viscosity associated with scales smaller than those suffering the relaxation. At a given scale size in an inertial range, the eddy diffusivity/viscosity effects are of the same order as the straining effects that act to increase intermittency. Thus power counting, order-of-magnitude arguments, and associated dimensional considerations, are inadequate to determine whether increase of intermittency with decrease of scale size eventually is halted by the relaxation effects [4].

Eddy relaxation effects characterize both NS dynamics and the advection of a passive scalar field by a stochastic velocity field. They take a degenerate form in Burgers dynamics, where nonlinearity produces shocks that eventually relax without loss of form under the combined action of molecular viscosity and self-advection. Burgers dynamics exhibits extreme intermittency of velocity gradients.

Turbulence may be examined in either the physical space (x space) or wavenumber (k space) domains. There are also hybrid representations, such as by wavelets or by subfields in x space that are band-limited in k space. There are some pitfalls in passing among different representations. In particular, one must be wary of asserting that certain quantities live exclusively in the inertial range.

Isotropic absolute-value structure functions for an isotropic, homogeneous velocity field $\mathbf{u}(\mathbf{x})$ may be defined by

$$S_n^{\mathbf{u}}(r) = \langle |\mathbf{u}(\mathbf{x}+\mathbf{r}) - \mathbf{u}(\mathbf{x})|^n \rangle , \tag{1}$$

where $\langle\ \rangle$ denotes ensemble average. If the inertial-range spectrum of the velocity field is $E(k) \propto k^{-5/3}$, or something near to that form, then there is a close link between description by structure functions and band decomposition: If the statistics are not too exotic, and n is not too large, the value of $S_n^{\mathbf{u}}(r)$ is dominated by contributions from $O(1/r)$ velocity-field wavenumbers. Thus there is justification for linking "scale size" r to a band of wavenumbers k and speaking of "inertial-range scales r".

The concept of a pure inertial-range of r for structure functions is less justified when one turns to dynamics. The equation of motion for $S_n^{\mathbf{u}}(r)$ involves molecular dissipation in an essential way, even when r is in the inertial range [2]. This is easily understood by taking the simplest case of Gaussian $\mathbf{u}(\mathbf{x})$, expanding the right side of (1), and decomposing the average into sums of products of covariances. If r is in middle of a long inertial range, the covariance $\langle \mathbf{u}(\mathbf{x}+r)\cdot\mathbf{u}(\mathbf{x}) \rangle$ decays negligibly from direct molecular dissipation. However, the variance $\langle |\mathbf{u}(\mathbf{x})|^2 \rangle$ also occurs. Its decay rate is finite and independent of r because its spectral support includes the dissipation range of wavenumbers. Molecular viscosity appears directly, and importantly, in the equation of motion for $S_n^{\mathbf{u}}(r)$ at inertial-range r. It should play a central role also in the construction of dynamical models of the inertial-range $S_n^{\mathbf{u}}(r)$.

Suppose that there is a power-law scaling range of r such that

$$S_n^{\mathbf{u}}(r) \propto r^{\zeta_n}, \tag{2}$$

where the exponents ζ_n are independent of r. It is useful to define the terms "regular scaling", "anomalous scaling", and "progressive scaling". Scaling shall be called regular here if $\zeta_n/\zeta_m = n/m$. This corresponds to full similarity of statistics at all r in the range. A more concrete description may be given in terms of the band-limited fields. Suppose that the entire scaling range of $k = 2\pi/r$ is divided into decade bands in wavenumber. Then regular scaling implies that all moments of the x-space velocity field in a band are independent of band location, provided that the moments are

normalized by the variance of the band-limited velocity. Regular scaling corresponds to the K41 picture of the inertial range.

All scaling that is not regular shall be called anomalous here. If the scaling range is infinitely long, and structure functions at macroscales r are finite, Hölder inequalities require $\zeta_n/n \leq \zeta_m/m$ if $n > m$; as n increases, anomalous exponents can only decrease below regular values. Progressive scaling shall denote anomalous scaling in which the exponent differences $\zeta_{n+1} - \zeta_n$ become ever smaller as n increases.

Burgers equation

$$\frac{\partial u}{\partial t} + u\frac{\partial u}{\partial x} = \nu\frac{\partial^2 u}{\partial x^2} \tag{3}$$

evolves the velocity $u(x,t)$ of an infinitely compressible fluid of viscosity ν. Shocks form under (3) as fast-moving fluid overtakes slow-moving fluid. The inertial range at large Reynolds number is asssociated with the neighborhoods of the shocks. The shocks have a characteristic sawtooth shape which represents coherence over a wide range of wavenumbers. Dissipation is concentrated within the shocks and thereby is highly intermittent. The structure functions $S_n^u(r) = \langle |u(x+r) - u(x)|^n \rangle$ for inertial-range r have the form

$$S_n^u(r) = u_0^n r/L, \tag{4}$$

where u_0 is the root-mean-square (rms) velocity and L is a macroscale for velocity fluctuations. The support of $S_n^u(r)$ is dominated by the shocks: r/L in (4) measures the probability that a major shock occurs between $x + r$ and x while u_0 measures the jump in velocity at a major shock.

Equation (4) is an extreme example of anomalous scaling. It is not progressive scaling. The differences $\zeta_{n+1} - \zeta_n$ degenerate to zero and so do not decrease as n increases. The strong intermittency of high-Reynolds-number Burgers flow arises from the shocks, which are structures involving coherence over a wavenumber range that extends from $1/L$ to dissipation wavenumbers. Nevertheless, it is easy to demonstrate that the cascade of energy toward higher wavenumbers is local in the wavenumber space [5]. The straining across a distance r that sharpens the shocks and maintains them in a sharp state is dominated by contributions from wavenumbers $O(1/r)$. Spatial coherence and dynamical locality in wavenumber do not preclude each other.

The scalings of $S_2^u(r)$ and $S_3^u(r)$, features closely associated with existence of shocks, are given correctly by an approximation that is quite incapable of explicit description of shocks or any coherent spatial structures. This is the Lagrangian-history direct-interaction approximation (LHDIA) [5]. The LHDIA uses only limited information from Burgers equation: conservation laws and invariance to Galilean transformations as incorporated in expressions quadratic in the interaction coefficients of individual wavenumber-triad amplitudes. Cross terms between different wavenumber-triad coefficients, which could express phase coherence in physical space, are absent. An implication of the success of this approximation is that relatively elementary properties of the interaction coefficients directly imply the scaling, so that it is possible to recover the latter without being able actually to describe the structures in space. In this picture, the shock structures are regarded not as the cause of the scaling but as a parallel manifestation of an underlying dynamics.

The equation of motion of a passive scalar field $T(\mathbf{x},t)$ advected by an incompressible velocity field $\mathbf{u}(\mathbf{x},t)$ is

$$\left(\frac{\partial}{\partial t} + \mathbf{u}(\mathbf{x},t)\cdot\boldsymbol{\nabla}\right) T(\mathbf{x},t) = \kappa\nabla^2 T(\mathbf{x},t), \tag{5}$$

where κ is molecular diffusivity. The inertial-range structure of T depends on that of $\mathbf{u}$. In order to clarify what causes what, it helps to start with a Gaussian $\mathbf{u}$ field rather than a solution of the NS equation. Maximum simplification occurs when $\mathbf{u}(\mathbf{x},t)$ has a correlation time that is infinitely short compared to any eddy circulation time. This limit yields exact expressions for the effects of

advection on scalar-field statistics [6,7]. It can be approached in such a way that the single-particle and two-particle eddy diffusivities resemble those of more realistic fields.

In the rapid-change limit, the exact evolution equation for the structure functions $S_{2n}^{\mathrm{T}}(r) = \langle |\Delta T(\mathbf{r})|^{2n} \rangle$, where $\Delta T(\mathbf{r})$ denotes $T(\mathbf{x}+\mathbf{r}) - T(\mathbf{x})$, can be derived as

$$\frac{\partial S_{2n}^{\mathrm{T}}(r)}{\partial t} - \frac{2}{r^{d-1}} \frac{\partial}{\partial r} \left(r^{d-1} \eta(r) \frac{\partial S_{2n}^{\mathrm{T}}(r)}{\partial r} \right) = \kappa J_{2n}(r). \tag{6}$$

Here d is space dimensionality, $\eta(r)$ is the two-particle eddy-diffusivity scalar defined by

$$\eta(r) = \frac{1}{2} \int_0^t \langle [\delta_{\parallel} u(\mathbf{r},t) \delta_{\parallel} u(\mathbf{r},t')\rangle \, dt', \tag{7}$$

with $\delta_{\parallel} u(\mathbf{r},t) = [\mathbf{u}(\mathbf{x},t) - \mathbf{u}(\mathbf{x}+\mathbf{r},t)] \cdot \mathbf{r}/r$, and

$$J_{2n}(r) = 2n \left\langle [\Delta T(\mathbf{r})]^{2n-1} (\nabla_x^2 + \nabla_{x'}^2) \Delta T(\mathbf{r}) \right\rangle, \tag{8}$$

is the dissipation term anticipated in the discussion following (1). It is assumed that the velocity field is switched on at $t = 0$ and that $T(\mathbf{x}, t = 0)$ is Gaussian [2].

The difficulties in turbulence theory usually are ascribed to the nonlinearity in stochastic quantities, which poses the so-called closure problem. In the present case, the dynamical effects on $S_{2n}^{\mathrm{T}}(r)$ of the advection term in (5), which contains all the stochastic nonlinearity, are fully and exactly described by the $\eta(r)$ term in (6), so what is usually called the closure problem disappears. However, another kind of closure problem remains: the dissipation term $J_{2n}(r)$ in (6) contains space derivatives in such a way that it cannot be expressed in a closed form that involves only the structure functions. Closed equations can be written for the general $2n$-point, single-time moment of T, but they are much more complicated than (6) [7]. Equations (6)–(8) do form a closed set for $n = 1$.

Despite the lack of closure of (6)–(8), it has been possible to make some progress in deducing the inertial-range scaling exponents from them. A key step is the introduction of the conditional mean

$$H[\Delta T(\mathbf{r})] = \left\langle (\nabla_x^2 + \nabla_{x'}^2) \Delta T(\mathbf{r}) | \Delta T(\mathbf{r}) \right\rangle, \tag{9}$$

where $\langle \cdot | \Delta T(\mathbf{r}) \rangle$ denotes ensemble average conditioned on a given value $\Delta T(\mathbf{r})$. $J_{2n}(r)$ may be written

$$J_{2n}(r) = 2n \left\langle [\Delta T(\mathbf{r})]^{2n-1} H[\Delta T(\mathbf{r})] \right\rangle. \tag{10}$$

It can then be argued persuasively (but not yet rigorously) that there are only two forms for $H[\Delta T(\mathbf{r})]$ that permit steady-state power-law scaling solutions of (6) in the inertial range [3]. Either H has the form $r^{-\zeta_2/2} h(\Delta T / r^{\zeta_2/2})$, where h is a function to be determined, or else H is a linear function of ΔT of the form $f(r)\Delta T(r)$. The former case yields regular scaling and the latter case leads to a fully-determined expression for $J_{2n}(r)$,

$$J_{2n}(r) = 2n S_{2n}^{\mathrm{T}}(r) A(r) / S_2^{\mathrm{T}}(r), \tag{11}$$

where $A(r) = \nabla^2 S_2^{\mathrm{T}}(r) - \nabla^2 S_2^{\mathrm{T}}(0)$, and anomalous scaling of a precise form:

$$\zeta_{2n} = \tfrac{1}{2} \sqrt{4nd\zeta_2 + (d - \zeta_2)^2} - \tfrac{1}{2}(d - \zeta_2), \tag{12}$$

where $\eta(r) \propto r^{\zeta(\eta)}$, $S_{2n}^{\mathrm{T}}(r) \propto r^{\zeta_{2n}}$ in the inertial range and $\zeta_2 = 2 - \zeta(\eta)$. As $n \to \infty$, $\zeta_{2n} \propto n^{1/2}$.

An independent argument involving realizability inequalities on the dissipation field $\nabla^2 T$ appears to rule out regular scaling [3], so that, if the analysis is valid, (12) remains as the only possible power-law scaling in the inertial range. This result was obtained under the special assumption of very rapidly changing velocity field, but some features may be of broad applicability. Plausible arguments can be made that the dependence of the ζ_{2n} on $\zeta(\eta)$ is unchanged if the velocity field has finite correlation times but remains Gaussian. Corrections to the ζ_{2n} are expected if the velocity field displays intermittent (anomalous) scaling.

It was noted earlier that some scaling properties of Burgers turbulence are correctly given by a statistical approximation (LHDIA) that is incapable of describing the shocks associated with the scaling. If (12) is correct, something analogous may be going on in the passive scalar case. The high-order anomalous exponents certainly are strongly affected by spatial structures in which the scalar gradient is exceptionally large. Such structures are not captured by statistical description in terms of the $S_{2n}^{\mathrm{T}}(r)$ alone, and the scalar-field analysis sketched above certainly takes no account of specific spatial structures. The hope raised is that it may be unnecessary to do so if only scaling exponents are sought.

The Burgers scaling discussed earlier can be obtained from a framework like that erected for the passive scalar by adding heuristic elements associated with LHDIA. The advection term in the equation of motion for $S_{2n}^{\mathbf{u}}(r)$ cannot be written exactly as for a passive scalar with rapidly changing velocity field. However, a very similar form is obtained by doing renormalized perturbation approximation based on LHDIA. The result is an equation like (6), but with an important difference: a factor of $2n$ appears in the advection term on the left side because, in contrast to the scalar case where there is only one $\mathbf{u}$ factor, any of the $2n$ factors u in $\left\langle u^{2n}\partial u/\partial x\right\rangle$ may be regarded as the advecting velocity.

For inertial range r, $\eta(r) \propto r$ in Burgers dynamics, where $S_2^{\mathbf{u}}(r) \propto r$. One way to see this is to note that the cascade rate $\eta(r)r^{-2}S_2^{\mathbf{u}}(r)$ mediated by eddy viscosity is then independent of r. The similar fact for NS under K41 assumptions is that $\eta(r)r^{-2}S_2^{\mathbf{u}}(r)$ is independent of r with $\eta(r) \propto r^{4/3}$, $S_2^{\mathbf{u}}(r) \propto r^{2/3}$. In both cases, ∇^2 is expressed by r^{-2}. With $\eta(r) \propto r$, the analog of (6) gives the correct Burgers scaling $S_{2n}^{\mathbf{u}}(r) \propto r$ by balance of advective and dissipative terms, if the dissipative term is taken in the form corresponding to (11). It is easy to see independently that this form is exact in the shock-dominated Burgers inertial range, where dissipation is confined to the shocks.

It is unclear to what extent similar procedures are meaningful in three-dimensional NS dynamics, where intense vortex tubes and sheets are expected to make major contributions to high-order structure functions in place of the shocks of Burgers dynamics. One can write a balance equation like (6) in steady state and argue as in [3] that, if both sides scale as as powers of r, then anomalous scaling is possible only if the conditional mean corresponding to (9) is linear so that the dissipation term has a form like (11).

To go further, some estimate must be made of the advective term. Here the vector character of $\mathbf{u}$, incompressibility, and pressure all make things more complicated than in the Burgers case. An LHDIA-like perturbative evaluation can be carried out, as in the Burgers case, but this has not yet been done. Plausibly, the Burgers and rapid-velocity-field passive scalar cases represent limits for three-dimensional NS scaling. Burgers presents the most rapid possible growth of intermittency with decrease of scale size; there is no disruption of coherence by eddy effects. The passive scalar, on the other hand, appears to give the best possible opportunity for relaxation of intermittency by eddy transport effects.

The stretching of vorticity in an incompressible three-dimensional NS field would seem much more analogous to stretching of scalar blobs than to the formation of shocks under Burgers equation. If so, the $n^{1/2}$ behavior for the scaling exponents of a scalar field given by (12) may be a meaningful zeroth approximation to the exponents of the NS velocity field. At the present time this is only

speculation. However, Nelkin has shown that models incorporating such behavior can be consistent with experimental data on NS structure functions [8]. He points out that the $n^{1/2}$ dependence can be related to a class of fractal processes recently described by Novikov [9].

In general, the determination of higher scaling exponents has proved very resistant to analytical treatment. The shock-mediated intermittency of Burgers and the scalar advected by a rapidly-changing velocity field are particularly friendly cases. It may be of general significance that the deduction of scaling exponents for the passive scalar reviewed above involves conditional means in an essential way. Most analytical work on turbulence has been related more or less closely to renormalized perturbation analysis. Systematic approximations for moments can be constructed fairly straightforwardly by such analysis, but this is very much not the case for conditional means. The present analysis suggests, therefore, that nonperturbative methods should be sought if higher statistics are the goal.

AKNOWLEDGEMENT

This work was supported by the U. S. Department of Energy under Grant DE-FG03-90ER14118.

REFERENCES

[1] "Turbulence and Stochastic Processes", ed. by J. C. R. Hunt, O. M. Phillips, and D. Williams, Proc. Roy. Soc. London A **434**, 1-240 (1991). This commemorative collection of articles gives a comprehensive picture of work on inertial-range scaling during the fifty years starting with Kolmogorov's 1941 papers on turbulence.

[2] R. H. Kraichnan, Phys. Rev. Lett. **72**, 1016 (1994).

[3] R. H. Kraichnan, V. Yakhot, and S. Chen, submitted to Phys. Rev. Lett. (1995).

[4] R. H. Kraichnan, J. Fluid Mech. **62**, 305 (1974)

[5] R. H. Kraichnan, Phys. Fluids **11**, 266 (1968).

[6] R. H. Kraichnan, Phys. Fluids **11**, 945 (1968).

[7] B. I. Shraiman and E. D. Siggia, Phys. Rev. E **49**, 2912 (1994).

[8] M. Nelkin, submitted to Phys. Rev. E (1995).

[9] E. A. Novikov, Phys. Rev. E **50**, R3303 (1994).

CONVECTION IN A NEMATIC LIQUID CRYSTAL WITH HOMEOTROPIC ALIGNMENT AND HEATED FROM BELOW

Guenter Ahlers

Department of Physics and
Center for Nonlinear Studies
University of California
Santa Barbara, CA 93106

ABSTRACT

Experimental results for convection in a thin horizontal layer of a homeotropically aligned nematic liquid crystal heated from below and in a vertical magnetic field are presented. A subcritical Hopf bifurcation leads to the convecting state. There is quantitative agreement between the measured and the predicted bifurcation line as a function of magnetic field. The nonlinear state near the bifurcation is one of spatio-temporal chaos which seems to be the result of a zig-zag instability of the straight-roll state.

INTRODUCTION

Convection in an *isotropic* fluid heated from below is well known as Rayleigh-Bénard convection (RBC).[1,2] However, this phenomenon is altered dramatically in the case of a nematic liquid crystal (NLC). Here we discuss what happens when the NLC has homeotropic alignment (*i.e.*, has a director which is aligned in the vertical direction parallel to the heat flux) and is heated from below.[3,4,5] The usual Rayleigh-Bénard destabilization due to a thermally-induced density gradient is opposed by the stiffness of the director field which is coupled to and distorted by any flow. It turns out that relaxation times of the director field are much longer than thermal relaxation times. For that reason it is possible for director fluctuations and temperature/velocity fluctuations to be out of phase as they grow in amplitude. This situation typically leads to an oscillatory instability (also known as overstability), and the bifurcation at which these time-periodic perturbations acquire a positive growth rate is known as a Hopf bifurcation.[6] This case is closely analogous to convection in binary-fluid mixtures with a negative separation ratio.[7,8] In that case, concentration gradients oppose convection, and concentration diffusion has the slow and heat diffusion the fast time scale. It turns out that the Hopf bifurcation in the NLC case is subcritical,[5] and that the fully developed nonlinear state no longer is time periodic. Instead, the statistically stationary state above the bifurcation is one of spatio-temporal chaos with a typical time scale which is about two orders of magnitude slower than the inverse Hopf frequency.[9]

However, it was possible to actually measure the Hopf frequency by looking at the growth or decay of small perturbations which were deliberately introduced when the system was close to the conduction state and near the bifurcation point.[5]

A convenient aspect of thermal convection in NLCs is that an external magnetic field will couple to the fluid because the diamagnetic susceptibility is anisotropic. A field of modest strength can have a dramatic effect on the phenomena which are observed. This adds greatly to the richness of the physics accessible to the experimentalist. In the case of homeotropic alignment to be discussed, the field is parallel to the heat current.

An interesting aspect of NLC convection is that we are dealing with a system whose equations of motion are well known,[10;11] but significantly more complicated than the Navier-Stokes equations for isotropic fluids. The usual viscosity η and conductivity λ are replaced by six viscosities $\alpha_i, i = 1, \ldots, 6$ and two conductivities $\lambda_{\|}$ and $\lambda_{\perp}$, and the equations for momentum and energy balance must be coupled to an equation for the director field which contains three elastic constants $k_{ii}, i = 1, 2, 3$. In spite of these complexities, it has been possible to carry out quantitative stability analyses, and under some conditions predictions in the weakly nonlinear regime have been made.[12,13,14] Thus, one may argue that comparison of quantitative experiments on thermal convection in NLC's with corresponding detailed theoretical calculations provides an excellent testing ground for the applicability of methods of stability analysis and of weakly nonlinear theory to systems which are more complex than isotropic fluids.

From another point of view, thermal convection in NLCs provides a rich system for the study of general problems in pattern formation. During the last two decades interest in this nonlinear topic has seen a revival in the physics community, and a great deal has been learned from experiments about nonlinear pattern-forming dissipative systems.[15,16] The case under consideration here leads to a spatio-temporally complex pattern often referred to as spatio-temporal chaos (STC).

The most common NLC for the study of Rayleigh-Bénard convection has been p-methoxy benzylidene-p-n-butylaniline (MBBA). The reason for this apparently is historical; MBBA was the first material for which all relevant physical properties, which are necessary for comparison between experiment and theory, had been measured. However, a recent survey of the literature revealed that the properties of some of the cyano-biphenyls are known nearly as well. These materials are far more stable and less toxic than MBBA, and thus have advantages for precise experimental work. They are also relatively inexpensive, and this is an important factor for thermal convection because comparatively large amounts (typically perhaps 30 cm^3) are required.[17] In the present work we have used 4–n–pentyl–4′–cyanobiphenyl (5CB).

THEORETICAL PREDICTIONS

As for Rayleigh-Bénard convection in an isotropic fluid, the conduction state has rotational symmetry in the horizontal plane because its director is oriented vertically and parallel to the magnetic field and the heat flow. Thus, patterns of arbitrary angular orientation should form unless the boundary conditions of the experiment select a particular direction.

The first instability should be a Hopf bifurcation, that is the disturbances which first acquire a positive growth rate should be time-periodic.[3,4] As the magnetic field is increased, the threshold for convection is predicted to shift to larger values.[5,13] This was confirmed by

early experimental work on this system.[5] For sufficiently high fields the primary bifurcation is predicted to be to a stationary state of convection.[13] There is a codimension-two point where the two bifurcation lines meet. The situation is somewhat similar to binary-mixture convection,[15] which has been studied extensively in recent years.

The quantitative aspects of the instabilities are determined by four dimensionless parameters which are formed from combinations of the fluid properties.[18] They are[12] the Prandtl number

$$\sigma = \frac{(\alpha_4/2)}{\rho\kappa_\parallel} \quad , \tag{1}$$

the ratio between the director relaxation time and the heat diffusion time

$$F = \frac{(\alpha_2/2)\kappa_\parallel}{k_{33}} \quad , \tag{2}$$

the Rayleigh number

$$R = \frac{\alpha g \rho d^3 \Delta T}{(\alpha_4/2)\kappa_\parallel} \quad , \tag{3}$$

and the dimensionless magnetic field

$$h = H/H_{F,\parallel} \tag{4}$$

with the Fréedericksz field

$$H_{F,\parallel} = \frac{\pi}{d}\sqrt{\frac{k_{33}}{\rho\chi a}} \quad . \tag{5}$$

The time scale of transients and pattern dynamics is measured in terms of

$$t_v = d^2/\kappa_\parallel \quad . \tag{6}$$

As usual, $\kappa_\parallel$ is the thermal diffusivity $\lambda_\parallel/\rho C_p$. Both h and R are easily varied in an experiment, and may be regarded as two independent control parameters. The availability of h in addition to R makes it possible to explore an entire line of instabilities. The parameters F, σ, and t_v are essentially fixed once a particular NLC and temperature range have been chosen, and even between different NLCs there is not a great range at our disposal. For 5CB at 26° we have $\sigma = 272$ and $F = 460$. The critical value R_c of R and the fluid parameters determine the critical temperature difference ΔT_c for a sample of a given thickness d. The realistic experimental requirement that $\Delta T_c \simeq$ a few °C dictates that the sample thickness should be a few mm. Typical values of $H_{F,\parallel}$ are near 20 *Gauss*. Thus modest fields of a *kGauss* or so are adequate to explore the entire range of interest.

A linear stability analysis was carried out by several investigators.[4,19,20,21] A very detailed analysis of this case was presented recently by Feng, Decker, Pesch, and Kramer (FDPK).[13] These authors also provided a weakly nonlinear analysis, and we shall briefly describe their results.

For low fields, FDPK predict that the first instability will be a subcritical Hopf bifurcation. The critical Rayleigh number $R_c(H)$ varies typically from about 1500 at small fields to about 3400 for $h \simeq 50$. The details of $R_c(H)$ depend upon σ and F, and have

to be computed for each particular case. The wavevector which first becomes unstable is predicted to vary from about 3.2 to 4.6 as the field increases from $h = 0$ to $h \simeq 50$. The Hopf frequency is expected to be between about 12 and 2 over this range. It would not be too helpful to be more specific here since the details of all these parameters depend upon σ and F. At $h = h^{ct} \simeq 50$ (assuming typical parameter values for MBBA), the Hopf bifurcation line meets a stationary bifurcation at a codimension-two point. At this point, the Hopf frequency is predicted to be finite (close to 2) and there is a discontinuity of about 10% in the wavevector. The stationary bifurcation for $h > h^{ct}$ initially is also predicted to be subcritical, but for $h \gtrsim 63$ (for typical MBBA parameters) it is expected to become supercritical. At $h = h^{ct} \simeq 63$, the coefficient of the cubic term in a Ginzburg-Landau equation vanishes and a tricritical point is predicted for the stationary bifurcation branch.

EXPERIMENTAL RESULTS

Early measurements for this system were made by Guyon, Pieranski, and Salan[5] (GPS). These authors used the NLC MBBA. Their sample had a thickness $d = 5\ mm$, yielding $H_{F,\|} \simeq 15\ Gauss$. It had a circular cross section, and a diameter of 54 mm.[22] At half-height, several thermocouples were mounted in the fluid to monitor the local temperature. A heater wire near the thermocouples also traversed the sample. It is difficult to say whether these intrusive devices had an influence on the hydrodynamics. The temperature stability of the water baths above and below the sample was of the order of 0.01°C. GPS measured the onset of convection by monitoring the response of their thermocouples to a temperature perturbation induced by a heat pulse delivered by the heater wire. If this response grew (decayed) as a function of time, the threshold of their system had (had not) been exceeded. They were also able to determine a characteristic frequency from the thermocouple response during the transients which led to the convecting nonlinear state. The results for ΔT_c are qualitatively consistent with the theoretical results[13] for the laterally infinite system. The magnitude of ΔT_c at a given field was within 10 or 20 % of the theoretical value. ΔT_c increased with H up to $H \simeq 580\ Gauss (h \simeq 33)$, and then decreased again. The maximum was interpreted[13] as the predicted codimension-two point which for the laterally infinite system is expected at $h^{ct} = 51$, although it occurred at a rather low field. The measurements also provided clear evidence for hysteresis at the primary bifurcation. The measured Hopf frequency had a maximum near $h = 13$, whereas the theory predicts the maximum to occur near $h = 32$. The frequency was generally of the same size as the one given by the theory, but at the highest field values $h \simeq 33$ it was still much larger than expected for $h = h^{ct}$. We conclude that these experiments clearly established a number of central features of the bifurcation. These include its subcritical nature and the time-periodic behavior of the growing perturbations of the conduction state. However, at the quantitative level there are substantial differences between the experiments and the theory for the laterally infinite system.

We used a circular cell with $d = 3.94\ mm$ and $r = 41.9\ mm$, corresponding to a radial aspect ratio $\Gamma \equiv r/d = 10.6$. The fluid was 5CB. For this system, $t_v = 136\ s$ and $H_{F,\|} = 21.1\ Gauss$. Monodomain homeotropic samples were prepared before each experimental "run". The heat current was increased in small steps while the top temperature was held fixed at 19°C, until convection occurred. The heat current then was decreased again in small steps until convection ceased. At each heat-current value, the bottom-plate temperature was measured at one-minute intervals for two hours ($\simeq 53 t_v$). The temperature measurements and the heat current were used to determine the Nusselt number, which

is given by

$$N \equiv \lambda_{eff}/\lambda_{\|} \quad . \tag{7}$$

Here $\lambda_{\|}$ is the conductivity of the homeotropically aligned sample, and

$$\lambda_{eff} \equiv -Qd/\Delta T \tag{8}$$

is the effective conductivity and contains contributions from diffusive conduction and from hydrodynamic flow. While the current was steady, images of the convection pattern were acquired by the computer-interfaced CCD camera.

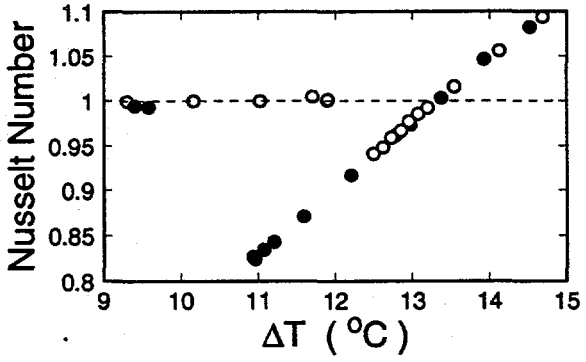

Figure 1. Nusselt number measurements for $h = 9.4$ ($H = 200$ *Gauss*). Open (filled) circles were obtained with increasing (decreasing) steps in ΔT.

Figure 1 shows N as a function of ΔT for $H = 200$ *Gauss* ($h \simeq 9.4$). Surprisingly, N decreased below one when convection started. This can be understood because the conductivity of a sample with parallel alignment, in which $\mathbf{Q}$ is perpendicular to $\hat{n}$ ($\lambda_{\perp}$), is much less than the conductivity of the homeotropic case ($\lambda_{\|}$).[23] The direct hydrodynamic contribution to the heat flux is smaller than the decrease in the heat flux due to the deviations of the director from parallel alignment caused by the flow. As the current decreased, the conduction state was reached at a value of ΔT equal to $\Delta T_s < \Delta T_c$, showing the predicted and previously observed[5] hysteresis. For small fields ($H < 250G$), the conduction state reached from the convecting state had a conductivity less than $\lambda_{\|}$, corresponding to $N < 1$, because the hydrodynamic flow experienced by the sample had introduced defects which reduced the average conductivity below $\lambda_{\|}$. At the field value of this experiment, the elimination of defects from the sample occurred on a time scale which was much longer than the duration of the experiment. The visual appearance of the conduction state reached after convection is interesting. It had the appearance of curdled milk, with the clusters of non-homeotropic alignment corresponding to the curds suspended in a nearly-clear background fluid of homeotropic alignment.

From data like those in Fig. 1, values of the critical temperature difference ΔT_c and of the temperature difference at the saddle node ΔT_s were determined with an uncertainty of about 0.5 %. The corresponding Rayleigh numbers are shown in Fig. 2 as a function of h^2 (solid circles: ΔT_c, open circles: ΔT_s). The solid line in the figure is the theoretical prediction,[13] evaluated for the properties of 5CB at the mean temperature of the experiment. As can be seen, the agreement with the measurements is excellent. The small deviations at large h are probably caused by excessive variations of the fluid properties over the temperature interval of the measurement when the temperature of the cell bottom is

rather close to T_{NI}. There are as yet no predictions for R_s. It is interesting that R_s is only about 10% below R_c. Nonetheless, a calculation may turn out to be difficult because there is already severe distortion of the originally homeotropic director field by the fluid flow, as evidenced by the defects encountered after the conduction state is reached once more.

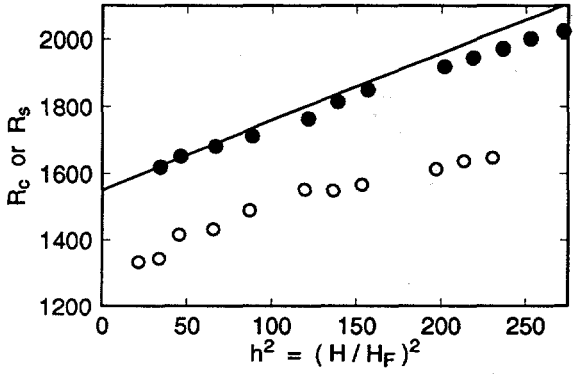

Figure 2. Solid circles: Critical Rayleigh numbers for the onset of convection as a function of h^2. Open circles: Rayleigh numbers at the saddle node where convection ceased when the heat current was lowered.

The pattern which evolves beyond the bifurcation is extremely interesting. The first two rows of Fig. 3 show typical images of the flow field immediately above the convective threshold for $h = 9.4$. By examining relatively rapid time sequences of images, it was found that, on the time scale of the inverse of the expected Hopf frequency, the convection rolls were steady rather than travelling or standing waves. This is not in contradiction to the predicted Hopf bifurcation because the subcritical nature of the bifurcation leads to a finite-amplitude state at threshold whereas the theory pertains to an infinitesimal perturbation of the conduction state. A similar situation is encountered in binary-mixture convection, where for a range of values of the separation ratio the convection rolls are steady when $\Delta T = \Delta T_c$ even though small perturbations of the conduction state are travelling waves. In our experiment, there unfortunately was no way to determine the frequency of small-amplitude transients as had been done by GPS.

On a much longer time scale, the pattern evolved continuously. This is illustrated by the images in Fig. 3, which are from a single experimental run with constant external conditions. They were taken at the times indicated in each image, in units of $t_v = 136\ s$, which had elapsed since an arbitrary origin at which the pattern already had been equilibrated for some time. Even in runs of much longer duration (up to two weeks or $9000t_v$) no steady state was reached. The nature of the pattern did not change noticeably over the field range $5 < h < 16$ covered by the experiments, although no quantitative studies as a function of h have been carried out. It appears that the patterns are disordered both in space and in time, providing an example of spatio-temporal chaos.

The bottom row of Fig. 3 gives the modulus of the Fourier transform. The transforms were base on the central parts of the images, by using the filter function $W(r) = cos^2[(\pi/2)(r/r_0)]$ for $r < r_0$ and $W(r) = 0$ for $r > r_0$. Here r_0 was set equal to 85% of the sample radius. The transforms for $t = 449$ and 1033 show that the nature of the pattern changed dramatically with time. The rightmost image in the bottom row of Fig. 3 (labeled "Avg") shows the square root of the time average of the square of the modulus of the Fourier transform [*i.e.* of the structure factor $S(k)$]. The average involved 250 images taken over a total time period of $1123t_v$ (nearly two days). It is seen to contain

contributions at all angles, consistent with the idea of a statistically stationary process of non-periodic pattern evolution and with the expected rotational symmetry of the system.

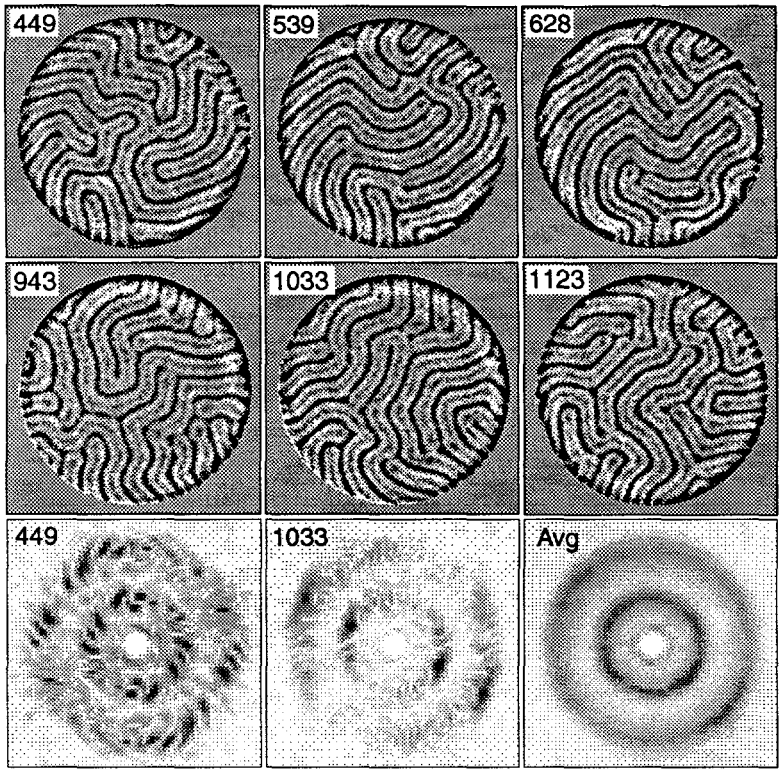

Figure 3. Top two rows: a sequence of images from the same run at 200 *Gauss* ($h = 9.4$), taken with constant external conditions. The time elapsed since the start of the run (in units of $t_v = 136\ s$) is given in the top left corner of each image. Bottom row: Square root of the structure factor of the central portions of two of the images shown above, and the average of the structure factor of the central portions of 250 images spanning a time interval of $1123 t_v$.

Figure 4a shows the azimuthal average $S(k)$ of the temporal average of the structure factor for the run described above, *i.e.* of the lower right image in Fig. 3. Both the fundamental and the second harmonic (corresponding to a roll width of half a wavelength) are well developed, but the higher harmonics are so weak as to be unobservable on the scale of the figure. The characteristic wavenumber of the pattern is about 3.4. This is fairly close to the theoretically predicted wavenumber for the mode which first acquires a positive growth rate; but since the observed state is one of finite amplitude, this agreement is not particularly significant. Figure 4b shows the average over k of $S(\mathbf{k})$ as a function of the azimuthal angle Θ [the average over k was computed only in the vicinity of the fundamental peak of $S(k)$]. Although there is a discernable maximum near $\Theta \approx 0.75$, the angular distribution is really quite uniform. Any remaining structure might well disappear if data were averaged over longer time periods. On the other hand, it could also be indicative of a slight asymmetry in the experimental cell.

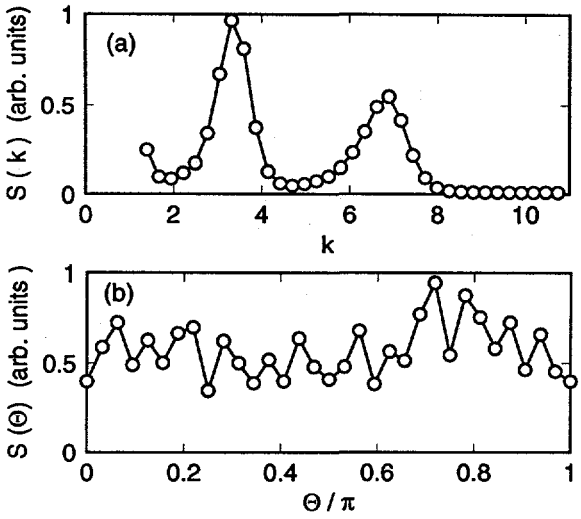

Figure 4. a): The azimuthally averaged structure factor $S(k)$ as a function of the modulus k of the wavevector. b): the radially averaged structure factor $S(\Theta)$ as a function of the azimuthal angle Θ.

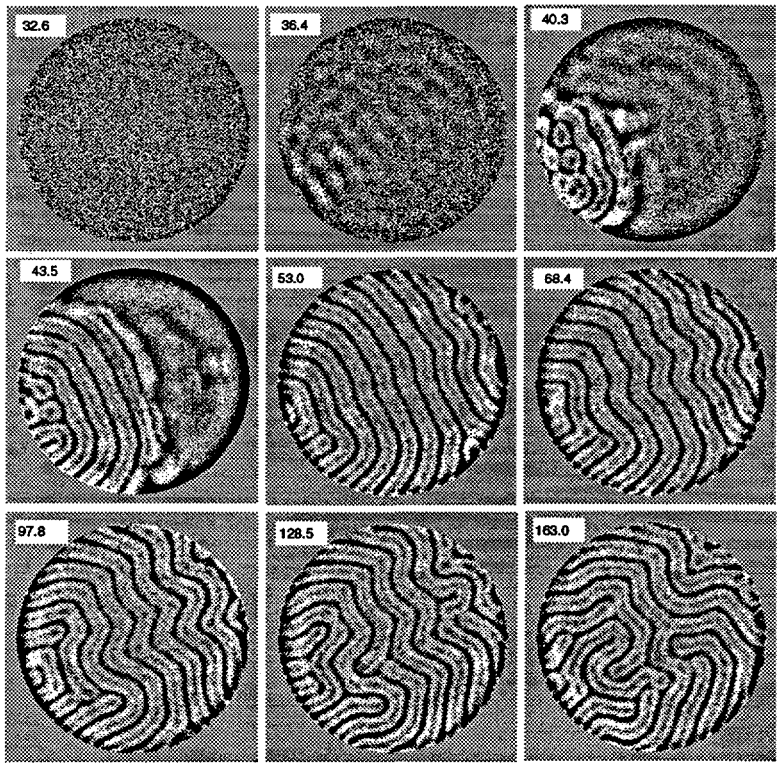

Figure 5. A temporal succession of images during the transient leading from conduction to convection when ΔT was raised slightly above ΔT_c. The field was $h = 9.4$. The numbers are the elapsed time, in units of t_v, since the threshold was exceeded.

It is instructive to examine the transients which lead from the conduction to the convecting state. This is done in Fig. 5. Here the number in each image gives the time, in units of t_v, which has elapsed since ΔT was raised slightly (1%) above ΔT_c. At $t = 32.6$,

there is still no evidence of convection; but at $t = 36.4$, there are noticeable fluctuations in the image which correspond to hydrodynamic flow. At $t = 40.3$, some of these fluctuations have grown to macroscopic amplitudes, and a front of convection is invading the quiescent fluid (t = 43.5). This creates a state of nearly-straight parallel convection rolls ($t = 53$). However, these straight rolls turn out to be unstable to a zig-zag instability. The zig-zag disturbance can be seen to grow at $t = 68.4$ and 97.4. In the end, this instability leads to the spatially and temporally disordered pattern shown for $t = 163$ and in Fig. 3.3. Thus, we see that a secondary instability led to a chaotic state rather than to a new time-independent pattern. This phenomenon most likely is analogous to the one encountered in very early experiments on spatio-temporal chaos using liquid helium[24,25], where ordinary RB convection became chaotically time dependent, probably because the skewed-varicose instability[26] was crossed (one cannot be absolutely sure about this because in the early work there was no flow visualization).

REFERENCES

1. H. BÉNARD, *Rev. Gen. Sci. Pure Appl.* **11**, 1261, 1309 (1900); and *Ann. Chim. Phys.* **23**, 62 (1901).
2. A large literature pertaining to this field has evolved. Particularly useful as introductions to early work are the reviews by E.L. KOSCHMIEDER, *Adv. Chem. Phys.* **26**, 177 (1974); and in *Order and Fluctuations in Equilibrium and Nonequilibrium Statistical Mechanics,* XVIIth International Solvay Conference, ed. by G. Nicolis, G. Dewel, and J.W. Turner (Wiley, NY, 1981), p. 168; and by F. BUSSE, in *Hydrodynamic Instabilities and the Transition to Turbulence,* edited by H.L. Swinney and J.P. Gollub (Springer, Berlin, 1981), p. 97; and in *Rep. Prog. Phys.* **41**, 1929 (1978).
3. H. LEKKERKERKER, *J. Phys. France Lett.* **38**, 277 (1977).
4. H. LEKKERKERKER, *J. Phys. Colloq. France* **40**, C3 (1979).
5. E. GUYON, P. PIERANSKI, and J. SALAN, *J. Fluid. Mech.* **93** 65, (1979).
6. For a summary of bifurcation types, see for instance Appendix A of P. BERGÉ, Y. POMEAU, and C. VIDAL, *Order within Chaos* (Wiley, NY, 1986).
7. D.T.J. HURLE and E. JAKEMAN, *J. Fluid Mech.* **47**, 667 (1971).
8. For a recent review, see for instance, M. C. CROSS and P.C. HOHENBERG, *Rev. Mod. Phys.* **65**, 851 (1993).
9. G. AHLERS, unpublished.
10. P.G. DE GENNES, *The Physics of Liquid Crystals* (Clarendon Press, Oxford, 1973).
11. M.J. STEPHEN and J.P. STRALEY, *Rev. Mod. Phys.* **46**, 617 (1974).
12. Q. FENG, W. PESCH, and L. KRAMER, *Phys. Rev. A* **45**, 7242 (1992).
13. Q. FENG, W. DECKER, W. PESCH, and L. KRAMER, *J. Phys. France* **II 2**, 1303 (1992).
14. L. KRAMER and W. PESCH, *Annu. Rev. Fluid Mech.* **27**, in print.

15. M.C. CROSS and P.C. HOHENBERG, *Rev. Mod. Phys.* **65**, 851 (1993).

16. G. AHLERS, in Proceedings of the XIIIth Sitges Conference, edited by M. Rubio (Springer), in print.

17. We obtained our 5CB from EM Industries, 5 Skyline Drive, Hawthorne, NY 10532.

18. For a discussion of the properties of 5CB, see G. AHLERS, in *Pattern Formation in Liquid Crystals*, edited by L. Kramer and A. Buka (Springer, 1995).

19. M. VELARDE and I. ZÚÑIGA, *J. Phys. France* **40**, 725 (1979).

20. P. BARRATT and D. SLOAN, *J. Fluid Mech.* **102**, 389 (1981).

21. P. BARRATT and J. MANLEY, *J. Non-Equilib. Thermodyn.* **8**, 143 (1983).

22. J. SALAN, private communication.

23. G. AHLERS, D.S. CANNELL, L.I. BERGE, and S. SAKURAI, *Phys. Rev. E* **49**, 545 (1994).

24. G. AHLERS, in *Fluctuations, Instabilities, and Phase Transitions*, edited by T. Riste (Plenum, NY, 1974), p. 181.

25. G. AHLERS, *Phys. Rev. Lett.* **33**, 1185 (1974).

26. F.H. BUSSE and R.M. CLEVER, *J. Fluid Mech.* **91**, 319 (1979).

MODELING OF MIXING PROCESSES: FLUIDS, PARTICULATES, AND POWDERS

J. M. Ottino and S. Hansen

Laboratory for Fluid Mechanics, Chaos and Mixing
Department of Chemical Engineering, Northwestern University
Evanston, Illinois 60208

ABSTRACT

Work under this grant involves two main areas: (i) *Mixing of Viscous Liquids,* this first area comprising aggregation, fragmentation and dispersion, and (ii) *Mixing of Powders.* In order to produce a coherent self-contained picture, we report primarily on results obtained under (i), and within this area, mostly on computational studies of particle aggregation in regular and chaotic flows.

Numerical simulations show that the average cluster size of compact clusters grows algebraically, while the average cluster size of fractal clusters grows exponentially; companion mathematical arguments are used to describe the initial growth of average cluster size and polydispersity. It is found that when the system is well mixed and the capture radius independent of mass, the polydispersity is constant for long-times and the cluster size distribution is self-similar. Furthermore, our simulations indicate that the fractal nature of the clusters is dependent upon the mixing.

INTRODUCTION

The overall objective of our work under this grant is to produce fundamental knowledge of viscous mixing processes involving multiphase fluids and particulate systems. Our goal is to generate broad-based understanding relevant to a variety of industrial applications. The motivation for such an approach is the belief that there is a broad common denominator underlying many of the mixing problems shared by industry.

Current problems of interest in mixing can be found in polymer processing, chemical reaction engineering and composites, food processing/consumer products, and the pharmaceutical industry. Work in these areas is being carried out by both industry and universities. However, mixing-related research in all these disciplines has developed in nearly independent fashion. Often one sees "practical" work that

is hard to generalize and "basic" results that are hard to apply. We believe that there is a need to generate a more fundamental understanding of mixing since, at a fundamental level, there are strong similarities in the basic science underlying all these applications.

As a step towards reaching the above goals we concentrate on two main areas: (i) *Mixing of Viscous Liquids*, this area involving work in aggregation, fragmentation and dispersion, and (ii) *Mixing of Powders*. Work carried out under (ii), initially perceived as an extension of on our work in suspensions, is rapidly becoming a distinct area involving a rather different approach, and future extensions may be carried out outside the bounds of this grant.

MIXING OF VISCOUS LIQUIDS: AGGREGATION, FRAGMENTATION AND DISPERSION

DISPERSION

The basic goal of work in this area is to obtain basic understanding of mixing of immiscible fluids leading to the determination of flow conditions which result in efficient breakup and dispersion of one mass of fluid in the bulk of another. Related issues are the prediction of the morphological structures and drop size distribution in complex flows. This area is relatively well developed. We are currently investigating dispersion and coalescence processes in non-homogeneous flows.

AGGREGATION AND FRAGMENTATION

Work in this area focuses on fundamental issues in flow-driven particle aggregation and fragmentation and dispersion of agglomerates in complex flows. An understanding of aggregation, the reverse of breakup, complements and enhances our studies of breakup of immiscible fluids.

On-going research investigates flow-driven aggregation in nonhomogeneous flows. We study, by dynamic modeling, aggregation of compact and fractal structures in model flows typifying regular and chaotic regimes. Emphasis is placed on two-dimensional flows but three-dimensional systems are considered as well. The goal is to put into evidence flow effects - kinetics of aggregation, cluster size distribution and structure of aggregates - with the long range goal of manipulating flows to tailor the structure of clusters.

Two aggregation scenarios are considered: in (i) the clusters retain a compact geometry - forming disks and spheres - whereas in (ii) fractal structures are formed. The primary focus of (i) is *kinetics and self-similarity* of size distributions, while the main focus of (ii) is the *fractal structure* of the clusters and its dependence with the flow.

Classically, irreversible aggregation is described by Smoluchowski's coagulation equation which can be written for a continuous distribution of cluster sizes as

$$\frac{\partial n(x,t)}{\partial t} = \frac{1}{2}\int_0^x K(x-y,y)n(x-y,t)n(y,t)dy - n(x,t)\int_0^\infty K(x,y)n(y,t)dy, \quad (1)$$

where n(x,t) is the concentration of clusters of mass x at time t and K(x,y) is the rate of aggregation of clusters of masses x and y. The first term, on the right-hand side, accounts for the formation of a cluster of size x due to aggregation of two clusters of size x-y and y, whereas the second term represents the loss of clusters of mass x. Typically, the analysis of aggregation can be simplified by use of the scaling ansatz [1]

$$n(x,t) = [s(t)]^{-2}\Phi\left(\frac{x}{s(t)}\right), \quad (2)$$

which reduces the number of variables from two (x and t) to one (x/s(t)). The function Φ is commonly referred to as the scaling distribution.

The scaling ansatz allows predictions of the long-time behavior of Smoluchowski's equation. However, the scaling does not address the initial evolution of the cluster size distribution. We have shown however, that it is possible to develop analytical estimates of this growth.

The primary goal of our work however, is to assess the effects of flow. A preliminary study [2], which does not explicitly address the fractal nature of the clusters, shows that islands of regularity may cause spatial variations in the rate of aggregation, and that aggregation in "well-mixed" chaotic systems is similar mathematically to Brownian aggregation and can be described by Smoluchowski's equation. The effect of chaotic mixing on the fractal nature of clusters is considered explicitly by Danielson, Muzzio and Ottino [3]. They determined the fractal dimension of the cluster is affected by mixing [for background on mixing and chaos, see 4]. This differs from a study by Torres et al. [5] which predicts that the flow field does not affect the fractal nature of the resulting clusters. The variation of fractal dimension with mixing is due to the nature of interactions of monomers and larger clusters in different mixing schemes. If the system is not well mixed, the large clusters do not interact with each other, the process resembles the particle-cluster aggregation [5]. However, if the system is well mixed, then larger clusters interact with each other and aggregation resembles cluster-cluster [5] aggregation. Thus, the fractal dimension of a cluster is expected to decrease with better mixing.

Computational studies were carried out in the so-called journal bearing flow. A particularly important aspect of this flow is that it can be realized experimentally and manipulated to produce both regular and chaotic flows [6]. Also, analytic streamfunctions, which allow for tractable computations, can be found in Wannier [7].

Our simulations mimic fast coagulation; particles seeded in the flow are convected passively and aggregate upon contact. Brownian motion is not considered and hydrodynamic interactions are neglected; passive particles move as fluid elements. The flows considered are regular, chaotic, and a combination of both. The clusters are compact (or spherical) and fractal (a typical fractal structure from our simulations can be seen below).

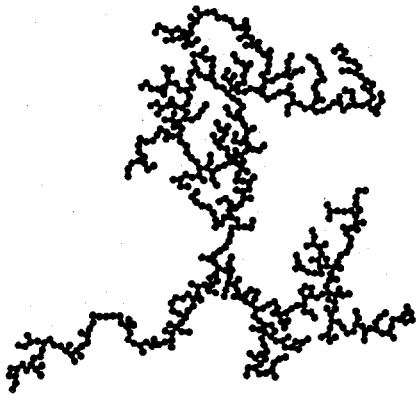

Figure 1: Typical fractal cluster from our simulations. The fractal dimension of this cluster is 1.54±0.001, and the radius of gyration is 40 times the particle radius.

An outline of the results obtained to date is shown in the following table:

	Growth of Average Cluster Size, s(t)				
Flow	Compact Structure				Fractal Structure
	constant capture radius, α		total area or volume constant		
	2 dimensions	3 dimensions	2 dimensions	3 dimensions	
Regular	for α=0.0025 $(1+0.22t)^{0.77}$ R=0.999	for α=0.0067 $(1+0.21t)^{0.7}$ R=0.997	for ρ=0.1 $(1+0.0065t)^{14}$ R=0.997	for ϕ=0.1 $(1+2.7t)^{0.85}$ R=0.998	for ρ=0.1 $(1+0.22t)^{0.7}$ R=0.999
"Poorly" mixed	for α=0.0025 $(1+0.29t)^{0.62}$ R=0.999 for α=0.00067 $(1+0.025t)^{0.55}$ R=0.999	for α=0.0067 $(1+0.44t)^{0.55}$ R=0.998	for ρ=0.02 $(1+0.018t)^{0.81}$ R=0.999 for ρ=0.1 $(1+0.0098t)^{25}$ R=0.988	for ϕ=0.1 $(1+25t)^{0.66}$ R=0.997	for ρ=0.02 exp(0.085t) R=0.999 for ρ=0.1 exp(0.79t) R=0.999
Chaotic	for α=0.0025 $(1+0.22t)^{1}$ R=0.995	for α=0.0067 $(1+0.21t)^{0.93}$ R=0.997	for ρ=0.02 $(1+0.012t)^{5.2}$ R=0.999 for ρ=0.1 $(1+0.06t)^{6.5}$ R=0.999	for ϕ=0.1 $(1+7.5t)^{1}$ R=0.998	for ρ=0.02 exp(0.21t) R=0.986 for ρ=0.1 exp(1.38t) R=0.976

Table 1: the growth rate of the average cluster size in the various studies. Here, α, ρ and ϕ are the capture radius, area fraction and volume fraction of clusters, respectively.

In general, the average cluster size and variance of the size distribution grow faster for fractal structures than compact structures, and the variance of the size distribution grows faster in poorly-mixed systems. Let us now consider a breakdown of the results: When the capture radius is constant, the average cluster size grows as $s(t) = s_0(1+t/t)^z$. The cluster size distributions are self-similar for the well mixed case and are given by

$$n(x,t) \approx M_1 s(t)^{-2} e^{-x/s(t)}. \tag{3}$$

However, the scaling ansatz does not hold for the poorly-mixed system. These results suggest that the size distribution may to some degree be controlled by the mixing. When the clusters are area conserving, formation of a large cluster dominates aggregation.

Significantly different kinetics are observed if fractal structure is considered; the average cluster size grows exponentially, as opposed to algebraically as in the case of compact structures.

Furthermore, due to the wide range of flow in the journal bearing flow, a distribution of fractal clusters is produced. When the area fraction of clusters is 0.02, the median fractal dimension of the clusters is dependent on the flow, similar to the study by Danielson et al. [3]. The median fractal dimension of clusters formed in the well-mixed system is 1.47 while the median fractal dimension of clusters formed in the poorly-mixed case is 1.55. Furthermore, the range of fractal dimension is higher in the well-mixed case.

The results are different when the area fraction of clusters increases. The median fractal dimension of the clusters is independent of the flow and is approximately 1.47. Since the fractal dimension of the clusters is closer to the dimension of the clusters in the well mixed system with a lower area fraction of clusters, this suggests that as the area fraction of clusters increases, the island of regularity gets broken up by the increasing capture radius of the clusters. Thus, aggregation in the poorly-mixed system behaves similarly to that in the well mixed system when aggregation occurs between the two disjoint regions of the flow. A more complete summary of these results appear in a paper under preparation [8].

MIXING OF SOLIDS

Let us consider now a few results pertaining to mixing of solids (dry powders). Our current understanding of solids mixing can scarcely be described as more than primitive: we can neither qualitatively nor quantitatively analyze the effectiveness of any given mixing mechanism in advance; we do not have a widely accepted set of equations - as in the companion case of liquid mixing - that govern solids mixing, and we cannot even establish whether a given set of solids will mix or de-mix under a given stirring regimen.

Recent work [9] has demonstrated that significant inroads can be made in this area using rather modest resources. We have shown that slow mixing processes can be imagined as a succession of avalanches and that processes can be divided into geometrical and dynamical parts. The geometrical aspects of the problems can be

cast in the language of maps. In depth aspects of dynamical aspects - leading for example to segregation effects - can be incorporated by means of molecular dynamic simulations. Simpler ad hoc methods capture gross aspects as well. Below we show a comparison between a experiment (left) and a computer simulation (right).

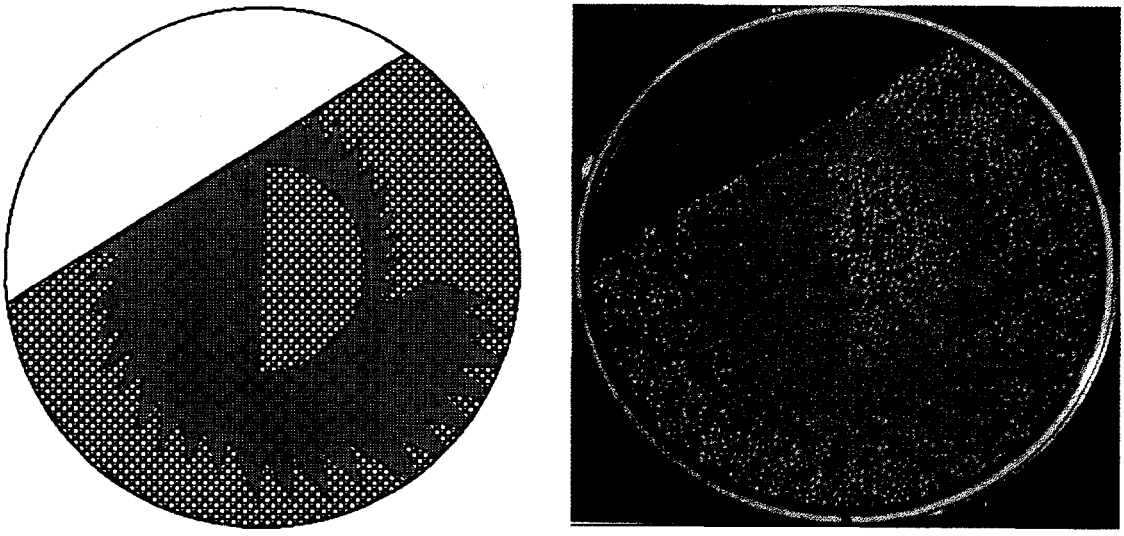

ACKNOWLEDGMENT

This work was supported by the U.S. Department of Energy, Division of Basic Energy Sciences.

REFERENCES

1. Meakin P., "Aggregation kinetics," *Physica Scripta* **46**, 295-331 (1992).

2. Muzzio, F. J. and Ottino, J. M., "Coagulation in chaotic flows," *Phys. Rev. A* **38**, 2516-2524 (1988).

3. Danielson, T. J., Muzzio, F. J. and Ottino, J. M., "Aggregation and structure formation in chaotic and regular flows," *Phys. Rev. Lett.* **66**, 3128-3131 (1991).

4. Ottino, J. M., *The kinematics of mixing: stretching, chaos, and transport*, Cambridge University Press: Cambridge, reprinted (1990).

5. Torres, F. E., Russel, W. B. and Schowalter, W. R., "Simulations of coagulation in viscous flows," *J. Colloid Interface Sci.* **145**, 51-73 (1991).

6. Swanson, P. D., and Ottino, J. M., "A comparative computational and experimental study of chaotic mixing of viscous fluids," *J. Fluid Mech.* **213**, 227-249 (1990).

7. Wannier, G. H., "A contribution to the hydrodynamics of lubrication," *Q. Appl. Maths.*, **8**, 1-32 (1950).

8. Hansen, S. and Ottino, J. M., "Aggregation and cluster size evolution in non-homogeneous flows," submitted to *J. Colloid Interface Sci.* (1995).

9. Metcalfe, G., Shinbrot, T., McCarthy, J. J., and Ottino, J. M., "Avalanche mixing of granular solids," *Nature* **374**, 38-41 (1995).

SPATIOTEMPORAL PATTERNS IN A REACTION-DIFFUSION SYSTEM AND IN A VIBRATED GRANULAR BED

Harry L. Swinney, K. J. Lee, W. D. McCormick, F. Melo, and P. Umbanhowar

Center for Nonlinear Dynamics and Department of Physics
The University of Texas at Austin
Austin, Texas 78712

ABSTRACT

Experiments on a quasi-two-dimensional reaction-diffusion system reveal transitions from a uniform state to stationary hexagonal, striped, and rhombic spatial patterns. For other reactor conditions lamellae and self-replicating spot patterns are observed. These patterns form in continuously fed thin gel reactors that can be maintained indefinitely in well-defined nonequilibrium states. Reaction-diffusion models with two chemical species yield patterns similar to those observed in the experiments. Pattern formation is also being examined in vertically oscillated thin granular layers (typically 3-30 particle diameters deep). For small acceleration amplitudes, a granular layer is flat, but above a well-defined critical acceleration amplitude, spatial patterns spontaneously form. Disordered time-dependent granular patterns are observed as well as regular patterns of squares, stripes, and hexagons. A one-dimensional model consisting of a completely inelastic ball colliding with a sinusoidally oscillating platform provides a semi-quantitative description of most of the observed bifurcations between the different spatiotemporal regimes.

INTRODUCTION

We are examining the formation of spatiotemporal patterns in two types of far-from-equilibrium systems that have been chosen in part because of their potential applications: (1) reaction-diffusion systems maintained by a continuous feed of chemicals, and (2) vertically oscillated thin layers of granular materials. Our earlier work on spatially extended chemical reactors demonstrated that in some cases a pattern forming chemical system can be used to achieve higher yield of certain species than can be achieved in the standard well-stirred batch or continuous flow (CSTR) reactors [1-2].

Shallow layers of granular materials ("vibrated beds") are used in industry because of their good heat and mass transfer properties [3-4]. A previous study observed square patterns in a vibrated bed [3], but the present work is the first to investigate systematically pattern formation in these systems.

Our goal is to understand the fundamental mechanisms leading to pattern formation and to determine the properties and parameter ranges of the different patterned regimes. Precision computer-controlled reactors and vibrated beds have been developed for these studies, and a high degree of reproducibility, unprecedented for these systems, is being achieved. The experiments are complemented by studies of models that provide insight into the spatiotemporal dynamics.

REACTION-DIFFUSION PATTERNS

Turing patterns

In a classic 1952 paper, Turing predicted that patterns could spontaneously form in reaction-diffusion systems. Turing considered systems with diffusion and chemical kinetic processes but no convection. We have developed reactors in which patterns form in a thin gel layer — the (essentially inert) gel prevents convection [5-11]. The gel layer is in contact on one or both sides with continuously refreshed reservoirs of the reagents of the reaction; thus the system can be maintained indefinitely in a well-defined nonequilibrium state.

In a study of a chlorite-iodide-malonic acid reaction, we found that patterns emerge spontaneously from an initially uniform background when critical values of the control parameters (chemical concentrations, temperature, gel thickness) are exceeded: the primary bifurcation leads to hexagonal patterns, as shown in Fig. 1(a) [5,7]. The wavelength λ of Turing patterns is predicted to depend not on the geometry (as in, e.g., fluid dynamic patterns), but only on the properties of the system: $\lambda = (2\pi\tau D)^{1/2}$, where D and τ are, respectively, a characteristic molecular diffusion coefficient of the reacting species and a characteristic time determined by the chemical kinetics. We have recently made direct measurements of D and τ and have confirmed the predicted dependence of λ on D and τ [6].

Fig. 1. Stationary chemical patterns formed in continuously fed gel reactors: (a) hexagons [5-8], (b) stripes [5-8], and (c) lamellae [9-10]. The gels are thin compared to the wavelength of the patterns so the patterns are approximately two-dimensional. Patterns (a) and (b), each 1 mm x 1 mm, were observed in a chlorite-iodide-malonic acid reaction [7]; variations in darkness correspond to variations in concentration of triiodide. Pattern (c), 13 mm x 10 mm, was observed in a ferrocyanide-iodate-sulfite reaction [9].

At the onset of instability the patterns consist of regular hexagons with 60° angles between all dots neighboring another dot [see, e.g., Fig. 1(a)], but beyond the onset of instability the hexagons can be slightly squashed — e.g., the angles between neighboring dots can be 57°, 66°, 57°, 57°, 66°, 57°; such rhombic structures have been found to be a consequence of the translational, rotational, and reflection symmetry of continuous planar continua [8].

With further increase in control parameter, we observe a bifurcation from hexagonal to striped patterns (cf. Fig. 1(b)) [5,7], and with yet further increase in control parameter the patterns can become disordered in both space and time [12].

Lamellae

Experiments on a bistable ferrocyanide-iodate-sulfite reaction have revealed a new type of spatial pattern, one in which fronts propagate at a constant speed until they reach a critical separation (typically 0.4 mm in the experiments) and stop [9-10]. This behavior contrasts with the behavior of waves in excitable media, where colliding fronts annihilate one another. The front patterns develop locally and spread to fill space, resulting in a stationary asymptotic pattern that is highly irregular, as Fig. 1(c) illustrates. The pattern forming process also contrasts with that leading to the regular hexagonal and striped patterns (Fig. 1(a)-(b)), which emerge spontaneously everywhere in the medium when a critical control parameter value is exceeded: the lamellae must be initiated by a finite amplitude perturbation.

Self-replicating spots

For conditions close to those yielding lamellae, patterns of spots are observed and are found to undergo a continuous process of birth through replication and death through overcrowding, as Fig. 2 illustrates. The spots do not form spontaneously, but once initiated by a perturbation (UV light or a boundary perturbation), the spot patterns are self-sustaining. These patterns are observed for a wide parameter range in the ferrocyanide-iodate-sulfite reaction.

Models

Simulations of several different reaction-diffusion models with two chemical species have been found to yield lamellae and self-replicating spots similar to those observed in the experiments (see refs. in [10]). (Replicating spots were actually first found in a model [13]). Even abstract models that could describe convection and other pattern forming systems as well as chemical systems have been found to form lamellae like those in Fig. 2(c). Thus, while lamellae and replicating spots have not been observed in other laboratory systems maintained far from equilibrium, the occurrence of these patterns in several models suggests that there is nothing remarkable about our ferrocyanide-iodate-sulfite system — lamellar and spot patterns can be expected to form in other chemical systems and perhaps in non-chemical systems as well.

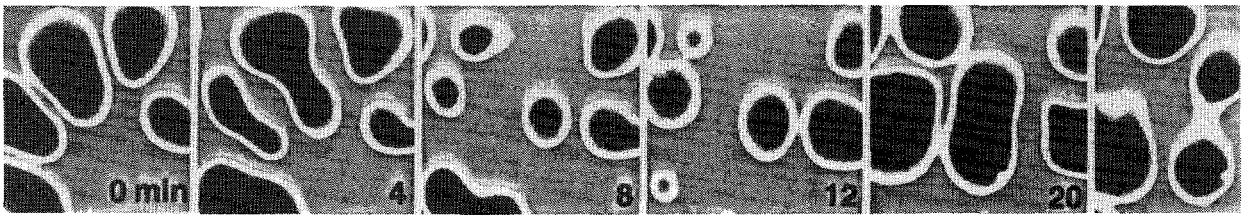

Fig. 2. Self-replicating spots evolving in time for 24 min. The behavior continues to evolve indefinitely as long as the reactor conditions are maintained [10-11]. Black represents the low pH state (pH ≅ 3); grey represents the high pH state (pH ≅ 7). The region shown is 7 mm x 7 mm.

PATTERNS IN VIBRATED GRANULAR BEDS

Granular materials are large assemblies of solid particles that interact mainly through nearest neighbor contacts; this is often a good approximation for granular systems in nature and industry, e.g., mined coal, concrete, cracking catalysts, rice, and pills. Granular materials comprise a unique state of matter with properties common to both fluids and solids. These shared properties make the application of statistical methods to the definition of mean quantities difficult, and cause phenomenological coefficients, such as viscosity or elasticity, to be strongly singular. Despite formidable challenges, the significant role of granular dynamics in industry and geology makes the understanding of these materials an important subject for science and engineering. Most research on granular materials has concerned static rather than dynamic properties, but in recent years some studies have begun to examine the time-dependent properties, and vibrating systems in particular have been found to exhibit some remarkable behavior [4, 14, 15].

The subject of our study, pattern formation in vibrated beds (shallow vertically oscillated layers), has not been previously examined in any detail [3-4]. We have found a variety of spatiotemporal patterns, some of which are illustrated in Fig. 3. We consider beds of particles that are sinusoidally oscillated with dimensionless acceleration amplitudes Γ in the range 0-9 (maximum acceleration relative to the gravitational acceleration) [16-17]. The particles (usually glass or bronze spheres in our experiments) have diameters in the range 0.1-1.0 mm. The layers are typically 3-30 particle diameters deep. The driving frequency ranges from 10 to 120 Hz. The container is 127 mm in diameter and 90 mm high. The container is evacuated to 0.1 torr, which is a pressure low enough so that volumetric effects of the remaining gas are negligible.

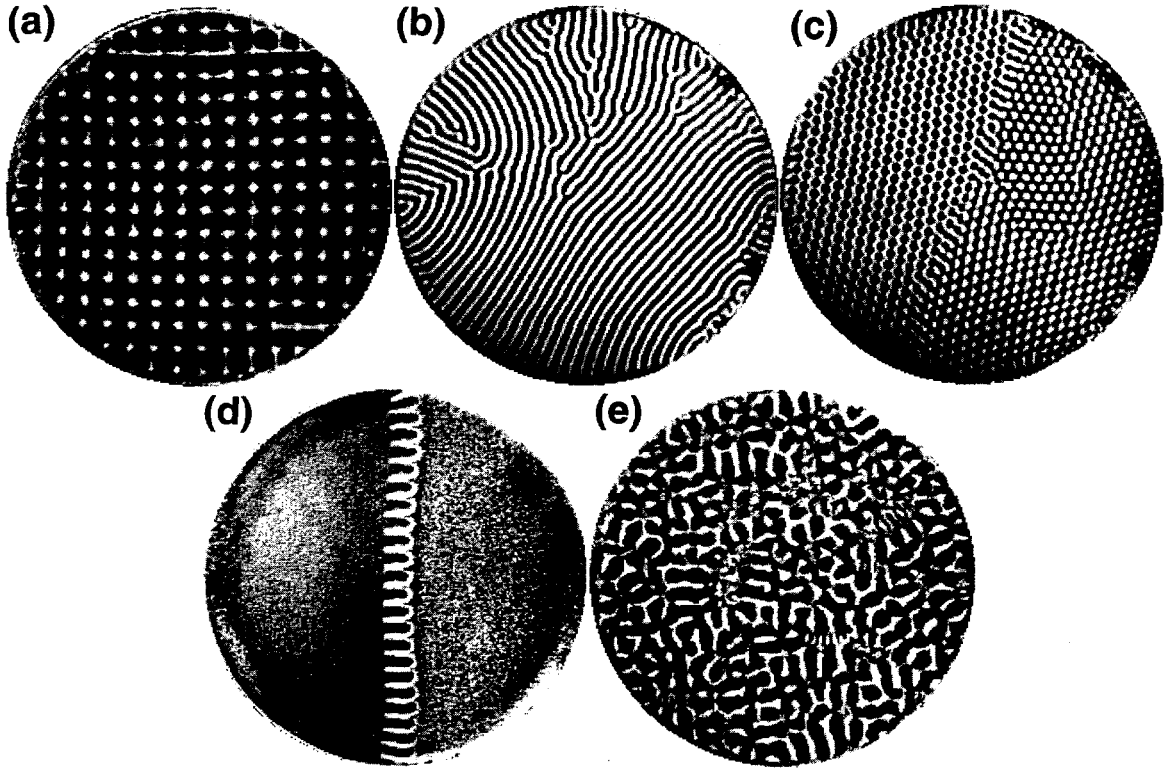

Fig. 3. Patterns observed for different dimensionless acceleration amplitudes Γ in a 1.2 mm thick layer of 0.15-0.18 mm diameter bronze spheres [16-17]: (a) squares (Γ = 2.7, f = 19 Hz), (b) stripes (Γ = 3.3, f = 67 Hz), (c) hexagons (Γ = 3.9, f = 67 Hz), (d) flat domains separated by kinks (Γ = 4.5, f = 37 Hz), and (e) disordered pattern (Γ = 8.5, f = 67 Hz).

We now describe some of the patterns.

Primary instability: squares and stripes

For small drive frequency f and increasing Γ, the flat surface bifurcates to a square standing wave pattern oscillating at f/2; see Fig. 3(a) [16-17]. For a drive frequency greater than a critical value (42 Hz for a 1.2 mm deep layer of 0.17 mm bronze spheres), the pattern is in the form of a stripes rather than squares, as Fig. 3(b) illustrates. The transition from a flat surface to squares is definitely hysteretic, while the hysteresis is small (perhaps absent) for the transition from a flat surface to a striped pattern.

Higher instabilities: hexagons, kinks, and disorder

As the acceleration is increased with the drive frequency fixed, we observe five successive regimes beyond the squares or stripes oscillating at f/2 (cf. Figs. 3 and 4) [17]: (i) hexagons (f/2); (ii) kinks (phase jumps of π) separating distinct flat domains; (iii) squares or stripes oscillating at f/4; (iv) hexagons (f/4); and (v) patterns disordered in both space and time. These different regimes are quite reproducible and the transitions between them are well defined.

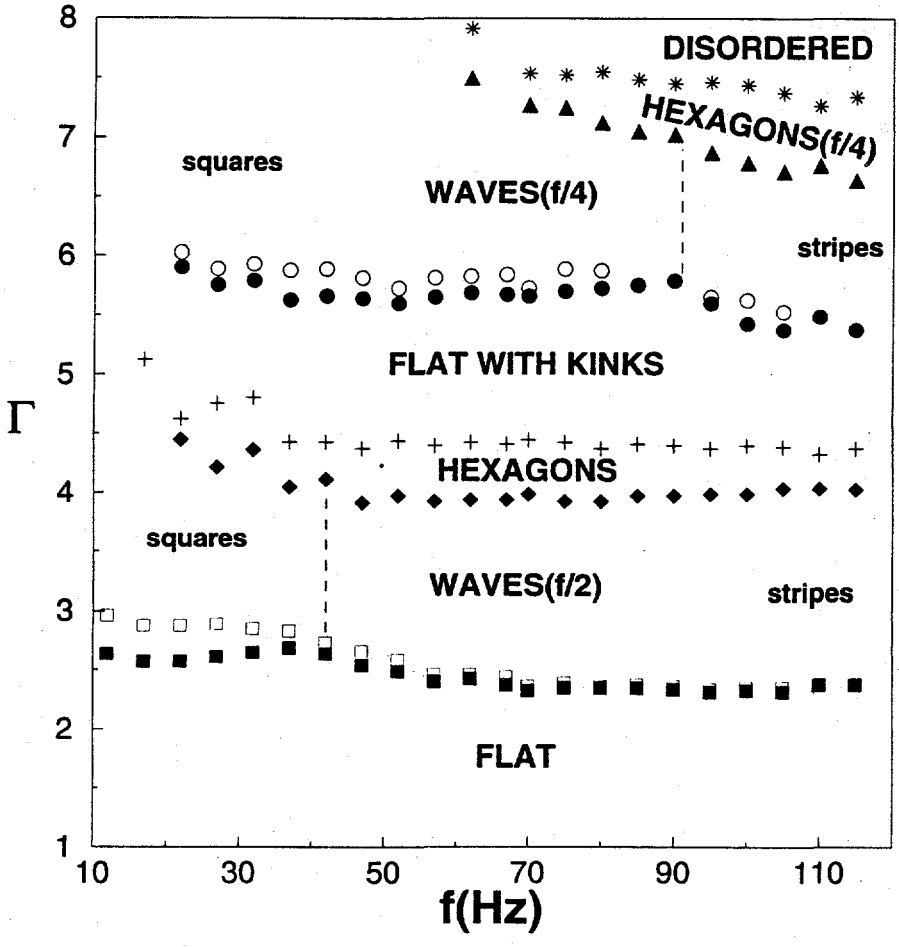

Fig. 4. Stability diagram showing different regimes in a granular layer (cf. Fig. 3) [17]. The transitions to squares (at frequency f/2 and f/4) are hysteretic, as indicated, while no hysteresis was measurable for the other transitions. The vertical dashed lines show the approximate center of the continuous transitions between squares and stripes.

Model

A one-dimensional model with a completely inelastic ball colliding with a sinusoidally oscillating platform indicates that the transitions from squares or stripes to hexagons and kinks are related to a period doubling bifurcation [17]. The model also provides insight into the higher bifurcations, even though of course the one-dimensional model cannot describe the form of the two-dimensional spatial patterns.

One goal of our study is to characterize and understand mixing in vibrated beds. Transport properties will be determined in the experiments by direct tracking of many particles, a technique that we have used in studying transport in quasi-geostrophic (oceanic-type) fluid flows [18]. The measurements will be compared with transport properties computed for two-dimensional models. This investigation should suggest ways in which the mixing properties of vibrated beds can be enhanced.

DISCUSSION

Our experiments have revealed new types of spatiotemporal patterns in reaction-diffusion systems and vibrated shallow granular beds. A fundamental understanding of the pattern forming processes in these systems should provide a stepping stone toward more efficient and innovative utilization of reaction-diffusion processes and vibrated beds.

ACKNOWLEDGEMENT

We gratefully acknowledge the participation of Qi Ouyang in some aspects of this research. This work was performed under the auspices of the U.S. Department of Energy Office of Basic Energy Sciences.

REFERENCES

1. R. D. VIGIL, Q. OUYANG, and H. L. SWINNEY, "Spatial variation of a short-lived intermediate chemical species in a Couette reactor," *J. Chem. Phys.* 96, 6126 (1992).

2. Q. OUYANG, H. L. SWINNEY, J. C. ROUX, P. DE KEPPER, and J. BOISSONADE, "Recovery of short-lived species in a Couette flow reactor," *AIChE J.* 38, 509 (1992).

3. B. THOMAS, M. O. MASON, Y. A. LIU, and A. M. SQUIRES, "Identifying states in shallow vibrated layers," *Powder Tech.* 57, 267 (1989).

4. B. J. ENNIS, J. GREEN, and R. DAVIES, "Particle Technology: the legacy of neglect in the U. S.," *Chem. Eng. Prog.* 90, 32 (1994).

5. Q. OUYANG and H. L. SWINNEY, "Transition from a uniform state to hexagonal and striped Turing patterns," *Nature* 352, 610 (1991).

6. Q. OUYANG, R. LI, G. LI, AND H. L. SWINNEY, "Dependence of Turing pattern wavelength on diffusion rate," *J. Chem. Phys.* 102, 2551 (1995).

7. Q. OUYANG and H. L. SWINNEY, "Onset and beyond Turing pattern formation," in *Chemical Waves and Patterns*, ed. by R. Kapral and K. Showalter, Kluwer Academic Publishers (1995), p. 269.

8. G. H. GUNARATNE, Q. OUYANG, and H. L. SWINNEY, "Pattern formation in the presence of symmetries," *Phys. Rev. E* 50, 2802 (1994).

9. K. J. LEE, W. D. McCORMICK, Q. OUYANG, and H. L. SWINNEY, "Pattern formation by interacting chemical fronts," *Science* 261, 192 (1993).

10. K. J. LEE and H. L. SWINNEY, "Lamellar structures and self-replicating spots in a reaction-diffusion system," *Phys. Rev. E* 51, 1899 (1995).

11. K. J. LEE, W. D. McCORMICK, J. E. PEARSON, and H. L. SWINNEY, "Experimental observation of self-replicating spots in a reaction-diffusion system," *Nature* 369, 215 (1994).

12. Q. OUYANG and H. L. SWINNEY, "Transition to chemical turbulence," *Chaos* 1, 411 (1991).

13. J. E. PEARSON, "Complex patterns in a simple system," *Science* 261, 189 (1993).

14. H. M. JAEGER, J. B. KNIGHT, C. H. LIU, and S. R. NAGEL, "What is shaking in the sandbox?," *MRS Bulletin* 19 (no. 5), 25 (1994).

15. H. K. PAK, E. VAN DOORN, AND R. P. BEHRINGER, "Effects of ambient gases on granular materials under vertical vibration," *Phys. Rev. Lett.*, to appear.

16. F. MELO, P. UMBANHOWAR, and H. L. SWINNEY, "Transition to parametric wave patterns in a vertically oscillated granular layer," *Phys. Rev. Lett.* 72, 172 (1994).

17. F. MELO, P. UMBANHOWAR, and H. L. SWINNEY, "Hexagons, kinks, and disordered patterns in a vertically oscillated granular layer," *to be published.*

18. T. H. SOLOMON, E. R. WEEKS, and H. L. SWINNEY, "Chaotic advection in a two-dimensional flow," *Physica D* 76, 70 (1995).

DEFORMATION AND CRACK GROWTH RESPONSE UNDER CYCLIC CREEP CONDITIONS

Frederick W. Brust, Jr.

Battelle Memorial Institute
Columbus, Ohio 43201, U.S.A.

ABSTRACT

To increase energy efficiency, new plants must operate at higher and higher temperatures. Moreover, power generation equipment continues to age and is being used far beyond its intended original design life. Some recent failures which unfortunately occurred with serious consequences have clearly illustrated that current methods for insuring safety and reliability of high temperature equipment is inadequate. Because of these concerns, an understanding of the high-temperature crack growth process is very important and has led to the following studies of the high temperature failure process.

This effort summarizes the results of some recent studies which investigate the phenomenon of high temperature creep fatigue crack growth. Experimental results which detail the process of creep fatigue, analytical studies which investigate why current methods are ineffective, and finally, a new approach which is based on the T*-integral and its ability to characterize the creep-fatigue crack growth process are discussed. The potential validity of this new predictive methodology is illustrated.

INTRODUCTION

As noted by Prager [1], the executive director of the Materials Property Council (MPC), historically equipment became obsolete, and was replaced with new designs, before the potential creep fatigue failure time was reached. As a result, experience with creep failures under nominal

design conditions has been limited. Some recent failures of high energy steam pipes in fossil power plants (see Lundin, et al. [2,3]), which were highly publicized and occurred with serious consequences, have clearly illustrated that creep rupture failures must be prevented. From the MPC studies (References [1] to [3]) and field experience it is now known that current engineering methods to predict the life of components that operate in these severe environments are ineffective. The reasons these current methods are ineffective are briefly summarized in the following paragraphs. Thorough and detailed discussion is provided in References [4-16].

The methods currently used for predicting the life of components that must operate in an environment where creep and creep/fatigue damage may develop are an extension of methods developed to predict elastic-plastic fracture. For an elastic-plastic cracked body, assuming deformation theory plasticity can adequately characterize the straining, one may show that the strength of the asymptotic field may be characterized by a path independent integral (the J-integral). Today, elastic plastic fracture is characterized in practice using J-integral tearing theory. It was quickly recognized that a creep analogue to plasticity using a Norton Creep Law (instead of deformation plasticity) leads to a path independent rate integral, C^*-integral, which characterizes the strength of the creep crack field. Following the same reasoning as that developed for elastic-plastic fracture, as adapted for creep crack growth, a creep fracture methodology was developed. The reason that the creep fracture analogy fails while the plasticity fracture technique works well are now clear: *deformation theory plasticity can accurately characterize plastic deformation near the high stresses which develop near the crack tip while Norton creep cannot characterize the creep deformations near a crack tip in a creeping body.* Moreover, when cyclic loads occur, the current methods for predicting creep-fatigue lives, which are based on Miner's rule, completely break down. Rather than use the strength of the asymptotic field as the creep fracture parameter, which depends on the chosen constitutive law, we have developed an energy-based fracture parameter which is independent of the chosen constitutive law. This method is discussed later.

CYCLIC CREEP DAMAGE

Consider a cracked body which is loaded and held at the load at a temperature which causes creep deformation to occur. The bulk of the creep strains will develop at the crack tip and emanate outward from the tip as time proceeds. A "creep zone" has thus developed at the crack tip. If the load is then removed from the body, the elastic strains surrounding the creep zone are prevented from going to zero because the inelastic creep strains prevent the body from attaining its original configuration. Hence, a compressive zone is induced in the crack region. This compressive zone can be quite large in size (see References [8,12,13] for calculations which illustrate the size of this zone). Figure 1 illustrates this effect with a blow up of the region near a crack tip produced from a detailed analysis of a 9Cr-Mo steel which experienced numerous cycles (see Reference [12] for details). If the load is then held at a zero or a negative load (or at any load smaller than the original load), a compressive creep zone which also emanates from the crack tip, and also grows with time, will develop in this compressive stress zone. If the load is then increased (positively) again, tensile stresses develop at the crack tip, a tensile creep zone re-

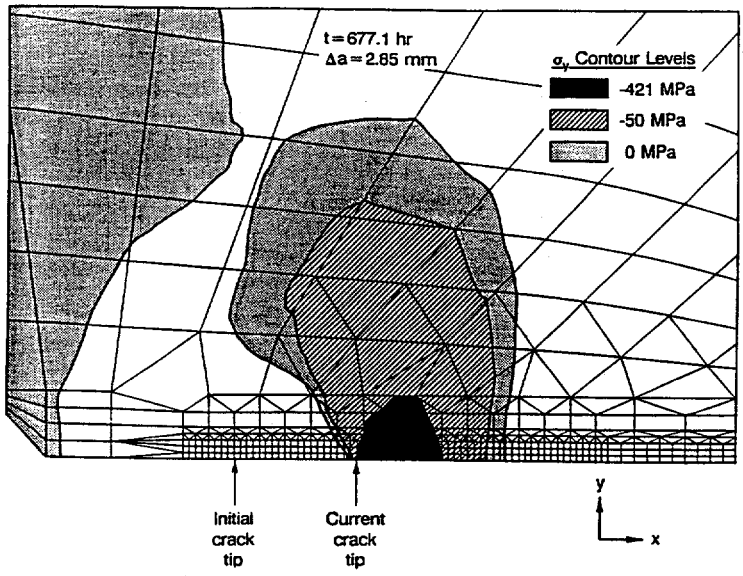

Figure 1. Contour Plots of the y-component of Stress at the End of an Unload/Hold Sequence forthe Analysis of a 9Cr-Mo Steel at 538 C. The Specimen Was Loaded and Held for 24 Hours, Unloaded and Held for 0.1 Hour, etc. The Results Shown Here are Near the End of the Test. Note the large size of the compressive stress zone even though the minimum load is zero.

develops, etc. It should be clear that, for any creep-fatigue situation where hold times occur, the crack tip region constantly experiences reversing tensile and compressive creep strains. Moreover, the creep strain rates which develop after each change in sign (ie., positive to negative or vice-versa) are greatly increased compared to the situation where no stress reversals occur [4,5]. This causes increased creep damage compared to the constant load case, and is the reason that classical creep fatigue crack growth methods break down.

EXPERIMENTAL OBSERVATIONS

The effect of the above described alternating tensile and compressive creep zones that develop near the crack tip during cyclic loading (even for R-ratios greater than zero) is increased creep damage and reduced life. A number of different tests were performed on 316 stainless steel at 650 C and 593 C, and on 9Cr-Mo steel at 538 C that illustrates this effect (see the cited References). Here we summarize some general trends.

Let us first examine some of the general conclusions which can be made regarding history-dependent loading in the time-dependent deformation regime. Figure 2 illustrates a load versus time sequence that was applied to one of the 9 Cr-Mo compact tension specimens at 538 C. An initial load period of 36 hours was made to ensure the development of an initial creep zone in the specimen. The unload hold times and subsequent reload times were continually decreased until about 90 hours, after which four-hour hold periods and one-hour unload periods were maintained until the specimen failed. This assured a truly variable load history.

An enlargement of the displacement versus time history for this experiment between 325

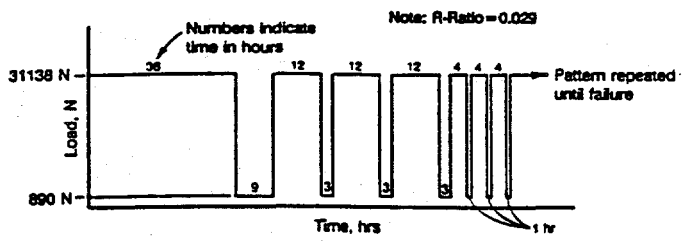

Figure 2. Load Time sequence (1st 9Cr-Mo test)

and 365 hours after beginning the test is illustrated in Figure 3. This specimen failed after about 400 hours. Another specimen was loaded to the same load level and was identical in all other ways to the above-described specimen except for a slightly larger initial crack. However, this specimen was held for 320 hours before unload/reload occurred, and only one cycle was applied. Figure 4 illustrates the displacement versus time history for this test. Note that this test failed at more than 600 hours.

Several important general conclusions can be drawn from these results:

- During the unload-hold period, load-point displacement recovery occurs. This is due to the compressive stresses which develop at the crack tip during unloading. The compressive stress zone size can be quite large, as was verified through computational studies, even though the global load is never less than zero.

- After reload, the displacement rates increase compared to the rates during the previous loading period. This is clearly seen in Figures 3 and 4. Note also that the displacement just after reloading is always smaller than the corresponding value just before unloading.

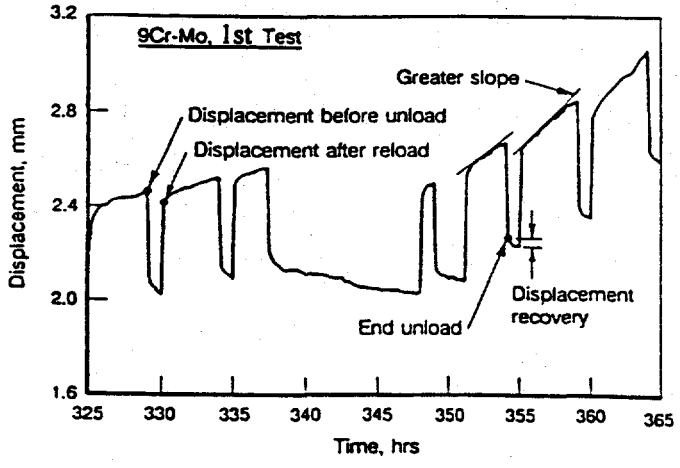

Figure 3. Displacement Time History 1st 9CrMo Test.

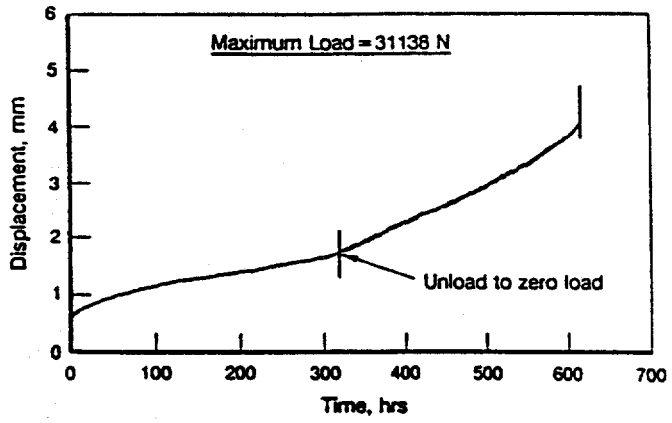

Figure 4. Displacement Time History - 2nd 9CrMo Test.

- Load-history effects significantly decrease life compared to the nearly constant load (only one unload) test, i.e., in this case the constant load test lasted nearly 1.5 times longer.

ANALYSIS SUMMARY

Here we briefly show results of an asymptotic study before showing results from an analysis of an experiment. Consider a stationary crack subjected to the following load sequence: (i) Load with 24-hour hold period, (ii) unload (to zero load) and hold for one hour, (iii) reload and hold for 24 hours, (iv) etc. This means that the end of the load-hold periods were 24, 49, 74, and 99 hours. An extremely refined symmetric finite element mesh was developed with 10 rings of six-noded isoparametric triangular elements surrounding the crack tip and eight-noded elements elsewhere with the crack-tip element size equal to .0005 times the uncracked ligament. This refinement is about 2.5 times more refined compared with the classical HRR field studies of Shih and German. A classical strain-hardening (S-H) and the Murakami-Ohno (M-O) cyclic creep law were used to model the problem. Creep properties for 9 Cr-Mo steel were used. Figure 4 illustrates the theta component (i.e., perpendicular to the crack) of creep strain as a function of the distance, R, ahead of, and parallel to, the crack. Note that the creep strain as calculated using the M-O law continuously drifts away from the strains evaluated using a classical law. This is because the creep strain rates after a *change in stress direction* which occurs near the crack during global load changes become very large. This is observed both experimentally and predicted using M-O. The S-H law cannot capture this effect. The importance of this is that the true deformation response of the cracked body must be accounted for in order to adequately predict the damage accumulation near the crack. Examination of stresses also reveals that the strength of the asymptotic field also changes from cycle to cycle. We thus conclude that current engineering methods, which are based on correlating creep-crack growth rates to the strength of an asymptotic field assuming a classical creep law (and constant load conditions), are not valid for variable load conditions.

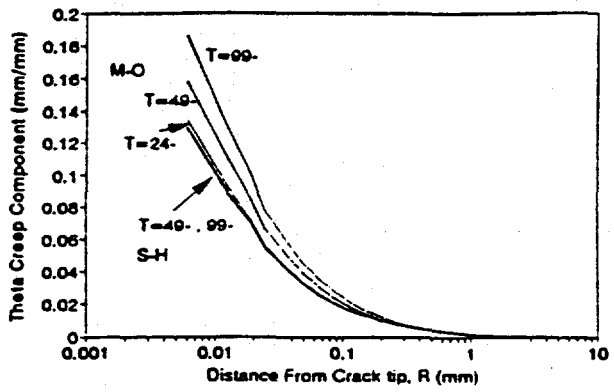

Figure 5 Asymptotic Creep Strains.

Finally, the analysis results of one of the 9 Cr-Mo tests (i.e., third test) are presented. This specimen had a load sequence consisting of (i) load and hold for 24 hours, (ii) unload and hold for 5 minutes, (iii) reload and hold for 24 hours, etc., (i.e., different from Figure 1 and 3). The maximum load was 23.353 KN, and the minimum load was zero.

The finite element model was forced to follow the load-time and crack-growth history. The constitutive law used to perform the analyses is based on the work of Murakami and Ohno. The numerical implementation of this law and the finite element model is detailed in References [7,13]. An implicit numerical scheme is used, crack growth is modeled in the two dimensional problems using a node release technique, and the T*-integral is evaluated using a direct approach. Other integral parameters are also evaluated. T* can be shown to represent the energy release rate to a process zone near the growing crack tip per unit crack growth. Reference [16] details the theory of T* as well as providing a number of verification examples for different conditions.

Load-line displacements were predicted as well as a number of integral fracture parameters. The fracture parameters considered here are integral parameters, which have an energetic physical interpretation. The T^*, J_W (Watanabe), J_M (McClintock), $\hat{J}$ (Aoki, et al.), and J_B (Blackburn) integrals were evaluated throughout the history (please see references for detailed discussions of these parameters). The crack initiated at about 192 hours and failure occurred after 700 hours in the test. Note that the entire load history was modeled.

Figure 6 shows a comparison of the maximum displacements (at the end of the load-hold period) and minimum displacements (at the end of the unload-hold periods). It is seen that the predicted displacements compare quite well with the experimental results, which suggests that the model is adequate. The predicted displacements begin to accelerate upward at about 600 hours while the experimental results begin to increase at about 650 hours, i.e., the analysis predictions are a little conservative here. The displacement trends of displacement recovery after unload, and displacement rates increasing after reload (of the type illustrated in Figure 3) were also predicted reasonably well compared to the data.

Figure 7 compares all of the integral parameters as a function of time. As indicated in Figure 7, crack growth begins at about 192 hours, after the eighth unloading. Note that, before crack growth, all of the integrals experience a step jump after a load cycle indicating that variable loads increase creep damage conditions as measured by these parameters. Note that the T^* and

J_W integrals attain a nearly constant value during the crack-growth phase (observe the horizontal lines in Figure 7). This result suggests that a constant value of T^* or J_W can characterize crack growth under creep fatigue conditions. Moreover, crack initiation can be predicted. At about 628 hours the integral parameters become unstable, suggesting that crack instability is predicted. The analysis results of the other tests also showed this same performance of the integral parameters. Energetic parameters can characterize load history dependent fracture while asymptotic methods must be abandoned.

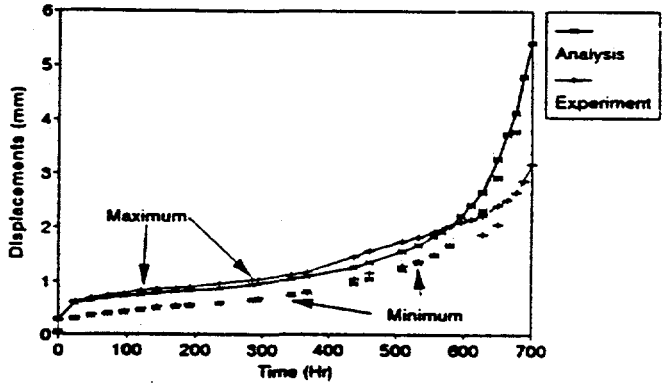

Figure 6. Displacement Comparisons for 3rd 9Cr-Mo test.

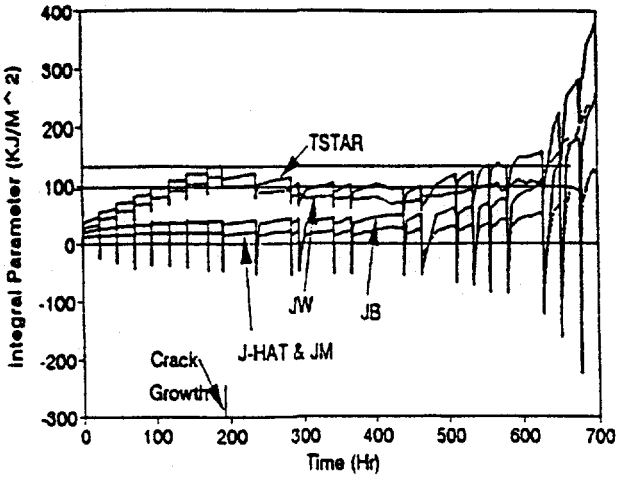

Figure 7. Behavior of Integral Parameters for 3rd 9Cr-Mo Test.

ACKNOWLEDGEMENTS

This work was performed under the auspices of the U.S. Department of Energy, Office of Basic Engineering Science. The authors thank Drs. O. Manley and James Welty for their support.

REFERENCES

1. M. PRAGER, "Issues in Life Assessment of Chrome-Moly Welds", *ASME PVP-Vol. 2391,* MPC-Vol. 33 (1992).

2. C. D. LUNDIN ET. AL., "Failure Analysis of a Service-Exposed Hot Reheat Steam Line in a Utility Steam Plant", Excerpt from WRC Bulletin 354, June (1990).

3. C. D. LUNDIN AND Y. WANG, "Repair Welding of Service Exposed Cr-Mo Steel Weldments", Excerpt from WRC Bulletin 348, November (1989).

4. P. KRISHNASWAMY, F. W. BRUST, AND N. D. GHADIALI, "A Finite Element Algorithm To Study Creep Crack Growth Based on the Creep Hardening Surface", *Int. J. Num. Meth. Eng.* 38 (6), 969-988 (1995).

5. F. W. BRUST, P. KRISHNASWAMY, AND B. S. MAJUMDAR, "Consideration of History Dependent Damage in Creep Crack Growth", *Proc. 10th Symp. Energy Eng. Sci.,* Argonne, Ill., May (1992).

6. P. KRISHNASWAMY, F. W. BRUST, AND N. D. GHADIALI, "Finite Element Analysis of History Dependent Damage in Time Dependent Fracture Mechanics", *ASME J. Pres. Ves. Tech.,* (115), 339-347 (1993).

7. F. W. BRUST AND P. KRISHNASWAMY, "A Computational Study of the Time Dependent Crack Growth Process", *ASME AD-Vol 27,* ed. A. Nagar (1992).

8. F. W. BRUST AND B. S. MAJUMDAR," Load History Effects on Creep Crack Growth", *Eng. Fract. Mech.,* 49 (6), 809-837 (1994).

9. F. W. BRUST AND B. S. MAJUMDAR, "Studies of Creep Crack Growth Under History Dependent Loading", *Proc. ICF-8,* Ukraine, June (1993). Also to Appear *J. Matl. Sci.*

10. F. W. BRUST, P. KRISHNASWAMY, AND B. S. MAJUMDAR, "Further Studies of History Dependent Loading in the Creep-Crack Growth Regime", in Fracture Mech. - Applications and New Matls., ed. A. Mehta, *ASME PVP Vol. 260,* July (1993).

11. P. KRISHNASWAMY AND F. W. BRUST, "Finite Element Modeling of Creep Crack Growth In 316 Stainless and 9 Cr-Mo Steels", *Proc. 11th Int. Invit. Symp. On the Unif. Of Anal., Comp., Sol. Meth.,* Boston, MA, August (1993).

12. F. W. BRUST, "Investigations of High Temperature Damage and Crack Growth Under Variable Load Histories", *Int. J. Sol. Structs.*, in press (1995).

13. F. W. BRUST, "Numerical Modeling and Experiments of Creep Crack Growth Under Cyclic Loading", *ASTM STP 1256,* (1995).

14. F. W. BRUST, "The Effects of Load History on Creep Damage Evolution", *ASME PVP Volume,* July (1995).

15. F. W. BRUST, "An Investigation of the Effects of History Dependent Damage in Time Dependent Fracture Mechanics", *To Appear Proc. ICES-95,* August (1995).

16. F. W. BRUST, "The T*-Integral: Definition and Use for Predicting Damage Accumulation and Fracture", invited pres. at *A. C. Eringen Medal of the Soc. Of Eng. Sci. Award*, New Orleans. Also to appear in *Recent Advances in Engineering Science,* November (1995).

ADVANCED LASER DIAGNOSTICS FOR DIAMOND DEPOSITION RESEARCH

C.H. Kruger, T.G. Owano, E.H. Wahl

High Temperature Gasdynamics Laboratory
Department of Mechanical Engineering
Stanford University
Stanford, CA 94305-3032

ABSTRACT

Chemical Vapor Deposition (CVD) using thermal plasmas is attractive for diamond synthesis applications due to the inherently high reactant densities and throughput, but the associated high gas-phase collision rates in the boundary layer above the substrate produce steep thermal and species gradients which can drive the complex plasma chemistry away from optimal conditions. To understand and control these environments, accurate measurements of temperature and species concentrations within the reacting boundary layer are needed. This is challenging in atmospheric pressure reactors due to the highly luminous environment, steep thermal and species gradients, and small spatial scales. The applicability of degenerate four-wave mixing (DFWM) as a spectroscopic probe of atmospheric pressure reacting plasmas has been investigated. This powerful, nonlinear technique has been applied to the measurement of temperature and radical species concentrations in the boundary layer of a diamond growth substrate immersed in a flowing atmospheric pressure plasma. In-situ measurements of CH and C_2 radicals have been performed to determine spatially resolved profiles of vibrational temperature, rotational temperature, and species concentration. Results of these measurements are compared with the predictions of a detailed numerical simulation.

INTRODUCTION

Thermal plasma CVD of diamond thin films is an attractive synthesis technique due to several inherent attributes. The high reactant densities available at atmospheric pressure can produce high radical fluxes to the deposition surface, resulting in high growth rates. Operation at atmospheric pressure also precludes the loading and unloading of samples to be coated from a vacuum system, yielding a corresponding decrease in process cost and complexity. From a modeling standpoint, the atmospheric pressure reacting flowfield is in the continuum, rather than the molecular or transitional flow regime and is more readily simulated. These beneficial attributes of atmospheric pressure deposition are tempered by the presence of a collision dominated, chemically reacting boundary layer above the substrate surface in which important

chemical species are both rapidly produced and destroyed. This aspect of atmospheric pressure techniques is strikingly different from low pressure deposition techniques in which production and diffusion of chemical species controls the deposition process

Previous studies of the atmospheric pressure deposition environment have yielded important knowledge of the parameters affecting diamond formation,[1-4] but have been limited to mostly post-deposition characterizations and comparisons. To further explore the nature of the atmospheric pressure diamond deposition environment and process, it is necessary to make accurate in-situ measurements of temperatures and species concentrations within the thin (< 1 cm) reacting boundary layer over the substrate, and compare these fundamental quantities with detailed simulations.

It is quite difficult, for many diagnostic techniques, to provide useful and accurate information from such a harsh and potentially nonequilibrium environment. Sensitive measurement of temperature and trace radical concentrations within a reacting boundary layer is a challenging problem in atmospheric pressure reactors due to the highly luminous environment, small spatial scales, and steep thermal and concentration gradients. It is in this environment where the application of sensitive, laser based diagnostic techniques can allow the detailed measurement of temperature and trace radical concentrations to be made, and compared to models of the deposition environment. The application of a powerful non-linear laser spectroscopy, degenerate four wave mixing (DFWM), as a gas-phase optical diagnostic has opened the door for significant advancement in the area of atmospheric pressure plasma chemistry, since it can provide high sensitivity and spatial resolution with a coherent, phase conjugate signal which can be readily discriminated against the plasma luminosity.[5-8]

The DFWM technique utilizes three laser beams of a single wavelength interacting with the plasma to produce a fourth spatially coherent, polarized signal beam that can be collected with high efficiency, and effectively filtered from the intense plasma luminosity. This feature is perhaps the greatest advantage of DFWM over other traditional diagnostic tools of atmospheric pressure plasmas which are often disabled or corrupted by the intense background luminosity. DFWM is found to be an extremely useful nonintrusive probe of the plasma, capable of providing high spectral and spatial resolution, and permitting measurements of temperature and relative species concentrations of trace radicals under conditions in which other spectroscopic techniques fail. Since DFWM can be used to probe the ground state of electronic transitions, it is much less subject to misinterpretation as a result of nonequilibrium effects[9] than conventional techniques such as optical emission spectroscopy (OES). Measurements of vibrational and rotational temperatures, as well as relative concentration profiles for CH and C_2 radicals have been measured in the thin boundary layer of a diamond-growth substrate immersed in a flowing atmospheric pressure plasma. DFWM measurements of temperature and relative species concentrations are compared with the results of a detailed numerical simulation[10] of the reacting plasma, and found to be in agreement.

EXPERIMENTAL FACILITY

The RF inductively coupled plasma (ICP) torch facility has been described in previous work.[1,4] The present experiments were conducted inside a water cooled quartz test section which is shown in schematic cut-away along with the plasma torch head in Figure 1. Open-ended laser access ports, approximately 6.5 cm downstream of the nozzle exit, enable the DFWM pump and

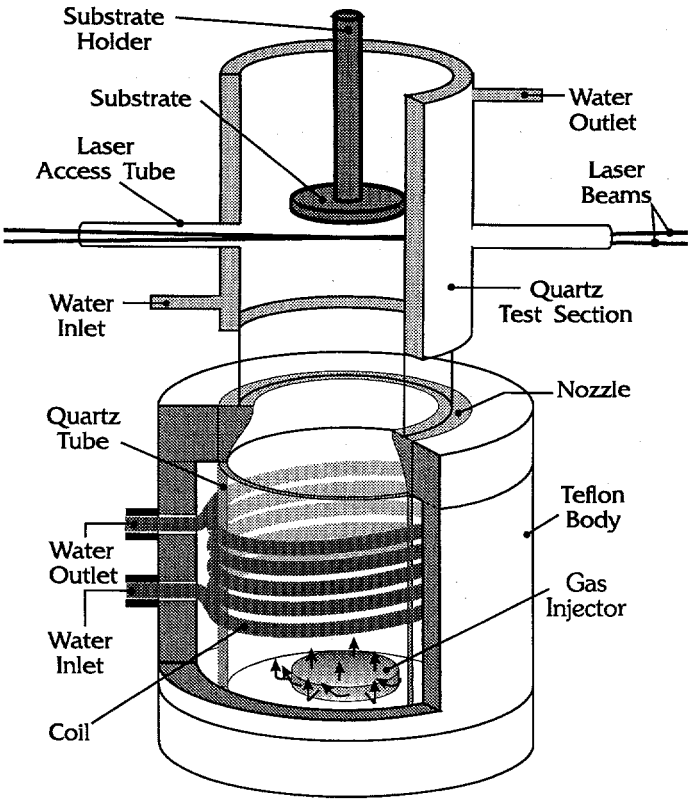

Figure 1. Schematic of RF-ICP reactor.

probe beams to enter and exit the reactor unhindered, and to cross at a location directly below the stagnation point of the substrate. Substrates are supported within the quartz test section in a stagnation point flow geometry by means of a water cooled holder. The substrate can be vertically translated in-situ to allow laser measurements to be made at various points through the boundary layer. Substrate temperature is monitored with a Minolta/Land Cyclops 152 infra-red optical pyrometer. Reactant gases (hydrogen and methane) are premixed with the carrier gas (argon) before passage through the RF discharge.

The optical configuration for this facility is shown schematically in Figure 2.. Laser beams for the DFWM experiments are produced using a Nd:YAG pumped dye laser system (~0.05 cm^{-1} bandwidth). The output of the laser is spatially filtered to improve beam quality, and reduced in intensity with a variably rotated half-wave plate, fixed polarizer combination. The beam is then split into three beams (of approximately equal energy at the test section), the backward pump beam (denoted E_b), the probe beam (denoted E_p), and the forward pump beam (denoted E_f). Polarization of the backward pump beam is rotated with a half-wave plate to be perpendicular to the polarization of the forward pump and probe beams, thus aiding signal isolation. Beam convergence is adjusted to produce a mild focus at the mid-line of the test section, producing beam waists of approximately 300 μm diameter. The forward and backward pump beams are brought coaxial and counterpropagating through the test section laser ports, and the probe beam crosses the pump beams at a slight angle (≈2.1°) directly beneath the stagnation region of the

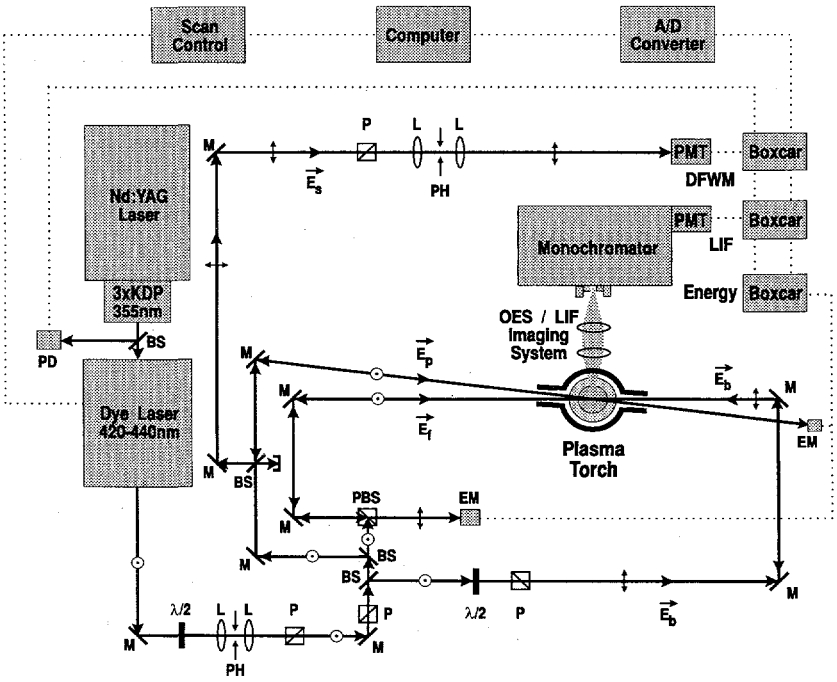

Figure 2. Schematic of optical configuration.

substrate. The three beams lie in a plane parallel to the substrate surface. Geometric interaction length of the pump and probe beams is approximately 16 mm (parallel to the substrate surface).

The phase-conjugate signal beam (denoted E_S) is generated within the interaction region and follows the reverse path of the probe beam out of the test section. This signal beam counterpropagating along the probe beam line is separated by means of a beamsplitter, spatially filtered to reject incoherent scattering, and detected with an unfiltered photomultiplier tube (Hamamatsu Model R212). Beam energy is continuously monitored by means of two joulemeters (Molectron J4-09) which terminate the probe and backward pump beams.

DEGENERATE FOUR-WAVE MIXING RESULTS

The applicability of in-situ DFWM to the atmospheric pressure diamond synthesis environment has been investigated using the well controlled, atmospheric pressure ICP reactor (Figure 1). It was desired to make in-situ measurements during normal operation of the atmospheric pressure RF-ICP diamond synthesis reactor - with a substrate in place, and growing diamond. The conditions chosen for these studies were indeed diamond growth conditions (although they were not optimized for best possible growth) and all measurements reported here were taken with the growing substrate in place. The reactor gas feed mixture was comprised of 106.5 l/min Ar, 12.0 l/min H_2, and 0.8% to 10% CH_4 (in H_2) premixed before introduction to the plasma torch. Calorimetric energy balance of the reactor indicates a net plasma enthalpy of 6 kW leaving the nozzle exit. The molybdenum substrate had a measured surface temperature of 1035°C.

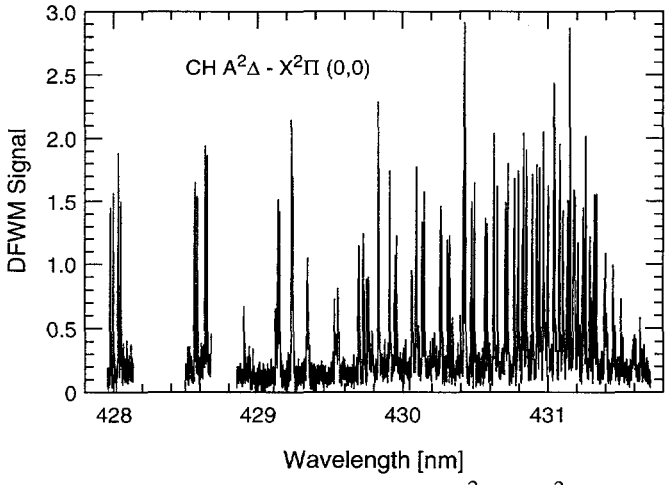

Figure 3. DFWM Spectra of CH $A^2\Delta \leftarrow X^2\Pi$ (0,0)

The CH radical was probed with in-situ DFWM measurements of the CH $A^2\Delta \leftarrow X^2\Pi$ (0,0) system near 431 nm. Figure 3 shows a DFWM spectrum of this region taken with approximately 10 μJ laser beam energies. The small groups of lines to the left side of Figure 3 are the grouped components of individual rotational lines in the R branch, while the closely spaced lines toward the right side of the figure are individual lines comprising the Q branch (the P branch is not shown). The v″=0 and v″=1 sets of individual R branch lines are closely grouped (Figure 4) and permit determination of vibrational temperatures. The Q branch region allows fairly rapid measurements of several v=0 lines, thus permitting rotational temperature measurements to be made throughout the

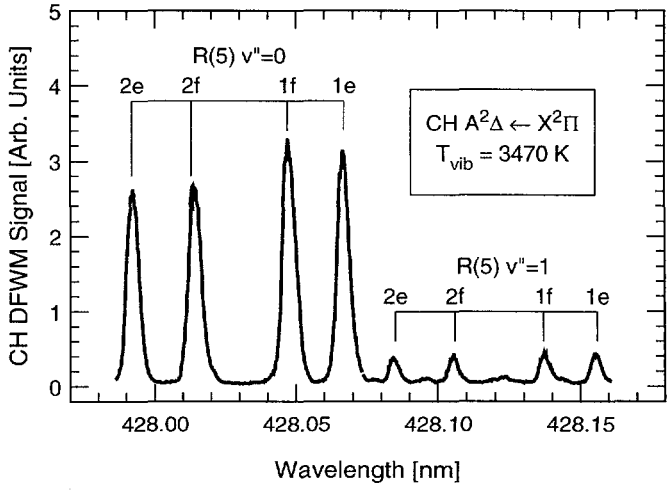

Figure 4. CH R(5) v"=0 and v"=1 components.

reacting boundary layer. An example of this rotational temperature determination is shown in Figure 5 where the intensity of measured Q branch lines (from N = 6 to 20) are plotted on a DFWM Boltzmann plot. This yields a straight line distribution (indicating rotational equilibration) corresponding to a rotational temperature of 3135 K. The C_2 radical was probed with in situ DFWM measurements of the C_2 $d^3\Pi_g \leftarrow a^3\Pi_u$ (3,1) system near 437 nm.

A stoichiometric study of the freestream concentrations of CH and C_2 radicals as a function of methane to hydrogen feed gas ratio was performed to address several questions. First, since the methane to hydrogen feed gas ratio is an important process parameter in controlling quality of the deposited diamond, it was of interest to determine the sensitivity of DFWM measurements of CH and C_2 radicals to this ratio. Secondly, an important assumption in modeling this environment[4-7,10] is that the freestream be a known input condition; more specifically that the freestream plasma is in chemical equilibrium at the measured freestream temperature. Although this a priori assumption is quite reasonable since the flowtime of the plasma from the region of excitation is chemically very long (10 ms compared to a chemical relaxation time of approximately 1 ms), it is nonetheless a prudent idea to test its validity for these trace radicals.

In Figure 6, the results of this stoichiometric study are shown for methane to hydrogen feed gas ratios ranging from approximately 0.8% to 10%, with measured freestream temperature constant at 3500 K. The closed and open circles correspond to the CH and C_2 relative mole fractions measured using DFWM, and the solid lines represent equilibrium chemical composition for the plasma mixture at 3500 K. (The CH and C_2 DFWM relative concentration data sets have been normalized to the equilibrium composition lines for comparison). The agreement between the equilibrium calculation and the measured relative mole fractions of CH and C_2 as a function of methane to hydrogen feed gas ratio is a very good indication that the freestream is indeed in chemical equilibrium.

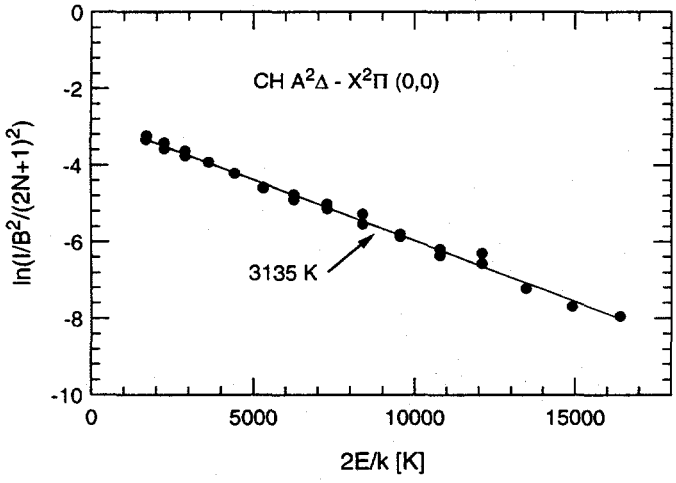

Figure 5. DFWM rotational Boltzmann plot

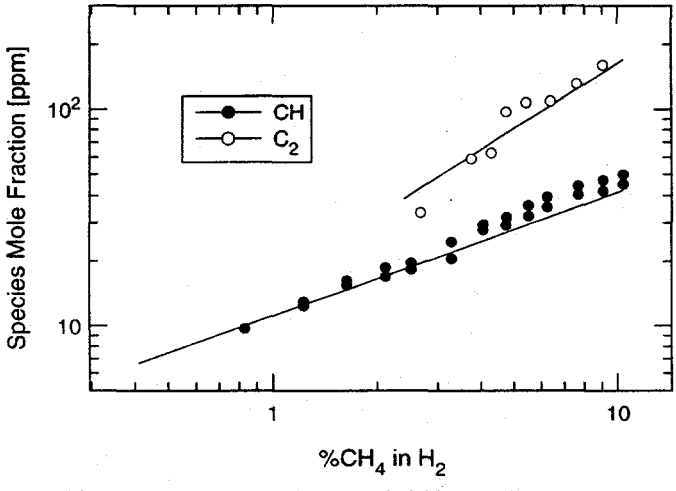

Figure 6. Freestream stoichiometric study.

Temperature and concentration profiles within the reacting boundary layer itself were also probed using DFWM. A comparison of measured CH vibrational and rotational temperatures along the stagnation line of the substrate with values from the computational simulation is shown in Figure 7. Boundary conditions for the simulation are the measured freestream temperature of 3900 K, an estimated freestream velocity of 8 m/s, and the measured substrate temperature of 1035°C. We can see in

Figure 7 the predicted thermal boundary layer (≈6mm thick) with a steep fall off in temperature very close to the substrate. The measured CH vibrational temperatures are in close agreement with the predictions, although the loss in signal of the v=1 transitions in the cooler region very near the substrate prevents accurate vibrational temperature measurement for distances < 2mm. Rotational temperatures measurements from the CH v=0 lines, which remain strong enough for accurate measurement closer to the substrate are in good agreement with both the measured vibrational temperatures and the computational simulation. It is possible to make rotational temperature measurements even closer to the substrate than shown in Figure 7, but for these experimental conditions the CH concentration in that region has dropped below approximately 2 ppm, which is our current detection limit.

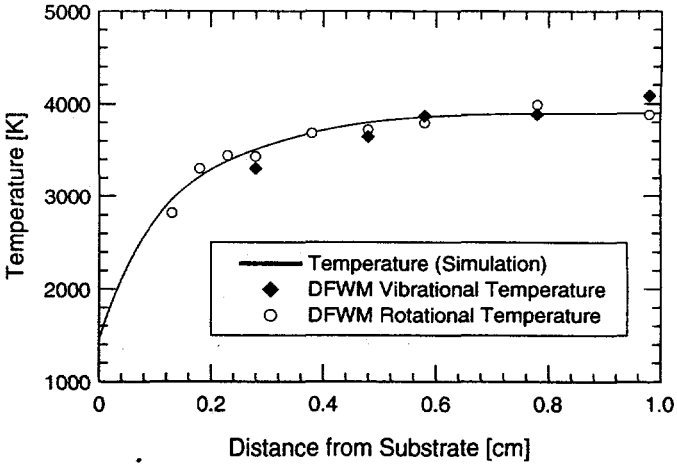

Figure 7. Boundary layer temperature profiles.

Measurements of the relative CH and C_2 mole fractions within the substrate boundary layer are compared to results of the computational simulation in Figures 8 and 9. In Figure 8, the CH mole fraction is approximately 20 ppm in the freestream (4100 K) and is predicted to first rise within the approximately 6 mm thick boundary layer (due to production) as the plasma cools toward approximately 3700 K, reaching a peak of approximately 55 ppm at 2 mm from the substrate surface, then to be destroyed as the plasma cools further on its approach to the substrate surface. In Figure 9, we see a similar behavior for the C_2 concentration profile with a much higher peak concentration (~300 ppm). We can see that the DFWM measurements of relative CH and C_2 mole fraction (which have been scaled to the peak of the predicted curve, and are in agreement with the calibrated equilibrium freestream) correspond closely to the predicted concentration in both trend and magnitude, accurately reflecting the production and destruction of the radicals within the boundary layer and demonstrating the ability of DFWM to probe this small, harsh reaction zone.

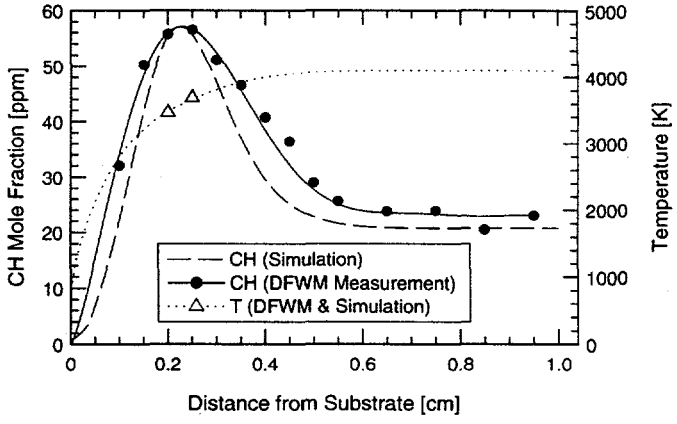

Figure 8. CH concentration profile.

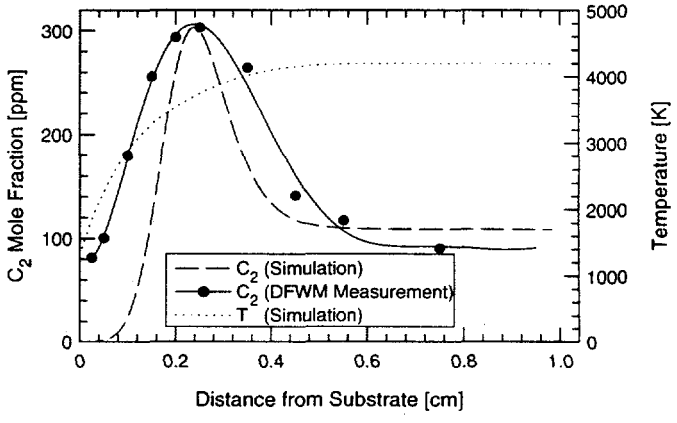

Figure 9. C_2 concentration profile.

CAVITY RING-DOWN SPECTROSCOPY RESULTS

Cavity ring-down spectroscopy is another emerging technique that also offers extremely sensitive, spatially resolved information from plasma environments via cavity-coupled laser absorption. By measuring the ring-down time of a laser pulse injected into an optical cavity which surrounds the plasma of interest, CRDS enables a very sensitive, absolute determination of the line-of-sight absorptivity of the plasma. Since this technique measures the ring-down time of the cavity, rather than the fractional absorbance ($I_{transmitted}/I_{incident}$), the measurement becomes insensitive to the intensity if the incident pulse which can be a major source of uncertainty in ordinary absorption (and multi-pass absorption) techniques. In this manner, plasma absorbance as small as one part in 10^5 (per cavity round-trip) can be accurately measured, thus yielding very sensitive measurements of absolute species concentrations.

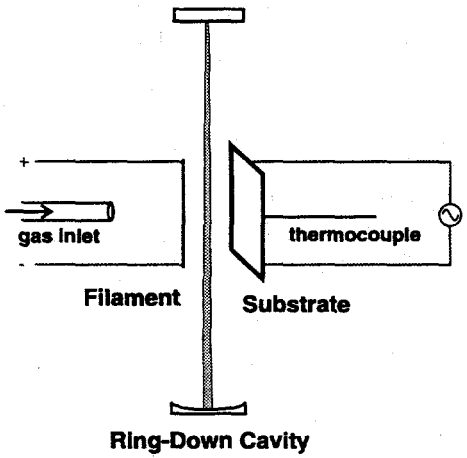

Figure 10. Schematic of CRDS system.

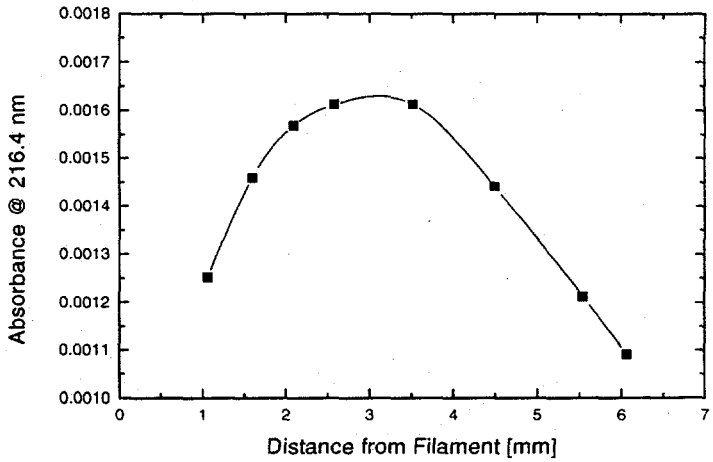

Figure 11. Spatial profile of methyl absorbance.

In the past year, we have been successful in applying cavity ring-down spectroscopy to the measurement of absolute concentration of methyl radicals in a hot filament reactor. The experimental schematic of these experiments is shown in Figure 10. Although this technique produces a line of sight averaged quantity, it provides high spatial resolution in the one spatial dimension of interest within this system, and more importantly provides absolute concentration measurements at single pass absorbances as low as $1x10^{-5}$. Using this technique, spatial profiles of methyl radical concentrations have been measured between the excitation filament and the deposition substrate, as a function of process variables such as flow direction, pressure, filament temperature, and substrate temperature. These preliminary investigations have provided evidence of the independence of flow direction within these reactors. CRDS measurements have also shown clear indications that for certain conditions, the methyl concentration peaks approximately 4 mm away from the filament surface, which is contrary to the currently accepted mechanism of methyl formation from excited hydrogen atoms close to the filament, but in agreement with more recent REMPI measurements of other investigators. A spatial distribution of methyl absorbance at 216.4 nm under typical hot-filamnet reactor operating conditions is shown in Figure 11. Many investigators are currently working to understand and model the complex plasma and surface chemistry within these systems, and CRDS appears to be a promising technique to experimentally validate those efforts.

CONCLUSIONS

Degenerate four-wave mixing has been demonstrated as a sensitive, spatially resolved diagnostic of boundary layer chemistry in thermal plasma CVD of diamond. The coherent, phase-conjugate signal produced in this technique enables the rejection of intense plasma luminosity, and allows the accurate interrogation of temperature and trace (ppm level) radical concentrations within the reacting plasma. In-situ measurements of vibrational and rotational temperatures, as well as relative CH and C_2 radical concentrations in the reacting boundary layer of a diamond growth substrate are found to be in good agreement with model predictions.

ACKNOWLEDGMENTS

The authors would like to acknowledge contributions by the companion research program of Prof. R.N. Zare, with Dr. P. Zalicki and Y. Ma (DOE Grant #DE-FG03-92ER14304)

REFERENCES

1. T.G. OWANO and C.H. KRUGER, "Parametric Study of Atmospheric-Pressure Diamond Synthesis with an Inductively Coupled Plasma Torch," *P. Chem. and P. Proc.* 13, 433 (1993).
2. B.W. WU and S.L. GIRSHICK, "Atomic Carbon Vapor as a Diamond Growth Precursor in Thermal Plasmas," *J. of Appl. Phys.* 75, 3914 (1993).
3. R. HERNBERG, T. LEPISTO, T. MANTYLA, T. STENBERG, and J. VATTULAINEN, "Diamond Film Synthesis on Mo in Thermal RF Plasma," *Diamond and Related Materials* **1** (1992) 255
4. S.K. BALDWIN, T.G. OWANO, and C.H. KRUGER, "Growth Rate Studies of CVD Diamond in an RF Plasma Torch," *P. Chem. and P. Proc.* 14, 383 (1994).
5. T.G. OWANO, C.H. KRUGER, D.S. GREEN, S. WILLIAMS, and R.N. ZARE, "Degenerate Four-Wave Mixing Diagnostics of Atmospheric Pressure Diamond Deposition," *Diamond and Related Materials* 2, 661 (1993).
6. D.S. GREEN, T.G. OWANO, S. WILLIAMS, D.G. GOODWIN, R.N. ZARE, and C.H. KRUGER, "Boundary Layer Profiles in Plasma Chemical Vapor Deposition," *Science* 259, 1726 (1993).
7. T.G. OWANO, E.H. WAHL, C.H. KRUGER, D.S. GREEN, and R.N. ZARE, "Degenerate Four-Wave Mixing as a Spectroscopic Probe of Atmospheric Pressure Reacting Plasmas," *Proceedings of the 11th International Symposium on Plasma Chemistry* 1, 416 (1993).
8. S. WILLIAMS, D.S. GREEN, S. SETHURAMAN, and R.N. ZARE, "Detection of Trace Species in Hostile Environments Using Degenerate Four-Wave Mixing: CH in an Atmospheric Pressure Flame," *J. Am. Chem. Soc.* 114, 9122 (1992).
9. C.H. KRUGER, M.H. GORDON, and T.G. OWANO, "Measurements of Nonequilibrium Effects in Thermal Plasmas," *J. of Pure and Appl. Chem.* 64, 637 (1992).
10) D.G. GOODWIN, and G.G. GAVILLET, "Numerical Modeling of the Filament-Assisted Diamond Growth Environment," *J. Appl. Phys.* 68, 6393 (1990).

Physical Models of Polarization Mode Dispersion

C. R. Menyuk and P. K. A. Wai

Department of Electrical Engineering, University of Maryland
Baltimore, MD 21228-5398

ABSTRACT

The effect of randomly varying birefringence on light propagation in optical fibers is studied theoretically in the parameter regime that will be used for long-distance communications. In this regime, the birefringence is large and varies very rapidly in comparison to the nonlinear and dispersive scale lengths. We determine the polarization mode dispersion, and we show that physically realistic models yield the same result for polarization mode dispersion as earlier heuristic models that were introduced by Poole. We also prove an ergodic theorem.

1. INTRODUCTION

There are two distinct data formats that are being actively studied for possible use in long-distance communication systems. The first data format uses solitons as 1-bits in the communication system. By balancing nonlinearity and dispersion, solitons avoid the bad effects that either phenomenon would lead to on its own. From a strict mathematical standpoint, the optical fiber does not support solitons—merely soliton-like pulses—because the equations that describe real-world fibers are not integrable. Nonetheless, the equations are closely related to the nonlinear Schrödinger equation, and there is ample theoretical and experimental evidence that solitons are robust in the sense that the soliton-like pulses that actually propagate in fibers have virtually all the properties of true solitons on the length scale over which experiments are done.[1] Soliton pulses are referred to in the vernacular of communication systems as RZ (return-to-zero) pulses. As shown in the top half of Fig. 1, the energy of the solitons is concentrated in the middle of the timing window, and the amplitude is always zero at the edge of the window. The second format is shown in the bottom half of Fig. 1 and is referred to as NRZ (non-return-to-zero). In this format, the

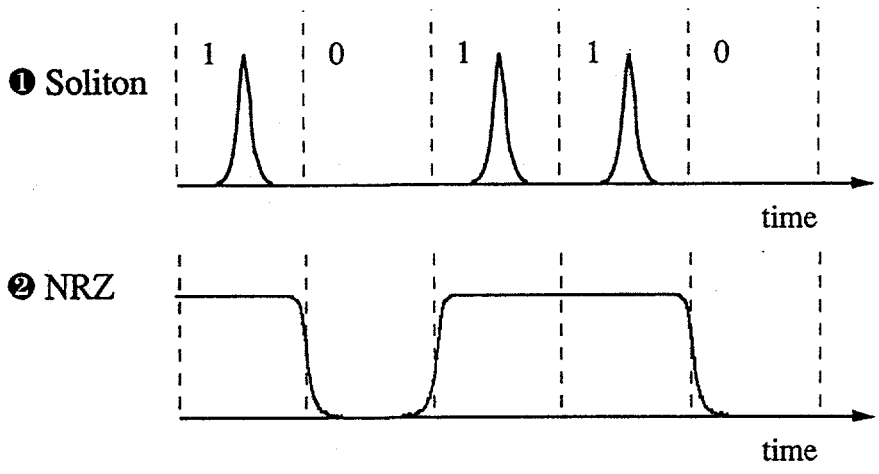

FIGURE 1. Intensity variation of a 10110 bit stream in both soliton and NRZ communications.

energy of a 1-bit is spread nearly evenly throughout the timing window. This format is the one that has been traditionally used in long-distance communications. Until a year ago, it was thought that solitons would eventually replace NRZ communications because of the demonstrated capability to do wavelength division multiplexing (WDM) with solitons. It was supposed that it would not be possible to do WDM with NRZ communications. However, it has recently been demonstrated that in fact WDM is possible with NRZ, and, while solitons are promising, NRZ systems remain a step ahead.[2] Thus, the future for solitons is unclear.

This situation is both an enigma and an enormous challenge to the theorist. Historically, NRZ communication systems came into vogue because in communication systems based on microwave RU-232 cable, signal distortion was dominated by dispersion and so it was desirable to minimize the bandwidth of the signal—something that NRZ signals accomplish quite well. For this reason, there has been a tendency to think of NRZ propagation as linear propagation, but that is simply not true! From a nonlinear standpoint, the behavior of soliton systems is not too hard too analyze because there is a well-defined sense in which a soliton is a pure mode of the nonlinear system.[1] By contrast, there is no sense in which NRZ pulses are modes, and, as a consequence, these systems are very difficult to study, and the theoretical work to date has had little predictive capability. Because neighboring NRZ bits interact, one must keep long strings of bits in the simulations which seriously slows down numerical calculations. The enigma and the challenge is to understand why these systems work as well as they do and to predict their ultimate limits.

It is already apparent that the large and rapidly varying birefringence that occurs in communication fibers plays a critical role in the distortion of NRZ pulses and in the ultimate bit error rates that can be achieved. Thus, understanding the impact of these variations is a crucial first step toward achieving an understanding of NRZ systems—not to mention that they play a vital role in soliton systems as well!

It is important to understand precisely what is meant when we describe the birefringence as large. Single mode optical fibers have one propagating mode that is referred to as the HE_{11} mode, but this mode is doubly degenerate. Doping and core anisotropies break the degeneracy, leading to birefringence, but typical values of $\Delta n/n$ are 10^{-7}–10^{-6}. While one might be tempted to think that this value is small, it implies a beat length that is on the order of 10 m, while nonlinear and dispersive effects occur on a length scale of 100–1000 km. Thus, it is actually very large! At the same time, one can infer from measurements to be described shortly that the fiber correlation length is on the order of 30–100 m, so that the birefringence is also rapidly varying. Thus, it makes sense to use multiple length scale techniques in which we first determine the evolution on the rapidly varying length scale of the randomly varying birefringence and then use the results to determine the evolution on the much longer dispersive and nonlinear length scales. Not only is this approach sensible from a conceptual standpoint, as it allows us to distinguish the phenomena occurring on the different length scales, but it will also allow us to create simulation codes that are significantly more efficient and accurate than those that are presently in use.

In this article, we will be concentrating on the rapidly varying length scale, and we will discuss its impact on the nonlinear evolution briefly at the end. We have actually only just begun to attack the full evolution, taking advantage of what we have learned on the rapidly varying length scale. The behavior on the rapidly varying length scale is linear but random, with the randomness being the major complication. At the end of the article, we will mention briefly some of the consequences of our calculations for the nonlinear evolution.

2. DIFFERENTIAL TIME DELAY

Experimentally, one finds that the randomly varying birefringence leads to a frequency-dependent differential time delay that in turn leads to pulse spreading.[3] One of the ways in which this delay manifests itself is that if the light from a multi-mode laser is injected into an optical fiber, it maps into a circle on the Poincaré sphere after propagating some length into the fiber. That implies that there are two orthogonal states, referred to as principal states, that to first order would not be spread on the Poincaré sphere by propagation through the fiber. The delay between these two states is the differential time delay because any other state is a combination of these two states and will arrive at some intermediate time. We begin by demonstrating the existence of the principal states and calculating the differential time delay. We then determine the expected distribution of the differential time delay as a function of distance along the fiber.

Taking a fixed set of axes, labeled 1 and 2, we may write the complex amplitudes of the two polarizations as a column vector $\mathbf{E} = (E_1, E_2)^t$, where E_1 and E_2 are functions of distance along the fiber z and frequency ω. The evolution of this column vector is governed by the linear equation

$$\frac{\partial \mathbf{E}(\omega, z)}{\partial z} = i\mathsf{K}(\omega, z)\mathbf{E}(\omega, z), \tag{1}$$

where

$$\mathsf{K} = k_0\mathsf{I} + \kappa_1\sigma_1 + \kappa_2\sigma_2 + \kappa_3\sigma_3, \tag{2}$$

and the σ_j are the usual Pauli matrices. We first note that if there is no polarization-dependent loss, then all the κ_j must be real. While, in fact, there is some polarization-dependent loss in the real systems, this loss occurs at the amplifiers, which are located 30–100 km apart, and its effect is small, although not unimportant. We will not consider it in this article. We include polarization-independent loss in the system by allowing k_0 to be complex, but it enters into the problem in a fairly trivial way. Making the transformation

$$\mathbf{A} = \mathbf{E} \exp\left[-i \int_0^z k_0(z')\, dz'\right], \tag{3}$$

we find that k_0 disappears from the evolution equation. Noting that optical fibers are linearly birefringent so that $\kappa_2 = 0$, we find that the evolution equation for A is

$$\frac{\partial \mathbf{A}(\omega, z)}{\partial z} = i\Theta(\omega, z)\mathbf{A}(\omega, z), \tag{4}$$

where

$$\Theta = \kappa_1\sigma_1 + \kappa_3\sigma_3 \equiv b\sin\theta\,\sigma_1 + b\cos\theta\,\sigma_3, \tag{5}$$

and b corresponds to the normalized birefringence strength while θ corresponds to the orientation of the birefringent axes. Since Θ is a traceless, Hermitian matrix at every ω, it follows that it generates a unitary transformation at every ω. Assuming now that this transformation matrix is sufficiently smooth as a function of ω, there must be at any z some traceless, Hermitian matrix F that satisfies

$$\frac{\partial \mathbf{A}}{\partial \omega} = i\mathsf{F}(\omega, z)\mathbf{A}(\omega, z). \tag{6}$$

Since this matrix F is traceless and Hermitian, its eigenvalues are real and have the same absolute values with opposite signs while its eigenvectors are orthogonal. Writing the eigenvectors as $\pm\tau_D/2$, it is not difficult to see that the eigenvalues correspond to $\pm$one-half the differential time delay while the eigenvectors correspond to the principal states. Solving Eq. (6), and writing the eigenvectors as S_p and $S_{p'}$, we find that

$$S_p(\omega, z) = S_p(0, z)\exp(i\tau_D\omega/2), \qquad S_{p'}(\omega, z) = S_{p'}(\omega, 0)\exp(-i\tau_D\omega/2). \tag{7}$$

When we use the Fourier transform to return to the time domain, it follows that an initial pulse that consists strictly of the initial state that transforms *via* Eq. (4) into S_p will have a time delay of $\tau_D/2$, and, similarly, an initial pulse that transforms into $S_{p'}$ will have a time delay $-\tau_D/2$. This result was obtained earlier by Poole and Wagner,[4] but their derivation was considerably more elaborate because they did not make use of the known properties of Hermitian matrices.

The next step is to determine the probability distribution of the differential time delay τ_D. Poole[5] has described an approach that applies in the limit in which there is a large and nearly fixed birefringence and in which there is a weak mode coupling. In this model $\cos\theta \simeq 1$ and $\sin\theta \simeq \theta$ in Eq. (4) so that Eq. (4) becomes

$$\frac{\partial A}{\partial z} = i\theta\sigma_1 + b\sigma_3, \tag{8}$$

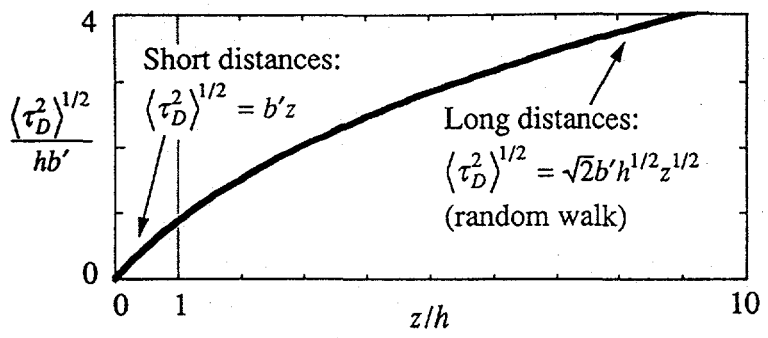

FIGURE 2. Variance of the differential time delay as a function of position along the fiber.

This limit is not really valid for communication fibers; however, we recently showed that a model that allows the birefringence orientation to vary randomly will yield the same results.[6] To obtain this result, it is useful to attempt to solve Eq. (5) through repeated diagonalization. Ignoring the variation of θ as a function of z, we could solve Eq. (4) by making the transformation $\mathbf{B}_1 = \mathsf{U}_1\mathbf{A}$ where

$$\mathsf{U}_1 = \cos(\theta/2)\,\mathsf{I} + i\sin(\theta/2)\,\sigma_3, \tag{9}$$

We then find that

$$\frac{\partial \mathbf{B}_1}{\partial z} = i\left(\mathsf{U}_1\Theta\mathsf{U}_1^{-1} - \mathsf{U}_1\frac{\partial \mathsf{U}_1^{-1}}{\partial z}\right)\mathbf{B}_1 \equiv i\Psi_1\mathbf{B}_1, \tag{10}$$

where U_1^{-1} is the inverse of U_1 and Ψ_1 can be written explictly as

$$\Psi_1 = \frac{1}{2}\frac{d\theta}{dz}\sigma_2 + b\sigma_3. \tag{11}$$

This equation is essentially the same as Eq. (8). The appearance of σ_2 rather than σ_1 makes no diffrence in the polarization mode dispersion. The only significant difference is that whereas Poole assumed that θ varies rapidly compared to the beat length, we must assume that $d\theta/dz$ varies rapidly compared to the beat length. In either case, one finds that the mean of the differential time delay is zero, and its variance is given by[5,6]

$$\langle \tau_D^2 \rangle^{1/2} = \sqrt{2}hb'\left[\exp(-z/h) - 1 + z/h\right]^{1/2}, \tag{12}$$

where $b' = db/d\omega$ is the derivative of the birefringence and h is a characteristic decorrelation length.

In the case of Poole's model, h corresponds to the length scale over which the polarizations mix. In the case of our model, it corresponds to the length over which the polarizations mix when measured in the frame that rotates with the local polarization axes. We note that in our model, $h = h_{\text{fiber}}$, where h_{fiber} is the correlation length for the optical fiber itself. Of course, in Poole's model, $h_{\text{fiber}} = \infty$ so that there is no relation

between h and h_{fiber}. Since one cannot directly measure the orientation of the polarization axes as a function of position along the fiber, it might appear at first that both models are equally plausible, but in fact, one can infer from the existence of solitons that the orientation must be randomly varying. Solitons tend to propagate naturally in a single polarization state,[7] and unless the orientation is randomly varying, solitons will be observed to split, and there is no evidence of that. Thus, we can use solitons to probe the structure of the fiber! We note that one can infer h from measurements of the differential time delay which is how it is measured in practice. Equation (12) is physically sensible. When z is small compared to the decorrelation length, then the two polarizations separate linearly in z. When z is large compared to the decorrelation length, then the two polarizations undergo a random walk and their separation is proportional to $z^{1/2}$.

To derive Eq. (12), we will present here an approach first described by Poole[5] and later modified by us so that it could be used to prove an ergodic theorem.[6] We have shown more recently that Eq. (12) can be derived more simply using the methods of stochastic differential equations; however, these results are still unpublished and cover a group of models that is less broad. Our starting point is to note that Eq. (10) that governs the evolution of $\mathbf{B}_1$ as a function of z is complemented by the equation

$$\frac{\partial \mathbf{B}_1}{\partial \omega} = i\mathsf{F}_1\mathbf{B}_1, \tag{13}$$

that governs the evolution of $\mathbf{B}_1$ as a function of ω, where F_1 is a traceless, Hermitian matrix. It then follows that $\tau_D^2 = -4\det \mathsf{F}_1 = 4\det(\partial \mathsf{T}_1/\partial\omega)$, where $\mathbf{B}_1(z,\omega) = \mathsf{T}_1(z,\omega)\mathbf{B}_{1,0}$. Defining now $\mathsf{S} = \exp\bigl[-i\phi(z)\sigma_3\bigr]\mathsf{T}_1$, where $\phi(z) = \int_0^z b(z')\,dz'$, we obtain

$$\frac{\partial \mathsf{S}}{\partial z} = \begin{pmatrix} 0 & \frac{1}{2}\theta_z \exp(-2i\phi) \\ -\frac{1}{2}\theta_z \exp(2i\phi) & 0 \end{pmatrix} \mathsf{S}, \tag{14}$$

where $\theta_z = d\theta/dz$. It now follows that

$$\tau_D^2 = 4\det(\mathsf{S}' + i\sigma_3\phi'\mathsf{S}), \tag{15}$$

where the primes indicate derivatives with respect to ω.

Writing the components of S explicitly so that

$$\mathsf{S} = \begin{pmatrix} s_1 & s_2 \\ -s_2^* & s_1^* \end{pmatrix}, \tag{16}$$

and taking the first derivative of τ_D^2, we obtain

$$\frac{\partial \tau_D^2}{\partial z} = 8b'\phi' + 8ib'(s_1 s_1'^* + s_2 s_2'^*), \tag{17}$$

where we assume that the elements of S are slowly varying so that we can neglect their variation with z. The key assumption is that the θ_z are small compared to b but vary rapidly so that their derivatives are large. Similarly, we find

$$\frac{\partial^2 \tau_D^2}{\partial z^2} = 4(b')^2 + 4\phi'\frac{db'}{dz} - 4ib'\theta_z\bigl(s_1 s_2' - s_1' s_2'\bigr)\exp(2i\phi) + \text{c.c.} \tag{18}$$

Although S is slowly varying, its z derivative varies rapidly, and we can use this fact to replace s_1 in Eq. (18) with the integral expression

$$s_1(z) \simeq s_1(\zeta) - \int_\zeta^z \frac{\theta_z(z')}{2} \exp\bigl[-2i\phi(z')\bigr]\, dz', \tag{19}$$

where $z-\zeta$ is a length that is long compared with the variation of θ_z and short compared with the variations of s_1 and s_2. The assumed existence of this intermediate length scale plays an important role in our argument. Similar results can be obtained for $s_2(z)$, $s_1'(z)$, and $s_2'(z)$. Defining

$$\begin{aligned} H(z) &= \mathrm{Re}\left[\int_\zeta^z \frac{\theta_z(z)\theta_z(z')}{4} \exp\bigl[2i\phi(z) - 2i\phi(z')\bigr]\, dz'\right] \\ &\simeq \frac{1}{2}\int_{-\infty}^{\infty} \frac{\theta(z)\theta(z')}{4} \exp\bigl[2i\phi(z) - 2i\phi(z')\bigr]\, dz', \end{aligned} \tag{20}$$

where we have used the assumed rapid variation of θ_z to extend the integral to $-\infty$, we may now rewrite Eq. (18) in the form

$$\frac{\partial^2 \tau_D^2}{\partial z^2} = 8(b')^2 + 8\phi'\frac{db'}{dz} - 32b'\phi' H(z) - 32ib' H(z)(s_1' s_1'^* + s_2 s_2'^*), \tag{21}$$

where we have dropped both small terms and rapidly varying terms that will not contribute on the length scale $z-\zeta$.

In order to obtain an ergodic theorem, our goal is to replace Poole's ensemble average over "a collection of statistically equivalent fibers" with an appropriate spatial average.[5,6] Since both b and θ change slowly by assumption, we may beplace $\phi(z)-\phi(z')$ with the local relationship $b(z-z')$. In general b and θ_z^2 are correlated; the latter is larger when the former is smaller. Consequently, b and H will be correlated. By contrast, we may assume that ϕ and $s_1 s_1'^* + s_2 s_2'^*$ are uncorrelated with b and H since these quantities are determined by integration from the origin and, over sufficiently long lengths, will be nearly independent of the local values of b and H. Physically, this length corresponds to the length over which the electric field samples the entire Poincaré sphere. Defining an ensemble average

$$\langle X(z)\rangle = \frac{1}{L}\int_{z-L}^{z} X(z')\, dz' \tag{22}$$

where L is this averaging length, we find, letting $\langle b'H\rangle = r\langle b'\rangle\langle H\rangle$, that

$$\langle \tau_D^2\rangle = \frac{\langle (b')^2\rangle}{2r^2\langle H\rangle^2}\bigl[\exp(-4r\langle H\rangle z) - 1 + 4r\langle H\rangle z\bigr]. \tag{23}$$

From the preceeding discussion, it should be apparent that this result is only meaningful in the limit $z \gg h$, where $h = 1/4r\langle H\rangle$.

Given $\langle \tau_D^2 \rangle$, the next task is to calculate the entire distribution function for τ_D^2. While this task has yet to be accomplished in general, it has been argued on physical grounds and verified in simulations that the actual distribution is given by

$$f(\tau_D^2) = \frac{2\tau_D^2}{\sqrt{\pi}\left(\langle \tau_D^2 \rangle / 3\right)^{3/2}} \exp\left(-3\tau_D^2 / \langle \tau_D^2 \rangle\right), \tag{24}$$

corresponding to a random walk on the Poincaré result. Determining the full evolution of the distribution function remains an important open problem.

3. DISCUSSION AND CONCLUSIONS

We showed in early work that in the limit of large but rapidly and randomly varying birefringence, the evolution of the field in the optical fiber is described by the Manakov equation,[7]

$$\begin{aligned} i\frac{\partial U}{\partial z} + \frac{1}{2}\frac{\partial^2 U}{\partial t^2} + \left(|U|^2 + |V|^2\right) U = 0, \\ i\frac{\partial U}{\partial z} + \frac{1}{2}\frac{\partial^2 U}{\partial t^2} + \left(|U|^2 + |V|^2\right) V = 0, \end{aligned} \tag{25}$$

where U and V correspond physically to the state that a linear, cw wave at the pulse's central frequency would occupy and its orthogonal complement. We now have models for the polarization mode dispersion that we know are physically correct. The next stage of this work is to combine the two effects to obtain a complete description of wave propagation through the fiber. This task is very important because large computational savings in modeling the fibers as well as an increase in understanding appear to be obtainable.

We expect to report progress along those lines in the very near future!

ACKNOWLEDGMENTS

This work was supported by the Department of Energy. Numerical work was carried out at SDSC and NERSC

REFERENCES

1. C. R. Menyuk, J. Opt. Soc. Am. B **10**, 1585 (1993).
2. See, N. S. Bergano, *et al.*, "40 Gbit/s WDM transmission of eight 5 Gb/s data channels over transoceanic distances using the conventional NRZ modulation format," presented at the OFC '95 meeting (February, 1995).
3. N. S. Bergano, C. D. Poole, and R. E. Wagner, J. Lightwave Technol. **5**, 1618 (1987).
4. C. D. Poole and R. E. Wagner, Electron. Lett. **22**, 1029 (1986).
5. C. D. Poole, Opt. Lett. **13**, 687 (1988).
6. C. R. Menyuk and P. K. A. Wai, J. Opt. Soc. Am. B **11**, 1288 (1994).
7. P. K. A. Wai, C. R. Menyuk, and H. H. Chen, Opt. Lett. **16**, 1231 (1991).

CONDITIONS FOR SYNCHRONIZATION IN JOSEPHSON-JUNCTION ARRAYS

A.A.Chernikov & G. Schmidt

Stevens Institute of Technology, Hoboken , NJ 07030

ABSTRACT

An effective perturbation theoretical method has been developed to study the dynamics of Josephson junction series arrays. It is shown that the inclusion of junction capacitances, often ignored, has a significant impact on synchronization. Comparison of analytic with computational results over a wide range of parameters shows excellent agreement.

INTRODUCTION

Josephson junctions are known to produce very high frequency oscillations and can be used to generate submillimeter range radiation [1-3]. The difficulty is the low power output of individual junctions. This could be remedied by the use of many synchronized coupled junctions. Fig.1 shows a sketch of N junctions in series, fed by a constant dc current source and shunted by a load of impedance Z. The junctions have an internal resistance as well as a capacitance.

In normalized units this circuit is described by

$$\beta\ddot{\varphi}_k + \dot{\varphi}_k + \sin(\varphi_k) + I_L = I \qquad (1)$$

where φ_k represents the phase difference of the wave function across the k-th junction, β corresponds to the capacitance of the junction, I_L is the load current. Without the load, the system can be visualized as a point particle of mass β sliding down an incline of steepness I, sinusoidally modulated, with air resistance represented by $\dot{\varphi}_k$. To maintain the motion and oscillations it is necessary that $I > 1$.

The load current depends on the voltage across the array, proportional to $\sum\dot{\varphi}_j$. For instance for a load made up of an inductance, capacitance and resistance in series one writes in normalized units

$$L\dot{I}_L + RI_L + (1/C)\int I_L dt = (1/N)\sum\dot{\varphi}_j \qquad (2)$$

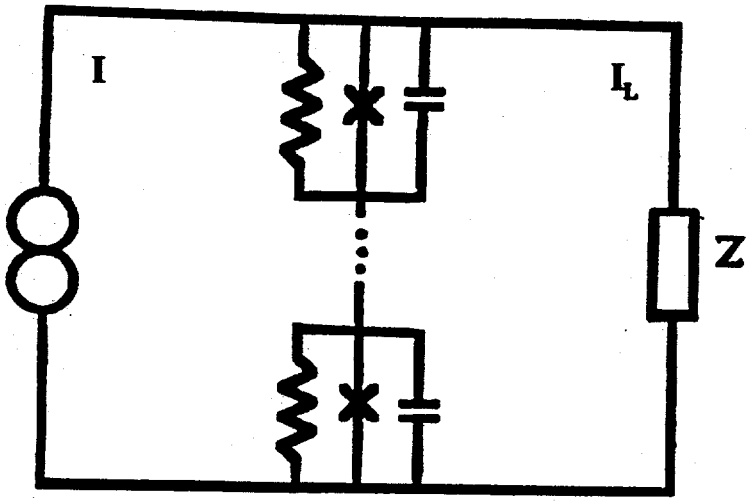

1. Sketch of the circuit investigated. Constant current I feeds the system, the junctions form an 1D array with resistive and capacitive characteristics, coupled to an impedance Z.

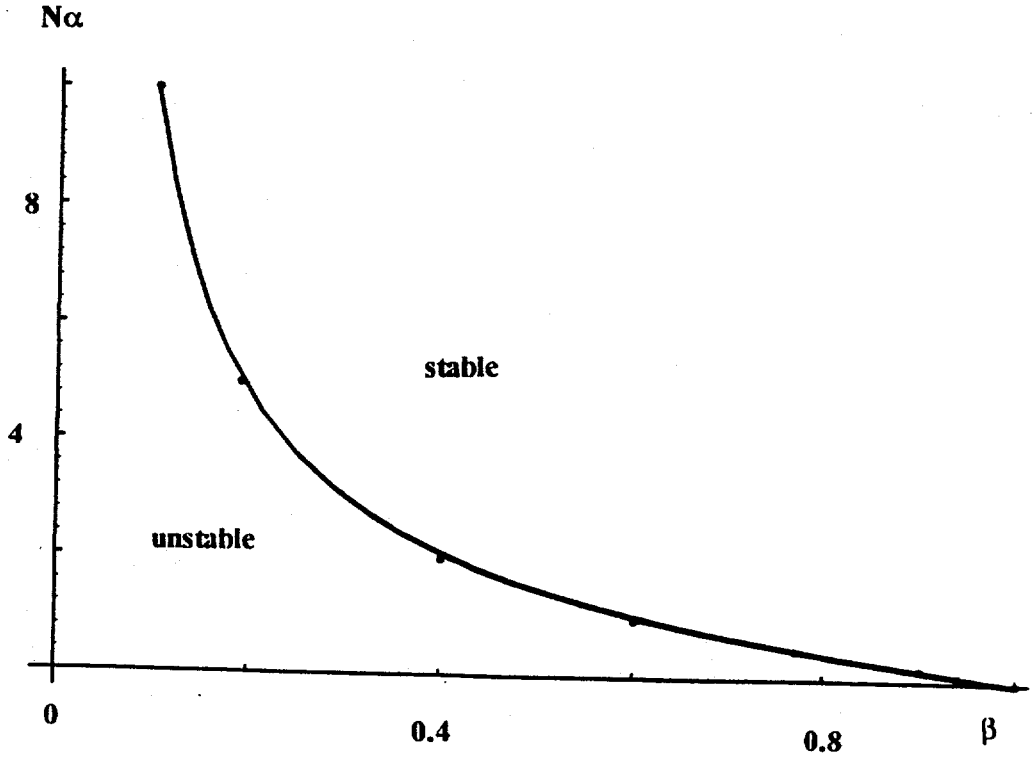

2. Computed dividing line between stable and unstable regions in β - αN parameter space of capacitively loaded arrays.

These equations are clearly nonlinear and no analytic solutions are available.

Recently several authors [4-9] investigated analytically a simplified version of these equations. The load capacitance has been ignored ($\beta = 0$) and the coupling to the load (I_L), has been assumed to be small, so perturbation theory could be used. Under these conditions it was shown that for a purely resistive load the equations are integrable [7] . The present authors have shown [9] that if a slight difference between the individual junction parameters is introduced, integrability fails and chaotic behavior follows. Quite recently Wiesenfeld and Swift [8] studied analytically the simplified equations of identical junctions with $\beta = 0$ in the weak coupling limit, and found that the synchronous solutions are stable if the load is predominantly inductive, and unstable if it is capacitive. The dividing line is at resonance when the Josephson junction frequency equals the resonant frequency of the load $(LC)^{-2}$.

Computed solutions of the equations show however that the junction capacitance has a significant effect on the stability of synchronized solutions, even for $\beta \ll 1$. Here a powerful perturbation theoretical method is developed where β as well as the coupling strength can be arbitrarily large, and excellent agreement is found with computer generated solutions.

CAPACITIVE LOAD; COMPUTATION

First we rewrite Eqs.(1) and (2), by dividing (1) by I, and rescaling time, $It \rightarrow t$, and $I\beta \rightarrow \beta$, to get

$$\beta\varphi_k + \varphi_k + b\sin(\varphi_k) + J = 1 \tag{3}$$

$$\mu_1 J + \mu_2 J + \int J dt = \alpha\sum\varphi_j \tag{4}$$

where $J = I_L/I$, $b = I^{-1}$, $\mu_1 = LCI^2$, $\mu_2 = RCI$, $\alpha = IC/N$. For a purely capacitive load $\mu_1 = \mu_2 = 0$, and these equations reduce to

$$\beta\,\varphi_k + \varphi_k + b\sin(\varphi_k) + \alpha\sum\varphi_j = 1 \tag{5}$$

In order to study the linear stability of the synchronous solution, one expand $\varphi_k = \varphi_0 + \delta\varphi_k$, where φ_0 satisfies the

$$\beta\varphi_0 + \varphi_0 + b\sin(\varphi_0) + N\alpha\varphi_0 = 1 \tag{6}$$

equation, while for $\delta\varphi_k$ one has

$$\beta\,\delta\varphi_k + \delta\varphi_k + b\cos(\varphi_0)\delta\varphi_k + \alpha\sum\varphi_j = 0 \tag{7}$$

Subtracting the k-th from l-th equation gives [5]

$$\beta\,\Delta_{l,k} + \Delta_{l,k} + b\cos(\varphi_0)\Delta_{l,k} = 0 \tag{8}$$

where $\Delta_{l,k} = \delta\varphi_l - \delta\varphi_k$. Linear stability implies that $\Delta_{l,k}$ asymptotically tends to zero. One solves Eq.(6) on the computer, for given parameters β, b and $N\alpha$, and the computed function φ_0 in Eq.(8) to determine, the long time behavior of $\Delta_{l,k}$. Since $I > 1$, the parameter b is always less than one.

b is always less than one.

Fig.2 shows the β - Nα curve constructed for b = 0.5, b = 0.25 and b = 0.1. Two important conclusions follow,

1., The three curves practically coincide, the differences are within the width of the line.

2., While for β = 0, the synchronous state is always linearly unstable, as expected [8] , for large coupling even the addition of small junction capacitance can stabilize the state. For example when Nα =10, $\beta > 0.1$ gives stability. When $\beta > 1$ stability persists for any value of the coupling.

The first condition suggest an analytic method. Since the solution is essentially independent of b, one can carry out an analytic calculation based on a small b expansion. Since b is the coefficient of the only nonlinear term, the expansion can be reduced to the solution of set of linear equations.

CAPACITIVE LOAD; ANALYSIS

To the lowest order in the expansion in b, Eq.(5) gives $\varphi_k = t + \theta_k$. First order terms are

$$\beta\ddot{\varphi}_k^{(1)} + \dot{\varphi}_k^{(1)} + \alpha\sum\ddot{\varphi}_j^{(1)} + b\sin(t + \theta_k) = 0 \qquad (9)$$

giving second order linear inhomogeneous equations, with oscillating solutions

$$\varphi_k^{(1)} = A_k \sin(t) + B_k \cos(t) \qquad (10)$$

where coefficients are determined from

$$\beta A_k + B_k + \alpha\sum A_j - b\cos\theta_k = 0, \qquad (11)$$

$$A_k - \beta B_k - \alpha\sum B_j + b\sin\theta_k = 0. \qquad (12)$$

Summation over all junctions gives

$$(\beta + N\alpha)\sum A_j + \sum B_j - b\sum\cos\theta_j = 0, \qquad (13)$$

$$-(\beta + N\alpha)\sum B_j + \sum A_j + b\sum\sin\theta_j = 0 \qquad (14)$$

with the solution

$$\sum A_j = b[1 + (\beta + N\alpha)^2]^{-1}[(\beta + N\alpha)\sum\cos\theta_j - \sum\sin\theta_j] \qquad (15)$$

$$\sum B_j = b[1 + (\beta + N\alpha)^2]^{-1}[(\beta + N\alpha)\sum\sin\theta_j + \sum\cos\theta_j] \qquad (16)$$

Substituting these expressions into Eqs.(11) and (12) gives

$$A_k = b(1 + \beta^2)^{-1}(-\sin\theta_k + \beta\cos\theta_k) + b\alpha(1 + \beta^2)^{-1}[1 + (\beta + \alpha N)^2]^{-1}$$
$$[(1 - \beta^2 - \beta\alpha N)\sum\cos\theta_j + (2\beta + \alpha N)\sum\sin\theta_j] \qquad (17)$$

$$B_k = b(1+\beta^2)^{-1}(\cos\theta_k + \beta\sin\theta_k) + b\alpha(1+\beta^2)^{-1}[1+(\beta + \alpha N)^2]^{-1}$$
$$[(1-\beta^2-\beta\alpha N)\sum\sin\theta_j - (2\beta+\alpha N)\sum\cos\theta_j] \quad (18)$$

The second order expansion of Eq.(5) gives

$$\beta\ddot{\varphi}_k^{(2)} + \dot{\varphi}_k^{(2)} + \alpha\sum\ddot{\varphi}_j^{(2)} + b\cos(t+\theta_k)\varphi_k^{(1)} = 0 \quad (19)$$

where $\varphi_k^{(1)}$ is given by Eqs.(10), (17) and (18). The driving term in Eq. (19) contains second harmonics as well as time independent terms. Synchronization as well as desynchronization is due to long time behavior, compared to the oscillation time scale. It is useful therefore to consider the time averaged term

$$\langle\, b\cos(t+\theta_k)\varphi_k^{(1)}\rangle = (b/2)(B_k\cos\theta_k - A_k\sin\theta_k) = (b^2/2)(1+\beta^2)^{-1} +$$
$$\alpha(b^2/2)(1+\beta^2)^{-1}[1+(\beta+\alpha N)^2]^{-1}[(1-\beta^2-\beta\alpha N)\sum\sin(\theta_j-\theta_k) - (2\beta+\alpha N)\sum\cos(\theta_j-\theta_k)] \quad (20)$$

So from Eqs. (19) and (20)

$$\varphi_k^{(2)} \sim -\langle\, b\cos(t+\theta_k)\varphi_k^{(1)}\rangle t + \text{second harmonic terms} \quad (21)$$

One may think of the φ_k-s as points moving on the unit circle. To lowest order they move with unit phase velocity separated by angles $\theta_j - \theta_k$. The first order solutions of Eq.(10) add oscillatory motion, while to second order, second harmonics of the oscillatory motion appear as well as a change in the time average velocity. The first term in Eq.(20) describes a slowing of all points to $1 - (b^2/2)(1+\beta^2)^{-1}$. The other two terms arise from the interaction of different points. Synchronization (or desynchronization) is described by the first of these terms. When $\beta = 0$ the angle differences $\theta_j - \theta_k$ grow toward a splay state. Past a threshold value of β the angle differences contract untill synchronization is achieved. This threshold is given by the equation

$$1 - \beta^2 - \beta\alpha N = 0 \quad (22)$$

This is an excellent fit to the curve in Fig.2.

Finally the last term in Eq.(20) describes the increase of phase velocities of points as they approach each other to the synchronous state, or the decrease of velocities as a splay state is approached.

ANALYSIS OF SYSTEM WITH RLC LOAD

A similar analysis can be carried out for the more general case described by Eqs. (3) and (4). This calculation is rather lengthy and here the detailes [10] are omitted, resulting in the synchronization condition

$$(1-\beta^2)(1-\mu_1) - \beta(2\mu_2 + \alpha N) < 0 \quad (23)$$

Various limiting cases follow. When the load is purely capacitive $\mu_1 = \mu_2 = 0$ and Eq.(22) is recovered.

When $\beta = 0$, the synchronization condition is

$$1 - \mu_1 = 1 - LCI^2 < 0 \qquad (24)$$

In our units the condition obtained by Wiesenfeld and Swift [8] is $LC(I^2 - 1) > 1$. For $b \ll 1$, $I \gg 1$ the two conditions agree.

When $\mu_1 = 1$, the system is in resonance and the synchronous state is always stable for $\beta > 0$.

Finally when driving current I is very large $\mu_1 \gg 1$, the condition becomes approximately

$$(1 - \beta^2) LI + \beta(2R + 1) > 0 \qquad (25)$$

independent of C.

It is clear that similar calculations can be carried out for an arbitrary load impedance Z (both for one-dimensional and two-dimensional arrays), leading to well defined conditions for synchronization or desynchronization. The growth rates of the instabilities leading to the final state are given by the coefficient of the $\sin(\theta_j - \theta_k)$ term.

ACKNOWLEDGEMENT

This work was sponsored by the U.S. Department of Energy, Contract No. DE-FGO2-87ER13740.

REFERENCES

1. K.Wan, A.K.Jain and J.E.Lukens, Appl. Phys. Lett., **51**, 1805 (1989).
2. S.Han, B.Bi, W.Zhang and J.E.Lukens, Appl. Phys. Lett., **64**, 1424 (1994).
3. M.J.Wengler, B.Guan and E.K.Track, IEEE Trans. on Microwave Theory and Techniques (submitted for publication).
4. K.Y.Tsang, R.E.Mirollo, S.H.Strogatz and K.Wiesenfeld, Physica D, **48**, 102 (1991).
5. P.Hadley, M.R.Beasley and K.Wiesenfeld, Appl. Phys. Lett., **32**, 1619 (1988).
6. S.Nichols and K. Wiesenfeld, Phys. Rev. E, **48**, 2569 (1993).
7. S.Watanabe and S.H.Strogatz, Physica D, **74**, 197 (1994).
8. K.Wiesenfeld and J.W.Swift, Phys. Rev. E, **51**, 1020 (1995).
9. A.Chernikov and G.Schmidt, Phys. Rev. E, **50** ,3436 (1994).
10. A.Chernikov and G.Schmidt, submitted for publication

MODELING ELECTRONEGATIVE PLASMA DISCHARGE

A. J. Lichtenberg and M. A. Lieberman

Department of Electrical Engineering and Computer Sciences
and the Electronics Research Laboratory
University of California, Berkeley, CA 94720

ABSTRACT

Macroscopic analytic models for a three-component electronegative gas discharge are developed. Assuming the negative ions to be in Boltzmann equilibrium, a positive ion ambipolar diffusion equation is derived. The discharge consists of an electronegative core and electropositive edges. The electron density in the core is nearly uniform, allowing a parabolic approximation to the plasma profile to be employed. The resulting equilibrium equations are solved analytically and matched to a constant mobility transport model of an electropositive edge plasma. The solutions are compared to a simulation of a parallel-plane r.f. driven oxygen plasma for $p = 50$ mTorr and $n_{eo} = 2.4 \times 10^{15}$ m^{-3}. The ratio α_0 of central negative ion density to electron density, and the electron temperature T_e, found in the simulation, are in reasonable agreement with the values calculated from the model. The model is extended to: (1) low pressures, where a variable mobility model is used in the electropositive edge region; and (2) high α_0 in which the edge region disappears. The inclusion of a second positive ion species, which can be very important in describing electronegative discharges used for materials processing, is a possible extension of the model.

I. INTRODUCTION

Considerable effort has gone into the development of equilibrium discharge models for electropositive plasmas. These include particle-in-cell (PIC) codes [1,2,3], fluid codes [4], and analytic approximations [5,6,7]. Plasma processing, however, usually involves electronegative gases and gas mixtures. The work presented here is based on and extends two models developed in our group to determine the behavior of oxygen discharges [8,9]. Oxygen is chosen both because of its usefulness in processing and because the reaction rates are relatively well known. In one study [8] a volume averaged two-dimensional model is developed, particularly for high plasma density (high power) low pressure discharges, which can be obtained, for example, in electron cyclotron resonance (ECR) and RF inductive sources. In a second study a theory is developed to treat an electronegative plasma with a planar spatial variation, at sufficiently high pressure that a constant mobility ion transport model is adequate, and when only a single positive ion species is important [9]. This situation applies to an oxygen discharge at low density and high pressure, in which dissociation of O_2 is not important. It was shown that the plasma is divided into a core electronegative region and an edge electropositive region, each with constant (but different) ambipolar diffusion coefficients [9]. Here, in addition to presenting some of the previous work, we develop a comprehensive, analytic, global model that is applicable over a wide range of pressures and powers. The model includes the relevant reaction rates appropriate to all of the significant ion and neutral species, as given in Ref. [8], which includes the presence of a second positive ion species. It also explicitly includes a core electronegative region with a surrounding electropositive region, but in a manner such that either region can essentially vanish in some parameter ranges. A Bohm condition for the particle flux at

the plasma-sheath edge, which is valid over the entire range of electronegativities, is used.

II. PHYSICS BASIS

A. *Global Equilibrium*

We previously considered the set of collisional reaction processes for an oxygen discharge as given in Table 1 [8].

Table 1. Model Reaction Set

Reaction			Rate Coefficients
$e + O_2$	$\longrightarrow$	$O_2^+ + 2e$	$k_1 = 9.0 \times 10^{-10} T_e^2 e^{-12.6/T}$ cm^3-s^{-1}
$e + O_2$	$\longrightarrow$	$O(^3P) + O(^1D) + e$	$k_2 = 5.0 \times 10^{-8} e^{-8.4/T}$ cm^3-s^{-1}
$e + O_2$	$\longrightarrow$	$O(^3P) + O^-$	$k_3 = 4.6 \times 10^{-11} e^{(2.91/T\ -12.6/T\ +6.92/T\ )}$cm^3-s^{-1}
$e + O(^3P)$	$\longrightarrow$	$O^+ + 2e$	$k_4 = 9.0 \times 10^{-9} T_e^{0.7} e^{-13.6/T}$ cm^3-s^{-1}
$O^- + O_2^+$	$\longrightarrow$	$O(^3P) + O_2$	$k_5 = 1.4 \times 10^{-7}$cm^3-s^{-1}
$O^- + O^+$	$\longrightarrow$	$O(^3P) + O(^3P)$	$k_6 = 2.7 \times 10^{-7}$cm^3-s^{-1}
$e + O^-$	$\longrightarrow$	$O(^3P) + 2e$	$k_7 = 1.73 \times 10^{-7} e^{(-5.67/T\ +7.3/T\ -3.48/T\ )}$cm^3-s^{-1}
$e + O_2$	$\longrightarrow$	$O(^3P) + O(^3P) + e$	$k_8 = 4.23 \times 10^{-9} e^{-5.56/T}$ cm^3-s^{-1}
$e + O(^3P)$	$\longrightarrow$	$O(^1D) + e$	$k_9 = 4.47 \times 10^{-9} e^{-2.286/T}$ cm^3-s^{-1}
$O(^1D) + O_2$	$\longrightarrow$	$O(^3P) + O_2$	$k_{10} = 4.1 \times 10^{-11}$cm^3-s^{-1}
$O(^1D) + O(^3P)$	$\longrightarrow$	$O(^3P) + O(^3P)$	$k_{11} = 8.1 \times 10^{-12}$cm^3-s^{-1}
$O(^1D)$	$\xrightarrow{\text{(wall)}}$	$O(^3P)$	$k_{12} = D_{\text{eff}}/\Lambda^2$ s^{-1}
$e + O(^1D)$	$\longrightarrow$	$O^+ + 2e$	$k_{13} = 9.0 \times 10^{-9} T_e^{0.7} e^{-11.6/T}$ cm^3-s^{-1}
O^+	$\xrightarrow{\text{(wall)}}$	$O(^3P)$	$k_{14} = 212.3\, T_e^{0.5}(2\pi r_p^2 h_L + 2\pi r_p 2\ell_p h_R)$ s^{-1}
O_2^+	$\xrightarrow{\text{(wall)}}$	O_2	$k_{15} = 149.9\, T_e^{0.5}(2\pi r_p^2 h_L + 2\pi r_p 2\ell_p h_R)$ s^{-1}

T_e [=] eV; p [=] mTorr.

Using these reactions for the creation and destruction of the various species, the simplest set of volume averaged global equilibrium equations assumes that the species densities are essentially constant in the bulk with density n, falling rapidly to a density n_s at the plasma-sheath edge. Keeping only the most important rate coefficients from Table 1, this yields the following equations: Neutral (O and O_2) particle balance:

$$2\,K_{diss} n_e n_{O2} = K_r n_O \quad ; \quad K_r = S/V, \tag{2.1}$$

$$G = K_{diss} n_e n_{O2} + K_r n_{O2} \tag{2.2}$$

Positive ion (O^+ and O_2^+) particle balance:

$$K_{iz1} n_e n_O = K_{rec1} n_- n_{1+} + n_{s1} u_{B1} (A_{loss}/V) \tag{2.3}$$

$$K_{iz2} n_e n_{O2} = K_{rec2} n_- n_{2+} + n_{s2} u_{B2} (A_{loss}/V) \tag{2.4}$$

Negative ion (O^-) particle balance:

$$K_{att} n_e n_{O2} = K_{rec1} n_- n_{1+} + K_{rec2} n_- n_{2+} \tag{2.5}$$

Power balance:

$$P_{abs} = (K_{iz1} n_e n_O \mathcal{E}_{c1} + K_{iz2} n_e n_{O2} \mathcal{E}_{c2}) V + (n_{s1} u_{B1} + n_{s2} u_{B2})(\mathcal{E}_{ew} + \mathcal{E}_{iw}) A_{loss} \tag{2.6}$$

Charge neutrality:

$$n_{1+} + n_{2+} = n_e + n_- \equiv n_e(1 + \alpha) \tag{2.7}$$

Here the densities n_{1+} and n_{2+} are the positive ion densities of O^+ and O_2^+, n_- is the density of O^-, S is the pumping speed, G is the O_2 source flow per unit volume, $\mathcal{E}_{c1}$ and $\mathcal{E}_{c2}$ are the collisional energy losses per ionization [8], $\mathcal{E}_{ew}$ and $\mathcal{E}_{iw}$ are the electron and ion energies lost per electron-ion pair lost to the wall, and V and A_{loss} are the plasma volume and plasma area for losses, respectively, and $u_{B1,2}$ are the Bohm velocities of O^+ and O_2^+. For ease of recognition we have renamed the reaction rates in Table 1: $K_{diss} \equiv k_8$, $K_{iz1} \equiv k_4$, $K_{iz2} \equiv k_1$, $K_{rec1} \equiv k_6$, $K_{rec2} \equiv k_5$, and $K_{att} \equiv k_3$. Reactions and rate coefficients omitted from the equations are of lesser importance, and excited states are ignored except in contributions to $\mathcal{E}_{c1}$ and $\mathcal{E}_{c2}$. For the neutral dynamics we assume a low fractional ionization and a low recombination coefficient at the walls for production of O_2 from O.

For a high power (high plasma density), low pressure (low neutral density) oxygen plasma discharge, as analyzed in Ref. [8], the neutral oxygen is nearly fully dissociated, the ratio $\alpha \equiv n_-/n_e \ll 1$, and the collisional regime is such that the variable mobility one dimensional solutions, as analyzed by Godyak and associates [5], are relative flat, except near the sheath edge. In this regime the set of equations (2.1)–(2.7) can be directly analyzed to obtain a reasonably accurate description of the plasma equilibrium.

B. *Spatially-Varying Three-Species Equilibrium*

In this model [9], we consider a subset (O_2^+, O^-, e) of charged particle species in a 1D (slab) geometry, and determine the spatially varying profiles of the species. We find that the discharge generally consists of an electronegative core, surrounded by electropositive edge regions in which $n_- \approx 0$. Depending on the parameters, the electropositive or electronegative regions can essentially vanish.

To determine the spatial variations, as in electropositive plasmas, for each charged species we write a flux equation

$$\Gamma_i = -D_i \nabla n_i \pm n_i \mu_i E_i, \tag{2.8}$$

where $D_i = kT_i/m_i\nu_i$, $\mu_i = |q_i|/m_i\nu_i$, with ν_i the total momentum transfer collision frequency and the $\pm$ corresponds to positive and negative carriers, respectively. In equilibrium the sum of the currents must balance,

$$\sum_{i=1}^{N} q_i \Gamma_i = 0. \tag{2.9}$$

If we make the additional assumption that both negative ion species are in Boltzmann equilibrium,

$$\frac{\nabla n_-}{n_-} = \gamma \frac{\nabla n_e}{n_e}, \tag{2.10}$$

where $\gamma = T_e/T_i$ (T_i is the temperature of both ionic species), then, using charge neutrality and the Einstein relations, together with (2.8)–(2.10), we obtain an approximate ambipolar diffusion coefficient for the positive ions

$$D_{a+} \approx D_+ \frac{1 + \gamma + 2\gamma\alpha}{1 + \gamma\alpha}. \tag{2.11}$$

The structure of D_{a+} is easily seen from (2.11). For $\alpha \gg 1$, γ cancels such that $D_{a+} \approx 2D_+$. When α decreases below 1, but $\gamma\alpha \gg 1$, $D_{a+} \approx D_+/\alpha$ such that D_{a+} increases inversely with decreasing α. For $\gamma\alpha < 1$, $D_{a+} \approx \gamma D_+$, which is the usual ambipolar diffusion without negative

ions. For plasmas in which $\alpha \gg 1$ at the plasma center the entire transition region takes place over a small range of $1/\gamma < \alpha < 1$, such that the simpler value of $D_{a+} = 2D_+$ holds over most of the electronegative plasma core, except near $n_- \approx 0$.

Consider now the positive ion diffusion equation, keeping only the dominant reaction rate constants, with only O_2^+ present. In plane-parallel geometry we have

$$-\frac{d}{dx}\left(D_{a+}(\alpha)\frac{dn_+}{dx}\right) = K_{iz}n_{O2}n_e - K_{rec}n_+n_-, \tag{2.12}$$

where n_{O2} is the neutral gas density. We eliminate n_e (through charge neutrality) and n_- (through α), to obtain

$$-\frac{d}{dx}\left(D_{a+}(n_+)\frac{dn_+}{dx}\right) = K_{iz}n_{O2}n_e(n_+) - K_{rec}n_+n_-(n_+) \tag{2.13}$$

where $D_{a+}(n_+)$ given by (2.11) is a complicated function of n_+ and three constants $\alpha_0 = n_{-0}/n_{e0}$ the ratio of n_- to n_e at the plasma center, n_{e0}, and T_e. To determine the three constants we use:

positive ion particle balance,

$$-D_{a+}\frac{dn_+}{dx}\bigg|_{x=\ell} = \int_0^\ell K_{iz}n_{O2}n_e dx - \int_0^\ell K_{rec}n_+n_-(n_+)dx; \tag{2.14}$$

negative ion particle balance,

$$\int_0^\ell K_{att}n_{O2}n_e dx - \int_0^\ell K_{rec}n_+n_-(n_+)dx = 0; \tag{2.15}$$

and energy balance,

$$P_{abs} = 2\mathcal{E}_c\int_0^\ell K_{iz}n_{O2}n_e dx + 2\mathcal{E}_w n_+(\ell_p)u_B \tag{2.16}$$

where $\mathcal{E}_c(T_e)$, the collisional energy lost per electron-positive ion pair created, is a known function of T_e, and $2\mathcal{E}_w n_+(\ell_p)u_B$ is the kinetic energy lost to the wall. Given the plasma length $2\ell_p$, and power P_{abs}, the three equations can be simultaneously solved for the three unknowns T_e, α_0, and n_{+0}. However, the plasma edge ℓ_p is not exactly known, but is dependent on the Bohm flux condition

$$-D_{a+}\frac{dn_+}{dx}\bigg|_{x=\ell} = n_+(\ell_p)u_B(T_e, T_i, \alpha), \tag{2.17}$$

which indicates where the sheath begins. Here $\alpha = \alpha(\ell_p) = n_-(\ell_p)/n_e(\ell_p)$. Since negative ions may be present when (2.17) is satisfied, the Bohm velocity may have the more general form [10]

$$u_B = \left[\frac{eT_e(1+\alpha)}{M_+(1+\gamma\alpha)}\right]^{1/2}, \tag{2.18}$$

which reduces to the usual expression $u_B = (eT_e/M_+)^{1/2}$ when $\alpha = 0$. For $\alpha > 1/\gamma$, the negative ions significantly reduce the Bohm velocity.

There are three different electronegative discharge equilibrium regimes depending on neutral pressure and applied power. (1) At low pressure and high power, α_0 is small. The negative ion density becomes quite small well within the plasma volume, such that the plasma can be treated as if it is essentially electropositive. (2) In the opposite limit of high pressure and low power, $\alpha_0 \gg 1$ and a significant density of negative ions may exist, which, from (2.18), gives a significantly depressed

Bohm velocity with essentially no electropositive edge regions. (3) An intermediate regime can exist where the central α may be quite large but a significant edge region has α near zero, allowing the usual Bohm velocity to be used at the plasma edge.

III. APPROXIMATE SOLUTIONS

A. *Three Component Model with Electronegative and Electropositive Regions*

Consider, as in previous work [9], that a central region of the discharge exists in which α is sufficiently large that $D_{a+} \approx 2D_+$, but that the effect of positive-negative ion recombination can be neglected in determining the spatial distribution. The diffusion equation (2.13) then takes the simple form

$$-2D_+ \frac{d^2 n_+}{dx^2} = K_{iz} n_{O2} n_{e0},$$

where (2.10) with $\gamma \gg 1$ allows us to set $n_e \approx n_{e0}$. In this approximation $n_+(x)$ has a simple parabolic solution of the form

$$\frac{n_+}{n_{e0}} = \frac{n_-}{n_{e0}} + 1 = \alpha_0 \left(1 - \frac{x^2}{\ell^2}\right) + 1, \tag{3.1}$$

where ℓ is the nominal position where $\alpha = 0$ (see Fig. 1). The $\alpha \gg 1$ solution is matched to an $\alpha = 0$ electropositive edge solution, which in turn determines the position of the plasma edge satisfying (2.17). The analysis is simplified by assuming that n_{e0} is known. The absorbed power P_{abs} is then obtained *a posteriori* from (2.16). If P_{abs} is specified rather than n_{e0}, then n_{e0} can be obtained iteratively, as is done for T_e, as described below.

In the development that follows we use the parabolic profile. However to allow the results to be used at small α_0, we use an average value of the diffusion coefficient obtained by substituting an average $\alpha = \bar{\alpha}$, where $\bar{\alpha} = \frac{2}{3}\alpha_0$ in the parabolic approximation.

Substituting this averaged $\bar{D}_{a+}$ in (2.14) and (2.15) and integrating, we obtain, respectively,

$$K_{iz} n_{O2} \ell = K_{rec} n_{e0} \left(\frac{8}{15}\alpha_0^2 + \frac{2}{3}\alpha_0\right) \ell + \frac{2\bar{D}_{a+}\alpha_0}{\ell}, \tag{3.2}$$

$$K_{att} n_{O2} \ell_p = K_{rec} n_{e0} \left(\frac{8}{15}\alpha_0^2 + \frac{2}{3}\alpha_0\right) \ell, \tag{3.3}$$

where in (3.2) the integration is only over the strongly electronegative plasma. At $x = \ell$ this electronegative solution is matched to an electropositive edge solution. The electropositive solution could be a sinusoidal profile, at higher pressures, a more nearly constant profile, at lower pressures, or a profile intermediate between the two. In previous work a parabolic profile was assumed in the electropositive region also, and the fluxes matched at the interface between the regions, to solve for the ratio ℓ/ℓ_p [9]. Here, in order to accommodate the flatter profile at lower pressures, we use a somewhat more general approach.

First, assuming ℓ/ℓ_p is known, we solve (3.3) to obtain

$$\alpha_0 = -\frac{5}{8} + \sqrt{\left(\frac{5}{8}\right)^2 + \frac{15}{8}\frac{K_{att}}{K_{rec}}\frac{n_{O2}}{n_{e0}}\frac{\ell_p}{\ell}}. \tag{3.4}$$

Since ℓ/ℓ_p is near unity for large α_0, the weak dependence on ℓ_p/ℓ is not significant; once a complete solution is found, the value of α_0 can be improved by iteration. For large α_0 (3.4) exhibits the important scaling $\alpha_0 \propto (n_{O2}/n_{e0})^{1/2}$. To obtain a relatively simple overall solution we also make

the assumption that the density in the electropositive solution is relatively constant, except very near the sheath, such that n_e can be set equal to n_{e0} in the integral term in (2.14). In this approximation particle conservation in the electropositive region yields

$$\frac{2\bar{D}_{a+}\alpha_0 n_{e0}}{\ell} + K_{iz} n_{O2} n_{e0}(\ell_p - \ell) = n_{e0} h_\ell u_B, \tag{3.5}$$

where $h_\ell \equiv n_s/n_{e0}$ can be obtained in various approximations. As in previous work [9], the temperature sensitive term K_{iz} can be eliminated by substituting K_{iz} from (3.2) into (3.5) to obtain

$$2\bar{D}_{a+}\alpha_0 \frac{\ell_p}{\ell^2} + K_{rec} n_{e0} \left(\frac{8}{15}\alpha_0^2 + \frac{2}{3}\alpha_0\right)(\ell_p - \ell) = h_\ell u_B. \tag{3.6}$$

which is valid provided $\ell/\ell_p < 1$. Equations (3.4), (3.6), and (3.2) can be solved simultaneously for α_0, ℓ/ℓ_p, and T_e, given n_{e0} as the independent parameter. Alternatively, a useful analytic method is to iteratively solve (3.4) and (3.6), which are not very sensitive to T_e, with an assumed T_e and then use (3.2) to iteratively improve the estimate of T_e. The procedure converges rapidly [9]. The power absorbed is then obtained from (2.16).

We give a comparison of the results of PIC simulation with the model, in Fig. 1, for a higher p case in which the constant mobility ion transport model for the electropositive edge is reasonable. The results indicate that the parabolic approximation is good in the electronegative region. Computing an effective electron temperature from $T_e = \frac{2}{3}\langle E \rangle$ we find $T_e = 2$eV in the PIC simulation and $T_e = 2.05$eV from the model, an excellent agreement. In Fig. 1 the central model density is normalized to that of the PIC simulation to compare the profiles. An $\alpha_0 = 11$, obtained from the model, is 30 percent larger than the $\alpha_0 = 8$ obtained from the simulation.

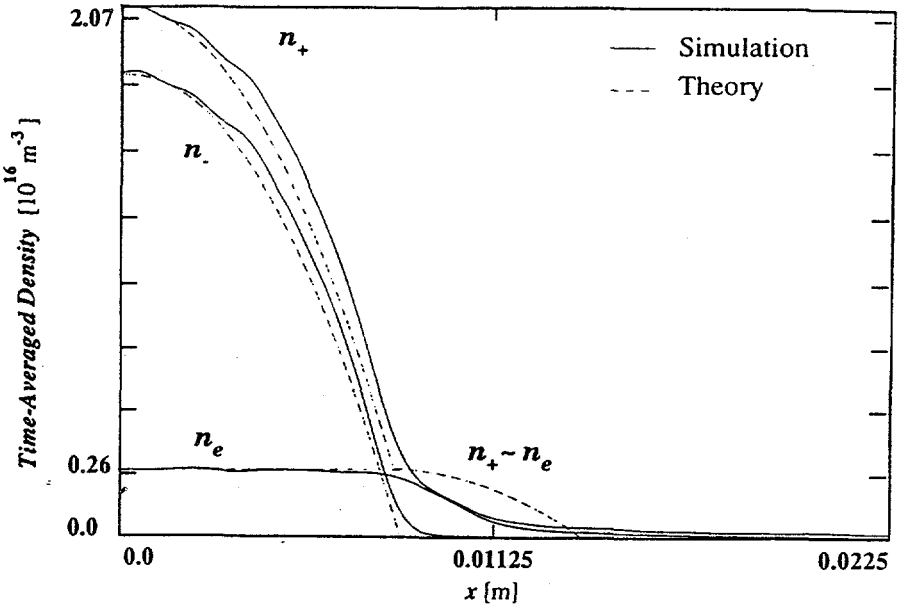

Figure 1. Comparison of analytic solution with simulation; n_{e0} and ℓ_p (at $u_i = u_B$) in the analytic solution are matched to the simulation; $p = 50$ mTorr and $n_{e0} = 2.4 \cdot 10^{15}$ m^{-3}; constant mobility model is used in the electropositive region.

B. *One Region Solution for Large Electronegativity*

For sufficiently large α_0 the electropositive edge region disappears. Assuming that the parabolic

solution is still a reasonable approximation for the negative ions

$$n_- = n_{e0}\alpha_0\left(1-\frac{x^2}{\ell^2}\right), \quad x < \ell_p,$$

but with $\ell > \ell_p$, then the particle balance equation for positive ions is

$$\begin{aligned} K_{iz}n_{O2}n_{e0}\ell_p =& K_{rec}n_{e0}^2\left\{\alpha_0^2\ell_p\left(1-\frac{2}{3}\frac{\ell_p^2}{\ell^2}+\frac{1}{5}\frac{\ell_p^4}{\ell^4}\right)+\alpha_0\ell_p\left(1-\frac{1}{3}\frac{\ell_p^2}{\ell^2}\right)\right\} \\ &+ n_{e0}\left[\alpha_0\left(1-\frac{\ell_p^2}{\ell^2}\right)+1\right]u_B \end{aligned} \tag{3.7}$$

where u_B is given by (2.18) with

$$\alpha = \alpha_0\left(1-\frac{\ell_p^2}{\ell^2}\right). \tag{3.8}$$

The negative ion particle balance is

$$K_{att}n_{O2}n_{e0}\ell_p = K_{rec}n_{e0}^2\left\{\quad\cdot\quad\right\}, \tag{3.9}$$

with the $\{\cdot\}$ repeated from (3.7). The third equation to complete the set is matching the positive ion edge flux

$$2\bar{D}_{a+}\alpha_0 n_{e0}\frac{\ell_p}{\ell^2} = n_{e0}\left[\alpha_0\left(1-\frac{\ell_p^2}{\ell^2}\right)+1\right]u_B. \tag{3.10}$$

For $\alpha_0 \gg 1$, keeping only the terms quadratic in α_0 in (3.9), we obtain

$$\alpha_0 = \left(\frac{K_{att}n_{O2}}{K_{rec}n_{e0}}\right)^{1/2}\left(1-\frac{2}{3}\frac{\ell_p^2}{\ell^2}+\frac{1}{5}\frac{\ell_p^4}{\ell^4}\right)^{-1/2}. \tag{3.11}$$

From (3.10)

$$\frac{\ell^2}{\ell_p^2} = \frac{\alpha_0\left(\dfrac{2\bar{D}_{a+}}{u_B\ell_p}+1\right)}{\alpha_0+1}. \tag{3.12}$$

Using these equations we have been able to explore the transition from a two region regime to a one region regime as the electronegativity α_0 increases. This is shown in Fig. 2, where the solid line for $\ell/\ell_p < 1$ (two region regime) is to be compared with the diamonds for $\ell/\ell_p > 1$ (entire plasma electronegative). The jump in ℓ/ℓ_p is caused by a jump in Bohm velocity in the somewhat idealized treatment. However, there is a hidden restriction, that has not been taken account in the two region model, which is that the ion flow cannot exceed the ion sound velocity. When this restriction is imposed (slightly modifying the theoretical treatment), the solid dots are obtained, giving an essentially continuous solution.

C. *Extensions to Multi-Component Plasmas and to Better Approximations*

The analysis presented above can be extended to additional plasma components. For oxygen, as described in Sec. II, O and O^+ must also be included if the analysis is to be applicable to a wide range of pressure and power. A set of equations have been obtained for two positive ion species

(four total species) using the same approximations as in sections A and B. We are in the process of determining the solutions to these equations over various ranges of pressure and power. We are also exploring better approximations to treat both the electronegative region at large α, and the electropositive edges at intermediate-to-low α.

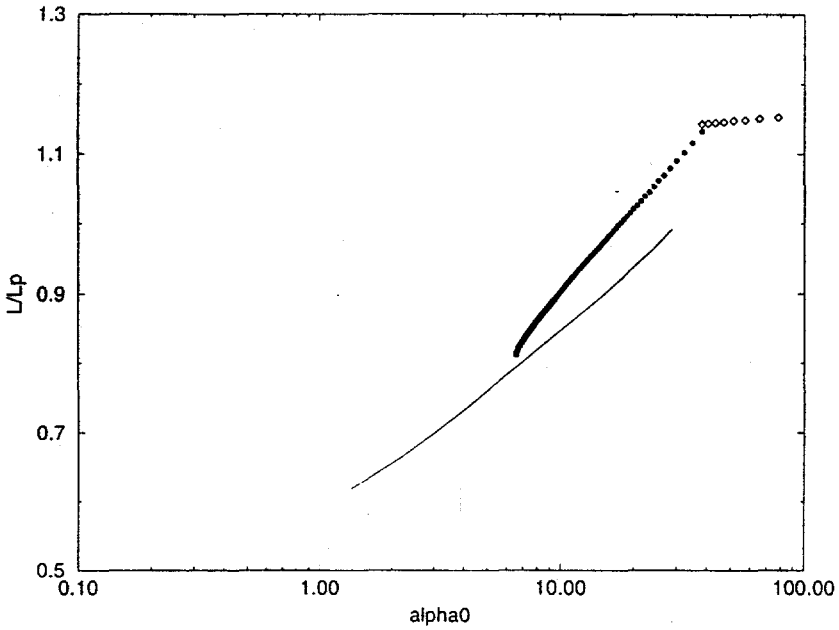

Figure 2. Analytic results of ℓ/ℓ_p is α_0 as n_{e0} is varied; $p = 50$ mTorr; variable mobility model is used in the electropositive region.

REFERENCES

1. D. Vender and R. Boswell, *IEEE Trans. Plasma Sci.*, **18,** 725 (1990).
2. M. Surendra and D. B. Graves, *IEEE Trans. Plasma Sci.*, **19,** 144 (1991).
3. B. Wood, "Sheath Heating in Low Pressure Capacitive R.F. Discharges," Thesis, University of California, Berkeley (1991).
4. D. B. Graves and K. F. Jensen, *IEEE Trans. Plasma Sci.*, **14,** 18 (1986).
5. V. A. Godyak, *Soviet Radio Frequency Discharge Research*, Delphic Assoc. Inc., Falls Church, VA (1986).
6. G. R. Misium, A. J. Lichtenberg, and M. A. Lieberman, *J. Vac. Sci. Technol.*, **A7,** 1007 (1989).
7. B. Wood, M. A. Lieberman, and A. J. Lichtenberg, *IEEE Trans. Plasma Sci.*, **23,** 89 (1995).
8. C. Lee, D. B. Graves, M. A. Lieberman, and D. W. Hess, *J. Electrochem. Soc.*, **141,** 1546 (1994).
9. A. J. Lichtenberg, V. Vahedi, M. A. Lieberman, and T. Rognlien, *J. Appl. Phys.*, **75,** 2339 (1994).
10. R. L. F. Boyd and J. B. Thompson, *Proc. Royal Soc.*, **A252,** 102 (1959).

PLASMA CHARACTERIZATION STUDIES FOR MATERIALS PROCESSING

E. Pfender and J. Heberlein

University of Minnesota
Minneapolis, MN 55455

ABSTRACT

New applications for plasma processing of materials require a more detailed understanding of the fundamental processes occurring in the processing reactors. We have developed reactors offering specific advantages for materials processing, and we are using modeling and diagnostic techniques for the characterization of these reactors. The emphasis is in part set by the interest shown by industry pursuing specific plasma processing applications. In this paper we report on the modeling of radio frequency plasma reactors for use in materials synthesis, and on the characterization of the high rate diamond deposition process using liquid precursors. In the radio frequency plasma torch model, the influence of specific design changes such as the location of the excitation coil on the enthalpy flow distribution is investigated for oxygen and air as plasma gases. The diamond deposition with liquid precursors has identified the efficient mass transport in form of liquid droplets into the boundary layer as responsible for high growth, and the chemical properties of the liquid for the film morphology.

INTRODUCTION

Plasma processing of materials continues to be a growing area, with specific applications ranging from plasma spray coatings to synthesis of ultrafine particles, from high rate deposition of diamond films using a thermal plasma CVD process to destruction of hazardous wastes. The increasing importance of this technical area is demonstrated by the fact that industry is increasingly making use of basic results obtained under this program, and providing additional funding thus leveraging the DOE funded effort.

In previous characterization efforts we had shown that many diagnostic techniques relying on line-of-sight or on time averaged measurements have limited value for characterizing plasma reactors with highly turbulent and reacting flows [1,2]. To improve our capability for describing plasma reactors used for materials processing, we have chosen (a) new diagnostic approaches relying on locally and/or temporally resolved measurement techniques, and (b) new modeling approaches. Two new diagnostic methods are being employed, the first being a high speed laser strobe video system, the second being based on laser scattering techniques developed at the Idaho

National Engineering Laboratory [3]. The new models have addressed issues of practical importance to materials processing reactors, such as radio frequency induction (RFI) plasma reactors with unusual geometries and different processing gases, and of d.c. arc jets either highly turbulent as used for atmospheric pressure plasma spraying, or possessing supersonic velocities with gases used for the deposition of diamond films. In this paper we will focus on two major efforts: (a) the description of the modeling approach and results of the RFI plasma reactor model, and (b) the experimental characterization of the novel method for diamond film deposition at ultra-high rates using liquid precursors. It should be noted that three additional efforts have been initiated for characterizing processing plasmas which cannot be discussed here due to space limitations: (1) the set-up and initial results of the laser scattering system for characterization of non-uniform, flowing plasmas, (2) the modeling of the diamond deposition process with liquid precursors, and (3) the application of the thermal plasma CVD process to the deposition of dense yttria stabilized zirconia films as they are used as electrolyte in solid oxide fuel cells.

MODELING OF HIGH-FREQUENCY (RF) PLASMA REACTORS

The application of RF plasma reactors for the synthesis of fine particles, for thermal plasma chemical vapor deposition (TPCVD), and for toxic waste destruction has been attracting increasing interest in recent years. RF plasmas are particularly suited for the synthesis of fine particles and for TPCVD if purity of the product is a primary concern, because electrode contamination is avoided. Toxic waste destruction with RF plasmas, on the other hand, offers the advantage of compatibility even with corrosive substances, since there are no electrodes in contact with the plasma.

For a better understanding of the characteristic features and for potential scale-up of such reactors, extensive modeling work has been conducted over the past two years. This work has laid the basis for additional funding from industry leveraging the DOE support.

Although modeling of RF plasma reactors has been previously reported, mainly with argon as working gas[1,2], in this modeling work, two different configurations and working gases have been considered, guided by potential applications. In case 1 our efforts focused on the conditions within the reactor itself with oxygen as working gas. In case 2, the plasma tail flame emanating from the reactor was of particular interest with air as the working gas. Because of space limitations, only the most important findings will be discussed in this paper.

Since the basic equations are the same for both cases, these equations will be briefly discussed in this paper.

Continuity: $$\frac{\partial(\rho u)}{\partial z}+\frac{1}{r}\frac{\partial(\rho r v)}{\partial r}=0 \qquad (1)$$

where ρ, u, v are the density, axial velocity and radial velocity respectively.

z-momentum:

$$\rho u\frac{\partial u}{\partial z}+\rho v\frac{\partial v}{\partial r}=-\frac{\partial P}{\partial r}+2\frac{\partial}{\partial z}\left(\mu_e\frac{\partial u}{\partial z}\right)+\frac{1}{r}\frac{\partial}{\partial r}\left[\mu_e r\left(\frac{\partial u}{\partial r}+\frac{\partial v}{\partial z}\right)\right]+\rho g+F_z \qquad (2)$$

where P is the pressure, F_z is the body force in the z-direction, and $\mu_e = \mu_l + \mu_t$ (μ_l : laminar viscosity, μ_t: turbulent viscosity)

r-momentum:

$$\rho u\frac{\partial u}{\partial z}+\rho v\frac{\partial v}{\partial r}=-\frac{\partial P}{\partial r}+\frac{2}{r}\frac{\partial}{\partial r}\left(\mu_e r\frac{\partial v}{\partial r}\right)+\frac{\partial}{\partial z}\left[\mu_e\left(\frac{\partial v}{\partial z}+\frac{\partial u}{\partial r}\right)\right]-\frac{2\mu_e v}{r^2}+\frac{\rho w^2}{r}+F_r \qquad (3)$$

where w is the tangential velocity and F_r is the body force in the r-direction.

θ-momentum:

$$\rho u\frac{\partial(rw)}{\partial z}+\rho v\frac{\partial(rw)}{\partial r}=\frac{\partial}{\partial z}\left(\mu_e\frac{\partial(rw)}{\partial z}\right)+\frac{1}{r}\frac{\partial}{\partial r}\left(\mu_e r\frac{\partial(rw)}{\partial r}\right)-\frac{2}{r}\frac{\partial}{\partial r}(\mu_e rw) \tag{4}$$

where w is the tangential velocity.

Energy:

$$\rho u\frac{\partial h}{\partial z}+\rho v\frac{\partial h}{\partial r}=\frac{\partial}{\partial z}\left(\frac{\lambda}{C_p}\frac{\partial h}{\partial z}\right)+\frac{1}{r}\frac{\partial}{\partial r}\left[\frac{\lambda}{C_p}r\frac{\partial h}{\partial r}\right]+\overline{q}_J-q_R \tag{5}$$

where h is the gas enthalpy, C_p is the specific heat, q_J is the Joule heating term, and q_R are the radiative heat losses.

Vector potential equations (see Ref. 3):

$$\frac{\partial^2 A_R}{\partial z^2}+\frac{1}{r}\frac{\partial}{\partial r}\left(r\frac{\partial A_R}{\partial r}\right)-\frac{A_R}{r^2}+\mu_0\sigma\omega A_I=0 \quad \frac{\partial^2 A_I}{\partial z^2}+\frac{1}{r}\frac{\partial}{\partial r}\left(r\frac{\partial A_I}{\partial r}\right)-\frac{A_I}{r^2}+\mu_0\sigma\omega A_R=0 \tag{6}$$

where A_R and A_I are the real and the imaginary parts of the vector potential A_θ. The electric and the magnetic fields are related to the vector potential by the following:

$$E_\theta=-i\omega A_\theta \qquad \mu_0 H_z=\frac{1}{r}\frac{\partial}{\partial r}(rA_\theta) \qquad \mu_0 H_r=-\frac{\partial}{\partial z}(A_\theta) \tag{7}$$

The radial and axial body forces acting on the plasma F_r, F_z, and the volumetric heat generation due to the Joule heating q_J are:

$$F_r=\frac{1}{2}\mu_0\sigma\mathrm{Real}\left[E_\theta H_z^*\right] \qquad F_z=-\frac{1}{2}\mu_0\sigma\mathrm{Real}\left[E_\theta H_r^*\right] \qquad q_J=\frac{1}{2}\sigma\left[E_\theta E_\theta^*\right] \tag{9}$$

where * denotes complex conjugate quantities.

Turbulent kinetic energy, k:

$$\rho u\frac{\partial k}{\partial z}+\rho v\frac{\partial k}{\partial r}=\frac{\partial}{\partial z}\left(\left(\mu_l+\frac{\mu_t}{\sigma_k}\right)\frac{\partial k}{\partial z}\right)+\frac{1}{r}\frac{\partial}{\partial r}\left[r\left(\mu_l+\frac{\mu_t}{\sigma_k}\right)\frac{\partial k}{\partial r}\right]+G-\rho\varepsilon \tag{10}$$

where

$$G=\mu_t\left\{2\left[\left(\frac{\partial u}{\partial z}\right)^2+\left(\frac{\partial v}{\partial r}\right)^2+\left(\frac{v}{r}\right)^2\right]+\left[r\frac{\partial}{\partial r}\left(\frac{w}{r}\right)\right]^2+\left(\frac{\partial u}{\partial r}+\frac{\partial v}{\partial z}\right)^2+\left(\frac{\partial w}{\partial z}\right)^2\right\} \tag{11}$$

Dissipation rate of turbulent kinetic energy, ε:

$$\rho u\frac{\partial \varepsilon}{\partial z}+\rho v\frac{\partial \varepsilon}{\partial r}=\frac{\partial}{\partial z}\left(\left(\mu_l+\frac{\mu_t}{\sigma_\varepsilon}\right)\frac{\partial \varepsilon}{\partial z}\right)+\frac{1}{r}\frac{\partial}{\partial r}\left[r\left(\mu_l+\frac{\mu_t}{\sigma_\varepsilon}\right)\frac{\partial \varepsilon}{\partial r}\right]+\frac{\varepsilon}{k}\left(C_{\varepsilon 1}f_{\varepsilon 1}G-C_{\varepsilon 2}f_{\varepsilon 2}\rho\varepsilon\right) \tag{12}$$

where C_μ, $C_{\varepsilon 1}$, $C_{\varepsilon 2}$, σ_h, σ_k and σ_ε are empirical constants of the k-ε turbulence model [4,5]:

C_μ	$C_{\varepsilon 1}$	$C_{\varepsilon 2}$	σ_h	σ_k	σ_ε
0.09	1.92	1.44	0.9	1.0	1.3

and the corrections $f_{\varepsilon 1}$ and $f_{\varepsilon 2}$ in the ε equations are given by

$$f_{\varepsilon 1}=1+\left(\frac{0.05}{f_\mu}\right) \qquad f_{\varepsilon 2}=1-\exp\left(-R_t^2\right)$$

The Lam-Bremhorst form of the Low-Reynolds-Number k-ε model is given by:

$$\mu_t = C_\mu f_\mu \frac{\rho k^2}{\varepsilon} \quad \text{where} \quad f_\mu = \left[1 - \exp\left(-0.0165 R_y\right)^2\right] \cdot \left(1 + \frac{20.5}{R_t}\right)$$

$$\text{with } R_y = \frac{\rho \sqrt{k}\, y}{\mu_t} \quad \text{and } R_t = \frac{\rho k^2}{\mu_t \varepsilon}$$

Results - Case 1:

A computer program has been developed to model the temperature and flow fields inside an RF plasma reactor for oxygen plasmas. This program is based on the SIMPLER algorithm [6]. The program solves the equations of conservation of mass (continuity), conservation of momentum and conservation of energy simultaneously. The source terms of the momentum and energy equations are supplied by the solutions from the vector potential equations (partial differential equations) of the electromagnetic field. In addition, a low Reynolds number, k-ε model is employed to model the turbulence in the plasma. The diffusive term of the momentum equations (effective viscosity) are supplied by solving the turbulent kinetic energy equations (k) and the turbulent kinetic energy dissipation rate equations (ε). The strong intercoupling between the partial differential equations makes modeling of RF plasmas a complex task.

A schematic of the RF plasma torch with the computational domain and geometry is shown in Figure 1. Based on the assumption of rotational symmetry, steady flow, local thermodynamic equilibrium (LTE), and optically thin conditions, solutions of the conservation equations have been obtained in terms of temperature and flow fields. Plasma properties and plasma compositions are calculated using the PLASMA code developed at the High Temperature Laboratory at the University of Minnesota.

As an example, Fig. 2 shows temperature and flow profiles at power levels from 10 to 30

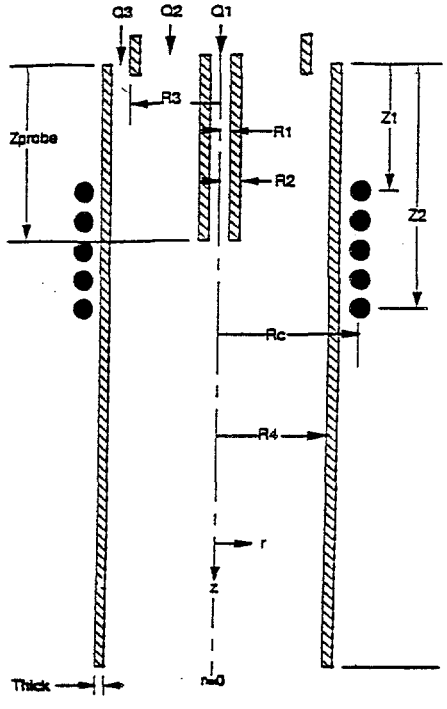

Fig. 1: Schematic of the RF plasma torch (Case 1)

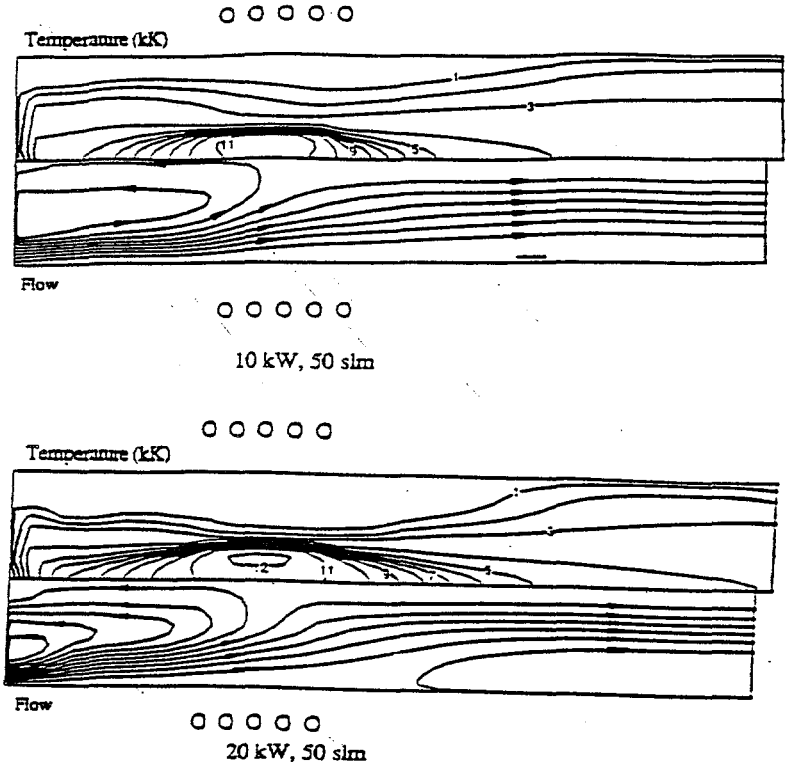

Fig. 2: Temperature and flow fields of oxygen plasmas at two power levels

kW and a gas flow rate of 50 slm. The maximum temperature in the plasma (approximately 12,000 K) remains almost the same as the power dissipation in the plasma increases, but the volume of hot plasma expands downstream. This behavior is typical for thermal RF plasmas.

Results - Case 2:

The same approach and essentially the same assumptions have been used to model temperature and flow fields for the RF plasma reactor configuration shown in Fig. 3, but in this case for air as the working gas (1 atm). It is obvious from the schematic of Fig. 3 that the emphasis for this calculation is on the tail flame of the RF plasma.

As an example, Fig. 4 shows temperature and flow fields for a plasma power of 25 kW. As the power level increases, the maximum temperature (approximately 11,000 K) remains almost the same as in case 1, but again, the hot plasma expands somewhat farther downstream and, at the same time, the velocity in the tail flame increases substantially as shown in Fig. 5. This leads to a substantial increase of the enthalpy far downstream from the exit nozzle (see Fig. 6).

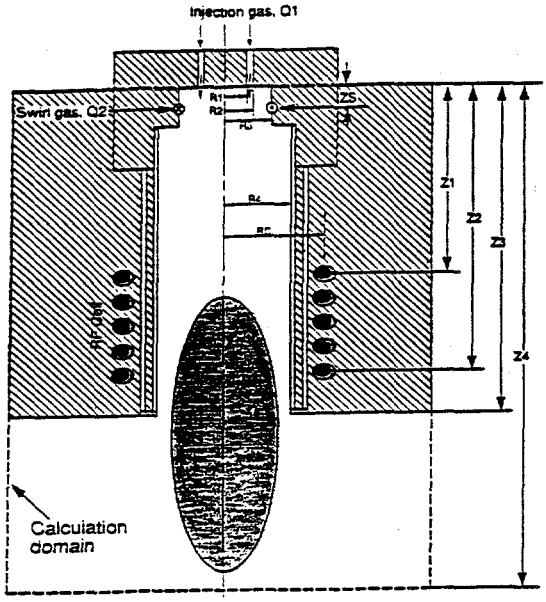

Fig. 3: Schematic of the RF plasma torch and the calculation domain (Case 2)

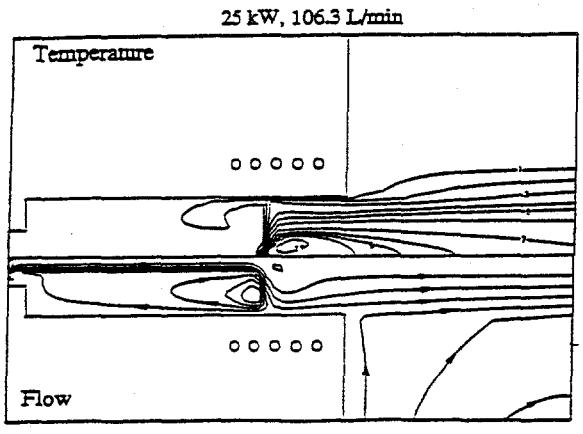

Fig. 4: Temperature and flow profiles of the air plasma torch

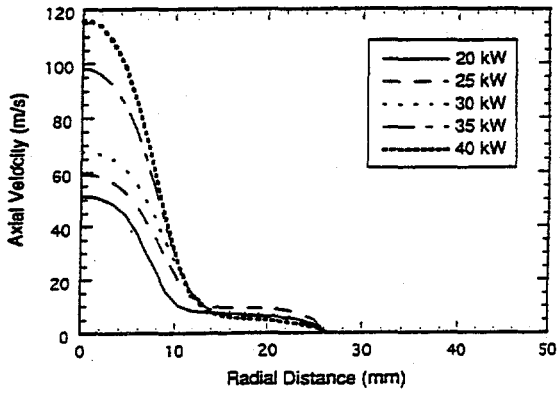

Fig. 5: Axial velocities at the downstream end of the coil

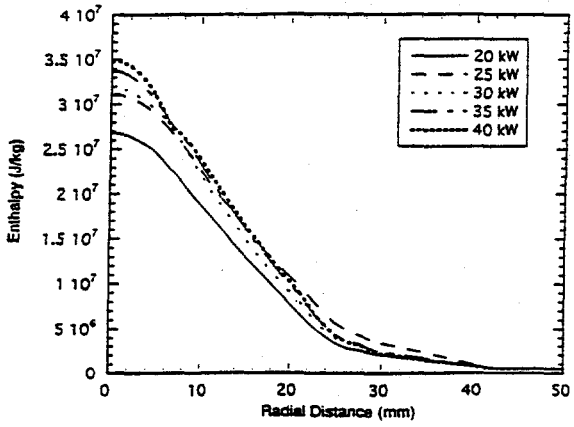

Fig. 6: Enthalpy profiles far downstream from the torch exit

DIAMOND DEPOSITION EXPERIMENTS WITH LIQUID PRECURSORS.

We have previously reported results of experiments in which very high growth rates of diamond films have been obtained by injecting liquids in form of an atomized jet in a counterflow arrangement into a plasma jet [10]. Liquids used in these studies included a variety of organics including PCB contaminated oils. We had demonstrated that jet fluctuations could lead to film non-uniformities. In order to obtain a better understanding of this deposition process, controlled experiments were performed in which the effect of mass transport was investigated. These investigations included (a) determination of the droplet size for different liquids using our atomizing nozzle in a particle size diagnostics wind tunnel, (b) an analysis of the evaporation behavior of the different liquid droplets used, and (c) observation of the droplet trajectories in the reactor for counterflow injection and for injection from the side parallel to the substrate. The specific liquids investigated were acetone, ethanol and toluene. It was found that differences in the physical characteristics of these liquids did not influence the mass transport to the substrate. The droplet trajectories were observed with the laser strobe video system. A new reactor had to be designed for this purpose with windows which would allow laser beam access and observation of the reflected signal without disturbing the flow pattern in the reactor. Fig. 7 shows schematically the set-up of the laser strobe video system. The electronic shutter of the CCD video head opens for 50 ns during which the nitrogen laser delivers a pulse. The light reflected by the droplets passes through a narrow line filter to block out background radiation and is captured by the video head. The images are recorded on tape and are then processed by computerized image analysis. Fig. 8 shows a computer enhanced image of droplets injected from the side 5 mm above the substrate interacting with the plasma jet coming from the top of the picture. It is apparent that droplets nearly reach the substrate providing efficient mass transport. We have found a dependence of growth rate on the plasma torch power, indicating that the diamond film growth may be limited by the amount of atomic hydrogen provided by the plasma jet. One observation which we cannot explain at present is that the diamond crystal size is quite different when different precursors are used. Fig. 9 shows SEM photos of films obtained with acetone and with ethanol, indicating the larger crystal size obtained with ethanol.

In order to guide further diagnostic experiments, we have initiated the modeling effort which includes description of the droplet formation, droplet - jet interaction, and the surface chemistry.

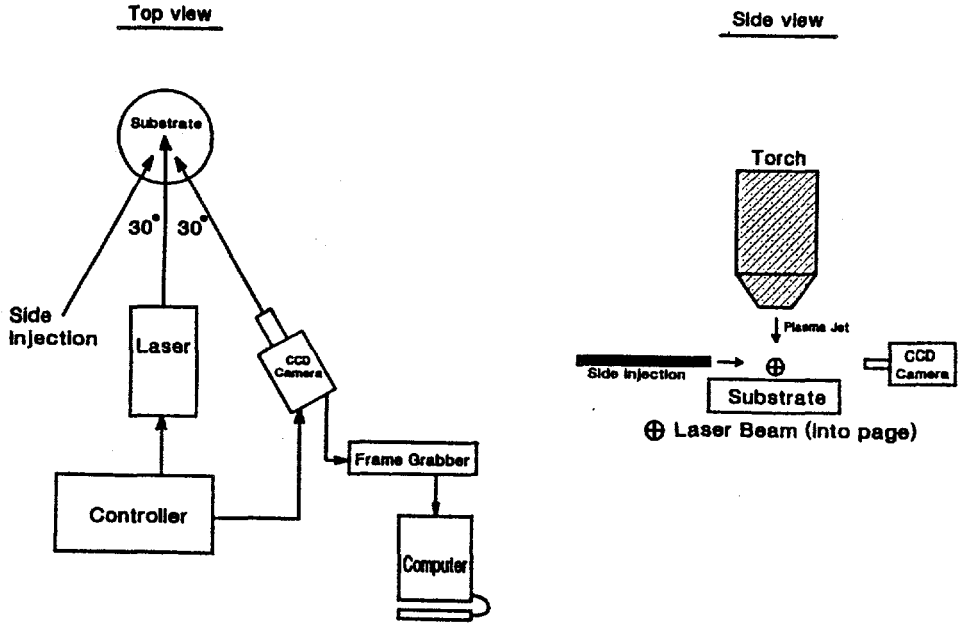

Fig. 7: Schematic of liquid droplet injection reactor and of laser strobe video set-up.

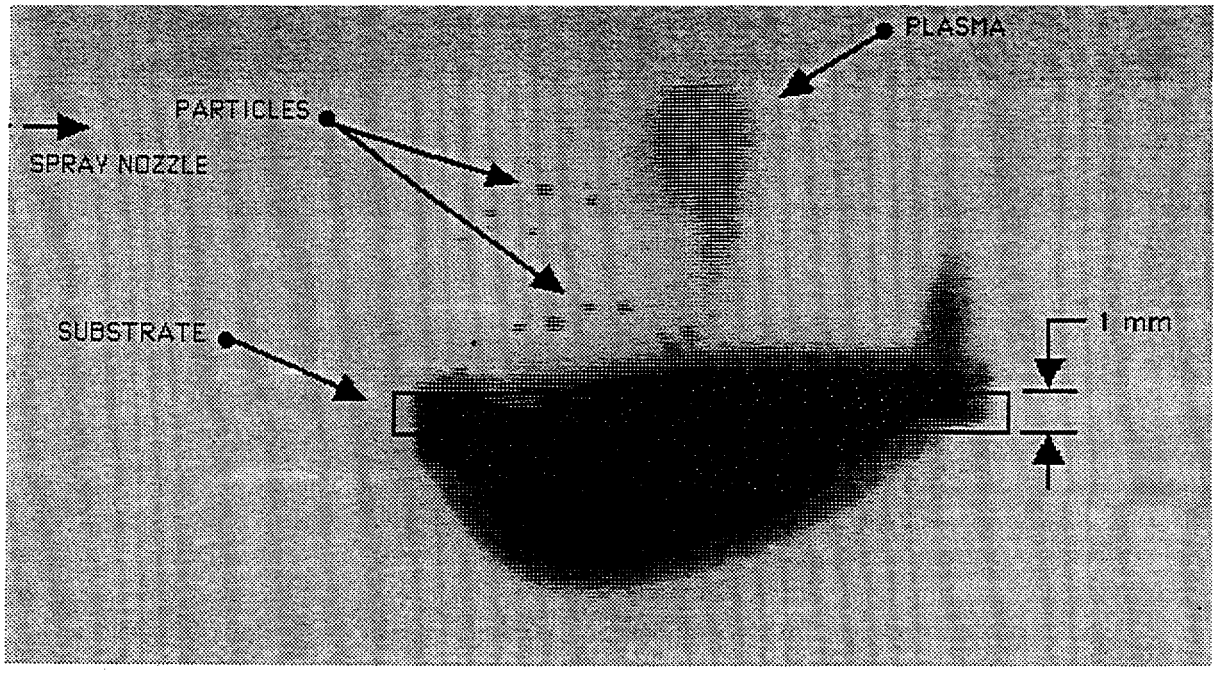

Fig. 8: Computer enhanced video image of plasma jet (center top) and of liquid droplets (injected from the left). The dark region in the center is a reflection from the substrate.
Injection probe position: 3 mm above the substrate;
Liquid: ethanol; atomizing gas: hydrogen;
Torch power: 10.5 kW.

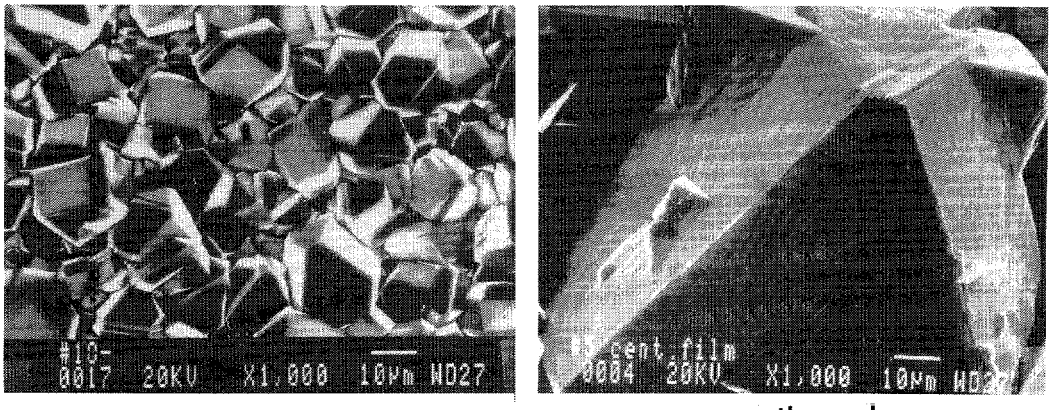

acetone ethanol

Fig. 9: Scanning Electron Micrographs of diamond films obtained from acetone and from ethanol with side injection for identical torch operating conditions.

CONCLUSIONS

Modeling of inductively-coupled RF plasmas indicates that with oxygen or air as the working gas, the maximum temperature in the plasma remains almost the same (around 11,000 K), regardless of the power input to the plasma. The hot plasma, however, extends farther downstream as the power input increases and, at the same time, the velocity in the plasma tail flame increases for the same mass flow rate. The quantitative description of the process details allow the derivation of scaling laws for process reactor design.

For a better understanding of the unusually high growth rates (up to mm/hr) of diamond films observed with liquid precursors injected into a thermal plasma jet, droplet visualization tests have been made, using a laser strobe system. The results show that the plasma jet accelerates the droplets towards the substrate, and some of the droplets almost reach the substrate surface, providing an efficient transport of chemically active species to the surface. The availability of atomic hydrogen seems to be a limiting factor for diamond growth in this case. The size of the well-faceted diamond crystals varies with different precursor materials (acetone, ethanol, benzene, etc.), an observation which remains unexplained at this point. Modeling of this process is necessary to enhance our understanding of the process details and to allow us to make full use of the high diamond film growth rates.

ACKNOWLEDGMENTS

The contributions by Mr. D. Or to the rf plasma modeling, and by Dr. D. Zhuang and Mr. P. Schwendinger to the characterization of the liquid injection reactor are gratefully acknowledged. This work has been supported by DOE under grant No.DOE/F602-85ER-13433.

REFERENCES

1. E. Pfender, J. Fincke, R. Spores, "Entrainment of Cold Gas into Thermal Plasma Jets", *Plasma Chem. Plasma Process.* **11**, 529-543 (1991).
2. W.L.T. Chen, J. Heberlein, and E. Pfender, "Diagnostics of a Thermal Plasma Jet by Optical Emission Spectroscopy and Enthalpy Probe Measurements," Plasma Chemistry and Plasma Processing, Vol. 14(3), pp. 317-332 (1994).
3. S,C. Snyder, L.D. Reynolds, J.R. Fincke, G.D. Lassahn, J.D. Grandy, T.E. Repetti, Electron-temperature and electron-density profiles in an atmospheric-pressure argon plasma jet," *Phys.Rev. E*, 50/1, 519-525 (1994).
4. G.Y. Zhao, J. Mostaghimi and M.I. Boulos, "The Induction Plasma Chemical Reactor, Part I: Equilibrium Model", *Plasma Chem. Plasma Process.* **10**, 133-150 (1990).
5. G.Y. Zhao, J. Mostaghimi and M.I. Boulos, "The Induction Plasma Chemical Reactor, Part II: Kinetic Model", *Plasma Chem. Plasma Process.* **10**, 151-166 (1990).
6. X. Chen and E. Pfender, "Modeling of RF Plasma Torch with a Metallic Tube Inserted for Reactant Injection", *Plasma Chemistry and Plasma Processing*, **11** (1), (1991).
7. C.K.G. Lam and K.A. Bremhorst, "Modified Form of the k-ε Model for Predicting Wall Turbulence", *J. Fluids Engineering*, **103**, 456 (1981).
8. W.P. Jones and B.E. Launder, "The Prediction of Laminarization with a Two-Equation Model of Turbulence", *Int. J. Heat Mass Transfer*, **15**, 301 (1972).
9. S.V. Patankar, *Numer. Heat Transfer Fluid Flow*, New York: McGraw Hill (1980).
10. E. Pfender, Q.Y. Han, T.W. Or, Z.P. Lu, and J. Heberlein, "Rapid synthesis of diamond by counter-flow liquid injection into an atmospheric pressure plasma jet," Diamond and Related Materials, Vol.1 (1), p.127, 1992.

HYDRODYNAMIC THEORY OF DIFFUSION IN TWO-TEMPERATURE MULTICOMPONENT PLASMAS

J. D. Ramshaw and C. H. Chang

Idaho National Engineering Laboratory
Idaho Falls, ID 83415

ABSTRACT

Detailed numerical simulations of multicomponent plasmas require tractable expressions for species diffusion fluxes, which must be consistent with the given plasma current density $\mathbf{J}_q$ to preserve local charge neutrality. The common situation in which $\mathbf{J}_q = \mathbf{0}$ is referred to as ambipolar diffusion. The use of formal kinetic theory in this context leads to results of formidable complexity. We derive simple tractable approximations for the diffusion fluxes in two-temperature multicomponent plasmas by means of a generalization of the hydrodynamical approach used by Maxwell, Stefan, Furry, and Williams. The resulting diffusion fluxes obey generalized Stefan-Maxwell equations that contain driving forces corresponding to ordinary, forced, pressure, and thermal diffusion. The ordinary diffusion fluxes are driven by gradients in pressure fractions rather than mole fractions. Simplifications due to the small electron mass are systematically exploited and lead to a general expression for the ambipolar electric field in the limit of infinite electrical conductivity. We present a self-consistent effective binary diffusion approximation for the diffusion fluxes. This approximation is well suited to numerical implementation and is currently in use in our LAVA computer code for simulating multicomponent thermal plasmas. Applications to date include a successful simulation of demixing effects in an argon-helium plasma jet, for which selected computational results are presented. Generalizations of the diffusion theory to finite electrical conductivity and nonzero magnetic field are currently in progress.

INTRODUCTION

There is a growing interest in the use of thermal plasmas for materials processing and synthesis applications. This has stimulated a parallel interest in the development and application of physical models and numerical methods for performing detailed space- and time-resolved

simulations of such plasmas [1,2]. Thermal plasmas are inherently multicomponent systems, so constitutive relations for the diffusional mass fluxes in the plasma are an essential ingredient in such models. Forced diffusion due to the electric field $\mathbf{E}$ is in turn an essential contribution to the diffusion fluxes. Even in the absence of an external electric field, an internal field spontaneously arises to preserve local charge neutrality, which would otherwise be disrupted by the natural tendency of the very light electrons to rapidly diffuse away from the much heavier ions and neutral atoms. The electric field is the mechanism by which the diffusion fluxes are constrained to produce an electrical current density $\mathbf{J}_q$ which preserves local charge neutrality. This implies $\nabla \cdot \mathbf{J}_q = \mathbf{0}$ at a minimum, but in many cases the stronger condition $\mathbf{J}_q = \mathbf{0}$ is satisfied. Diffusion in this latter situation is referred to as ambipolar diffusion [3].

Ambipolar diffusion in simple situations is treated in textbooks, but the resulting expressions are inadequate to deal with the arbitrary multicomponent mixtures of present concern. The required general expressions could in principle be derived from the kinetic theory of gases, but this theory is usually developed under the assumption that all the species or components share a common translational temperature. This assumption is frequently violated in thermal plasmas, where a variety of nonequilibrium effects can cause the electron temperature T_e to be significantly different from the heavy-particle temperature T [2]. This complication presents formidable difficulties in the kinetic theory, and is a serious obstacle to the development of simple and tractable approximations for the diffusion fluxes. We have therefore pursued an alternative hydrodynamic approach [4] which captures the essential physics within a much simpler and more transparent framework, and permits the derivation of a simple multitemperature ambipolar diffusion formulation [5] suitable for practical calculations and numerical implementation.

The hydrodynamic theory of diffusion has a distinguished history dating back to Maxwell and Stefan [6,7], and has been further elaborated in more recent times by Furry [8], Williams [9], and Ramshaw [4]. This theory has largely been superseded by the more accurate treatment made possible by the general kinetic theory of gases [6,10], but the latter theory has the disadvantage of being much more intricate and complex. For this reason, the hydrodynamic theory still retains value as a simple and physically transparent approach which leads to essentially correct results in a very straightforward manner. Indeed, the results of the hydrodynamic theory are surprisingly accurate; in the special case when $T_e = T$, they are in precise agreement with first-order Chapman-Enskog theory [4].

THE MULTITEMPERATURE STEFAN-MAXWELL EQUATIONS

The starting point of the hydrodynamic theory of diffusion is a conventional multifluid description with separate continuity and momentum equations for each of the N species in the mixture. These momentum equations contain frictional terms proportional to species velocity differences and thermophoretic force terms proportional to temperature gradients [4]. A reduction of the multifluid description to a diffusional description results when the friction coefficients are large, so that the slip velocities between species are reduced to very small values. The separate species accelerations then become very nearly equal to the mean acceleration of the plasma as a whole, whereupon the species momentum equations reduce to Stefan-Maxwell equations of the form [4]

$$\sum_j \frac{z_i z_j}{D_{ij}} (\mathbf{u}_j - \mathbf{u}_i) = \mathbf{H}_i - \left(\frac{\rho_i q_i}{p} \right) \mathbf{E} \tag{1}$$

where $z_i = p_i/p$, p_i is the partial pressure of species i, $p = \sum_i p_i$ is the total pressure, D_{ij} is the binary diffusion coefficient for the pair (i,j) (which depends on an effective pair temperature $T_{ij} = (m_i T_j + m_j T_i)/(m_i + m_j)$, where T_i and m_i are respectively the temperature and molecular mass of species i [4]), $\mathbf{u}_i$ is the specific velocity of species i, $\mathbf{H}_i = \nabla z_i + (z_i - y_i)\nabla \ln p + \mathbf{K}_i$, ρ_i and q_i are respectively the partial mass density and charge per unit mass of species i, $y_i = \rho_i/\rho$, $\rho = \sum_i \rho_i$ is the total mass density, $\mathbf{K}_i$ represents thermophoretic force terms proportional to temperature gradients [4], and we have assumed that the only external forces present are those of gravity (which cancels out) and the electric field. It is noteworthy that Eqs. (1) have the same form as the usual single-temperature Stefan-Maxwell equations [10], but with the mole fractions x_i replaced by the corresponding pressure fractions z_i. In the present context, all the heavy species have the same common temperature T, so that $T_i = T$ for $i \neq e$, while $T_i = T_e$ for $i = e$.

Only $N - 1$ of Eqs. (1) are linearly independent, as their sum over i yields $\mathbf{0} = \mathbf{0}$. These equations contain $N + 1$ unknowns, namely the $\mathbf{u}_i$ and $\mathbf{E}$. The two additional equations needed to close the system are

$$\sum_i \rho_i \mathbf{u}_i = \rho \mathbf{u} \tag{2}$$

$$\sum_i \rho_i q_i \mathbf{u}_i = \mathbf{J}_q \tag{3}$$

where $\mathbf{u}$ is the mass-averaged plasma velocity determined by the mean momentum equation, and $\mathbf{J}_q = \mathbf{0}$ in the ambipolar case. Equations (1)–(3) constitute a system of $N + 1$ linear equations for the $\mathbf{u}_i$ and $\mathbf{E}$, which must in general be solved at each point in space and time. The resulting $\mathbf{u}_i$ then determine the species diffusion fluxes $\mathbf{J}_i = \rho_i(\mathbf{u}_i - \mathbf{u})$, which in turn determine the time evolution of the ρ_i via the species continuity equations [4].

SIMPLIFICATIONS DUE TO SMALL ELECTRON MASS

The diffusion coefficients D_{ij} are of order $\mu_{ij}^{-1/2}$, where $\mu_{ij} = m_i m_j/(m_i + m_j)$. Since $m_e \ll m_j$ $(j \neq e)$, it follows that $\mu_{ej} \cong m_e$ and $D_{ej} \sim m_e^{-1/2}$. The entire left member of Eq. (1) for $i = e$ is therefore of order $m_e^{1/2}$, which is very small and may ordinarily be neglected. We thereby obtain

$$\mathbf{E} = \frac{p}{\rho_e q_e} \mathbf{H}_e \tag{4}$$

which is a general expression for the ambipolar electric field in an arbitrary two-temperature multicomponent plasma. It may now be used to eliminate $\mathbf{E}$ from Eq. (1) for $i \neq e$, in which the term $j = e$ may now be omitted from the summation as it is also of order $m_e^{1/2}$. The $i = e$ term in Eq. (2) may be omitted *a fortiori*, as it is of order m_e. When all this is done, Eqs. (1) (for $i \neq e$) and (2) no longer involve $\mathbf{u}_e$, and only $N - 2$ of Eqs. (1) for $i \neq e$ remain linearly independent. These equations, together with Eq. (2), then constitute a linear system of $N - 1$ equations for the $N - 1$ unknowns $\mathbf{u}_i$ with $i \neq e$. The final unknown $\mathbf{u}_e$ is then determined by Eq. (3).

The electrical conductivity of the plasma is of order $m_e^{-1/2}$ [6], so the resistivity is of order $m_e^{1/2}$. By neglecting terms of order $m_e^{1/2}$, we have effectively approximated the resistivity by zero; *i.e.*, the plasma has been approximated as a perfect conductor. Indeed, Eq. (4) for $\mathbf{E}$ may be interpreted as the generalized Ohm's law for the plasma in the limit of infinite conductivity.

THE SELF-CONSISTENT EFFECTIVE BINARY DIFFUSION APPROXIMATION

Self-consistent effective binary diffusion approximations are frequently used to avoid solving the linear system of Eqs. (1)–(3). A rational basis for such approximations has recently been presented [11] and applied in the present context [3–5]. In the limit of small electron mass, the resulting expressions for the $\mathbf{J}_i$ ($i \neq e$) take the form [5]

$$\mathbf{J}_i = \mathbf{J}_i^0 - y_i \sum_{j \neq e} \mathbf{J}_j^0 \tag{5}$$

where

$$\mathbf{J}_i^0 = -\frac{m_i D_i}{k_B T}(p\mathbf{H}_i - \rho_i q_i \mathbf{E}) \tag{6}$$

where k_B is Boltzmann's constant. These equations provide explicit approximate expressions for the diffusion fluxes of the heavy species. The diffusion flux for the electrons is then determined by Eq. (3). Notice that Eqs. (5) and (6) involve the effective binary diffusivities D_i [11] and temperature T for the heavy species only. They are therefore well suited for numerical implementation, where the very large value of D_e might otherwise have given rise to unacceptably restrictive stability and/or accuracy restrictions. These equations are currently in use in our LAVA computer code for simulating nonequilibrium thermal plasma processes [1,2]. Some illustrative computational results are presented in the next section.

DEMIXING IN ARGON-HELIUM PLASMA JETS

Demixing effects in plasma torches [12] provide a particularly interesting example of multicomponent diffusive phenomena in thermal plasmas. For example, in an argon-helium plasma jet discharging into quiescent air, the helium mole fraction in the jet core at the torch exit is substantially enhanced relative to the premixed feed gas due to diffusive demixing in the discharge region [12]. This effect results from an interplay between diffusion and ionization. The ionization potential of argon (15.8 eV) is considerably lower than that of helium (24.6 eV), so the argon is preferentially ionized near the torch centerline where the temperature is highest. This creates radial concentration gradients in both argon ions and electrons, resulting in radial outward ambipolar diffusion of argon ions. In addition, each ionization event produces two particles from one, which reduces the helium mole fractions near the centerline. This causes helium to diffuse radially inward, resulting in an enrichment of helium near the centerline and a corresponding depletion near the torch wall. The degree of demixing is primarily determined in the discharge region, but the diffusional separation process continues to operate for some distance downstream of the nozzle exit. Eventually, however, recombination occurs as temperatures drop and the argon and helium remix to regenerate the initial mixture ratio.

A suitable formulation for multicomponent ambipolar diffusion is essential to an accurate physical description of this and similar effects involving coupling between concentrations and diffusion fluxes of individual ionized and neutral species. Previous simplified approaches, such as those in which the plasma is approximated as a two-component mixture of the plasma gas and air [13,14], are fundamentally incapable of capturing such effects, as they neglect individual species diffusion fluxes as well as interactions between the multiple dissociation and ionization reactions occurring in the plasma. For example, ionization of argon is suppressed by the electrons produced by ionization of other species. Ionization processes are highly energetic and strongly

temperature dependent, so interaction effects of this type are essential to a quantitative description of multicomponent thermal plasmas.

The present ambipolar diffusion formulation, as implemented in the LAVA code [1,2], has been used to perform detailed numerical simulations of demixing in argon-helium plasma jets and comparisons with corresponding experimental data [12]. LAVA is a fluid-dynamical model which represents the plasma as an ideal gas mixture with temperature-dependent specific heats and transport properties. The equations solved consist of the mixture momentum equation for the plasma, separate thermal internal energy equations for the mixture and electrons, continuity equations for each component of the mixture, ideal-gas state relations, chemical kinetic rate expressions, and transport equations for turbulence parameters. The numbers of components and chemical reactions are arbitrary. Detailed descriptions of the theoretical model and numerical scheme are available elsewhere [1,2].

The present simulations were performed in two-dimensional cylindrical coordinates, as the plasma torch is presumed to be axisymmetric. Gravity and swirl were neglected, and complete local thermodynamic equilibrium (LTE) was assumed. This implies both chemical and thermal equilibrium, so the electron and heavy-particle temperatures were taken to be equal. Eleven species were included in the calculations, namely Ar, Ar^+, e^-, He, He^+, N_2, N, N^+, O_2, O, and O^+. The formation of NO_x is neglected due to the fact that negligible amounts were observed experimentally. The following six chemical reactions were included: The chemical reactions are

$$\begin{aligned} Ar &\rightleftharpoons Ar^+ + e^- \\ He &\rightleftharpoons He^+ + e^- \\ N_2 &\rightleftharpoons 2N \\ O_2 &\rightleftharpoons 2O \\ N &\rightleftharpoons N^+ + e^- \\ O &\rightleftharpoons O^+ + e^- \end{aligned}$$

all of which are assumed to be in equilibrium.

The geometry and operating conditions of the plasma torch are typical of a commercial unit (Miller SG-100). This torch has an 8 mm nozzle exit diameter and was operated subsonically. Torch operating conditions for the data presented are 800 A at 37 V, for a total power input of 29.6 kW, approximately 2/3 of which is deposited in the torch gas. The argon and helium flow rates were 3200 ℓ/hr and 1331 ℓ/hr respectively, resulting in a premixed [Ar]/[He] mixture ratio of 2.4. The inflow profiles of Ar and He concentrations, velocity, and temperature at the torch exit were obtained from the experimental data 0.5 cm from the nozzle exit [12].

Figure 1 shows the computed and experimental argon/helium cold mole fraction ratios along the centerline. The experimental results were obtained by enthalpy probe measurements using a differentially pumped quadrapole mass spectrometer system to determine species concentrations [12]. The cold mole fraction of argon is defined by

$$x^c_{Ar} = \frac{[Ar] + [Ar^+]}{[Ar] + [Ar^+] + [He] + [He^+] + [N_2] + [O_2] + \frac{1}{2}([N] + [N^+] + [O] + [O^+])} \qquad (7)$$

where [X] is the molar concentration of species X in the plasma. This is the argon mole fraction measured by sampling the plasma and cooling it to room temperature at constant elemental composition. The cold mole fractions of helium and air are given by analogous expressions.

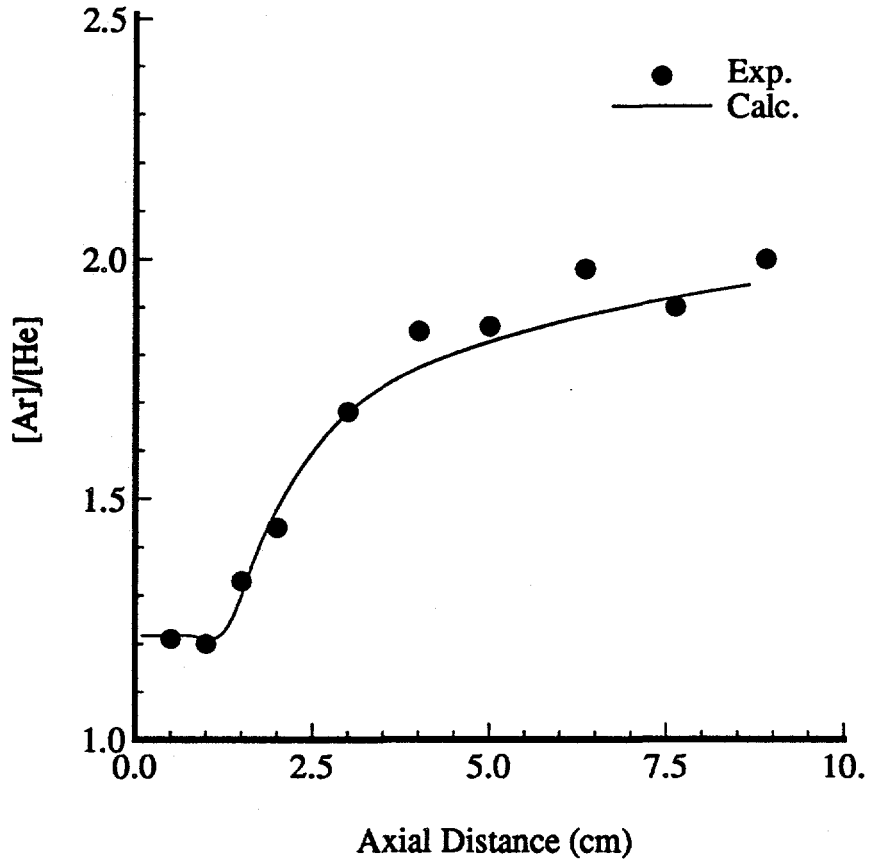

Figure 1. Calculated and Experimental Argon to Helium Cold Mole Fraction Ratio Along the Centerline.

Figure 1 shows that the centerline argon/helium cold mole fraction ratio is approximately 1.2 at the 0.5 cm axial location. This ratio is 2.4 for the premixed plasma gas, so the diffusive demixing effect is quite dramatic. The experimental data show a slight further decrease in this ratio between 0.5 cm and 1.0 cm, indicative of continued diffusive demixing in this region. Note that the simulation also captures this effect. Beyond 1.0 cm, the plasma rapidly cools and remixing again begins to occur, as discussed above.

Figure 2 shows radial plots of the Ar-He cold mole fraction ratio at axial locations of 0.5 cm (inflow condition), 2.0 cm, and 5.0 cm. After the shear layer surrounding the jet encroaches into the centerline (which occurs at about 1.0 cm [12]), turbulent mixing overcomes diffusive demixing and the Ar-He ratio begins to increase again. By 5.0 cm, the profile of Ar-He mole fraction ratio has been flattened by the mixing process and is approaching a value of about 2.0 on the centerline.

ACKNOWLEDGMENTS

We are grateful to Jim Fincke for helpful discussions and collaboration. This work was performed under the auspices of the U. S. Department of Energy under DOE Field Office, Idaho Contract DE-AC07-94ID13223, supported by the U. S. Department of Energy, Office of Energy Research, Office of Basic Energy Sciences, Division of Engineering and Geosciences.

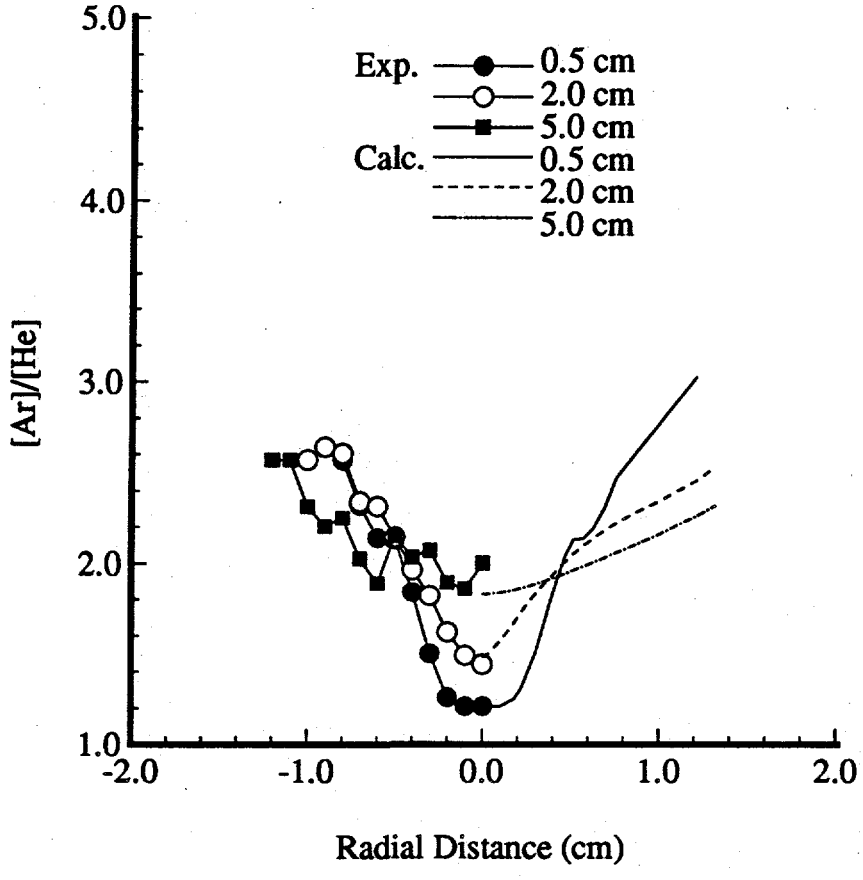

Figure 2. Calculated and Experimental Radial Profiles of Argon to Helium Cold Mole Fraction Ratio.

REFERENCES

1. J. D. Ramshaw and C. H. Chang, "Computational Fluid Dynamics Modeling of Multicomponent Thermal Plasmas," *Plasma Chem. Plasma Process.* **12**, 299 (1992).

2. C. H. Chang and J. D. Ramshaw, "Numerical Simulation of Nonequilibrium Effects in an Argon Plasma Jet," *Phys. Plasmas* **1**, 3698 (1994).

3. J. D. Ramshaw and C. H. Chang, "Ambipolar Diffusion in Multicomponent Plasmas," *Plasma Chem. Plasma Process.* **11**, 395 (1991).

4. J. D. Ramshaw, "Hydrodynamic Theory of Multicomponent Diffusion and Thermal Diffusion in Multitemperature Gas Mixtures," *J. Non-Equilib. Thermodyn.* **18**, 121 (1993).

5. J. D. Ramshaw and C. H. Chang, "Ambipolar Diffusion in Two-Temperature Multicomponent Plasmas," *Plasma Chem. Plasma Process.* **13**, 489 (1993).

6. S. Chapman and T. G. Cowling, *The Mathematical Theory of Non-Uniform Gases,* 3rd ed. Cambridge University Press, Cambridge, UK (1970).

7. C. Truesdell, "Mechanical Basis of Diffusion," *J. Chem. Phys.* **37**, 2336 (1962).

8. W. H. Furry, "On the Elementary Explanation of Diffusion Phenomena in Gases," *Am. J. Phys.* **16**, 63 (1948).

9. F. A. Williams, "Elementary Derivation of the Multicomponent Diffusion Equation," *Am. J. Phys.* **26**, 467 (1958).

10. J. O. Hirschfelder, C. F. Curtiss, and R. B. Bird, *Molecular Theory of Gases and Liquids,* Wiley, New York (1964).

11. J. D. Ramshaw, "Self-Consistent Effective Binary Diffusion in Multicomponent Gas Mixtures," *J. Non-Equilib. Thermodyn.* **15**, 295 (1990).

12. J. R. Fincke, C. H. Chang, W. D. Swank, and D. C. Haggard, "Entrainment and Demixing in Subsonic Thermal Plasma Jets: Comparison of Measurements and Predictions," *Int. J. Heat Mass Transfer* **37**, 1673 (1994).

13. Y. P. Chyou and E. Pfender, "Modeling of Plasma Jets with Superimposed Vortex Flow," *Plasma Chem. Plasma Process.* **9**, 291 (1989).

14. A. H. Dilawari, J. Szekely, and R. Westhoff, "A Comparison of Experimental Measurements and Theoretical Predictions Regarding the Behavior of a Turbulent Argon Plasma Jet Discharging into Air," *Plasma Chem. Plasma Process.* **10**, 501 (1990).

Final List of Participants

THIRTEENTH SYMPOSIUM ON ENERGY ENGINEERING SCIENCES

May 15-17, 1995

Argonne National Laboratory
Argonne, Illinois

Guenter Ahlers
University of California-Santa Barbara
Department of Physics
Santa Barbara, CA 93106

Chong H. Chang
Idaho National Engineering Laboratory
P.O. Box 1625, Mail Stop 3808
Idaho Falls, ID 83415

Paul I. Barton
Massachusetts Institute of Technology
Department of Chemical Engineering
Room 66-464
Cambridge, MA 02139

Ezechiel G. D. Cohen
The Rockefeller University
Physics Department
1230 York Avenue
New York, NY 10021-6399

Haim H. Bau
University of Pennsylvania
Department of Mechanical Engineering
Philadelphia, PA 19104-6315

Eiichi Fukushima
The Lovelace Institutes
2425 Ridgecrest Drive SE
Albuquerque, NM 87108

Frederick W. Brust, Jr.
Battelle
Engineering Mechanics Group
505 King Avenue
Columbus, OH 43201-2693

Robert Goulard
George Washington University
SEAS Department
801 22nd Street NW
Washington, DC 70052

Brent D. Butler
NIST
Chemical Sciences & Tech. Lab, Thermophysics Div.
325 Broadway
Boulder, CO 80303

Howard J. M. Hanley
NIST
Thermophysics Division
325 Broadway
Boulder, CO 80303

Shrikar Chakravarti
University of Wisconsin-Madison
Department of Chemical Engineering
1415 Johnson Drive
Madison, WI 53706-1691

Thomas J. Hanratty
University of Illinois
Department of Chemical Engineering
205 Roger Adams Laboratory
600 South Mathews
Urbana, IL 61801

Shawn G. Hausen
Northwestern University
Department of Chemical Engineering
2145 Sheridan Road
Evanston, IL 60208

Oscar Manley
U.S. Department of Energy
Division of Engineering and Geosciences
Office of Basic Energy Sciences, ER-15
Washington, DC 20585

Joachim V. R. Heberlein
University of Minnesota
Department of Mechanical Engineering
111 Church Street SE
Minneapolis, MN 55455

John B. McLaughlin
Clarkson University
Department of Chemical Engineering
Potsdam, NY 13699-5705

Frank P. Incropera
Purdue University
School of Mechanical Engineering
1288 Mechanical Engineering Building
West Lafayette, IN 47907

Eckart H. Meiburg
University of Southern California
Department of Aerospace Engineering
Los Angeles, CA 90089-1191

Daniel Kaftori
University of California-Santa Barbara
Dept. of Chemical & Nuclear Eng., Mechanical Eng.
Santa Barbara, CA 93106

Curtis R. Menyuk
University of Maryland-Baltimore County
Department of Electrical Engineering
TRC 201A
Baltimore, MD 21228-5398

Robert H. Kraichnan
369 Montezuma 108
Santa Fe, NM 87501

Issam Mudawar
Purdue University
Department of Mechanical Engineering
1288 Mechanical Engineering
West Lafayette, IN 47907

Allan J. Lichtenberg
University of California
Dept. of Electrical Engineering and Comp. Sci.
Cory Hall
Berkeley, CA 94720

Evgeny A. Novikov
University of California-San Diego
Institute for Nonlinear Science
La Jolla, CA 92093-0402

Julio M. Ottino
Northwestern University
Department of Chemical Engineering
2145 Sheridan Road
Evanston, IL 60208

George Schmidt
Stevens Institute of Technology
Department of Physics & Engineering Physics
Hoboken, NJ 07030

Thomas G. Owano
Stanford University
Department of Mechanical Engineering
Bldg. 520, Rm. 521Q
Stanford, CA 94305-3032

Daphne L. Stoner
Idaho National Engineering Laboratory
Department of Biotechnology
Lockheed Idaho Technologies Company
2351 North Boulevard, P.O. Box 1625
Idaho Falls, ID 83415

Walter Polansky
U.S. Department of Energy
Advanced Energy Projects Division, ER-33
19901 Germantown Road
Germantown, MD 20874-1290

Harry L. Swinney
University of Texas-Austin
Center for Nonlinear Dynamics
Austin, TX 78712

Gerald C. Pomraning
University of California-Los Angeles
Department of Mechanical, Aerospace, and Nuclear
405 Hilgard Avenue
Los Angeles, CA 90024-1597

Stephen L. Teitel
University of Rochester
Department of Physics and Astronomy
Rochester, NY 14627

W. Harmon Ray
University of Wisconsin
Department of Chemical Engineering
1415 Johnson Drive
Madison, WI 53706

Chang-Lin Tien
University of California-Berkeley
Office of the Chancellor
200 California Hall #1500
Berkeley, CA 94720-1500

John Ross
Stanford University
Department of Chemistry
Stanford, CA 94305

Salvatore Torquato
Princeton University
Department of Civil Engineering
Princeton Materials Institute
Princeton, NJ 08544

James M. Wallace
The University of Maryland
Department of Mechanical Engineering
College Park, MD 20742

Graham B. Wallis
Dartmouth College
Thayer School of Engineering
Hanover, NH 03755-8000

James R. Welty
U.S. Department of Energy
Division of Engineering and Geosciences
Office of Basic Energy Sciences, ER-15
Washington, DC 20585

Arthur W. Westerberg
Carnegie Mellon University
Department of Chemical Engineering
5000 Forbes Avenue
Pittsburgh, PA 15213